NASA Conference Publication 3011

Flight Mechanics/Estimation Theory Symposium 1988

(NASA-CP-3011) FLIGHT MECHANICS/ESTIMATION THEORY SYMPOSIUM 1988 (NASA) 611 p CSCL 22A
N89-15934
--THRU--
N89-15962
Unclas
H1/13 0184888

Proceedings of a symposium held at
Goddard Space Flight Center
Greenbelt, Maryland
May 10-11, 1988

NASA

1Front CP 3011

NASA Conference Publication 3011

Flight Mechanics/Estimation Theory Symposium 1988

Thomas Stengle, *Editor*
Goddard Space Flight Center
Greenbelt, Maryland

Proceedings of a symposium sponsored by
NASA Goddard Space Flight Center and held at
Goddard Space Flight Center
Greenbelt, Maryland
May 10-11, 1988

NASA
National Aeronautics
and Space Administration

Scientific and Technical
Information Division

1988

1Ban

FOREWORD

The papers presented here have been derived primarily from speakers' summaries of talks presented at the Flight Mechanics/Estimation Theory Symposium held May 10-11, 1988 at Goddard Space Flight Center. Papers included in this document are presented as received from the authors with little or no editing.

PRECEDING PAGE BLANK NOT FILMED

CONTENTS

FOREWORD

Page

SESSION 1

A General Model for Attitude Determination Error Analysis
F. Markley, E. Seidewitz (GSFC), M. Nicholson (CSC) 3

Accuracy Study of the Upper Atmosphere Research Satellite (UARS) Definitive Attitude Determination
F. Snow (GSFC), K. Krack, Y. Sheu, W. Bosl (CSC) 26

Maneuvering Strategies Using CMGs
H. Oh, S. Vadali (Texas A&M University) 42

Minimal Parameter Solution of the Orthogonal Matrix Differential Equation
I. Bar-Itzhack (Technion-Israel Institute of Technology).
F. Markley (GSFC) 62

The Optical Field Angle Distortion Calibration Feasibility Study for the Hubble Space Telescope Fine Guidance Sensors
K. Luchetti, G. Abshire, L. Hallock, R. McCutcheon (CSC) 89

Algorithm for In-flight Gyroscope Calibration
P. Davenport (GSFC), G. Welter (CSC) 114

SESSION 2

Optimal Post-experiment Estimation of Poorly Modeled Dynamic Systems
D. Mook (State University of New York) 131

Computation of Orbits Using Total Energy
V. Bond, D. Mulcihy (McDonnell Douglas Astronautics Co.) 153

A Multi-satellite Orbit Determination Problem in a Parallel Processing Environnment
M. Deakyne, R. Anderle (GE) 166

The Landsat/Global Positioning System Project
T. Wood 186

Relative Motion Using Analytical Differential Gravity
R. Gottlieb (McDonnell Douglas Astronautics Co.) 209

Preliminary Orbit Determination System (PODS) for Tracking and Data Relay Satellite System (TDRSS)–Tracked Target Spacecraft Using the Homotopy Continuation Method
S. Kirschner, M. Samii (CSC), S. Broaddus, C. Doll (GSFC) 217

PRECEDING PAGE BLANK NOT FILMED

Trajectory Computation During a Maneuver: Thrust Estimation with the Goddard Trajectory Determination System (GTDS)
A. Beri, M. Samii (CSC), C. Doll (GSFC) 238

SESSION 3

A Gamma Ray Observatory Ground Attitude Error Error Analysis Study Using the Generalized Calibration System
E. Ketchum (GSFC) 267

An Analysis of the Kalman Filter in the Gamma Ray Observatory (GRO) On-board Attitude Determination Subsystem
F. Snow, R. Harman, J. Garrick (GSFC) 289

In-flight Determination of Spacecraft Magnetic Bias Independent of Attitude
P. Davenport (GSFC), W. Rumpl, G. Welter (CSC) 326

Three Axis Attitude Determination via Kalman Filtering of Magnetometer Data
F. Martel, P. Pal (Ithaco), M.Psiaki (Cornell) 344

Attitude Analysis of the Earth Radiation Budget Satellite (ERBS) Yaw Turn Anomaly
J. Kronenwetter, M. Phenneger (CSC), W. Weaver (LaRC) 368

Evaluation of ERBE Scanner Pointing Accuracy Based Upon a Coastline Detection Algorithm
W. Weaver, L. Hoffman, J. Kibler (LaRC) 391

Attitude Motion of a Non-attitude-controlled Cylindrical Satellite
C. Wilkinson (Textron) 412

GOES Dynamic Propagation of Attitude
F. Markley, E. Seidewitz (GSFC), D. Chu, J. Rowe (CSC) 430

SESSION 4

Controlled Reentry of the Gamma Ray Observatory (GRO)
E. Brown (GSFC) 459

EUVE/XTE Orbit Decay Study
K. Richon (GSFC), J. Hashmall, M. Lambertson, T. Phillips (CSC) 486

Remote Chance of Recontact?
S. Abeyagunawardene, D. Elkin (CSC), R. DeFazio (GSFC) 507

Comparison of Circular Orbit and Fourier Power Series Ephemeris Representations for Backup Use by the Upper Atmosphere Research Satellite On-board Computer
J. Kast (CSC) 530

GOES Next Navigation Operations
J. Fiorello, I. Oh (CSC), R. Ranne (NOAA) 553

Correlations Between Solar Activity and Operationally Determined Satellite Drag Variation Parameters
E. Smith (CSC) 571

Evaluation of Advanced Geopotential Models for Operational Orbit Determination
M. Radomski, B. Davis, M. Samii (CSC), C. Engel, C. Doll (GSFC) 595

FLIGHT MECHANICS/ESTIMATION THEORY SYMPOSIUM

SESSION 1

N89-15935

A GENERAL MODEL FOR ATTITUDE DETERMINATION ERROR ANALYSIS

F. Landis Markley
Ed Seidewitz
Code 554 / Flight Dynamics Analysis Branch
Goddard Space Flight Center
Greenbelt MD 20771

Mark Nicholson
Computer Sciences Corporation
Lanham / Seabrook MD

ABSTRACT

This paper gives an overview of a comprehensive approach to filter and dynamics modeling for attitude determination error analysis. The models presented include both batch least-squares and sequential attitude estimation processes for both spin-stabilized and three-axis stabilized spacecraft. The discussion includes a brief description of a dynamics model of strapdown gyros, but it does not cover other sensor models. Model parameters can be chosen to be *solve-for parameters*, which are assumed to be estimated as part of the determination process, or *consider parameters*, which are assumed to have errors but not to be estimated. The only restriction on this choice is that the time evolution of the consider parameters must not depend on any of the solve-for parameters. The result of an error analysis is an indication of the contributions of the various error sources to the uncertainties in the determination of the spacecraft solve-for parameters. The model presented in this paper gives the uncertainty due to errors in the *a priori* estimates of the solve-for parameters, the uncertainty due to *measurement noise*, the uncertainty due to *dynamic noise* (also known as *process noise* or *plant noise*), the uncertainty due to the consider parameters, and the overall uncertainty due to all these sources of error.

PRECEDING PAGE BLANK NOT FILMED

1. INTRODUCTION

Spacecraft attitude determination involves estimating the orientation of a spacecraft relative to inertial space, based on measurements from onboard sensors. Attitude determination error analysis is the computation of the attitude determination accuracy obtainable with sensor data of prescribed error characteristics, without processing real or simulated sensor data. This analysis takes into account the presence of certain errors in modeling the sensors and the attitude motion of the spacecraft [Wertz].

This paper gives an overview of a comprehensive approach to filter and dynamics modeling for attitude determination error analysis. The models presented include both batch least-squares and sequential attitude estimation processes for both spin-stabilized and three-axis stabilized spacecraft. Model parameters can be chosen to be *solve-for parameters*, which are assumed to be estimated as part of the determination process, or *consider parameters*, which are assumed to have errors but not to be estimated. The only restriction on this choice is that the time evolution of the consider parameters must not depend on any of the solve-for parameters. Great freedom is also allowed in specifying sensor types and measurement scheduling.

The result of an error analysis is an indication of the contributions of the various error sources to the uncertainties in the determination of the spacecraft solve-for parameters. The model presented in this paper gives the uncertainty due to errors in the *a priori* estimates of the solve-for parameters, the uncertainty due to *measurement noise*, the uncertainty due to *dynamic noise* (also known as *process noise* or *plant noise*), the uncertainty due to the consider parameters, and the overall uncertainty due to all these sources of error. This approach was developed as part of the mathematical specification of algorithms for the computer-based Attitude Determination Error Analysis System (ADEAS) [Nicholson].

2. DYNAMICS MODEL

The *state vector* $\boldsymbol{x}$ is an N-dimensional vector of parameters that completely characterizes the system. For spacecraft attitude determination, the state vector includes spacecraft attitude parameters and sensor calibration parameters. The state vector is assumed to evolve in time according to the dynamics model

$$\dot{\boldsymbol{x}}(t) = \boldsymbol{f}(\boldsymbol{x}(t), t) + \boldsymbol{u}(t) \qquad (2\text{-}1)$$

where the dynamic noise $\boldsymbol{u}(t)$ is a Gaussian white noise process with mean and covariance given by

$$E[\boldsymbol{u}(t)] = 0 \qquad \text{and} \qquad E[\boldsymbol{u}(t)\boldsymbol{u}^T(t')] = Q\,\delta(t - t') \qquad (2\text{-}2)$$

with $E[\ldots]$ denoting the expectation value. In this equation Q is the NxN *dynamic noise spectral density matrix* and $\delta(t - t')$ denotes the Dirac delta, or unit impulse, function. The state vector includes all the parameters needed to compute $\boldsymbol{x}$, even though some of these parameters may have zero derivative.

The true value of the state vector is never exactly known, but can only be estimated. The *state estimate vector* $\boldsymbol{x}^*(t)$ evolves in time according to

$$\dot{\boldsymbol{x}}^*(t) = \boldsymbol{f}(\boldsymbol{x}^*(t), t) \qquad (2\text{-}3)$$

The *state error vector*, given by

$$\Delta x(t) = x(t) - x^*(t) \qquad (2\text{-}4)$$

is assumed to always remain small, so linear error analysis techniques can be used. Then, to first order,

$$\Delta\dot{\mathbf{x}}(t) = \dot{\mathbf{x}}(t) - \dot{\mathbf{x}}^*(t) = f(\mathbf{x}(t), t) - f(\mathbf{x}^*(t), t) + \mathbf{u}(t) \approx (\partial f/\partial\mathbf{x})(t)\,\Delta\mathbf{x}(t) + \mathbf{u}(t). \tag{2-5}$$

Integrating this formally gives

$$\Delta\mathbf{x}(t) = \Phi(t, t')\,\Delta\mathbf{x}(t') + \psi(t, t') \tag{2-6}$$

where the *state transition matrix* $\Phi(t, t')$ is the solution of the differential equation

$$\dot{\Phi}(t, t') = (\partial f/\partial\mathbf{x})(t)\,\Phi(t, t') \tag{2-7a}$$

with the initial condition

$$\Phi(t', t') = I_N = \text{the NxN identity matrix} \tag{2-7b}$$

and the *random excitation vector* $\psi(t, t')$ is given by the integral

$$\psi(t, t') = \int_{t'}^{t} \Phi(t, t'')\,\mathbf{u}(t'')\,dt''. \tag{2-8}$$

It follows from equations (2-7) and (2-8) that the transition matrix obeys the *group property*

$$\Phi(t, t') = \Phi(t, t'')\,\Phi(t'', t') \tag{2-9}$$

and that the random excitation vector obeys the relation

$$\psi(t, t') = \Phi(t, t'')\,\psi(t'', t') + \psi(t, t''). \tag{2-10}$$

Equations (2-2) and (2-8) give the relationship

$$E[\psi(t, t'')\psi^T(t'', t')] = 0 \qquad \text{for } t \geq t'' \geq t'. \tag{2-11}$$

The estimation computations require the *random excitation covariance matrix*

$$D(t, t') \equiv E[\psi(t, t')\psi^T(t, t')] = \int_{t'}^{t} \Phi(t, t'')\,Q\,\Phi^T(t, t'')\,dt'', \tag{2-12}$$

which equations (2-10) and (2-11) show to obey the relation

$$D(t, t') = \Phi(t, t'')\,D(t'', t')\,\Phi^T(t, t'') + D(t, t''). \tag{2-13}$$

2.1 Spin-Stabilized Spacecraft Dynamics Model

For spin-stabilized spacecraft, the attitude matrix $A_{BI}(t)$ which transforms vectors from an inertial frame I to the spacecraft body frame B is given as the product

$$A_{BI}(t) = A_{BL}(t)\,A_{LI}(t) \tag{2-14}$$

where the subscript L denotes an intermediate frame in which the total spacecraft angular momentum vector $\mathbf{L}$ is oriented along the positive z-axis. The matrix $A_{LI}(t)$ is given in terms of the right ascension

$\alpha(t)$ and declination $\delta(t)$ of the angular momentum vector as

$$A_{LI}(t) = A_2(\pi/2 - \delta)\, A_3(\alpha) \tag{2–15}$$

where $A_i(\theta)$ denotes a rotation by angle θ about axis i. The matrix $A_{BL}(t)$ is parameterized by a 3-1-3 Euler axis sequence as

$$A_{BL}(t) = A_3(\psi)\, A_1(\theta)\, A_3(\phi)\,. \tag{2–16}$$

For torque-free motion of an axially-symmetric rigid body $\alpha(t)$, $\delta(t)$, and $\theta(t)$ are constant, and

$$\dot{\phi}(t) = \omega_I(t) \tag{2-17a}$$
$$\dot{\psi}(t) = \omega_p(t), \tag{2-17b}$$

where $\omega_I(t)$ and $\omega_p(t)$ are the *inertial nutation rate* and *body nutation rate*, respectively [Wertz].

The state vector $x(t)$ for the spin-stabilized case is

$$x(t) = [\alpha(t), \delta(t), \phi(t), \theta(t), \psi(t), \omega_I(t), \omega_p(t), x_m^T(t)]^T, \tag{2–18}$$

where x_m is a μ-dimensional vector of measurement parameters depending on the sensor complement of the spacecraft being modeled. We assume that the measurement parameters are constant and that any deviations of the dynamics from torque-free motion of an axially symmetric rigid body can be approximated by independent white noise processes $u_\alpha(t)$, $u_\delta(t)$, $u_\phi(t)$, $u_\theta(t)$, $u_\psi(t)$, $u_I(t)$, and $u_p(t)$. The equations of motion for spin-stabilized spacecraft give the dynamics model

$$\dot{x}(t) = \begin{bmatrix} 0 & 0 & 0 & 0 & 0 & 0 & 0 & \mathbf{0}_\mu^T \\ 0 & 0 & 0 & 0 & 0 & 0 & 0 & \mathbf{0}_\mu^T \\ 0 & 0 & 0 & 0 & 0 & 1 & 0 & \mathbf{0}_\mu^T \\ 0 & 0 & 0 & 0 & 0 & 0 & 0 & \mathbf{0}_\mu^T \\ 0 & 0 & 0 & 0 & 0 & 0 & 1 & \mathbf{0}_\mu^T \\ 0 & 0 & 0 & 0 & 0 & 0 & 0 & \mathbf{0}_\mu^T \\ 0 & 0 & 0 & 0 & 0 & 0 & 0 & \mathbf{0}_\mu^T \\ \mathbf{0}_\mu & \mathbf{0}_\mu & \mathbf{0}_\mu & \mathbf{0}_\mu & \mathbf{0}_\mu & \mathbf{0}_\mu & \mathbf{0}_\mu & 0_{\mu x \mu} \end{bmatrix} x(t) + \begin{bmatrix} u_\alpha(t) \\ u_\delta(t) \\ u_\phi(t) \\ u_\theta(t) \\ u_\psi(t) \\ u_I(t) \\ u_p(t) \\ \mathbf{0}_\mu \end{bmatrix} \tag{2-19}$$

where $\mathbf{0}_\mu$ is a μ-dimensional vector of zeros and $0_{\mu x \mu}$ is a $\mu x \mu$ matrix of zeros. Since the dynamics model for spin-stabilized spacecraft is linear in the state vector, the state error vector $\Delta x(t)$ obeys an equation of the same form as equation (2-19). Thus the state transition matrix, as defined by equation (2-7), is

$$\Phi(t, t') = \begin{bmatrix} 1 & 0 & 0 & 0 & 0 & 0 & 0 & \mathbf{0}_\mu^T \\ 0 & 1 & 0 & 0 & 0 & 0 & 0 & \mathbf{0}_\mu^T \\ 0 & 0 & 1 & 0 & 0 & \Delta t & 0 & \mathbf{0}_\mu^T \\ 0 & 0 & 0 & 1 & 0 & 0 & 0 & \mathbf{0}_\mu^T \\ 0 & 0 & 0 & 0 & 1 & 0 & \Delta t & \mathbf{0}_\mu^T \\ 0 & 0 & 0 & 0 & 0 & 1 & 0 & \mathbf{0}_\mu^T \\ 0 & 0 & 0 & 0 & 0 & 0 & 1 & \mathbf{0}_\mu^T \\ \mathbf{0}_\mu & \mathbf{0}_\mu & \mathbf{0}_\mu & \mathbf{0}_\mu & \mathbf{0}_\mu & \mathbf{0}_\mu & \mathbf{0}_\mu & I_\mu \end{bmatrix} \tag{2-20}$$

where

$$\Delta t \equiv t - t' . \tag{2-21}$$

The inverse of the state transition matrix is

$$\Phi^{-1}(t, t') = \begin{bmatrix} 1 & 0 & 0 & 0 & 0 & 0 & 0 & \mathbf{0}_\mu^T \\ 0 & 1 & 0 & 0 & 0 & 0 & 0 & \mathbf{0}_\mu^T \\ 0 & 0 & 1 & 0 & 0 & -\Delta t & 0 & \mathbf{0}_\mu^T \\ 0 & 0 & 0 & 1 & 0 & 0 & 0 & \mathbf{0}_\mu^T \\ 0 & 0 & 0 & 0 & 1 & 0 & -\Delta t & \mathbf{0}_\mu^T \\ 0 & 0 & 0 & 0 & 0 & 1 & 0 & \mathbf{0}_\mu^T \\ 0 & 0 & 0 & 0 & 0 & 0 & 1 & \mathbf{0}_\mu^T \\ \mathbf{0}_\mu & \mathbf{0}_\mu & \mathbf{0}_\mu & \mathbf{0}_\mu & \mathbf{0}_\mu & \mathbf{0}_\mu & \mathbf{0}_\mu & I_\mu \end{bmatrix} \tag{2-22}$$

and the random excitation covariance matrix is

$$D(t, t') = \begin{bmatrix} Q_\alpha & 0 & 0 & 0 & 0 & 0 & 0 & \mathbf{0}_\mu^T \\ 0 & Q_\delta & 0 & 0 & 0 & 0 & 0 & \mathbf{0}_\mu^T \\ 0 & 0 & Q_\phi + (1/3)Q_\zeta(\Delta t)^2 & 0 & 0 & (1/2)Q_\zeta\Delta t & 0 & \mathbf{0}_\mu^T \\ 0 & 0 & 0 & Q_\theta & 0 & 0 & 0 & \mathbf{0}_\mu^T \\ 0 & 0 & 0 & 0 & Q_\psi + (1/3)Q_\rho(\Delta t)^2 & 0 & (1/2)Q_\rho\Delta t & \mathbf{0}_\mu^T \\ 0 & 0 & (1/2)Q_\zeta\Delta t & 0 & 0 & Q_\zeta & 0 & \mathbf{0}_\mu^T \\ 0 & 0 & 0 & 0 & (1/2)Q_\rho\Delta t & 0 & Q_\rho & \mathbf{0}_\mu^T \\ \mathbf{0}_\mu & \mathbf{0}_\mu & \mathbf{0}_\mu & \mathbf{0}_\mu & \mathbf{0}_\mu & \mathbf{0}_\mu & \mathbf{0}_\mu & 0_{\mu\times\mu} \end{bmatrix} \Delta t , \tag{2-23}$$

where Q_α is defined by

$$E[u_\alpha(t) u_\alpha(t')] = Q_\alpha \delta(t - t') \tag{2-24}$$

with similar relations for Q_δ, Q_ϕ, Q_θ, Q_ψ, Q_ζ, and Q_p.

2.2 Three-Axis Stabilized Spacecraft Dynamics Model

For three-axis stabilized spacecraft, the attitude matrix $A_{BI}(t)$ is given as the product

$$A_{BI}(t) = A_{BR}(t) A_{RI}(t) \tag{2-25}$$

where the subscript R denotes a reference frame, which can be, for example, Earth-pointing, Sun-pointing, or inertial. The inertial-to-reference matrix $A_{RI}(t)$ for any reference system is computed from the reference vectors defining that system. The nominal spacecraft attitude with respect to the reference frame evolves over time according to

$$\dot{A}_{BR}(t) = - \tilde{\omega}_{BR}(t) A_{BR}(t) , \tag{2-26}$$

where $\tilde{\omega}_{BR}(t)$ is the $3x3$ antisymmetric matrix

$$\tilde{\omega}_{BR}(t) \equiv \begin{bmatrix} 0 & -[\omega_{BR}(t)]_z & [\omega_{BR}(t)]_y \\ [\omega_{BR}(t)]_z & 0 & -[\omega_{BR}(t)]_x \\ -[\omega_{BR}(t)]_y & [\omega_{BR}(t)]_x & 0 \end{bmatrix} \tag{2-27}$$

defined from the column vector $\omega_{BR}(t)$ containing the components in the body frame of the spacecraft angular velocity relative to the reference frame. The nominal attitude profile is used for determining measurement geometry, sensor line-of-sight occultation, and related effects.

The attitude error is defined in terms of a three-component *attitude error vector* $\Delta\theta(t)$, whose components are the small rotations about each of the spacecraft body axes that would align the true body axes with the estimates of these axes. In terms of the true attitude $A_{BR}(t)$ relative to the reference frame and the estimate $A_{BR}^*(t)$ of this attitude,

$$A_{BR}^*(t) \approx [I_3 + \Delta\tilde{\theta}(t)] A_{BR}(t), \tag{2-28}$$

where I_3 is the 3x3 identity matrix and the antisymmetric matrix $\Delta\tilde{\theta}(t)$ is defined similarly to equation (2-27).

The true attitude relative to inertial space evolves according to

$$\dot{A}_{BI}(t) = - \tilde{\omega}_{BI}(t) A_{BI}(t) , \tag{2-29}$$

where $\omega_{BI}(t)$ is the column vector of components in the body frame of the spacecraft angular velocity

2 from CF 3011

relative to inertial space. Similarly, the estimated attitude relative to inertial space evolves according to

$$\dot{A}_{BI}^*(t) = -\tilde{\omega}_{BI}^*(t)\, A_{BI}^*(t)\,, \tag{2-30}$$

where $\omega_{BI}^*(t)$ is the column vector of estimates of $\omega_{BI}(t)$. These equations form the basis of the attitude error propagation, since this is assumed to be based on information obtained from gyros, which provide the estimates $\omega_{BI}^*(t)$ of the angular rates relative to inertial space. The attitude estimate relative to inertial space is related to the estimate relative to the reference frame by the analog of equation (2-25):

$$A_{BI}^*(t) = A_{BR}^*(t)\, A_{RI}(t). \tag{2-31}$$

Then from equations (2-25) - (2-31) we have

$$\begin{aligned} d(\Delta\tilde{\theta})/dt = d(A_{BR}^*\, A_{BR}^T)/dt = d(A_{BI}^*\, A_{BI}^T)/dt &= \dot{A}_{BI}^*(t)\, A_{BI}^T(t) + A_{BI}^*(t)\, \dot{A}_{BI}^T(t) \\ &= -\tilde{\omega}_{BI}^*(t)\, A_{BI}^*(t)\, A_{BI}^T(t) + A_{BI}^*(t)\, A_{BI}^T(t)\, \tilde{\omega}_{BI}(t) \\ &= -\tilde{\omega}_{BI}^*(t)\, [I_3 + \Delta\tilde{\theta}(t)] + [I_3 + \Delta\tilde{\theta}(t)]\, \tilde{\omega}_{BI}(t). \end{aligned} \tag{2-32}$$

We now define the angular velocity measurement error vector by

$$\Delta\omega_{BI}(t) \equiv \omega_{BI}^*(t) - \omega_{BI}(t) \tag{2-33}$$

and assume that its components are small. Then, to first order in $\Delta\omega_{BI}$ and $\Delta\theta$

$$d(\Delta\tilde{\theta})/dt = -\tilde{\omega}_{BI}(t)\, \Delta\tilde{\theta}(t) + \Delta\tilde{\theta}(t)\, \tilde{\omega}_{BI}(t) - \Delta\tilde{\omega}_{BI}(t), \tag{2-34}$$

which is, in vector form

$$\Delta\dot{\theta}(t) = -\tilde{\omega}_{BI}(t)\, \Delta\theta(t) - \Delta\omega_{BI}(t)\,. \tag{2-35}$$

The angular velocity measurement errors arise from gyro errors, and a general model for these errors gives [Nicholson]

$$\Delta\omega_{BI}(t) = \Delta b(t) + \Omega(t)\, \Delta k - \tilde{\omega}_{BI}(t)\, \Delta\varepsilon - u_\theta(t) \tag{2-36}$$

where $\Delta b(t)$ is a vector of first-order Markov processes representing the *gyro drift rate biases*, Δk is a vector of constant *gyro scale factor errors*, $\Delta\varepsilon$ is a vector of constant *gyro misalignment errors*, $u_\theta(t)$ is a vector of white-noise processes representing the *gyro drift rate noise*, and

$$\Omega(t) \equiv \mathrm{diag}\, [\omega_{BI}^T(t)\,], \tag{2-37}$$

which means that $\Omega(t)$ is the diagonal matrix with the components of $\omega_{BI}(t)$ as the diagonal elements. The drift rate bias vector is assumed to evolve according to

$$\Delta\dot{b}(t) = -\Delta b(t)/\tau + u_b(t), \tag{2–38}$$

where τ is the correlation time of the Markov processes and $\mathbf{u}_b(t)$ is a vector of white-noise processes representing the *gyro drift rate ramp noise*. The white noise processes $\mathbf{u}_\theta(t)$ and $\mathbf{u}_b(t)$ have means and covariances given by

$$E[\mathbf{u}_\theta(t)] = 0\,, \qquad E[\mathbf{u}_\theta(t)\mathbf{u}_\theta^T(t')] = Q_\theta\, \delta(t - t') \tag{2-39a}$$

$$E[\mathbf{u}_b(t)] = 0\,, \qquad E[\mathbf{u}_b(t)\mathbf{u}_b^T(t')] = Q_b\, \delta(t - t') \tag{2-39b}$$

$$\text{and} \qquad E[\mathbf{u}_\theta(t)\mathbf{u}_b^T(t')] = 0, \tag{2-39c}$$

where Q_θ and Q_b are 3x3 symmetric, non-negative-definite matrices that are assumed to be constant. This gyro error model is a generalization of the model in [Lefferts] to include scale factor and misalignment errors.

The state error vector for the three-axis stabilized case is

$$\Delta\mathbf{x}(t) = [\Delta\boldsymbol{\theta}^T(t),\, \Delta\mathbf{b}^T(t),\, \Delta\mathbf{k}^T,\, \Delta\boldsymbol{\varepsilon}^T,\, \Delta\mathbf{x}_m{}^T(t)]^T \tag{2-40}$$

where $\Delta\mathbf{x}_m$ is the error in a μ-dimensional vector of measurement parameters depending on the sensor complement of the spacecraft being modeled, as in the spin-stabilized case. The time evolution of this vector is given, using the above models, by

$$\Delta\dot{\mathbf{x}}(t) = \begin{bmatrix} -\tilde{\omega}_{BI}(t) & -I_3 & -\Omega(t) & \tilde{\omega}_{BI}(t) & 0_{3x\mu} \\ 0_{3x3} & -I_3/\tau & 0_{3x3} & 0_{3x3} & 0_{3x\mu} \\ 0_{3x3} & 0_{3x3} & 0_{3x3} & 0_{3x3} & 0_{3x\mu} \\ 0_{3x3} & 0_{3x3} & 0_{3x3} & 0_{3x3} & 0_{3x\mu} \\ 0_{\mu x3} & 0_{\mu x3} & 0_{\mu x3} & 0_{\mu x3} & 0_{\mu x\mu} \end{bmatrix} \Delta\mathbf{x}(t) + \begin{bmatrix} \mathbf{u}_\theta(t) \\ \mathbf{u}_b(t) \\ \mathbf{0}_3 \\ \mathbf{0}_3 \\ \mathbf{0}_\mu \end{bmatrix} \tag{2-41}$$

where $\mathbf{0}_3$ is a 3-dimensional vector of zeros and 0_{jxk} is a jxk matrix of zeros. The state transition matrix, as defined by equation (2-7) is then

$$\Phi(t, t') = \begin{bmatrix} \Phi_{\theta\theta}(t, t') & \Phi_{\theta b}(t, t') & \Phi_{\theta k}(t, t') & I_3 - \Phi_{\theta\theta}(t, t') & 0_{3x\mu} \\ 0_{3x3} & \Phi_{bb}(t, t') & 0_{3x3} & 0_{3x3} & 0_{3x\mu} \\ 0_{3x3} & 0_{3x3} & I_3 & 0_{3x3} & 0_{3x\mu} \\ 0_{3x3} & 0_{3x3} & 0_{3x3} & I_3 & 0_{3x\mu} \\ 0_{\mu x3} & 0_{\mu x3} & 0_{\mu x3} & 0_{\mu x3} & I_\mu \end{bmatrix} \tag{2-42}$$

where

$$\Phi_{\theta b}(t, t') = -\int_{t'}^{t} \Phi_{\theta\theta}(t, t'') \exp[-(t'' - t')/\tau]\, dt'' \tag{2-43a}$$

$$\Phi_{\theta k}(t, t') = -\int_{t'}^{t} \Phi_{\theta\theta}(t, t'')\, \Omega(t'')\, dt'' \tag{2-43b}$$

$$\Phi_{bb}(t, t') = I_3 \exp[-(t - t')/\tau]\,. \tag{2-43c}$$

The *attitude error propagation matrix* $\Phi_{\theta\theta}(t, t')$ is given by the differential equation

$$\dot{\Phi}_{\theta\theta}(t, t') = -\tilde{\omega}_{BI}(t)\, \Phi_{\theta\theta}(t, t') \tag{2-44a}$$

with the initial condition

$$\Phi_{\theta\theta}(t', t') = I_3\,. \tag{2-44b}$$

The form of equation (2-44a) is identical to that of equation (2-29) for the attitude matrix $A_{BI}(t)$. Thus $\Phi_{\theta\theta}(t, t')$ must also act as a transition matrix for the attitude:

$$A_{BI}(t) = \Phi_{\theta\theta}(t, t')\, A_{BI}(t'), \tag{2-45}$$

or

$$\Phi_{\theta\theta}(t, t') = A_{BI}(t)\, A_{BI}^{T}(t'). \tag{2-46}$$

Equations (2-43) reduce to quadrature after substitution of equation (2-46), where $A_{BI}(t)$ is given in terms of the nominal attitude profile by equation (2-25). The matrix $\Omega(t)$, which is needed to evaluate equation (2-43b), is also given in terms of the nominal profile by the following argument. The integral is broken up into time steps of length Δt, chosen to keep integration errors below a specified tolerance [Nicholson]. The contribution of the interval between t and $t + \Delta t$ requires the matrix $\Omega\, \Delta t$, where Ω denotes the average value of $\Omega(t)$ over the time interval. This matrix has the same elements, rearranged by row and column, as the matrix $\tilde{\omega}_{BI}\, \Delta t$, where ω_{BI} denotes the time average of $\omega_{BI}(t)$ over the interval. This is given in terms of the result of integrating equation (2-29) over the interval, and ignoring terms of higher than first order in Δt;

$$A_{BI}(t + \Delta t) \approx [\, I_3 - \tilde{\omega}_{BI}\, \Delta t\,]\, A_{BI}(t), \tag{2-47}$$

or

$$\tilde{\omega}_{BI}\, \Delta t = (1/2)[A_{BI}(t)\, A_{BI}^{T}(t + \Delta t) - A_{BI}(t + \Delta t)\, A_{BI}^{T}(t)]. \tag{2-48}$$

Since the submatrix $\Phi_{\theta\theta}(t, t')$ is seen from equation (2-46) to be orthogonal, the inverse of the state transition matrix is given by

$$\Phi^{-1}(t, t') = \begin{bmatrix} \Phi_{\theta\theta}^T & -\Phi_{\theta\theta}^T\Phi_{\theta b}\Phi_{bb}^{-1} & -\Phi_{\theta\theta}^T\Phi_{\theta k} & I_3 - \Phi_{\theta\theta}^T & 0_{3x\mu} \\ 0_{3x3} & \Phi_{bb}^{-1} & 0_{3x3} & 0_{3x3} & 0_{3x\mu} \\ 0_{3x3} & 0_{3x3} & I_3 & 0_{3x3} & 0_{3x\mu} \\ 0_{3x3} & 0_{3x3} & 0_{3x3} & I_3 & 0_{3x\mu} \\ 0_{\mu x3} & 0_{\mu x3} & 0_{\mu x3} & 0_{\mu x3} & I_\mu \end{bmatrix} \tag{2-49}$$

where the time arguments of the submatrices, which have been omitted for compactness, are the same as the arguments of the full matrix, and

$$\Phi_{bb}^{-1}(t, t') = I_3 \exp[(t - t')/\tau]. \tag{2–50}$$

The random excitation covariance matrix is

$$D(t, t') = \begin{bmatrix} D_{\theta\theta}(t, t') & D_{\theta b}(t, t') & 0_{3x3} & 0_{3x3} & 0_{3x\mu} \\ D_{\theta b}^T(t, t') & D_{bb}(t, t') & 0_{3x3} & 0_{3x3} & 0_{3x\mu} \\ 0_{3x3} & 0_{3x3} & 0_{3x3} & 0_{3x3} & 0_{3x\mu} \\ 0_{3x3} & 0_{3x3} & 0_{3x3} & 0_{3x3} & 0_{3x\mu} \\ 0_{\mu x3} & 0_{\mu x3} & 0_{\mu x3} & 0_{\mu x3} & 0_{\mu x\mu} \end{bmatrix} \tag{2-51}$$

where

$$D_{\theta\theta}(t, t') = \int_{t'}^{t} [\Phi_{\theta\theta}(t, t'')\, Q_\theta\, \Phi_{\theta\theta}^T(t, t'') + \Phi_{\theta b}(t, t'')\, Q_b\, \Phi_{\theta b}^T(t, t'')]\, dt'' \tag{2-52a}$$

$$D_{\theta b}(t, t') = \int_{t'}^{t} \Phi_{\theta b}(t, t'')\, Q_b\, \Phi_{bb}(t, t'')\, dt'' \tag{2-52b}$$

$$D_{bb}(t, t') = \int_{t'}^{t} \Phi_{bb}(t, t'')\, Q_b\, \Phi_{bb}(t, t'')\, dt''. \tag{2-52c}$$

with Q_θ and Q_b given by equations (2-39).

3. ESTIMATION AND COVARIANCE ANALYSIS

A filter produces state estimates based on information obtained from measurements made at discrete times. Let $\boldsymbol{y}_i$ be an n_i-dimensional vector of measurement values obtained at time t_i. Measurements are related to the state vector by the following measurement model:

$$\boldsymbol{y}_i = \boldsymbol{g}_i(\boldsymbol{x}(t_i)) + v_i \tag{3-1}$$

where v_i is a Gaussian white noise process with mean and covariance given by

$$E[v_i] = \boldsymbol{0} \tag{3-2a}$$

$$E[v_i v_i^T] = R_i \tag{3-2b}$$

$$E[v_i v_j^T] = 0 \quad \text{for } i \neq j. \tag{3-2c}$$

The functions $\boldsymbol{g}_i$ are assumed to be known functions of imprecisely known arguments. Therefore, it is possible to compute predicted measurement values by

$$\boldsymbol{y}_i^* = \boldsymbol{g}_i(\boldsymbol{x}^*(t_i)) \tag{3-3}$$

The measurement residual between the actual and computed measurements is then

$$\Delta \boldsymbol{y}_i = \boldsymbol{y}_i - \boldsymbol{y}_i^* = \boldsymbol{g}_i(\boldsymbol{x}(t_i)) - \boldsymbol{g}_i(\boldsymbol{x}^*(t_i)) + v_i \approx G_i\, \Delta \boldsymbol{x}(t_i) + v_i \tag{3-4}$$

where $$G_i \equiv \partial \boldsymbol{g}_i / \partial \boldsymbol{x}(t_i) \tag{3-5}$$

and $\Delta \boldsymbol{x}$ is assumed to be small.

It is usually not necessary to estimate all of the state parameters. Therefore, a filter may produce estimates for a set of *solve-for parameters* which are a subset of the state parameters. The filter does not account for the remaining state parameters, which are called *consider parameters* since they contain uncertainties that are considered in the error analysis. The state error vector is thus partitioned as follows:

$$\Delta \boldsymbol{x}(t) = \begin{bmatrix} \Delta \boldsymbol{s}(t) \\ \Delta \boldsymbol{c}(t) \end{bmatrix} \tag{3-6}$$

where $\Delta \boldsymbol{s}(t) \equiv$ solve-for parameter error vector
$\Delta \boldsymbol{c}(t) \equiv$ consider parameter error vector.

The random excitation vector, the state transition matrix and the random excitation covariance matrix have similar partitionings:

$$\psi(t, t') = \begin{bmatrix} \psi_S(t, t') \\ \psi_C(t, t') \end{bmatrix} \tag{3-7a}$$

$$\Phi(t, t') = \begin{bmatrix} \Phi_{ss}(t, t') & \Phi_{sc}(t, t') \\ 0 & \Phi_{cc}(t, t') \end{bmatrix} \tag{3-7b}$$

and

$$D(t, t') = \begin{bmatrix} D_{ss}(t, t') & D_{sc}(t, t') \\ D_{sc}^T(t, t') & D_{cc}(t, t') \end{bmatrix} . \tag{3-7c}$$

The error propagation equation (2-6) can then be rewritten as

$$\Delta s(t) = \Phi_{ss}(t, t')\Delta s(t') + \Phi_{sc}(t, t')\Delta c(t') + \psi_s(t, t') \tag{3-8}$$

$$\Delta c(t) = \Phi_{cc}(t, t')\Delta c(t') + \psi_c(t, t') . \tag{3-9}$$

The partitioning used in equations (3-6) to (3-9) is not the same as the partitioning of the state vector used in section 2. The two partitionings are related by row and column interchanges, depending on the selection of solve-for and consider parameters. The zero in the state transition matrix in equation (3-7b) reflects an assumption that the time evolution of the consider parameters does not depend on any of the solve-for parameters. This restriction assures that solve-for parameter errors do not induce additional consider parameter errors during propagation. In the case of the three-axis stabilized case discussed in section 2.2 this means that it is impossible to solve for any gyro parameters without also solving for the attitude. Work is continuing on removing this restriction from the model.

There are four basic contributions to the total solve-for parameter error:

$$\Delta s(t) = \Delta s_a(t) + \Delta s_n(t) + \Delta s_c(t) + \Delta s_u(t) \tag{3-10}$$

where $\Delta s_a(t) \equiv$ the error at time t due to an *a priori* error at the *epoch time* t_o

$\Delta s_n(t) \equiv$ the error due to measurement noise

$\Delta s_c(t) \equiv$ the error at time t due to consider parameter errors at time t_o

$\Delta s_u(t) \equiv$ the error due to dynamic noise.

Substituting equation (3-10) into equation (3-8), and using equation (3-9), gives

$$\Delta s_a(t) = \Phi_{ss}(t, t')\Delta s_a(t') \tag{3-11a}$$

$$\Delta s_n(t) = \Phi_{ss}(t, t')\Delta s_n(t') \tag{3-11b}$$

$$\Delta s_c(t) = \Phi_{ss}(t, t')\Delta s_c(t') + \Phi_{sc}(t, t')\Phi_{cc}(t', t_o)\Delta c(t_o) \tag{3-11c}$$

$$\Delta s_u(t) = \Phi_{ss}(t, t')\Delta s_u(t') + \Phi_{sc}(t, t')\psi_c(t', t_o) + \psi_s(t,t'). \tag{3-11d}$$

The function of a full estimation system is to determine an estimate $s^*(t)$ given measurements y_i. Error analysis, however, does not require the actual computation of an estimate, but determines how good an estimate would be if it were produced in a given situation. This is done by computing the *estimation covariance matrix* defined by

$$P(t) \equiv E[\Delta s(t)\Delta s^T(t)]. \tag{3-12}$$

The covariance matrix $P(t)$ provides a statistical measure of how good an estimate could be produced at time t of a given scenario. We assume that at the *epoch time* t_o the solve for error $\Delta s(t_o)$ and the consider error $\Delta c(t_o)$ are uncorrelated. If all the various error sources are also initially uncorrelated, then by equations (3-11) they remain uncorrelated at all times. Thus, substituting equation (3-10) into equation (3-12) gives

$$P(t) = P_a(t) + P_n(t) + P_c(t) + P_u(t) \tag{3-13}$$

where

$$P_a(t) \equiv E[\Delta s_a(t)\Delta s_a^T(t)] \tag{3-14a}$$

$$P_n(t) \equiv E[\Delta s_n(t)\Delta s_n^T(t)] \tag{3-14b}$$

$$P_c(t) \equiv E[\Delta s_c(t)\Delta s_c^T(t)] \tag{3-14c}$$

$$P_u(t) \equiv E[\Delta s_u(t)\Delta s_u^T(t)] \ . \tag{3-14d}$$

In addition to providing a solve-for parameter estimate, an estimation system will generally also compute an estimate P^* of the estimation covariance P. Since the true *a priori* error and noise covariance matrices may not be known, the estimation system must use *assumed* values for the covariances of these error sources. Further, the estimation filter, by definition, does not account for consider parameter errors. Therefore, there are three basic contributions to P^*:

$$P^*(t) = P_a^*(t) + P_n^*(t) + P_u^*(t) \tag{3-15}$$

where

$P_a^*(t) \equiv$ the covariance contribution at time t induced by the assumed *a priori* covariance

$P_n^*(t) \equiv$ the covariance contribution induced by the assumed measurement noise covariance

$P_u^*(t) \equiv$ the covariance contribution induced by the assumed dynamic noise covariance

If the assumed covariances do not reflect the actual values (the filter is *mistuned*) then there will be some covariance contribution due to residual *a priori* error, measurement noise and dynamic noise. Thus

$$P(t) = P^*(t) + P_c(t) + \Delta P_a(t) + \Delta P_n(t) + \Delta P_u(t) \tag{3-16}$$

where

$$\Delta P_a(t) = P_a(t) - P_a^*(t) \tag{3-17a}$$

$$\Delta P_n(t) = P_n(t) - P_n^*(t) \tag{3-17b}$$

$$\Delta P_u(t) = P_u(t) - P_u^*(t) \ . \tag{3-17c}$$

Note that these matrices may not be non-negative-definite.

3.1 Batch Filter Covariance Analysis

A batch filter produces an estimate $\mathbf{s}^*(t_o)$ at an epoch time t_o, based on a single batch of measurements $\mathbf{y}$ that may have been made at various times. Thus

$$\mathbf{y} \equiv \begin{bmatrix} \mathbf{y}_1 \\ \cdots \\ \mathbf{y}_m \end{bmatrix}, \quad \mathbf{y}^* \equiv \begin{bmatrix} \mathbf{y}_1^* \\ \cdots \\ \mathbf{y}_m^* \end{bmatrix} \quad \text{and} \quad \Delta\mathbf{y} \equiv \begin{bmatrix} \Delta\mathbf{y}_1 \\ \cdots \\ \Delta\mathbf{y}_m \end{bmatrix}. \tag{3-18}$$

The batch filter produces an estimate $\mathbf{s}^*(t_o)$ that gives the computed measurement $\mathbf{y}^*$ which minimizes the cost function

$$V \equiv \Delta\mathbf{y}^T W \Delta\mathbf{y} + \Delta\mathbf{s}_o^{*T} W_o \Delta\mathbf{s}_o^* \tag{3-19}$$

with
$$\Delta\mathbf{s}_o^* \equiv \mathbf{s}^*(t_o) - \mathbf{s}_o^* = \mathbf{s}^*(t_o) - \mathbf{s}(t_o) + \mathbf{s}(t_o) - \mathbf{s}_o^* = \Delta\mathbf{s}_o - \Delta\mathbf{s}(t_o) \tag{3-20a}$$
$$\Delta\mathbf{s}_o \equiv \mathbf{s}(t_o) - \mathbf{s}_o^* \tag{3-20b}$$

where
$W \equiv$ positive-definite symmetric measurement weight matrix
$\mathbf{s}_o^* \equiv$ *a priori* estimate of $\mathbf{s}(t_o)$
$W_o \equiv$ non-negative-definite symmetric *a priori* weight matrix.

Since the batch filter determines $\mathbf{s}^*(t_o)$, it is necessary to relate $\Delta\mathbf{y}$ to $\Delta\mathbf{s}(t_o)$. Substituting equation (2-6) into equation (3-4), and using the partitioning of equations (3-6) and (3-7b), gives

$$\Delta\mathbf{y}_i = G_i\,[\Phi(t_i, t_o)\Delta\mathbf{x}(t_o) + \psi(t_i, t_o)] + \mathbf{v}_i = F_i\,\Delta\mathbf{s}(t_o) + C_i\,\Delta\mathbf{c}(t_o) + \mathbf{U}_i + \mathbf{v}_i \tag{3-21}$$

where

$$F_i \equiv G_i \begin{bmatrix} \Phi_{ss}(t_i, t_o) \\ 0 \end{bmatrix}, \quad C_i \equiv G_i \begin{bmatrix} \Phi_{sc}(t_i, t_o) \\ \Phi_{cc}(t_i, t_o) \end{bmatrix} \quad \text{and} \quad \mathbf{U}_i \equiv G_i\,\psi(t_i, t_o). \tag{3-22}$$

Then
$$\Delta\mathbf{y} = F\Delta\mathbf{s}(t_o) + \Delta\mathbf{e} \tag{3-23}$$

where
$$\Delta\mathbf{e} \equiv C\Delta\mathbf{c}(t_o) + \mathbf{U} + \mathbf{v} \tag{3-24a}$$

and

$$F \equiv \begin{bmatrix} F_1 \\ \cdots \\ F_m \end{bmatrix} \tag{3-24b}$$

with C, $\mathbf{U}$ and $\mathbf{v}$ defined similarly from C_i, $\mathbf{U}_i$ and $\mathbf{v}_i$.

Substituting equations (3-20a) and (3-23) into equation (3-19) for the cost function gives

$$\begin{aligned} V &= \Delta s^T(t_o)\,(W_o + F^TWF)\,\Delta s(t_o) + \Delta s^T(t_o)\,(F^TW\Delta e - W_o\Delta s_o) \\ &\quad + (\Delta e^TWF - \Delta s_o{}^TW_o)\,\Delta s(t_o) + \Delta e^TW\Delta e + \Delta s_o{}^TW_o\Delta s_o \\ &= [\Delta s(t_o) + W_n^{-1}(F^TW\Delta e - W_o\Delta s_o)]^T\,W_n\,[\Delta s(t_o) + W_n^{-1}(F^TW\Delta e - W_o\Delta s_o)] \\ &\quad - (F^TW\Delta e - W_o\Delta s_o)^T\,W_n^{-1}\,(F^TW\Delta e - W_o\Delta s_o) + \Delta e^TW\Delta e + \Delta s_o{}^TW_o\Delta s_o \end{aligned} \qquad (3\text{-}25)$$

where $$W_n \equiv W_o + F^TWF\ . \qquad (3\text{-}26)$$

The matrix W_n is known as the *normal matrix*. The final equality in equation (3-25) is valid as long as W_n is nonsingular. The singularity (or ill-conditioning) of the normal matrix indicates a lack of observability of the solve-for parameters from the measurements $\mathbf{y}$.

If W_n is nonsingular, then it is clear from the form of equation (3-25) that V is minimized when

$$\begin{aligned} \Delta s(t_o) &= -\,W_n^{-1}\,(F^TW\Delta e - W_o\Delta s_o) \\ &= -\,W_n^{-1}\,\{F^TW\,[C\Delta c(t_o) + \mathbf{U} + v] - W_o\Delta s_o\} \\ &= \Delta s_a(t_o) + \Delta s_n(t_o) + \Delta s_c(t_o) + \Delta s_u(t_o) \end{aligned} \qquad (3\text{-}27)$$

where $$\Delta s_a(t_o) \equiv W_n^{-1}W_o\Delta s_o \qquad (3\text{-}28a)$$

$$\Delta s_n(t_o) \equiv -\,W_n^{-1}F^TWv \qquad (3\text{-}28b)$$

$$\Delta s_c(t_o) \equiv -\,W_n^{-1}F^TWC\Delta c(t_o) \qquad (3\text{-}28c)$$

$$\Delta s_u(t_o) \equiv -\,W_n^{-1}F^TW\mathbf{U}\ . \qquad (3\text{-}28d)$$

The estimate $s^*(t_o)$ at the epoch time t_o may be propagated to any other time using equation (2-3). The solve-for parameter errors at these other times are given by equations (3-11), with $t' = t_o$ and with equations (3-28) as initial conditions.

Using equations (3-11a) and (3-28a) in equation (3-14a) gives the *a priori* error induced contribution to the solve-for covariance:

$$P_a(t) = \Phi_{ss}(t, t_o)\,P_a(t_o)\,\Phi_{ss}{}^T(t, t_o) \qquad (3\text{-}29)$$

where $$P_a(t_o) = W_n^{-1}W_oP_oW_oW_n^{-1} \qquad (3\text{-}30)$$

with $$P_o \equiv E[\Delta s_o\Delta s_o{}^T]\ . \qquad (3\text{-}31)$$

Using equations (3-11b) and (3-28b) in equation (3-14b) gives the measurement noise induced contribution to the solve-for covariance:

$$P_n(t) = \Phi_{ss}(t, t_o)\, P_n(t_o)\, \Phi_{ss}^T(t, t_o) \tag{3-32}$$

where $$P_n(t_o) = W_n^{-1} F^T W R W F W_n^{-1} \tag{3-33}$$

with $$R \equiv E[vv^T]\ . \tag{3 34}$$

Using equations (3-11c) and (3-28c) in equation (3-14c) gives the consider parameter induced contribution to the solve-for covariance:

$$P_c(t) = (\partial s/\partial c)(t)\, E[\Delta c(t_o)\Delta c^T(t_o)]\, (\partial s/\partial c)^T(t) \tag{3-35}$$

where $$(\partial s/\partial c)(t) \equiv -\, \Phi_{ss}(t, t_o)\, W_n^{-1} F^T W C + \Phi_{sc}(t, t_o)\ . \tag{3-36}$$

The computation of the dynamic noise contribution P_u is complicated by the fact that the U in equation (3-28d) is correlated with the $\psi_s(t, t_o)$ term introduced by the propagation equation (3-11d). Using equations (3-11d) and (3-28d) in equation (3-14d) gives

$$\begin{aligned} P_u(t) = {} & \Phi_{ss}(t, t_o)\, P_u(t_o)\, \Phi_{ss}^T(t, t_o) - \Phi_{ss}(t, t_o)\, W_n^{-1} F^T W\, E[U\psi_s^T(t, t_o)] \\ & - E[\psi_s(t, t_o) U^T]\, W F W_n^{-1} \Phi_{ss}^T(t, t_o) + D_{ss}(t, t_o) \end{aligned} \tag{3-37}$$

where $$P_u(t_o) = W_n^{-1} F^T W E[UU^T] W F W_n^{-1}\ . \tag{3-38}$$

From equation (3-22) we have

$$E[UU^T] = \begin{bmatrix} G_1 D(t_1, t_o) G_1^T & \cdots & G_1 D'(t_1, t_m) G_m^T \\ \cdots & \cdots & \cdots \\ G_m D'(t_m, t_1) G_1^T & \cdots & G_m D(t_m, t_o) G_m^T \end{bmatrix} \tag{3-39a}$$

$$E[U\psi_s^T(t, t_o)] = \begin{bmatrix} G_1 D'_s(t_1, t) \\ \cdots \\ G_m D'_s(t_m, t) \end{bmatrix} \tag{3-39b}$$

where $$\begin{aligned} D'(t_i, t_j) &\equiv E[\psi(t_i, t_o)\psi^T(t_j, t_o)] = [D'_s(t_i, t_j), D'_c(t_i, t_j)] \\ &= \Phi(t_i, t_j)\, D(t_j, t_o) = \Phi(t_i, t_o)\, \Phi^{-1}(t_j, t_o)\, D(t_j, t_o) \qquad \text{for } t_i \geq t_j \\ &= D(t_i, t_o)\, \Phi^T(t_j, t_i) = [\Phi(t_j, t_o)\, \Phi^{-1}(t_i, t_o)\, D(t_i, t_o)]^T \qquad \text{for } t_j \geq t_i\ . \end{aligned} \tag{3-40}$$

The last equality on the first line of equation (3-40) indicates a partitioning of $D'(t_i, t_j)$ into submatrices $D'_s(t_i, t_j)$ and $D'_c(t_i, t_j)$, and the equalities on the last two lines follow from equations (2-9) to (2-11).

A *minimum variance* batch estimator produces solve-for parameter estimates with minium covariance due to noise sources known to the filter [Sorenson, Wertz]. The weights for such a filter are chosen as follows:

$$W = R^{*-1} \quad \text{and} \quad W_o = P_o^{*-1} \tag{3-41}$$

where $R^* \equiv$ an assumed value for the measurement noise covariance

$P_o^* \equiv$ an assumed value for the *a priori* error covariance.

The estimated covariance at the epoch time $P^*(t_o)$ is obtained by substituting equations (3-41) into equations (3-30) and (3-33), and assuming that $R = R^*$ and $P_o = P_o^*$, giving

$$P^*(t_o) = P_a^*(t_o) + P_n^*(t_o) = W_n^{-1}(W_o + F^TWF)W_n^{-1} = W_n^{-1} \tag{3-42}$$

with

$$P_a^*(t_o) = W_n^{-1}W_oW_n^{-1} \tag{3-43a}$$

$$P_n^*(t_o) = W_n^{-1}F^TWFW_n^{-1}\ . \tag{3-43b}$$

Note that the $P_u^*(t_o) = 0$ because the batch filter does not account for dynamic noise at all. The covariance estimate is propagated to other times by using equations (3-29) and (3-32), which give

$$P^*(t) = \Phi_{ss}(t, t_o)\, P^*(t_o)\, \Phi_{ss}^T(t, t_o)\ . \tag{3-44}$$

Using equations (3-30), (3-33), (3-41) and (3-43) in equations (3-17) gives the residual covariance contributions:

$$\Delta P_a(t_o) = W_n^{-1}W_o(P_o - P_o^*)W_oW_n^{-1} \tag{3-45a}$$

$$\Delta P_n(t_o) = W_n^{-1}F^TW(R - R^*)WFW_n^{-1} \tag{3-45b}$$

$$\Delta P_u(t_o) = P_u(t_o)\ . \tag{3-45c}$$

The matrices propagate in the same manner as P_a, P_n and P_u, respectively.

3.2 Sequential Filter Covariance Analysis

A sequential filter produces an estimate $\mathbf{s}^*(t)$ based on measurements taken at discrete times $t_i \le t$. Between the measurement times t_i, the state estimate $\mathbf{x}^*(t)$ is propagated using equation (2-3). At each time t_i, the solve-for parameters are updated based on the propagated state $\mathbf{x}^*(t_i)$ and the measurements $\mathbf{y}_i$. Typically, this update has the following form:

$$\mathbf{s}^*(t_i) = \mathbf{s}^*(t_i-) + K_i\Delta \mathbf{y}_i \tag{3-46}$$

where $\mathbf{s}^*(t_i)$ and $\mathbf{s}^*(t_i-)$ denote estimates of the solve-for parameters immediately after and immediately before incorporating the information contained in the measurements at time t_i. The gain matrix K_i determines how much the propagated state is corrected, based on the measurement residuals $\Delta \mathbf{y}_i$.

The estimation error immediately after an update is

$$\Delta s(t_i) = s(t_i) - s^*(t_i) = s(t_i) - s^*(t_i-) - K_i\Delta y_i = \Delta s(t_i-) - K_i\Delta y_i \tag{3-47}$$

since the true state is continuous at t_i. Substituting equation (3-4) for Δy_i and using the partitioning of equation (3-6) gives

$$\begin{aligned}\Delta s(t_i) &= \Delta s(t_i-) - K_i\,[G_i\Delta x(t_i-) + v_i]\\ &= (I - K_iG_{si})\,\Delta s(t_i-) - K_i\,[G_{ci}\Delta c(t_i-) + v_i]\end{aligned} \tag{3-48}$$

where G_i has been partitioned as

$$G_i = [G_{si},\ G_{ci}]\ . \tag{3-49}$$

Substituting equation (3-10) into equation (3-48), and using equation (3-9), gives update equations for each of the contributions to the total solve-for error:

$$\Delta s_a(t_i) = (I - K_iG_{si})\,\Delta s_a(t_i-) \tag{3-50a}$$

$$\Delta s_n(t_i) = (I - K_iG_{si})\,\Delta s_n(t_i-) - K_iv_i \tag{3-50b}$$

$$\Delta s_c(t_i) = (I - K_iG_{si})\,\Delta s_c(t_i-) - K_iG_{ci}\Phi_{cc}(t_i\,,t_o)\,\Delta c(t_o) \tag{3-50c}$$

$$\Delta s_u(t_i) = (I - K_iG_{si})\,\Delta s_u(t_i-) - K_iG_{ci}\Psi_c(t_i,t_o)\ . \tag{3-50d}$$

Each of these error contributions may be propagated individually between measurement times using equations (3-11), with the initial conditions:

$$\Delta s_a(t_o) = \Delta s_o \tag{3-51a}$$

$$\Delta s_n(t_o) = \Delta s_c(t_o) = \Delta s_u(t_o) = \mathbf{0}\ , \tag{3-51b}$$

where Δs_o is defined in equation (3-20b).

Using equation (3-11a) in equation (3-14a) gives the propagation equation for the *a priori* error induced contribution to the solve-for covariance:

$$P_a(t) = \Phi_{ss}(t,\,t_i)\,P_a(t_i)\,\Phi_{ss}{}^T(t,\,t_i) \quad \text{for } t_i \le t < t_{i+1} \tag{3-52}$$

where $$P_a(t_o) = P_o \tag{3-53}$$

with the *a priori* covariance P_o defined in equation (3-31). Substituting equation (3-50a) into equation (3-14a) gives the update equation:

$$P_a(t_i) = (I - K_iG_{si})\,P_a(t_i-)\,(I - K_iG_{si})^T\ . \tag{3-54}$$

Using equation (3-11b) in equation (3-14b) gives the propagation equation for the measurement noise induced contribution to the solve-for covariance:

$$P_n(t) = \Phi_{SS}(t, t_i)\, P_n(t_i)\, \Phi_{SS}^T(t, t_i) \quad \text{for } t_i \le t < t_{i+1} \tag{3-55}$$

where

$$P_n(t_o) = 0 \tag{3-56}$$

Substituting equation (3-50b) into equation (3-14b) gives the update equation:

$$P_n(t_i) = (I - K_i G_{Si})\, P_n(t_i-)\, (I - K_i G_{Si})^T + K_i R_i K_i^T \tag{3-57}$$

with R_i defined by equation (3-2b).

The consider parameter induced contribution to the covariance can be most easily expressed in terms of the partial derivative $(\partial s/\partial c)(t)$ implicitly defined by

$$\Delta s_c(t) = (\partial s/\partial c)(t)\, \Delta c(t_o)\, . \tag{3-58}$$

Substituting this into equation (3-11c) gives the propagation equation:

$$(\partial s/\partial c)(t) = \Phi_{SS}(t, t_i)\, (\partial s/\partial c)(t_i) + \Phi_{SC}(t, t_i)\Phi_{CC}(t_i, t_o) \quad \text{for } t_i \le t < t_{i+1} \tag{3-59}$$

where

$$(\partial s/\partial c)(t_o) = 0\, . \tag{3-60}$$

Substituting equation (3-58) into equation (3-50c) gives the update equation:

$$(\partial s/\partial c)(t_i) = (I - K_i G_{Si})\, (\partial s/\partial c)(t_i-) - K_i G_{Ci} \Phi_{CC}(t_i, t_o)\, . \tag{3-61}$$

From equations (3-14c) and (3-58), the consider parameter contribution to the solve-for covariance is then

$$P_c(t) = (\partial s/\partial c)(t)\, E[\Delta c(t_o) \Delta c^T(t_o)]\, (\partial s/\partial c)^T(t)\, . \tag{3-62}$$

As in the case of a batch filter, the dynamic noise contribution is more complicated to compute than the other contributions. Substituting equation (3-11d) into equation (3-14d) and using equation (2-11) gives:

$$\begin{aligned} P_u(t) = {} & \Phi_{SS}(t, t_i)\, P_u(t_i)\, \Phi_{SS}^T(t, t_i) + \Phi_{SS}(t, t_i)\, P_{uc}(t_i)\, \Phi_{SC}^T(t, t_i) \\ & + \Phi_{SC}(t, t_i)\, P_{uc}^T(t_i)\, \Phi_{SS}^T(t, t_i) + \Phi_{SC}(t, t_i)\, D_{CC}(t_i, t_o)\, \Phi_{SC}^T(t, t_i) \\ & + D_{SS}(t, t_i) \end{aligned} \tag{3-63}$$

for $t_i \le t < t_{i+1}$, where

$$P_u(t_o) = 0 \tag{3-64}$$

and

$$P_{uc}(t) \equiv E[\Delta s_u(t) \psi_C^T(t, t_o)] \tag{3-65}$$

and the random excitation covariance D is partitioned as in equation (3-7c). It follows from equations

(2-10), (3-7a) and (3-7b) that

$$\psi_c(t,t_o) = \Phi_{cc}(t,t_i)\,\psi_c(t_i,t_o) + \psi_c(t,t_i)\,. \tag{3-66}$$

Using this and equations (2-11) and (3-11d) in equation (3-65) gives the equation for propagating $P_{uc}(t)$;

$$\begin{aligned} P_{uc}(t) = {} & \Phi_{ss}(t, t_i)\, P_{uc}(t_i)\, \Phi_{cc}^T(t, t_i) + \Phi_{sc}(t, t_i)\, D_{cc}(t_i, t_o)\, \Phi_{cc}^T(t, t_i) \\ & + D_{sc}(t, t_i) \end{aligned} \tag{3-67}$$

for $t_i \leq t < t_{i+1}$, where

$$P_{uc}(t_o) = 0\,. \tag{3-68}$$

From equations (3-14d), (3-50d) and (3-65), the update equations for $P_u(t)$ and $P_{uc}(t)$ are:

$$\begin{aligned} P_u(t_i) = {} & (I - K_iG_{si})\, P_u(t_i\text{-})\, (I - K_iG_{si})^T - (I - K_iG_{si})\, P_{uc}(t_i\text{-})\, G_{ci}^T K_i^T \\ & - K_iG_{ci}\, P_{uc}^T(t_i\text{-})\, (I - K_iG_{si})^T + K_iG_{ci}\, D_{cc}(t_i,t_o)\, G_{ci}^T K_i^T \end{aligned} \tag{3-69a}$$

$$P_{uc}(t_i) = (I - K_iG_{si})\, P_{uc}(t_i\text{-}) - K_iG_{ci}\, D_{cc}(t_i,t_o)\,. \tag{3-69b}$$

A *Kalman filter* is a sequential filter which produces solve-for parameter estimates with minimum covariance due to noise sources known to the filter [Gelb, Lefferts]. In addition to the solve-for parameter estimates, a Kalman filter maintains an estimate P^* of the solve-for parameter covariance, and uses this to compute an optimal gain K_i at each time t_i. The covariance estimate P^* is given by algorithms similar to those for P, with the full state error vector replaced by the solve-for parameter error vector. The resulting propagation equation for P^* is

$$P^*(t) = \Phi_{ss}(t, t_i)\, P^*(t_i)\, \Phi_{ss}^T(t, t_i) + D_{ss}^*(t, t_i) \quad \text{for } t_i \leq t < t_{i+1} \tag{3-70}$$

where the matrix D_{ss}^* is the estimate of the random excitation covariance used by the filter. It is based on an assumed spectral density Q_{ss}^* of the dynamic noise on the solve-for parameters:

$$D_{ss}^*(t, t_i) \equiv \int_{t_i}^{t} \Phi_{ss}(t, t'')\, Q_{ss}^*\, \Phi_{ss}^T(t, t'')\, dt''. \tag{3-71}$$

The update equation for the covariance estimate is

$$P^*(t_i) = (I - K_iG_{si})\, P^*(t_i\text{-})\, (I - K_iG_{si})^T + K_iR_i^*K_i^T \tag{3-72}$$

where $\quad R_i^* \equiv$ an assumed value for the measurement noise covariance

and the *Kalman gain* is given by [Gelb, Lefferts]

$$K_i = P^*(t_i\text{-})\, G_i^T\, [G_iP^*(t_i\text{-})G_i^T + R_i^*]^{-1}\,. \tag{3-73}$$

Substituting equation (3-15) into equation (3-70), gives the following propagation equations for the component contributions to P^*:

$$P_a{}^*(t) = \Phi_{ss}(t, t_i)\, P_a{}^*(t_i)\, \Phi_{ss}{}^T(t, t_i) \tag{3-74a}$$

$$P_n{}^*(t) = \Phi_{ss}(t, t_i)\, P_n{}^*(t_i)\, \Phi_{ss}{}^T(t, t_i) \tag{3-74b}$$

$$P_u{}^*(t) = \Phi_{ss}(t, t_i)\, P_u{}^*(t_i)\, \Phi_{ss}{}^T(t, t_i) + D_{ss}{}^*(t, t_i) \tag{3-74c}$$

for $t_i \le t < t_{i+1}$, with initial conditions

$$P_a{}^*(t_o) = P_o{}^* \equiv \text{an assumed value for the } a\ priori \text{ error covariance.} \tag{3-75a}$$

$$P_n{}^*(t_o) = P_u{}^*(t_o) = 0\,. \tag{3-75b}$$

Substituting equation (3-15) into equation (3-72), gives the corresponding update equations:

$$P_a{}^*(t_i) = (I - K_i G_{si})\, P_a{}^*(t_i\text{-})\, (I - K_i G_{si})^T \tag{3-76a}$$

$$P_n{}^*(t_i) = (I - K_i G_{si})\, P_n{}^*(t_i\text{-})\, (I - K_i G_{si})^T + K_i R_i{}^* K_i{}^T \tag{3-76b}$$

$$P_u{}^*(t_i) = (I - K_i G_{si})\, P_u{}^*(t_i\text{-})\, (I - K_i G_{si})^T\,. \tag{3-76c}$$

A Kalman filter will produce an estimate with the minimum covariance P^* due to the *assumed* covariances $P_o{}^*$, $R_i{}^*$ and $Q_{ss}{}^*$. If the filter is mistuned, the true covariance will *not* be minimized. Using equations (3-52), (3-55), (3-63) and (3-74) in equations (3-17) gives propagation equations for the residual covariance contributions:

$$\Delta P_a(t) = \Phi_{ss}(t, t_i)\, \Delta P_a(t_i)\, \Phi_{ss}{}^T(t, t_i) \tag{3-77a}$$

$$\Delta P_n(t) = \Phi_{ss}(t, t_i)\, \Delta P_n(t_i)\, \Phi_{ss}{}^T(t, t_i) \tag{3-77b}$$

$$\begin{aligned}\Delta P_u(t) = {} & \Phi_{ss}(t, t_i)\, \Delta P_u(t_i)\, \Phi_{ss}{}^T(t, t_i) + \Phi_{ss}(t, t_i)\, P_{uc}(t_i)\, \Phi_{sc}{}^T(t, t_i) \\ & + \Phi_{sc}(t, t_i)\, P_{uc}{}^T(t_i)\, \Phi_{ss}{}^T(t, t_i) + \Phi_{sc}(t, t_i)\, D_{cc}(t_i, t_o)\, \Phi_{sc}{}^T(t, t_i) \\ & + D_{ss}(t, t_i) - D_{ss}{}^*(t, t_i)\end{aligned} \tag{3-77c}$$

for $t_i \le t < t_{i+1}$, where

$$\Delta P_a(t_o) = P_o - P_o{}^* \tag{3-78a}$$

$$\Delta P_n(t_o) = \Delta P_u(t_o) = 0\,. \tag{3-78b}$$

Using equations (3-54), (3-57), (3-69a) and (3-76) in equations (3-17) gives update equations for the residual covariance contributions:

$$\Delta P_a(t_i) = (I - K_i G_{si})\, \Delta P_a(t_i\text{-})\, (I - K_i G_{si})^T \tag{3-79a}$$

$$\Delta P_n(t_i) = (I - K_i G_{si})\, \Delta P_n(t_i\text{-})\, (I - K_i G_{si})^T + K_i\, (R_i - R_i{}^*)\, K_i{}^T \tag{3-79b}$$

$$\begin{aligned}\Delta P_u(t_i) = {} & (I - K_i G_{si})\, \Delta P_u(t_i\text{-})\, (I - K_i G_{si})^T - (I - K_i G_{si})\, P_{uc}(t_i\text{-})\, G_{ci}{}^T K_i{}^T \\ & - K_i G_{ci}\, P_{uc}{}^T(t_i\text{-})\, (I - K_i G_{si})^T + K_i G_{ci}\, D_{cc}(t_i, t_o)\, G_{ci}{}^T K_i{}^T\,.\end{aligned} \tag{3-79c}$$

4. CONCLUSIONS

Error analysis can be crucial during mission design, providing assistance in the specification of a sensor complement and a calibration plan, possibly requiring a set of scheduled attitude maneuvers, to deliver the pointing accuracy necessary to satisfy the mission objectives. Error analysis is also necessary to determine what level of ground-based processing will be needed to meet high-accuracy attitude determination requirements. Thus, to ensure the achievement of mission objectives, it is critical that the analyst produce accurate estimates of determination uncertainties, especially the often-underestimated contributions of process noise and consider parameter errors. In this paper we have presented a general, comprehensive approach to filter and dynamics modeling for spacecraft attitude determination error analysis.

The model is general in that it allows great freedom in specifying orbit geometry, sensor types, measurement scheduling and parameter selection. Further, it covers both spin-stabilized and three-axis stabilized spacecraft, with process noise appropriate to the two types of stabilization, and both batch least-squares and sequential attitude estimation processes. This paper does not include models of sensors, with the exception of a model for strapdown gyros used for dynamics model replacement in the three-axis stabilized case. However, the only restriction on sensor modeling is that the measurement noise must be additive.

The model is comprehensive in that it considers all the major sources of error in the determination process. The model gives the separate contributions to the solve-for parameter uncertainty arising from errors in the *a priori* estimates of the solve-for parameters, from measurement noise, from process noise, and from consider parameter uncertainties, as well as the overall uncertainty due to all these sources of error. This allows the analyst to judge the importance of various sources of error, and make informed recommendations to reduce the effect of the largest contributors.

The analysis of the effect of dynamics errors in the batch estimation case is particularly important, since batch filters generally do not account for this source of error. Indeed, for both the batch and the sequential cases, the model carefully separates the estimation covariance based on *true* sources of error from the estimation covariance based on sources of error *assumed* by the filter. This gives the analyst the ability to study *mistuned* filters. While the concept of tuning is primarily associated with sequential filters, the presentation here makes it clear that it may also be an important consideration in the batch case.

The model for attitude determination error analysis presented here was developed as part of the mathematical specification of algorithms for the computer-based Attitude Determination Error Analysis System. This software system incorporates the dynamics model presented in this paper for three-axis stabilized spacecraft, a simplified dynamics model for spin-stabilized spacecraft, slightly simplified batch and sequential filter models and a wide variety of sensor models, including digital and analog sun sensors, scanning and fixed-head star trackers, gimballed line-of-sight sensors, horizon sensors, and magnetometers. The Attitude Determination Error Analysis System is currently undergoing acceptance testing, and will be an important component of the institutional flight support software of the Goddard Space Flight Center Flight Dynamics Division when this testing has been successfully completed.

3Front CP3011

REFERENCES

[Gelb] Arthur Gelb, ed., *Applied Optimal Estimation*, The MIT Press, 1974.

[Lefferts] E. J. Lefferts, F. L. Markley, and M. D. Shuster,"Kalman Filtering for Spacecraft Attitude Estimation," *Journal of Guidance, Control, and Dynamics,* Vol. 5, No. 5, September-October 1982, pp. 417-429.

[Nicholson] M. Nicholson, F. Markley, and E. Seidewitz, *Attitude Determination Error Analysis System (ADEAS) Mathematical Specifications Document,* CSC/TM-88/6001, Computer Sciences Corporation, December 1987.

[Sorenson] Harold W. Sorenson, *Parameter Estimation: Principles and Problems*, Marcel Dekker, New York, 1980

[Wertz] James R. Wertz, ed., *Spacecraft Attitude Determination and Control,* D. Reidel Publishing Company, 1978.

N89-15936

ACCURACY STUDY OF THE UPPER ATMOSPHERE RESEARCH SATELLITE (UARS) DEFINITIVE ATTITUDE DETERMINATION

Frank Snow
Goddard Space Flight Center

and

Kenneth Krack, Yi-Tsuei Sheu, and William Bosl
Computer Sciences Corporation

ABSTRACT

The Upper Atmosphere Research Satellite (UARS) has two definitive attitude determination requirements: the definitive attitude of the Modular Attitude Control Subsystem (MACS) and the definitive attitude of the gimbaled Solar-Stellar Pointing Platform (SSPP). The onboard computer (OBC) will compute the MACS attitude using a Kalman filter and will transform this attitude solution through the SSPP gimbals to calculate the SSPP attitude. The attitude ground support system (AGSS) will compute the MACS attitude using a batch least-squares differential corrector algorithm and will also transform this solution through the gimbals to obtain the SSPP attitude. This paper reports the results of a prelaunch study to predict the accuracy of the OBC attitude solutions and the accuracy of the AGSS attitude solutions. The OBC and AGSS solution accuracies are then compared to establish the relative quality. The effects of star observability, sensor noise, and sensor misalignment uncertainties on attitude determination accuracy are analyzed for each case.

~~s~~

N89-15937

1.0 INTRODUCTION

The Upper Atmosphere Research Satellite (UARS) has two definitive attitude determination requirements: the definitive attitude of the Modular Attitude Control Subsystem (MACS) and the definitive attitude of the gimbaled Solar-Stellar Pointing Platform (SSPP). The onboard computer (OBC) will compute the MACS attitude using a Kalman filter and will transform this attitude solution through the SSPP gimbals to calculate the SSPP attitude. The attitude ground support system (AGSS) will compute the MACS attitude using a batch least-squares differential corrector algorithm and will also transform this solution through the gimbals to obtain the SSPP attitude. This paper reports the results of a prelaunch study to predict the accuracy of the OBC attitude solutions and the accuracy of the AGSS attitude solutions. The OBC and AGSS solution accuracies are then compared to establish the relative quality.

The software that was used for both the OBC and the AGSS study is the Attitude Determination Error Analysis System (ADEAS) Program, Release 3 (CSC, 1986; Fang, 1983). ADEAS has the ability to estimate the accuracies of both a Kalman filter and a batch differential corrector. The ADEAS program has not at this time completed formal acceptance testing; therefore, while the results presented here are considered essentially correct, they may be updated in the future.

The attitude sensors that can be used by the OBC or the AGSS are two fixed-head star trackers (FHSTs), the inertial reference unit (IRU), and the fine Sun sensor (FSS) on the MACS. Normally, two FHSTs will be used for attitude determination and control. In the event that one FHST fails, the FSS on the MACS is to be used in conjunction with the remaining FHST. In this study, the attitude uncertainty has been estimated for the case of two FHSTs. The IRU drift rate bias uncertainties are always solved in addition to the attitude uncertainties.

The stars used in this analysis are taken from the combined OBC primary and secondary catalogs as presented in Sheldon (1986). Every estimate of the attitude uncertainty was repeated for two cases of star observability: (1) When the spacecraft is flying in an orbit such that each FHST can see the maximum number of stars (29 stars) with minimum star separation angles, this represents the best-case star observability during the UARS mission. (2) When the spacecraft is flying in an orbit such that each FHST can see the minimum number of stars (5 stars) with maximum star separation angles, this represents the worst-case star observability during the UARS mission. These two cases will be referred to as the 29-star case and the 5-star case, respectively. The timespan for all cases is one full orbit, 5796 seconds (sec). The resulting attitude uncertainties presented are those at the end of the data batch.

The UARS ephemeris is generated internally in ADEAS with no orbit perturbations and no atmospheric drag. For the 29-star case, the spacecraft is flying forward and the FHSTs are pitching about the axis of negative orbit normal, which is at a right ascension (RA) of 306 degrees (deg) and a declination (dec) of -33 deg. For the 5-star case, the spacecraft is flying backward and the two FHSTs are pitching about the axis of orbit normal, which is at RA of 118 deg and dec of 33 deg. The Keplerian orbital elements used in the study represent the nominal mission orbit:

Semimajor axis = 6.978065×10^6 meters
Eccentricity = 0.001486
Inclination = 57.017788 deg
Argument of perigee = 60.9378 deg
Mean anomaly = 299.162 deg

$$\text{Right ascension of ascending node} = \begin{cases} 216 \text{ deg for 29-star case} \\ 208 \text{ deg for 5-star case} \end{cases}$$

The epoch time is not important in the uncertainty analysis, as it is only used as a time reference in the calculation.

2.0 PRELAUNCH SENSOR PARAMETERS

This section reviews values of the sensor parameters that will be known at the time of launch, including the prelaunch estimates for sensor noise and alignment uncertainties and the nominal alignments of the sensors. The nominal orientations of the attitude sensors on the spacecraft are represented by Euler angle rotations from the MACS frame.

2.1 FHST

The nominal orientations of the FHSTs are given as a 2-1-3 Euler sequence. The Euler angles and the nominal fields of view (FOVs) are given in Table 1.

Table 1. Nominal FHST Alignments and FOV Sizes

Sensor	Rotation Angles (Degrees)			FOV (Degrees)
	θ_1	θ_2	θ_3	
FHST A	-114.27	-49.27	0	8 × 8
FHST B	114.27	-49.27	0	8 × 8

The prelaunch value of the FHST noise is derived from the 3σ error budget for an 8-degree-diameter circular FOV as presented in GE (1983). The components of the total noise are given in Table 2. The values are given in both radians and arc-seconds (arc-sec).

Table 2. Prelaunch FHST Noise Sources (GE, 1983)

Noise Source	Value (3σ)	
	(Radians)	(Arc-Sec)
Noise Equivalent Angle	1.193×10^{-4}	24.6
Quantization Error	3.394×10^{-5}	7.0
Signal Lag Error (Unsynch)	3.636×10^{-5}	7.5
Calibration Error	1.454×10^{-4}	30.0

The noise equivalent angle and the signal lag error are assumed to be random white noise. The quantization error listed in Table 2 is actually the quantization interval. The standard deviation of the random error generated by a quantized process is $\sqrt{1/12}$ times the quantization interval (Bendat, 1971). The 3σ value, therefore, for the quantization error should be 2.939×10^{-5} radians (6.1 arc-sec). The root-sum-square (RSS) of these four noises is

1.939×10^{-4} radians (40.0 arc-sec). This number is adopted for the FHST noise.

The 3σ prelaunch FHST alignment uncertainties are provided by GE (1988): 2.681×10^{-4} radians (55.3 arc-sec) for both the X- and Y-axes and 2.676×10^{-4} radians (55.2 arc-sec) for the boresight direction, the Z-axis.

2.2 IRU

If a spacecraft is moving with constant angular velocity, the IRU misalignments and scale factors are indistinguishable from the drift rate biases. This condition is very closely met by UARS when it is in normal pointing mode. Because both the OBC and the AGSS solve for the IRU biases as well as the attitude, the contribution to the attitude uncertainty by the misalignment and scale factor uncertainties is automatically taken into account. The IRU noise does not contribute significantly to the attitude uncertainty and was, therefore, not considered in this study.

2.3 SSPP

The SSPP is mounted on a two-axis gimbal system. When both gimbals are in their nominal zero positions, the SSPP coordinate system aligns with the MACS frame. The α-gimbal is fixed to the spacecraft and rotates about the MACS Y-axis. It has a range of 0 to 360 degrees although, in actual use, the range is restricted by spacecraft and Earth blockage. The β-gimbal is carried by the α-gimbal and rotates about the SSPP X-axis. The β-gimbal has a range of 0 to 90 degrees; however, in normal Sun-tracking operation, β will not exceed 80 degrees. (This is the sum of the UARS orbital inclination and the maximum elevation of the Sun.) A more complete description of the SSPP geometry is presented in the UARS FDSS Mathematical Background (Kast, 1987b).

The relevant uncertainties with regard to the SSPP are the alignment uncertainty from the MACS to the SSPP gimbals, the uncertainties of the gimbal measurements, the alignment uncertainty from the gimbals to the SSPP FSS, and the noise of the SSPP FSS. The prelaunch estimates of each of these uncertainties are given below. All values are 3σ.

The uncertainties σ_α and σ_β in the two gimbal measurements have values of 9.696×10^{-5} radians (20.0 arc-sec) each (GE, 1986).

The SSPP FSS noise uncertainty is taken from Adcole (1986). The value of the uncertainty is $\sigma_{FSS} = 1.745 \times 10^{-4}$ radians (36.0 arc-sec).

The prelaunch alignment uncertainties are taken to be diagonal matrices of the form

$$P_{\alpha m} = \begin{bmatrix} \sigma^2_{\alpha m} & 0 & 0 \\ 0 & \sigma^2_{\alpha m} & 0 \\ 0 & 0 & \sigma^2_{\alpha m} \end{bmatrix} \qquad P_{N\beta} = \begin{bmatrix} \sigma^2_{N\beta} & 0 & 0 \\ 0 & \sigma^2_{N\beta} & 0 \\ 0 & 0 & \sigma^2_{N\beta} \end{bmatrix}$$

where $P_{\alpha m}$ and $P_{N\beta}$ are the covariance matrices of the MACS-to-gimbals and gimbals-to-SSPP-FSS alignments, respectively. The uncertainties $\sigma_{\alpha m}$ and $\sigma_{N\beta}$ were derived from data in Neste (1987). The values used are 6.545×10^{-4} and 2.424×10^{-4} radians (135 and 50.0 arc-sec), respectively.

3.0 FHST ON-ORBIT ALIGNMENT ACCURACY

The on-orbit alignment for the two FHSTs will be performed shortly after launch. The algorithm presented in Shuster (1982) is used by the UARS AGSS. This scheme minimizes the overall deviation of the sensor alignments from their prelaunch values. The covariances of the misalignments after on-orbit alignment for two sensors can be estimated by

$$P(\mathrm{post})^{-1} = \left[\begin{array}{c|c} G & -G \\ \hline -G & G \end{array}\right] + \left[\begin{array}{c|c} P_1(\mathrm{pre})^{-1} & 0 \\ \hline 0 & P_2(\mathrm{pre})^{-1} \end{array}\right]$$

where

$P(\mathrm{post})$ = 6 by 6 postcalibration misalignment covariance matrix

$$G = \sum_{m=1}^{N} \frac{\left(\hat{W}_1^m \times \hat{W}_2^m\right)\left(\hat{W}_1^m \times \hat{W}_2^m\right)^T}{\left(\sigma_1^2 + \sigma_2^2\right)\left|\hat{W}_1^m \times \hat{W}_2^m\right|^2}$$

N = number of observations

σ_i^2 = sensor noise for sensor i

$\hat{W}_i^m$ = m^{th} star vector observation tracked by sensor i, expressed in spacecraft body coordinates

$P_i(pre)$ = 3 by 3 precalibration misalignment covariance matrix for sensor i

Because this alignment algorithm is attitude independent, it requires that the star observations in the two sensors be simultaneous. Based on this algorithm, a small program simulating the two FHSTs on UARS was developed to estimate the uncertainties of the misalignments after on-orbit alignment.

In estimating the uncertainties, it is assumed that UARS will be deployed on October 26, 1991 (an arbitrary date in late October 1991). To maximize the period before the first yaw maneuver, it is also assumed that the spacecraft is flying backward in an orbit whose right ascension of the ascending node is equal to the right ascension of the Sun. The two FHSTs are assumed to be aligned shortly after deployment using two orbits of FHST data with a total of 21 simultaneous star observations. The resultant alignment uncertainties are given in Table 3.

Table 3. FHST On-Orbit Alignment Uncertainties

Sensor	Axis	Alignment Uncertainty (3σ)	
		(Radians)	(Arc-Sec)
FHST A	X Y Z	2.123×10^{-4} 2.468×10^{-4} 2.642×10^{-4}	43.8 50.9 54.5
FHST B	X Y Z	2.123×10^{-4} 2.482×10^{-4} 2.633×10^{-4}	43.8 51.2 54.3

Further simulation runs indicate that these accuracies are not significantly improved by using more data.

4.0 UARS ATTITUDE DETERMINATION ACCURACY USING A KALMAN FILTER

The UARS OBC attitude determination algorithm is a Kalman filter. This filter propagates the previous attitude solution using IRU data whenever there are no valid star observations. When there is a valid star observation, the OBC updates its estimate of the state vector, which consists of the IRU drift rate bias and the attitude. This update occurs at intervals of 32.768 seconds. When there are valid star observations in both FHSTs, the OBC updates the state vector using data from the FHST that was used longest ago. This situation produces an effective FHST sampling rate of 65.536 seconds with the observations being taken alternately for the two sensors.

The error estimation software used in this study cannot model an alternating sampling of the FHSTs. To estimate the effect of the alternating sampling, the program was run for both a 32.768-second and a 65.536-second sampling rate. The resulting variances were averaged together with a weighting proportional to the fraction of time that observations overlapped, that is, the fraction of time when there were valid observations in both FHSTs. In the 5-star case, there is no overlap; in the 29-star case, there is approximately a 65 percent overlap.

In the 5-star case, the attitude uncertainties were taken at the end of a three-orbit run because the Kalman filter had not converged at the end of the first orbit.

4.1 RESULTS USING PRELAUNCH PARAMETERS

The OBC attitude solution uncertainties using the prelaunch values of the attitude sensor uncertainties presented in Section 2.0 are given below. For the two cases of star observability, as discussed in the introduction, the attitude uncertainties are given in Table 4.

Table 4. OBC Attitude Uncertainties Using Prelaunch Alignment Uncertainties

Case	Axis	Attitude Uncertainty (3σ)	
		(Radians)	(Arc-Sec)
5-star	X Y Z	1.572×10^{-4} 3.132×10^{-4} 1.584×10^{-4}	32.4 64.6 32.7
29-star	X Y Z	1.352×10^{-4} 3.092×10^{-4} 1.321×10^{-4}	27.9 63.8 27.2

4.2 RESULTS USING ON-ORBIT ALIGNMENT ESTIMATES

The AGSS attitude solution uncertainties using the on-orbit estimates of the FHST alignment uncertainties presented in Section 3.0 are given in Table 5.

Table 5. OBC Attitude Uncertainties Using On-Orbit FHST Alignment Uncertainties

Case	Axis	Attitude Uncertainty (3σ)	
		(Radians)	(Arc-Sec)
5-star	X Y Z	1.406×10^{-4} 2.875×10^{-4} 1.262×10^{-4}	29.0 59.3 26.0
29-star	X Y Z	1.195×10^{-4} 2.830×10^{-4} 1.036×10^{-4}	24.7 58.4 21.4

5.0 UARS ATTITUDE DETERMINATION ACCURACY USING A DIFFERENTIAL CORRECTOR

The AGSS definitive attitude determination system is a batch least-squares differential corrector that estimates an epoch attitude and drift rate biases of the IRU over a batch of approximately one orbit of sensor data. This epoch attitude is propagated to uniform time intervals using the IRU data and the solved IRU biases. The results given in this section are the attitude covariances at the end of a one-orbit batch of data. It is assumed that data from both FHSTs are available every 32.768 seconds when there are valid stars in the FOV.

5.1 RESULTS USING PRELAUNCH PARAMETERS

The AGSS attitude solution uncertainties using the prelaunch values of the attitude sensor uncertainties presented in Section 2.0 are given below. For the two cases of star observability, as discussed in the introduction, the attitude uncertainties are given in Table 6.

Table 6. AGSS Attitude Uncertainties Using Prelaunch Alignment Uncertainties

Case	Axis	Attitude Uncertainty (3σ)	
		(Radians)	(Arc-Sec)
5-star	X Y Z	1.733×10^{-4} 3.143×10^{-4} 0.800×10^{-4}	35.7 64.8 16.5
29-star	X Y Z	1.582×10^{-4} 3.009×10^{-4} 1.452×10^{-4}	32.6 62.1 29.9

5.2 RESULTS USING ON-ORBIT ALIGNMENT ESTIMATES

The AGSS attitude solution uncertainties using the on-orbit estimates of the FHST alignment uncertainties presented in Section 3.0 are given in Table 7.

Table 7. AGSS Attitude Uncertainties Using On-Orbit FHST Alignment Uncertainties

Case	Axis	Attitude Uncertainty (3σ)	
		(Radians)	(Arc-Sec)
5-star	X Y Z	1.395×10^{-4} 2.900×10^{-4} 0.679×10^{-4}	28.8 59.8 14.0
29-star	X Y Z	1.384×10^{-4} 2.763×10^{-4} 1.156×10^{-4}	28.5 57.0 23.8

6.0 SSPP ATTITUDE DETERMINATION ACCURACY

This section reports estimates of the SSPP on-orbit misalignment determination accuracy and the SSPP attitude accuracies using both the estimated OBC attitude solution accuracy and the estimated AGSS attitude solution accuracy.

The SSPP attitude is represented as a transformation from the geocentric inertial (GCI) coordinate system to the SSPP coordinate system. This transformation can be expressed as a series of rotations

$$M_{NI} = M_{N\beta}\, M_{\beta\alpha}\, M_{\alpha m}\, M_{mI}$$

where M_{NI} is the SSPP attitude matrix, $M_{N\beta}$ and $M_{\alpha m}$ represent misalignments of the β-gimbal and the α-gimbal, respectively, $M_{\beta\alpha}$ is the product of two Euler rotation matrices about the two gimbal axes:

$$M_{\beta\alpha} = M_1(\beta)\; M_2(\alpha)$$

and M_{mI} represents the MACS attitude. The total SSPP attitude covariance matrix, P_{NI}, may be calculated from the transformations in the above equations and their corresponding covariance matrices as follows (Kast, 1987a, Section 3.1.1.7):

$$P_{NI} = M_{N\beta}\left[M_{\beta\alpha}(M_{\alpha m}P_{mI}M^T_{\alpha m} + P_{\alpha m})M^T_{\beta\alpha} + P_{\beta\alpha}\right]M^T_{N\beta} + P_{N\beta}$$

P_{mI} is the attitude covariance of either the OBC or the ground AGSS attitude solution, $P_{\alpha m}$ and $P_{N\beta}$ are the covariance matrices for the SSPP misalignment matrices, and $P_{\beta\alpha}$ is the covariance of the gimbal rotation. $P_{\beta\alpha}$ is computed from the prelaunch values for the gimbal rotation uncertainties and depends on the measured α and β angles:

$$P_{\beta\alpha} = \begin{bmatrix} \sigma_\beta^2 & 0 & 0 \\ 0 & \sigma_\alpha^2 \cos^2\beta & -\sigma_\alpha^2 \cos\beta \sin\beta \\ 0 & -\sigma_\alpha^2 \cos\beta \sin\beta & \sigma_\alpha^2 \sin^2\beta \end{bmatrix}$$

6.1 SSPP ON-ORBIT ALIGNMENT ESTIMATION RESULTS

In solving for the on-orbit estimate of the SSPP misalignment, the misalignment matrices are assumed to be small angle rotations of the form

$$M_{\alpha m} = \begin{bmatrix} 1 & \varepsilon_3 & -\varepsilon_2 \\ -\varepsilon_3 & 1 & \varepsilon_1 \\ \varepsilon_2 & -\varepsilon_1 & 1 \end{bmatrix}, \qquad M_{N\beta} = \begin{bmatrix} 1 & \delta_3 & -\delta_2 \\ -\delta_3 & 1 & \delta_1 \\ \delta_2 & -\delta_1 & 1 \end{bmatrix}$$

The angles ε_1, ε_2, ε_3 represent small rotations about the MACS axes, and the angles δ_1, δ_2, δ_3 represent small rotations about the SSPP axes. The angles ε_2 and δ_1 are equivalent to α- and β-gimbal angle biases, respectively.

A FORTRAN program was written to estimate the misalignment covariance matrices, $P_{\alpha m}$ and $P_{N\beta}$. Following Section 13.4 of Spacecraft Attitude Determination and Control (Wertz, 1984), a single 6-by-6 covariance matrix containing $P_{\alpha m}$ and $P_{N\beta}$ in the upper left and lower right, respectively, is computed assuming that the misalignment matrices were computed using a batch least squares differential corrector having the state vector (ε_1, ε_2, ε_3, δ_1, δ_2, δ_3).

To compute the misalignment covariances, it is necessary to assume a MACS attitude covariance for use in constructing an observation weight matrix. Because the SSPP misalignments will be calculated on the ground, the covariance used was the differential corrector results after on-orbit alignment of the FHSTs for the 29-star case as described in Section 5.0. Estimates of the accuracies of only the angles ε_1, ε_2, ε_3, and δ_1 are made as the remaining two angles were found to have poor observability. The resulting SSPP misalignment covariance matrices (in radians^2) are as follows:

$$P_{\alpha m} = \begin{bmatrix} 3.317 \times 10^{-11} & -1.337 \times 10^{-11} & -0.353 \times 10^{-11} \\ -1.337 \times 10^{-11} & 3.003 \times 10^{-11} & 1.494 \times 10^{-11} \\ -0.353 \times 10^{-11} & 1.494 \times 10^{-11} & 3.369 \times 10^{-11} \end{bmatrix}$$

and

$$P_{N\beta} = \begin{bmatrix} 3.839 \times 10^{-11} & 0 & 0 \\ 0 & 6.529 \times 10^{-9} & 0 \\ 0 & 0 & 6.529 \times 10^{-9} \end{bmatrix}$$

More information concerning the SSPP misalignment accuracy estimation is provided by Bosl (1987).

6.2 SSPP ATTITUDE ACCURACY USING KALMAN FILTER RESULTS

Table 8 presents the SSPP attitude uncertainties using the MACS attitude covariance of the OBC solution and the equations presented in Section 6.1. The values reported are after on-orbit alignment of the FHSTs. Because the SSPP attitude uncertainty for each SSPP axis depends on the gimbal angles, a typical gimbal position of α equal to 180 degrees and β equal to 45 degrees was chosen for reporting the per-axis uncertainty. The RSS of the three axes is independent of the gimbal angles and is also reported in Table 8.

Table 8. SSPP Attitude Uncertainties Using OBC Attitude Uncertainties After On-Orbit FHST Alignment

Case	Axis	Attitude Uncertainty (3σ)	
		(Radians)	(Arc-Sec)
5-star	X	1.726×10^{-4}	35.6
	Y	3.434×10^{-4}	70.8
	Z	3.289×10^{-4}	67.8
	RSS	5.059×10^{-4}	104.3
29-star	X	1.560×10^{-4}	32.2
	Y	3.374×10^{-4}	69.6
	Z	3.232×10^{-4}	66.7
	RSS	4.926×10^{-4}	101.6

6.3 SSPP ATTITUDE ACCURACY USING DIFFERENTIAL CORRECTOR RESULTS

The SSPP attitude uncertainties resulting from the AGSS attitude solution covariance after on-orbit FHST alignment are given in Table 9. As in Section 6.2, these values are at gimbal angles of α equal to 180 degrees and β equal to 45 degrees.

Table 9. SSPP Attitude Uncertainties Using AGSS Attitude Uncertainties After On-Orbit FHST Alignment

Case	Axis	Attitude Uncertainty (3σ)	
		(Radians)	(Arc-Sec)
5-star	X	1.718×10^{-4}	35.4
	Y	3.293×10^{-4}	67.9
	Z	3.283×10^{-4}	67.7
	RSS	4.957×10^{-4}	102.2
29-star	X	1.708×10^{-4}	35.2
	Y	3.387×10^{-4}	69.9
	Z	3.201×10^{-4}	66.0
	RSS	4.963×10^{-4}	102.4

7.0 CONCLUSIONS

Comparison of the estimates of the OBC and AGSS attitude determination uncertainties shows no significant differences. The ADEAS results indicate that most of the uncertainty for both the OBC and the AGSS is due to the effect of the FHST alignment uncertainties. This effect is the reason that there is little difference between the 5-star case and the 29-star case. The FHST alignment uncertainties given in Table 3 are not much less than the prelaunch values. This result is due to attempting to estimate six uncertainty values when three of the six degrees of freedom are unobservable. There is, therefore, a strong, unavoidable dependence on the prelaunch alignment uncertainties.

For all cases, the X- and Z-axes have 3σ uncertainties of approximately 1.454×10^{-4} radians (30 arc-sec), and the Y-axis has a 3σ uncertainty of approximately 2.909×10^{-4} radians (60 arc-sec). Based on the results of this study, it is recommended that these uncertainties be used in UARS error budget analyses.

REFERENCES

Adcole Corporation, "Critical Design Review Data Package: Platform Sun Sensor," SVS 11064, November 19, 1986

Bendat, J. S. and A. G. Pierool, Random Data: Analysis and Measurement Procedures, New York: Wiley-Interscience, 1971

Bosl, W., "Solar-Stellar Pointing Platform (SSPP) Definitive Attitude Accuracy Study," Computer Sciences Corporation, CSC/TM-87/6020, Mission Report 87004, 1987

Computer Sciences Corporation, Attitude Determination Error Analysis System (ADEAS) User's Reference Manual, CSC/SD-86/6025, December 1986

Fang B. and W. Davis, Attitude Determination Error Analysis (ADEAS) Program Requirements and Mathematical Specifications, Computer Sciences Corporation, CSC/TM-83/6175, December 1983

General Electric, Instrument Module Attitude Determination Study for Upper Atmosphere Research Satellite, 83SDS4202, January 1983

General Electric, "SSPP Controls Presentation", June 13, 1986

General Electric, UARS Attitude Determination and Control Subsystem Level, Critical Design Review, February 2, 1988

Kast, J. K., K. Krack, et al., Upper Atmosphere Research Satellite (UARS) Flight Dynamics Support System (FDSS) Specifications Volume II: Functional Specifications, Computer Sciences Corporation, CSC/TR-86/6003, May 1987a

Kast, J. K., K. Krack, et al., Upper Atmosphere Research Satellite (UARS) Flight Dynamics Support System (FDSS) Mathematical Background, Computer Sciences Corporation, CSC/TM-86/6060, May 1987b

Neste, S. L., UARS Pointing Error Budgets, General Electric PIR U-1K21-UARS-517A, March 20, 1987

Sheldon, K., On-Board Star Catalog for UARS, General Electric PIR U-1k21-UARS-318, January 1986

Shuster, M.D, "In-Flight Estimation of Spacecraft Attitude Sensor Accuracies and Alignments," J Guidance, July-August 1982, vol. 5, vo. 4, pp. 339-343

Wertz, J. R. (ed.), Spacecraft Attitude Determination and Control, Dortrecht, Holland: D. Reidel Publishing Co., 1984

Maneuvering Strategies Using CMGs

H.S. Oh and S.R. Vadali
Department of Aerospace Engineering
Texas A&M University
College Station, TX 77843

ABSTRACT

This paper considers control strategies for maneuvering spacecraft using Single-Gimbal Control Momentum Gyros. A pyramid configuration using four gyros is utilized. Preferred initial gimbal angles for maximum utilization of CMG momentum are obtained for some known torque commands. Feedback control laws are derived from the stability point of view by using the Liapunov's Second Theorem. The gyro rates are obtained by the pseudo-inverse technique. The effect of gimbal rate bounds on controllability are studied for an example maneuver. Singularity avoidance is based on limiting the gyro rates depending on a singularity index.

INTRODUCTION

Control Moment Gyros (CMGs) are attractive spacecraft attitude control devices. They require no expendable propellant, which are of limited quantity and may contaminate the spacecraft environment. Their fixed rotor speeds minimize structure dynamic excitations. They are also capable of rapid slewing maneuvers and precision pointing. There are two types of CMGs; single-gimbal and double-gimbal.

The single-gimbal CMGs have the advantages of possessing relative mechanical simplicity and producing amplified torques directly on the spacecraft. However, development of control laws for their use is made difficult by the existence of internal singular states. External singular states correspond to directional angular momentum saturation. For any system of n CMGs and any direction in space, there exists a set of 2^n gimbal angles for which no torque can be produced in that direction [1]. For double-gimbal CMGs in parallel configuration, Kennel's law [2] has seen wide applications. In this paper, four single-gimbal CMGs in a pyramid configuration (as depicted in Fig. 1) are utilized.

Margulies and Aubrun [1] present a geometric theory of CMG systems. They characterize the momentum envelope of a cluster of CMGs and identify the internal singular states. Yosnikawa [3] presents a steering law for a roof-type configuration with four CMGs. His steering law is based on making all the internal singular states unstable by providing two jumps with hystereses around the singularities. Cornick [4] developed singularity avoidance control laws for the pyramid configuration. His technique is based on the ability to calculate the instantaneous locations of all singularities. Hefner and McKenzie [5] developed a technique for maximizing the minimum torque capability of a cluster of CMGs in the pyramid configuration. Recently Bauer

[6] showed that it is impossible to avoid some singularities and in general, no global singularity avoidance steering law can exist.

In the existing literature, the most commonly used steering law is based on the pseudo-inverse technique. Neglecting the effect of spacecraft rotation, the angular momentum H of the CMG cluster evolves as

$$\frac{d\underline{H}}{dt} = \underline{T} \tag{1}$$

where $\underline{T}$ is the torque demand.
This can also be written as

$$\frac{d\underline{H}}{dt} = C\underline{\dot{\sigma}} \tag{2}$$

where C is a matrix function of the gimbal angles $\underline{\sigma}$. From Eq. (1) and (2), we obtain

$$C\underline{\dot{\sigma}} = \underline{T} \tag{3}$$

Generally at least four CMGs are used for three-axis attitude control. Hence the pseudo-inverse is utilized to obtain gimbal rate commands from the torque command:

$$\underline{\dot{\sigma}} = C^T(CC^T)^{-1}\underline{T} \tag{4}$$

Some steering laws also employ null motion, i.e. gyro rate commands that produce no torque. Any null motion rate command $\underline{\dot{\sigma}}_N$ can be expressed as

$$\dot{\underline{\sigma}}_N = ([I] - C^T(CC^T)^{-1}C)\,\underline{V} \tag{5}$$

where $[I]$ is the identity matrix of the same dimension as the number of gyros and $\underline{V}$ is any arbitrary vector of appropriate dimension. The fact that $\dot{\underline{\sigma}}_N$ commands do not produce any torques can be verified by premultiplying C throughout Eq. (5).

The basis for singularity avoidance has been to provide appropriate null motion along with torque providing motion so that the required torques are produced as well as singular states are avoided. Typically, at singular states some of the gyros develop anti-parallel momentum configurations. Thereby their full momentum capability cannot be utilized.

In this paper we present results pertaining to the following aspects of torque generation using CMGs:

1) Investigation of the existence of preferred initial gimbal angles at zero momentum, for given torque commands such that the maximum momentum capability is utilized.

2) Feedback control of rotational maneuvers of spacecraft by using Liapunov's second theorem and investigation of the effects of gimbal rate bounds on controllability and performance.

SYSTEM EQUATIONS OF MOTION

An arbitrary asymmetric spacecraft, with the location of the ith single-gimbal gyro, is shown in Fig. 2. Spacecraft attitude is represented by Euler parameter vector $\underline{\beta}$. The differential equations for the attitude are given by the angular velocity vector $\bar{\omega}$ of the vehicle and an orthogonal attitude matrix $G(\beta)$ as follows:

$$\dot{\underline{\beta}} = \frac{1}{2} G(\beta) \bar{\omega} \tag{6}$$

where $\bar{\omega} = \begin{Bmatrix} 0 \\ \omega_x \\ \omega_y \\ \omega_z \end{Bmatrix}$ and $G(\beta) = \begin{bmatrix} \beta_0 & -\beta_1 & -\beta_2 & -\beta_3 \\ \beta_1 & \beta_0 & -\beta_3 & \beta_2 \\ \beta_2 & \beta_3 & \beta_0 & -\beta_1 \\ \beta_3 & -\beta_2 & \beta_1 & \beta_0 \end{bmatrix}$

To derive the equations of motion, we follow Junkins and Turner |7|. The detailed notation appears at the end of the paper. Ross and Melton |8| present an alternate formulation for double-gimbal CMG systems.

The total angular momentum of the system $\underline{H}^{s/c}$ about the system mass center c is composed of the vehicle's angular momentum and that of the CMGs as follows

$$\underline{H}^{s/c} = \underline{H}^{v/c} + \sum_{i=1}^{n} \underline{H}^{G_i/c} .$$

Each angular momentum can be expressed in vehicle frame $(\hat{\underline{v}})$ as

$$\underline{H}^{v/c} = I^{v/c} \underline{\omega} , \text{ and}$$

$$\underline{H}^{G_i/c} = m_i(r_i \times \dot{\underline{r}}_i) + \underline{H}^{G_i/cG_i}$$

$$= M_i \underline{\omega} + \underline{H}^{G_i/cG_i} .$$

Then the system angular momentum can be written as

$$\underline{H}^{s/c} = (I^{v/c} + \Sigma M_i)\underline{\omega} + \Sigma\,\underline{H}^{G_i/cG_i}$$

$$= I\underline{\omega} + \Sigma\,\underline{H}^{G_i/cG_i}$$

where $I = I^{v/c} + \Sigma M_i$, i.e. the inertia matrix of vehicle body and point-massed gyro cluster about the c in vehicle frame.

For the convenience of simulation, we assume that

1) the center of the pyramid bottom surface coincides with the mass center c of the system.

2) the principal axes coincide with the axes of the vehicle frame $(\hat{\underline{v}})$.

3) Only the relative axial angular momenta of the gyros are retained.

With these assumptions, the system angular momentum in vehicle frame can be expressed as

$$\underline{H}^{s/c} = I\,\underline{\omega} + \Sigma C_i^T\,\underline{h}_i \tag{7}$$

where C_i is the direction cosine matrix of each gimbal frame $(\hat{G})$ with respect to vehicle frame $(\hat{\underline{v}})$,i.e. $(\hat{\underline{G}}_i) = C_i(\hat{\underline{v}})$.

The time derivatives of the total angular momentum of the system with respect to inertial frame $(\hat{\underline{n}})$ is equal to the external torque $\underline{L}_c$ exerted on the system about the mass center c:

$$\underline{L}_c = \frac{d}{dt}\,(\underline{H}^{s/c})_N \tag{8}$$

The above equation can be rewritten as

$$\underline{L}_C = I\dot{\underline{\omega}} + \tilde{\omega} I \underline{\omega} + \Sigma(\tilde{\omega}\, C_i^T \underline{h}_i + C_i^T\, \tilde{\dot{\sigma}}_i \underline{h}_i) + \Sigma\, C_i^T\, \dot{\underline{h}}_i$$

where $\tilde{\omega} = \begin{bmatrix} 0 & -\omega_z & \omega_y \\ \omega_z & 0 & -\omega_x \\ -\omega_y & \omega_x & 0 \end{bmatrix}$ and $\tilde{\dot{\sigma}}_i = \begin{bmatrix} 0 & -\dot{\sigma}_i & 0 \\ \dot{\sigma}_i & 0 & 0 \\ 0 & 0 & 0 \end{bmatrix}$.

In the absence of external torques and when the spin rate of wheel is constant, $\underline{L}_C = 0$ and $\dot{\underline{h}}_i = 0$. Thus the system equations of motion are

$$\dot{\underline{\omega}} = -I^{-1}\tilde{\omega}\; I\; \underline{\omega} - I^{-1}\; \Sigma(\tilde{\omega}\; C_i^T \underline{h}_i + C_i^T \tilde{\dot{\sigma}}_i \underline{h}_i) \tag{9}$$

SYSTEM CONFIGURATION

In this paper, the pyramid configuration for four CMGs is considered as depicted in Fig. 1. With this configuration, the CMG angular momentum in Eq. (7) can be written as

$$\sum_{i=1}^{4} C_i^T \underline{h}_i = h \begin{bmatrix} -C\delta S\sigma_1 - C\sigma_2 + C\delta S\sigma_3 + C\sigma_4 \\ C\sigma_1 - C\delta S\sigma_2 - C\sigma_3 + C\delta S\sigma_4 \\ S\delta S\sigma_1 + S\delta S\sigma_2 + S\delta S\sigma_3 + S\delta S\sigma_4 \end{bmatrix} \tag{10}$$

where h is the magnitude of each CMG's angular momentum and $\Sigma\, C_i^T\, \tilde{\dot{\sigma}}_i \underline{h}_i$ in Eq. (9) can be written as

$$\sum_{i=1}^{4} C_i^T\, \tilde{\dot{\sigma}}_i \underline{h}_i = C\dot{\underline{\sigma}} = \begin{bmatrix} -C\delta C\sigma_1 & S\sigma_2 & C\delta C\sigma_3 & -S\sigma_4 \\ -S\sigma_1 & -C\delta C\sigma_2 & S\delta_3 & C\delta C\sigma_4 \\ S\delta C\sigma_1 & S\delta C\sigma_2 & S\delta C\sigma_3 & S\delta C\sigma_4 \end{bmatrix} \begin{Bmatrix} \dot{\sigma}_1 \\ \dot{\sigma}_2 \\ \dot{\sigma}_3 \\ \dot{\sigma}_4 \end{Bmatrix}$$

We select $\delta = 54.74^\circ$ in this configuration to minimize the angular momentum requirements as recommended by Meffe [9]. With this configuration, we consider the preferred initial gimbal angles for some known torque profiles.

Determination of Preferred Initial Gimbal Angles

Perhaps the most severe demand on the CMGs is a unidirectional torque. Bauer [6] shows that for the present CMG configuration and pseudo-inverse steering law, if the torque demand is 1 unit about the x-axis, the CMG cluster encounters an internal singularity at a momentum value of 1.15h. This corresponds to an antiparallel situation. The initial gimbal angles are $\underline{\sigma} = [0^\circ\ \ 0^\circ\ \ 0^\circ\ \ 0^\circ]^T$ and the angles at the singularity are $\underline{\sigma} = [-90^\circ\ \ 0^\circ\ \ 90^\circ\ \ 0^\circ]^T$. From Eq. (10), it can be observed that the CMG angular momentum distribution at the singularity is $\underline{H} = [2hc\delta\ \ 0\ \ 0]^T$. To utilize the maximum momentum capability, we calculate the desired final angular momentum corresponding to saturation. At saturation, all the momentum vectors should point along the x-axis, i.e. $\underline{\sigma} = [-90^\circ\ \ 180^\circ\ \ 90^\circ\ \ 0^\circ]^T$ and $\underline{H} = [h(2c\delta + 2)\ \ \ 0\ \ \ 0]^T = [3.1545\ h\ \ \ 0\ \ \ 0]^T$.

With the desired final gimbal angles (perturbed slightly) and a torque demand of $[-1\ \ 0\ \ 0]^T$, we integrate Eq. (4) backward until the zero angular momentum stage is reached. The preferred set of gimbal angles is obtained as $\underline{\sigma} = [-60^\circ\ \ 60^\circ\ \ 120^\circ\ \ -120^\circ]^T$. Similarly, several initial gimbal angles are obtained for other desired torques as shown in Table 1. It should be noted that the set $[-120^\circ\ \ -60^\circ\ \ 60^\circ\ \ 120^\circ]$ is also good for a torque demand of $[1\ \ 0\ \ 0]^T$. During our experimentation, we found this gimbal angle set could avoid singularities for torques constrained to the x, y directions. However, we did not experiment with time varying torques.

TABLE 1. Preferred Initial Gimbal Angles

Torque Demand	Initial Gimbal Angles
[1 0 0]	[-60° 60° 120° -120°]
[0 1 0]	[-120° -60° 60° 120°]
[0 0 1]	[0° 0° 0° 0°]
[1 1 1]	[0° 0° 0° 0°]
[4 2 0]	[-60° 60° 120° -120°]
[2 4 0]	[-120° -60° 60° 120°]

FEEDBACK CONTROL

Feedback control laws can be determined using the Liapunov stability theory. Vadali and Junkins [10] developed the feedback control laws for spacecraft maneuvers with external torques and reaction wheels. In this section we derive a feedback control law for a slewing maneuver of a spacecraft with CMGs when no external torques exist.

The general equations for attitude and dynamics of the system are given by Equations (6) and (9). Let the target orientation $\underline{\beta}_f^T = [1 \;\; 0 \;\; 0 \;\; 0]$ and the final target angular velocity of vehicle $\underline{\omega}_f^T = [0 \;\; 0 \;\; 0]$. The error vectors $\underline{e}_1$, and $\underline{e}_2$ which represent the departure of the instantaneous states from the desired terminal states can be written as

$$\underline{e}_1 = \underline{\beta} - \underline{\beta}_f$$

$$\underline{e}_2 = \underline{\omega} - \underline{\omega}_f = \underline{\omega}$$

Let V(e) be a trial Liapunov function defined as

$$V(e) = k\, \underline{e}_1^T\, \underline{e}_1 + \frac{1}{2}\, \underline{e}_2^T\, I\, \underline{e}_2$$

where k is a positive constant. The time derivative of V is given by

$$\dot{V}(e) = 2k\, \underline{e}_1^T\, \dot{\underline{e}}_1 + \underline{e}_2^T I\, \dot{\underline{e}}_2$$

$$= 2k(\underline{\beta}^T - \underline{\beta}_f^T)\, \dot{\underline{\beta}} + \underline{\omega}^T I \dot{\underline{\omega}}$$

Using the identities

$$\underline{\beta}^T \dot{\underline{\beta}} = 0 \quad ,$$

$$\dot{\underline{\beta}} \quad = \frac{1}{2}\, G(\beta)\bar{\omega} \text{ , and}$$

$$I\dot{\underline{\omega}} \quad = -\tilde{\omega}\, I\underline{\omega} - \Sigma(\tilde{\omega}\, C_i^T \underline{h}_i + C_i^T\, \dot{\tilde{\sigma}}_i \underline{h}_i) \text{ ,}$$

$\dot{V}(\underline{e})$ can be written as

$$\dot{V}(e) = -k\, \underline{\beta}_f^T\, G(\beta)\bar{\omega} + \underline{\omega}^T(-\tilde{\omega} I \underline{\omega} - \Sigma(\tilde{\omega} C_i^T \underline{h}_i + C_i^T\, \dot{\tilde{\sigma}}_i \underline{h}_i))$$

However, $\underline{\omega}^T \tilde{\omega} = 0$ and $-k\beta_f^T G(\underline{\beta})\bar{\omega} = -\underline{\omega}^T(-k\bar{\beta})$
where $\bar{\beta}^T = |\beta_1\ \beta_2\ \beta_3|$. Hence $\dot{V}(\underline{e})$ can be simplified as

$$\dot{V}(e) = -\underline{\omega}^T(-k\bar{\beta} + \Sigma C_i^T\, \dot{\tilde{\sigma}}_i \underline{h}_i).$$

For $\dot{V}(e)$ to be negative definite, we can choose a linear feedback control as

$$-k\bar{\beta} + \Sigma\, C_i^T\, \dot{\tilde{\sigma}}_i \underline{h}_i = K\underline{\omega}$$

where K is a positive definite constant matrix

$$K = \begin{bmatrix} K_1 & 0 & 0 \\ 0 & K_2 & 0 \\ 0 & 0 & K_3 \end{bmatrix} .$$

$\Sigma\, C_i^T\, \dot{\tilde{\sigma}}_i \underline{h}_i$ can be written as $C\dot{\underline{\sigma}}$ where C is a matrix whose rows compose of first row of directoin cosine matric C_i of each CMG gimbal frame with respect to $(\hat{\underline{V}})$. Then the feedback control law becomes

$$C\dot{\underline{\sigma}} = K\underline{\omega} + k\bar{\beta}.$$

Usually the number of CMGs cluster is more than three. Then we can choose the minimum norm solution for a rate control $\dot{\underline{\sigma}}$ as

$$\dot{\underline{\sigma}} = C^{+}\,(K\underline{\omega} + k\bar{\beta}) \tag{11}$$

where C^{+} is a pseudo-inverse of C.
Thus we have the same form for $\dot{\underline{\sigma}}$ as Eq. (4).

Simulation

Equations (6), (9) and (11) are a complete set of equations which are needed for a simulation. With a pyramid configured CMG cluster as depicted in

Fig. 1, we present a simulation of a slewing maneuver. For critical damping, the gains K and k are chosen as [10]

$$K_i^2 = 2I_i k \qquad (i = 1,2,3)$$

The numerical data and boundary conditions are shown in Table 2 and Table 3. Near a singularity, the determinant of CC^T becomes almost zero. The required magnitude of control rate $|\dot{\sigma}_i|$ increases enormously and exceeds the control limit $|\dot{\sigma}|_{limit}$. To avoid a singularity, Cornick [4] suggests a method using the "null" motion. However, in this paper we choose the determinant test to avoid a singularity. That is, when det. (CC^T) is less than Det._{limit}, we simply hold $\dot{\sigma}$ at its most previous value. After escaping from a singularity, we use the pseudo-inverse technique again. The selection of Det._{limit} is based on the required $|\dot{\sigma}_{limit}|$.

The simulation results show that without any method of avoiding singularity, the determinant of CC^T becomes almost zero many times as depicted in Fig. 3. When using the determinant test method, many would-be singular points are passed through with reasonable gyro rates although during the passages there are some fluctuations in gyro rates as depicted in Fig. 4 and Fig. 5. However, the feedback control law works very well as shown in Figs. 6 and 7. The gimbal angles are shown in Fig. 8 and the demanded torques in Fig. 9. The maneuver takes about 170 sec.

TABLE 2. Numerical Data

Item	Values
I_x	86.215 kg-m^2
I_y	85.07 kg-m^2
I_z	113.565 kg-m^2
h	1.8 kg-m^2
k_1	13.13 N-m-sec
k_2	13.04 N-m-sec
k_3	15.08 N-m-sec
k	1.0 N-m
δ	54.74°
Det_{limit}	0.1

TABLE 3. Boundary Conditions

State	Initial Conditions	Final Conditions
β_0	0.7071	1
β_1	0.7071	0
β_2	0	0
β_3	0	0
ω_x	0.01 r/sec	0
ω_y	0.05 r/sec	0
ω_z	0.001 r/sec	0

CONCLUSION

Rotational maneuvers of spacecraft with single-gimbal CMGs is treated. The fact that some sets of initial gimbal angles avoid singularities for unidirectional and planar torque demands is observed. The feedback control law based on Liapunov theory works well with the single-gimbal CMG system. Avoidance of large fluctuations in $\dot{\underline{\alpha}}$ needs further study.

REFERENCES

|1| Margulies, G and Aubrun, J.N., "Geometric Theory of Single-Gimbal Control Moment Gyro Systems," J. of Astronautical Sciences, Vol. XXVI, No. 2, pp. 159-191, April-June 1978.

|2| Kennel, H.F., "Steering Law for Parallel Mounted Double-Gimballed Control Moment Gyros - Revision A," NASA TM-82390, Jan. 1981.

|3| Yoshikawa, T., "Steering Law for Roof Type Configuration Control Moment Gyro System," Automatica, Vol. 12, pp. 359-368, 1977.

|4| Cornick, D.E., "Singularity Avoidance Control Laws for Single Gimbal Control Moment Gyros," AIAA paper No. 79-1698, Aug. 1979.

|5| Hefner, R.D. and McKenzie, C.H., "A Technique for Maximizing the Torque Capability of Control Moment Gyro Systems," AAS paper No. 83-387.

|6| Bauer, S.R., "Single Gimbal CMG Steering Laws," SGNM No. 10E-87-06, 10E-87-09, Charles Stark Draper Laboratory, Inc., May 1987.

|7| Junkins, J.L. and Turner, J.D., Optimal Spacecraft Rotational Maneuvers, studies in Astronautics 3, Elsevier Scientific Publishing Company, New York, 1985.

|8| Ross, I.M. and Melton, R.G., "Quaternion Formulation of Rotational Dynamics for a Double-Gimbaled Momentum Wheel Control System," AAS paper No. 87-510, August 1987.

|9| Meffe, M., "Control Moment Gyroscope Configurations for the Space Station," AAS paper No. 88-040, Jan.-Feb. 1988.

|10| Vadali, S.R. and Junkins, J.L., "Optimal Open-Loop and Stable Feedback Control of Rigid Spacecraft Attitude Maneuvers," J. of the Astronautical Sciences, Vol. 32, No. 2, April-June 1984, pp. 105-122.

NOMENCLATURE

$\underline{H}^{s/c}$: angular momentum of system about mass center c in vehicle frame $\{\hat{\underline{v}}\}$

$\underline{H}^{v/c}$: angular momentum of vehicle about mass center c in $\{\hat{\underline{v}}\}$

$\underline{H}^{G_i/c}$: angular momentum of gyro about mass center c in $\{\hat{\underline{v}}\}$

$\underline{H}^{G_i/cG_i}$: angular momentum of gyro about gyro mass center cG_i in $\{\hat{\underline{v}}\}$

$I^{v/c}$: inertia matrix of vehicle about c with respect to vehicle frame $\{\hat{\underline{v}}\}$

I : inertia matrix of vehicle and point-massed gyro clusters about c with respect to $\{\hat{\underline{v}}\}$

M_i : i^{th} gyro point-massed inertia matrix about c with respect to $\{\hat{\underline{v}}\}$.

$\underline{h}_i$: i^{th} gyro relative angular momentum in gimbal frame, $\underline{h}_i^T = [0\ h\ 0]$

m_i : i^{th} gyro mass

$c\delta$: $\cos(\delta)$

$s\delta$: $\sin(\delta)$

δ : configuration angle of pyramid

$\underline{\omega}$: spacecraft angular velocity, $\underline{\omega}^T = [\omega_x\ \omega_y\ \omega_z]$

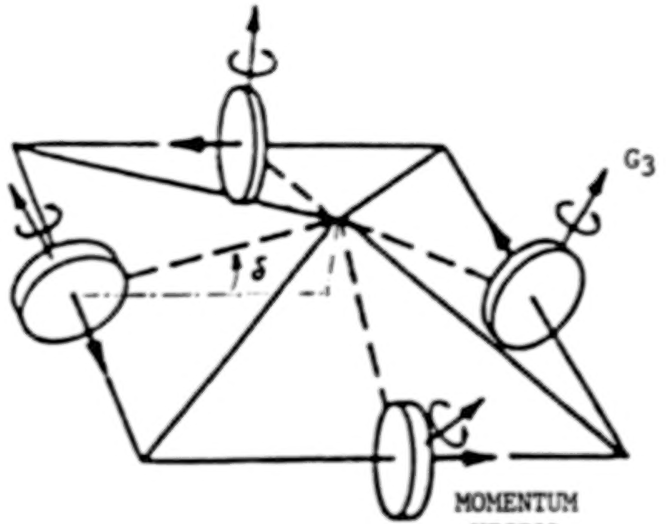
G3
δ
MOMENTUM VECTOR

Fig. 1. CMG Configuration

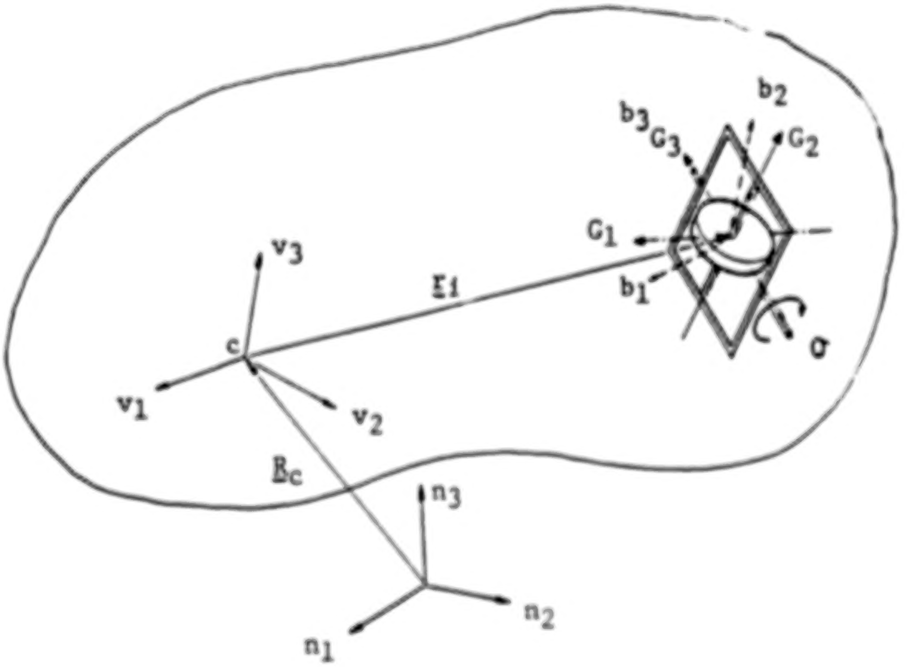
b2
b3
G3
G2
G1
b1
σ
v3
ri
c
v1
v2
Rc
n3
n2
n1

Fig. 2. System with i^{th} gyro

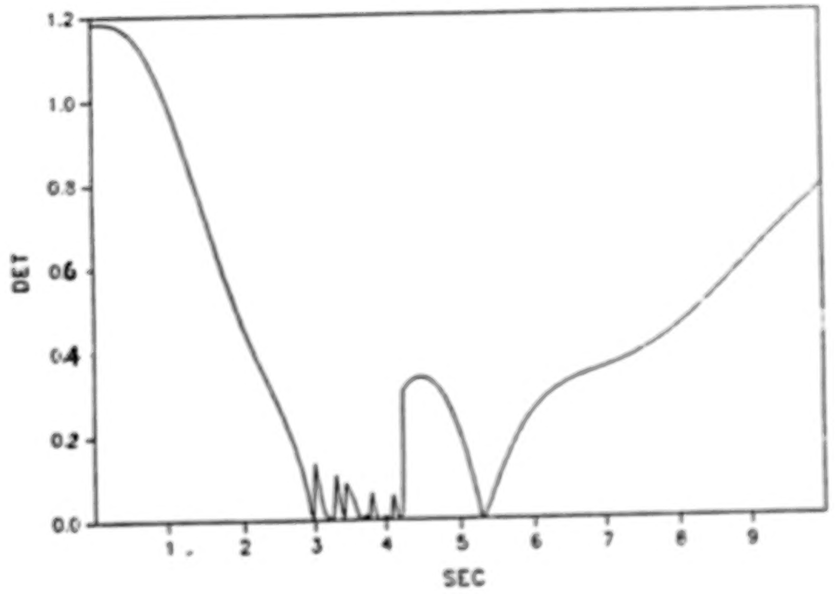

Fig. 3. Determinant of (CC^T) w/o bounds on control

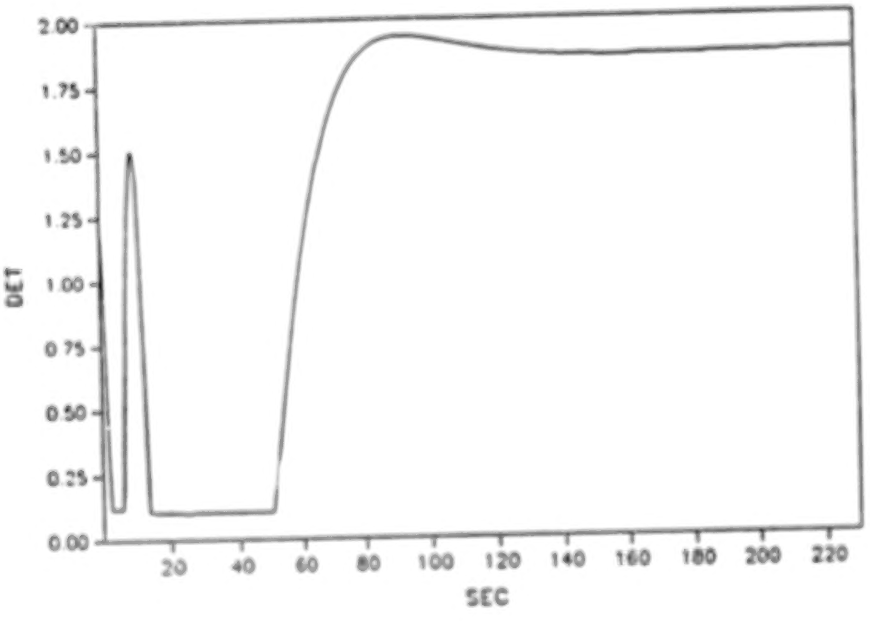

Fig. 4. Determinant of (CC^T) with limit $\text{Det.}_{\text{lim.}}$

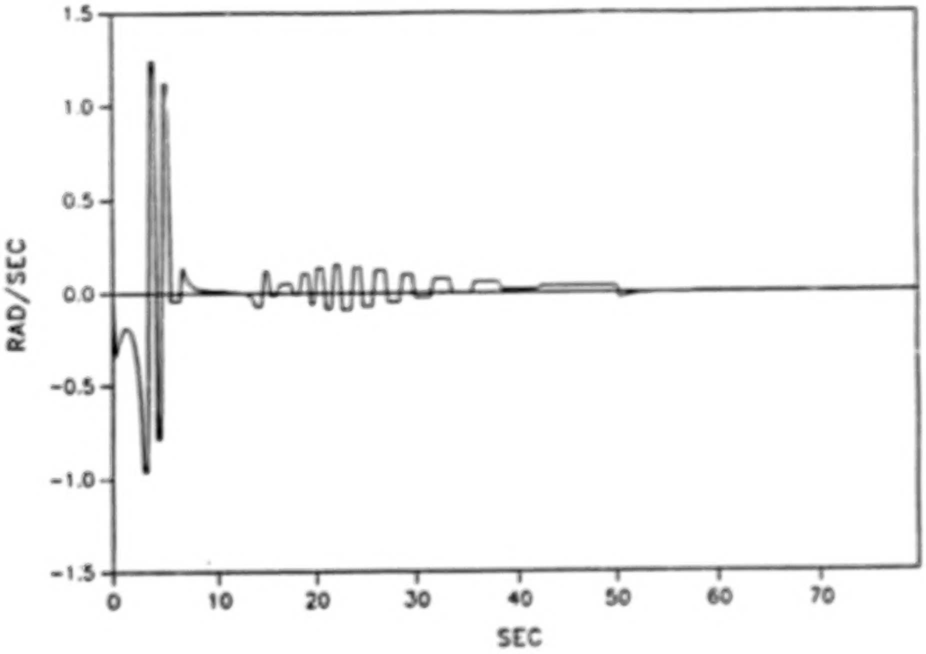

(a) The 1st gyro gimbal rate

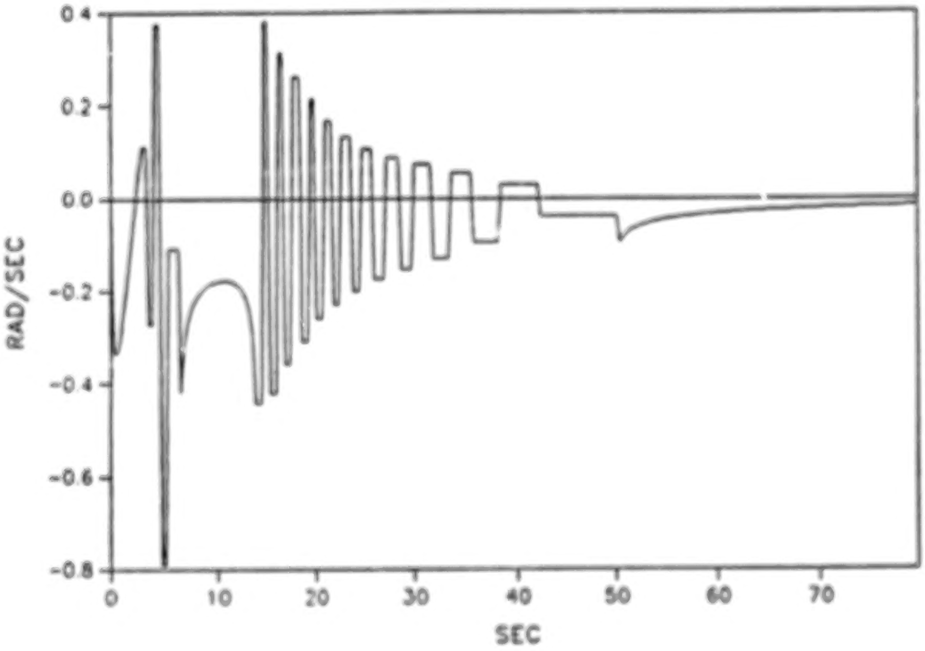

(b) The 2nd gyro gimbal rate

Fig. 5 Gyro gimbal rates

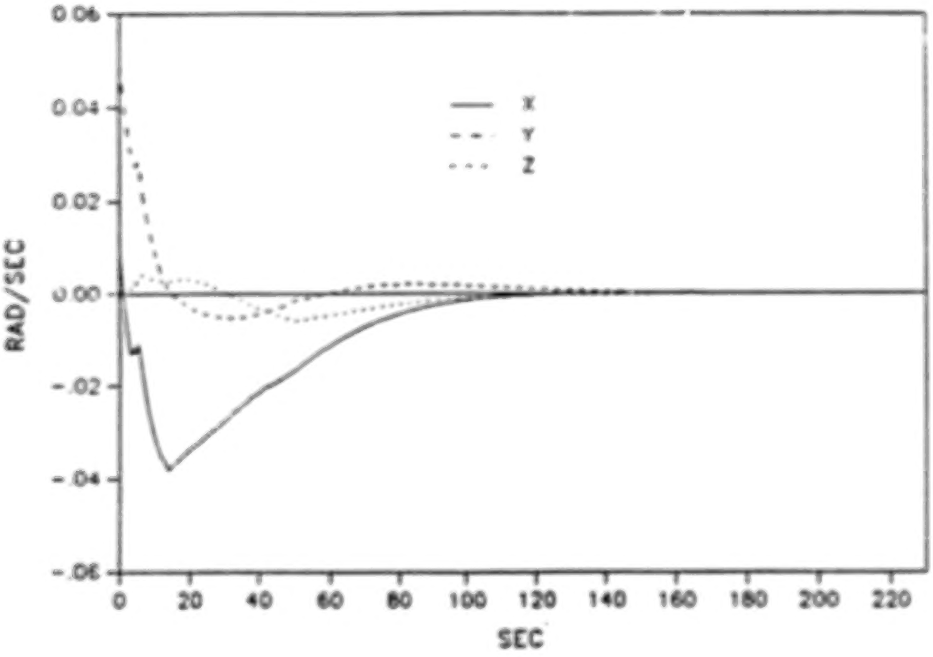

Fig. 6. Angular velocities of spacecraft

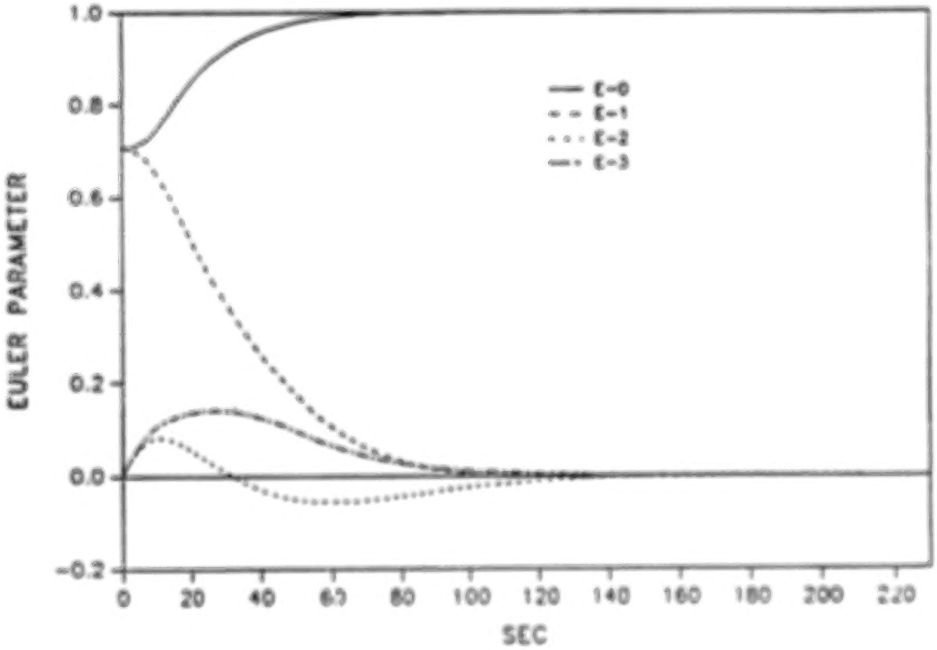

Fig. 7. Attitude of spacecraft

ORIGINAL PAGE IS
OF POOR QUALITY

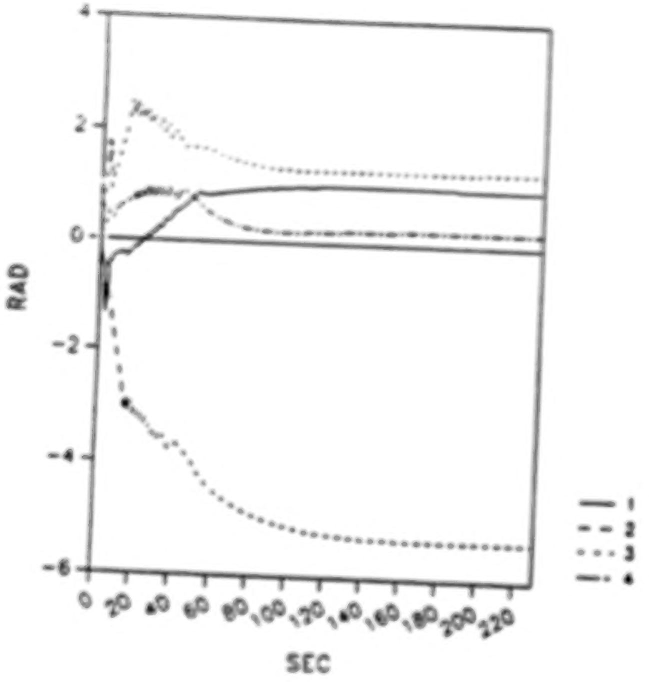

Fig. 8. Gimbal angles

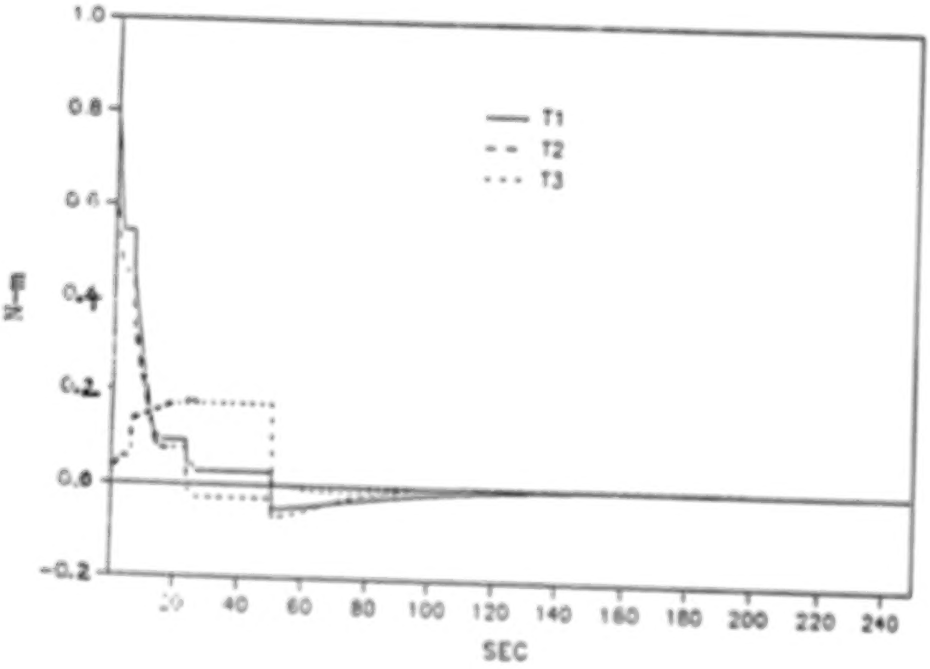

Fig. 9. Torque demands

N89-15938

MINIMAL PARAMETER SOLUTION
OF THE
ORTHOGONAL MATRIX DIFFERENTIAL EQUATION

by

Itzhack Y. Bar-Itzhack* and F. Landis Markley**

NASA - Goddard Space Flight Center
Greenbelt, MD 20771

Abstract

As proven in this work, all orthogonal matrices solve a first order differential equation. The straightforward solution of this equation requires n^2 integrations to obtain the elements of the the n-th order matrix. There are, however, only n(n-1)/2 independent parameters which determine an orthogonal matrix. The questions of choosing them, finding their differential equation and expressing the orthogonal matrix in terms of these parameters are considered in this work. Several possibilities which are based on attitude determination in three dimensions (3-D) are examined. It is shown that not all 3-D methods have useful extensions to other dimensions. It is also shown why the rate of change of the matrix elements, which are the elements of the angular rate vector in 3-D, are the elements of a tensor of the second rank (dyadic) in spaces other than three dimensional. It is proven that the 3-D Gibbs vector (or Cayley Parameters) are extendible to other dimensions. An algorithm is developed employing the resulting parameters, which are termed Extended Rodrigues Parameters, and numerical results are presented of the application of the algorithm to a fourth order matrix.

---

* National Research Council - NASA Resident Research Associate, Flight Dynamics Analysis Branch. On Sabbatical leave from the Aeronautical Engineering Department, Technion-Israel Institute of Technology, Haifa 32000, Israel.

** Head, Mathematical Analysis Section, Systems Development Branch.

I. INTRODUCTION

In a recent paper [1] a new algorithm for solving the matrix Riccati equation was introduced. The algorithm requires the solution of two matrix differential equations. The solution of one of the equations yields a diagonal matrix of the eigenvalues of P, the solution matrix of the Riccati equation. The other equation is

$$\dot{V}(t)=W(t)V(t) \tag{1}$$

where V is a matrix of the eigenvectors of P. Since P is a real symmetric matrix its eigenvectors are orthonormal, consequently V is an orthonormal matrix. (In the ensuing we will refer to an orthonormal matrix as an orthogonal one). The matrix W is a skew-symmetric matrix. (Note that in [1] the order of V and W on the right-hand side of (1) is reversed. This difference should cause no difficulty since V is the transpose of the corresponding matrix in [1] and W is the negative of its corresponding matrix).

Let n be the order of the square matrix V. The number of scalar integrations implied by (1) is n^2 ; however, the orthogonality of V invokes $n(n+1)/2$ relations among its elements. Therefore there are really only $m=n(n-1)/2$ independent elements in V. The superfluous computational burden involved in the solution of (1) can, then, be reduced by properly defining the m independent parameters of V, solving a differential equation only for them and then performing an algebraic computation in order to transform these m elements into V.

We observe that (1) is identical to the famous differential equation of the transformation matrix in the three dimensional Euclidean space which is solved on-line for attitude determination of navigation and satellite systems. That matrix, of course, is also orthogonal, and W is a skew-symmetric matrix whose entries are the three components of the angular velocity vector at which the body rotates with respect to some reference coordinates. One question that comes immediately to mind is: does (1) always yield a solution which is orthogonal? and conversely, do all orthogonal matrices solve such a differential equation?

The answer to these two questions is formulated in the following two theorems.

Theorem I.1: Given equation (1) for $t_o < t < t_1$ where

$$W^T(t) = -W(t) \tag{2}$$

then:

(I) The matrix $V^T(t)V(t)$ is a constant matrix.

(II) If the initial matrix $V(t_o)$ is orthogonal, then $V(t)$ is orthogonal too.

Proof:

$$\frac{d}{dt}\,[V^T(t)V(t)] = \dot{V}^T(t)V(t) + V^T(t)\dot{V}(t) \tag{3}$$

substituting (1) into (3) yields

$$\frac{d}{dt}\,[V^T(t)V(t)] = V^T(t)W^T(t)V(t) + V^T(t)W(t)V(t) \tag{4}$$

and when (2) is substituted into (4), it is seen that

$$\frac{d}{dt}\,[V^T(t)V(t)] = 0 \tag{5}$$

Consequently

$$V^T(t)V(t) = \text{Const.} \tag{6}$$

and thus (I) has been proven.

Now when $V(t_o)$ is orthogonal, then

$$V^T(t_o)V(t_o) = I$$

(where I denotes the identity matrix) and due to (6) also

$$V^T(t)V(t) = I$$

which proves assertion (II). ■

Theorem I.2: Any time varying orthogonal matrix, $V(t)$, satisfies the matrix differential equation

$$\dot{V}(t) = W(t)V(t) \tag{7}$$

where

$$W^T(t) = -W(t) \tag{8}$$

Proof: Since $V(t)$ is orthogonal

$$\dot{V}(t) = \dot{V}(t)V^T(t)V(t) \tag{9}$$

Denote

$$W(t) = \dot{V}(t)V^T(t)$$

then (9) can be written as

$$\dot{V}(t) = W(t)V(t) \tag{10}$$

which is (7).

Using (10) we write

$$\dot{V}^T(t)V(t) + V^T(t)\dot{V}(t) = V^T(t)W^T(t)V(t) + V^T(t)W(t)V(t)$$

$$= V^T(t)\ [W^T(t) + W(t)]\ V(t) \qquad (11)$$

The left-hand side of (10) is the time derivative of $V^T(t)V(t)$ hence (10) can be written as

$$\frac{d}{dt}\ [V^T(t)V(t)] = V^T(t)\ [W^T(t) + W(t)]\ V(t) \qquad (12)$$

But

$$V^T(t)V(t) = I$$

hence the left-hand side of (11) is zero which implies that

$$W^T(t) = -W(t)$$

as stated in (8). This completes the proof. ■

In view of the preceding, it is realized that the problem we are concerned with is an extension of the three dimensional attitude determination problem and conversely, the latter is a special case of the problem at hand. It is interesting to investigate the correspondence of the various elements involved in three dimensional attitude determination with the eventual solution and features of our present problem. For this reason the pertinent background material of attitude determination will be reviewed in Section III following a formal definition of the problem in the next section. In Section IV we discuss a possible solution using Extended Euler Angles followed, in Section V, by an introduction of the chosen Extended Rodrigues Parameter solution. In Section VI we probe the issue of presenting angular rate in n-D and in Section VII we discuss numerical issues involved in the implementation of the solution. Numerical results are then presented and conclusions are drawn in Section VIII.

II. PROBLEM STATEMENT

We state our problem as follows. Given the matrix differential equation

$$\dot{V}(t) = W(t)V(t)$$

in which W is a skew symmetric matrix and for which the initial matrix $V(t_o)$ is known to be orthogonal, find the following:

a) $m=n(n-1)/2$ parameters which unambiguously define V,

b) the differential equation needed to be solved in order to compute these parameters,

c) the functional relations between the parameters and V which will enable the computation of V based on the parameters, and

d) a simple algorithm to implement the solution of the differential equation as well as the computation of V.

III. BACKGROUND IN THREE DIMENSIONAL SPACE

Euler Angles [2-6]

The best known parameters describing a 3-D rotation and the resulting transformation matrix are Euler Angles. Three such angles are necessary and sufficient to describe any transformation from one Cartesian coordinate system to any other one. There are 12 sequences of 3 right-hand Euler Angle rotation sequences. If for example one chooses the sequence z-y-x rotations by the respective angles p, t and f, then the corresponding differential equations of the Euler Angles are

$$\dot{p} = (w_y \,\mathrm{sinf} + w_z \,\mathrm{cosf})/\mathrm{cost} \qquad (13.a)$$

$$\dot{t} = w_y \,\mathrm{cosf} - w_z \,\mathrm{sinf} \qquad (13.b)$$

$$\dot{f} = w_x + \mathrm{tant}\,(w_y \,\mathrm{sinf} + w_z \,\mathrm{cosf}) \qquad (13.c)$$

where w_x, w_y and w_z are the three components of the angular rate vector at which the final coordinate system turns with respect to the initial one when this vector is resolved in the final system. The transformation matrix, D, which transforms vectors from the initial coordinate system into the rotated one is computable using the solution of (13) in the following expression

$$D = \begin{bmatrix} \mathrm{cp\ ct} & \mathrm{sp\ ct} & \mathrm{-st} \\ \mathrm{-sp\ cf} + \mathrm{cp\ st\ sf} & \mathrm{cp\ cf} + \mathrm{sp\ st\ sf} & \mathrm{ct\ sf} \\ \mathrm{sp\ sf} + \mathrm{sp\ st\ cf} & \mathrm{-cp\ sf} + \mathrm{sp\ st\ cf} & \mathrm{ct\ cf} \end{bmatrix}$$

where s denotes the sine and c denotes the cosine functions.

We note two shortcomings of this method. First, we run into a singularity problem as t approaches 90° or -90° and, secondly we need to compute trigonometric functions. For this reason the use of Quaternions is usually preferred.

Quaternion [2,5,6]

Quaternions consist of 4 elements; that is, the Quaternion is a 4 parameter rotation specifier. One parameter is, of course, superfluous but this is acceptable since, using Quaternions, the two aforementioned shortcomings, involved in the usage of Euler Angles, are eliminated. Denote the 4 elements of the Quaternion of rotation by q_0, q_1, q_2 and q_3 then the differential equation of the Quaternion elements is

$$\frac{d}{dt}\begin{bmatrix} q_0 \\ q_1 \\ q_2 \\ q_3 \end{bmatrix} = \frac{1}{2}\begin{bmatrix} 0 & -w_x & -w_y & -w_z \\ w_x & 0 & w_z & -w_y \\ w_y & -w_z & 0 & w_x \\ w_z & w_y & -w_x & 0 \end{bmatrix}\begin{bmatrix} q_0 \\ q_1 \\ q_2 \\ q_3 \end{bmatrix} \tag{14}$$

The solution of (14) yields the components of the Quaternion which can be used to compute D as follows

$$D = \begin{bmatrix} q_0{}^2+q_1{}^2-q_2{}^2-q_3{}^2 & 2(q_1q_2-q_0q_3) & 2(q_3q_1+q_0q_2) \\ 2(q_1q_2+q_0q_3) & q_0{}^2-q_1{}^2+q_2{}^2-q_3{}^2 & 2(q_2q_3-q_0q_1) \\ 2(q_3q_1-q_0q_2) & 2(q_2q_3+q_0q_1) & q_0{}^2-q_1{}^2-q_2{}^2+q_3{}^2 \end{bmatrix}$$

The Quaternion of rotation is based on Euler's theorem which states that any orientation of a 3-D Cartesian coordinate system with respect to any reference system can be obtained by a single rotation of the initial coordinate system about an axis fixed in both systems. Let the positive direction (according to the right-hand rule) of this axis be denoted by a unit vector $\hat{f}$ and the rotation angle by f, then the components and the magnitude of the rotation vector $\hat{f}f$ (also known as Euler Vector) are used to define the Quaternion as follows

$$q_0=\cos(f/2) \quad ; \quad q_1=\sin(f/2)f_x/f$$

$$q_2=\sin(f/2)f_y/f \; ; \; q_3=\sin(f/2)f_z/f$$

were f_i, i=x,y,z, are the 3 components of the rotation vector.

The Quaternion is, then, a 4 component element constructed on a 3 component vector.

Rodrigues Parameters [7,8,6]

Another 3 parameter representation of 3-D rotation is due to Rodrigues [7]. Denote the parameters by g_1, g_2 and g_3 then the differential equation which these parameters satisfy is

$$\frac{d}{dt}\begin{bmatrix} g_1 \\ g_2 \\ g_3 \end{bmatrix} = \frac{1}{2}\begin{bmatrix} 1+g_1^2 & g_3+g_1g_2 & -g_2+g_1g_3 \\ -g_3+g_1g_2 & 1+g_2^2 & g_1+g_2g_3 \\ g_2+g_1g_3 & -g_1+g_2g_3 & 1+g_3^2 \end{bmatrix}\begin{bmatrix} w_x \\ w_y \\ w_z \end{bmatrix} \qquad (15)$$

The solution of (15) can, then, be used to compute D as follows

$$d = 1+g_1^2+g_2^2+g_3^2$$

$$D = \frac{1}{d}\begin{bmatrix} 1+g_1^2-g_2^2-g_3^3 & 2(g_1g_2-g_3) & 2(g_1g_3+g_2) \\ 2(g_1g_2+g_3) & 1-g_1^2+g_2^2-g_3^2 & 2(g_2g_3-g_1) \\ 2(g_1g_3-g_2) & 2(g_2g_3+g_1) & 1-g_1^2-g_2^2+g_3^2 \end{bmatrix}$$

The relationship between the Rodrigues Parameters and the rotation vector are

$$g_1 = \tan(f/2)f_x/f \quad ; \quad g_2 = \tan(f/2)f_y/f \quad ; \quad g_3 = \tan(f/2)f_z/f$$

Since both the Quaternion of rotation and Rodrigues Parameters are based in a similar manner on the rotation vector, there is a rather simple relationship between them; namely, $g_i = q_i/q_o$ $i=1,2,3$.

The preceding equations for the time change of the Rodrigues Parameter and for converting the parameters into D can be cast in matrix form as follows [9,10]. Define a G matrix such that

$$G = \begin{bmatrix} 0 & g_3 & -g_2 \\ -g_3 & 0 & g_1 \\ g_2 & -g_1 & 0 \end{bmatrix} \qquad (16)$$

and, similarly a W matrix

$$W = \begin{bmatrix} 0 & w_3 & -w_2 \\ -w_3 & 0 & w_1 \\ w_2 & -w_1 & 0 \end{bmatrix} \qquad (17)$$

then

$$\dot{G} = -\frac{1}{2}(I+G)W(I-G) \qquad (18)$$

$$D = (I-G)(I+G)^{-1} \qquad (19)$$

where I is the identity matrix. Like with the 3 parameter Euler Angle representation, here too singularity may occur whenever the size of the rotation vector reaches a magnitude of 180°.

After having discussed the possible solutions to the problem in 3-D we will consider, next, the possibility of extending these solutions to n-D (whenever mentioning n dimensional spaces we mean Euclidean spaces whose dimension $n \neq 3$).

IV. POSSIBLE SOLUTIONS

Extended Euler Angles

When trying to solve our problem (as defined in Section II) the first question that comes to mind is: can the Euler Angle parametrization presented in the preceding section be extended to higher dimensional Euclidean spaces? As it turns out [11], Euler himself showed that this was possible. This was also shown later by Lagrange [12]. (See also Jacobi's observation on their and others' work [13]). However, the use of the Extended Euler Angles for $n > 3$ is cumbersome since, for calculating V, the sine and cosine functions of $m=n(n-1)/2$ angles must be computed, these functions have to be multiplied through in a long string of multiplications, and the resultant products have to be added and subtracted. For $n=4$, for example, the 1,1 element of V is

$$v_{1,1} = \cos a_1 \cos a_3 \cos a_5 + \sin a_1 \sin a_4 \sin a_5$$

and there are 16 elements, all equally long, in V. When compared with the simplicity of the solution which we will eventually choose the complexity of the present one will be striking. Moreover, to complete the algorithm it is necessary to find the differential equations governing the Extended Euler Angles and solve them. Merely finding the equations, let alone solving them, is a formidable task. As an example for the work involved in deriving those equations, consider the following approach. Let the Extended Euler Angles be denoted by a_1, a_2, ..., a_m. Denote the column vector whose elements are the these angles by $\underline{a}$. We may express V as a product of the individual matrices $V(a_i)$ of the transformation matrix related to a single angle a_i, thus

$$V(\underline{a}) = \prod_{i=1}^{m} V(a_i) \qquad (20)$$

Differentiation of (20) yields

$$\dot{V}(\underline{a}) = \sum_{j=1}^{m} \dot{a}_j [\prod_{i=1}^{j-1} V(a_i)] \frac{dV(a_j)}{da_j} [\prod_{i=j+1}^{m} V(a_i)] \qquad (21)$$

On the other hand (20) and (1) yield

$$\dot{V}(\underline{a}) = W \sum_{i=1}^{m} V(a_i) \qquad (22)$$

equating the right-hand sides of (21) and (22) yields m equations in $\dot{a}_j$. After cumbersome manipulations we obtain the required m differential equations for a_j, j=1,2,...,m whose solution yields $\underline{a}$, the elements of which are needed in order to compute V. We conclude that finding the differential equations for the Extended Euler Angles, solving them, and then using the solutions to compute the corresponding V matrix, while possible, is indeed a formidable task which we reject in favor of the method which we will eventually select.

Extended Quaternion

The use of the quaternion of rotation in 3-D is motivated by the following considerations. It does not suffer from singularities, it does not require the computation of trigonometric functions, it has a simple linear differential equation and a simple geometric interpretation related to the rotation vector. Finally, the only price paid for using it, is the need to deal with 4 (rather than 3) parameters. Because of these merits, one is motivated to try to extend the notion of quaternions to n-D. This approach though does not seem to yield a non -singular parametrization even even if one is willing to use m+1 parameters to define an extended quaternion.

Of the three 3-D parametrization methods reviewed in Section III only the Rodrigues Parameters are extendible to a compact easily implementable algorithm. This will be shown in the next section.

V. EXTENDED RODRIGUES PARAMETERS

We start the presentation of this parametrization method in n-D with two lemmas which will be helpful in the ensuing.

Lemma V.1: Let A be an nxn matrix, then the matrix (I+A) is invertible iff none of the eigenvalues of A is equal to -1.

Proof:

The eigenvalues b_i , i=1,2,...,n of (I+A) are the roots of the polynomial

$$|(I+A) - bI| = 0 \tag{23}$$

which can be written as

$$|A - (b-1)I| = 0 \tag{24}$$

or

$$|A-aI| = 0 \tag{25}$$

where

$$a=b-1 \tag{26}$$

The condition for (I+A) to be invertible is $b_i \neq 0$, i=1,2,...,n or, in view of (26), $a_i \neq -1$, i=1,2,...,n. But in view of (25), a_i are the eigenvalues of A. This ends the proof. ■

Lemma V.2: Let $(I+A)^{-1}$ exist and let

$$B = (I-A)(I+A)^{-1}$$

then (I+B) is invertible.

Proof:

$$\begin{aligned}(I+B) &= I + (I-A)(I+A)^{-1} \\ &= (I+A)(I+A)^{-1} + (I-A)(I+A)^{-1} \\ &= 2(I+A)^{-1}\end{aligned}$$

Obviously, $(I+A)^{-1}$ has an inverse which is (I+A), thus

$$(I+B)^{-1} = (I+A)/2.$$ ■

With these lemma on hand we can proceed and prove the following theorem.

Theorem V.1: Let V be an n-th order orthogonal matrix with none of its eigenvalues equal to -1 then

I) there exists a matrix G defined as follows

$$G = (I-V)(I+V)^{-1} \tag{27}$$

II) G is skew-symmetric

III) V is the following function of G

$$V = (I-G)(I+G)^{-1} \tag{28}$$

IV) the rate of change of G is given by

$$\dot{G} = -\frac{1}{2}(I+G)W(I+G)^T \tag{29}$$

Proof: From lemma V.1 the matrix (I+V) has an inverse; thus G as defined in (27) exists. To show that G is skew-symmetric use (27) to write

$$G^T = (I+V)^{-T}(I-V)^T$$

where -T is the inverse of the transpose (or vice-versa). Using the last equation and the orthogonality of V we observe that

$$\begin{aligned} G^T &= (I+V^T)^{-1}(I-V^T) = (V^TV+V^T)^{-1}(V^TV-V^T) \\ &= [V^T(V+I)]^{-1}V^T(V-I) \\ &= (I+V)^{-1}VV^T(V-I) = (I+V)^{-1}(V-I) \\ &= -(I+V)^{-1}[2I-(I+V)] = -2(I+V)^{-1} + I \end{aligned} \tag{30}$$

Now

$$\begin{aligned} -2(I+V)^{-1} + I &= -2(I+V)^{-1} + (I+V)(I+V)^{-1} \\ &= [-2I+(I+V)](I+V)^{-1} \\ &= -(I-V)(I+V)^{-1} = -G \end{aligned} \tag{31}$$

Substitution of (31) into (30) yields the result $G^T = -G$, i.e. G is skew-symmetric.

From lemma V.2, (I+G) is invertible which gives legitimacy to the right-hand side of (28). To prove the truth of (28) re-write (30) as

$$G^T = I-2(I+V)^{-1}$$

hence

$$G = I-2(I+V^T)^{-1}$$

from which we obtain

$$I-G = 2(I+V^T)^{-1} \qquad (32)$$

and

$$I+G = 2I - 2(I+V^T)^{-1} \qquad (33)$$

We can further write

$$\begin{aligned} 2I-2(I+V^T)^{-1} &= 2(I+V^T)(I+V^T)^{-1} - 2(I+V^T)^{-1} \\ &= 2V^T(I+V^T)^{-1} \end{aligned}$$

thus

$$I+G = 2V^T(I+V^T)^{-1}$$

and

$$(I+G)^{-1} = \frac{1}{2}(I+V^T)V \qquad (34)$$

Substitution of (32) and (34) in the right-hand side of (28) yields the proof of III.

To prove (29) differentiate (27)

$$\begin{aligned} \dot{G} &= -\dot{V}(I+V)^{-1} - (I-V)(I+V)^{-1}\dot{V}(I+V)^{-1} \\ &= -[I+(I-V)(I+V)^{-1}]\dot{V}(I+V)^{-1} \end{aligned}$$

Substitute (27) in the last equation to obtain

$$\dot{G} = -(I+G)\dot{V}(I+V)^{-1}$$

Using (1) the last equation can be written as

$$\dot{G} = -(I+G)WV(I+V)^{-1}$$

Substitution of (28) into the last equation yields

$$\dot{G} = -(I+G)W(I-G)(I+G)^{-1}[I+(I-G)(I+G)^{-1}]^{-1} \qquad (35)$$

The expression in the brackets can be written as follows

$$I + (I-G)(I+G)^{-1} = (I+G)(I+G)^{-1} + (I-G)(I+G)^{-1} = 2(I+G)^{-1}$$

therefore (35) can be written as

$$\dot{G} = -(I+G)W(I-G)(I+G)^{-1}[2(I+G)^{-1}]^{-1} = -\frac{1}{2}(I+G)W(I-G)$$

and since G is skew-symmetric the last equation can be written also as

$$\dot{G} = -\frac{1}{2}(I+G)W(I+G)^T$$

which ends the proof. ■

Note, from lemma V.1, that the condition for the invertibility of (I+G) is that it has no eigenvalues at -1, which is analogous to the condition for (I+V) to be invertible, i.e. that V has no eigenvalues at -1. However while V always exists, G does not exist when V has an eigenvalue at -1. The parametrization of V by G fails when the latter is the case. However this can be overcome as will be shown in Section VII.

The parametrization of V by the Extended Rodrigues Parameters is n-dimensional since the foregoing proofs were not restricted to any value of n, nor did they hinge on a rotation vector or any other geometric quality in n-D. In fact, the Extended Rodrigues Parameters, which are the elements of G, are the answer to the first three parts of our problem as posed in Section II. That is we found m parameters which define the n-dimensional orthogonal matrix, V. We also found a first order differential equation for G, and we showed how to calculate V, once G is found.

What is needed to fully answer our problem is a simple algorithm to implement the solution; this will be presented in Section VII. For now, after having obtained a parametrization in n-D, we are prepared to discuss the meaning of the skew-symmetric matrix, W, its geometric interpretation, and the difference between W in 3 and in n-D.

VI. ANGULAR RATE IN n-D

Recall (1)

$$\dot{V}(t) = W(t)V(t) \qquad (1)$$

The matrix V can be viewed as a transformation matrix which transforms vector components in an n-D Euclidean space. In particular it transforms a set of unit vectors, which form a Cartesian coordinate system, to another such set. Let us denote the former as the initial coordinate system and the latter as the final one. The rows of V are components of unit vectors of the initial set resolved in the final Cartesian coordinate system such that $v_{i,j}$ is the i-th component in the final system of the j-th unit vector of the initial coordinate system. From (1)

$$\dot{v}_{i,j} = \sum_{k=1}^{n} w_{i,k} v_{k,j}$$

hence $w_{i,k}$ is the relative weight that the k-th component in the final system, of a unit vector in the initial system, has on the rate of change of the i-th component in the final system of the same unit vector in the initial system. Note that this weight is independent of j; i.e. of which unit vector in the initial system we consider. To give $w_{i,j}$ a more descriptive interpretation and to see the role of W more clearly, consider the 3-D case where, for example

$$\dot{v}_{3,1} = w_{3,1}v_{1,1} + w_{3,2}v_{2,1} \tag{36}$$

(note that the term $w_{3,3}v_{3,1}$ was dropped since $w_{3,3} = 0$ for skew-symmetric W). In 3-D (36) can be written as

$$\dot{v}_{3,1} = w_2v_{1,1} - w_1v_{2,1} \tag{37}$$

where w_1 and w_2 are the respective angular rates at which the final coordinate system instantaneously rotates about its 1 and 2 axes. The components w_i, i=1,2,3, are those of the 3-D angular rate vector describing the instantaneous rotation of the final system. In 3-D w_i is also the angular rate at which the j axis turns towards the k axis, and so on in a cyclic manner for w_j and w_k. Indeed a comparison between (36) and (37) reveals that

$$w_2 = w_{3,1}$$

$$-w_1 = w_{3,2}$$

We conclude that the following can be said about W in 3-D

(A) The elements of W are angular rates.

(B) Each components of W is a rate of turn of one coordinate axis towards another such that $w_{p,q}$ is the angular rate at which axis p turns towards axis q. Obviously, $w_{p,q} = -w_{q,p}$.

(C) Both the p and the q axes turn at the angular rate $w_{p,q}$ about the third axis r.

(D) The elements of W are components of an angular rate vector.

When we turn now to n-D, we realize that the preceding observation cannot be fully extended from 3 to n-D. In n-D W has m=n(n-1)/2 independent components such that the elements of W cannot be components of a rate vector whose number is necessarily only n. We cannot, therefore, consider the elements of W as angular rates about (coordinate) axes. Consequently, of the four features of the elements of W in 3-D, mentioned above, the only ones which also prevail in n-D are (A) and (B).

Realizing that the angular rates in n-D cannot be described by a vector, one is motivated to examine the possibility of expressing the angular rate by a tensor. To accomplish that, choose one, say the i-th, column of V(t) and the i-th column of V(t) and denote them correspondingly by $\dot{v}$ and v such that $\dot{v} = [\dot{v}_1, \dot{v}_2, \ldots\ldots, \dot{v}_n]^T$ and $v = [v_1, v_2, \ldots\ldots, v_n]^T$. Using their components express them as vectors in the same arbitrarily chosen coordinate system such that

$$\dot{\bar{v}} = \bar{i}_1\dot{v}_1 + \bar{i}_2\dot{v}_2 + \ldots\ldots + \bar{i}_n\dot{v}_n$$

where $\bar{i}_1, \bar{i}_2, \ldots, \bar{i}_n$ are unit vectors along the coordinate axes 1, 2, ..., n respectively. Similarly

$$\bar{v} = \bar{i}_1 v_1 + \bar{i}_2 v_2 + \ldots\ldots + \bar{i}_n v_n$$

Define a tensor of the second rank, $\bar{W}$, using the elements of W as follows

$$\begin{aligned} \bar{W} = {} & \bar{i}_1\bar{i}_1 0 + \bar{i}_1\bar{i}_2 w_{1,2} + \ldots\ldots + \bar{i}_1\bar{i}_n w_{1,n} \\ & + \bar{i}_2\bar{i}_1 w_{2,1} + \bar{i}_2\bar{i}_2 0 + \ldots\ldots + \bar{i}_2\bar{i}_n w_{2,n} \\ & \qquad \vdots \\ & + \bar{i}_n\bar{i}_1 w_{n,1} + \bar{i}_n\bar{i}_2 w_{n,2} + \ldots\ldots + \bar{i}_n\bar{i}_n 0 \end{aligned}$$

then obviously

$$\dot{\bar{v}} = \bar{W}\,\bar{v}$$

that is, when the angular rate components are treated as elements of a tensor of the second rank, (1) is fully satisfied. A tensor of the second rank is also known as dyadic [14].

The fact that the angular rate in 3-D is basically a tensor is known [8,15] but is not reflected in the applied literature. The reason for it stems, perhaps, from the unique possibility to express angular rates in 3-D by a vector such that its description as a tensor might have been perceived merely as a philosophical formalism. (Even when treated as a tensor, the angular rate is usually that of a 3-D coordinate system). Indeed, the creation, in 3-D, of the so called "vector cross-product matrix" based on the angular velocity vector is conceived as a useful gimmick rather than a restoration of the true mathematical description of the angular rate. So far, the consideration of angular rates in dimensions higher than 3 probably was not required nor known. Thus it was not recognized that in higher dimensions the angular rate cannot be described by a vector but must be described as another entity, and that the ability to describe it in 3-D by a vector is just a matter of good fortune. (In fact, even in 2-D the angular rate is not truly expressible as a vector. This is evident when we note that the that the expression of rotation in a plane by a vector normal to it is necessarily a 3-D expression. The correct and only 2-D expression is

$$\dot{\bar{v}} = (\bar{i}_1\bar{i}_2 w - \bar{i}_2\bar{i}_1 w)\bar{v}$$

or

$$\dot{\begin{bmatrix} v_1 \\ v_2 \end{bmatrix}} = \begin{bmatrix} 0 & w \\ -w & 0 \end{bmatrix} \begin{bmatrix} v_1 \\ v_2 \end{bmatrix}$$

where the first expression is in a tensor form and the second is in a matrix form). Another possible cause for the disregard of the fact that angular rate is a tensor stems from the fact that the tensor of the second rank; that is, the dyadic, is replaceable by a matrix (as demonstrated in the last 2-D representation and in equation 1). Therefore all practical work in any dimension can be carried out without resorting to the tensor concept.

After having cleared the issue of angular rate representation we are prepared to consider the implementation of the algorithm for solving (1) using the Extended Rodrigues Parameters, thereby solving our problem in its entirety.

VII. NUMERICAL IMPLEMENTATION

Recall the differential equation (1)

$$\dot{V} = WV \tag{1}$$

in which W is given. We wish to solve (1) using the extended Rodrigues Parameters. The solution process requires first the solution of

$$\dot{G} = -\frac{1}{2}(I+G)W(I+G)^T \tag{29}$$

and then the computation of V according to (28)

$$V = (I-G)(I+G)^{-1} \tag{28}$$

There are two caveats which we have to be alerted to. One of them is the non-existence of G when V has an eigenvalue at -1, and the other is the need to invert the matrix (I+G), which may be so burdensome as to render the whole approach inefficient in comparison with the direct solution of (1). The first problem can be easily avoided if we can keep the elements of G small, for then, as can be readily seen from (28), V is close to I whose eigenvalues are all equal to +1. That is, if we are free to control its size, we can always choose G so small as to make the eigenvalues of V as close to +1 (and thus as far from -1) as we wish. Indeed, we are able to control the magnitude of G. The ability to do it is based on the following proposition.

Proposition: Given the differential equation of (1)

$$\dot{V}(t) = W(t)V(t) \tag{1}$$

with the initial condition $V(t_o)$ where $V(t_o)$ is orthogonal, then $V(t)$, the solution of (1) at time $t > t_o$, can be written as a product of two matrices as follows

$$V(t) = V(t,t_o)V(t_o) \tag{38}$$

where $V(t,t_o)$ is the solution of (1) at time t given the initial condition $V(t_o,t_o) = I$.

Proof: Since $V(t_o)$ is orthogonal it always has an inverse. Therefore one can always compute a matrix

$$V(t,t_o) = V(t)V^T(t_o) \tag{39}$$

such that (38) holds. Now if (38) is differentiated with respect to time the following is obtained

$$\dot{V}(t) = \dot{V}(t,t_o)V(t_o)$$

Equating the right-hand side of the last equation to that of (1) and using (38) results in

$$\dot{V}(t,t_o)V(t_o) = W(t)V(t,t_o)V(t_o)$$

Since $V(t_o)$ is invertible, the last equation yields

$$\dot{V}(t,t_o) = W(t)V(t,t_o)$$

hence $V(t,t_o)$ solves (1). Finally setting t in (39) to t_o results in

$$V(t_o,t_o) = I$$

which ends the proof. ■

In computing V(t) we make use of the last proposition when we consider V(t) as a product of $V(t,t_o)$ and $V(t_o)$ as follows

$$V(t) = V(t,t_o)V(t_o) \qquad (40)$$

and instead of computing $V(t)$ directly we compute $V(t,t_o)$ from time t_o to t and then use (40) to compute $V(t)$. Actually instead of computing $V(t,t_o)$ we use (29) to compute G, the parametrization of $V(t,t_o)$, from time t_o to t with the initial condition $G(t_o) = 0$ which corresponds to $V(t,t_o) = I$. The computation of G is stopped periodically at, say, t_1 and $V(t_1)$ is computed according to (28) yielding

$$V(t_1,t_o) = [I-G(t_1)][I+G(t_1)]^{-1}$$

and then $V(t_1)$ is computed using (40) as follows

$$V(t_1) = V(t_1,t_o)V(t_o)$$

Next the computation of $V(t)$ proceeds into the following time interval using the same algorithm that produced $V(t_1)$ once $V(t_o)$ was given. We start, of course, with the initial condition $G(t_1) = 0$ which corresponds to $V(t,t_1) = I$. Using this algorithm we proceed to compute G and V at times t_2, t_3, ..., t_k. By properly choosing the size of the intervals t_2-t_1, t_3-t_2, ..., t_k-t_{k-1} we can impose an upper bound on G which can practically be as small as we wish. We term the operation of resetting the value of V and G at the beginning of an interval reset operation.

The foregoing policy rids us of the singularity problem. In fact, if singularity were the only issue, one can choose the time intervals t_i-t_{i-1} quite large and still not encounter singularity. However, we are still left with the second problem mentioned before; namely, the inversion of $[I+G(t_i)]$. We overcome this problem by approximating the inverse without really performing any matrix inversion. Before discussing the options for approximating this inverse we list without proof two well known theorems (e.g. Ref. 16 p.129) needed in the ensuing.

Theorem VII.1: Let G be a square matrix then the series $\sum_{i=0}^{\infty}(-1)^i G^i$ converges to $(I+G)^{-1}$ iff all the eigenvalue of G lie inside the unit circle about the origin of the complex plane.

Theorem VII.2: Denote the elements of the nxn matrix G by $g_{i,j}$. If the sums

$$\sum_{j=1}^{n}|g_{i,j}| \qquad i=1,\ 2,\ \ldots,\ n$$

are all less than 1, or if

$$\sum_{i=1}^{n} |g_{i,j}| \qquad j=1, 2, \ldots, n$$

are all less than 1, then all the eigenvalues of G lie inside the unit circle about the origin of the complex plane.

The algorithm we use to approximate the inverse of (I-G) is based on the fact that if the matrix X_i is a good approximation of the inverse of some matrix A then a better approximation, X_{i+1}, can be obtained using the Newton-Raphson-type iteration [16 p.52, 17]

$$X_{i+1} = X_i(2I - AX_i) \qquad (41)$$

This algorithm converges if and only if the eigenvalues of $I-AX_i$ are all of absolute value less than 1 [16, p.52]. If indeed X_i is almost the inverse of A then this condition is met. If now V is computed without reset taking place at the end of the previous time increment, then we use as a first approximation of $[I+G(t)]^{-1}$, the value used as an inverse at the previous time point. This is based on the presumption that the time increments of the integration are small enough such that the change of the inverse is small too, hence its previous accurate value can serve now as an approximate value. If, however, reset did take place at the previous time point then G was set to zero and the previous inverse of I+G is simply I. For the sake of computation reduction it is desired to keep at minimum the number of iterations used to compute an accurate inverse. Normally one iteration is sufficient. However, when reset takes place and consequently the previous inverse of I+G (i.e. the inverse of $I+G_o$ for $G_o = 0$) is taken as I then a single iteration produces

$$(I+G_1)^{-1} \simeq I-G_1 \qquad (42)$$

where G_1 is G at the present time. If, however, we enter the iteration with the value $X_o= I-G_1$ then, due to the quadratic convergence characteristic of the process, a single iteration produces

$$(I+G_1)^{-1} \simeq I-G_1+G_1^{\,2}-G_1^{\,3} \qquad (43)$$

obviously the approximate inverse given in (43) is more accurate than that of (42) since it contains more terms of the series which expresses the inverse of $(I+G_1)$. Note that the series generated by (41) converges since due to the reset operation, G is kept at a very small value such that the condition of theorem VII.2 is met. Thus the eigenvalues of G are in the unit circle which, in view of theorem VII.1, assures convergence.

Another point of interest is the ability to use an alternate equation for computing G. From (31) it is obvious that

$$2(I+V)^{-1} = I+G$$

which yields

$$V = 2(I+G)^{-1} - I \tag{44}$$

The computation of V using (44) is simpler than when (28) is used. However, if the reset operation took place at the previous time point then the use of (28) at the present time point yields better results. This is evident in particular when the previous inverse, $(I+G_{i-1})^{-1}$, is approximated by I. In this case the use of (41) yields the approximation of (42) for which the use of (44) yields

$$V(t_i,t_{i-1}) = I- 2G_i$$

whereas the use of (28) yields

$$V(t_i,t_{i-1}) = I - 2G_i + G_i^2$$

which is more accurate than the preceding result. Even when the approximation of (43) is used, the use of (28) yields better results than that obtained using (44). Then, however, the difference is smaller since the term of the series which is being added is smaller than the added term in the previous case which was G_i^2. If, of course, an exact inverse is used then the use of (44) rather than (28) is preferable since then the computation of $V(t_i,t_{i-1})$ is simplified without the penalty of accuracy degradation.

The algorithm which results from the preceding considerations is shown in Table I. Note that (28) rather than (44) is implemented for the reasons discussed above.

If one chooses to perform reset after each integration step of $\dot{G}$ then the computation of $V(t_i,t_o)$ as given in Table I produces

$$V(t_i,t_o) = I - 2G_i + 2G_i^2 - 2G_i^3 + G_i^4 \tag{45}$$

where $G_i = G(t_i)$. This is a truncated series of the expression for V as a function of G given in (28) with the special feature that the last term in the series lacks the multiplier 2. A more computationally efficient algorithm than that is

$$V(t_i,t_o) = I - G_i(2I - G_i[2I - G_i(2I - G_i)]) \tag{46}$$

or better yet, if G_i^4 is added to (45) to generate the true truncation of the series expansion of $(I-G_i)(I+G_i)^{-1}$ then the new expression can be written as

$$V(t_i,t_o) = I - 2G_i(I - G_i[I - G_i(I - G_i)]) \tag{47}$$

Consequently one can use either the algorithm of Table I as is or compute $V(t_i,t_o)$ using either (45) or(46) or(47). These, however are not the only possible variants of the algorithm. As a result of the discussions presented in this section it is clear that one has the following additional choices:

Table I

```
Given:  $V(t_o) = V_o$  and  $W(t)$

(1) Set the initial condition  $G(t_o) = 0$.
(2) Solve  $\dot{G}(t) = -\frac{1}{2}[I+G(t)]W(t)[I+G(t)]^T$  from  $t_o$  to  $t_i$.
(3) If reset didn't take place at the end of the preceding
    cycle, go to (4).
    compute  $X_i = I - G(t_i)$  and go to (5).
(4) Compute  $X_i = X^*_{i-1}$
(5) Compute  $A_i = I + G(t_i)$  and  $X_i^* = X_i(2I-A_iX_i)$
(6) If reset is not requested go to (8).
(7) Perform a reset as follows. If reset didn't take place
    at the end of the preceding cycle compute (b).
    (a)  $V(t_i,t_o) = X_iX_i^*$  and go to (c).
    (b)  $V(t_i,t_o) = [I-G(t_i)]X_i^*$
    (c)  $V(t_i) = V(t_i,t_o)V(t_o)$
    (d)  set  $t_o = t_i$
(8) If the current time is equal to the final time go to
    step (10).
(9) If (7) was executed go to (1).  Otherwise go to (2)
    and increase all indices by 1.
(10) Stop.
```

- Perform or not perform resets.
- Use more terms of the series

$$V(t_i,t_{i-1}) = I + 2\sum_{n=1}^{\infty}(-1)^n G_i^{\,n}$$

- Use either (28) or (44) to compute $V(t_1,t_o)$ from G_i.

The choices should correspond to the particular problem on hand.

As an example we ran a 4th dimensional case where

$$V(0) = I \quad ; \quad W(t) = \begin{bmatrix} 0 & -0.1 & -1.0 & -7.5 \\ 0.1 & 0 & 3.0 & 0 \\ 1.0 & -3.0 & 0 & -0.9 \\ 7.5 & 0 & 0.9 & 0 \end{bmatrix} * \sin(6.28t)$$

the initial time $t_o = 0.$

the final time $t_f = 1_{sec}$

the integration time $dt = 0.001_{sec}$

The algorithm used in the solution of V was the one given in Table I where reset was performed after each integration step. Equation (1) was solved to yield a reference with which the algorithm output was compared. The reference matrix was denoted by V_r and the one generated by the algorithm was denoted by V. The integration routine which was used to solve the differential equation for V_r as well as for G was a 4-th order Runge-Kutta routine. The difference matrix between the two solutions was computed and denoted by $E = V-V_r$. A scalar which constitutes a measure of the size of the error was defined as follows

$$e = [\mathrm{Tr}(EE^T)]^{1/2}$$

The scalar e is the square root of the sum of the squares of the elements of E. The results at $t = 0.5_{sec}$ were:

V_r

```
-.72765515E+00   .15285696E+00  -.24387237E+00  -.62263874E+00
 .10217642E-01   .58373643E+00   .79194147E+00  -.17881859E+00
-.13935294E+00  -.79737729E+00   .53481405E+00  -.24237192E+00
 .67156112E+00  -.87171959E-02  -.16531458E+00  -.72221933E+00
```

```
                                   V

 -.72765512E+00   .15285696E+00  -.24387236E+00  -.62263872E+00
  .10217638E-01   .58373643E+00   .79194147E+00  -.17881859E+00
 -.13935294E+00  -.79737729E+00   .53481405E+00  -.24237191E+00
  .67156110E+00  -.87171923E-02  -.16531458E+00  -.72221930E+00


                                   E

  .29723949E-07  -.18713478E-09   .83326148E-08   .24813960E-07
 -.35405291E-08  -.25268088E-09  -.11170641E-08   .71958844E-09
  .42739559E-09   .12413215E-08   .86561824E-09   .83593105E-08
 -.25932268E-07   .35672249E-08   .95984923E-09   .29599694E-07

                          e = .56724776E-07
```

As mentioned earlier the algorithm of Table I with a reset at the end of each integration cycle amounts to the use of (46) in the computation of $V(t_i,t_o)$. As suggested, (47) can be used instead. In Table II we show a comparison between the use of (46) and (47) for different series lengths. The table presents the error measure, e, for the two series truncated after different powers, n, of G. The error measure was recorded at $t = 0.5_{sec}$ for at that point, which is half the period of the oscillating W, the value of e is the highest during the first period, i.e., in the domain $0. < t < 1._{sec}$. As can be seen from the results, algorithm 2 is superior. It can be also seen that there is a distinct power beyond which the addition of more terms yields little return. In view of these conclusions we recommend the use of the algorithm listed in Table III which in fact was used in the first example.

Table II

	n				
	1	2	3	4	5
1. $V(t_i,t_o)=I-2G_i+2G_i^2- \dots G_i^n$	.17 E 01	.52 E-02	.17 E-04	.57 E-07	.13 E-09
2. $V(t_i,t_o)=I-2G_i+2G_i^2- \dots 2G_i^n$	.10 E-01	.34 E-04	.11 E-06	.33 E-09	.63 E-10

Table III

```
Given: $V(t_o) = V_o$ and $W(t)$
==========================================
(1) Initialize $i = 0$
(2) Set the initial condition $G(t_i) = 0$.
(3) Solve $\dot{G}(t) = -\frac{1}{2}[I+G(t)]W(t)[I+G(t)]^T$
        from $t_i$ to $t_{i+1}$.
(4) Compute
        $V(t_{i+1},t_i) = I-2G_{i+1}(I-G_{i+1}[I-G_{i+1}(I-G_{i+1})])$
        $V(t_{i+1}) = V(t_{i+1},t_i)V(t_i)$
(5) If the current time is smaller than the final
    time go back to step (2) and increase all
    indices by 1, otherwise STOP.
```

VIII. CONCLUSIONS

This work addressed the problem of solving the first order differential equation, which every orthogonal matrix satisfies, using the minimum number of parameters necessary to uniquely determine the matrix. The major question was: which are the parameters that do determine this matrix. The other questions were: what are the differential equation which one has to solve in order to find the parameters, and: once the parameters are found, how to use them in order to find the corresponding matrix. All these questions were answered and several algorithms for computing the orthogonal matrix via the parameters were suggested and investigated.

In search for solutions the familiar special 3-D case was examined with the purpose of extending the methods used there to the general n-D case. Accordingly, the first thought that came to mind was the idea of extending the concept of Euler angles to the n-D case. It turned out that, although not well known, Euler himself succeeded in using Euler angles to parametrize higher dimensional orthogonal matrices. Euler, however, was not concerned with the dynamic case; that is, with the differential equation which describe their change in time (neither did he do it for the 3-D case). Lagrange improved Euler's approach and presented it in the first edition of his book on analytic mechanics. We did not adopt this approach because of the multitude of the trigonometric functions that one has to trace and compute and because of the complexity of the differential equations which describe the time change of the extended Euler angles.

Another popular 3-D parametrization which was considered was the quaternion of rotation. This approach did not seem to lead to any solution and was abandoned. The last parametrization which was examined was that of Rodrigues. In the vast literature on 3-D methods the elements of this parametrization are known as: Gibbs vector or Cayley-Rodrigues parameters; however, the presentation of these parameters by Rodrigues in 1840 [7] preceded the work of Cayley who, as a matter of fact, credits Rodrigues with their discovery [18,19]. Rodrigues' work certainly preceded that of Gibbs who first published his research of these parameters in 1884 (see Ref. 9, p. 17). Although it seems that Rodrigues was the first one to present them, it turns out, as noted by Jacobi [13] and by Roberson [8], that even these parameters were first presented by Euler [20] although in a different form. Ironically, while Rodrigues based his development on the, by now, very famous theorem of Euler [21], Euler himself was not aware of the possible use of his own theorem in the derivation of these parameters. (The theorem states that any final sequence of 3-D rotations can be represented by just one rotation about a single fixed axis)*. It is, however, Rodrigues who developed the parameters in their present known form. For this reason we refer to their extension to n-D as the Extended Rodrigues Parameters. It was shown that the parameters can be conveniently extended to n-D. In fact there is nothing that limit their validity to 3-D only. Indeed, the theorems used in the presentation of the Extended Rodrigues Parameters in this work do not assume any restriction on the dimensionality of the space in which they are used.

Projecting the 3-D concepts into n-D raises the question of the correct mathematical representation of angular rates in spaces whose dimension is not 3. It is shown that angular rate has to be represented by a tensor of the second rank, also known as dyadic. The ability to represent angular rate as a vector is unique to 3-D. This fact, while known before, was not paid sufficient attention because the vectorial representation satisfied the intuition and the practical needs of its users. In other dimensions the vectorial representation fails and the use of the dyadic representation is required. Finally it should be pointed out that when, as in our case, matrices are used, the skew-symmetric dyadic which represents angular rate in n-D is simply represented by a skew symmetric matrix.

---

* As noted by Jacobi, Lagrange too presented this theorem in the first edition of his book on analytic mechanics [12] but dropped it as well as the treatment of rotations from the second edition of this book.

Acknowledgment

The authors wish to thank Ms Constance Carter of the US Library of Congress for her unyielding search which culminated with the discovery of the original Russian and French journals in which Euler's and Rodrigues' papers were published respectively.

REFERENCES

[1] Y. Oshman and I. Y. Bar-Itzhack, "Eigenfactor Solution of the Matrix Riccati Equation - a Continuous Square Root Algorithm," IEEE Transactions on Automatic Control, Vol. AC-30, No. 10, October 1985, pp. 971-978.

[2] P. L. Pio, "Euler Angle Transformations," IEEE Transactions on Automatic Control, Vol. AC-11, No. 5, October 1960, pp. 707-715.

[3] H. Goldstein, Classical Mechanics, 2nd edition, Addison-Wesley, Reading Mass, 1980.

[4] E. T. Whittaker, A Treatise on the Analytical Dynamics of Particles and Rigid Bodies, 4th edition, Cambridge University Press, England, 1964.

[5] T. F. Wiener, "Theoretical Analysis of Gimballess Inertial Reference Equipment Using Delta-Modulated Instruments," Doctoral Dissertation, M.I.T. Cambridge Mass. 1962.

[6] J. R. Wertz (ed.), Spacecraft Attitude Determination and Control, D. Reidel, Dordrecht Holland, 1978.

[7] M. O. Rodrigues, "Des Lois Geometriques Qui Regissent les Deplacement d'un Systeme Solide dans L'espace, et de la Variation des Coordonnees Provenant de ces Deplacements Consideres Independamment des Causes qui Peuvent les Produire," J. de Mathematiques Pures et Appliquees, (Liouville), Vol. 5, 1840, pp. 380-440.

[8] R. E. Roberson, "Kinematic Equations for Bodies Whose Rotation is Described by the Euler-Rodrigues Parameters," AIAA Journal, Vol.6, No. 5, January 1968, pp. 916,917.

[9] J. W. Gibbs Scientific Papers, Vol. II, Dover Publication Inc., New-York, 1961, p. 65.

[10] J. Stuelpnagel, "On the Parametrization of the Three-Dimensional Rotation Group," SIAM Review, Vol. 6 No. 4, October 1964, pp. 422-430.

[11] L. Euler, "Problema Algebraicum ob Affectiones Prorsus Singulares Memorabile," Novi Comm. Acad. Sci. Petrop., Vol. 15, 1770, pp. 75-126

[12] J. L. Lagrange, Mecanique Analytique, 1st edition, part II, Section VI: Sur la Rotation des Corpes, Chez La Veuve de Saint, Libraire, Rue du Foin S. Jacques, 1788, p.353.

[13] C. G. J. Jacobi, "Bemerkungen zu Einer Abhandlung Euler's uber die Orthogonale Substitution," in C. G. J. Jacobi's Gesammelte Werke, 2nd edition, Vol. III, Chelsea Publishing Co. New-York, 1969, pp. 601-609.

[14] L. P. Page, Introduction to Theoretical Physics, 3rd edition, Van Nostrand, Princeton NJ, 1952, pp. 46-55.

[15] A. M. Goodbody, Cartesian Tensors: with Application to Mechanics, Fluid Mechanics and Elasticity, Ellis Horwood Ltd. Publishers, Chichester UK, 1982, pp. 221, 222.

[16] J. R. Westlake, A Handbook of Numerical Matrix Inversion and Solution of Linear Equations, John Wiley and Sons, New-York, 1968.

[17] G. E. Forsyth and C. B. Moler, Computer Solution of Linear Algebraic Systems, Prentice-Hall, Englewood Cliffs NJ, 1967, p.78.

[18] A. Cayley, "On the Motion of Rotation of a Solid Body," Cambridge Mathematical Journal, Vol. III, 1843, pp. 224-232, also in The Collected Mathematical Papers of Arthur Cayley, Vol. I, The Cambridge University Press, 1889. Johnson Reprint Corp. New York, 1963, pp.28-35.

[19] A. Cayley, "On certain Results Relating to Quaternions," Cambridge Mathematical Journal, Vol. III, 1843, pp. 141-145, also in The Collected Mathematical Papers of Arthur Cayley, Vol. I, The Cambridge University Press, 1889. Johnson Reprint Corp. New York, 1963, pp.123-126.

[20] L. Euler, "Nova Methodus Motum Corporum Rigidorum Determinandi," Novi Comm. Acad. Sci. Petrop., Vol. 20, 1775, pp. 208-238.

[21] L. Euler, "Formulae Generales pro Translatione Quacunque Corporum Rigidorum," Novi Acad. Sci. Petrop., Vol. 20, 1775, pp. 189-207.

From CP 3011

N89-15939

THE OPTICAL FIELD ANGLE DISTORTION CALIBRATION FEASIBILITY STUDY FOR THE HUBBLE SPACE TELESCOPE FINE GUIDANCE SENSORS

K. Luchetti, G. Abshire, L. Hallock, and R. McCutcheon
Computer Sciences Corporation

ABSTRACT

The results of an analytical study to investigate the feasibilty of calibrating the Hubble Space Telescope's (HST's) fine guidance sensors (FGSs) within HST mission accuracy limits are presented. The study had two purposes: (1) to determine the mathematical feasibility of the optical field angle distortion (OFAD) calibration algorithm and (2) to confirm that the OFAD, plate scale, and FGS-to-FGS alignment calibration algorithms produced a calibration of the FGSs that satisfied mission requirements. The study concluded that the mathematical specification of the OFAD algorithm is adequate and permits a determination of the FGS calibration parameters (accurate to better than 0.003 arc-second) sufficient to meet the mission requirements. The algorithms implemented, the characteristics of the simulated data and procedures for data analysis, and the study's results are discussed. In addition, several useful techniques for improving the stability and accuracy of the OFAD solution are outlined.

1. INTRODUCTION

1.1 STUDY BACKGROUND AND PURPOSE

The success of the Hubble Space Telescope (HST) depends critically on the capabilities to accurately place a target in the desired fine guidance sensor (FGS) aperture, precisely control HST pointing, and track moving targets in any FGS aperture. These capabilities depend, in turn, on precise determination of the optical field angle distortion (OFAD), plate scale, and relative alignments of the FGSs. Failure in any of these calibrations means failure to meet HST mission accuracy requirements. Using data as realistic as possible, we conducted a feasibility study to verify that the HST Payload Operations Control Center (POCC) Applications Software Support (PASS) algorithms for these calibrations will, in concert, satisfy mission accuracy requirements.

We performed the study using PASS software implementing the current form of the optical telescope assembly (OTA) calibration algorithms, original versions of which were specified by Perkin-Elmer (P-E) in 1984 (References 1 through 4). The current forms of the algorithms incorporate corrections and enhancements recommended by Computer Sciences Corporation (CSC), Goddard Space Flight Center (GSFC), Marshall Space Flight Center (MSFC), W. Jefferys of the astrometry team, and K. Minka of Computer Technology Associates (CTA). The baselined source specifying the mathematical details of the OTA algorithms is the PASS requirements specification document (Reference 5).

Performance of the feasibility study required the careful coordination of eight separate software functions: data simulation, telemetry processing, data adjustment, plate scale calibration using the calibrated plate method, optical distortion calibration using the mini-OFAD algorithm, plate scale calibration using the moving asteroid method, optical distortion calibration using the P-E-supplied OFAD algorithm, and FGS-to-FGS alignment calibration. We used the PASS attitude data simulator, which was originally developed to test attitude determination software, to generate data for all of the calibration functions studied. Reference 5 provides a detailed description of the simulator's algorithms and capabilities. We used the PASS offline telemetry processor (OTP) to convert the necessary HST FGS data to usable engineering format for the study; Reference 5 provides a detailed description of the OTP.

1.2 ARTICLE OVERVIEW AND TERM/CONCEPT DEFINITION

Section 2 of this article briefly describes the algorithms for the data adjustment and calibration functions analyzed in the OFAD feasibility study. Section 3 outlines the evolution of the OFAD algorithm in response to various problems encountered during OFAD prototype software testing. Section 4 details the data simulation and data reduction activities of the feasibility study; in addition, that section specifies the calibration scenario followed in the study, as well as the original strawman scenario recommended by P-E. Section 5 discusses the results of the study, and Section 6 specifies the conclusions.

The following paragraphs briefly define terms used and concepts referred to throughout this article:

FGSs -- Each of the HST's three FGSs consists of a system of photomultiplier tubes (PMTs) and amplitude interferometers in white light (Koesters' prism). Because only two

FGSs are required at any particular time for guidance, the third FGS can be used to conduct high-precision astrometric observations.

Image and Object Space -- An image space measurement is the direction of the observed star as measured by the FGS. An object space measurement is the true direction of the observed star. The difference between object and image space measurements is the magnification of the FGS.

Star Selector Deviation and Offset Angles -- Two beam deflectors, called star selectors, rotate to bring light from an object anywhere in the FGS field of view (FOV) into the 5-by-5-arc-second square aperture of the FGS detector assembly. Each of the two star selectors (star selectors A and B) provides a conical scan vector with a diameter of 7.1 arc-minutes in object space. Figure 1 illustrates the star selector deviation and offset angles:

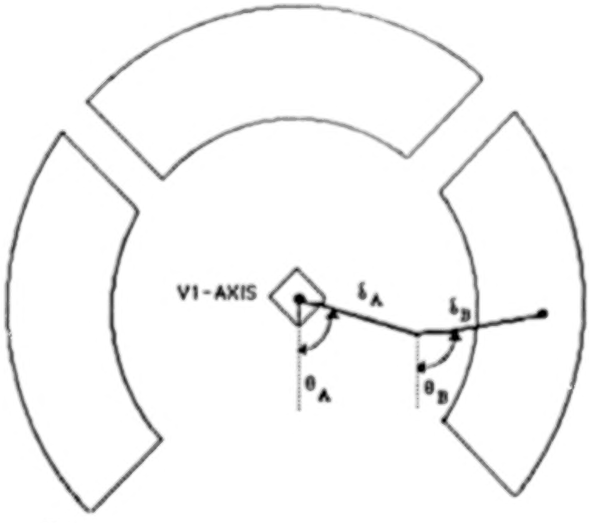

Note:

θ_A and θ_B = star selector A and B deviation angles, respectively
δ_A and δ_B = star selector A and B offset angles, respectively

Figure 1. FGS Star Selector Deviation and Offset Angles

Distortion Polynomials -- The OFAD algorithm solves for distortion coefficients for use in converting distorted star positions to undistorted star positions in object space. Although the distortion coefficients (also referred to as distorted-to-true coefficients) are not required by any elements of the HST software system except OFAD, the PASS software converts them into coefficients that are used throughout the HST system, as specified below.

Coefficient Type	Used By
Distorted-to-undistorted image space	PASS attitude determination software PASS OTA calibration software
Undistorted-to-distorted image space	PASS mission scheduling software PASS attitude simulation software
Undistorted-to-distorted object space	Onboard flight software (OBC)

Observation Sets and Maneuver Sequence -- Because of the OFAD algorithm's complexity and the large number of parameters solved for in an OFAD execution, the algorithm requires a large quantity of input data (i.e., FGS measurements) to obtain a valid distortion calibration. The HST collects the data by taking FGS measurements of a star field at several different spacecraft attitudes. The measurements of a star field at a specific attitude are referred to as an observation set or frame.

The maneuver sequence for collection of OFAD data consists of 13 pitch-yaw maneuvers and 2 roll manuevers from a reference attitude. The pitch-yaw maneuvers include nine manuevers forming an ellipsoid about the reference attitude and four larger offset maneuvers toward the FGS wings. Each observation set consists of approximately 30 stars.

2. BRIEF ALGORITHM DESCRIPTIONS

Calibration of the HST's FGSs involves four major software functions: data adjustment (initial data reduction), plate scale calibration, optical distortion calibration, and FGS-to-FGS alignment calibration. This section briefly describes the algorithms for these functions, which were originally provided by P-E and revised by CSC and P-E as required.

2.1 INITIAL DATA REDUCTION

The purpose of initial data reduction is to read onboard computer (OBC) quaternion and FGS data from the OTA engineering data file (output from the OTP), edit these data to eliminate any irregularities, locate FGS star tracks, and form and identify FGS observation vectors corresponding to these tracks. The primary output from initial data reduction is the OTA prepared data file, which contains the computed FGS image space vectors and associated information. The OTA prepared data file is the primary input to the OFAD, plate scale, and FGS-to-FGS alignment calibration algorithms.

2.2 PLATE SCALE CALIBRATION

The purpose of plate scale calibration is to compute the scale factor that converts FGS measurements from image to object space. The PASS software currently provides two methods for computing the plate scale: (1) the calibrated plate method and (2) the moving asteroid method. The calibrated plate method uses ground-measured star observations to determine the plate scale. Because this method cannot produce the accuracy required, it serves as an interim technique. The moving asteroid method uses minor planets, specially selected by the astrometry team, that move across the length of the FGS FOV. The use of these planets, whose ephemerides are well known (i.e., to within approximately 0.5 milliarc-second), enables a high level of accuracy in plate scale calibration. In both cases the primary input is the OTA prepared data file produced by the initial data reduction function, and the output is the FGS plate scale.

2.3 OPTICAL DISTORTION CALIBRATION

The purpose of distortion calibration is to compensate for any biases in FGS-measured star directions that cannot be modeled by a rotation (via FGS-to-FGS alignment calibration) or by a scale (via plate scale calibration). P-E models distortion using polynomial functions of the direction cosines, as specified by the following equations:

$$X_U = X_D - \sum_{L,M} a_{LM} \; X_D^L Y_D^M$$

$$Y_U = Y_D - \sum_{L,M} b_{LM} \; X_D^L Y_D^M$$

where X_U, Y_U = undistorted X and Y object space direction cosines, respectively

X_D, Y_D = FGS-measured distorted X and Y object space direction cosines, respectively

a_{LM} = distorted-to-undistorted object space distortion coefficient for the X-polynomial for which the exponent of the X direction cosine is L and the exponent of the Y direction cosine is M

b_{LM} = distorted-to-undistorted object space distortion coefficient for the Y-polynomial for which the exponent of the X direction cosine is L and the exponent of the Y direction cosine is M

The PASS software currently includes two algorithms for calibrating distortion: (1) the method provided by P-E and referred to as the OFAD algorithm and (2) the mini-OFAD algorithm. The mini-OFAD algorithm, the simpler of the two, solves only for the distortion polynomial coefficients, whereas the OFAD algorithm solves for many peripheral parameters, specifically the star direction cosines and the attitude maneuver angles. Because the mini-OFAD algorithm determines fewer parameters than does its more complex counterpart, it requires less FGS data for input. However, the mini-OFAD algorithm must use ground-measured star directions as input when specifying star reference directions; and because the error in the ground measurements is expected to be an order of magnitude higher than the OFAD error budget, the simpler algorithm cannot generate final distortion calibration values. The mini-OFAD algorithm can initialize the OFAD algorithm, which internally computes reference star direction cosines and therefore does not require input of ground measurements. The OFAD algorithm can also solve for offset and deviation angles, a capability that currently is not present in the mini-OFAD algorithm. For both algorithms, the primary input is the OTA prepared data file produced by the initial data reduction function. The user can reject any suspect observation in this file before it is used by the algorithm. Sections 2.3.1 and 2.3.2 describe the two OFAD calibration algorithms in greater detail.

2.3.1 Mini-OFAD Algorithm

The mini-OFAD algorithm calibrates the distortion coefficients using a least-squares procedure (References 6 and 7) that compares the direction cosines of an FGS-measured star field to ground-measured values. The equations of condition are of the form

$$X_D - \sum_{L,M} a_{LM} \, X_D^L Y_D^M - \left\{ [R_{MINI}] \hat{\xi}_A \right\}_X = 0$$

$$Y_D - \sum_{L,M} b_{LM} \; X_D^L Y_D^M \; - \left\{ [R_{MINI}] \hat{\xi}_A \right\}_Y = 0$$

where $[R_{MINI}]$ = rotation error matrix

$\hat{\xi}_A$ = differential aberration-perturbed ground-measured star vector rotated into FGS object space

and X_D, Y_D, a_{LM}, and b_{LM} are as defined in Section 2.3. The algorithm generates a pair of equations of condition (X and Y) for each star observation.

The distortion calibration using the mini-OFAD algorithm proceeds as follows. First, the FGS-measured image space direction cosines are transformed to object space (generating the parameters X_D and Y_D for each star observation) using the current plate scale value. Next, the ground-measured background star right ascensions and declinations are transformed to geocentric inertial (GCI) reference frame vectors (GCI coordinates are Earth-centered celestial coordinates), and full velocity aberration effects corresponding to the observation time are applied to the GCI vector. Using the telemetered attitude and the current alignment value, the full velocity aberration-perturbed GCI vector is rotated to FGS object space, yielding the vector $\hat{\xi}_A$, which contains differential velocity aberration perturbations. In the first distortion calibration sequence, the rotation error matrix $[R_{MINI}]$ is initialized to the identity matrix. Using these values for X_D, Y_D, $\hat{\xi}_A$, and $[R_{MINI}]$ and initial estimates for a_{LM} and b_{LM}, updated distortion coefficients are determined to provide the best fit to the equations of condition.

Following convergence (or upon exceeding a maximum number of iterations), an updated value of $[R_{MINI}]$ is determined as follows. Using the updated distortion coefficients, the undistorted FGS-measured direction cosines (X_U and Y_U) are determined using the equations specified in Section 2.3. Least-squares computation of the distortion coefficients followed by q-method calculation of the rotation error matrix is iterated until convergence is achieved or a maximum number of iterations is exceeded. Using the q-method (Reference 8), the rotation matrix $[R_{MINI}]$, which maps the vector $\hat{\xi}_A$ into the undistorted measurement vector, $(X_U, Y_U, Z_U)^T$, is determined. In effect, $[R_{MINI}]$ is an error matrix that corrects for errors in the FGS alignment matrix and telemetered attitude quaternion.

The only output from distortion calibration using the mini-OFAD algorithm is the distortion polynomial coefficients, which are used as initial estimates to the OFAD algorithm and can also be used as input to the other OTA calibration algorithms described in this article.

2.3.2 OFAD Algorithm

The OFAD algorithm calibrates the distortion coefficients, as well as offset and deviation angles, using a least-squares procedure (References 6 and 7) that compares the direction cosines of a star field at several spacecraft attitudes (referred to hereafter as observation sets). A somewhat simplified version of the equations of condition (ignoring terms relative to offset and deviation angle biases) is

$$X_D - \sum_{L,M} a_{LM} \; X_D^L Y_D^M \; - \left\{ [D_A] \, [R_{MAXI}] \, \hat{\xi}_T \right\}_X = 0$$

$$Y_D - \sum_{L,M} b_{LM} \; X_D^L Y_D^M \; - \left\{ [D_A] \, [R_{MAXI}] \, \hat{\xi}_T \right\}_Y = 0$$

where $[D_A]$ = matrix that adds differential velocity aberration at the time of the observation to the "true" star direction vector at the given attitude

$[R_{MAXI}]$ = attitude change Euler angle matrix for transformation from the reference observation set to other observation sets

$\hat{\xi}_T$ = "true" star direction cosines in FGS object space at the reference observation set

and X_D, Y_D, a_{LM}, and b_{LM} are as defined in Section 2.3. The algorithm generates a pair of equations of condition (X and Y) for each star observation.

Distortion calibration using the OFAD algorithm proceeds as follows. FGS-measured image space direction cosines are transformed to object space (generating the parameters X_D and Y_D for each star observation) using the current plate scale value. Initial estimates of the vector $\hat{\xi}_T$ are obtained by removing distortion (using the initial distortion coefficient values) and differential velocity aberration from FGS measurements of star directions at the reference observation set attitude. Initial estimates of $[R_{MAXI}]$ are obtained using the q-method. The matrix $[R_{MAXI}]$ that transforms the reference observation set to the reference observation set is defined to be the identity matrix. Updated values of $\hat{\xi}_T$ and the Euler angles defining $[R_{MAXI}]$ are determined as part of the least-squares process that determines updated values of the distortion coefficients, along with updated offset and deviation angles. Using these values for X_D, Y_D, $\hat{\xi}_T$, and $[R_{MAXI}]$ and initial estimates for a_{LM} and b_{LM}, updated distortion coefficients, offset and deviation angles, true direction cosines, and attitude change Euler angles are determined to provide a best fit to the equations of condition. The iterative process is continued until convergence is achieved or a maximum number of iterations is exceeded. Once a satisfactory solution is achieved, the final coefficients, offset angle, and deviation angle(s) are output.

2.4 FGS-TO-FGS ALIGNMENT CALIBRATION

The purpose of FGS-to-FGS alignment calibration is to determine the orientation of FGS-1 and FGS-3 relative to FGS-2. FGS-2 defines the HST vehicle reference frame. The primary input is the OTA prepared data file produced by the initial data reduction function, and the output is alignment matrices for transformation from the FGS-1 and FGS-3 frames to the HST vehicle frame.

3. EARLY OFAD PROBLEMS, STUDIES, AND SOLUTIONS

Following our implementation of the basic OFAD algorithm in the prototype software, we began a series of new tests using simulated data corrupted by noise and solving for a broad spectrum of distortion coefficients and offset angle/deviation angle combinations. These tests revealed previously unexpected accuracy, observability, and numerical stability problems. W. Jefferys confirmed many of these problems using his independent software implementation of the OFAD algorithm. Because of the OFAD algorithm's high level of complexity and the difficulties experienced during attempts to solve many of these new problems, GSFC and MSFC decided to create an OFAD technical team to coordinate the efforts of those individuals in the HST community most knowledgeable in the subtleties of the OFAD algorithm. The team, headed by P. Davenport of GSFC, also included F. VanLandingham, G. Abshire, and L. Hallock of CSC; M. Margulies and L. Abramowicz-Reed of P-E; R. Jayroe of MSFC; and W. Jefferys of the University of Texas. The insights of the team into the inner workings of OFAD produced many highly successful enhancements to the original algorithm and resulted in improvements to prelaunch operational procedures and maneuver planning.

This section briefly discusses several of the contributions of the OFAD technical team toward creating a reliable OFAD algorithm.

3.1 OBSERVABILITY AND NUMERICAL STABILITY PROBLEMS

The standard P-E distortion polynomial, consisting of 11 terms in each axis, has the form

$$\begin{aligned}\sum_{L,M} a_{LM}\, X_D^L Y_D^M = {} & a_{1,0}X_D + a_{2,0}X_D^2 + a_{1,1}X_DY_D + a_{0,2}Y_D^2 + a_{3,0}X_D^3 \\ & + a_{2,1}X_D^2Y_D + a_{1,2}X_DY_D^2 + a_{0,3}Y_D^3 + a_{5,0}X_D^5 \\ & + a_{3,2}X_D^3Y_D^2 + a_{1,4}X_DY_D^4\end{aligned}$$

$$\begin{aligned}\sum_{L,M} b_{LM}\, X_D^L Y_D^M = {} & b_{0,1}Y_D + b_{2,0}X_D^2 + b_{1,1}X_DY_D + b_{0,2}Y_D^2 + b_{3,0}X_D^3 \\ & + b_{2,1}X_D^2Y_D + b_{1,2}X_DY_D^2 + b_{0,3}Y_D^3 + b_{0,5}Y_D^5 \\ & + b_{2,3}X_D^2Y_D^3 + b_{4,1}X_D^4Y_D\end{aligned}$$

where a_{LM}, b_{LM}, X_D, and Y_D are as defined in Section 2.3. Most of the early "perfect" data tests (i.e., tests with simulated data uncorrupted by noise) executed using the OFAD prototype software and data generator studied only a subset of the full 11-term polynomial, specifically the 3 quadratic and 4 cubic coefficients. The next step in the algorithm test procedure was to expand the scope of the tests to include linear and fifth-order coefficients. These tests produced algorithm failures centering on the inability of the software to invert the large matrices (having dimensions greater than 100) used in the least-squares calculations.

In the case of the linear coefficients, the inversion problem had two causes. First, we determined empirically in testing that unless roll maneuvers were included in the OFAD maneuver sequence (nominally the simulated data included two observations sets consisting of a +10-degree roll and a -10-degree roll from the reference attitude), no linear coefficients could be determined. Jefferys confirmed this finding analytically and soon afterward modified the planned OFAD observing sequence to include two pure roll maneuvers. The second anomaly discovered during testing was that the $a_{1,0}$ and $b_{0,1}$ coefficients (linear terms), when taken together, contain a plate scale component, which is not observable by the OFAD algorithm. The initial solution to this problem was to hold the $b_{0,1}$ coefficient constant and solve for only the $a_{1,0}$ coefficient. A later enhancement (discussed in Section 3.3) constrained the solved-for distortion polynomial's $a_{1,0}$ and $b_{0,1}$ coefficients from having a scale component and thereby permitted solving for both linear coefficients. The $a_{0,1}$ and $b_{1,0}$ coefficients (linear cross-terms), when taken together, contain a rotation component, which is not observable by the OFAD algorithm. To solve for the linear cross-terms, the required procedure at that time was to hold the $b_{1,0}$ coefficient constant while solving for the $a_{0,1}$ coefficient. (The current implementation of both the mini-OFAD and OFAD algorithms allows the user to select any polynomial up through fifth order, with a default to the P-E 11-term polynomial.) A later enhancement (discussed in Section 3.3) constrained the solved-for distortion polynomial's $a_{0,1}$ and $b_{1,0}$ coefficients from having a rotation component and thereby permitted solving for both linear coefficients.

Numerical underflow produced the matrix inversion problems in solving for fifth-order coefficients. We solved this problem by adding numerical scaling parameters to the calculations. With appropriately selected values, these parameters provide adequate underflow protection and eliminate a purely numerical source of instability.

3.2 NOISE-CORRUPTED DATA PROBLEM

The effect of corrupting data with noise was the most difficult of all the OFAD problems to solve. Efforts to solve this problem resulted in the enhancement of the original OFAD algorithm with constraints and led to the creation of the mini-OFAD algorithm (Section 3.4). We discovered the problem during our first tests with simulated data corrupted by noise. With perfect data the OFAD algorithm could solve for the "true" distortion polynomial coefficients (i.e., the coefficients simulated in the data generator) to a precision of eight significant figures, even with a very poor initialization. However, with the addition of noise, the effective difference between a solved-for coefficient and the corresponding true value of the coefficient appeared to be one to two orders of magnitude higher than the noise in the data. To determine more quantitatively the size of the discrepancy, we coded a small prototype software utility (called the goodness-of-fit utility). This utility revealed that the resulting error in the undistorted vector computed using the solved-for coefficients was between 60 and 100 times the noise. We therefore referred to the anomaly as "noise magnification."

Jefferys explained the nature of the noise magnification effect empirically (Reference 9), and Davenport explained it analytically (References 10 and 11). Jefferys analyzed the difference between expected and solved-for values and demonstrated that the error could be modeled by an affine transformation (linear translations plus rotation). After removal of the affine fit, the remaining errors were approximately the same size as the original noise. Davenport demonstrated analytically that over the small FOV of an FGS, without input ground measurements to constrain the solution, the polynomial solution could be expected to acquire undesired affine terms. Soon afterward, Davenport further refined his result by proving that the dominant error term can be characterized by a similarity transformation, i.e., a combination of translations in X and Y, a rotation about Z, and a change in plate scale. Jefferys also observed this empirically (Reference 12). The OFAD algorithm can observe none of the four components of a similarity transformation. However, determination of the combined translations and rotations, at least in a relative sense, is possible via FGS-to-FGS alignment calibration (Section 2.4), and, of course, determination of the change in plate scale is possible via plate scale calibration (Section 2.2). It was clear that unless the undesired similarity terms could be kept out of the polynomial solution, the only way to verify the accuracy of the OFAD solution would be to undertake a massive simulation effort in which a complete set of FGS calibration parameters (distortion coefficients, plate scales, and FGS-to-FGS alignments) would be determined for each FGS with highly realistic simulated data, following which the overall accuracy of the complete parameter set would be evaluated. Even if such a simulation indicated that the overall accuracy of the whole parameter set met mission requirements, the necessity of relying on an OFAD algorithm that under operational conditions would displace the solved-for distortion coefficients from the initial values by a large, unpredictable similarity transformation was clearly undesirable.

To alleviate this problem, Davenport recommended introducing four constraints on the OFAD state vector that he believed would inhibit formation of the observed similarity transformation between the solved-for distortion coefficients and the truth (Reference 13). The effect of the constraints was to prohibit the solved-for true direction cosines from picking up similarity terms that could be passed on to the solved-for distortion polynomial. Because no constraint features existed in the original OFAD formulation,the software was enhanced with the new equations specified by Jefferys (Reference 14) and Abramowicz-Reed (Reference 15) incorporating Davenport's constraints in OFAD. Section 3.3 discusses the results of our tests using OFAD software containing this constraint capability.

Finally, the technical team made tentative plans to carry out a full-scale simulation to test the validity of the combined OFAD, plate scale, and alignment calibration solutions in the event that the results of the upcoming tests on the enhanced OFAD algorithm did not prove unambiguously successful. In particular, CSC and P-E began identification and specification of a complete set of biases and physical effects required for generation of realistic simulated data.

3.3 INITIAL ESTIMATES FOR CONSTRAINTS

After implementing in prototype software Davenport's constraints on the solved-for reference observation set star direction cosines (Section 3.2), we began testing the enhanced algorithm with a variety of input polynomials. We determined that the constrained version of the OFAD algorithm, unlike the unconstrained version, was highly sensitive to the accuracy of the distortion coefficient initialization values. The cause of the problem was that the values of the reference direction cosines used to initialize the OFAD least-squares process were determined by removing distortion (using the initial estimates of the coefficients) from FGS measurements of star directions at the reference attitude. Because these initial values of the direction cosines were used to constrain the solved-for values of the direction cosines, once an error was induced in the direction cosines (via the initial coefficient estimates), the algorithm could not recover from the error. As a result, the OFAD algorithm tended to converge to a polynomial solution very close to the initial estimates. In particular, if the OFAD algorithm was initialized with a polynomial having different similarity properties than the "true" polynomial, the effect of the constraints would be to prohibit the OFAD algorithm from solving for the truth.

Soon afterward, Davenport discovered the highly data-dependent nature of the OFAD polynomial's similarity component (References 16 and 17). Therefore, even if the development of undesirable similarity transformations when solving for distortion coefficients could be prohibited, the solved-for coefficients could appear to have nonzero similarity terms when applied to other data. This result emphasized further that tests of the validity of the OFAD algorithm performed in isolation from the plate scale and alignment algorithms would not be reliable, and therefore a full-scale simulation of all three algorithms was required to demonstrate feasibility.

Two approaches to the constraint initialization problem developed. First, CSC recommended that a simpler, more stable form of the OFAD algorithm, a mini-OFAD algorithm using ground-based data (Section 2.3.1), be developed in the hope that it could be used to detect at an early stage any large biases in the prelaunch distortion coefficient estimates and also be used to provide a more accurate initialization of the full OFAD algorithm. Section 3.4 describes the results of our tests using the mini-OFAD algorithm. The second approach to the constraint initialization anomaly was Davenport's continuing efforts to improve on the existing constraint formulation. Section 3.4 also discusses the new constraints he developed and their applicability to both the mini-OFAD and OFAD algorithms.

3.4 ALIGNMENT/ATTITUDE ERRORS IN MINI-OFAD ALGORITHM

The mini-OFAD algorithm iterates between the least-squares computation of the distortion polynomial coefficients and the q-method calculation of a rotation error matrix. The algorithm can perform the q-method calculation either before or after the least-squares calculation of the distortion polynomial, at user option. Initially, we conducted algorithm tests with data-generator-produced input data that were corrupted by noise but contained no alignment bias. When performing the least-squares calculation of the coefficients prior to computing the rotation error matrix, the mini-OFAD algorithm determined coefficients to an accuracy comparable with the amount of noise in the data and the error in the ground-measured background stars. When the order was reversed, the rotation matrix determination picked up any rotational differences in similarity terms between the initial values of the distortion coefficients and the true values of the distortion coefficients, resulting in a poor solution. Therefore, for the first series of tests, as long as error matrix determination followed coefficient calculation, the mini-OFAD algorithm performed well enough to provide early bias detection capability and an accurate initialization for the OFAD algorithm. However, the addition of a simulated alignment bias (operationally, for mini-OFAD, an apparent alignment bias could be generated by an alignment or attitude error) resulted in undesirable coefficient perturbation. So although the mini-OFAD algorithm was rather insensitive to noise, it unfortunately was highly sensitive to alignment biases or attitude errors, neither of which was a problem to the OFAD algorithm, which uses such information only for aberration calculations.

Davenport's modified constraints (Reference 18) provided the solution to the problems of both algorithms. In his new constraint formulation, the distortion coefficients were constrained such that the similarity content of the distortion polynomial was required to remain the same through all iterations of the OFAD algorithm. When applied to the mini-OFAD algorithm, the constraints prohibited the coefficients from picking up an alignment bias and/or attitude error. When applied to the OFAD algorithm, the constraints prevented the coefficients from modifying the similarity terms to provide a better fit to the noise. Initially the constraints used fixed points outside the FGS FOV to maintain a constant similarity content. However, because of the data-dependent nature of the similarity components, the use of actual measurement points as input to the constraints produced better results. All OFAD and mini-OFAD runs performed in the feasibility study constrained the distortion polynomial with measured star direction cosines. Implementation of Davenport's new constraints in both OFAD algorithms constituted the last major software enhancement required to support the combined simulation effort.

4. FEASIBILITY STUDY

From February through July 1987, we conducted a feasibility study to test the combined accuracy of FGS calibration parameters determined with the OFAD, plate scale, and FGS-to-FGS alignment calibration software. The study required the simulation of a massive quantity of FGS data that realistically modeled all conceivable sensor biases, telemetry characteristics, and physical phenomena that could affect the in-flight calibration of the FGSs. In addition, the unique characteristics of the FGSs and the unusually high accuracy requirements placed on the calibration process necessitated considerable effort to determine a successful operational scenario for utilizing available software calibration tools. This section provides a detailed account of these activities.

4.1 DATA SIMULATION AND DATA REDUCTION ACTIVITIES

The OFAD feasibility study used a modified version of the PASS attitude simulation software that enabled the realistic simulation of the most important aspects of the HST's FGSs.

4.1.1 Simulation Procedure

Our procedure for generation of data for the full-scale simulation was as follows. First, the PICKLES program, developed by W. Jefferys, was executed to select an appropriate cluster of stars for each observation set being simulated. Capabilities provided by this program included shifting the FGS FOV and deleting any undesirable stars in the FOV. Input to this program was the NGC 188 star catalog; output was the right ascension, declination, and magnitude of each star chosen for the specific observing sequence. Using the MAC Terminal utility program and the VAX screen editor, the output data file from PICKLES was transferred from the Macintosh personal computer on which the program had been executed to the VAX 11/785; the file was then used as input to a utility program (developed especially for the simulation) for creation of a NAMELIST for use by the PASS simulation software.

Next, the simulator was executed to simulate the attitude profile (defining parameters that have a first-order dependence on attitude) for the observation set and to create astrometry and guide star files, and the data generated were used as input to the attitude simulator for creation of OTA telemetry data. All attitude simulator executions were in batch mode; all other executions were in interactive mode. The telemetry data generated were then used as input to the PASS OTP for creation of an engineering data file. The engineering data file contains attitude quaternion data, fine mode PMT counts, star selector angle data, and engineering data status flags.

The OTA initial data reduction software (IDR) was executed to reduce the engineering data file to the OTA prepared data file, and the prepared data file was then used as input to the plate scale, mini-OFAD, OFAD, and FGS-to-FGS alignment calibration software. Finally, all data created prior to initial data reduction were written to tape.

4.1.2 Errors and Biases

Each type of error and the magnitude of each error to be simulated were specified jointly by CSC and P-E and then submitted to the OFAD technical team for comment. The major sources of the errors simulated were as follows: initialization in the attitude simulator of the distortion coefficients, plate scale values, offset and deviation angles, and FGS alignments; FGS measurements; HST dynamics; and ground measurements of the star positions.

The distortion polynomial used in the attitude simulator executions was a 17-term undistorted-to-distorted image space polynomial specified by P-E. The distortion polynomial used in the IDR executions was a modified version of an 11-term polynomial provided by P-E; the distorted-to-undistorted object and image space coefficients used were identical to those specified by P-E except for the X linear term in the X-polynomial and the Y linear term in the Y-polynomial, which were modified to remove the effects of scale and rotation.

The P-E-specified discrepancy of no more than ±2 percent in simulator versus IDR plate scale values was adhered to in the simulation. The errors simulated in plate scale values were between 1.0 and 1.4 percent depending on the FGS involved. Errors were also introduced into the deviation and offset angles.

The discrepancies in alignment were computed using small-angle approximation. The error in FGS-1 was computed with a pitch of 1.5 arc-seconds, a roll of -295 arc-seconds, and a yaw of -0.5 arc-second. In both the simulator and IDR executions, FGS-2 and FGS-3 had the same alignment.

The FGS measurements were the second most important source of errors in the simulation. The FGS fine error signal consists of measurements of the number of photons selected by four PMTs and so is subject to Poisson statistics as specified by the square root of the number of photons detected. The two sources of error in star selector angle measurement were the 7-bit correction and the 14-bit correction. These corrections are due to mechanical encoder errors. Both corrections were simulated. Only the 7-bit correction was compensated for in the OTP to within ±0.32 milliarc-second. The 14-bit correction is a time-independent, low-frequency correction to the star selector angles of about 0.5 arc-second that is not compensated for by the IDR or the OTP. However, because this is a low-frequency correction, it can be compensated for using the distortion coefficients. All of the fine error signals were adjusted for a background with the amount of light generated by a 20th-magnitude star in addition to the expected star.

An HST attitude error of 3 milliarc-seconds due to jitter was simulated, but no error due to uncompensated rate gyro assembly drift was included. The stars in the guide star and astrometry header data files generated by the profile simulator had random position errors of 15 milliarc-seconds from their true locations in the sky.

4.1.3 Data Quantity

The full-scale data simulation was a massive effort requiring heavy use of computer resources. For a single FGS, 17 observation sets were required for distortion coefficient determination, 1 simulator execution was required for mini-OFAD calibration, and 3 simulator executions were required for plate scale calibration. An additional 10 executions were required for FGS-to-FGS alignment calibration, for a grand total of 73. Each observation set consisted of about 40 minutes of simulated data, for a total of

2,920 minutes, or 4.9 hours. We used the observing sequence described in Section 1.2 for the OFAD calibration.

4.2 DATA ANALYSIS SCENARIOS

Because each of the three FGS calibration functions (OFAD, plate scale, and FGS-to-FGS alignment calibration) requires as input the output of the other two, an iterative procedure among the three software modules is required to generate an FGS calibration parameter set that meets the HST mission accuracy requirements.

4.2.1 Strawman Scenario

To provide a starting point for the feasibility study, P-E prepared a preliminary procedure for calibrating the FGSs (Reference 19). This procedure was as follows:

1. Excluding the fifth-order distortion coefficients, iterate between the calibrated plate method for plate scale calibration and the mini-OFAD algorithm for distortion calibration until the change in the plate scale on successive iterations falls to below 0.002 percent.

2. Perform a preliminary alignment calibration.

3. Solving for the full 11-term polynomial, iterate between the OFAD algorithm for distortion calibration and the moving asteroid method for plate scale calibration until convergence is achieved.

4. Calibrate the FGS-to-FGS alignment.

5. Iterate among the OFAD algorithm for distortion calibration, the moving asteroid method for plate scale calibration, and FGS-to-FGS alignment calibration until the alignment matrix changes on successive iterations by less than 0.2 percent.

In the course of performing the feasibility study, we discovered that a number of improvements to the strawman scenario could be made. Section 4.2.2 describes the final calibration procedure used in the study.

4.2.2 Final Operational Scenario

Using the P-E strawman scenario as a starting point, we gradually refined the scenario to improve the accuracy and stability of the solution. The final procedure is described below.

First, as in the P-E scenario, an iterative procedure between the calibrated plate method for plate scale calibration and the mini-OFAD algorithm for distortion calibration was performed until the change in the plate scale on successive iterations fell to below 0.002 percent. In practice, this convergence condition required four executions of the plate scale software and three executions of the mini-OFAD calibration software. In each execution of the mini-OFAD calibration software, three iterations between the least-squares computation of the coefficients and the q-method computation of the rotation error matrix were performed. In the least-squares distortion coefficient computation, three to six iterations were usually performed (on the third cycle with the q-method, at least six iterations were always performed). As in the P-E scenario, no fifth-order coefficients were solved for. In earlier test results, the solution appeared to be somewhat unstable when fifth-order coefficients were included. Because the initial estimates of the linear coefficients ($a_{1,0}$ in the X-polynomial and $b_{0,1}$ in the Y-polynomial) did not satisfy Davenport's constraint for these terms (Reference 18), both linear coefficients could not be determined (using this constraint) without displacing the coefficients from their initial values by a large amount. Instead, the $a_{1,0}$ coefficient in the X-polynomial was determined, whereas the $b_{0,1}$ coefficient in the Y-polynomial was held constant. The remaining coefficients (i.e., the three quadratic and four cubic coefficients) in the standard 11-term polynomial were determined.

After the iterative procedure between the calibrated plate method and the mini-OFAD algorithm converged, a preliminary alignment was determined. Because a complete set of FGS calibration parameters was then available, the goodness-of-fit utility was executed. Of course, in a real operations situation, where the truth is unknown, the goodness-of-fit utility is not usable. The preliminary alignment was used for accuracy checking only; it was not used to initialize the OFAD algorithm or the moving asteroid method. The output from the calibrated plate method and the mini-OFAD algorithm were, however, used to initialize the moving asteroid method and the OFAD algorithm.

Next, an iterative procedure between the moving asteroid method and the OFAD algorithm was performed until convergence was achieved. The convergence criterion selected was that the change in the plate scale on successive iterations be no more than 0.00001 percent.

In a departure from the P-E approach, an asteroid plate scale was determined to initialize the OFAD algorithm. For the OFAD algorithm executions, the full set of 11-term polynomial coefficients, except for the $b_{0,1}$ coefficient in the Y-polynomial, were determined. As in the case of the mini-OFAD algorithm executions, the $b_{0,1}$ coefficient in the Y-polynomial was held constant to avoid a conflict with the requirements of the associated constraint. Also, the B deviation angle and the B offset angle were determined. Solving for more than one deviation or offset angle in a single execution resulted in erratic displacements of the solved-for direction cosines (Section 5.1). Satisfaction of the convergence criterion required four executions of the moving asteroid plate scale calibration software and three executions of the OFAD algorithm. In one execution of the OFAD algorithm, six iterations were usually performed. At the end of each plate scale calculation using the moving asteroid method, the most recent OFAD algorithm and moving asteroid plate scale solutions were checked for consistency using the mini-OFAD algorithm. Unlike the goodness-of-fit utility, the mini-OFAD algorithm can be used to check the consistency of the OFAD algorithm solutions even in an operational setting. However, the goodness-of-fit utility was used in the feasibility study to check the accuracy of the OFAD algorithm solutions on an intermittent basis. The last step of the scenario was to perform an alignment calibration. It was determined that because the OFAD algorithm and the moving asteroid method are relatively insensitive to alignment errors, no iteration among the OFAD algorithm, the moving asteroid method of plate scale calibration, and FGS-to-FGS alignment was required. The final parameter set was consistency checked with the mini-OFAD software and accuracy checked with the goodness-of-fit utility.

5. RESULTS OF FEASIBILITY STUDY

In addition to achieving the study's primary objective of demonstrating feasibility, we also discovered many useful techniques for improving the stability and accuracy of the OFAD solution.

5.1 QUALITATIVE RESULTS

The feasibility study provided an excellent opportunity to test the behavior of the OTA algorithms using realistically simulated data with different combinations of state vector element sets and constraints. The most important discovery was the high sensitivity of both the mini-OFAD and OFAD algorithms to bad data points. As part of the simulation, a star observation was produced with an erroneous 14-bit correction and a consequent error of approximately 0.5 arc-second. Even using the mini-OFAD algorithm, which is more stable than the OFAD algorithm, this single bad data point out of 38 data points resulted in a level of data degradation sufficient to produce an unacceptably high error in the solved-for polynomial. Considerable effort was required during the study to detect and identify bad data points. In response to this problem, we proposed the enhancement of all the OTA algorithms to include a more sophisticated data validation capability and a series of statistical summary displays to display the vector of conditions and other large arrays. Such summary displays would identify which stars/observation sets constitute the poorest fit to the current distortion polynomial values without requiring the operator to page through an impractically large number of array elements and visually identify the outliers. These enhancements were implemented in the PASS OFAD software after the completion of this study.

One expected problem experienced during the study was some instability when solving for fifth-order coefficient values. To minimize the impact of the instability, the fifth-order terms were held constant in the mini-OFAD algorithm. This helped the mini-OFAD algorithm solve for stable, accurate polynomial coefficients. Having been initialized with a reliable distortion estimate, the OFAD algorithm had no difficulty solving for the fifth-order terms when a higher accuracy solution was required. We believe that some additional improvement could be achieved if better numerical scaling of the coefficients were added to the OFAD algorithms. The improvement of the numerical scaling is currently being studied.

We observed a new, unexpected instability in the first set of mini-OFAD algorithm executions. All the solved-for distortion coefficients (one linear in the X distortion polynomial, three quadratic in X and three in Y, and four cubic in X and four in Y) moved by unrealistically large amounts from their initial estimates during the first least-squares computation before the Euler angle calculation with the q-method. This effect was most observable in the linear term and was amplified when, in test executions, fifth-order terms were determined. Upon recomputation of the coefficients following Euler angle calculation, considerable recovery of the solution occurred, although a larger-than-expected displacement of the solution from the initial estimates remained. Further, but not complete, recovery was achieved on iteration with the plate scale calibration software and upon refinement with the OFAD algorithm. There is currently no explanation for this phenomenon, but this particular instability apparently (on the basis of the calculated accuracy of the solution (Section 5.2)) caused no lasting damage.

We executed the OFAD algorithm numerous times to solve for different combinations of offset and deviation angles. The more parameters solved for, the greater the displacement of the solved-for star direction cosines from their initial estimates. In solving for two deviation angles and one offset angle, the shift in the star direction cosines was as much as 1 arc-second even though the accuracy of the mini-OFAD distortion estimate was expected to be no worse than about 20 milliarc-seconds. The standard parameter set was one deviation angle and one offset angle. For such cases the maximum displacement of direction cosines was between 0.2 and 0.5 arc-second. Although no degradation in the achieved accuracy was observed (Section 5.2), such a large movement in the star field is quite unsettling. The reason for the displacement could be nonutilization (during the feasibility study) of the old constraints on the direction cosines (Section 3.2). These constraints might, in conjunction with the new constraints on the coefficients used during the study (Section 3.4), provide for an accurate, stable solution without unrealistic displacement of the state vector's non-calibration elements. Since completion of the study, the additional four constraints have been added to the PASS OFAD software.

5.2 QUANTITATIVE RESULTS

The primary reason for conducting this study was to determine if, with a proper operational scenario, the three FGS calibration algorithms (plate scale, OFAD, and FGS-to-FGS alignment calibration) could determine an FGS calibration parameter set of sufficient accuracy to meet HST mission requirements. As shown in Table 1, for the standard 11-term polynomial case, the accuracy of an FGS relative to itself (i.e., the combined accuracy of plate scale and OFAD parameters) was always below 1.5 milliarc-seconds, as against an accuracy requirement of 3 milliarc-seconds. The accuracy of either FGS-1 or FGS-3 relative to FGS-2 (i.e., the combined accuracy of the plate scale, OFAD, and alignment parameters) was less than 3 milliarc-seconds, as against an accuracy requirement of 5 milliarc-seconds. Furthermore, the error in inverting the solved-for polynomial for onboard use was negligible. These results are outstanding and provide good reason for optimism about the probability for success of the in-flight calibration activity.

Results achieved using a 17-term polynomial (adding in the linear cross-term and the 5 fourth-order terms) were similar to the 11-term polynomial results, with one major exception. The inversion error when transforming a 17-term distorted-to-undistorted object space polynomial to an 11-term undistorted-to-distorted object space polynomial was much higher than when inverting the 11-term distorted-to-undistorted object space polynomial.

Table 1. OFAD and Mini-OFAD Algorithm Accuracies

CONDITIONS	Mean FGS-1 (mas)			Mean FGS-2 (mas)		Mean FGS-3 (mas)		
	wrt FGS-1	wrt FGS-2	Inversion	wrt FGS-2	Inversion	wrt FGS-3	wrt FGS-2	Inversion
OFAD: 17 TERMS, θ_B, δ_B	1.0 ± 0.8	2.0 ± 1.4	1.2 ± 1.0	0.5 ± 0.4	1.2 ± 1.2	1.7 ± 0.9	2.5 ± 1.8	7.7 ± 5.5
OFAD: 11 TERMS, θ_B, δ_B	0.8 ± 0.7	2.3 ± 1.7	0.03 ± 0.01	0.7 ± 0.7	0.02 ± 0.01	1.1 ± 0.7	2.1 ± 1.6	0.04 ± 0.02
MINI-OFAD: 17 TERMS	10.3 ± 14.0	N/A	3.0 ± 3.4	5.3 ± 4.1	2.3 ± 1.5	21.8 ± 16.9	N/A	13.5 ± 8.0
MINI-OFAD: 17 TERMS	9.8 ± 10.5	N/A	0.07 ± 0.04	4.0 ± 3.3	0.10 ± 0.06	37.1 ± 29.5	N/A	0.61 ± 0.47

NOTE: mas = milliarc-second
wrt = with respect to
N/A = not applicable

For FGS-3, the inversion error was greater than the total error budget. We determined the major contributor to the inversion error to be the linear cross-term. Provided the distortion encountered in flight contains no components that are best modeled by linear cross-terms, solving for the standard 11-term polynomial in flight should be no problem.

Table 1 also specifies the accuracies of the mini-OFAD solutions (in conjunction with asteroid-method-computed plate scales) used to initialize the OFAD algorithm computations. For FGS-1 and FGS-2, the accuracy of the calibration of the FGS relative to itself was about 10 milliarc-seconds or better. Because the expectation had been that the mini-OFAD algorithm would calculate distortion coefficients accurate to about 20 to 30 milliarc-seconds (largely due to error in the reference vectors), the accuracies achieved with FGS-1 and FGS-2 were surprisingly good. In fact, for FGS-2, the accuracies with the mini-OFAD algorithm almost met the 3-milliarc-second mission requirement. For FGS-3, the accuracies (relative to FGS-3) were much worse, due to the presence of additional bad simulated data points. However, even with FGS-3, the approximate distortion values supplied by the mini-OFAD algorithm provided the OFAD algorithm with a sufficiently accurate initialization to allow the latter to compute coefficients accurate to better than 3 milliarc-seconds. In addition, the errors experienced when inverting mini-OFAD solutions followed the same pattern as with OFAD solutions, i.e., the inversion errors for the 11-term polynomial were small, but the errors for a 17-term polynomial were unacceptably large.

6. CONCLUSIONS

We believe that our study of FGS calibration accuracy demonstrates that the current versions of the PASS plate scale, OFAD, and FGS-to-FGS alignment calibration algorithms are capable of meeting the HST mission's very stringent accuracy requirements, provided the actual distortion encountered in flight can be represented with the current P-E 11-term polynomial. In particular, it is essential that the distortion encountered in flight not contain any components best modeled by linear cross-terms, because no such terms are present in the current 11-term model. Should any linear cross-terms or other important, unrepresented terms be present, the PASS software has the capability to solve for a larger polynomial including the extra terms, but the flight software's inverse polynomial is limited to 11 terms. The study did not obtain an accurate inversion from a larger, more general polynomial to the standard 11-term polynomial within accuracy limits. Therefore, to the extent that the distortion simulated in this study resembles the real distortion that will be encountered in flight, the study shows the OFAD algorithm to be adequate to support HST launch.

CSC acknowledges the valuable assistance of the OFAD technical team, headed by P. Davenport of GSFC, in determining the initial parameter values for this study and in interpreting the study's results. Other non-CSC members of the team include R. Jayroe of MSFC, L. Abramowicz-Reed and M. Margulies of P-E, and W. Jefferys of the University of Texas. Also, CSC extends thanks to W. Lindboe and W. Rumpl of CSC for program runs made in support of the simulation activities for this study.

CSC performed the OFAD calibration feasibility study in support of contract NAS 5-26685.

REFERENCES

1. L. Abramowicz-Reed, "Space Telescope Plate Scale Calibration Algorithm," Memorandum ST-SE-3360, Perkin-Elmer, April 2, 1984
2. G. Dente and L. Abramowicz-Reed, "Space Telescope Optical Field Angle Distortion Calibration Algorithm," Memorandum ST-SE-3336, Perkin-Elmer, March 23, 1984
3. Perkin-Elmer, PR-1011, Algorithms for Fine Guidance Sensor/V1, V2 , V3 Alignment (Part 1) and Fine Guidance Sensor/Scientific Instrument Alignment (Part 2), December 7, 1984
4. --, PR-1005, Initial Data Reduction Techniques for Star Selector Positions, December 7, 1984

5. Computer Sciences Corporation, CSC/TM-82/6045, SpaceTelescope POCC Applications Software Support (PASS) Requirements Specification (Revision E), September 1987
6. W. Jefferys, "On the Method of Least Squares, " The Astronomical Journal, February 1980, vol. 85, no. 2, pp. 177- 181
7. --, "On the Method of Least Squares II," The Astronomical Journal, January 1981, vol. 86, no. 1, pp. 149-155
8. Computer Sciences Corporation, CSC/TM-77/6034, Analysis of Least-Squares Attitude Determination Routine, DQAOP, February 1971
9. W. Jefferys, Attachment to Minutes of May 1, 1986, OFAD Technical Meeting, May 12, 1986
10. P. Davenport, "Deficiency of Linear Distortion Coefficients in OFAD, " Memorandum, National Aeronautics and Space Administration, Goddard Space Flight Center, May 19, 1986
11. --, "Analysis of OFAD Noise Problem," Memorandum, National Aeronautics and Space Administration, Goddard Space Flight Center, May 30, 1986
12. W. Jefferys, "Why Only Four Constants?," Memorandum, University of Texas at Austin, May 30, 1986
13. P. Davenport, "The OFAD Noise Problem, A Review and the Solution," Memorandum, National Aeronautics and Space Administration, Goddard Space Flight Center, June 25, 1986
14. W. Jefferys, "Constraints in OFAD," Memorandum, University of Texas at Austin, July 9, 1986
15. L. Abramowicz-Reed, Memorandum on OFAD Constraints, P-E, August 12, 1986
16. P. Davenport, "Additional Problems With Polynomial Representing Distortion," Memorandum, National Aeronautics and Space Administration, Goddard Space Flight Center, October 3, 1986
17. --, Attachment to Minutes of October 2, 1986, OFAD Technical Meeting, November 5, 1986
18. --, "Modification of the OFAD Constraints and Distortion Polynomial," Memorandum, National Aeronautics and Space Administration, Goddard Space Flight Center, January 28, 1987
19. L. Abramowicz-Reed, "Procedure for Processing Data in the OTA Algorithms," Memorandum, Perkin-Elmer, March 9, 1987

N89-15940

ALGORITHM FOR IN-FLIGHT GYROSCOPE CALIBRATION

by
P. B. Davenport
Goddard Space Flight Center
and
G. L. Welter
Computer Sciences Corporation

ABSTRACT

An optimal algorithm for the in-flight calibration of spacecraft gyroscope systems is presented. Special consideration is given to the selection of the loss function weight matrix in situations in which the spacecraft attitude sensors provide significantly more accurate information in pitch and yaw than in roll, such as will be the case in the Hubble Space Telescope mission. The results of numerical tests that verify the accuracy of the algorithm are discussed.

I. INTRODUCTION

A spacecraft gyroscope system, sometimes referred to as the rate gyro assembly (RGA), is used to measure angular rotation rates of the spacecraft. This is required for proper control of the spacecraft, particularly for the proper positioning of spacecraft sensors with respect to desired targets. We present here an algorithm for RGA calibration that was used for the High Energy Astronomy Observatory (HEAO) missions and enhanced for use in the Hubble Space Telescope (HST) mission. Section II of this article presents the basic algorithm; Section III, the statistical weighting scheme; Section IV, the results of numerical tests of the algorithm; and Section V, our conclusions.

II. BASIC RGA CALIBRATION ALGORITHM

Any RGA must be composed of at least three gyroscopes whose axis directions taken together completely span the space of possible rotations (i.e., pitch, roll, and yaw). An RGA consisting of K gyros produces as output a response "vector" $\mathbf{R} = (r_1, r_2, \ldots, r_K)^T$, where r_k is the response of the kth gyro. The response vector is translated into a measured angular velocity, Ω_M, of the spacecraft (in the spacecraft frame) via the relation

$$\Omega_M = G_0 \mathbf{R} - \mathbf{D}_0 , \tag{1}$$

where G_0 is the RGA 3-by-K scale factor / alignment matrix, and $\mathbf{D}_0$ is the RGA drift rate bias. If G_0 and $\mathbf{D}_0$ deviate from their true values, because of either poor initial calibration or temporal changes of the RGA, then Ω_M will deviate from the true angular rate, Ω. The goal of the algorithm is to determine correction matrices M and $\mathbf{d}$ that may be applied to G_0 and $\mathbf{D}_0$ so that a modified equation (1) will yield the true angular rate:

$$G = M G_0 , \tag{2a}$$

$$\mathbf{D} = M \mathbf{D}_0 + \mathbf{d} , \tag{2b}$$

$$\Omega = G \mathbf{R} - \mathbf{D} = M \Omega_M - \mathbf{d} . \tag{2c}$$

The angular rate deviation, ω, between the measured and true rates is given by

$$\omega = \Omega_M - \Omega = -m \Omega_M + \mathbf{d} , \tag{3}$$

where $m = M - I$, and I is the identity matrix. The algorithm will solve for m and $\mathbf{d}$. The correction matrices m and $\mathbf{d}$ are dimensioned 3-by-3 and 3, respectively; we emphasize this because it ties directly to the fact that the algorithm being developed here provides correction information for the RGA as a whole in its capacity as a device for measuring three-dimensional angular motion. Unless the RGA under consideration consists of only three gyros, m and $\mathbf{d}$ will not contain sufficient information to allow separate calibration updates of scale, alignment, and drift for the individual gyros.

We wish now to relate the angular rate deviation as integrated over some calibration maneuver to the difference in attitude changes as determined for the maneuver by the RGA and by some independent attitude sensing devices (e.g., fixed-head star trackers). This derivation is conveniently done using quaternion notation; see Reference 1 for a discussion of the mathematics of quaternions. First, an expression for the time derivative of a quaternion is required. If $\mathbf{Q}(t)$ is the quaternion representing spacecraft attitude at time t, then the quaternion representing a change in attitude over a time interval Δt is given by $\mathbf{Q}^{-1}(t)\,\mathbf{Q}(t+\Delta t)$. If Δt is small, the attitude change may be expressed as

$$\mathbf{Q}^{-1}(t)\,\mathbf{Q}(t+\Delta t) = \mathbf{1} + \mathbf{q}(\Omega\Delta t/2)\,, \tag{4}$$

where $\mathbf{1}$ is the identity quaternion, and $\mathbf{q}(\Omega\Delta t/2)$ is a differential quaternion with vector component $\Omega\Delta t/2$ and scalar component zero. Defining $\Delta\mathbf{Q}(t)$ as $\mathbf{Q}(t+\Delta t) - \mathbf{Q}(t)$ and combining this definition with equation (4) yields

$$\Delta\mathbf{Q}(t) = \mathbf{Q}(t)\,\mathbf{q}(\Omega\Delta t/2)\,. \tag{5}$$

Dividing equation (5) by Δt produces the desired quaternion time derivative, $\mathbf{Q}'(t)$:

$$\mathbf{Q}'(t) = \Delta\mathbf{Q}(t)/\Delta t = \mathbf{Q}(t)\,\mathbf{q}(\Omega/2)\,. \tag{6}$$

Equation (6) applies as well for the quaternion time derivative corresponding to the attitudes as measured by the RGA, with subscript M placed appropriately.

Next, the time derivatives specified above are used to construct the time derivative of the attitude error quaternion and the definite integral of that quaternion over the time of the maneuver. The attitude error quaternion, $\delta\mathbf{Q}$, is defined as

$$\delta\mathbf{Q} = \mathbf{Q}_M\,(\,\mathbf{Q}_M^{-1}\,\mathbf{Q}\,)\,\mathbf{Q}_M^{-1} = \mathbf{Q}\,\mathbf{Q}_M^{-1}\,, \tag{7}$$

which is a quaternion expressing a rotation from the RGA-determined postmaneuver attitude to the true postmaneuver attitude, transformed to the premanuever reference frame. It follows by the chain rule of differentiation that

$$\delta\mathbf{Q}' = \mathbf{Q}'\,\mathbf{Q}_M^{-1} + \mathbf{Q}\,\mathbf{Q}'^{-1}_M \tag{8a}$$

$$= \mathbf{Q}\,\mathbf{q}(\Omega/2)\,\mathbf{Q}_M^{-1} + \mathbf{Q}\,\mathbf{q}^{-1}(\Omega_M/2)\,\mathbf{Q}_M^{-1}\,. \tag{8b}$$

Combining equation (8b) with the relations $\omega = \Omega_M - \Omega$ and $\mathbf{q}^{-1}(\Omega_M/2) = \mathbf{q}(-\Omega_M/2)$ produces

$$\delta\mathbf{Q}' = \mathbf{Q}\,\mathbf{q}(-\omega/2)\,\mathbf{Q}_M^{-1} \ . \tag{9}$$

Integrating both sides of equation (9) over the maneuver yields

$$\delta\mathbf{Q} - \mathbf{1} = \int \mathbf{Q}\,\mathbf{q}(-\omega/2)\,\mathbf{Q}_M^{-1}\ dt \ , \tag{10}$$

where the constant of integration (i.e., the identity quaternion) is removed from **δQ** because the integral in equation (10) is a definite integral. The attitude error quaternion can be expressed in terms of the rotation $\mathbf{Q}_{R1}^{-1}\,\mathbf{Q}_{R2}$ from the first reference attitude to the second (i.e., as determined using the attitude sensors against which the RGA is being calibrated) and the rotation $\mathbf{Q}_{G1}^{-1}\,\mathbf{Q}_{G2}$ between the first RGA-propagated attitude and the second. Equation (10) thereby becomes

$$(\mathbf{Q}_{R1}^{-1}\,\mathbf{Q}_{R2})\,(\mathbf{Q}_{G2}^{-1}\,\mathbf{Q}_{G1}) - \mathbf{1} = \int \mathbf{Q}\,\mathbf{q}(-\omega/2)\,\mathbf{Q}_M^{-1}\ dt \ . \tag{11}$$

No approximations have been made in the derivation to this point. We now make two approximations, each of which is accurate to first order in the error. First, $\mathbf{Q}_M$ is substituted for **Q** in the integrand in equation (11). This substitution yields

$$(\mathbf{Q}_{R1}^{-1}\,\mathbf{Q}_{R2})\,(\mathbf{Q}_{G2}^{-1}\,\mathbf{Q}_{G1}) - \mathbf{1} = \int \mathbf{Q}_M\,\mathbf{q}(-\omega/2)\,\mathbf{Q}_M^{-1}\ dt \ . \tag{12}$$

The integrand in equation (12) is simply the quaternion representation for a rotation of the vector $-\omega/2$ through a rotation defined by $\mathbf{Q}_M$, i.e., the rotation that transforms $-\omega/2$ from spacecraft coordinates at time t to spacecraft coordinates in the premaneuver reference frame. Equation (12) can therefore be written in matrix notation as

$$\mathbf{Z}_i = -1/2 \int \boldsymbol{T}_i\ \omega\ dt \tag{13a}$$

$$= 1/2 \int \boldsymbol{T}_i\ (\boldsymbol{m}\ \Omega_M - \mathbf{d})\, dt \ , \tag{13b}$$

where $\mathbf{Z}_i$ is the vector component of **δQ**, $\boldsymbol{T}_i$ is the matrix for transforming vectors to premaneuver spacecraft coordinates, and i is a subscript designating maneuver number. The second approximation is made implicitly in the definition of $\mathbf{Z}_i$ as the vector component of $\delta\mathbf{Q}_i$; the fourth component of $\delta\mathbf{Q}_i$, which is actually equal to the cosine of the error rotation angle, is approximated as equal to 1. Because of the two approximations made in going from equation (11) to (13b), the calibration algorithm described here will be inherently iterative; the vector $\mathbf{Z}_i$ and matrix $\boldsymbol{T}_i$ must be reevaluated on each iteration.

Equation (13b) is linear in the unknowns $\boldsymbol{m}$ and $\mathbf{d}$ and thus lends itself naturally to standard least-squares techniques. First, the matrix equation that represents equation (13b) applied to N calibration maneuvers is written as

$$\mathbf{Z} = \boldsymbol{H}\,\mathbf{x}\,, \tag{14}$$

where $\mathbf{Z}$ and the state vector $\mathbf{x}$ are defined via

$$\mathbf{Z} = \{\, \mathbf{Z}_1^{\mathrm{T}}, \mathbf{Z}_2^{\mathrm{T}}, \ldots, \mathbf{Z}_N^{\mathrm{T}} \,\}^{\mathrm{T}}\,, \tag{15}$$

$$\mathbf{x} = 1/2\,\{\, m_{11}, m_{12}, m_{13}, m_{21}, m_{22}, m_{23}, m_{31}, m_{32}, m_{33}, d_1, d_2, d_3 \,\}^{\mathrm{T}}\,, \tag{16}$$

and $\boldsymbol{H}$ is a 3N-by-12 matrix of the form

$$\boldsymbol{H} = \begin{bmatrix} \boldsymbol{U}_1 & -\boldsymbol{Y}_1 \\ \vdots & \vdots \\ \boldsymbol{U}_N & -\boldsymbol{Y}_N \end{bmatrix}\,. \tag{17}$$

Each $\boldsymbol{U}_i$ is a 3-by-9 matrix, the components of which are given by

$$(U_{j\,k+3(l-1)})_i = \int (T_{j\,k})_i\,(\Omega_M)_l\,dt\,, \tag{18}$$

and each Y_i is a 3-by-3 matrix with components

$$(Y_{jk})_i = \int (T_{jk})_i \, dt . \tag{19}$$

The least-squares solution for the state vector **x** in equation (14) minimizes the linear Bayesian weighted least-squares loss function, J, given by

$$J = 1/2 \, [\, \mathbf{E}^T \boldsymbol{W} \mathbf{E} \; + \; (\mathbf{x} - \mathbf{x}_a)^T \boldsymbol{S}_a \, (\mathbf{x} - \mathbf{x}_a) \,] , \tag{20}$$

where

$$\mathbf{E} = \mathbf{Z} - \boldsymbol{H} \mathbf{x} , \tag{21}$$

W and S_a are symmetric nonnegative definite weighting matrices, and $\mathbf{x}_a$ is an a priori estimate of **x**. The desired solution for **x** is given by

$$\mathbf{x} = (H^T W H + S_a)^{-1} (H^T W \mathbf{Z} \; + \; S_a \mathbf{x}_a) . \tag{22}$$

Equations (20) and (22) include S_a and $\mathbf{x}_a$ for mathematical completeness. In what follows, we will assume $S_a = [0]$, i.e., no a priori knowledge of **x**. In applying equation (22) to determine **x**, it is clear that at least four calibration intervals are required and at least three of these must span the space of possible rotations. An acceptable minimum set of calibration intervals would be one maneuver each of pitch, roll, and yaw, together with a period of constant attitude to define the drift rate bias. In selecting calibration maneuvers to be used for the algorithm, a user should be aware that, at least in the equations specified above, a rotation of greater than 180 degrees is indistinguishable from a smaller rotation in the opposite direction. The use of such large rotations could lead to errors in the calibration and should therefore be avoided. The basic algorithm being discussed here lends itself easily to being broken into two separate algorithms, one to determine the scale factor / alignment portion of **x** and a separate one to determine the drift rate bias.

III. SPECIFICATION OF THE WEIGHT MATRIX

In principle, the specification of the weight matrix $\boldsymbol{W}$ in equation (22) depends on the scale size of random errors associated with the RGA itself, as well as the errors associated with the determination of reference attitudes. In practice, random errors associated with the RGA tend to be much smaller than those of the reference attitude sensors. This is true in particular for the sensors used for the HST mission. The HST uses two types of sensors for high-accuracy attitude determination: fixed-head star trackers (FHSTs) and fine guidance sensors (FGSs). The three FGS fields of view are clustered tightly (within 14 arc-minutes) about the principle axis of the spacecraft (hereafter called the V1-axis). When calibrated, the accuracy of the FGSs should be better than 0.010 arc-second. In most circumstances, however, their effective accuracy will be limited by the accuracy of the reference star catalog against which the FGS observations are compared during attitude computation; this will be about 0.3 arc-second. Because of the tight clustering of the FGSs about the V1-axis, this accuracy of 0.3 arc-second pertains only to the pitch and yaw components. The roll accuracy is determined by the accuracy of the FHSTs, whose fields of view are more widely distributed in direction about the spacecraft than those of the FGSs. The accuracy of the FHSTs used for the HST is about 10 arc-seconds. The fact that the reference attitudes for the HST are substantially better in pitch and yaw than in roll presented a special problem for the HST ground software. For spacecraft that have equal attitude accuracies about all axes, setting the weight matrix in equations (20) and (22) to the identity matrix, i.e., treating the accuracies of all components of all maneuvers as equal and uncorrelated, would be legitimate. This is not the case for the HST; consequently, significantly improved results for HST RGA calibration can be expected if a proper weight matrix is used. The need for a proper weight matrix is enhanced by the possible requirement to combine data sets for maneuvers in which some of the attitudes were determined using only FHSTs or only FGSs. This possibility arises because of potential sensor occultation by the Earth during parts of the spacecraft orbit.

The net effect of the considerations discussed above is that the simple product $\mathbf{E}^T \mathbf{E}$ ($\mathbf{E}$ defined in equation (21)) does not represent a squared sum of normalized, independent random variables as is required for an optimized least-squares loss function (e.g., see Reference 2). The determination of $\boldsymbol{W}$ depends upon the measurement uncertainties of the components of $\mathbf{E}$, both in magnitude for the individual components and in any correlation of errors between the individual components. The 3N-vector $\mathbf{E}$ is composed of N 3-vectors, the relation being

$$\mathbf{E} = (\mathbf{e}_1^T, \mathbf{e}_2^T, \ldots, \mathbf{e}_N^T)^T, \tag{23}$$

where $\mathbf{e}_i$ is the error associated with the ith calibration maneuver. If the errors for the maneuvers are assumed to be independent, then $\boldsymbol{W}$ can be represented as a block diagonal matrix, with each block being a 3-by-3 matrix, $\boldsymbol{w}_i$. The loss function becomes

$$J = \Sigma\, j_i, \tag{24a}$$

$$j_i = 1/2\ \mathbf{e}_i^T \boldsymbol{w}_i\, \mathbf{e}_i\ . \tag{24b}$$

The assumption is not strictly valid in cases where the same attitude data are used at both the end of one maneuver and the beginning of another. In such cases $\boldsymbol{W}$ would appropriately contain elements representing a cross-correlation of errors between maneuvers. Because this complication is both awkward to include computationally and of substantially smaller effect than that of the accuracy asymmetries in attitude produced by the use of FHSTs and FGSs together, we will neglect it. We will also make use of the fact that the random RGA errors are negligible when compared with the reference attitude errors. For notation simplification, hereafter we will suppress the subscript i (for maneuver number) unless it is explicitly required.

Using the approximations described above, the components of $\mathbf{e}$ may be written as

$$e_j = a_j + \Sigma\, t_{jk}\, b_k, \tag{25}$$

where a_j is the premaneuver attitude determination error about the jth spacecraft axis, b_k is the postmaneuver error about the kth axis, and is t_{jk} the (j,k) component of the postmaneuver-attitude-to-premaneuver-attitude transformation matrix. The numbers a_1, a_2, a_3, b_1, b_2, and b_3 may be assumed to be independent random variables, but the numbers e_1, e_2, and e_3 will in general be correlated because of the mixing of the postmaneuver errors via the maneuver transformation matrix. For cases where the a_j and b_k are all approximately equal (as would be true for attitudes determined using a number of well-separated sensors of equal accuracy), the correlation between the components of e would be small because of the combining in each of a number of random variables in different ways. Here, however, we are particularly interested in contexts where a_1 and b_1 (the roll errors) are large compared with a_2, a_3, b_2, and b_3. For such cases a maneuver with significant components about all axes will have errors given to first order by

$$e_1 = a_1 + t_{11} b_1 + O(\delta) , \tag{26a}$$
$$e_2 = t_{21} b_1 + O(\delta) , \tag{26b}$$
$$e_3 = t_{31} b_1 + O(\delta) , \tag{26c}$$

where δ is a generic random variable with variance like that of a_2, a_3, b_2, or b_3. The correlation, particularly between e_2 and e_3, is clear. The goal now is to construct from the components of e three independent, normalized random variables that may be used in defining a least-squares loss function. The components of the weight matrix *w* can then be solved for by setting this new loss function equal to 1/2 ($\mathbf{e}^T \boldsymbol{w}\, \mathbf{e}$). For this derivation we will consider two cases: (1) where the maneuver has a significant nonroll component (i.e., $t_{21}{}^2\sigma_{b1}{}^2 > \sigma_\delta{}^2$ and/or $t_{31}{}^2\sigma_{b1}{}^2 > \sigma_\delta{}^2$, where $\sigma_{b1}{}^2$ and $\sigma_\delta{}^2$ represent the variances of b_1 and δ, respectively) and (2) where the maneuver is essentially pure roll (i.e., $t_{21}{}^2\sigma_{b1}{}^2 < \sigma_\delta{}^2$ and $t_{31}{}^2\sigma_{b1}{}^2 < \sigma_\delta{}^2$).

In case 1 (a maneuver with a significant nonroll component), the quantities e_1, e_2 and e_3 may be used to construct three essentially independent random variables $\langle a_1 \rangle$, $\langle b_1 \rangle$, and c, where $\langle a_1 \rangle$ and $\langle b_1 \rangle$ are estimators of a_1 and b_1, and c is a variable with variance like that of δ. We specifically construct c to eliminate the large roll errors:

$$c = t_{31} e_2 - t_{21} e_3 . \tag{27}$$

The variance of c over an ensemble of maneuvers is given by

$$\sigma_c{}^2 = \mathrm{var}\,\{ t_{31} e_2 - t_{21} e_3 \} \tag{28a}$$
$$= (t_{31}{}^2\, C_2 + t_{21}{}^2\, C_3)\, \sigma_\delta{}^2 , \tag{28b}$$

where

$$C_2 = 1 + t_{22}^2 + t_{23}^2, \tag{29a}$$

$$C_3 = 1 + t_{32}^2 + t_{33}^2. \tag{29b}$$

We construct $<b_1>$ to be a good estimator of b_1:

$$<b_1> = [\, t_{21}^2 / (t_{21}^2 + t_{31}^2)\,]\,(e_2/ t_{21}) + [\, t_{31}^2 / (t_{21}^2 + t_{31}^2)\,]\,(e_3/ t_{31}). \tag{30}$$

The quantities e_2/t_{21} and e_3/t_{31} estimate b_1 to within δ/t_{21} and δ/t_{31}, respectively. The quantities in brackets are normalized weights inversely proportional to the square of the uncertainty of the corresponding estimate. For convenience we rewrite $<b_1>$ as

$$<b_1> = B_2\, e_2 + B_3\, e_3, \tag{31}$$

where

$$B_2 = t_{21} / (t_{21}^2 + t_{31}^2), \tag{32a}$$

$$B_3 = t_{31} / (t_{21}^2 + t_{31}^2). \tag{32b}$$

The variance of $<b_1>$ over an ensemble of maneuvers can be shown to be

$$\sigma_{<b1>}^2 = \sigma_{b1}^2 + (B_2^2\, C_2 + B_3^2\, C_3)\, \sigma_\delta^2. \tag{33}$$

The variance of $<b_1>$ increases as the maneuver approaches being pure roll; if $t_{21}^2\sigma_{b1}^2 = t_{31}^2\sigma_{b1}^2 = \sigma_\delta^2$, then $\sigma_{<b1>}^2 = (1 + C_2/4 + C_3/4)\,\sigma_{b1}^2 = 2\sigma_{b1}^2$. Finally, we construct $<a_1>$ to be a good estimator of a_1:

$$<a_1> = e_1 - t_{11} <b_1> = e_1 - A_2\, e_2 - A_3\, e_3, \tag{34}$$

where

$$A_2 = t_{11}\, B_2, \tag{35a}$$

$$A_3 = t_{11}\, B_3. \tag{35b}$$

The variance of $\langle a_1 \rangle$ over an ensemble of maneuvers can be shown to be

$$\sigma_{\langle a1 \rangle}{}^2 = \sigma_{a1}{}^2 + (t_{12}{}^2 + t_{13}{}^2 + A_{22} C_2 + A_{32} C_3) \sigma_\delta{}^2 . \qquad (36)$$

The variance of $\langle a_1 \rangle$ also increases as the maneuver approaches being pure roll; if $t_{21}{}^2 \sigma_{b1}{}^2 = t_{31}{}^2 \sigma_{b1}{}^2 = \sigma_\delta{}^2$, then $\sigma_{\langle a1 \rangle}{}^2 = \sigma_{a1}{}^2 + (C_2/4 + C_3/4) \sigma_{b1}{}^2 = \sigma_{a1}{}^2 + \sigma_{b1}{}^2$. Although $\langle a_1 \rangle$ is defined using $\langle b_1 \rangle$, it is specifically tailored to remove the correlation with b_1 from e_1. To lowest order $\langle a_1 \rangle = a_1$, $\langle b_1 \rangle = b_1$, and $c = f(a_2, a_3, b_2, b_3)$, from which it is clear that $\langle a_1 \rangle$, $\langle b_1 \rangle$, and c are essentially independent. To find expressions for the weight matrices $\boldsymbol{w}$, we construct a loss function from the squared sum of $\langle a_1 \rangle$, $\langle b_1 \rangle$, and c after normalization and set it equal to the original loss function, i.e.,

$$2j = \mathbf{e}^T \boldsymbol{w}\, \mathbf{e} = c / \sigma_c{}^2 + \langle b_1 \rangle^2 / \sigma_{\langle b1 \rangle}{}^2 + \langle a_1 \rangle^2 / \sigma_{\langle a1 \rangle}{}^2 . \qquad (37)$$

The corresponding elements of $\boldsymbol{w}$ are

$$w_{11} = 1 / \sigma_{\langle a1 \rangle}{}^2 , \qquad (38a)$$

$$w_{22} = A_2{}^2 / \sigma_{\langle a1 \rangle}{}^2 + B_2{}^2 / \sigma_{\langle b1 \rangle}{}^2 + t_{31}{}^2 / \sigma_c{}^2 , \qquad (38b)$$

$$w_{33} = A_3{}^2 / \sigma_{\langle a1 \rangle}{}^2 + B_3{}^2 / \sigma_{\langle b1 \rangle}{}^2 + t_{21}{}^2 / \sigma_c{}^2 , \qquad (38c)$$

$$w_{12} = w_{21} = - A_2{}^2 / \sigma_{\langle a1 \rangle}{}^2 , \qquad (38d)$$

$$w_{13} = w_{31} = - A_3{}^2 / \sigma_{\langle a1 \rangle}{}^2 , \qquad (38e)$$

$$w_{23} = w_{32} = A_2 A_3 / \sigma_{\langle a1 \rangle}{}^2 + B_2 B_3 / \sigma_{\langle b1 \rangle}{}^2 + t_{21} t_{31} / \sigma_c{}^2 . \qquad (38f)$$

In case 2 (an essentially pure roll maneuver), the components of $\mathbf{e}$ can be expressed as

$$e_1 = a_1 + b_1 , \qquad (39a)$$

$$e_2 = a_2 + t_{21} b_1 + (\cos \theta) b_2 + (\sin \theta) b_3 , \qquad (39b)$$

$$e_3 = a_3 + t_{31} b_1 - (\sin \theta) b_2 + (\cos \theta) b_3 , \qquad (39c)$$

where θ is the roll angle. Because b_2 and b_3 are assumed to have equal variance, the variables r_+ and r_-, defined as

$$r_+ = (\cos\theta)\, b_2 + (\sin\theta)\, b_3 , \tag{40a}$$

$$r_- = -(\sin\theta)\, b_2 + (\cos\theta)\, b_3 , \tag{40b}$$

are independent random variables with the same variance σ_δ^2. The components of **e** are therefore of the form

$$e_1 = a_1 + b_1 , \tag{41a}$$

$$e_2 = r_2 + t_{21}\, b_1 , \tag{41b}$$

$$e_3 = r_3 + t_{31}\, b_1 , \tag{41c}$$

where r_2 and r_3 are independent random variables with variance $2\sigma_\delta^2$. The components of **e** are mildly correlated via b_1; b_1 contributes half of the variance of e_1 and at most one-third of the variances of e_2 and e_3 (for $t_{21}^2 = t_{31}^2 = \sigma_\delta^2 / \sigma_{b1}^2$). We neglect this mild correlation for maneuvers that are essentially pure roll by treating them as exactly pure roll, i.e., by setting $t_{21} = t_{31} = 0$. The weight matrix elements that follow from this assumption are

$$w_{11} = 1 / (\sigma_{a1}^2 + \sigma_{b1}^2) , \tag{42a}$$

$$w_{22} = w_{33} = 1 / 2\sigma_\delta^2 , \tag{42b}$$

$$w_{12} = w_{21} = w_{23} = w_{32} = w_{13} = w_{31} = 0 . \tag{42c}$$

The equations specified above provide the functional relationship between the elements of $\boldsymbol{w}$ and the uncertainties in attitude determination with respect to the spacecraft axes. These uncertainties can be derived from the attitude covariance matrix (e.g., see Reference 3), given by

$$\boldsymbol{P} = \sigma_t^2 \left[\boldsymbol{I} - \sum_{k=1,n} (\sigma_t^2 / \sigma_k^2)\, \mathbf{V}_k\, \mathbf{V}_k^T \right]^{-1} \tag{43}$$

where

n = number of measurements,

$\mathbf{V}_k$ = kth star vector used for attitude determination, as expressed in the spacecraft frame,

σ_k = uncertainty of kth measurement,

$\sigma_t^2 = [\ \Sigma\ (\ \sigma_k^2\ )^{-1}\ ]^{-1}$.

For spacecraft such as the HST, whose sensor orientations allow attitude determinations with uncorrelated estimates of pitch, roll, and yaw, the diagonal elements of the matrix ***P*** may be used as the attitude error variance required in the expressions for the elements of ***w***.

IV. NUMERICAL TESTING

The scheme specified above for applying statistical weights to RGA maneuver data has been implemented in the Payload Operations Control Center (POCC) Applications Software Support (PASS) system to be used in support of the HST mission. As indicated at the end of Section II, the algorithm was implemented in a way that allows independent calibration of the RGA scale factor / alignment and the RGA drift rate bias. RGA, FGS, and FHST data appropriate for a number of different calibration intervals were generated using the PASS attitude simulator (this is a simulator that produces data like that expected from the HST). The FGS and FHST errors were of order 0.5 and 10 arc-seconds, respectively. The data consisted of nine independent 90-degree maneuvers (three each of pitch, roll, and yaw) and one extended period of constant attitude data. The 90-degree maneuvers would require approximately 16 minutes of spacecraft time, whereas the constant attitude data represented approximately 45 minutes of spacecraft time. These data were in turn processed through the PASS attitude determination and RGA calibration software. Final residuals were calculated for each maneuver component by comparing the RGA-measured maneuver with the "true" maneuver as supplied to the simulator. The results were good. The final residuals for the components of **E** were in magnitude appropriate for the sensor type governing those residuals (e.g., e_2 for a pure pitch maneuver was in size like the simulated FGS errors, whereas e_1 was like the simulated FHST errors). Furthermore, the scheme described above allows for the combining of data sets in which different attitudes were determined with various different sensor combinations (i.e., FHST and FGS, FHST only, and FGS only). To test this aspect, we processed our simulated data through two RGA calibration scenarios: (1) with both FHST and FGS data used for all attitude determinations and (2) with each maneuver processed twice, once with FHSTs only and once with FGSs only. The final accuracy of the RGA calibration was essentially the same for both scenarios. For the nine-maneuver simulation, the largest deviation (when comparing the measured maneuver magnitude after calibration with the true maneuver magnitude) was found to be about 30 parts per million. This is both appropriate for the magnitude of the sensor errors and sufficiently accurate to support the needs of the HST mission.

V. CONCLUSIONS

We have presented a general algorithm for the calibration of a spacecraft rate gyro assembly, as well as a data weighting scheme that produces a statistically optimal solution. The weighting scheme, although explicitly tailored for use during the Hubble Space Telescope mission, is applicable to any three-axis stabilized spacecraft. Numerical simulations demonstrate that the algorithm works as expected in theory and is capable of supporting the needs of the HST mission.

The work reported in this article was supported in part by NASA contract NAS 5-26685 for the development of ground support software for the Hubble Space Telescope mission.

REFERENCES

1. L. Fallon, *Quaternions*, Appendix D of Spacecraft Attitude Determination and Control, J. R. Wertz, ed. Dordrecht, Holland: D. Reidel Publishing Company, 1978
2. K. A. Brownlee, Statistical Theory and Methodology in Science and Engineering. New York: John Wiley & Sons, Inc., 1960
3. M. Shuster and S. Oh, *Three-Axis Attitude Determination from Vector Observations*, Journal of Guidance and Control, January 1981, vol. 4, no. 1, p. 70

FLIGHT MECHANICS/ESTIMATION THEORY SYMPOSIUM

SESSION 2

PRECEDING PAGE BLANK NOT FILMED

N89-15941

Optimal Post-Experiment Estimation
of
Poorly Modeled Dynamic Systems

D. Joseph Mook
Department of Mechanical and Aerospace Engineering
State University of New York at Buffalo
Buffalo, New York 14260

Abstract

Recently, a novel strategy for post-experiment state estimation of discretely-measured dynamic systems has been developed. The method accounts for errors in the system dynamic model equations in a more general and rigorous manner than do filter-smoother algorithms. The dynamic model error terms do not require the usual process noise assumptions of zero-mean, symmetrically distributed random disturbances. Instead, the model error terms require no prior assumptions other than piecewise continuity. The resulting state estimates are more accurate than filters for applications in which the dynamic model error clearly violates the typical process noise assumptions, and the available measurements are sparse and/or noisy. Estimates of the dynamic model error, in addition to the states, are obtained as part of the solution of a two-point boundary value problem, and may be exploited for numerous reasons. In this paper, the basic technique is explained, and several example applications are given. Included among the examples are both state estimation and exploitation of the model error estimates.

PRECEDING PAGE BLANK NOT FILMED

1.0 Introduction

A large number of applications exist in the general area of "post-experiment" or "post-flight" estimation, wherein estimates of the state histories of a dynamic system are obtained using an assumed state dynamic model and sets of discrete measurements. In general, both the assumed model and the available measurements are imperfect. The motivation for applying an "optimal estimation" algorithm is to combine the model output with the available measurements in such a way as to obtain estimates of the state histories which are superior to both the model and the measurements, and, in addition, satisfy an optimality criterion. In this paper, a new estimation strategy is described which includes both a new optimality criterion and a new algorithm for obtaining estimates based on this condition.

The following generic problem statement for post-experiment estimation of a dynamic process is used to motivate the discussion. Given a system whose state vector dynamics is modeled by the (linear or nonlinear) system of equations,

$$\dot{\underline{x}} = \underline{f}[\underline{x}(t), \underline{u}(t), t] \tag{1}$$

where

$\underline{x} \equiv n \times 1$ *state vector*

$\underline{f} \equiv n \times 1$ *vector of model equations*

$\underline{u} \equiv p \times 1$ *vector of forcing terms,*

and given a set of discrete measurements modeled by the (linear or nonlinear) system of equations,

$$\tilde{\underline{y}}(t_k) = \underline{g}_k[\underline{x}(t_k), t_k] + \underline{v}_k \ , \ k \ = \ 1, ..., m \tag{2}$$

where

$\tilde{\underline{y}}(t_k) \equiv r \times 1$ *measurement set at* t_k

$\underline{g} \equiv r \times 1$ *measurement model equations*

$m \equiv$ *total number of measurement sets*

$\underline{v}_k \equiv r \times 1$ *measurement error vector,*

and v_k is assumed to be a zero-mean, gaussian random sequence of known covariance R_k, determine the optimal estimate for $\underline{x}(t)$ (denoted by $\hat{\underline{x}}(t)$), during some specified time interval $t_0 \leq t \leq t_f$. Clearly, the definition of optimal is subjective, and we begin by discussing optimality criteria.

2.0 Optimality Criteria

The typical approach for obtaining an optimal estimate of the system state trajectories is the minimization of a function of the estimate error,

$$\underline{e}_{\hat{x}} \equiv E\{(\hat{\underline{x}} - \underline{x})\} \tag{3}$$

or its covariance,

$$P_{\hat{x}\hat{x}} \equiv E\{(\hat{\underline{x}} - \underline{x})(\hat{\underline{x}} - \underline{x})^T\} \tag{4}$$

Among these criteria are the well-known "maximum likelihood" and "minimum variance" strategies (e.g., Gelb[1]). For example, the minimum variance criterion requires the minimization of the trace of $P_{\hat{x}\hat{x}}$. Many other criteria which rely on estimating the estimate error statistics (Eqs. (3), (4)) have also been used as bases for estimation algorithms. A practical problem arises during actual implementation of these methods. In order to determine the estimate error statistics, it is necessary to assume that any errors in the system model Eq. (1) are noise of known probability distribution. Most often, the probability distribution is assumed to be zero-mean gaussian, whose covariance is treated as a known quantity ("process noise"). The state estimation proceeds without any adjustment to the system model equations.

In general, it is difficult, if not impossible, to rigorously justify process noise assumptions for the model error. For real physical systems, error is likely to be due to modeling simplifications such as linearization, neglect of higher-order terms, etc., or, perhaps, just plain ignorance. Many of these likely sources are deterministic and non-zero mean. Consequently, the estimate error statistics in Eqs. (3) and (4) cannot be calculated rigorously. Estimates based on their optimization are sub-optimal, e.g., the minimum variance estimate is not truly minimum variance if the variance which is minimized is not the true variance.

These observations are well-known and are repeated here only to motivate the discussion. The optimal estimation strategies which require process noise assumptions work well in many applications, whether or not the model error assumption is justifiable, and filter algorithms are the most commonly used estimators in practice. The filters must generally be artistically "tuned", but this is often possible and sufficient for a reasonably accurate estimate.

However, filter accuracy may deteriorate substantially under a number of conditions. The filter algorithms rely on the integration of the original dynamic model Eq. (1) for the between-measurement estimate. If the model is poor and the measurements are sparse, the accumulated integration error between measurements may become very large. Even if the measurements are dense, if they are particularly noisy, and the model is poor, then the filter estimate may be of poor accuracy. Under certain conditions, the filter may become unstable. Divergence of filters when process noise assumptions are violated may be found in Fitzgerald[2], Huber[3], and Breza and Bryson[4], among others.

With this motivation, Mook and Junkins[5] developed a new estimation strategy which eliminates any *apriori* assumptions about the model error except that it is continuous between the measurement times. The method, called Minimum Model Error (MME) estimation, is based on an optimality criterion which does not require estimation of the estimate error statistics, Eqs. (3)-(4). In the remainder of this paper, a summary of the method is given, followed by several application examples.

3.0 The Covariance Constraint Optimality Criterion

In the MME, a novel optimality criterion is used. The probability distribution of the state estimate error is not estimated. Instead, the optimal state trajectory estimate is determined on the basis of the assumption that the measurement-minus-estimate error covariance matrix must match the measurement-minus-truth error covariance matrix. This condition is referred to as the "covariance constraint". The covariance constraint is defined mathematically by requiring the following approximation to be satisfied:

$$\left\{[\underline{\tilde{y}}(t_j) - \underline{g}(\underline{\hat{x}}(t_j),t_j)][\underline{\tilde{y}}(t_j) - \underline{g}(\underline{\hat{x}}(t_j),t_j)]^T\right\} \approx R_j \qquad (5)$$

Thus, the *estimated measurements* $\underline{g}(\underline{\hat{x}}(t_j),t_j)$ are required to fit the *actual measurements* $\underline{\tilde{y}}(t_j)$ with approximately the same error covariance as the actual measurements fit the truth. An algorithm for obtaining the estimates is described shortly.

The covariance constraint may be evaluated without knowledge of the estimate error statistics. Consequently, there is no need for process noise-like assumptions for the model error. In the next section, an algorithm which produces estimates which satisfy the covariance constraint is derived, treating model error as an unknown which is estimated along with the states.

The interpretation of the "approximately equal" sign in the covariance constraint may be adjusted according to the particular application. If the measurements are repeated samples of the same quantities, as is usual in a filtering problem, then a good approach is to calculate the covariance of the measurement-minus-estimate residuals using all of the measurements simultaneously. Thus, the covariance constraint is averaged over all of the measurements. In problems where several distinct sets of measurements are repeated, each set may be averaged separately. An example is spacecraft navigation, where the measurements may include sets of attitude measurements and sets of angular velocity measurements. These two sets are normally taken independently and contain different noise levels, so they should be averaged separately.

4.0 MME Algorithm

If the dynamic model Eq. (1) contains significant error, then its output generally cannot predict the measurements with enough accuracy to satisfy the covariance constraint. The estimated measurement set at time t_k is based on the current state estimate, $\hat{\underline{x}}(t_k)$, as shown in Eq. (2). The between-measurement state estimate is based on integration of the system dynamic model. Thus, if the system dynamic model contains errors, the integration does not yield the correct state estimate, and the residuals between the estimated and the actual measurements are too large. Consequently, the model error must be reduced in order to satisfy the covariance constraint. To accomplish this, a model correction term $\underline{d}(t)$ is added to the original dynamic model as

$$\dot{\underline{x}} = \underline{f}[\underline{x}(t), \underline{u}(t), t] + \underline{d}(t) \tag{6}$$

In general, an infinite number of $\underline{d}(t)$'s exist which are capable of correcting the model to satisy the covariance constraint. The minimum correction is sought, thereby providing the least adjustment to the original model. Accordingly, the following cost functional is minimized with respect to $\underline{d}(t)$:

$$J = \sum_{j=1}^{m} \left\{ [\tilde{\underline{y}}(t_j) - \underline{g}(\hat{\underline{x}}(t_j), t_j)]^T R_j^{-1} [\hat{\underline{y}}(t_j) - \underline{g}(\hat{\underline{x}}(t_j), t_j)] \right\}$$
$$+ \int_{t_0}^{t_f} \underline{d}^T(\tau) W \underline{d}(\tau) d\tau \tag{7}$$

where W is a $k \times k$ weight matrix chosen to satisfy the covariance constraint as described shortly. The functional J in Eq. (7) is the sum of two penalty terms, whose relative weighting is controlled by W. If W is near zero, then the integral term is nearly zero. Consequently, the allowable $\underline{d}(t)$ is virtually unlimited and thus the model is corrected until the measurements are predicted almost exactly (i.e., the summation term goes to zero). However, this is only appropriate when the measurements are perfect. If the measurements are noisy, then the covariance constraint implies that the summation term should not be zero. The weight matrix, W, is chosen such that the covariance constraint is satisfied, allowing just enough correction $\underline{d}(t)$. Generally, determination of W requires a search procedure. However, unlike the tuning of a filter, which is essentially artistic, W is specified by satisfaction of the covariance constraint.

In Figure (1), the concept of the covariance constraint is demonstrated for a one-dimensional (n=1) system. Figure (1a) shows the ratio of the left-hand side of Eq. (5) to the right-hand

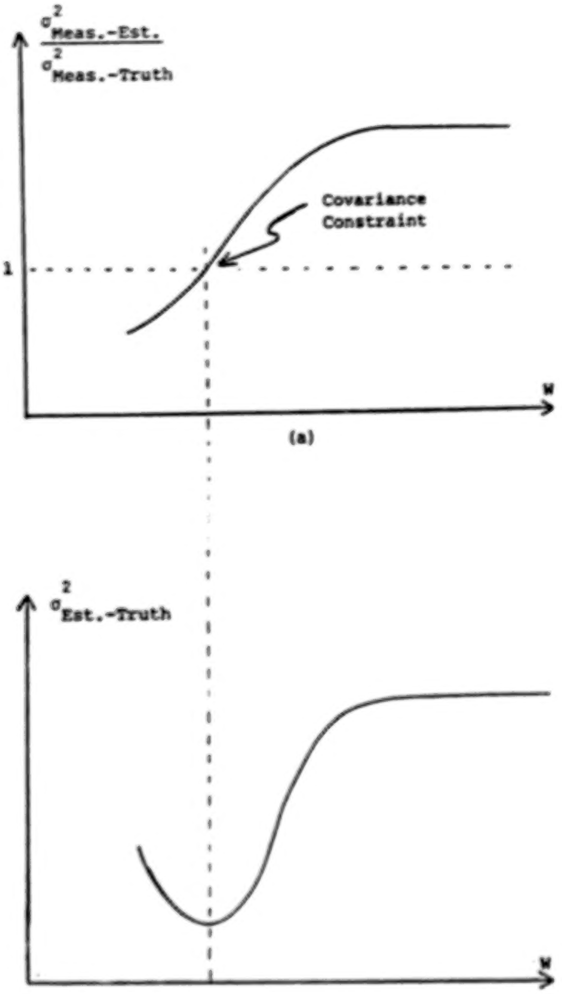

Figure 1. Choosing W to satisfy the covariance constraint leads to the optimal state estimate.

side, plotted versus W. As the weight is decreased, the corrected model predicts the actual measurements more closely as shown in the figure. In Figure (1b), the estimate variance is plotted versus W. The covariance constraint implies that the optimal estimate occurs when the covariance constraint is satisfied.

An algorithm for the minimization of J in Eq. (7) follows directly from a modification (e.g., Geering[6]) of the so-called Pontryagin's necessary conditions (e.g., Rozonoer[7]). For a given W, the minimization of J in Eq. (7) with respect to $\underline{d}(t)$ leads to the two-point boundary value problem (TPBVP) summarized as:

$$\dot{\underline{x}} = \underline{f}[\underline{x}(t), \underline{u}(t), t] + \underline{d}(t) \tag{6}$$

$$\dot{\underline{\lambda}} = -\left(\frac{\partial \underline{f}}{\partial \underline{x}}\right)^T \underline{\lambda} \tag{8}$$

$$\underline{d} = -\frac{1}{2} W^{-1} \left[\frac{\partial \underline{f}}{\partial \underline{u}}\right]^T \underline{\lambda} \tag{9}$$

$$\underline{x}(t_0) = specified, \quad or\ \underline{\lambda}(t_0^-) = \underline{0} \tag{10}$$

$$\underline{\lambda}(t_j^+) = \underline{\lambda}(t_j^-) + 2H_j^T R_j^{-1}\left[\tilde{\underline{y}}(t_j) - \underline{g}(\hat{\underline{x}}(t_j), t_j)\right] \tag{11}$$

$$\underline{x}(t_f) = specified, \quad or\ \underline{\lambda}(t_f^+) = \underline{0} \tag{12}$$

where

$$H \equiv \left.\frac{\partial \underline{g}}{\partial \underline{x}}\right|_{\hat{\underline{x}}(t_j), t_j}$$

This TPBVP contains jump discontinuities in the costates at each measurement time where the predicted measurement does not exactly match the actual measurement. The size of the jump is proportional to the measurement residual $\left[\tilde{\underline{y}}(t_j) - \underline{g}(\hat{\underline{x}}(t_j), t_j)\right]$, which, via the covariance constraint, is proportional to the measurement noise. From Eq. (9), these costate jumps lead to jumps in the estimated model error. Thus, for noisy measurements, the model error estimates are jump discontinuous proportional to the measurement residuals. Note that this is identical to a filter except that in a filter, the jumps are in the state estimates. The MME state estimates are continuous.

The algorithm Eqs. (6)-(12) exhibits several desirable features of both batch and sequential estimation techniques. The state estimate is obtained by processing all of the available measurements, much like a batch estimator such as least squares. Thus, the estimate is optimized in a *global* sense. In addition, the state estimate is continuous, eliminating the jump discontinuities present in filter estimates. For many physical systems, jump discontinuities in the states are not possible; thus, jump discontinuities in the filter state estimates must be reconciled in an artful manner. In addition to the batch algorithm-like advantages, the minumum model error algorithm calculations are based upon sequential processing of the measurements, which, like the filter algorithms, greatly reduces the memory requirements and eliminates the need for large matrix manipulations. From the standpoint of algorithmic calculations, the minimum model error technique shares advantages of both batch and sequential estimation techniques.

If the assumed model in the MME algorithm is linear, then a multiple shooting technique may be used to solve the TPBVP described by Eqs. (6)-(12) (Lew and Mook[8]). This technique converts the TPBVP into a set of linear algebraic equations which may be solved using any linear equation solver.

When the covariance constraint has been satisfied, the estimate is considered to have been optimized. As a byproduct of the solution, the estimates $\underline{d}(t)$ of the model error required to satisfy the optimality criterion are available. The results of the examples clearly indicate that these terms may provide highly accurate estimates of the actual model errors, leading to potential improvements in the model.

5.0 Examples

In this section, several example applications are summarized which demonstrate the present method and explore the accuracy of both the state estimates and the model error estimates obtained using it. The examples include both linear and nonlinear systems, varying degrees of model error, varying levels of measurement noise, measurement frequency, and total number of measurements. Exploitation of the model error estimates is also demonstrated.

5.1 Simple Example of Minimum Model Error Estimation

To illustrate the application of the minimum model error approach, consider estimation of a scalar function of time for which noisy measurements are the only information available. No prior knowledge of the underlying dynamics is assumed. Thus, the system dynamic model equation is

$$\dot{x} = 0 \tag{13}$$

Using the minimum model error approach, the system model is modified by the addition of a to-be-determined unmodeled effect as

$$\dot{x} = 0 + d(t) \tag{14}$$

where $d(t)$ represents the dynamic model error. For simplicity, the measurements are direct measurements of the state itself, and the measurement noise is a zero mean gaussian process with a variance of σ^2, given as

$$\tilde{x}(t_k) = x(t_k) + v_k \ , \quad k \ = \ 0, ..., m \tag{15}$$

where $\tilde{x}_k$ is the measurement at time t_k, x_k is the true state at time t_k, and v_k is a zero-mean gaussian sequence of variance σ^2. The cost functional to be minimized (see Eq. (7)) is

$$J = \frac{1}{\sigma^2}\sum_{k=0}^{m}[\tilde{x}(t_k) - \hat{x}(t_k)]^2 + \int_{t_0}^{t_m} d^2(\tau) W \, d\tau \tag{16}$$

where W is the to-be-determined weight on the integral sum-square model error term. The TPBVP which results from the minimization of J with respect to $d(t)$ may be summarized as (see Eqs. (6)-(12))

$$\begin{aligned} d &= -\frac{\lambda}{2W} \\ \dot{x} = d &= -\frac{\lambda}{2W} \\ \dot{\lambda} &= -\frac{\partial f}{\partial x}\lambda = 0 \\ \lambda(t_0^-) &= \lambda(t_f^+) = 0 \\ \lambda(t_k^+) &= \lambda(t_k^-) + \frac{2}{\sigma^2}(\tilde{x}_k - \hat{x}_k) \end{aligned}$$

where $\underline{\lambda}$ is the vector of costates. The boundary conditions indicate that the state is unknown at t_0 or t_f. The algorithm proceeds according to the following steps:

1) Choose W
2) Solve the TPBVP
3) Check the covariance constraint
4) If the covariance constraint is not satisfied, go to step 1

The true state history for this example is taken as $x(t) = cos(t)$. In Fig. 2, a set of 101 simulated measurements spanning the time interval $t_0 = 0$ to $t_f = 10$ is shown. The measurements were simulated by adding a computer-generated gaussian random sequence to the true state as

$$\tilde{x}_k = cos(t_k) + v_k \tag{17}$$

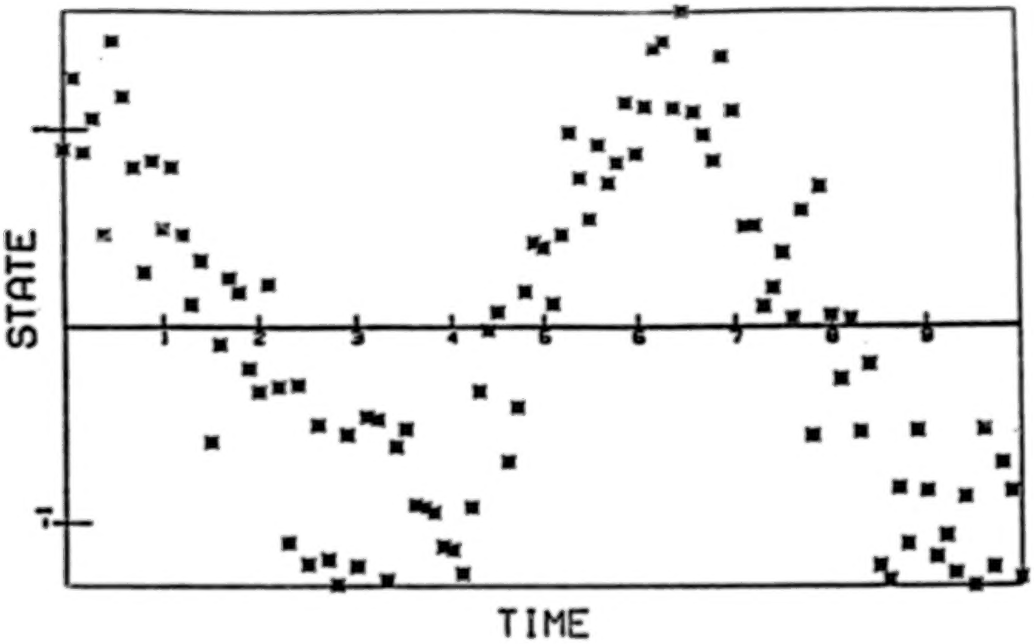

Figure 2. Simulated measurements of $cos(t)$ with $\sigma^2 = 0.114$.

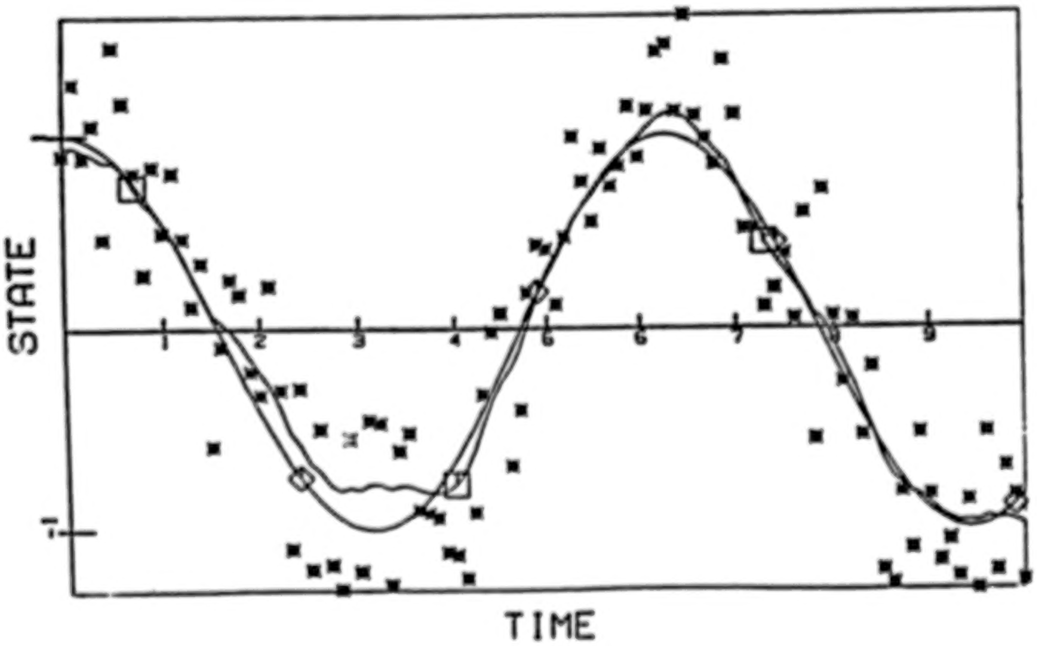

Figure 3. MME estimates using the Figure (2) measurements with no model. * denotes measurement, ◇ denotes truth ($cos(t)$), □ denotes MME estimate.

The nominal variance of v_k in Fig. 2 is 0.1, although the actual variance depends on the seed supplied to the random number generator. This variance is 10% of the peak amplitude. Thus, the average measurement error is approximately 50% of the average amplitude.

In Fig. 3, the minimum model error state estimate is shown along with the measurements and the true state history. Note that the state has been reconstructed to an error variance of .0085, considerably better than the measurement variance even in the total absence of a model. Note also that the model prediction variance (i.e., constant $x = 0$) is 0.717.

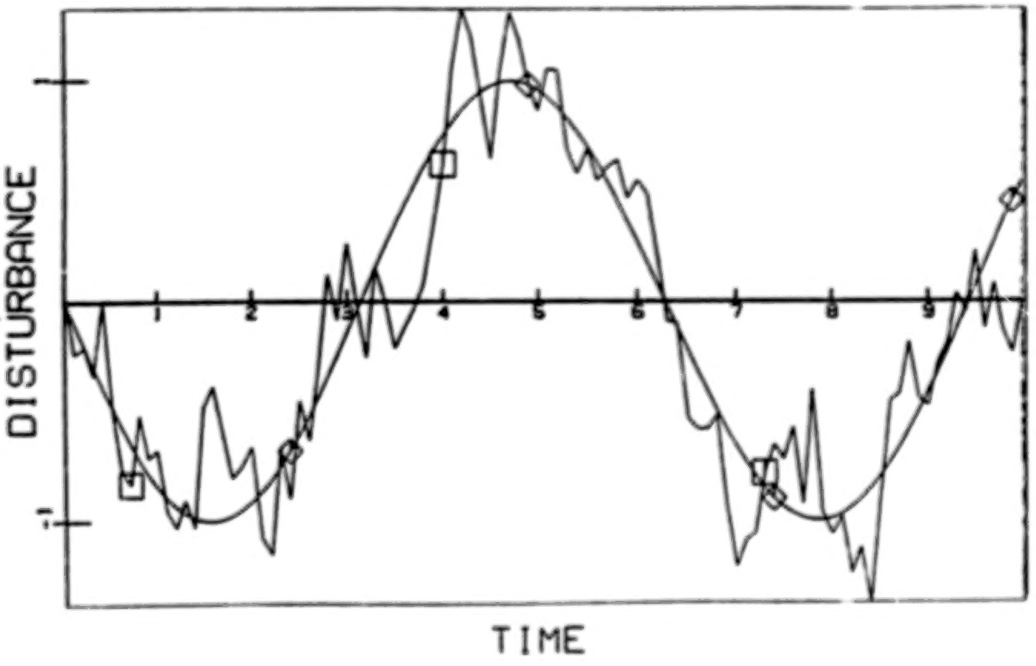

Figure 4. MME model error estimates using the Figure (2) measurements with no model. ◇ denotes true model error ($-sin(t)$), □ denotes MME estimate.

In Fig. 4, the model error term is plotted along with the true model error, $-sin(t)$. Although the model error estimate contains considerable noise, due to the noisy measurements, it is an accurate representation of the actual model error. Based on an examination of Fig. 4, a user might easily conclude that the dynamic model error is indeed $-sin(t)$. If the dynamic model is amended from $\dot{x} = 0$ to $\dot{x} = -sin(t)$, and the estimation process repeated, the state estimate is virtually exact and the model error estimate is virtually zero.

5.2 System State Estimation from MME

Several applications examples are now presented for system state estimation using the MME method. Other examples have also been investigated but are omitted here due to space limitations.

5.2.1 Modal Space State Estimation

In these examples, taken from Mook and Lin[9] and Lin[10], the state histories of the output measurements of a system described by a linear sum of system modes are obtained using the MME. The simulated measurements are created by assuming a truth as a sum of several modes, and then adding gaussian noise to the truth. The assumed model for the MME estimation is taken as the first mode in the sum. All of the other modes are ignored in the assumed model. Figures (5) shows the results from a case with a five mode truth. The one-mode model is plotted along with the MME estimate and the truth. The model is seen to be very poor, but the estimate is essentially perfect. The measurement noise is gaussian with $\sigma^2 = 0.04$, and the measurement interval is 0.1

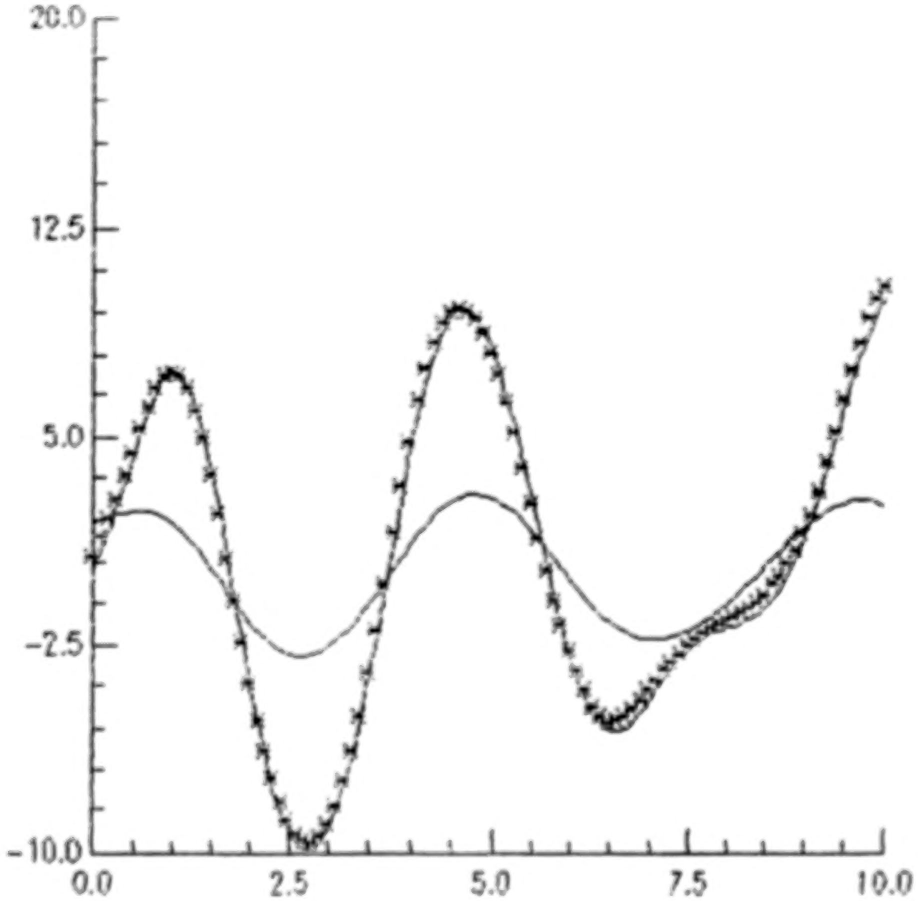

Figure 5. One-mode assumed model, five-mode truth, and MME estimate (*).

seconds.

Clearly, the MME is able to recover from a very poor model to produce accurate state estimates. This result can be very helpful for structural modelers who are uncertain about whether or not a modal model has been truncated with the correct number of retained modes.

5.2.2 Nonlinear State Estimation

The following example is taken from Mook[11]. Consider the single-degree-of-freedom system modeled by

$$\ddot{x} + \omega_0^2 x = f(x(t), \dot{x}(t)) + F(t) \tag{18}$$

where x and $\dot{x}$ are the system states, $F(t)$ is a known external excitation, and $f(x(t), \dot{x}(t))$ contains terms which may be nonlinear in the states. The external excitation is assumed to be independent of the states. Eq. (18) may be converted to state-space form as

$$\dot{\underset{\sim}{z}} = \begin{pmatrix} 0 & 1 \\ -\omega_0^2 & 0 \end{pmatrix} \underset{\sim}{z}(t) + \begin{pmatrix} 0 \\ F(t) \end{pmatrix} + \begin{pmatrix} 0 \\ f(x(t), \dot{x}(t)) \end{pmatrix} \tag{19}$$

where $\underset{\sim}{z} \equiv \{x(t) \quad \dot{x}(t)\}^T$. A specific example, after Thompson and Stewart[12], is given by

$$2.56\ddot{x} + 0.32\dot{x} + x + 0.05x^3 = 2.5cos(t) \tag{20}$$

This example exhibits two distinct possible steady-state solutions, depending on the initial conditions. The assumed model for the MME algorithm is used in two different forms. First, the nonlinear system is modeled for the MME as a linear oscillator. Measurements are simulated with a variety of different noise levels and frequencies. In each case, the MME is able to obtain accurate state estimates. Results are shown in Figures (6) through (8). In part (a) of each figure, the measurements are plotted along with the linear model output, thus showing the information given to the MME method. In part (b) of each figure, the truth, measurements, and MME estimate are shown. The accuracy of the state estimate is apparent from the figures, even for measurement frequency less than 4/cycle and total measurements as low as 15 (Figure (7)), and for noise levels with σ equal to 30% of the peak amplitude (Figure (8)).

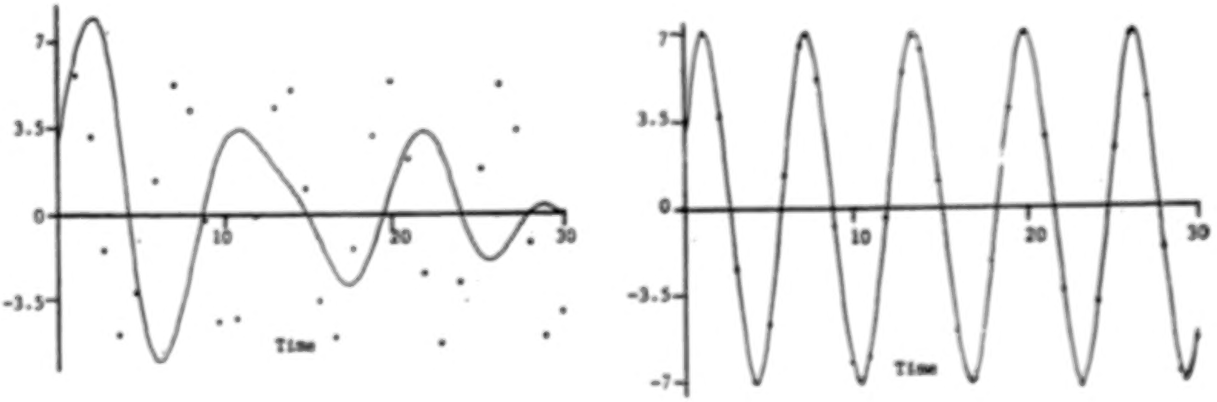

(a) (b)

Figure 6. (a) Nonlinear estimation with 30 noiseless measurements, using assumed linear oscillator model. (b) Truth, measurements, and MME estimates.

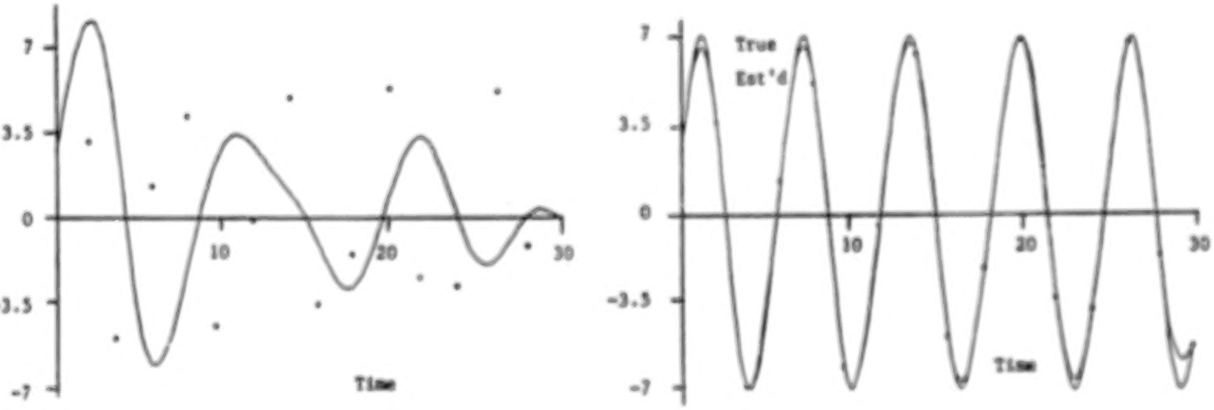

(a) (b)

Figure 7. (a) Nonlinear estimation with 15 noiseless measurements, using assumed linear oscillator model. (b) Truth, measurements, and MME estimates.

Second, the assumed model for the MME consisted only of the external forcing, so that no knowledge of the system is assumed. Results are shown in Figure (9), where the MME estimate pictured in part (b) is seen to be very accurate despite the very poor model pictured in part (a).

ORIGINAL PAGE IS
OF POOR QUALITY

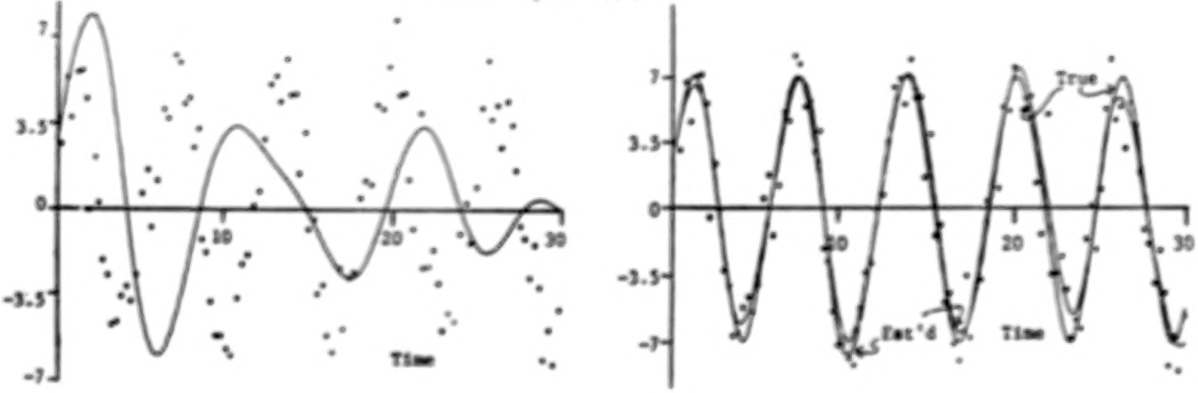

(a) (b)

Figure 8. (a) Nonlinear estimation with 100 noisy measurements, with noise level approximately 30%. (b) Truth, measurements, and MME estimates.

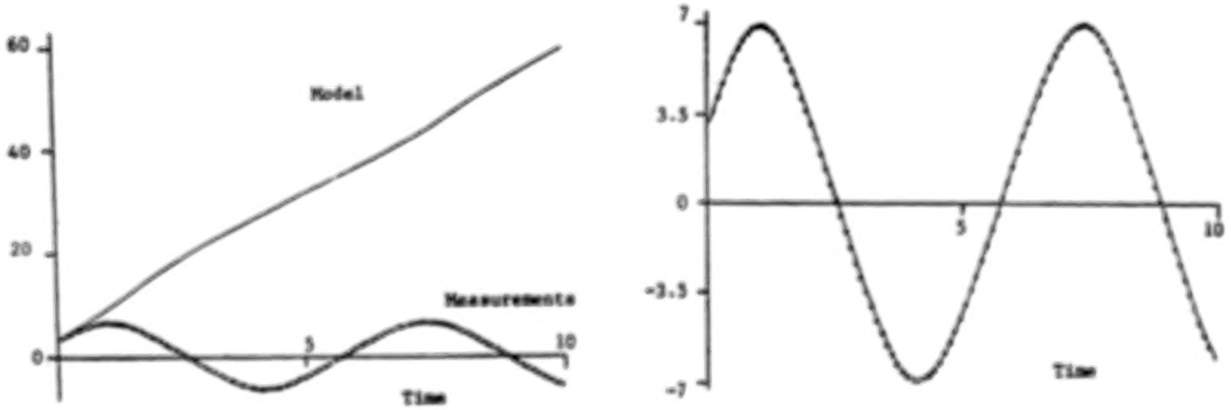

(a) (b)

Figure 9. (a) Nonlinear estimation with 100 noiseless measurements, using no assumed model. (b) Truth, measurements, and MME estimates.

5.3 System Identification From Model Error Estimates

An area of considerable interest in many engineering disciplines is identification, the process of obtaining an accurate model of a dynamic process using measured data. State estimation and identification are most often two separate processes. Some versions of Kalman filters have been implemented which treat unknown constant parameters in a model as states, so that they are estimated as part of the state vector. This approach, like most other identification techniques, requires the user to construct a model of appropriate form and order *apriori*. The filter then estimates the constant parameters in the model. However, the filters still assume that any model error is a gaussian white noise, so this approach usually works well only if the model order and form are correctly chosen by the user. The MME, by estimating the model error, may be used to determine the form of the model error before attempting to estimate the parameters.

Several studies have been conducted to investigate the use of the MME as an aid to system

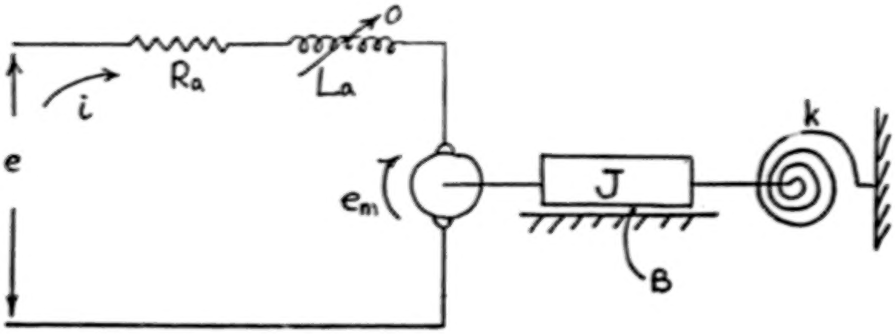

$$\underline{\dot{z}} = \begin{pmatrix} 0 & 1 \\ -\frac{K}{J} & -\frac{BR_a+K_TK_b}{JR_a} \end{pmatrix} \underline{z} + \begin{pmatrix} 0 \\ \frac{K_T}{JR_a} \end{pmatrix} e$$

Figure 10. Armature-controlled motor drives a rotating shaft assembly with inertia J, damping B, and stiffness k. The motor constants are K_T and K_b, and $\underline{z} = \{\theta\ \dot{\theta}\}^T$.

identification. These results are presented next.

5.3.1 Linear State Space Parameter Identification

The simplest form of model to identify is the linear, time-invariant state-space model. This is also the most commonly used model form in practice. Some examples of linear system identification are given in Mook, Liu, and Ho[13], and some results of that study are repeated here. Two assumed true systems are studied; an armature-controlled motor system driving a rotating shaft assembly, shown in Figure (10), and a linear, two-degree-of-freedom model nominally represented by two masses, springs, and dampers, as shown in Figure (11). In Figure (10), the term $A_{22} = -\frac{BR_a+K_TK_b}{JR_a}$, which represents damping, is assumed to be unknown and is to be estimated. In Figure (11), the three damper constants are to be estimated from the free response. Simulated measurements are created for both cases by adding gaussian white noise to the truth, and several cases are presented for varying noise, measurement frequency, and record length. In addition, the assumed model used for the MME is varied from case to case by altering the assumed values for the unknown constants.

The parameter estimation is carried out by a least-squares fit of the estimated model error. Since the model error estimate is continuous except at the measurement times, it may be sampled at an arbitrary number of points away from the measurements to create an overdetermined system of algebraic equations in the unknown parameters. Then, a least-squares algorithm is used to produce the parameter estimates. Results for the system in Figure (10) are shown in Table (1), and for the system in Figure (11), in Table (2).

5.3.2 Nonlinear System Identification

In section 5.2.2, results are given which demonstrate very accurate state estimation of a nonlinear system, given poor dynamic models and noisy, sparse data. In this section, identification results are given for those same examples. More detail is available in Mook[11].

The model error estimates corresponding to Figures (6)-(9) are shown in Figures (12)-

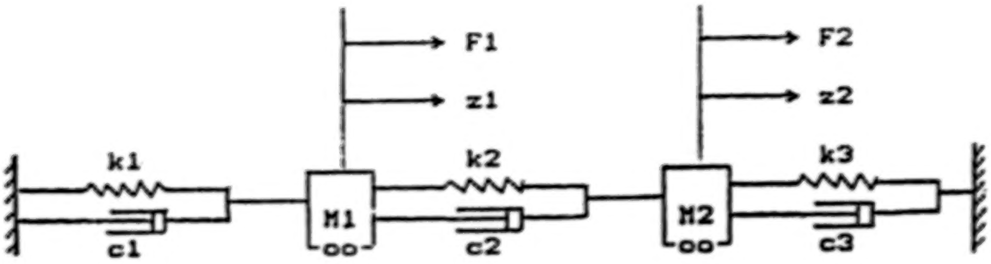

$$\dot{z} = \begin{pmatrix} 0 & 1 & 0 & 0 \\ -(k_1+k_2) & -(c_1+c_2) & -k_2 & -c_2 \\ 0 & 0 & 0 & 1 \\ -k_2 & -c_2 & -(k_2+k_3) & -(c_2+c_3) \end{pmatrix} z + \begin{pmatrix} 0 \\ F_1 \\ 0 \\ F_2 \end{pmatrix}$$

Figure 11. Mass-spring-damper system, where F is applied force.

Table 1. Parameter estimates for the system in Figure (10).

Measurement Frequency (meas/10 sec)	Measurement Variance	True A_{22}	Estimated A_{22}	Error %
41	0.	-0.4	-0.4000	0.00
41	0.00018	-0.4	-0.394691	1.33
21	0.00014	-0.4	-0.395293	1.18
11	0.00015	-0.4	-0.415468	3.87
41	0.0045	-0.4	-0.361596	9.60

(15). Clearly, the model error estimates are dependent on the accuracy and frequency of the measurements. For more accurate and more frequent measurements, the model error estimates are smoother and more accurate. However, the accuracy of the model error is not dependent on the accuracy of the assumed model. This is a very significant result for identification.

In order to identify the nonlinear model from the model error estimates, a parameterized model of the model error is constructed and then the parameters are estimated using a least-squares algorithm. For demonstration purposes, the assumed model for identification contained more terms than the actual model error, including the case when no prior model is assumed for the MME (Figures (9) and (15)). The least squares fit produced near-zero parameter estimates for the assumed model error terms which are not in the model, and near-perfect parameter estimates for the assumed terms which are in the model.

Table 2. Parameter estimates for the system in Figure (11).

values of c's measurements	true	guess	estimate	error (%)
perfect	.2,.1,.3	0.,0.,0.	0.207 0.092 0.291	3.5 8.0 3.0
noisy			0.210 0.108 0.278	5.0 8.0 [illegible].0
perfect		.4,.2,.6	0.205 0.097 0.286	2.5 3.0 4.6
noisy			0.208 0.095 0.277	4.0 5.0 7.7

(values are in the order of c1, c2, c3)

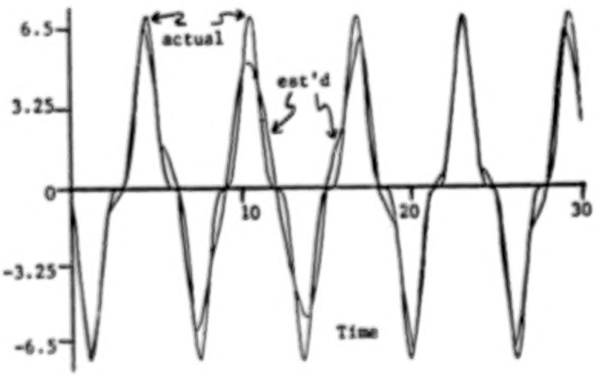

Figure 12. Model error estimation with 30 noiseless measurements, using assumed linear model.

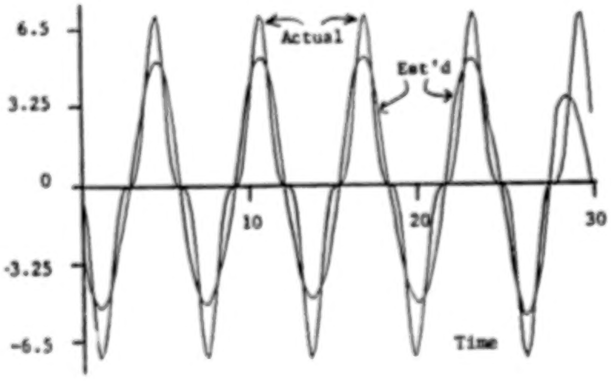

Figure 13. Model error estimation with 15 noiseless measurements, using assumed linear model.

5.2.3 Modal Space Realization/Identification

Recently, considerable interest in the identification of modal space models for large flexible systems has arisen in conjunction with such proposed projects as the space station. Several methods which produce accurate modal models from time-domain data have been developed (e.g., Ibrahim and Mikulcik[14]; Rajaram and Junkins[15]; Hendricks *et al*[16]; Chen *et al*[17]). The recently developed Eigensystem Realization Algorithm (Juang and Pappa[18]) is particularly attractive because it first determines the model order and then estimates the model parameters. This alleviates a very serious drawback of most methods, which require that the model order be known *apriori*. However, Juang and Pappa[19] found that for high noise levels in the measurements, the ERA could not determine the correct number of modes in the model, and the parameter estimates for the model were of low

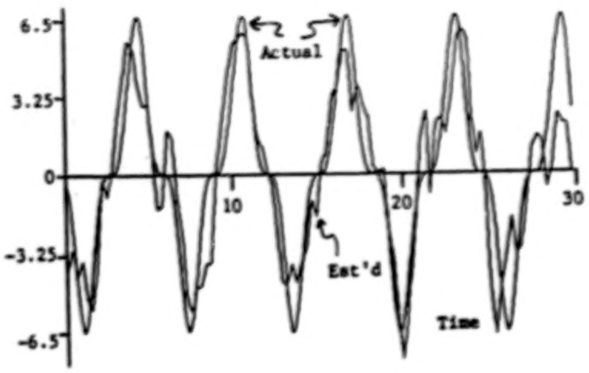

Figure 14. Model error estimation with 100 noisy measurements, using assumed linear model.

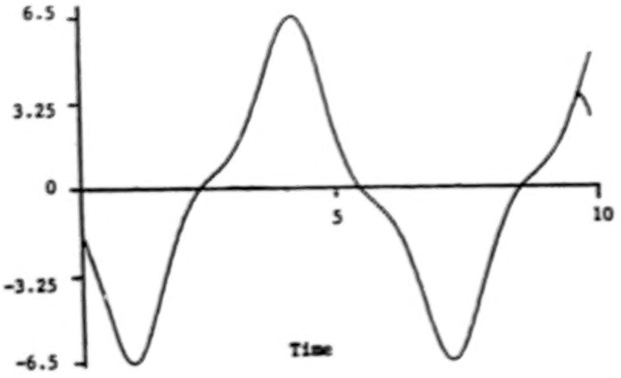

Figure 15. Model error estimation with 100 noiseless measurements, using no assumed model.

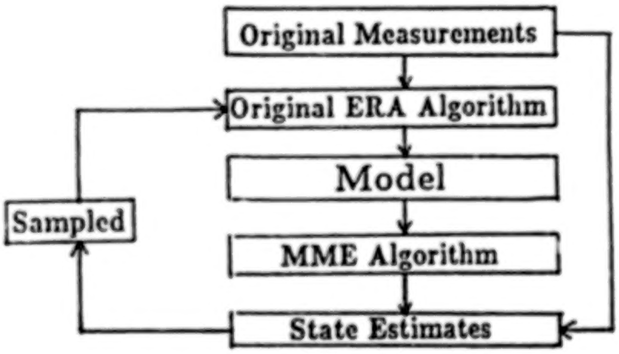

Figure 16. Algorithm flowchart for modal identification.

accuracy.

In Mook and Lew[20], the MME method is used in conjunction with the ERA to produce an algorithm which is significantly less sensitive to noise. The algorithm may be summarized as (i) apply ERA to the original measurements, (ii) use the ERA-produced model and the original measurements in the MME to produce state estimates of the measurements, (iii) sample the MME-produced state estimates to create simulated measurements of higher accuracy than the original measurements, and (iv) apply ERA to the simulated measurements in order to realize/identify the correct model. The steps (ii)-(iv) may be repeated, since the MME will produce more accurate state estimates if a more accurate model is used. Consequently, if the first pass through steps (ii)-(iv) produces more modes than step (i), a second pass through steps (ii)-(iv) may further improve the accuracy of the realization/identification. The entire procedure is represented by the flowchart in Figure (16).

The combined algorithm has been investigated for identification of the modes of a clamped-clamped beam. The true model is given by

$$y(t) = 1.0sin(t) + 0.05sin(2.76t) + 0.001sin(5.4t) \tag{21}$$

Measurement data was created with several noise levels, including $\sigma = 0.001$, $\sigma = 0.003$, $\sigma = 0.01$,

$\sigma = 0.05$, and $\sigma = 0.1$. Note that the highest noise level corresponds to approximately 10% of the measurement amplitude, while the lowest noise level is approximately 0.1% of the amplitude. Moreover, the highest noise level is twice as high as the second, and 100 times as high as the third, modal amplitudes, while the lowest noise level is equal to the smallest modal amplitude.

Table 3. Singular values from the ERA algorithm.

$\sigma=0.1$	$\sigma=0.05$	$\sigma=0.01$	$\sigma=0.003$	$\sigma=0.001$	$\sigma=0.0$
29.484	29.468	29.458	29.457	29.457	29.456
20.038	20.030	20.028	20.028	20.028	20.028
2.166	1.675	1.331	1.279	1.264	1.257
1.638	1.199	0.904	0.862	0.851	0.845
1.196	0.593	0.118	0.035	0.023	0.026
1.181	0.590	0.113	0.034	0.019	0.022
1.134	0.566	0.110	0.033	0.012	10^{-12}
1.124	0.561	0.108	0.031	0.011	10^{-12}
1.083	0.541	0.106	0.030	0.011	10^{-13}
1.031	0.516	0.102	0.029	0.010	10^{-13}
0.965	0.483	0.097	0.029	0.010	10^{-13}
0.942	0.471	0.094	0.028	0.009	10^{-13}

The model order is determined from the singular values of the singular value decomposition of $H(0)$, where H is the so-called "Hankel matrix". The model order is determined by the number of pairs of singular values between which there is a significant drop in magnitude. Table (3) gives the singular values in order from largest to smallest for each of the five noise levels. It appears that the model order is one, perhaps two, for $\sigma = 0.1$, since the singular value pairs beginning with the second pair are approximately the same magnitude. Consequently, for noise levels of $\sigma = 0.1$, the ERA method indicates one mode from the measurements. This seems intuitively reasonable since the level of noise exceeds the amplitude of modes 2 and 3.

Table 4. Parameter identification from the ERA algorithm.

	Mode 1		Mode 2		Mode 3	
Noise	Frequency	Damping	Frequency	Damping	Frequency	Damping
$\sigma=0.1$	1.007	-2.25×10^{-2}	2.473	-2.410	11.48	-31.44
$\sigma=0.05$	1.013	-1.37×10^{-2}	2.660	-0.967	12.87	-31.36
$\sigma=0.01$	1.003	-3.23×10^{-3}	2.739	-0.048	26.26	-10.54
$\sigma=0.003$	1.001	-8.37×10^{-4}	2.753	2.11×10^{-3}	26.22	-10.45
$\sigma=0.001$	1.000	-3.14×10^{-4}	2.756	3.18×10^{-3}	5.487	-4.27
True	1.000	0	2.760	0	5.400	0

After the model order is determined, the ERA algorithm estimates the modal frequencies and damping factors. Note that the true frequencies for this example are given in Eq. (21), and the true damping factors are 0. The frequencies and damping factors estimated by the ERA method are given in Table (4), along with the true values. In constructing Table (4), we have chosen the number of modes as three in all cases, even though this is not clear from the singular values. The damping and frequency parameters in Table (4) clearly indicate that modes 2 and 3 have not been discerned from the noisier measurements.

We now proceed to apply the combined ERA/MME algorithm to the same five sets of measurements used in the ERA algorithm. The assumed dynamic model varies from case to case. The results from Tables (3) and (4) were used to construct the models which were assumed for the MME algorithm. Thus, for the three highest noise levels, the MME used only the first mode identified by the ERA, and for the lower two noise levels, used the first two modes identified by the ERA. The MME algorithm produced state estimates for the measurement position. These estimates were then sampled at the original measurement times to produce "simulated" measurements which contain significantly less noise than the original measurements. Finally, the ERA algorithm is again applied, this time to the simulated measurements. Although a second application of this procedure may improve the realization/identification, as illustrated in Figure (1), we present results for a single pass only. The singular values obtained by ERA processing of the sampled MME estimates are given in Table (5). These singular values indicate three modes for every noise level. The parameter identification results are given in Table (6). All three frequencies are identified at all noise levels. The damping identification for the first two modes is also very good at all noise levels.

Table 5. Singular values from the ERA/MME algorithm.

σ =0.1	σ =0.05	σ =0.01	σ =0.003	σ =0.001	σ =0.0
29.613	29.496	29.461	29.460	29.456	29.456
20.094	20.048	20.039	20.030	20.028	20.028
0.960	1.091	1.168	1.2790	1.264	1.257
0.706	0.760	0.788	0.8610	0.851	0.845
0.234	0.175	0.052	0.0085	0.0154	0.026
0.209	0.160	0.046	0.0074	0.0125	0.022
0.106	0.078	0.024	0.0045	0.0031	10^{-12}
0.075	0.058	0.021	0.0031	0.0025	10^{-12}
0.073	0.057	0.021	0.0023	0.0020	10^{-13}
0.072	0.056	0.020	0.0014	0.0014	10^{-13}
0.069	0.055	0.020	0.0013	0.0013	10^{-13}
0.066	0.050	0.017	0.0012	0.0012	10^{-13}

The results presented in Tables (5) and (6) indicate that the combined algorithm is capable of identifying modes with amplitudes as low as 1% of the noise. In each case, we have assumed the minimum model identified by the first pass of the ERA. Thus, for example, at $\sigma = 0.1$, which is twice the amplitude of mode 2 and 100 times the amplitude of mode 3, the ERA algorithm identifies a single mode. Using only this one-mode model as input to the MME, the combined algorithm is still able to determine that the true model order is three, and give good accuracy in the parameter estimates.

Table 6. Parameter identification from the ERA/MME algorithm.

	Mode 1		Mode 2		Mode 3	
Noise	Frequency	Damping	Frequency	Damping	Frequency	Damping
σ =0.1	0.996	1.44×10^{-3}	2.910	-4.09×10^{-2}	5.408	-0.408
σ =0.05	0.998	4.14×10^{-4}	2.827	-7.97×10^{-3}	5.517	-0.554
σ =0.01	0.999	-7.18×10^{-5}	2.768	2.22×10^{-3}	5.678	-0.766
σ =0.003	1.000	-4.30×10^{-5}	2.766	-1.62×10^{-3}	5.589	-0.142
σ =0.001	1.000	-4.61×10^{-5}	2.763	2.00×10^{-4}	5.397	0.044
True	1.000	0	2.760	0	5.400	0

5.4 Sample Comparison With Extended Kalman Filter-Smoother

To illustrate the potential advantages of the model error terms in the MME compared with process noise in filters, consider the following nonlinear problem. The truth is given by the equation

$$\dot{x} = -\frac{x + t^2}{2x + t} \tag{22}$$

For illustration, the assumed model for the estimation algorithms is

$$\dot{x} = 0 \tag{23}$$

The measurements are perfect measurements of x. The MME is applied to this problem, and, for comparison, an extended Kalman filter-smoother is also used. The EKFS is modeled after the well-known Rauch-Tung-Streibel[21] filter-smoother, extended for the nonlinear problem. Since the assumed model is zero, the EKFS estimate must be constant between the measurements. The results of the two estimation approaches are shown in Figure (17). The model correction capability of the MME enables it to produce state estimates using a corrected version of the original model, so that the MME is not constant between measurements. The advantage of this approach is clear in Figure (17). Even though the measurements are perfect, the EKFS estimates between the measurements are poor.

Summary and Conclusions

In this paper, a new method for optimal post-experiment estimation has been described and its application demonstrated by numerous examples. The method is formulated to account for model error in a much more general and rigorous fashion than the process noise assumptions of typical filter algorithms. The state estimates are continuous and based on global measurement fits, compared with filter estimates which are discrete and based on local measurement fits. The MME method may give vastly improved state estimates when compared with filters for dynamic problems with significant model error, especially if the measurements are sparse and/or noisy.

In the MME, model error is treated as an unknown and estimated along with the states. The estimated model error is automatically corrected in the original model in order to obtain the state estimates. For poorly modeled systems, this produces two significant benefits. First, the state

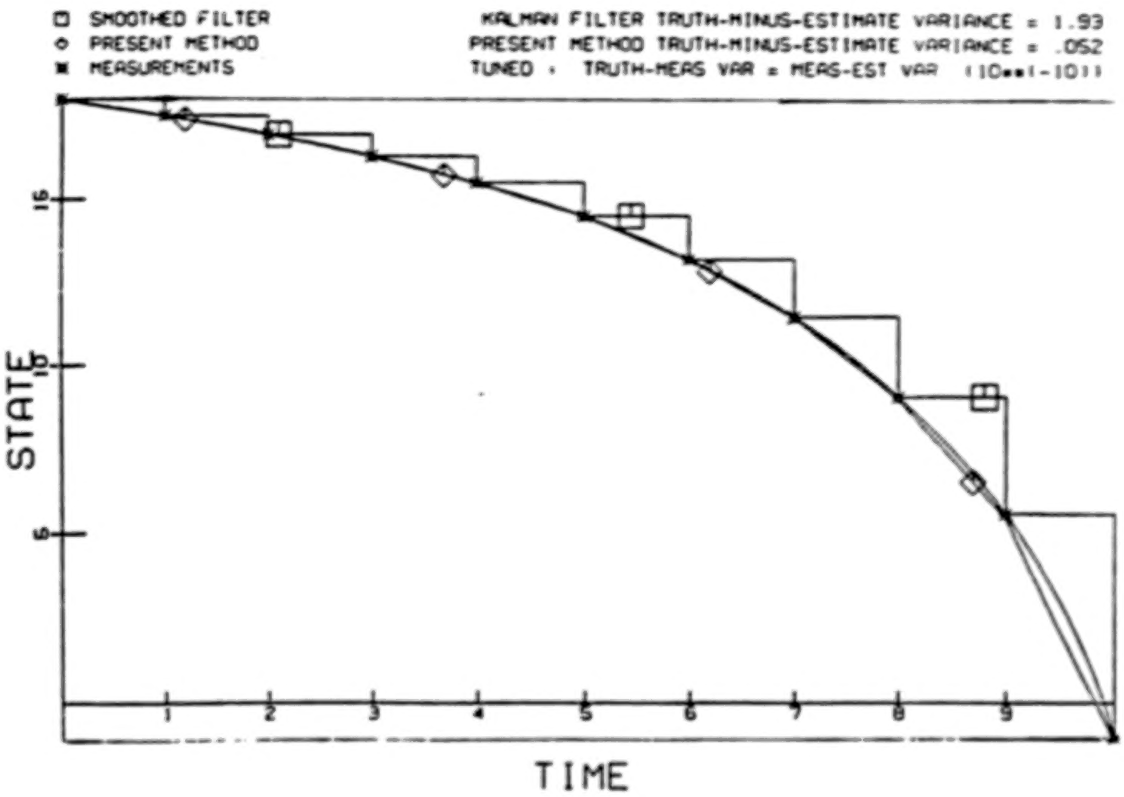

Figure 17. Comparison of the MME with an extended Kalman filter-smoother in the absence of a model. The EKFS estimate must be constant between measurements, but the model correction in the MME shows clear advantages.

estimates are based on a corrected model (unlike filters), and second, the model error estimates are available to aid in identification of an accurate model for subsequent use.

Examples are given which demonstrate state estimation and exploitation of the model error estimates for both system identification and external force identification. The MME method shows considerable promise for use in numerous post-experiment estimation and identification problems, and should be considered for any application in which significant model error is suspected.

REFERENCES

1. Gelb, A., editor, **Applied Optimal Estimation**, MIT Press, Cambridge, Massachusetts, 1984.

2. Fitzgerald, R. J., "Divergence of the Kalman Filter," **IEEE Transactions on Automatic Control**, Vol. AC-16, p. 736, 1971.

3. Huber, P. J., "The 1972 Wald Lecture: Robust Statistics: A Review," **Annals of Mathematical Statistics**, Vol. 43, p. 1041, 1972.

4. Breza, M. J., and Bryson, A. E., "Minimum-Variance Steady-State Filters With Eigenvalue Constraints", 5th Symposium on Nonlinear Estimation Theory and its Applications, San Diego, 1974.

5. Mook, D.J., and Junkins, J.L., "Minimum Model Error Estimation for Poorly Modeled Dynamic Systems", **AIAA Journal of Guidance, Control, and Dynamics**, to appear.

6. Geering, H.P., "Continuous-Time Optimal Control Theory for Cost Functionals Including Discrete State Penalty Terms", **IEEE Transactions on Automatic Control**, Volume AC-21, pp. 866-869, 1976.

7. Rozonoer, L.I., "L.S. Pontryagin Maximum Principle in Optimal System Theory", **Avtomat. I. Telemekh**, Vol. 20, 1959. Also in **Optimal and Self-Optimizing Control**, R. Oldenburger, editor, MIT Press, 1966.

8. Lew, J.S., and Mook, D.J., "Two-Point Boundary Problems Containing Jump Discontinuities", in review.

9. Mook, D.J., and Lin, J.-C., "Minimum Model Error Estimation of Modal Truncation Errors", Proceedings of the 1987 Spring Meeting of the Society for Experimental Mechanics, Houston, TX, June 1987.

10. Lin, J. C., "Minimum Model Error Estimation of Modal Truncation Errors", M.S. Thesis, State University of New York at Buffalo, 1988.

11. Mook, D.J., "Estimation and Identification of Nonlinear Dynamic Systems", Proceedings of the 29th Structures, Structural Dynamics, and Materials Conference, Williamsburg, Virginia, April 1988. Also, to appear, **AIAA Journal**.

12. Thompson, J. M. T., and Stewart, **Nonlinear Dynamics and Chaos**, John Wiley and Sons, 1986.

13. Mook, D. J., Liu, S.-A., and Ho, F.-S., "Linear Model Parameter Identification From State Measurements", Proceedings of the 18th Annual Pittsburgh Conference on Modeling and Simulation, Pittsburgh, April 1987.

14. Ibrahim, S.R., and Mikulcik, E.C., "A Method for the Direct Identification of Vibration Parameters from the Free Response," **Shock and Vibration Bulletin**, No. 47, Pt. 4, pp. 183-198, Sept. 1977.

15. Rajaram, S., and Junkins, J.L., "Identification of Vibrating Flexible Structures", **AIAA Journal of Guidance, Control, and Dynamics**, Vol. 8, No. 4, pp. 463-470, July-Aug. 1985.

16. Hendricks, S.L., et. al., "Identification of Mass, Damping, and Stiffness Matrices for Large Linear Vibratory Systems", **AIAA Journal of Guidance, Control, and Dynamics**, Vol. 7, No. 2, pp. 244-245, March-April 1984.

17. Chen, J.C., et.al., "Direct Structural Parameter Identification by Modal Test Results", 24th Structures, Structural Dynamics, and Materials Conference, Pt. 2, 1983.

18. Juang, J.-N., and Pappa, R.S., "An Eigensystem Realization Algorithm (ERA) for Modal Parameter Identification and Model Reduction", **AIAA Journal of Guidance, Control, and Dynamics**, Vol. 8, No. 5, pp. 620-627, Sept.-Oct. 1985.

19. Juang, J.N., and Pappa, R.S., "Effects of Noise on Modal Parameters Identified by the Eigensystem Realization Algorithm", **AIAA Journal of Guidance, Control, and Dynamics**, Vol. 9, No. 3, pp. 294-303, May-June 1986.

20. Mook, D. J., and Lew, J., "A Combined ERA/MME Algorithm For Robust System Realization/Identification", AIAA/ASME/ASCE/AHS 29^{th} Structures, Structural Dynamics, and Materials Conference, Williamsburg, Virginia, April 1988.

21. Rauch, H. E., Tung, F., and Streibel, C. T., "Maximum Likelihood Estimates of Linear Dynamic Systems", **AIAA Journal**, Vol. 3, No. 8, pp. 1445-1450, 1965.

N89-15942

COMPUTATION OF ORBITS USING TOTAL ENERGY

by

Victor R. Bond

and

David D. Mulcihy

MCDONNELL DOUGLAS ASTRONAUTICS CO.
16055 SPACE CENTER BLVD.
HOUSTON, TEXAS 77062

Presented at the

FLIGHT MECHANICS/ESTIMATION THEORY SYMPOSIUM
GODDARD SPACE FLIGHT CENTER
GREENBELT, MARYLAND 20771

MAY 10-11, 1988

This work was performed for NASA
under Contract NAS 9-17650

COMPUTATION OF ORBITS USING TOTAL ENERGY

1.0 SUMMARY

The computation of orbits can be done more efficiently by the use of any of several new formulations (Reference 1, 2, 3, 4, 5) of the perturbed two body problem which consider the total energy of the orbital system as one of the dependent variables. The total energy is the osculating two body energy plus the potential energy due to perturbing masses. The use of the total energy as the dependent variable instead of the two body energy is a relatively new idea (Reference 1). The advantage of using total energy arises from the fact that the more perturbing potential energy that is accounted for in the total energy variable, the more nearly constant is the total energy. In fact, except for dissipative forces such as drag, the only reason for the total energy not being constant is the rotation or revolution of the perturbing mass. This near constancy of the total energy has the effect of inhibiting error growth during numerical solution (Reference 1). This paper will present the results of an application of total energy formulation (Reference 2) to the problem of the precise computation of orbits.

2.0 INTRODUCTION

The differential equation of motion of the perturbed two-body problem can be expressed as,

$$\ddot{\underline{r}} + \frac{\mu}{r^3}\,\underline{r} = \underline{F} = \underline{P} - \frac{\partial V}{\partial \underline{r}} \tag{1}$$

where $\underline{r}$ is the position vector of one of the bodies relative to the other. The perturbations, those derivable from a potential $\partial V/\partial \underline{r}$, as well as other forces $\underline{P}$, are included in the total perturbation $\underline{F}$.

The total energy element formulations (References 1, 2, 3, 4, 5) of the perturbed two-body problem are developed such that $\partial V/\partial t$ is used as well as $\partial V/\partial \underline{r}$. The perturbations are split into those derivable from a potential and those which are included in the perturbation $\underline{P}$. The perturbation $\underline{P}$ normally includes non-conservative perturbations, but it can also include perturbations derivable from a potential when convenient. For the total energy formulations, the right-hand sides of all differential equations, except that for the total energy, include the perturbation factors $\underline{P}$ and $\partial V/\partial \underline{r}$. The total energy differential equation has the form

$$\dot{h} = \dot{\underline{r}} \cdot \underline{P} + \frac{\partial V}{\partial t} \tag{2}$$

where h is the total energy,

$$h = \frac{1}{2} \dot{\underline{r}} \cdot \dot{\underline{r}} - \frac{\mu}{r} + V(\underline{r},t) \tag{3}$$

Equation (2) is derived by taking the time derivative of equation (3) and substituting equation (1) into this result to eliminate $\ddot{\underline{r}}$. Note that this differential equation includes the perturbations $\underline{P}$ and $\partial V/\partial t$, but does not include $\partial V/\partial \underline{r}$.

There are three options available in the total energy formulations depending upon the way in which the perturbations derivable from a potential are used in the differential equations. These options are categorized as follows:

(A) The entire perturbing potential is considered with its effect including $\partial V/\partial \underline{r}$ and $\partial V/\partial t$. This is the option which is developed and discussed in this paper.

(B) The perturbing potential can be portioned, including some of the perturbation in $\partial V/\partial \underline{r}$ and some in $\underline{P}$. This has been the approach most often used when the geopotential is the perturbation. The zonal terms have been included in $\partial V/\partial \underline{r}$, while the explicitly time dependent terms (the tesseral and sectorial terms) have been included in $\underline{P}$. This approach has been used in order to avoid the computation of $\partial V/\partial t$. The potential used is that of the zonal terms only.

(C) The perturbing potential is not considered at all. The $\partial V/\partial \underline{r}$ are included in the perturbation $\underline{P}$. The potential is set to zero.

It must be emphasized that all three options are correct. The advantage that any of the options has over the others is numerical accuracy and speed in computation. The advantage of option (B) over option (C) in accuracy and speed is considerable and is discussed at length in References 1, 2, and 4.*

In order to properly implement the differential equation (2) for the total energy as discussed in option (A), the partial derivative $\partial V/\partial t$ must be computed. This report will derive a simple formula for this computation. This formula will be developed for the general case of any perturbation derivable from a potential. Then the particular case of a geopotential perturbation acting on an Earth satellite will be used as an example to show the advantage of using $\partial V/\partial t$ in the computation.

3.0 DEVELOPMENT OF $\partial V/\partial t$

Let $\underline{r}$ be the position vector in an inertial system and let $\underline{r}_G$ be the same position vector in a system rotating with angular velocity $\underline{\omega}$ with respect to the inertial system. Then,

$$\underline{r} = \underline{r}_G \tag{4}$$

The velocity vectors are related by,

$$\dot{\underline{r}} = \dot{\underline{r}}_G + \underline{\omega} \times \underline{r}_G \tag{5}$$

In the inertial system, the potential function is expressed as an explicit function of time,

$$V = V(\underline{r},t) \tag{6}$$

---

* For these formulations a slightly different energy parameter α_0, where $h = -2\alpha_0$, is used and a new independent variable called fictitious time is introduced. With these changes, equation (2) becomes

$$\alpha_0' = -\frac{r}{2}\frac{\partial V}{\partial t} - \frac{1}{2}\underline{r}'\cdot\underline{P}$$

where ( )' = d( )/ds and s is the independent variable such that dt/ds = r.

having the total derivative

$$\frac{dV}{dt} = \frac{\partial V}{\partial \underline{r}} \cdot \dot{r} + \frac{\partial V}{\partial t} \tag{7}$$

In a properly chosen rotating system, the same potential function can be expressed as a function of position only,

$$V = V(\underline{r}_G) \tag{8}$$

having the total derivative,

$$\frac{dV}{dt} = \frac{\partial V}{\partial \underline{r}} \cdot \dot{\underline{r}}_G \tag{9}$$

since in the rotating system the potential has no explicit dependence on time, $\partial V(\underline{r}_G)/\partial t = 0$.

Using equations (4) and (5), equation (7) becomes

$$\frac{dV}{dt} = \frac{\partial V}{\partial \underline{r}_G} \cdot (\dot{\underline{r}}_G + \underline{\omega} \times \underline{r}_G) + \frac{\partial V}{\partial t} \tag{10}$$

Comparing equations (9) and (10), we obtain

$$\frac{\partial V}{\partial t} = - \frac{\partial V}{\partial \underline{r}_G} \cdot \underline{\omega} \times \underline{r}_G \tag{11}$$

Note that to this point, we have not considered any particular potential function. The result, equation (11), can be applied under proper conditions to the case where V represents the perturbing geopotential function or to the case of a lunar, solar, or planetary perturbation on a satellite.

4.0 APPLICATION TO THE GEOPOTENTIAL

We now consider the case of the perturbing geopotential which can be divided into two parts,

$$V(\underline{r},t) = V_Z(\underline{r}) + V_T(\underline{r},t) \tag{12}$$

where $\underline{r}$ is expressed in an inertial system having one axis normal to the Earth equatorial plane and the other two orthogonal axes in the equatorial plane. The portion of the perturbing geopotential $V_Z(\underline{r})$ arising from the zonal terms has no explicit time dependence. The portion of the perturbing geopotential $V_T(\underline{r},t)$ arising from the sectorial and tesseral terms are explicitly dependent upon time.

For the case of a perturbing geopotential equation (11) can be reduced further. Define the rotating system X_G, Y_G, Z_G such that Z_G is in a direction normal to the Earth equatorial plane and the X_G and Y_G axes lie in the Earth equatorial plane and are fixed in the Earth. The zonal portion of the perturbing geopotential is

$$V_Z = -\frac{\mu}{r} \sum_{n=2}^{\infty} C_{n,o} \left(\frac{a_e}{r}\right)^n P_n\,(Z_G/r)$$

where, $C_{n,o}$ are the zonal coefficients
a_e is the equatorial radius of the Earth
P_n is the nth degree Legendre polynomial which is a function of Z_G/r.

Now, $\underline{r}_G = \hat{i}_G X_G + \hat{j}_G Y_G + \hat{k}_G Z_G$, $\quad r = |\underline{r}_G|$

where $\hat{i}_G, \hat{j}_G, \hat{k}_G$ are unit vectors along the X_G, Y_G, Z_G axes. The partial derivative $\partial V_Z/\partial \underline{r}_G$ has the form,

$$\frac{\partial V_Z}{\partial \underline{r}_G} = f_1(r,Z_G)\underline{r}_G + f_2(r,Z_G)\hat{k}_G$$

Note that since $\underline{\omega} = \omega \hat{k}_G$,

$$\frac{\partial V_Z}{\partial \underline{r}_G} \cdot \underline{\omega} \times \underline{r}_G = 0.$$

Thus , the zonal part V_Z of the perturbing geopotential does not contribute to $\partial V/\partial t$. Equation (11) becomes

$$\frac{\partial V}{\partial t} = - \frac{\partial V_T}{\partial \underline{r}_G} \cdot \underline{\omega} \times \underline{r}_G . \qquad (13)$$

Consider the first two options given in Section 2.0 for the formulation of the differential equation (2) for the total energy.

4.1 Option A – All zonal, sectorial, and tesseral terms of the perturbing geopotential are included in the potential and hence in the total energy.

Let $\quad V = V_Z(\underline{r}) + V_T(\underline{r})$

then $\quad \dfrac{\partial V}{\partial \underline{r}} = \dfrac{\partial V_Z}{\partial \underline{r}} + \dfrac{\partial V_T}{\partial \underline{r}}$

also $\quad \underline{P} = 0$

and from equation (13), we compute $\partial V/\partial t$.

Further, since $\underline{r} = \underline{r}_G$, we can express equation (2) as

$$\dot{h}_A = \frac{\partial V}{\partial t} = - \frac{\partial V_T}{\partial \underline{r}} \cdot \underline{\omega} \times \underline{r} . \qquad (14)$$

4.2 Option B – Only the zonal terms of the perturbing geopotential are included in the potential and hence in the total energy.

Let $\quad V = V_Z(\underline{r})$

then $\quad \dfrac{\partial V}{\partial \underline{r}} = \dfrac{\partial V_Z}{\partial \underline{r}}$

and $\quad \dfrac{\partial V}{\partial t} = 0$

The sectorial and tesseral terms are considered to be in the perturbation $\underline{P}$,

$$\underline{P} = - \frac{\partial V_T}{\partial \underline{r}}$$

and the total energy differential equation (2) becomes,

$$\dot{h}_B = \dot{\underline{r}} \cdot \underline{P} = - \frac{\partial V_T}{\partial \underline{r}} \cdot \dot{\underline{r}} \tag{15}$$

4.3 Comparison of Options A and B:

Both equations (14) and (15) depend directly upon the factor $\partial V_T/\partial \underline{r}$, which is a small term depending only upon the sectorial and tesseral terms. But we also observe that for Option B, $\dot{h}_B$ is proportional to the inertial velocity, $\dot{\underline{r}}$, whereas for Option A, $\dot{h}_A$ is proportional to the component ($\underline{\omega} \times \underline{r}$) of the inertial velocity which arises from the rotation of the axes fixed in the Earth.

For near Earth satellite orbits,

$$\left| \underline{\omega} \times \underline{r} \right| < \left| \dot{\underline{r}} \right| \tag{16}$$

and also

$$\left| \dot{h}_A \right| < \left| \dot{h}_B \right|$$

In fact, if the Earth were not rotating ($\omega = 0$), then $\dot{h}_A$ would be zero. For satellite orbits which are at large distances from the Earth, the inequality (16) does not always hold. However, at large distances from the Earth, the perturbing geopotential is not as significant as perturbations due to the Sun or Moon. The global region for which the inequality (16) holds is complicated and depends upon the semi-major axis, the eccentricity, and the true anomaly (or angular position) of the satellite trajectory.

For near circular orbits, it can be shown that the ratio

$$\dot{h}_A / \dot{h}_B = \frac{\omega}{n}\left(1 - (Z/r)^2\right)^{1/2}$$

where n is the mean motion of the satellite and the factor $\left(1 - (Z/r)^2\right)$ is always less than unity. For orbits within the geosynchronous distance, the inequality (16) holds since

$$n > \omega$$

For near Earth orbits,

$$\frac{\omega}{n} \approx \frac{1}{16}$$

and so

$$\dot{h}_A / \dot{h}_B < \frac{1}{16}$$

The formulations of the perturbed two-body problem discussed in References 1, 2, and 4 are in effect perturbed harmonic oscillators having frequencies which are dependent upon the total energy. The use of the full geopotential as shown in Option A in the computation of the total energy causes $\dot{h}_A$ to be small. Thus, h_A is nearly constant and the resulting frequency of the perturbed oscillator equations is nearly constant. Options A and B as well as Option C are also compared in Table I.

5.0 NUMERICAL RESULTS

The numerical effect of using the full geopotential as in Option A is shown in Figure 1. A near circular orbit was propagated for ten days first using Option A and then using Option B. This computation was done using the KSUR12 total energy formulation (Reference 2) and the RK4(5) variable step numerical integrator (Reference 6). The geopotential model used was the complete GEM-L2 (Reference 7). The results of these computations were compared to a reference trajectory computed with very high precision as given in Reference 8 and originally provided in Reference 9. Figure 1 shows the RSS of the position vector of Options A and B, with each compared to the reference.

Option B (using only the zonal part of the geopotential in the total energy) required an average of 59.4 variable steps per revolution with a maximum error of 25 meters. Option A (using the full geopotential in the total energy) required an average of 45.2 variable steps per revolution with a maximum error of about 8 meters. The two options are also compared on Figure 1 using 30 fixed steps per revolution. Option B showed a rapidly growing error reaching 25 meters after 4 days and still diverging. Option A reached a maximum error of about 15 meters after 10 days.

6.0 REFERENCES

1. Stiefel, E. and Scheifele, G.: Linear and Regular Celestial Mechanics. Springer-Verlag (1971).

2. Bond, V.: Celestial Mechanics 10 (1974) pp 303-318.

3. Bond, V.: Celestial Mechanics 13 (1976) pp 287-311.

4. Bond, V. and Hanssen, V.: "The Burdet Formulation of the Perturbed Two-body Problem with Total Energy As An Element," NASA-JSC-Internal Note No. 73-FM-86 (JSC-08004), June 8, 1973.

5. Bond, V. and Janin, G.: Celestial Mechanics 23 (1981) pp 159-172.

6. Fehlberg, E.: 1969, "Low Order Classicial Runge - Kutta Formulas with Step Size Control and Their Application to Some Heat Transfer Problem", NASA TR R-315.

7. Lerch, F.J., et al: A Refined Gravity Model From Lageos (GEM-L2). NASA TM-84986, February 1983.

8. Bond, V. and Tillett, H.: Performance of KSUR12 Program on the HP9000 (Preliminary Results). McDonnell Douglas Astronautics Co., Houston. Working Paper No. 1.2-WP-FM86028-10, May 1986.

9. Lear, W.M.: Personal Communication, 19 November 1985.

Table I. Comparison of Options A, B, and C for perturbing geopotential.

	Option A	Option B	Option C
Perturbing Geopotential (V)	$V_Z + V_T$	V_Z	0
Total Energy (h) equation (3)	$\frac{1}{2}\dot{\underline{r}}\cdot\dot{\underline{r}} - \frac{\mu}{\underline{r}} + V_Z + V_T$	$\frac{1}{2}\dot{\underline{r}}\cdot\dot{\underline{r}} - \frac{\mu}{\underline{r}} + V_Z$	$\frac{1}{2}\dot{\underline{r}}\cdot\dot{\underline{r}} - \frac{\mu}{r}$
Perturbation $\left(\frac{\partial V}{\partial \underline{r}}\right)$	$\frac{\partial V_Z}{\partial \underline{r}} + \frac{\partial V_T}{\partial \underline{r}}$	$\frac{\partial V_Z}{\partial \underline{r}}$	0
Perturbation (P)	0	$-\frac{\partial V_T}{\partial \underline{r}}$	$-\left(\frac{\partial V_Z}{\partial \underline{r}} + \frac{\partial V_T}{\partial \underline{r}}\right)$
Derivative of total energy $(\dot{h})$ equation (2)	$-\frac{\partial V_T}{\partial \underline{r}} \cdot \underline{\omega} \times \underline{r}$	$-\frac{\partial V_T}{\partial \underline{r}} \cdot \dot{\underline{r}}$	$-\left(\frac{\partial V_Z}{\partial \underline{r}} + \frac{\partial V_T}{\partial \underline{r}}\right)\cdot\dot{\underline{r}}$

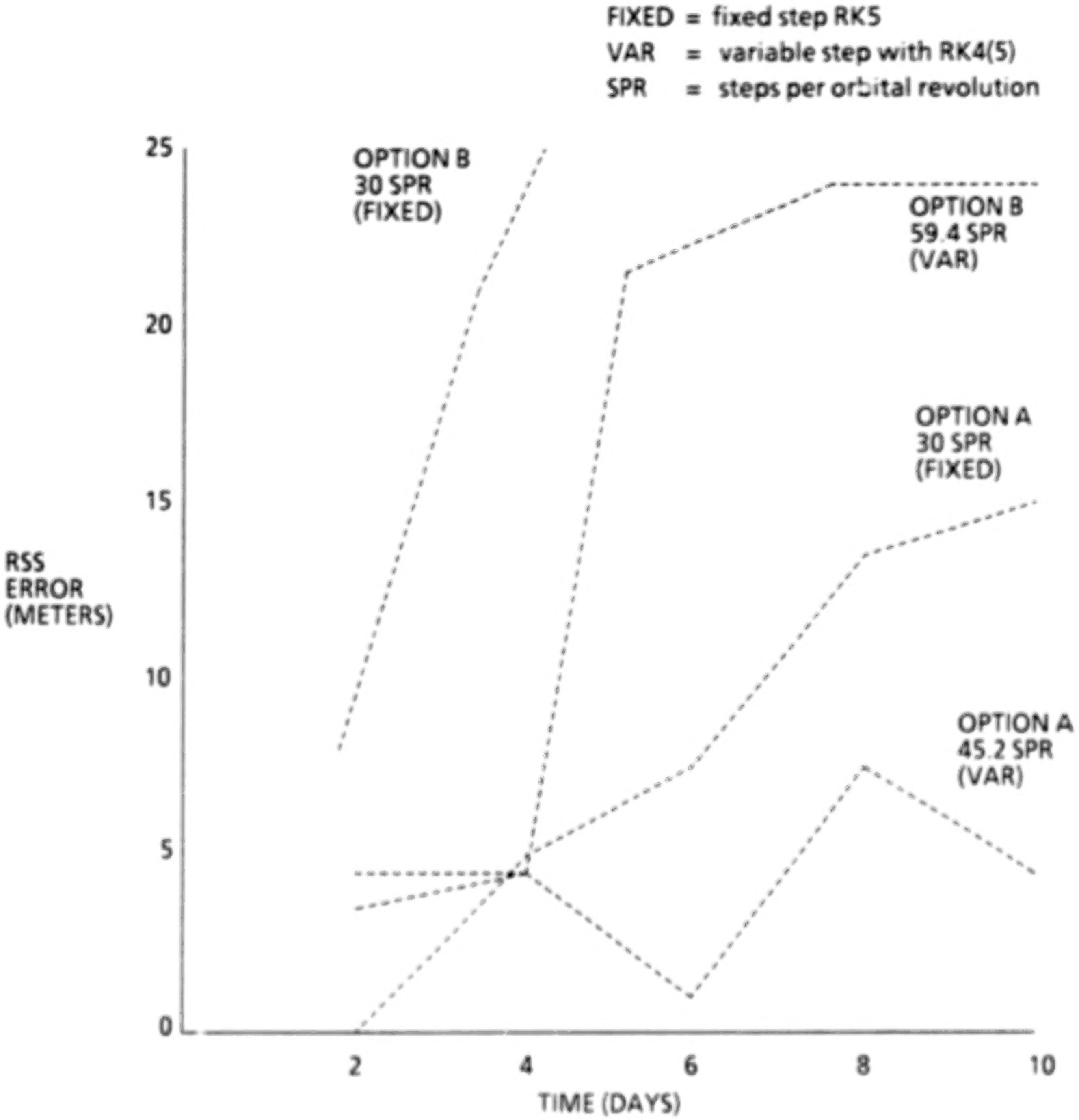

Figure 1. Comparison of RSS errors for near Earth trajectories computed using only the zonal terms of the perturbing geopotential in the total energy (Option B) and using the full perturbing geopotential in the total energy (Option A).

N89-15943

A MULTI-SATELLITE ORBIT DETERMINATION PROBLEM IN A PARALLEL PROCESSING ENVIRONMENT

M. S. Deakyne and R. J. Anderle

General Electric Valley Forge
Military and Data Systems Operations
Engineering Orbit Analysis Unit

ABSTRACT:

The Engineering Orbit Analysis Unit at GE Valley Forge had available to it an Intel Hypercube Parallel Processor. It was decided to investigate the performance and gain experience of parallel processors with a multi-satellite orbit determination problem. A general study was selected in which major blocks of computation for the multi-satellite orbit computations would be used as units to be assigned to the various processors on the Hypercube. Problems encountered or successes achieved in addressing the orbit determination problem would be more likely to be transferable to other parallel processors.

Our prime objective was to study the algorithm to allow processing of observations later in time than those employed in the state update. We would exploit our expertise in ephemeris determination in addressing these problems and use the facility to bring a realism to the study which would highlight the problems which may not otherwise be anticipated. Our secondary objectives were to gain experience of a non-trivial problem in a parallel processor environment, explore the necessary interplay of serial and parallel sections of the algorithm in terms of timing studies, to explore the granularity (coarse vs. fine grain) to discover the granularity limit above which there would be a risk of starvation where the majority of nodes would be idle or under the limit where the overhead associated with splitting the problem may require more work and communication time than is useful. We could also see the pros and cons of local versus shared memory.

Traditional algorithms for filtering and smoothing within the orbit determination problem have been sequential in nature. Real time filter algorithms imposes constraints on the implementation of the problem on any parallel computer. The computations preceding the state update are extensive and can be solved by small vector processor(s). The computations, arrays and execution time of the update are all extensive, and the third component of concern would be the algorithmic bottleneck which occurs in the updating of the parameters of the state when process noise is used to represent unmodeled errors.

A MULTI-SATELLITE ORBIT DETERMINATION PROBLEM IN A PARALLEL PROCESSING ENVIRONMENT

M. S. Deakyne and R. J. Anderle

INTRODUCTION:

The Orbit Determination Algorithm is a computational intensive problem which can be investigated in terms of increased efficiency with vector, pipeline, and parallel processors. As described below, the approach most intimately connected with the physics of the problem is parallel processing. In 1987, our objective was to decide if parallel processors could be used effectively to determine the orbits of satellites and use the Hypercube to bring a realism to the study which would highlight problems which may not otherwise be anticipated.

The first basic challenges were to become familiar with the many intricate details of the computer architecture and operating system and then to transfer the structure of the algorithm onto the machine architecture of the Hypercube. The complexity and high computational demands of the Orbit Determination Algorithm lent itself to be first logically decomposed into relatively big, computationally independent units. These units would be used as the major blocks of computation assigned to the various processors on the Hypercube. At this stage, we were gaining experience of the Orbit Determination problem in a parallel computing environment. We were discovering the extent of the parallelism within the existing traditional algorithm.

Our next challenge and our prime objective was to study the algorithm to allow processing of observations later in time than those employed in the state update - 'Look Ahead Techniques'. In this stage, we were trying to invent a new piece to the filter algorithm, fundamentally parallel in nature to solve our problem. Problems encountered and successes achieved on the algorithmic level would be more likely to be transferrable to other parallel processors.

THE ALGORITHM:

Traditional algorithms for filtering and smoothing within an Orbit Determination problem have been sequential in nature. Real time filter algorithms impose constraints on the implementation of the problem on any parallel processor. The major segments of an orbit determination problem are:

1. The evaluation of the accelerations of the satellites due to the forces modeled.
2. The numerical integration of these equations of motion.
3. The calculation of the process noise representing unmodeled forces.
4. The calculation of the residuals between the models and the observation.
5. The update of the parameter estimates and the covariance of the estimates.

The update is referred to as filtering when the current time estimates of the parameters are made based on observations prior to that time. Smoothing is when the parameter estimates at a given time are based on observations made after, as well as before, the given time.

The computations preceding the state update are extensive and can be solved by small vector processors. The computations, arrays, and execution time of the update are extensive and can be addressed by vector and/or pipeline processors. The third major area of concern is the algorithmic bottleneck which occurs in the updating of the parameters of the state when process noise is used to represent unmodeled errors.

Within an orbit determination process, using an extended Kalman filter, one must integrate the equations of motion and perturbation equations for all satellites and then compute the process noise before a time update of the covariance can be computed. The residual is found before the Gain is computed, and the measurement update must await for all of the above before its calculation can be performed. Then onto the next measurement. With a single satellite, the force and integration can be done in parallel and the different process noise contributions (i.e. drag, gravity, solar radiation pressure, and clocks) can be done in parallel, independently of each other. With a multi-satellite configuration, the parallelism can be increased by doing all of the above for each satellite in parallel. In the mode of the extended Kalman filter, the algorithmic bottleneck is the measurement update of the state and covariance. The update works in isolation.

APPLYING THE ALGORITHM TO THE MACHINE:
The Hypercube machine is a loosely coupled 32 node multi-processor connected together with a binary n-cube network. Each node had its own sizeable memory with no shared memory and no global synchronization with the host. Communication was achieved by message passing and the computation was data driven.

For a first attack to the parallelism within the orbit determination problem, the Hypercube was a good match to the Orbit Determination problem since the algorithm could be decomposed naturally into logically large and separate independent sub-algorithms. However, the Orbit Determination problem sub-algorithms were diverse in terms of requiring unsynchronized communicating with other pieces of the algorithm which put a challenge on balancing the load and interprocessor communication. Because of the amount of data exchanged, the lack of shared memory was felt as message passing became more and more cumbersome and stilted. And we had no advantage with the Hypercube in terms of dealing with the intensive computational aspect of our problem. We came to believe that the ideal machine would be a coarse grain machine which would allow the underlying concepts of the algorithm to be expressed via the division of the nodes, implementation of the vector package within each node and more efficient mode of communication among the nodes.

However, given our problem and Hypercube facility, we proceeded. The total problem was broken into coarse large sub-problems divided logically along physical concept boundaries. Chunks of code, each dealing with a physical concept, had been then extracted from various sources of standard sequential filter software. Each sub-problem was assigned to a separate process and placed on a separate node. The solution of each node had to be exchanged among the different nodes as the algorithm proceeded. Message passing was a point to point communication path. If there were no direct communication paths between the nodes, the message was routed by intermediate nodes. To handle these messages, a message-delivery scheme was written - the node executive - and was placed on each node as the control center of the flow of data and to coordinate the various node processors.

PRELIMINARY RESULTS:
We achieved a cycling program and began to immediately output timing data. Timing information was difficult to interpret since all the clocks were independent from each other. Intervals of time, concerning wait time, calculation time, and communication time, were output. Reconstructing relative time was difficult. However, from our preliminary results, we found at the end of 1986 an unexplained difference in total run time on the host computer and the overall wait time on each of the nodes. Also, we found that each of the nodes was spending an unacceptable amount of time waiting for information. Placing a synchronization handshake between nodes and the controller did not decrease the difficulty because no message could be broadcast simultaneously and the handshake introduced additional pauses.

During all the work of 1986, the Hypercube machine was physically separated from the group of engineers (i.e. We and the machine were in two different rooms). In 1987, the engineers and the machine were placed in the same room and we could run our program and watch the interplay of the nodes via blinking lights. (Each node on the Hypercube had two lights. When the red light was on, the node was waiting for data; When the green light was on, it was in its calculation mode.) Only then, by viewing these lights did we realize our problems and constraints of implementing this non-trivial problem into the parallel environment. One of our objectives was to explore the algorithm in terms of timing studies. However, by merely observing the lights during an execution of our software, we found that the serial sections of the algorithm were completely dominating the time over the parallel sections. In fact, it was so dominating that it masked completely any saving of time in our different implementations in the parallel sections. Not only was this discovered but also several sections we thought we implemented in a parallel mode were being executed in a sequential mode.

These blinking lights also emphasized the newness and difference of the parallel environment. As we watched the interplay of lights and correlated them to the running sections of the algorithm, we realized that to think of a certain number of processors performing the same task in the same time interval was easy to grasp. But to think and be logically able to handle the different tasks in parallel requiring different intervals of time for calculation and communication and then to tie them together in an efficient parallel mode without reverting to standard inefficient modes of sequential thinking was a challenge.

At this point, we scanned the literature in terms of parallel software techniques and re-visited the existing software package on the Hypercube. Our main objectives now were to explore the necessary interplay of serial and parallel sections of the algorithm in terms of the timing studies, to explore the granularity (coarse vs. fine), and to explore the granularity limit above which there would be a risk of starvation where the majority of nodes would be idle or under the limit where the overhead associated with splitting the problem may require more work and communication time than is useful. We were also exploring the pros and cons of local memory versus shared memory.

Implementing changes into existing software and trying to debug the software was horrific. Unless the debug information messages were written to specifically isolate only certain nodes and certain processes, the person would receive a torrent of messages from all the nodes and the information would be lost in the deluge. All operations on the multiple processors would not necessarily occur in precisely the same order from execution to execution and would not even be time ordered within the same execution. All debug messages affected the timing of the processes and had to be commented out for timing studies. Often the program would cycle with the debug messages in the system only to crash when the messages were removed. Debugging had to be done in a fine grain piecemeal fashion with the messages being highly restrictive to certain nodes and certain processes.

FINAL RESULTS OF THE HYPERCUBE STUDY:

Over the course of the study, we were able to decrease the original run time of the overall execution time by a factor of eight and we did find a proportionate reduction in execution time with the increasing number of nodes employed in the problem. See Table 1 and Table 2 for a summary of the Four Test Cases in terms of calculation time and wait times for 1986 and 1987, respectively. See Table 3 for a Summary of overall run time for the Four Test Cases. See the Appendix for information and explanation of the different Test Cases and a summary of the 1986 Results.

At this stage of experience and output, we were able to finally hone into the new algorithmic aspects of our study. We defined four different 'Look Ahead Techniques' to attack directly the algorithmic bottleneck of the update. See Table 4.

As we began to implement these 'Look Ahead Techniques', we continually bumped up against the machine architecture in terms of memory allocation on the nodes, message passing, and the demands of load balancing and inter-processor communication. To preserve the generality of our study, we scanned the literature and established contacts with Corporate Research Development Labs (CRD). Our evolving approach was to bring together the estimation expertise, the experience of the users in the parallel environment, and the architectural expertise and computing resources of the laboratories. If this approach was followed, it would make it possible to review the real-time speed and numerical performance of the orbit determination package in terms of the implementation, independent of the particular machine architecture, while maintaining the correct view on the algorithmic level.

Our objective now was to define a benchmark orbit determination problem to use to evaluate and demonstrate new improvements to the algorithm using various mapping architectures of existing parallel computers. We developed and wrote a sequential orbit determination package which contained the same realistic models of the satellite dynamics, gravity, drag, solar radiation, GPS, and ground clock noise contained in the Hypercube program.

CONCLUSIONS:

The test results finally showed an improvement in efficiency of ephemeris computations with an increase in the number of nodes utilized. Experimentation and experience caused us to stop our implementation of the 'Look Ahead Techniques' on the Hypercube and re-direct the IR&D effort to a broader baseline. The Hypercube machine was a viable necessary tool to gain experience in parallel processing and bring the realism to the study. However, the Hypercube type of machine architecture, which we used in this study, is not the best one which matches the structure of the orbit determination problem in terms of increased efficiency. (New Upgrades to the Hypercube have been noted in the literature which eases message passing.) But the Orbit Determination problem is still a viable problem for parallel processing.

Our experience should be expanded to machines such as the Warp II, Cray, the Butterfly, and the Connection Machine to determine the efficiency of the implementation with the focus on the measurement update.

The project should be conducted with parallel support from M&DSO and CRD. The achievable throughput, cost, and reliability of large scale filters in a parallel environment is a very important and known next step to accomplish.

ORIGINAL PAGE IS
OF POOR QUALITY

TABLE 1

1987 HYPERCUBE EPHEMERIS PROJECT

TIMING DATA
1986
15 OBSERVATIONS

PROCESS	NODE ASSIGNMENTS				TOTAL WAIT TIME (SEC)				TOTAL CALCULATION TIME(SEC)			
	1	2	3	4	1	2	3	4	1	2	3	4
INTEGRATOR	1	1	1	7	422	402	414	428	9.2	9.4	9.3	52.1
INTEGRATOR	2	2	2		422	400	412		9.4	9.6	9.5	
INTEGRATOR	3	3	3		422	405	395		7.1	7.1	18.1	
INTEGRATOR	4	4	4		422	400	422		8.1	7.1	2.7	
INTEGRATOR	5	5			434	410			1.5	1.7		
INTEGRATOR	6	6			438	409			0.0	1.3		
INTEGRATOR	7	7			434	418			1.3	0.0		
INTEGRATOR	8				437				0.0			
INTEGRATOR	9				437				0.0			
INTEGRATOR	10				437				0.0			
GRAVITY NOISE	12	1	1	7	425	396	409	449	3.1	7.8	7.9	24.5
GRAVITY NOISE	13	2	2		425	394	412		3.4	7.9	8.1	
GRAVITY NOISE	14	3	3		408	372	393		11.1	12.5	14.7	
DRAG NOISE	15	6	3	7	422	397	407	475	4.1	5.0	9.4	15.3
DRAG NOISE	16	7	4		421	392	410		4.4	3.7	6.4	
S. RAD. NOISE	17	1	1	7	422	395	408	475	4.5	13.9	13.9	14.6
S. RAD. NOISE	18	5	2		422	392	419		4.6	5.7	6.0	
CLOCK NOISE (GPS)	19	4	4	7	404	359	393	475	10.8	18.2	15.6	11.7
CLOCK NOISE (GRD)	20	2	3	7	401	396	394	477	10.9	18.9	16.8	13.4
RESIDUAL	11	3	21	21	426	387	415	496	2.7	6.4	4.1	3.9
UPDATE	21	21	21	21	345	329	343	423	75.4	74.9	74.9	75.1

	TIME PER OBSERVATION (SEC)			
	1	2	3	4
1	25	24	24	31
2	31	30	32	36
3	30	30	32	38
4	27	27	28	34
5	27	27	28	33
6	27	27	27	33
7	29	26	28	34
8	27	27	28	33
9	28	27	28	33
10	27	28	28	33
11	28	27	28	33
12	27	27	27	33
13	31	27	28	33
14	32	27	28	32
15	29	27	28	33
TOTAL RUN TIME	425	408	422	503

NOTE:
- SIGNIFICANT AMOUNT OF DEBUG DATA TRANSMITTED
- NO FLICK (50 MILLISECOND WAIT TIME AWAITING EACH MESSAGE)

ORIGINAL PAGE IS
OF POOR QUALITY

TABLE 2

1987 HYPERCUBE EPHEMERIS PROJECT

TIMING DATA
1987
15 OBSERVATIONS

PROCESS	NODE ASSIGNMENTS				TOTAL WAIT TIME (SEC)				TOTAL CALCULATION TIME(SEC)			
	1	2	3	4	1	2	3	4	1	2	3	4
INTEGRATOR	1	1	1	7	33	34	47	65	9.2	9.4	9.3	35.0
INTEGRATOR	2	2	2		33	35	47		9.1	9.0	9.1	
INTEGRATOR	3	3	3		36	37	44		6.2	6.2	12.6	
INTEGRATOR	4	4	4		36	37	46		6.2	6.2	2.2	
INTEGRATOR	5	5			34	34			1.2	1.2		
INTEGRATOR	6	6			0.0	32			0.0	1.0		
INTEGRATOR	7	7			32	0			0.9	0.0		
INTEGRATOR	8				0.0				0.0			
INTEGRATOR	9				0.0				0.0			
INTEGRATOR	10				0.0				0.0			
GRAVITY NOISE	12	1	1	7	39	40	53	90	1.4	1.6	1.3	5.1
GRAVITY NOISE	13	2	2		39	40	53		1.6	1.5	1.4	
GRAVITY NOISE	14	3	3		39	41	53		2.4	2.4	2.4	
DRAG NOISE	15	6	3	7	38	40	53	90	2.0	1.9	1.9	3.9
DRAG NOISE	16	7	4		38	40	53		2.0	2.1	1.9	
S. RAD. NOISE	17	1	1	7	40	41	52	89	1.9	2.0	1.9	3.8
S. RAD. NOISE	18	5	2		40	41	52		2.0	2.3	1.9	
CLOCK NOISE (GPS)	19	4	4	7	40	41	53	93	0.8	0.8	0.7	0.7
CLOCK NOISE (GRD)	20	2	3	7	40	41	54	93	0.8	0.8	0.8	0.8
RESIDUAL	11	3	21	21	40.5	42	53	94	1.2	1.4	1.2	1.2
UPDATE	21	21	21	21	31	32	49	84	7.2	7.3	7.3	7.3

	TIME PER OBSERVATION (SEC)			
	1	2	3	4
1	5	3	4	
2	2	2	3	
3	3	2	4	
4	3	2	3	
5	2	2	3	
6	2	2	3	
7	2	2	3	
8	2	2	3	
9	4	2	4	
10	2	2	3	
11	2	4	3	
12	2	2	3	
13	2	2	3	
14	2	2	3	
15	2	2	4	
TOTAL RUN TIME	37	33	49	94

NOTE:
- OBSERVATION FILE REFORMATTED PRIOR TO CYCLING
- GLOBAL BROADCAST TREE INCORPORATED

TABLE 3

EPHEMERIS PROCESSING IN PARALLEL PROCESSORS
IR&D STATUS REVIEW

RESULTS OF EXECUTION TIME

- PROPORTIONATE REDUCTION IN EXECUTION TIME WITH INCREASING NUMBER OF NODES EXPECTED

NUMBER OF NODES UTILIZED IN TEST CASE	21	8	5	2
RUN TIME (JAN 1987) (SEC)	425	408	422	503
RUN TIME (JUNE 1987) (SEC)	37	33	49	94

TABLE 4

EPHEMERIS PROCESSING IN PARALLEL PROCESSORS
IR&D STATUS REVIEW

LOOK AHEAD TECHNIQUES

METHOD 1 (PRESENTLY EMPLOYED)

- o MAINTAIN STATES AT SAME EPOCH BY RESTARTING INTEGRATION OF ALL SATELLITES AT THE TIME OF OBSERVATION OF ANY SATELLITE
- o SOLUTION EXACT BUT ALL SATELLITE INTEGRATIONS ARE STALLED FOR UPDATE CALCULATION

METHOD 2

- o ALLOW STATES OF DIFFERENT SATELLITES TO HAVE DIFFERENT EPOCHS FOR THE TIME OF UPDATE
- o RESTART OF INTEGRATION ONLY AT RESPECTIVE OBSERVATION TIMES
- o INTEGRATION FOR EACH SATELLITE MUST AWAIT ITS OWN UPDATE
- o NET RESULT MAY BE APPROXIMATE DUE TO PROCESS NOISE CORRELATIONS
- o FOR TRAJECTORY/COVARIANCE OUTPUT, RESTARTS ARE NECESSARY DURING LONG OBSERVATION GAPS FOR ANY GIVEN SATELLITE

METHOD 3

- o BATCH SEQUENTIAL
- o SPECIFIED BATCH LENGTH, SAME EPOCH FOR ALL SATELLITES
- o RESTART AT OBSERVATION TIMES ONLY IF UPDATE PARAMETERS EXCEED PROPOGATED STATE BY SOME TOLERANCE

METHOD 4

- o BATCH SEQUENTIAL
- o MINIMUM AND MAXIMUM BATCH LENGTH SPECIFIED
- o DIFFERENT EPOCHS FOR DIFFERENT SATELLITES
- o MAXIMUM BATCH LENGTH DEFINED AS INTERVAL BETWEEN OBSERVATIONS OF RESPECTIVE SATELLITES

APPENDIX

ALGORITHM TASKS

EPHEMERIS

OBJECTIVE
The objective of the hypercube ephemeris task was to decide if parallel processors can be used effectively to determine the orbits of satellites.

APPROACH
Within a satellite ephemeris computer program, there are many vector-type operations that could be performed in parallel and, thus, improve the throughput of the computations. However, exploiting this capability of parallel or vector processors would require a large number of processors; furthermore, the results of such a study would be highly dependent on the type of computers used. A general study was selected in which the major blocks of computation for multisatellite orbit computations were used as the units to be assigned to various processors. A multisatellite orbit solution including observations between satellites is a challenging problem for parallel processors, since there is a natural bottleneck that occurs in the updating of the parameters of such a solution when process noise is used to represent unmodeled errors. Problems encountered or successes achieved in addressing this problem are more likely to be transferrable to other computers.

TEST CONDITIONS
A typical multisatellite test problem was selected which consisted of the configuration shown in Table 1. The program that was designed has the capability of processing the above observations for 3 primary satellites, such as Landsat or Topex, 3 relay satellites, and 18 GPS satellites. The number of Doppler stations can be greater than the 15 selected for the test, but provision was not made for time-overlapping Doppler observations since it would not have contributed to the test objectives. The process noise models account for the statistical effects of atmospheric drag variations and unmodeled errors in the earth's gravity field, computed effects of solar radiation forces, and clocks aboard the primary satellites that are used to make measurements of range to the GPS satellites or Doppler effects seen at ground stations.

The processor modules shown in Table 2 consist of:

1. An executive for each node

2. Integrator-force assignable to nodes for any groupings of satellites

3. Residual computation assignable to nodes for any groupings of observation types and satellites

4. Process noise for gravity assignable to nodes for any grouping of host vehicles and relay satellites

5. Process noise for drag assignable to nodes for any grouping of host vehicles

6. Process noise for solar radiation pressure assignable to nodes for any groupings of relay satellites

7. Process noise for clocks assignable to nodes for any groupings of host satellites

8. A single time and observation update module

The controller receives input assigning the processes to nodes, initializes the computations, and sends extended observation messages to the appropriate nodes where the executive (on the basis of the codes contained in the observation record) determines which processes are to be performed on the respective node and where to send the results. As the current solution is performed, the update module sends it to the controller for output, and this signals readiness for another observation. An IBM 3090 program supports the system by generating simulated data which is down-loaded to the hypercube controller.

DESCRIPTION OF TEST CASES

The orbit computations were performed for 15 simulated observations using the node assignments shown in Tables 3 and 4. All the processes were loaded on each node except for Update which was loaded on node 21 with no other processes (excluding the node executive which was common to all nodes). Test 4 node assignments were selected to approach the computer run time expected for sequential processing. Tests 2 and 3 provide measures of gain to be achieved in parallel processing. Of course, in actual implementation, the processes would be decomposed into smaller elements in order to make maximum utilization of available nodes. Test 1 was designed to determine the approximate computation time required for each process. Although the length of time spent in the computation portion of each process was recorded, it included time spent during the 50-msecond samplings of other processors. Although the exits to the node executive were included in the process times obtained in Test 1, the results were as close to the actual computation time as could be obtained. Refer to Table 5 for memory requirements for processors.

TABLE 1

TEST CONDITIONS

Satellites:

- Landsat Mapping Satellite
- Topex Altimetry Satellite
- Tracking and Data Relay Satellite System (TDRSS) -1 Relay Satellite
- TDRSS -2 Relay Satellite
- 6 Global Positioning System (GPS) Satellites (Orbits Assumed to be Known)

Observations:

- Ground Doppler Observations of Landsat and Topex
- Range Observations From a Ground Site to TDRSS Satellites
- Range-Sum Observations Through Relays to Landsat and Topex
- Range Observations From Topex and Landsat to GPS

Process Noise:

- Gravity for Landsat, Topex and Relays
- Drag for Landsat and Topex
- Radiation Pressure for Relays
- GPS Receiver Clocks on Landsat and Topex
- Doppler Beacons on Landsat and Topex

TABLE 2

PROCESSOR MODULES

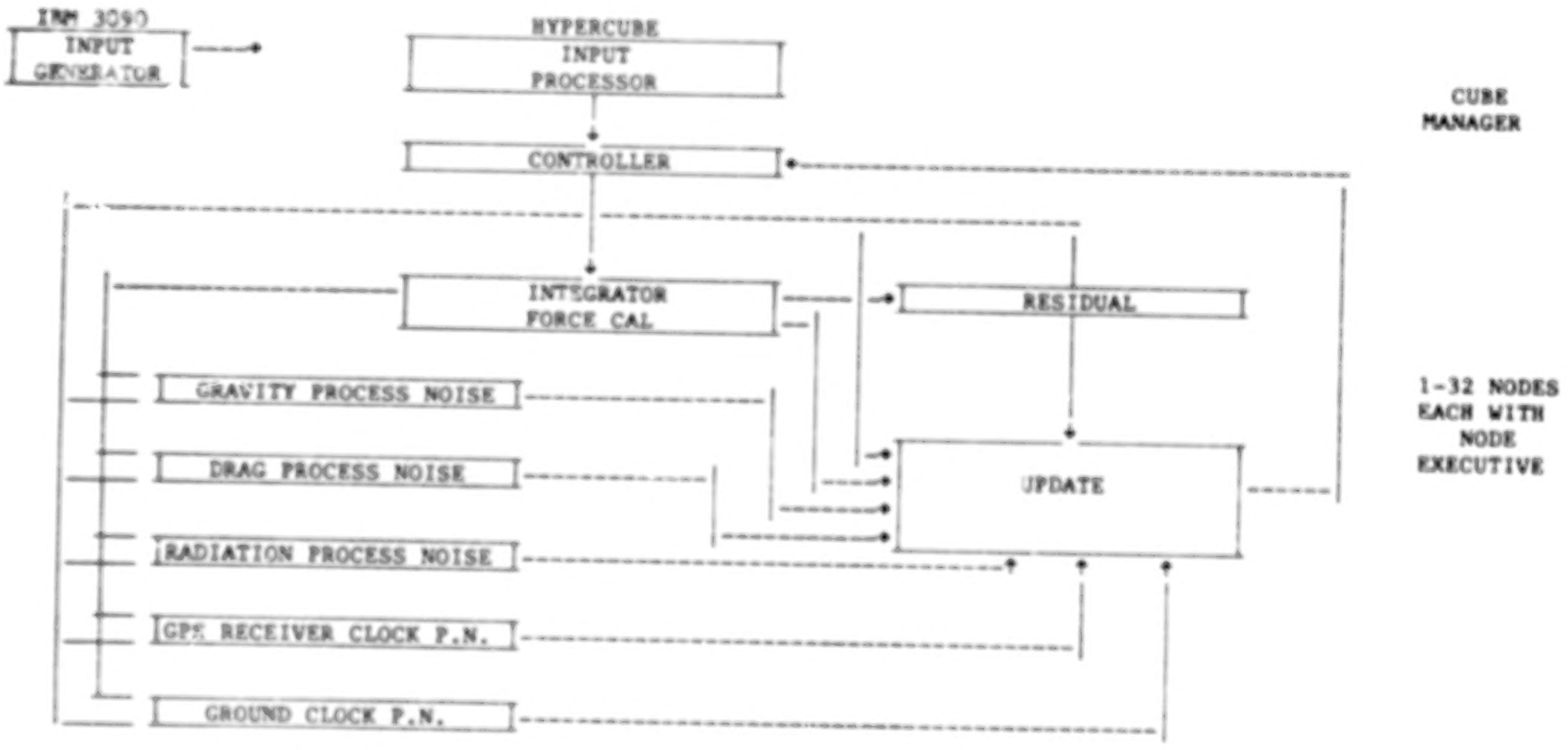
IBM 3090
INPUT
GENERATOR
HYPERCUBE
INPUT
PROCESSOR
CUBE
MANAGER
CONTROLLER
INTEGRATOR
FORCE CAL
RESIDUAL
GRAVITY PROCESS NOISE
DRAG PROCESS NOISE
RADIATION PROCESS NOISE
GPS RECEIVER CLOCK P.N.
GROUND CLOCK P.N.
UPDATE
1-32 NODES
EACH WITH
NODE
EXECUTIVE

TABLE 3
NODE ASSIGNMENTS - INTEGRATOR/FORCE

Processor	Test 1	Test 2	Test 3	Test 4
Integrator/Force				
Landsat	1	1	1	7
Topex	2	2	2	7
Relay-1	3	3	3	7
Relay-2	4	4	3	7
GPS-1	5	5	4	7
GPS-2	6	5	4	7
GPS-3	7	6	4	7
GPS-4	8	6	4	7
GPS-5	9	7	4	7
GPS-6	10	7	4	7
Residuals	11	3	21	21

TABLE 4
NODE ASSIGNMENTS - PROCESS NOISE

Processor	Test 1	Test 2	Test 3	Test 4
Process Noise				
Gravity P.N. Landsat	12	1	1	7
Gravity P.N. Topex	13	2	2	7
Gravity P.N. Relay 1	14	3	3	7
Gravity P.N. Relay 2	14	3	3	7
Drag Noise Landsat	15	6	3	7
Drag Noise Topex	16	7	4	7
Rad. Noise Relay 1	17	1	1	7
Rad. Noise Relay 2	18	5	2	7
Clock 1 Landsat	19	4	4	7
Clock 1 Topex	19	4	4	7
Clock 2 Landsat	20	2	3	7
Clock 2 Topex	20	2	3	7
Update	21	21	21	21

TABLE 5
MEMORY REQUIREMENTS FOR PROCESSORS

Process	Memory Requirement (Bytes)	
	IBM 3090	Hypercube
Node Executive	N/A	47769
Integrator/Force	175005	42251
Residuals	74688*	3185*
Gravity Noise	67848*	26935
Radiation Noise	72168*	34349
Clock (GPS)	55144*	14277
Clock (Ground)	55984*	14577
Update		231988*

* Combination of these processes in one processor would reduce the storage requirements for these five routines from 398000 to 174000 bytes through the use of shared subroutines and common data.

** This figure is the memory requirement for the full computational Update. For test purposes, an abbreviated Update was used. The test version required 182825 bytes.

RESULTS

The execution times initially obtained for the previous test cases are given in Table 6. Supplementary timing data showed that the small reduction in run time with increase in the number of nodes was accompanied by large wait times (100-600 seconds) on the nodes and large execution time (75 seconds) for update. The best estimate of the actual computation time (as opposed to execution time, which includes the wait time) for sequential processing is that obtained for Test 4, which gave a value of 211 seconds, including 75 seconds for Update computations, or a computation time of 135 seconds for all processes except Update. Using this value as a base, the differences in execution time for the other test cases were used to estimate the computation times for those cases. The measured computation time for the processors in those cases could not be used because the time measured within each processor also included time spent in other processors on the same node during the 50 millisecond sequencing among processors. The computation time for Update was considered separately for the comparisons, since proportionate reduction in computation time with increasing number of nodes would not be expected for Update, which was on a separate node in each case.

The reduction in estimated computation time from Test 4 to Test 3 to Test 2 is within a factor of two of that expected for the increase in number of nodes. Proportional reduction in execution time is not expected for Test 1, since the processor assignments required that several of the nodes operate in sequence in this case; however, the increase in execution time is anomalous.

Although the estimated reduction in computation time with increase in number of nodes was satisfactory, the excessive wait time for the nodes is not acceptable. The second major concern was the extent of the time required for update processing. The time was particularly disappointing because the matrix operations required for an actual update were bypassed during these tests to expedite test results which were more pertinent to the objectives of the test. The initial test results were obtained while a significant amount of debug data was being transmitted from the nodes to the system log. They were also made without the benefit of the use of the Flick command which prevents

TABLE 6
NODE LOADING COMPARISONS

	Test 1	Test 2	Test 3	Test 4
1. Observed Results				
Number of Nodes Used	21	8	5	2
Execution Time (Seconds)	425	408	422	502
2. Estimated Calculation Time Excluding Update				
Number of Nodes Used	20	7	4	1
Estimated Calculation Time (Seconds)	58	41	55	135

C 3

an unnecessary 40-millisecond wait time in a processor that is awaiting information each time the node sequences through the processor. A rerun of the test was made with the debug communication deleted and with the Flick command installed in the node executives (but not in the processors, which were thought to be of lesser concern). The execution time was nearly halved with these modifications, and the computation time reduced to a third of the original value for Test 4. The computation time for Update was reduced in order of magnitude to about 7 seconds. However, the computation time did not decrease with an increase in the number of nodes; in fact, the execution time increased slightly.

The cause of the failure of the execution time to decrease significantly with increase in number of nodes has not been specifically identified. The timing data accumulated to date fails to account for more than half the wait time recorded by the processors. In addition to the difficulty of interpreting timing results for a sequencing node, reruns of the same test case occasionally gave different results. A rerun of the test cases with the revised INTEL operating system would resolve that question, or additional timing data installed in the processors would identify the source of the unexpected wait time.

There are two modifications to the existing hypercube ephemeris program that would have a dramatic effect on the efficient utilization of the processors, even after the cause of the current anomalous results is identified:

1. The integration/force computations can be separated and performed in different processors. Since the integration and force computation for a given satellite are essentially sequential operations, the nodes with either an integration or force processor must also be assigned other processes, in order that the gain in efficiency can be realized.

2. Computations for some satellites can proceed ahead of the update computations, which would allow additional parallel computations to be performed. This modification would require some revision of the update algorithm and some additional logic in the controller and node executive.

CONCLUSIONS

The test results failed to show an improvement in efficiency of ephemeris computations with an increase in the number of nodes because of unexplained wait times occurring during execution. It is expected that additional testing would reveal the cause of the unexpected wait times, and tests with a modified program would demonstrate that ephemeris programs could be run efficiently on parallel processors.

RECOMMENDATIONS

It is recommended that:

1. The test cases be rerun with the latest INTEL operating system
2. Test 1 be rerun with additional timing data recorded to determine the cause of the unidentified wait times
3. The current processor modules be further subdivided, particularly by separating the integration and force computations
4. The update and integrator processors be modified to hold the epoch of the states fixed for scheduled periods of time, and the controller and node executives be modified to allow observation to be processed at controlled intervals ahead of the observation time for the last update
5. Studies and tests be conducted to develop an algorithm for automatic assignment of processors to nodes as a function of the available number of nodes and the nature of the ephemeris task

N89-15944

THE LANDSAT/GLOBAL POSITIONING SYSTEM PROJECT

TERRI WOOD
SYSTEMS DEVELOPMENT BRANCH
GODDARD SPACE FLIGHT CENTER
GREENBELT ROAD, GREENBELT, MD. 20771

ABSTRACT

A GPSPAC/Landsat-D Interface (GLI) Ground Support System was built to validate the performance and to calibrate the accuracy of the experimental navigation package, GPSPAC, flown on the Landsat-4 and 5 spacecraft. Although the GLI system operated successfully to give the orbit information needed to validate the GPSPAC, it also detected two anomalies: one is characteristic of the GLI system and the other is characteristic of the pre-operational phase of GPS. Several methods were applied to resolve or reduce the anomalies. This paper presents a description of the problems, the methods applied to resolve or reduce them, and the results.

2.0 GLOBAL POSITIONING SYSTEM BACKGROUND

The Global Positioning System (GPS) is an advanced satellite-based navigation system, being deployed by the Department of Defense, that will provide extremely accurate position, velocity, and time information to a variety of users 24 hours a day, 7 days a week. Both the Landsat-4 and 5 spacecraft carried an experimental navigation package, the Global Positioning System Package (GPSPAC), to assess the performance and the accuracy of the onboard use of GPS data.

The GPS configuration consists of a Master Control Station (MCS) and a constellation of Navigation Development Satellites (NDSs). In its operational configuration, the NDS constellation will consist of 18 Space Vehicles (SVs) in six nearly circular orbits of 12-hour periods (20,200 km altitude) each inclined 55 degrees to the equator. However, when Landsat-5 was launched in March 1984, the NDS constellation consisted of five operating SVs in two orbit planes with ascending nodes at 120 and 240 degrees, respectively.

The navigation process of GPS proceeds as follows: First, the MCS uplinks messages, consisting of time synchronization and SV ephemeris information, to the NDSs and the NDSs, in turn, continuously broadcast these messages to the user spacecraft. Subsequently, the GPSPAC Receiver/Processor Assembly (R/PA), which is the principle GPSPAC subsystem, records and uses the information onboard and processes pseudorange and delta-pseudorange observations with an Extended Kalman Filter (EKF) to calculate an estimate of the user spacecraft's orbit. (This information is retained to be analyzed and compared with the Landsat definitive ephemeris tape files which are derived from independent sources). If no SVs are in view of the user spacecraft, the R/PA of the user spacecraft must propagate its own orbit by using a numerical integrator.

One aspect of the GPSPAC experiment was to validate and to calibrate the accuracy of the orbit information produced by GPS data; another aspect of the GPSPAC experiment was to determine ways to improve the GPSPAC Kalman Filter's navigation performance by investigating various data base constant changes or by adopting algorithmic changes to the GPSPAC software. To support these efforts, a ground-support-modular system called the GPSPAC/Landsat-D Interface (GLI) System was developed in March 1982 by GSFC's Systems Development Branch. The GLI system consists of five subsystems and the function of each subsystem is described below.

First, the GPSPAC Experiment Data Preprocessor (GEDAP) is the front-end of the system; it reads, sorts, and reformats telemetry strip tape files containing raw GPSPAC measurement data (observations and residuals) and GPSPAC Kalman Filter parameter estimates. Second, the COMPAR subsystem compares ephemeris files from different sources. Next, the PLOT subsystem generates graphs of observations, residuals, and filter parameter estimates as well as ephemeris differences from COMPARE. Finally, the last two subsystems, RECON and ONPAC, are used sequentially. RECON recombines files from GEDAP output to produce data in a form ready for ONPAC to use. ONPAC, the onboard navigation package, is a menu-driven system which has two functions: (1) It uses the recombined files generated from RECON to produce estimates of the GPSPAC navigation solutions by emulating the GPSPAC Kalman Filter data processing scheme. (2) It simulates estimates of the GPSPAC navigation solutions by allowing the user to change various filter parameters; therefore, one can analyze the effect on the GPSPAC navigation solutions once the options are invoked.

The telemetry strip tape files and the Landsat definitive ephemeris tape files, which the GLI system processes, are provided by the Landsat Operations Control Center and by the Ground Spaceflight Tracking and Data Network (GSTDN) Center, respectively. The Landsat Operations Control Center, located at GSFC Building 28, retrieves the telemetry strip tape information from the playback recordings of the GPSPAC during the satellite flyby of a ground tracking station. The GSTDN center, located at GSFC Building 25, collects Unified S-Band (USB) range and range-rate data. Then, the Goddard Trajectory Determination System (GTDS) is used to process the GSTDN USB data and to compute the definitive orbits by performing batch-least squares orbit fits.

3.0 ONPAC AND GPSPAC ANOMALIES

From March 1982 until August 1986, the GLI system was operated successfully to give the orbit information needed to validate the GPSPAC. Namely, comparisons with definitive ephemeris indicated that errors in Landsat-4 and 5 position and velocity from GPSPAC were consistently less than 50 meters and 6 cm/sec, respectively, during periods of good NDS SV visibility (generally speaking 4 SVs in view), and that the peak position errors were generally less than 1,500 meters during periods of poor SV visibility. Although the GLI system helped us to assess the validity of the GPSPAC, it has also enabled us to detect two anomalies: one pertains to the GLI system and the other pertains to the pre-operational phase of GPS. A description of these anomalies is given in the next subsections.

3.1 The ONPAC Anomaly

A problem which pertains to the ONPAC system is depicted by the graphs of the ONPAC position (velocity) uncertainty parameters; these graphs are inconsistent with the graphs of the GPSPAC position (velocity) uncertainty parameters. For instance, figures 1 and 2 illustrate the inconsistencies between the two position uncertainty parameters where each graph was generated during the same arbitrary time span. These inconsistencies suggest that possibly the ONPAC orbit propagator does not match the models of GPSPAC entirely. To understand why the ONPAC position uncertainty parameters graphs differ from the GPSPAC position uncertainty parameters graphs, the ONPAC position differences graphs were analyzed; to resolve the ONPAC inconsistencies, the ONPAC software was investigated and modified. Briefly, the steps taken to resolve the ONPAC inconsistencies involved comparing the GPSPAC navigation code against the supposedly equivalent ONPAC code, modifying the non-conforming routines, and comparing hand-calculated values of various filter parameters (based on the GPSPAC algorithms) with the values used by ONPAC. A detailed explanation of these methods is given in section 4.1.

3.2 The GPSPAC Anomaly

A problem which is characteristic of the pre-operational phase of GPS, is that the GPSPAC/GSTDN definitive position (velocity) differences tend to fluctuate tremendously, when the user spacecraft is forced to propagate its own orbit because of poor SV visibility. For instance, figure 3 illustrates a typical graph of the GPSPAC/GSTDN definitive position difference fluctuations. Also, Figure 4 shows the NDS visibility to the Landsat-4 spacecraft for that period (only NDS SV numbers 5,6,8 & 9 were operational for that period). Notice how the GPSPAC/GSTDN definitive position differences graph peaks whenever there are less than two SVs in view during any particular time span. These fluctuations suggest that there could have been some inconsistencies between the way that the GPSPAC orbit propagator was designed and implemen[illegible]. Therefore, to investigate this suggestion fully, the GP[illegible] navigation software design was compared and analyzed wi[illegible]e software code. In addition to this, ONPAC was used to simulate runs of the GPSPAC definitive position difference fluctuations which enabled us to recommend ways to reduce the actual GPSPAC fluctuations. Briefly, the steps taken to reduce the simulated GPSPAC fluctuations involved studying the GPSPAC navigation design, comparing the design with the actual code (to see if the formulas were implemented correctly), documenting the differences, and changing various ONPAC filter parameters. A detailed explanation of these methods is given in section 4.2.

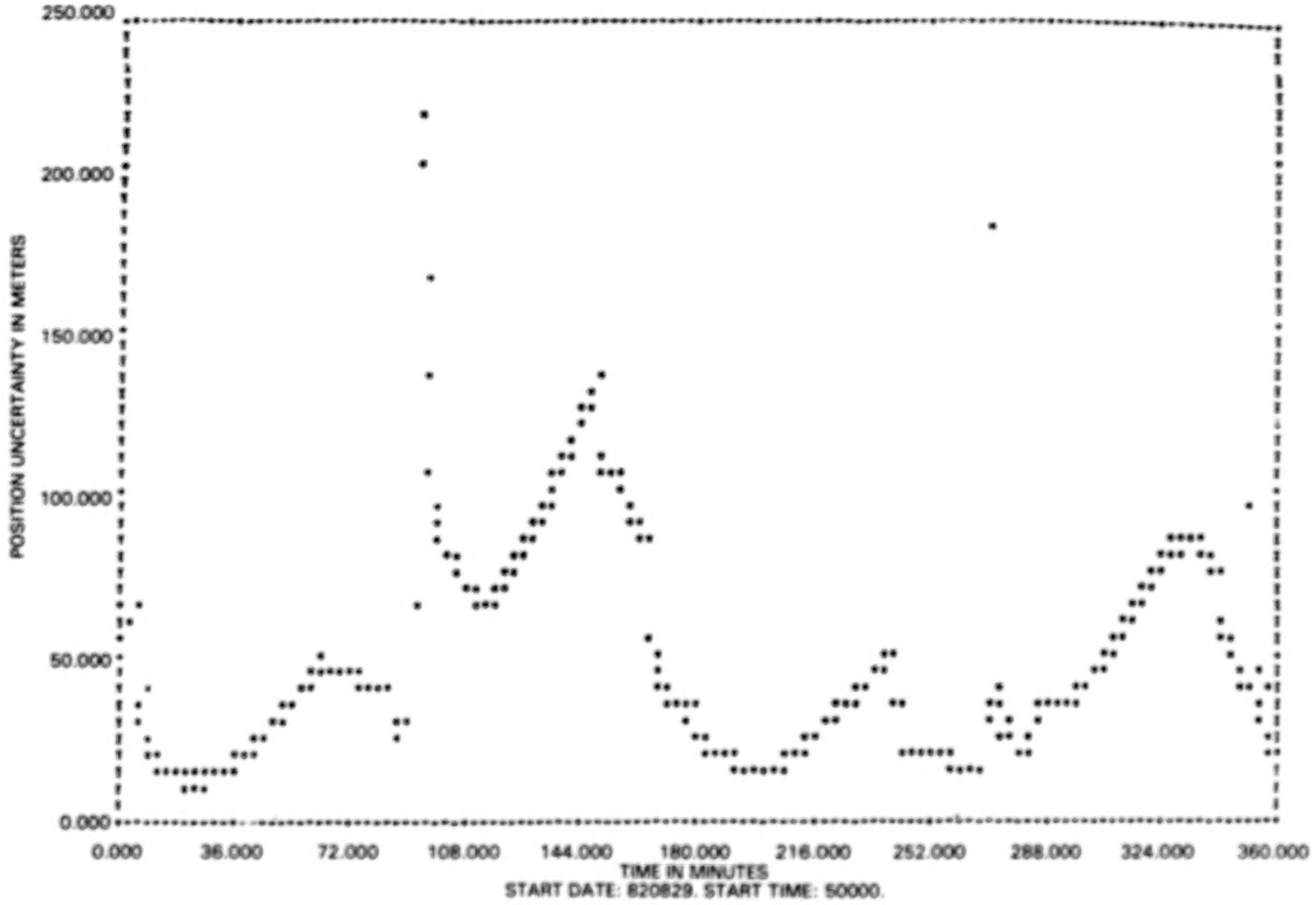

Figure 1. ONPAC Position Uncertainty Parameters

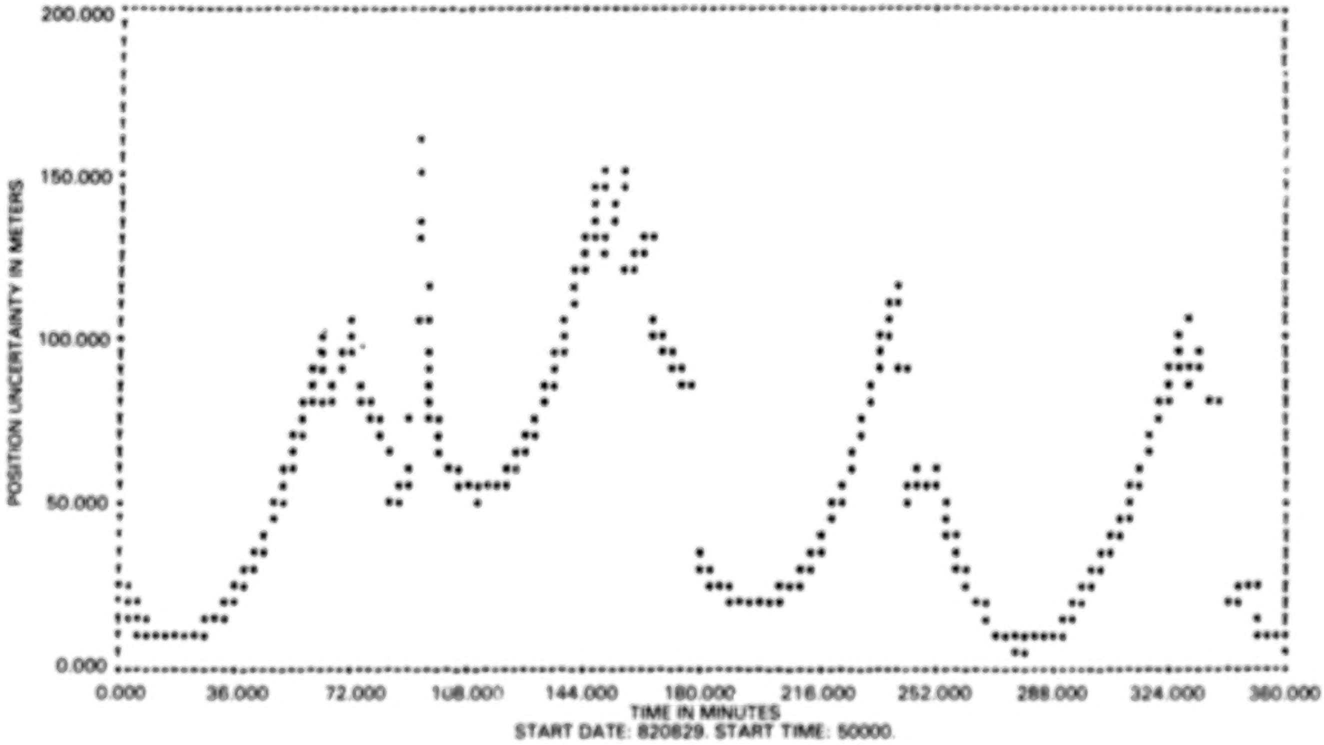

Figure 2. GPSPAC Position Uncertainty Parameters

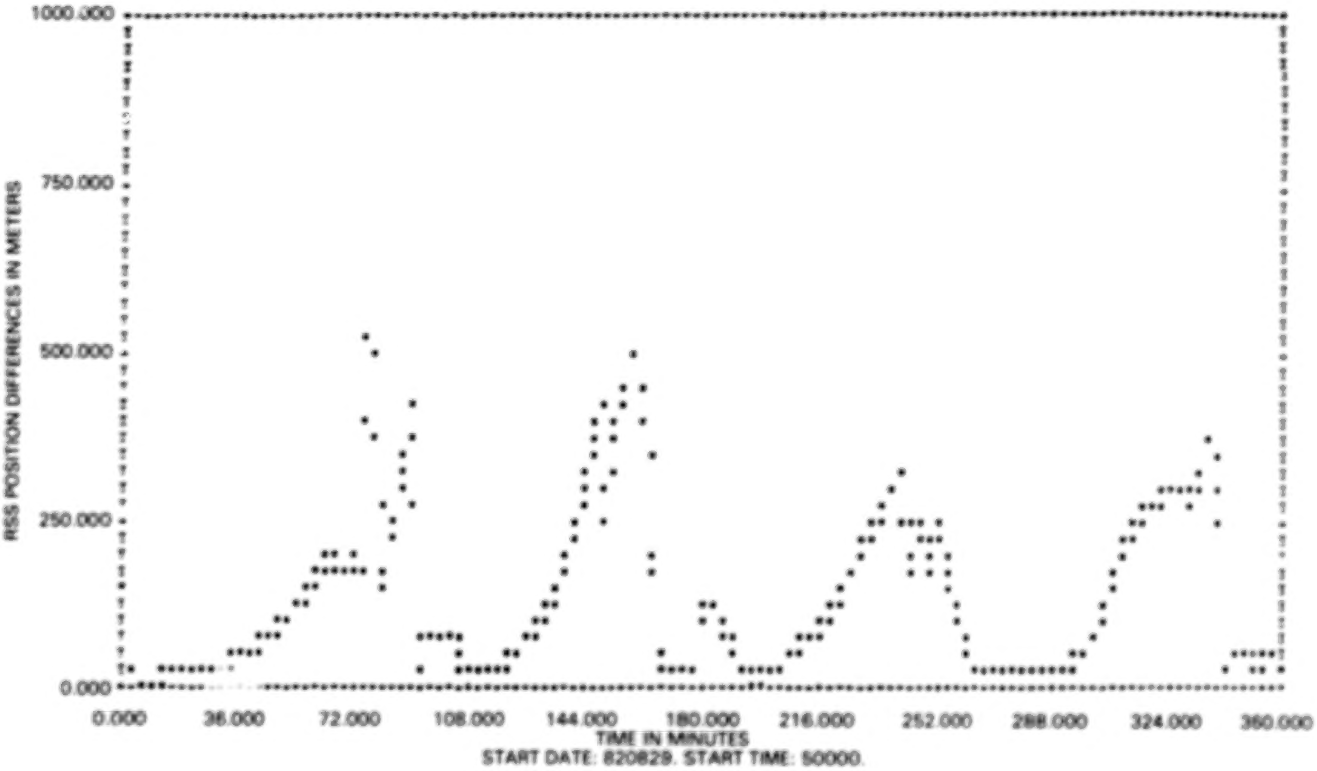

Figure 3. GPSPAC/GSTDN Definitive Position Difference Fluctuations

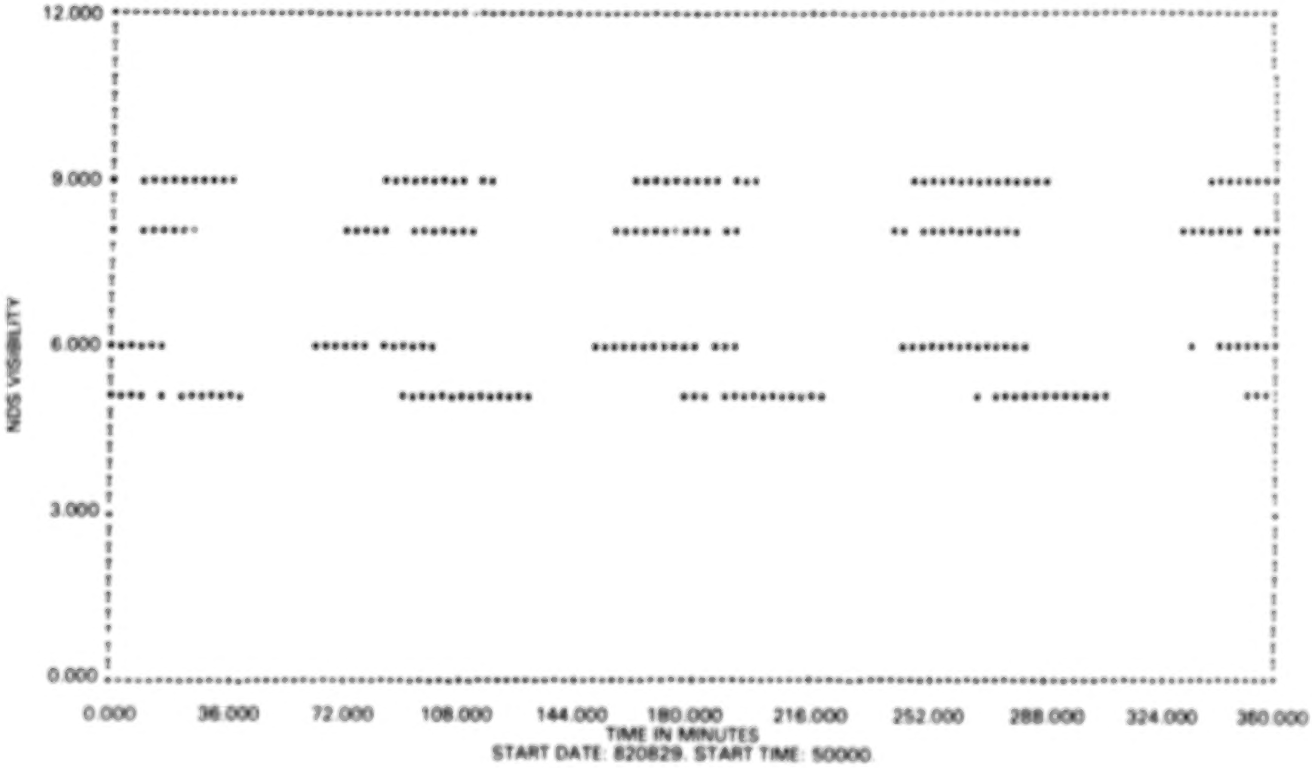

Figure 4. NDS Visibility to Landsat-4

4.0 STEPS TAKEN TO RESOLVE/REDUCE THE ANOMALIES

4.1 Steps Taken to Resolve the ONPAC Anomaly

Since the ONPAC orbit propagator did not match the orbit propagation model of GPSPAC entirely, the ONPAC software was compared with the GPSPAC software to see where the differences occurred. Moreover, several of the filter parameters were calculated by hand to check the computed answers given by ONPAC. A brief description of the GPSPAC/ONPAC code differences, the filter parameters calculated, and the implications of the changes is given in the next subsections.

The GPSPAC/ONPAC Code Differences

The GPSPAC/ONPAC code differences that were found by comparing the two software systems were minor and the following modifications were made to the ONPAC code: First, the geopotential force model in ONPAC, which is one of the modeled external forces used to describe the equations of motion for orbit propagation, was upgraded from a 4x4 earth geopotential model to a 5x5 earth geopotential model to match that of GPSPAC. Next, the atmospheric density model in ONPAC, which is used to model the external drag force (another external force used in orbit propagation), was assigned the same lowest altitude threshold value as that of GPSPAC. Finally, a variable used in ONPAC to validate the pseudorange observations, was replaced with another variable to help simulate the measurement error computation better.

The Filter Parameters Calculated

Another vehicle used to help locate the GPSPAC/ONPAC code differences was to calculate by hand the following EKF parameters given the GPSPAC EKF software, an arbitrary state vector, and the corresponding state-error covariance matrix (see the heading entitled "The EKF Background" for a detailed explanation of these EKF parameters): (1) The arbitrary state vector and the state-error covariance matrix were propagated to the pseudorange measurement time. (2) The pseudorange measurement residual and Kalman Gain were calculated. (3) The state vector was updated by

ORIGINAL PAGE IS
OF POOR QUALITY

adding the Kalman update to it. These hand calculations were done for at least 2 distinctive pseudorange cycles.

The Implications of the Steps Taken to Resolve the ONPAC Inconsistencies

When the ONPAC software code was modified to emulate the GPSPAC propagation model better, the modified ONPAC code was executed, using the same data as before, to generate a better graph of the ONPAC position uncertainty parameters. However, the second graph shows more inconsistencies with the graph of the GPSPAC position uncertainty parameters as did the first graph which was generated using the original ONPAC code (refer to figures 1, 2, and 5 for the comparison). And, to make matters even worse, all of the answers generated from the hand calculations discussed earlier, agreed with the computed answers given by the revised version of the ONPAC software. Consequently, neither of the steps taken to resolve the ONPAC inconsistencies helped; but, it turns out that a method used to reduce the simulated GPSPAC fluctuations also reduces the ONPAC inconsistencies as well and a description of this method is given in the next subsection.

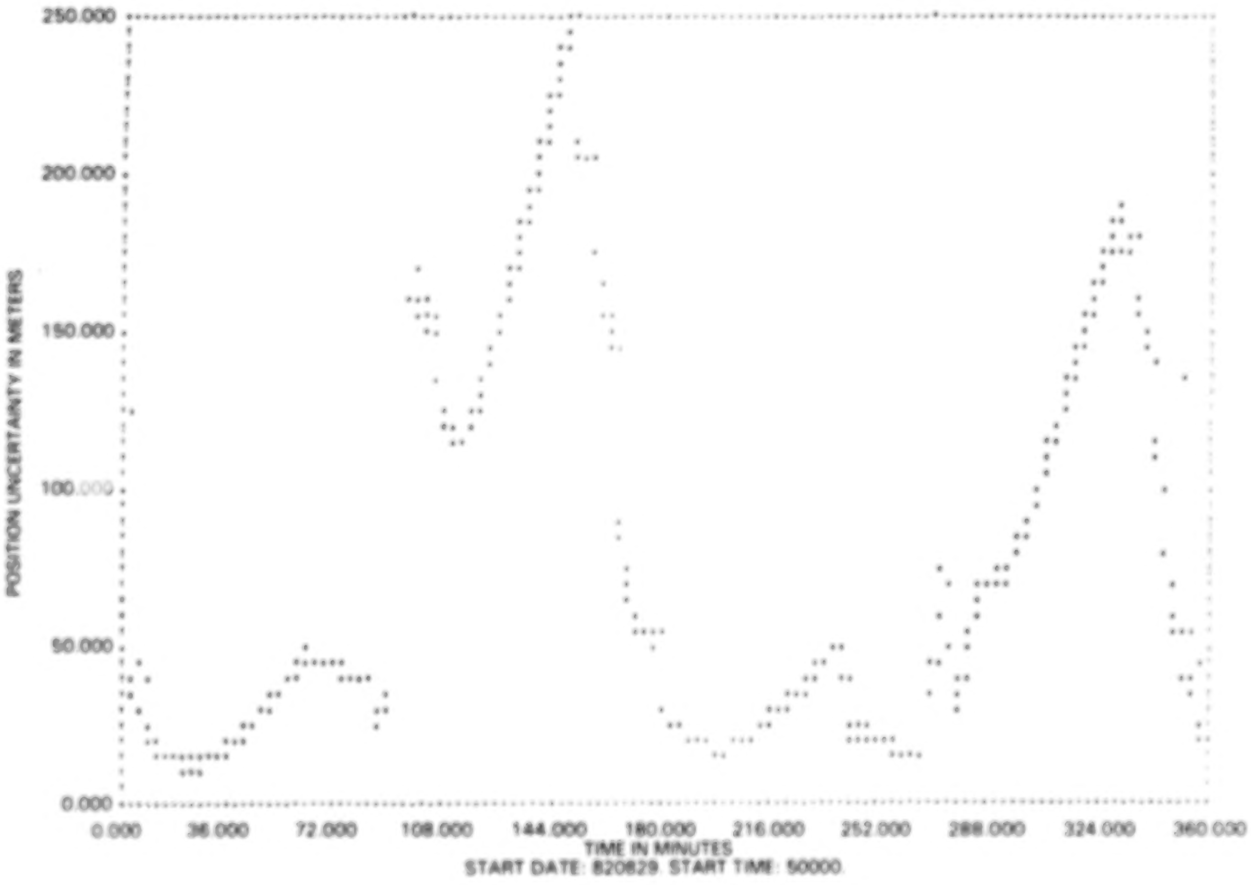

Figure 5. ONPAC Position Uncertainty Parameters using the modified code

4.2 Steps Taken to Reduce the Simulated GPSPAC Anomaly

In order to find out why the GPSPAC fluctuations were occurring, the design of the GPSPAC software and the actual software code were compared to see if there were any inconsistencies between the way the navigation scheme was designed and implemented. Basically, this involved studying the EKF algorithms to see how the navigation solution was propagated and estimated. In order to reduce the simulated GPSPAC fluctuations, various filter parameter changes were invoked using ONPAC. What follows in the next subsections is a description of the EKF (the source of the design-code differences), the results of filter parameter changes, and the implications of these steps taken to reduce the simulated GPSPAC fluctuations.

The GPSPAC Design-Code Differences

The Extended Kalman Filter Background

The Extended Kalman Filter (EKF) is the essential element of the GPSPAC navigation software. The EKF is an algorithm that computes an optimal estimate of the state of a non-linear system, given measurements, initial conditions, and statistical parameters. The filtering algorithm requires two input parameters: an estimate of the state at a previous measurement time and an estimate of the state-error covariance matrix at a previous measurement time. Given the input parameters, the filtering process proceeds as follows:

(1) The previous filter state, defined as a 9-state vector where components 1-3 and 5-7 are the current position and velocity of the state and components 4, 8, and 9 are the user spacecraft's receiver clock time bias, receiver clock frequency bias, and satellite drag factor, respectively, is propagated to the pseudorange measurement time (distance from the NDS satellite to the user spacecraft divided by the speed of light uncorrected for user clock error).

(2) The previous filter state-error covariance matrix, defined as a 9x9 matrix where the filter state error is given on the main diagonal, is propagated to the pseudorange measurement time.

ORIGINAL PAGE IS
OF POOR QUALITY

(3) The pseudorange measurement gain is calculated to determine how much can be "gained" from the measurement; then the measurement residual is used to determine an estimate of the state error at the pseudorange measurement time.

(4) The delta-pseudorange measurement (the difference between two pseudorange measurements) gain is calculated and the measurement residual is used to update the state error estimate of step 3.

(5) The updated state error estimate is used to correct the propagated filter state from step 1 and the measurement gain calculated is used to update the propagated filter state-error covariance matrix from step 2. This results in a new filter state and a new state-error covariance matrix applicable at the pseudorange measurement time.

Uyeminami describes the EKF process in detail (2).

Figure 6 illustrates the five steps of the filtering process.

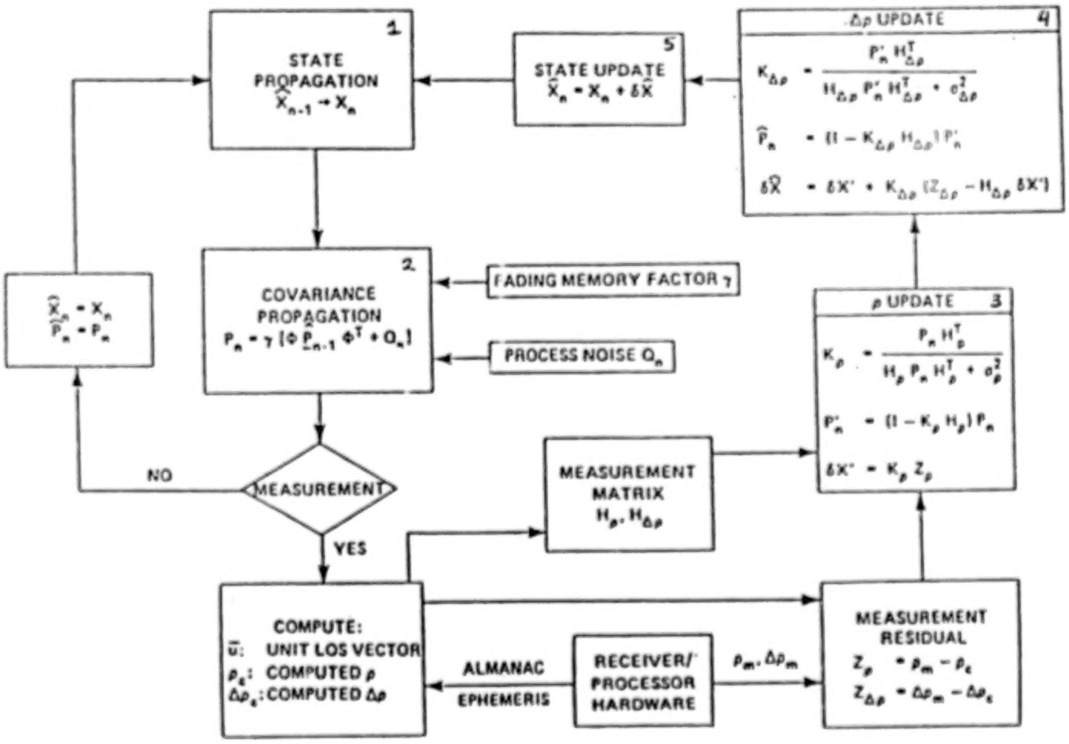
1
STATE PROPAGATION
$\hat{X}_{n-1} \rightarrow X_n$
5
STATE UPDATE
$\hat{X}_n = X_n + \delta\hat{X}$
$\Delta\rho$ UPDATE
4
$K_{\Delta\rho} = \frac{P'_n H^T_{\Delta\rho}}{H_{\Delta\rho} P'_n H^T_{\Delta\rho} + \sigma^2_{\Delta\rho}}$
$\hat{P}_n = (I - K_{\Delta\rho} H_{\Delta\rho}) P'_n$
$\delta\hat{X} = \delta X' + K_{\Delta\rho} (Z_{\Delta\rho} - H_{\Delta\rho} \delta X')$
$\hat{X}_n = X_n$
$\hat{P}_n = P_n$
2
COVARIANCE PROPAGATION
$P_n = \gamma [\Phi \hat{P}_{n-1} \Phi^T + Q_n]$
FADING MEMORY FACTOR γ
PROCESS NOISE Q_n
ρ UPDATE
3
$K_\rho = \frac{P_n H^T_\rho}{H_\rho P_n H^T_\rho + \sigma^2_\rho}$
$P'_n = (I - K_\rho H_\rho) P_n$
$\delta X' = K_\rho Z_\rho$
NO
MEASUREMENT
YES
MEASUREMENT MATRIX
$H_\rho, H_{\Delta\rho}$
COMPUTE:
$\bar{u}$: UNIT LOS VECTOR
ρ_c: COMPUTED ρ
$\Delta\rho_c$: COMPUTED $\Delta\rho$
ALMANAC
EPHEMERIS
RECEIVER/ PROCESSOR HARDWARE
$\rho_m, \Delta\rho_m$
MEASUREMENT RESIDUAL
$Z_\rho = \rho_m - \rho_c$
$Z_{\Delta\rho} = \Delta\rho_m - \Delta\rho_c$

Figure 6. R/PA Extended Kalman Filter

The Source of the Design-Code Differences
The State-Error Covariance Matrix

The major design-code differences that were found pertained to the implemented state-error covariance matrix, P_n. The state-error covariance matrix at the current measurement time is computed as: $P_n = \gamma [\Phi \hat{P}_{n-1} \Phi^T + Q_n]$. Briefly, the state transition matrix, Φ ,propagates the state-error covariance matrix forward in time and the state-process-noise covariance matrix, Q_n, is computed to compensate for the neglected terms in the force model of the state. See the Mathematical Specifications of the Onboard Navigation Package (ONPAC) Simulator for a detailed description of the state-error covariance matrix derivation (3).

Now, the only way to verify that the software was computing the elements of the state-error covariance matrix exactly the way the design plans had specified was to check and see if the code was computing the elements of the component matrices properly--namely, Φ and Q_n. So, we inspected the equations in the software for both the Φ and Q_n matrices and computed,by hand, the 81 elements in each matrix; as a result, we discovered that the design plan was inconsistent with the code for both matrices.

The Φ Matrix Design-Code Differences

Nine elements near the bottom left-hand side of the Φ matrix pertain to the modeled geopotential acceleration; these elements appeared in the design plans of the matrix, yet, for reasons unknown, they were not computed in the GPSPAC software code (see figure 7). Consequently, the equations of acceleration due to the geopotential were not modeled in the GPSPAC software's version of the estimated corrections to the state.

The Q_n Matrix Design-Code Differences

The design plans for the Q_n matrix is the following:

$$Q_n = \begin{bmatrix} Q_{11} & & Q_{12} & & Q_{13} \\ & Q_b & & Q_{b\dot{b}} & \\ Q_{12}^T & & Q_{22} & & Q_{23} \\ & Q_{b\dot{b}} & & Q_{\dot{b}} & \\ Q_{13}^T & & Q_{23}^T & & Q_{33} \end{bmatrix}$$

ORIGINAL PAGE IS
OF POOR QUALITY

$$
\begin{array}{|c|c|c|c|c|c|c|c|c|l}
\hline
1 & 0 & 0 & 0 & \Delta t & 0 & 0 & 0 & -\frac{1}{2}\rho_n v_n \Delta t^2 \dot{x}_n & x \\
\hline
0 & 1 & 0 & 0 & 0 & \Delta t & 0 & 0 & -\frac{1}{2}\rho_n v_n \Delta t^2 \dot{y}_n & y \\
\hline
0 & 0 & 1 & 0 & 0 & 0 & \Delta t & 0 & -\frac{1}{2}\rho_n v_n \Delta t^2 \dot{z}_n & z \\
\hline
0 & 0 & 0 & 1 & 0 & 0 & 0 & \Delta t & 0 & b_{s/c} \\
\hline
-\frac{\mu}{r_n^3}\left(1-3\frac{x_n^2}{r_n^2}\right)\Delta t & 3\mu\frac{x_n y_n}{r_n^5}\Delta t & 3\mu\frac{x_n z_n}{r_n^5}\Delta t & 0 & 1-\left(\frac{d\rho}{v}\right)_n (v_n^2+\dot{x}_n^2)\Delta t & -\left(\frac{d\rho}{v}\right)_n \dot{x}_n\dot{y}_n\Delta t + 2\Omega_e\Delta t & -\left(\frac{d\rho}{v}\right)_n \dot{x}_n\dot{z}_n\Delta t & 0 & -\rho_n v_n \Delta t\, \dot{x}_n & \dot{x} \\
\hline
3\mu\frac{y_n x_n}{r_n^5}\Delta t & -\frac{\mu}{r_n^3}\left(1-3\frac{y_n^2}{r_n^2}\right)\Delta t & 3\mu\frac{y_n z_n}{r_n^5}\Delta t & 0 & -\left(\frac{d\rho}{v}\right)_n \dot{y}_n\dot{x}_n\Delta t - 2\Omega_e\Delta t & 1-\left(\frac{d\rho}{v}\right)_n (v_n^2+\dot{y}_n^2)\Delta t & -\left(\frac{d\rho}{v}\right)_n \dot{y}_n\dot{z}_n\Delta t & 0 & -\rho_n v_n \Delta t\, \dot{y}_n & \dot{y} \\
\hline
3\mu\frac{z_n x_n}{r_n^5}\Delta t & 3\mu\frac{z_n y_n}{r_n^5}\Delta t & -\frac{\mu}{r_n^3}\left(1-3\frac{z_n^2}{r_n^2}\right)\Delta t & 0 & -\left(\frac{d\rho}{v}\right)_n \dot{z}_n\dot{x}_n\Delta t & -\left(\frac{d\rho}{v}\right)_n \dot{z}_n\dot{y}_n\Delta t & 1-\left(\frac{d\rho}{v}\right)_n (v_n^2+\dot{z}_n^2)\Delta t & 0 & -\rho_n v_n \Delta t\, \dot{z}_n & \dot{z} \\
\hline
0 & 0 & 0 & 0 & 0 & 0 & 0 & 1-\frac{\Delta t}{T_F} & 0 & \dot{b}_{s/c} \\
\hline
0 & 0 & 0 & 0 & 0 & 0 & 0 & 0 & 1-\frac{\Delta t}{T_D} & d_{s/c} \\
\hline
\end{array}
$$

Geopotential
Acceleration
Elements →

Figure 7. State Transition Matrix Φ

where the submatrices Q_{ij} are defined by equations below and elements not indicated in Q_n are taken to be zero.

$$Q_{11} = \frac{1}{4}\sigma_a^2 \Delta t^4 I + \frac{1}{20}\rho_n^2 v_n^2 \sigma_d^2 \Delta t^5 \underline{\dot{r}}_n \underline{\dot{r}}_n^T$$

$$Q_{12} = \frac{1}{2}\sigma_a^2 \Delta t^3 I - \underline{\frac{1}{4}\sigma_a^2 \Delta t^4 (2\underline{\Omega} \times I)^T} + \alpha_n(v_n^2 I + \underline{\dot{r}}_n \underline{\dot{r}}_n^T)^T$$

$$+ \frac{1}{8}\sigma_d^2 \rho_n^2 v_n^2 \Delta t^4 \underline{\dot{r}}_n \underline{\dot{r}}_n^T$$

$$Q_{13} = \frac{-1}{6}\rho_n v_n \sigma_d^2 \Delta t^3 \underline{\dot{r}}_n$$

$$Q_{22} = \sigma_a^2 \Delta t^2 I - \underline{\frac{1}{2}\sigma_a^2 \Delta t^3 \left[(2\underline{\Omega} \times I) + (2\underline{\Omega} \times I)^T\right]} +$$

$$\sigma_a^2 \alpha_n \Delta t^3 (v_n^2 I + \underline{\dot{r}}_n \underline{\dot{r}}_n^T) + \underline{\frac{1}{4}\sigma_a^2 \Delta t^4 \Big[(2\underline{\Omega} \times I)(2\underline{\Omega} \times I) -}$$

$$\underline{\alpha_n (v_n^2 I + \underline{\dot{r}}_n \underline{\dot{r}}_n^T)(2\underline{\Omega} \times I)^T - \alpha_n (2\underline{\Omega} \times I)(v_n^2 I + \underline{\dot{r}}_n \underline{\dot{r}}_n^T) +}$$

$$\alpha_n^2 (v_n^2 I + \underline{\dot{r}}_n \underline{\dot{r}}_n^T)^2\Big] + \frac{1}{3}\rho_n^2 v_n^2 \sigma_d^2 \Delta t^3 \underline{\dot{r}}_n \dot{r}_n^T$$

$$Q_{23} = \frac{-1}{2}\rho_n v_n \sigma_d^2 \Delta t^2 \underline{\dot{r}}_n$$

$$Q_{33} = \sigma_d^2 \Delta t$$

I = 3x3 Identity Matrix

Q_b = The user spacecraft's process noise time bias term

$Q_{\dot{b}}$ = The user spacecraft's process noise frequency bias term

$Q_{b\dot{b}}$ = The user spacecraft's process noise time bias/frequency bias coupling term

This formulation includes several terms that pertain to a modeled rotational force; these terms are underlined above. They were not computed in the GPSPAC software code because, during the design-code phase, the magnitude of these terms were judged to be insignificant by the design team. Consequently, the rotational force was not modeled in the GPSPAC software's version of the state-process-noise covariance matrix.

The Results of the Filter Parameter Changes

Heuberger used Landsat-4 data and ONPAC to analyze the effect on various navigation solutions by invoking the option to reduce the integration step size, by invoking the option to expand the state transition matrix Φ and by invoking the option to "tune" the state-process-noise covariance matrix Q_n. He discovered that by incorporating these changes before a simulated run, the simulated GPSPAC fluctuations were reduced considerably. Consequently, he recommended that these changes should be incorporated into the GPSPAC Kalman Filter software. For a detailed explanation of his results, see his paper entitled, "The Landsat-4/GPS Experiment Final Report".

A follow-up study was done with Landsat-5 data to test Heuberger's results and to reinforce his recommendations. This was accomplished by studying 2 specific arcs from the Landsat-5 data collection and by using ONPAC to invoke the same filter parameter options discussed above. These results, which concur with Heuberger's, are presented below in tabular and graphical form; also, a description of the filter parameters invoked is provided.

TABLE 1

GSTDN DEFINITIVE EPHEMERIS MAXIMUM ERRORS
OVER SELECTED 10-HOUR DATA ARCS

Arc #	Start Time	Position (m)	Velocity (cm/sec)
1	June 12, 1984, 05^h	48.7	4.2
2	July 24, 1985, 03^h	40.4	3.3

In Table 1 the two selected 10-hour data arcs are defined by their start dates and times. Furthermore, the maximum position/velocity errors of the GSTDN definitive ephemeris are given over each of the 10-hour data arcs. The maximum position/velocity errors were obtained by performing orbit fits over 24 to 32-hour tracking arcs with some overlap between successive arcs. The comparison of the two sets of GSTDN definitive ephemeris over the common time span gives one a measure of the consistency between the two orbit solutions. It was assumed that the maximum error in position (velocity) over the two definitive arcs was less than the maximum position (velocity) difference in the overlap if the RMS of the USB range (range-rate) residuals from the two least squares fit was small (i.e. if the data fits were good).

TABLE 2

GPSPAC vs. ONPAC NAVIGATION ACCURACY

Arc #	Filter Options			Ephemeris Differences			
	h(sec)	Geopotential terms in Φ	σ_a^2 (m^2/sec^4)	Position(m) MAX	Position(m) RMS	Velocity(cm/sec) MAX	Velocity(cm/sec) RMS
1*	3.0	No	10^{-8}	720	268	184	43
1	1.0	No	10^{-8}	625	170	70	22
1	1.0	Yes	10^{-8}	526	165	65	22
1	1.0	Yes	10^{-6}	466	160	65	21
2*	3.0	No	10^{-8}	539	128	83	19
2	1.0	No	10^{-8}	346	102	63	15
2	1.0	Yes	10^{-8}	288	88	63	14
2	1.0	Yes	10^{-6}	238	83	57	12

*GPSPAC Solution

In Table 2, the ONPAC results from invoking the various filter parameter changes are summarized. The GSTDN definitive ephemeris was compared with the navigation solutions from GPSPAC as well as the navigation solutions from ONPAC. The runs were compared during the last 6 hours of each data arc to decrease the length of time required for ONPAC to process the navigation solutions. Moreover, the maximum position/velocity differences and their corresponding RMS for each one of the filter parameter changes invoked are given for one to analyze and to compare the effect on each navigation solution. A plot of GPSPAC/GSTDN definitive position differences over the last 6 hours of arc #1 is shown in Figure 8 and the NDS visibility for this period is plotted in Figure 9. Similarly, the corresponding plots over the last 6 hours of arc #2 are shown in Figures 10 and 11.

By comparing the graphs of the GPSPAC/GSTDN definitive position differences, Figures 8 and 10, with the graphs of the NDS visibility Figures 9 and 11, one concludes that the GPSPAC fluctuations are large due to state error growth during periods of prolonged propagation. Also, the fact that GPSPAC uses a simple integration scheme—modified Euler with one derivate evaluation per step—definitely increases the risk of incurring large error growth during poor SV visibility. However, just by reducing the step size from 3 seconds to 1 second, the error growth became significantly bounded. For the comparison using arc #1, refer to Figure 8, the GPSPAC/GSTDN definitive position differences; Figure 12, the ONPAC/GSTDN definitive position differences with no changes and Figure 13, the ONPAC/GSTDN definitive position differences with 1.0 step size. Likewise, Figures 10, 16, and 17 give the corresponding comparison for arc #2.

A previous section of the paper explains the fact that the design plans for the state transition matrix, Φ , included the modeled geopotential acceleration terms, yet, for reasons unknown, these terms were not included in the code. However, ONPAC offers the capability of including the gravity acceleration terms as a filter parameter option. So this option was exercised over both data arcs and Table 2 shows just how much the maximum position/velocity differences decreased by expanding Φ to include the geopotential acceleration terms. Figures 14 and 18 illustrate the reduction seen in the GPSPAC fluctuations by using a smaller step size, 1.0 second and by using an expanded Φ which included the geopotential acceleration terms for each time span.

A process called "tuning the filter" was exercised over the 2 arcs in order to compensate for the GPSPAC Kalman Filter's underestimate of the true error during periods of poor SV visibility. To "tune the filter" one has to adjust the position-velocity components of the state-process-noise covariance matrix, Q_n, which are proportional to the date base constant σ_a^2 —the unmodeled acceleration variance; so by changing σ_a^2 accordingly, the filter is kept from diverging and hence, it produces a better estimate of the true error during periods of prolonged propagation due to poor SV visibility. The constant was increased from $10^{-8} m^2/sec^4$ to $10^{-6} m^2/sec^4$ (see Table 2). This filter parameter adjustment improved the error dynamics model significantly. Figures 15 and 19 show the ONPAC/GSTDN definitive position differences with all three filter parameter options invoked: the 1.0 step size reduction, the expanded Φ matrix which included the geopotential acceleration terms, and the tuned filter result from increasing σ_a^2.

ORIGINAL PAGE IS
OF POOR QUALITY

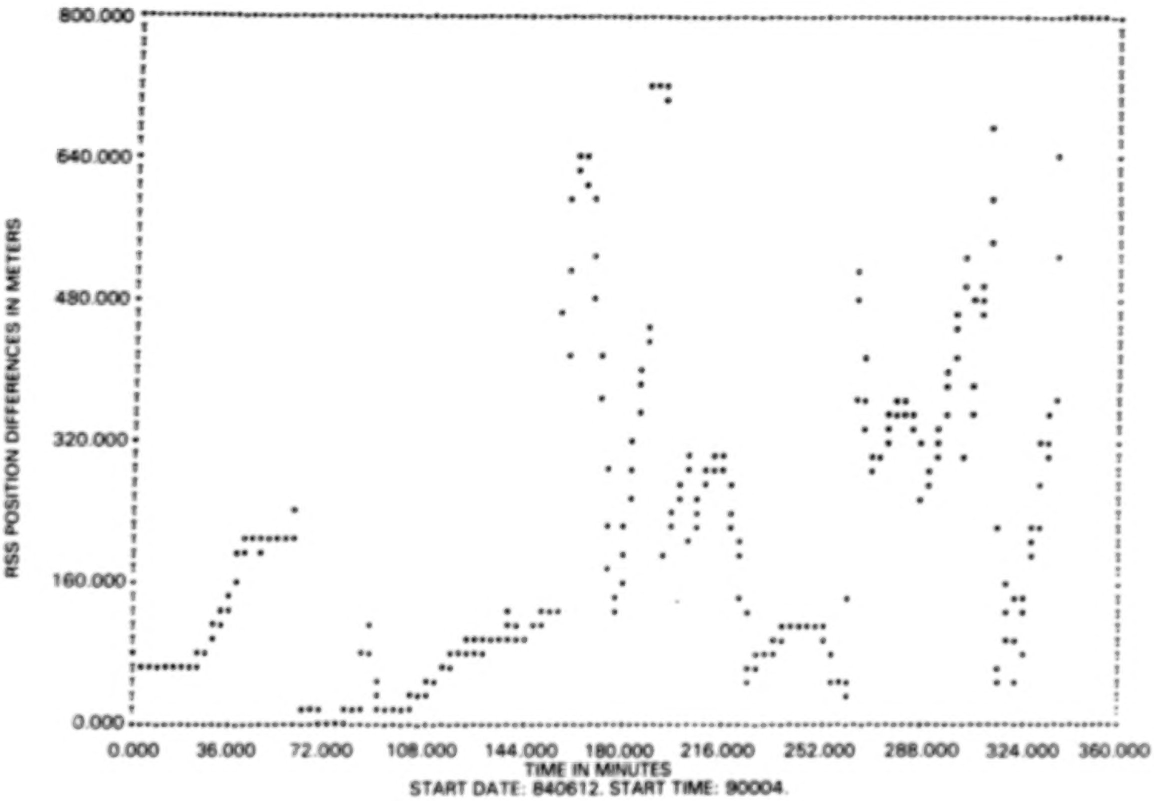

Figure 8. GPSPAC/GSTDN Definitive Position Differences - Arc #1

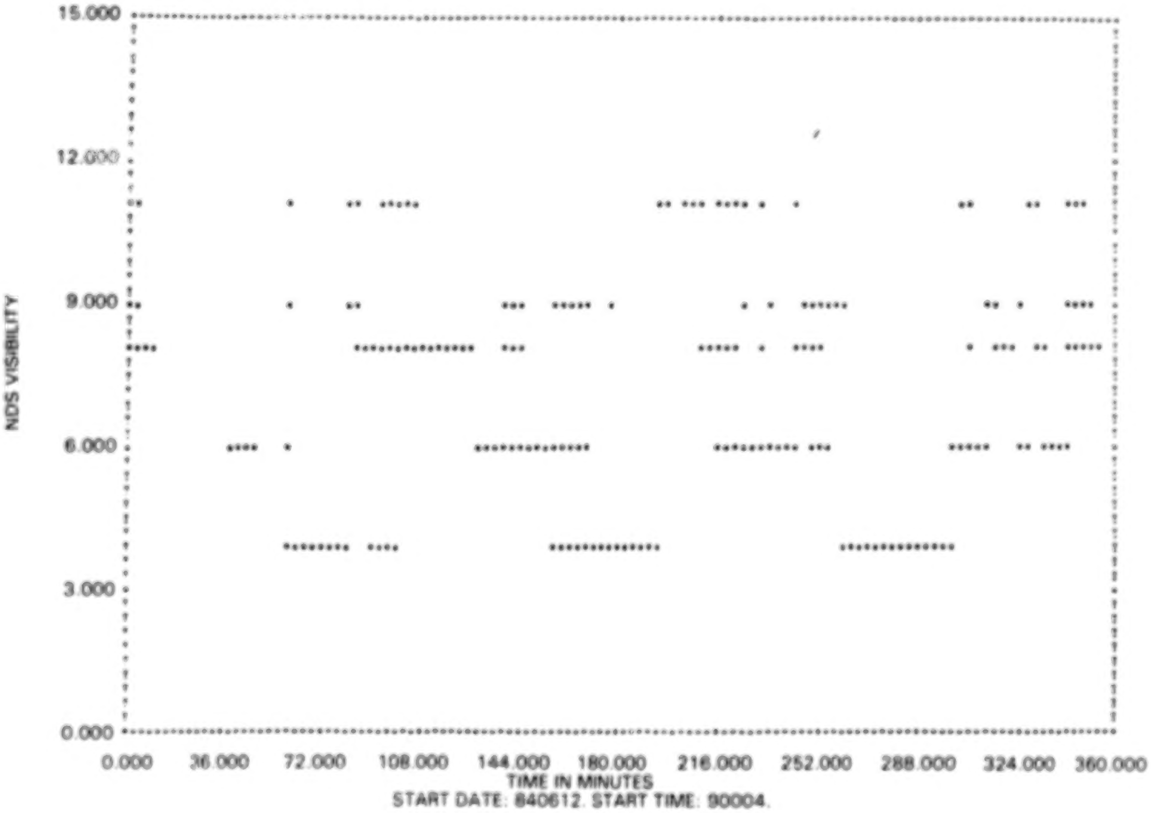

Figure 9. NDS Visibility to Landsat-5 - Arc #1

ORIGINAL PAGE IS
OF POOR QUALITY

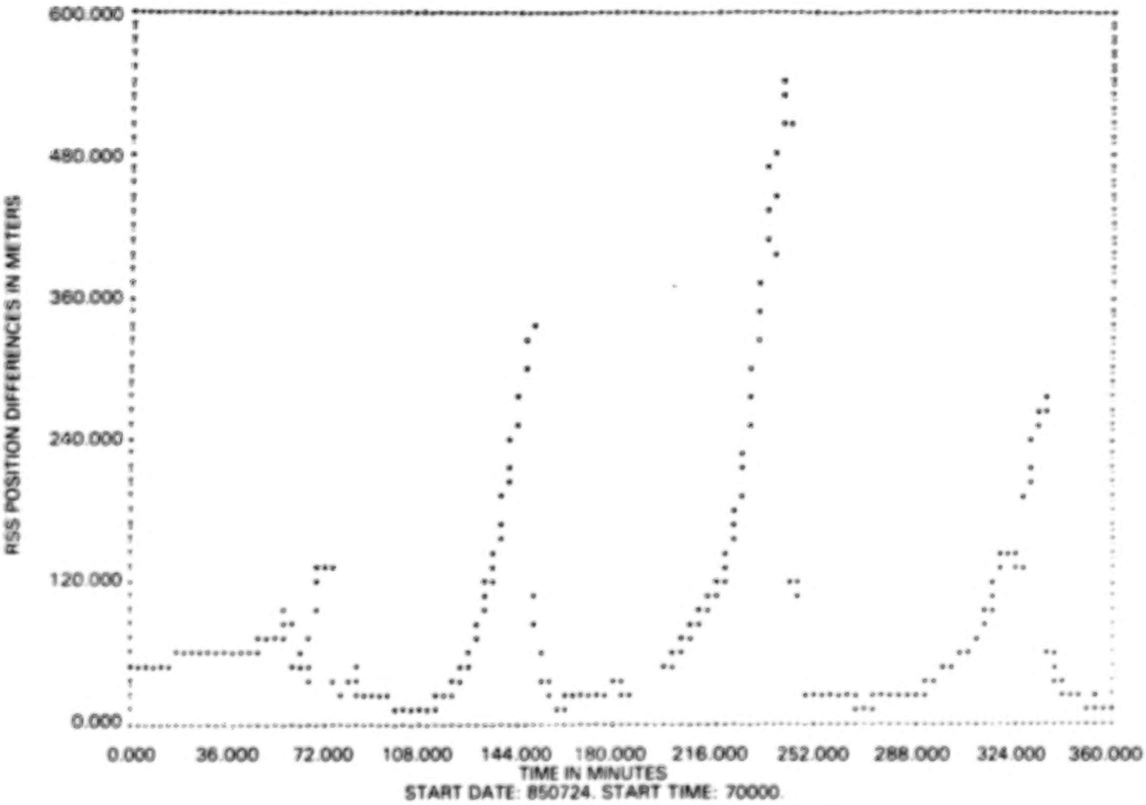

Figure 10. GPSPAC/GSTDN Definitive Position Differences - Arc #2

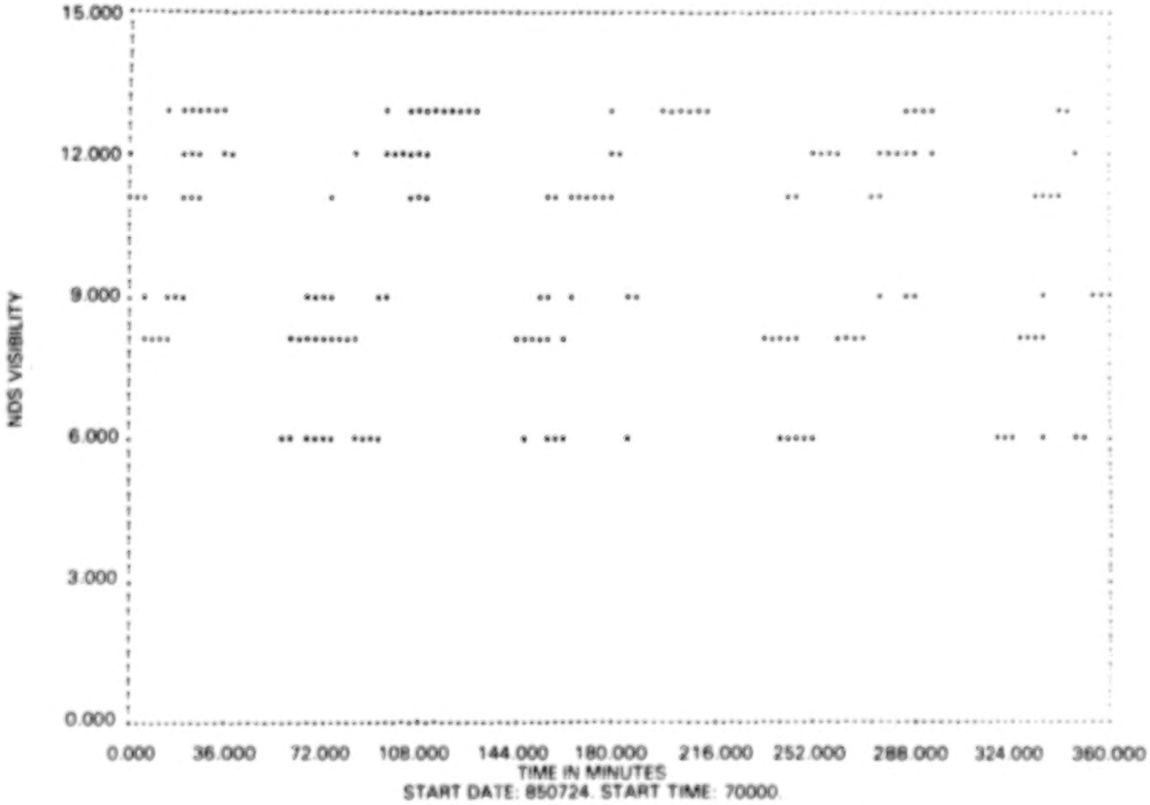

Figure 11. NDS Visiblity to Landsat-5 - Arc #2

ORIGINAL PAGE IS
OF POOR QUALITY

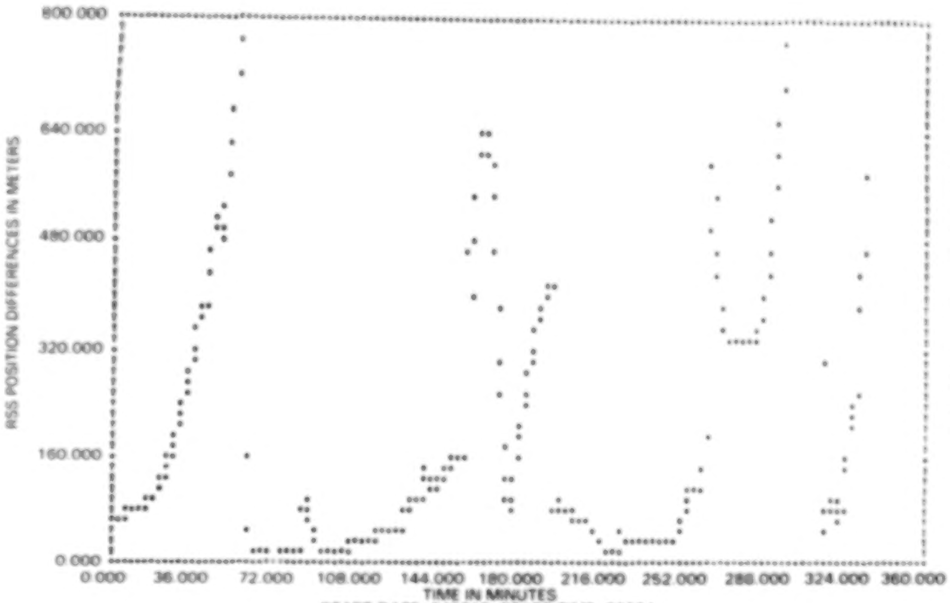

Figure 12. ONPAC/GSTDN Definitive Position Differences - Arc #1 (No changes)

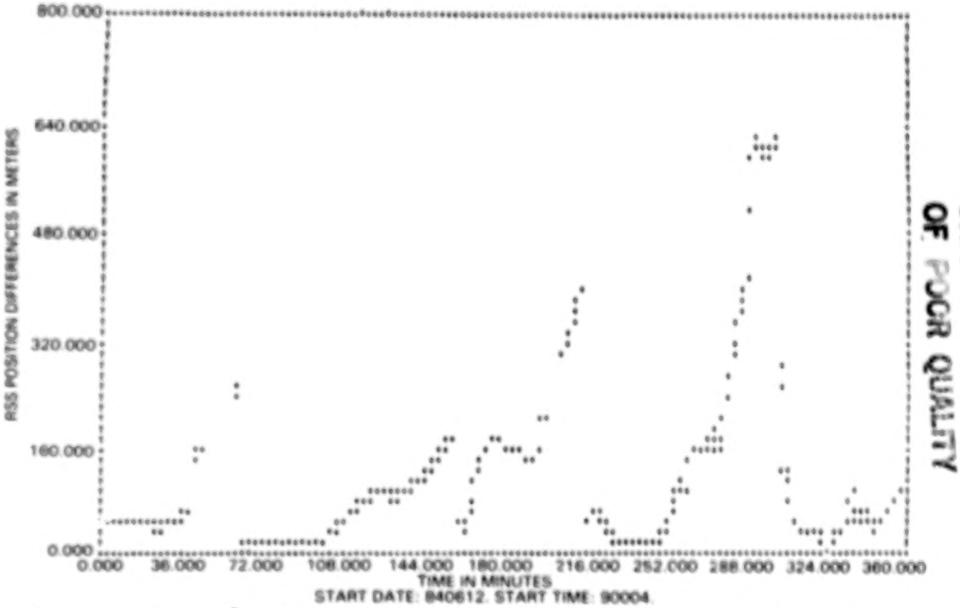

Figure 13. ONPAC/GSTDN Definitive Position Differences - Arc #1 (h + 1 second)

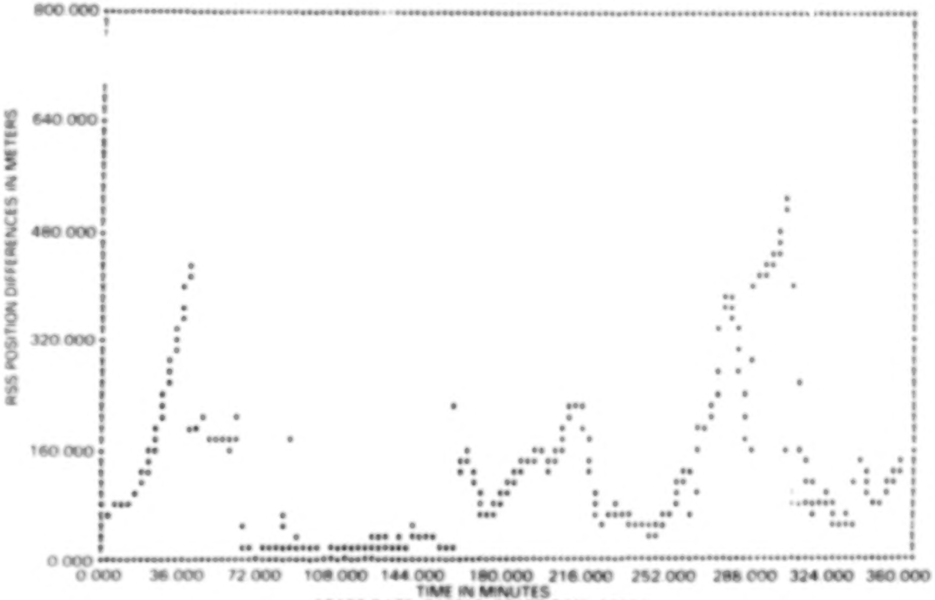

Figure 14. ONPAC/GSTDN Definitive Position Differences (h + 1 second, Geopotential terms in Φ)

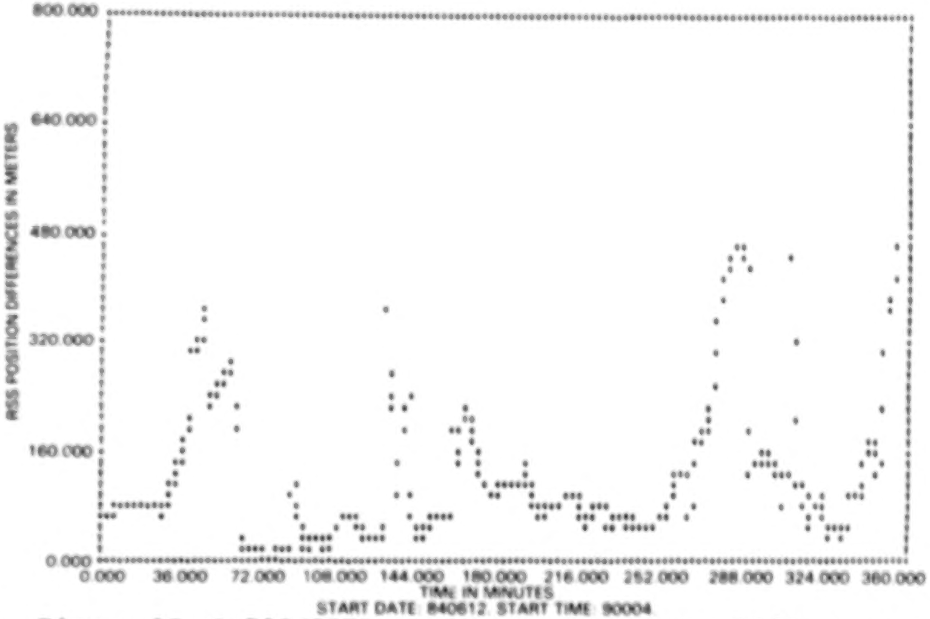

Figure 15. ONPAC/GSTDN Definitive Position Differences - Arc #1 (h + 1 second, Geopotential terms in Φ, $\sigma_a^2 = 10^{-6}\ m^2/sec^4$)

ORIGINAL PAGE IS
OF POOR QUALITY

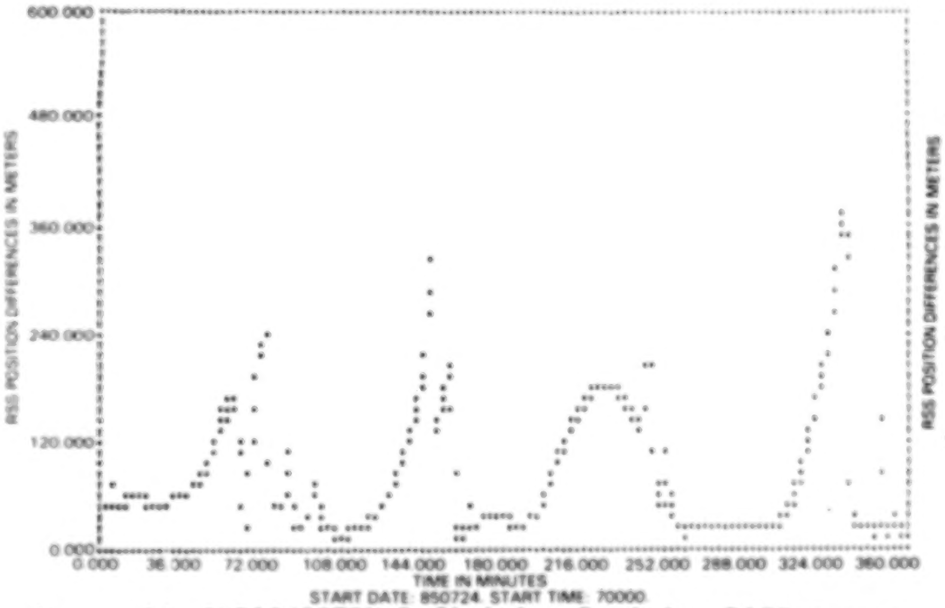

Figure 16. ONPAC/GSTDN Definitive Position Differences - Arc #2 (No changes)

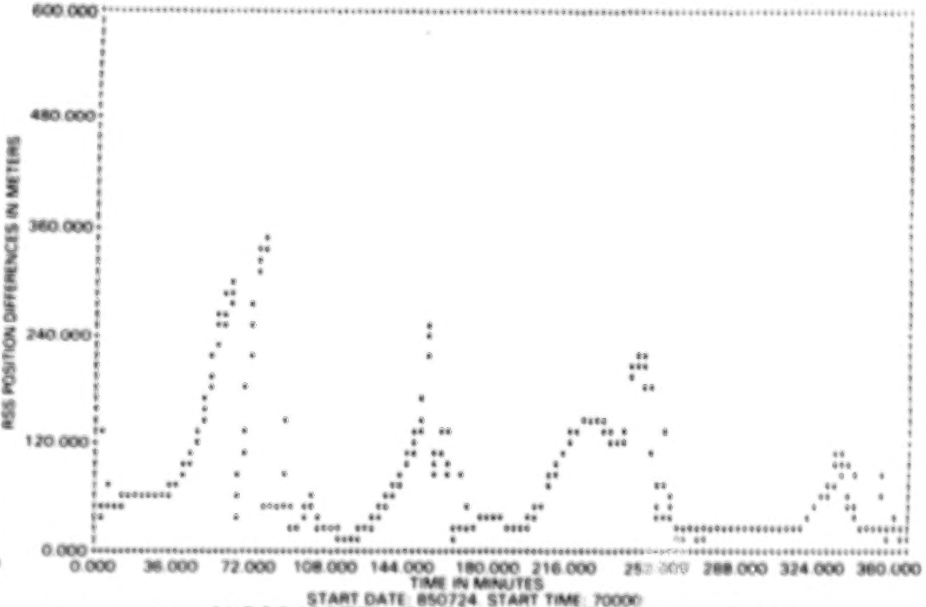

Figure 17. ONPAC/GSTDN Definitive Position Differences - Arc #2 (h + 1 second)

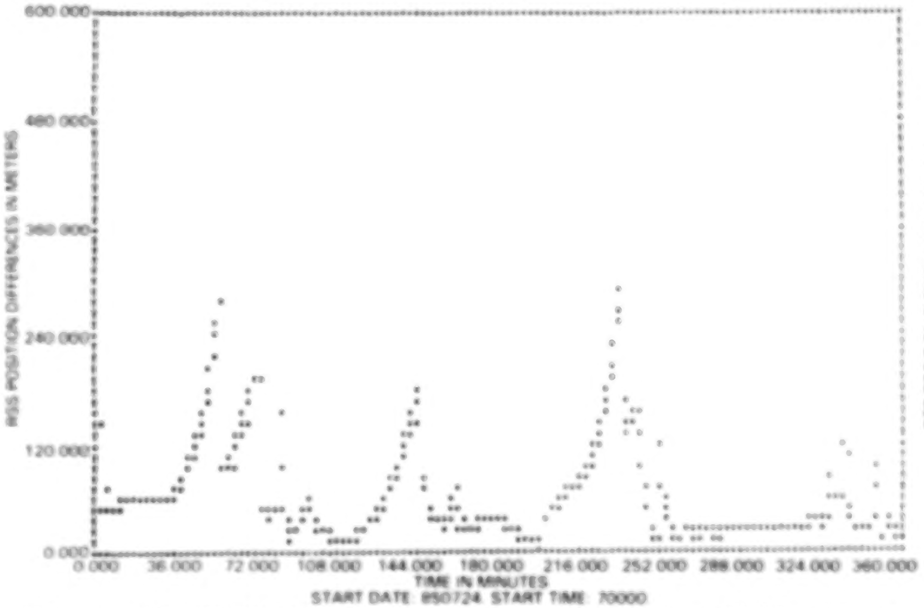

Figure 18. ONPAC/GSTDN Definitive Position Differences - Arc #2 (h + 1 second, Geopotential terms in Φ)

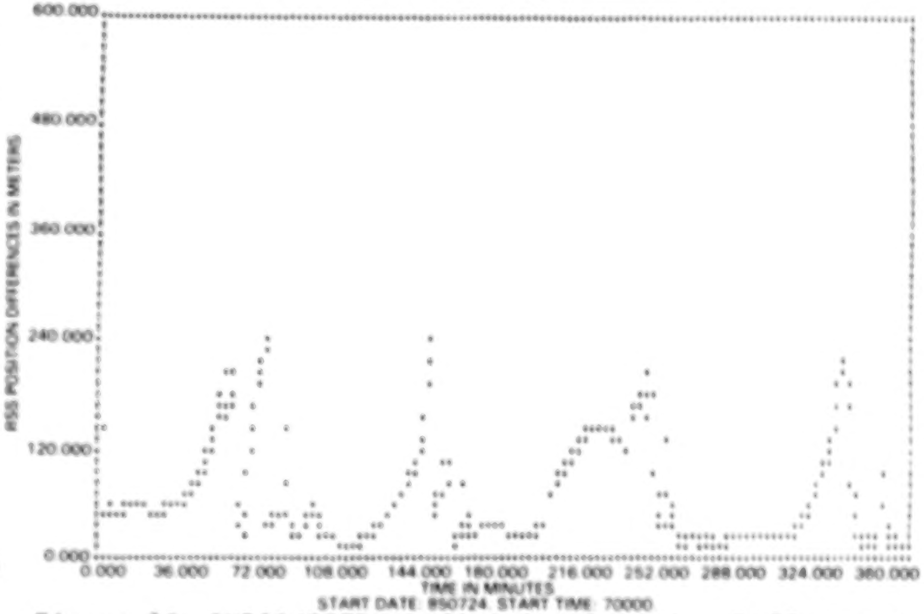

Figure 19. ONPAC/GSTDN Definitive Position Differences - Arc #2 (h + 1 second, Geopotential terms in $\sigma_a^2 = 10^{-6}\ m^2/sec^4$)

The Implications of the Steps Taken to Reduce the Simulated GPSPAC Fluctuations

The comparison of the GPSPAC navigation design with the code proved to be a step in the right direction for two reasons. First of all, it helped us detect a couple of problems that occurred in the way the EKF state-error covariance matrix was designed and implemented—namely, the Φ and Q_n design-code differences. Secondly, although the magnitude of the rotational force terms of the Q_n matrix were indeed insignificant (proven by hand calculations), expanding Φ to include the geopotential acceleration terms did help to reduce the simulated GPSPAC fluctuations considerably (this result is shown in the section entitled, "The Results of the Filter Parameter Changes").

In addition to the expanded Φ matrix, two other filter parameter options invoked during a ONPAC simulated run also helped to reduce the simulated GPSPAC fluctuations: decreasing the integration step size and increasing σ_a^2 to tune the filter. Because these results were shown in a follow-up study using Landsat-5 data, Heuberger's software recommendations are reinforced and are very easy to accommodate—the step size can easily be reduced to 1.0 second; the Φ matrix can easily be expanded to include the geopotential acceleration terms; and the Q_n matrix can easily be tuned by just changing the data base constant, σ_a^2.

5.0 CONCLUSIONS

A GPSPAC/Landsat-D Interface (GLI) ground support system was built to validate the performance and to calibrate the accuracy of the experimental navigation package, GPSPAC, flown on the Landsat-4 and 5 spacecraft. Although the GLI system has operated successfully to give the orbit information needed to validate the GPSPAC, it also detected the following two anomalies. The first problem which pertains to the ONPAC system is that the ONPAC orbit propagator is inconsistent with the orbit propagation model of GPSPAC. The second problem, which pertains to the pre-operational phase of GPS, is that the GPSPAC position (velocity) difference fluctuations are large whenever the user spacecraft is forced to propagate its own orbit because of poor SV visibility. Two attempts were made to resolve the ONPAC inconsistencies: (1) comparing the GPSPAC navigation code against the supposedly equivalent ONPAC code and modifying the non-conforming routines. (2) hand-calculating various filter parameters (to see if these answers matched the answers given by ONPAC). However, neither one of them helped; but, it turned out that by invoking the same filter parameter options which were used to reduce the simulated GPSPAC fluctuations also helped to reduce the ONPAC inconsistencies. The steps taken to reduce the simulated GPSPAC fluctuations were discovered by Heuberger. He recommended that the following changes should be made to the GPSPAC software: (1) reducing the integration step size from 3.0 seconds to 1.0 second, (2) expanding the state transition matrix to include the geopotential acceleration terms, (3) increasing the unmodeled acceleration variance to tune the Extended Kalman Filter. A follow-up study using ONPAC and Landsat-5 data was done to test Heuberger's recommended changes. The results of the study concurred with his; therefore, his recommendations are reinforced.

Theoretically, several possible software changes could be made to ONPAC to reduce the simulated GPSPAC fluctuations, such as upgrading the numerical integration scheme to a Runge-Kutta integration scheme. But, the software would have to be re-designed, re-built, and re-tested which would be costly. However, the recommendations mentioned above can be easily incorporated in the GPSPAC software thereby making them the preferred solution.

The future of GPSPAC remains to be seen since it is uncertain if Landsat or any other spacecraft, for that matter, will ever fly another GPS navigation package. However, since August 1986, the Systems Development Branch was finished with the project in terms of collecting, processing, and analyzing GPSPAC data; we will always keep a consolidated collection of good GPSPAC continuous data arcs from the Landsat-4 and 5 spacecraft for future independent studies of autonomous onboard navigation systems--for example, there is speculation that GPS may be used on Space Station and we will remain as a point of contact for obtaining various information pertaining to the GPSPAC/Landsat-D Interface ground support system.

ACKNOWLEDGMENT

I would like to thank Mr. Howard Heuberger of Johns Hopkins Applied Physics Laboratory for the time, effort, and assistance that he gave to me on the Landsat/Global Positioning System project.

REFERENCES

1. Sielski, H. M. and Dunham, J. B., "GPSPAC/Landsat-D Interface (GLI) System User's Guide", Systems Technology Laboratory Series, STL/882/002, March 1982, pp. 1-3, 6-1.
2. Uyeminami, R. T., "Navigation Filter Mechanization for a Spaceborne GPS User", Proc. IEEE Position Location and Navigation Symposium, November 1978, pp. 330.
3. Dunham, J. B., "Mathematical Specifications of the Onboard Navigation Package (ONPAC) Simulator (Revision 1)", Computer Sciences Corporation, CSC/SD-8116028, February 1981, pp. 3-13, 5-1.
4. Heuberger, H. S., "Landsat-4/GPS Experiment Final Report", NASA/Goddard Space Flight Center, December 1983, pp. 34-40.

N89-15945

RELATIVE MOTION USING ANALYTICAL DIFFERENTIAL GRAVITY

by

Robert G. Gottlieb

MCDONNELL DOUGLAS ASTRONAUTICS CO.
16055 SPACE CENTER BLVD.
HOUSTON, TEXAS 77062

Presented at the

FLIGHT MECHANICS/ESTIMATION THEORY SYMPOSIUM
GODDARD SPACE FLIGHT CENTER
GREENBELT, MARYLAND 20771

MAY 10-11, 1988

This work was performed for NASA
under Contract NAS 9-17885

Relative Motion Using Analytical Differential Gravity

1.0 INTRODUCTION

This paper presents a new approach to the computation of the motion of one satellite relative to another. The trajectory of the reference satellite is computed accurately subject to geopotential perturbations. This precise trajectory is used as a reference in computing the position of a nearby body, or bodies.

The problem that arises in this approach is differencing nearly equal terms in the geopotential model, especially as the separation of the reference and nearby bodies approaches zero. By developing closed form expressions for differences in higher order and degree geopotential terms, the numerical problem inherent in the differencing approach is eliminated.

2.0 ANALYSIS

The equations of motion for a satellite moving under the influence of gravity are written

$$\ddot{\underline{r}} = - \frac{\partial V}{\partial \underline{r}} \tag{1}$$

where $\underline{r}^T = (r_1 \; r_2 \; r_3)$

where V is the potential function

$$V = - \frac{\mu}{r} - \sum_{n=2}^{\infty} \sum_{m=0}^{n} \frac{\mu}{r} \left(\frac{a_e}{r} \right)^n P_{nm}(\mathcal{E}) \quad (C_{nm} \cos m \lambda + S_{nm} \sin m \lambda) \tag{2}$$

and where $P_{nm}(\mathcal{E})$ is the Legendre polynomial of degree n and order m, $\mathcal{E}$ is r_3/r, C_{nm} and S_{nm} are the geopotential model coefficients, $\tan \lambda = r_2/r_1$, and a_e is earth equatorial radius.

Using the recursive formulation given in [2], and considering only terms through $n = 2, m = 2$, the equation for $\ddot{\underline{r}}$ may be written:

$$\ddot{\underline{r}} = - \frac{\mu}{r^2} \left(\frac{\underline{r}}{r} + \left(\frac{a_e}{r} \right)^2 \left\{ (\Gamma_2 + \mathcal{E} H_2) \frac{\underline{r}}{r} - \begin{pmatrix} J_2 \\ K_2 \\ H_2 \end{pmatrix} \right\} \right) \tag{3}$$

where Γ_2, J_2, K_2 and H_2 may be shown to be

$$\Gamma_2 = \frac{\underline{r}^T}{r} \, G \, \frac{\underline{r}}{r} - \frac{3}{2} C_{20}$$

where

$$G = \begin{bmatrix} 15C_{22} & (12S_{21} + 30S_{22}) & 12C_{21} \\ 0 & -15C_{22} & 0 \\ 0 & 0 & \frac{9}{2} C_{20} \end{bmatrix}$$

$$J_2 = \underline{j}^T \frac{\underline{r}}{r}$$

where

$$\underline{j}^T = (6C_{22} \;\; 6S_{22} \;\; 3C_{21})$$

$$K_2 = \underline{k}^T \frac{\underline{r}}{r}$$

where

$$\underline{k}^T = (6S_{22} \;\; 6C_{22} \;\; 3C_{21})$$

and

$$H_2 = \underline{h}^T \frac{\underline{r}}{r}$$

where

$$\underline{h}^T = (3C_{21} \;\; 3S_{21} \;\; 3C_{20})$$

Using these, we may write equation (3) as,

$$\ddot{\underline{r}} = -\frac{\mu}{r^2}\left(\frac{\underline{r}}{r} + \left(\frac{a_e}{r}\right)^2 \left\{ \left(\frac{\underline{r}^T}{r} G \frac{\underline{r}}{r} - \frac{3C_{20}}{2} + \frac{r_3}{r} \underline{h}^T \frac{\underline{r}}{r} \right) \frac{\underline{r}}{r} - \begin{bmatrix} \underline{j}^T \\ \underline{k}^T \\ \underline{h}^T \end{bmatrix} \frac{\underline{r}}{r} \right\}\right) \quad (4)$$

by noting that r_3 may be written

$$r_3 = \underline{r}^T \underline{a}$$

where

$$\underline{a} = \begin{pmatrix} 0 \\ 0 \\ 1 \end{pmatrix}$$

and then defining

$$\Theta = G + \underline{a}\,\underline{h}$$

$$\Phi = I - \begin{bmatrix} \underline{j}^T \\ \hdashline \underline{k}^T \\ \hdashline \underline{h}^T \end{bmatrix}$$

we may write equation (4) as

$$\ddot{\underline{r}} = - \mu \Phi \frac{\underline{r}}{r^3} + \frac{3}{2} \mu C_{20} a_e^2 \frac{\underline{r}}{r^5} - \mu a_e^2 (\underline{r}^T \Theta \underline{r}) \frac{\underline{r}}{r^7} \tag{5}$$

In fact, it can be shown that in general for the geopotential

$$\ddot{\underline{r}} = M \underline{r}$$

where M is a matrix whose elements may depend on $\underline{r}$.

Assume that we have two satellites, the first with position vector $\underline{r}$ and the second with position vector $\underline{\rho}$. Both must satisfy equation (5). Subtracting the two differential equations and defining the difference between the two solution vectors to be

$$\underline{\delta} \equiv \underline{\rho} - \underline{r}$$

we may write

$$\ddot{\underline{\delta}} = - \mu \Phi \left(\frac{\underline{\rho}}{\rho^3} \frac{-\underline{r}}{r^3} \right) + 3 \mu \frac{C_{20}}{2} a_e^2 \left(\frac{\underline{\rho}}{\rho^5} \frac{-\underline{r}}{r^5} \right) - \mu a_e^2 \left[(\underline{\rho}^T \Theta \underline{\rho}) \frac{\underline{\rho}}{\rho^7} \cdot (\underline{r}^T \Theta \underline{r}) \frac{\underline{r}}{r^7} \right] \tag{6}$$

Now collect coefficients of $\frac{1}{r^3}$, $\frac{1}{r^5}$, $\frac{1}{r^7}$ to get

$$\ddot{\underline{\delta}} = \frac{-\mu}{r^3}\,\Phi\left(\underline{\delta} + (\frac{r^3}{\rho^3} - 1)\,\underline{\rho}\right) + 3\,\mu\,\frac{C_{20}}{2}\,\frac{a_e^{\;2}}{r^5}\left(\underline{\delta} + (\frac{r^5}{\rho^5} - 1)\,\underline{\rho}\right)$$

$$\frac{-\,\mu\,a_e^{\;2}}{r^7}\left\{\left[(\underline{\rho}^T\Theta\underline{\rho})\,(\frac{r^7}{\rho^7} - 1) + 2\,(\underline{\delta}^T\,\Theta\,\underline{\rho}) - (\underline{\delta}^T\Theta\,\underline{\delta})\right]\underline{\rho} + (\underline{r}^T\Theta\underline{r})\,\underline{\delta}\right\} \quad (7)$$

Note that the factors

$$\frac{r^3}{\rho^3} - 1\ , \quad \frac{r^5}{\rho^5} - 1\ , \quad \text{and} \quad \frac{r^7}{\rho^7} - 1$$

should each approach zero as $\underline{\delta}$ approaches zero. Numerically this presents a problem since r and ρ are large and nearly equal.

These can all be computed using Potter's [1] approach by noting that

$$r^2 = (\,\underline{\rho} - \underline{\delta}\,) \cdot (\,\underline{\rho} - \underline{\delta}\,) \;=\; \rho^2 - 2\,\underline{\rho}\,\cdot\,\underline{\delta}\,+\delta^2$$

and

$$r^n = (\,\rho^2 - 2\,\underline{\rho}\,\cdot\,\underline{\delta}\,+\delta^2\,)^{\,n/2}$$

and that

$$\rho^n \;=\; (\,\rho^2)^{\,n/2}$$

$$\therefore \quad \frac{r^n}{\rho^n} - 1 \;=\; \left(\frac{\rho^2 - 2\,\underline{\rho}\,\cdot\,\underline{\delta}\,+\delta^2}{\rho^2}\right)^{n/2} - 1 \qquad (8)$$

and we can write

$$\frac{r^n}{\rho^n} - 1 = \frac{(1+q)^n - 1}{(1+q)^{n/2} + 1} \qquad (9)$$

where

$$q = \frac{\delta^2 - 2\underline{\rho} \cdot \underline{\delta}}{\rho^2}$$

Note that q ⟶ 0 as δ ⟶ 0

We can now write these factors as

$$\frac{r^3}{\rho^3} - 1 = \frac{f}{(1+q)^{3/2} + 1} \qquad (10)$$

where

$$f = 3q + 3q^2 + q^3$$

$$\frac{r^5}{\rho^5} - 1 = \frac{f+(f+1)(2q+q^2)}{(1+q)^{5/2} + 1} \qquad (11)$$

and

$$\frac{r^7}{\rho^7} - 1 = \frac{q+(q+1)(2f+f^2)}{(1+q)^{7/2} + 1} \qquad (12)$$

Note that from the definition of q and f, these factors approach zero directly as δ approaches zero.

3.0 DISCUSSION AND RECOMMENDATIONS

Equations (10), (11), (12) when substituted into equation (7) yield the companion set of differential equations for the second satellite relative to the first. The terms in the resulting equation all go to zero directly as δ approaches zero and do not contain differences of large nearly equal terms. These equations would be quite useful for both space station and tethered satellite analysis.

The technique presented here extends, albeit with effort, to higher order and degree terms in the geopotential. A recursive approach to the computation of the coefficient matrices would be a welcome development.

4.0 REFERENCES

1. Battin, R. H., Astronautical Guidance, McGraw-Hill Book Company, 1964.
2. Gottlieb, R. G., "A Fast Recursive Singularity Free Algorithm for Calculating the First and Second Derivatives of the Geopotential", MDAC Report No. AA:0028, 1988.

N89-15946

PRELIMINARY ORBIT DETERMINATION SYSTEM (PODS) FOR TRACKING AND DATA RELAY SATELLITE SYSTEM (TDRSS)-TRACKED TARGET SPACECRAFT USING THE HOMOTOPY CONTINUATION METHOD*

S. M. Kirschner and M. V. Samii, Computer Sciences Corporation (CSC)
S. R. Broaddus and C. E. Doll, Goddard Space Flight Center (GSFC)

ABSTRACT

The Preliminary Orbit Determination System (PODS) provides early orbit determination capability in the Trajectory Computation and Orbital Products System (TCOPS) for a Tracking and Data Relay Satellite System (TDRSS)-tracked spacecraft. PODS computes a set of orbit states from an a priori estimate and six tracking measurements, consisting of any combination of TDRSS range and Doppler tracking measurements. PODS uses the homotopy continuation method to solve a set of nonlinear equations, and it is particularly effective for the case when the a priori estimate is not well known. Since range and Doppler measurements produce multiple states in PODS, a screening technique selects the desired state.

PODS is executed in the TCOPS environment and can directly access all operational data sets. At the completion of the preliminary orbit determination, the PODS-generated state, along with additional tracking measurements, can be directly input to the differential correction (DC) process to generate an improved state.

To validate the computational and operational capabilities of PODS, tests were performed using simulated TDRSS tracking measurements for the Cosmic Background Explorer (COBE) satellite and using real TDRSS measurements for the Earth Radiation Budget Satellite (ERBS) and the Solar Mesosphere Explorer (SME) spacecraft. The effects of various measurement combinations, varying arc lengths, and levels of degradation of the a priori state vector on the PODS solutions were considered.

In this paper, it is demonstrated that a poorly known a priori estimate that does not converge in the DC process can be improved through PODS processing, resulting in a solution that is accepted by the DC process. An overview of the system, the test results, and an analysis of these results are presented.

---

*This work was supported by the National Aeronautics and Space Administration (NASA)/Goddard Space Flight Center (GSFC), Greenbelt, Maryland, under Contract NAS 5-31500.

1. INTRODUCTION

The purpose of preliminary orbit determination methods is to derive an orbit state corresponding to an available set of measurements when, initially, the orbit state is not well known or not known at all. Characteristically, preliminary orbit determination methods use approximate physical models and measurements collected over a limited timespan, usually less than one revolution. These methods are a necessary part of orbit operations procedures. With the expansion at the National Aeronautics and Space Administration (NASA) of spacecraft tracking from the ground-based system [i.e., the Ground Spaceflight Tracking and Data Network (GSTDN)] to a satellite relay system [i.e., the Tracking and Data Relay Satellite System (TDRSS)], it is necessary to have a reliable preliminary orbit determination method available in the Goddard Space Flight Center (GSFC) Flight Dynamics Division (FDD) that functions with TDRSS tracking. This paper reports on the development and provides an evaluation of such a method, called the Preliminary Orbit Determination System (PODS).

The remainder of this section presents background information on preliminary orbit determination, gives requirements for PODS, and lists the topics covered in Sections 2 through 4 of the paper.

1.1 BACKGROUND

Earlier preliminary orbit determination methods in the FDD used angular antenna-pointing observations collected at the ground stations (Reference 1). The capability to process these tracking measurements is a feature of the FDD Goddard Trajectory Determination System (GTDS) Early Orbit Determination (EARLYORB) Program (Reference 2). TDRSS range and Doppler tracking measurements offer a primary source of tracking support for many spacecraft by the FDD. However, the open-loop TDRSS angular antenna-pointing measurements (beam angles azimuth and elevation) are too inaccurate for use even in preliminary orbit determination. Therefore, a preliminary orbit determination method that uses the precise TDRSS range and Doppler tracking exclusively is required. The problem is basically one of solving a set of nonlinear equations, which specify that the predicted values of the measurements match the observed values. The homotopy continuation method of solving nonlinear systems of equations is particularly well suited for preliminary orbit determination using range and Doppler measureents, especially with inaccurate or even unavailable a priori estimates of the solution (Reference 3 and 4).

1.2 REQUIREMENTS

PODS satisfies the following requirements:

- PODS processes precise TDRSS range and Doppler measurements by one or more Tracking and Data Relay Satellites (TDRSs).
- PODS uses a preliminary orbit determination method with the ability to overcome an inaccurate (or no) a priori value for the target state to be solved for. PODS also resolves multiple solutions that result from TDRSS range and Doppler data. The final solution is accurate enough for subsequent tracking acquisition.
- PODS is operable under the current Flight Dynamics Facility (FDF) operational system, i.e., the Trajectory Computation and Orbital Products System (TCOPS). PODS is flexible in accessing the relay state(s), the a priori target state, and the tracking measurements from different available sources of these data.

1.3 PAPER ORGANIZATION

Section 2 of this paper discusses the theory of the homotopy continuation algorithm and its application to preliminary orbit determination. It also describes the operational use of PODS.

Section 3 of the paper discusses several evaluation studies that were performed to test PODS. These studies include the effects of choosing various a priori target states, data arc lengths, and data types in obtaining different states. It is demonstrated that the final target state solution selected by PODS is good enough to be successfully used by the GTDS Differential Correction (DC) Program as an a priori target state vector.

Section 4 reviews the results from the evaluation studies, provides a conclusion summary, and lists future enhancements for PODS.

2. THEORY AND APPLICATION OF PRELIMINARY ORBIT DETERMINATION METHODS

The basic equation to be solved to obtain the target state vector, $\vec{X}$, relates the measured value of the range or Doppler data, O_i, to the modeled value, C_i, as follows:

$$O_i - C_i(\vec{X}) = 0 \qquad (i = 1, 2, \ldots, 6) \tag{1}$$

There are six equations for the six unknown components of $\vec{X}$, usually the spacecraft position and velocity in Cartesian coordinates at a specified epoch. For simplicity, the modeled values are determined from geometrical distances without atmospheric and measurement corrections.

A procedure for solving Equation (1) was developed using the homotopy continuation method; this procedure is described in Section 2.1. Section 2.1 also contains a discussion of the multiple solutions that arise from TDRSS symmetry in the range and Doppler measurements and presents a method for screening the candidate solutions. Section 2.2 outlines the operational use of PODS under TCOPS.

2.1 HOMOTOPY CONTINUATION METHOD

A general way to solve Equations (1) is the homotopy continuation method. In this method, a continuous mapping parameter, λ, is first introduced as follows:

$$O_i^\lambda \equiv O_i^0 + \lambda\,(O_i^1 - O_i^0) \qquad (i = 1, 2, \ldots, 6) \tag{2}$$

where O_i^0 = modeled measurement corresponding to the a priori estimate, $\vec{X}^0$

O_i^1 = real measurement at the unknown solution state $\vec{X}^1$

The quantity X must then be solved for from

$$O_i^\lambda - C_i(\vec{X}) = 0 \qquad (i = 1, 2, \ldots, 6) \tag{3}$$

by following the solution curve in the seven-dimensional $(\lambda, \vec{X})$ space, starting at $\lambda = 0$, keeping track of each solution whenever $\lambda = 1$ along the curve.

As an aid in visualizing the solution curve, Figure 1 shows its projection onto the λ-z plane, where z is the third Cartesian component of position, for a typical orbit (Reference 3). The curve-following begins at the point marked initial state, where $\lambda = 0$, and then passes through four solutions along the line at $\lambda = 1$ before returning to the start. Since this is a smooth curve embedded in seven-dimensional space, the apparently sharp changes and intersections in the figure do not really exist but result from the projection onto the λ-z plane.

The following is a brief summary of the procedure for following solution curves (Reference 3):

- Given the a priori state at $\lambda = 0$ as the first point, a bootstrap starter is used to develop the second point on the solution curve.

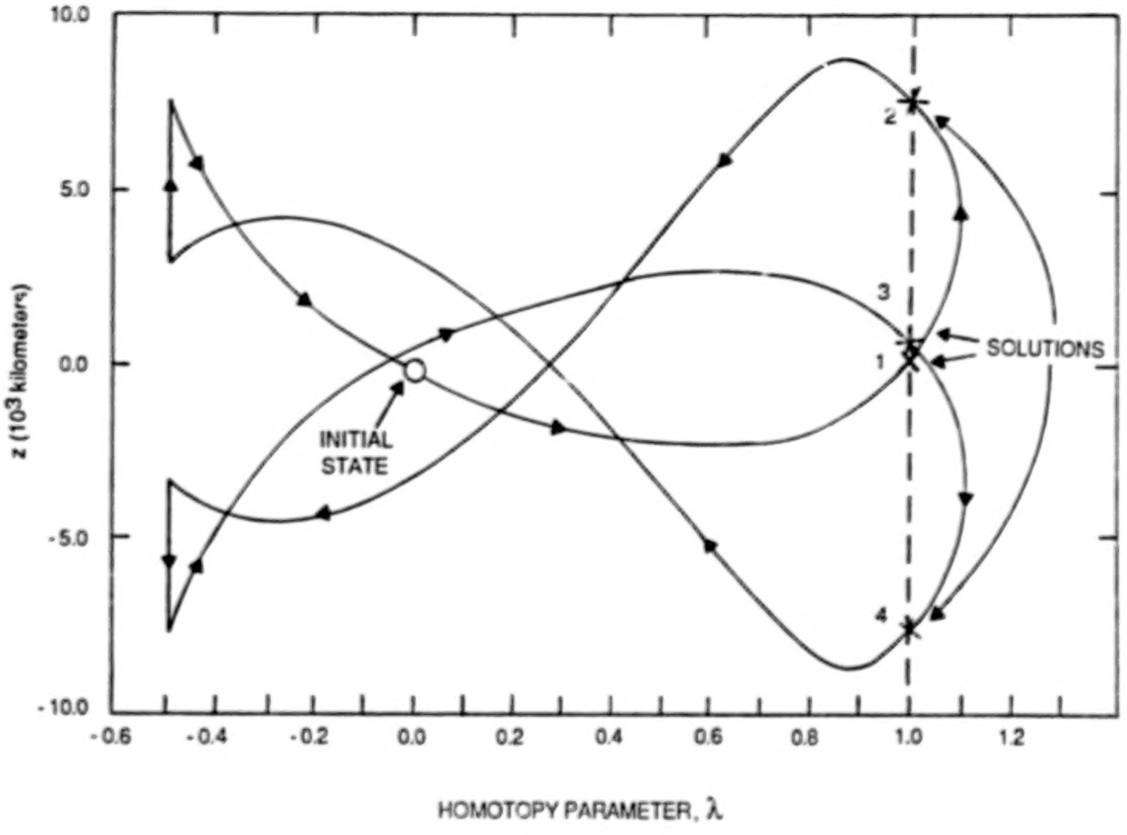

Figure 1. Projection of Solution Curve Onto λ-z Plane

- A preliminary value for the next step size change is selected.
- The next curve point along the arc is predicted by fitting a polynomial to the previous N backpoints (predictor step) (see Figure 2).
- The Newton-Raphson method is used to iteratively refine the predicted state to the corrected state along the hyperplane locally perpendicular to the extrapolating polynomial at the predicted state (corrector step).
- The new point is discarded and the step size is corrected, or the new point is accepted and a check is made to see if any candidate solution states have been determined at λ = 1.

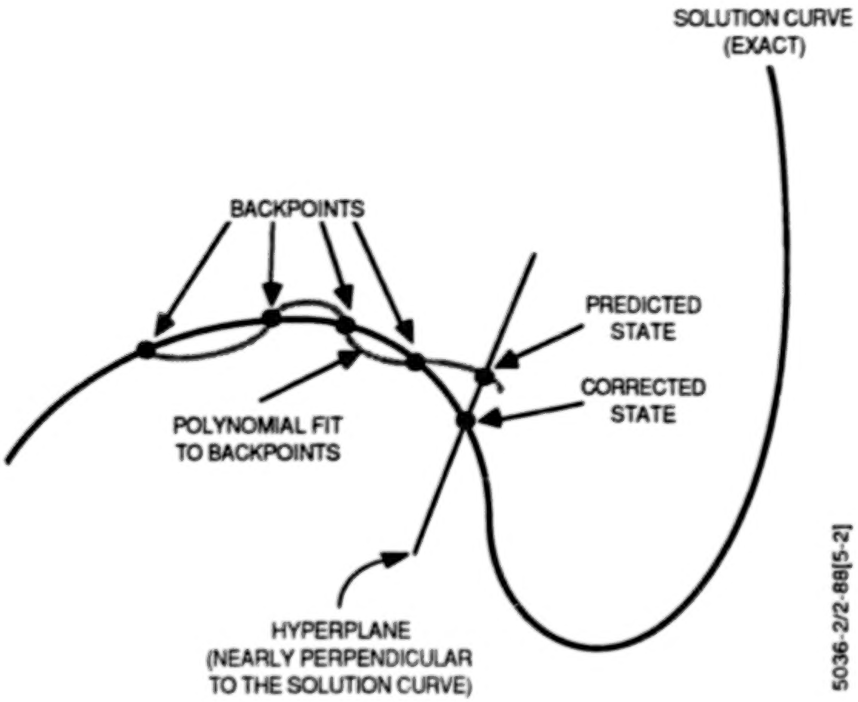
SOLUTION CURVE
(EXACT)
BACKPOINTS
PREDICTED
STATE
CORRECTED
STATE
POLYNOMIAL FIT
TO BACKPOINTS
HYPERPLANE
(NEARLY PERPENDICULAR
TO THE SOLUTION CURVE)
5036-2/2-88[5-2]

Figure 2. Predictor-Corrector Technique for Following a Solution Curve

- If the solution curve has returned to its start, the procedure is terminated.

Usually there are multiple solutions at $\lambda = 1$, as seen, for example, in Figure 1. Solutions 1 and 3 (and solutions 2 and 4) are mirror images of each other in the TDRS orbit plane.[1] These multiple solutions are due to the symmetry of range and Doppler data for TDRSS tracking (Reference 3). To determine which of the solutions is correct, a solution screening algorithm is required. Some solution candidates can be rejected because they are not physically correct, for example, when the semimajor axis, eccentricity, or inclination is not within the allowed limits for a particular target's orbit. Usually the candidate solutions are not near each other. TDRSS beam angles, which approximately locate the actual orbit, can then be used to reject most candidates, especially one or both of the mirror-image solution pairs.

---

[1] The TDRS orbit plan nearly coincides with the x-y plane. Thus, the mirror image solutions, evident in the projection of the solution curve onto the λ-z plane in Figure 1, are not apparent in similar projections onto the λ-x and λ-y planes.

When no solutions are accepted by the screening process and the candidate solutions are not paired by mirror images, a second solution loop exists that is the mirror image of the first; this solution loop may contain the desired solution. Consequently, each candidate solution, as well as its mirror image, is checked during solution screening.

The homotopy continuation method can be further generalized (Reference 3) to contain up to six continuation parameters (λ_n) and multiple disconnected loops. For an inaccurate value of the a priori target state that lies on one loop, this generalized method allows jumping from one loop to another at critical points in the search for candidate solutions at $\lambda_n = 1$.

2.2 OPERATIONAL USE OF PODS

To use PODS operationally for an event associated with a particular target, specific steps are followed prior to and immediately after the event. The preliminary steps include setting up sources for observations, relay states, and the a priori target state; generating a generic list of input parameter values; and allocating output files for summary reports and the target solution. Immediately after the event, the operator selects values for the solution epoch, the observations, the a priori target state, the relay state, and the input parameters. (See Reference 5 for detailed requirements specifications for these and a description of the operational steps.)

PODS is then executed operationally within the TCOPS User Interface (UI) environment. Figure 3 shows an overview of the system and its operational environment, including all required input and output interfaces. The foreground and background divisions in this figure indicate the modes of execution of the two separate parts of the system. (A more detailed description of the system is given in Reference 6.)

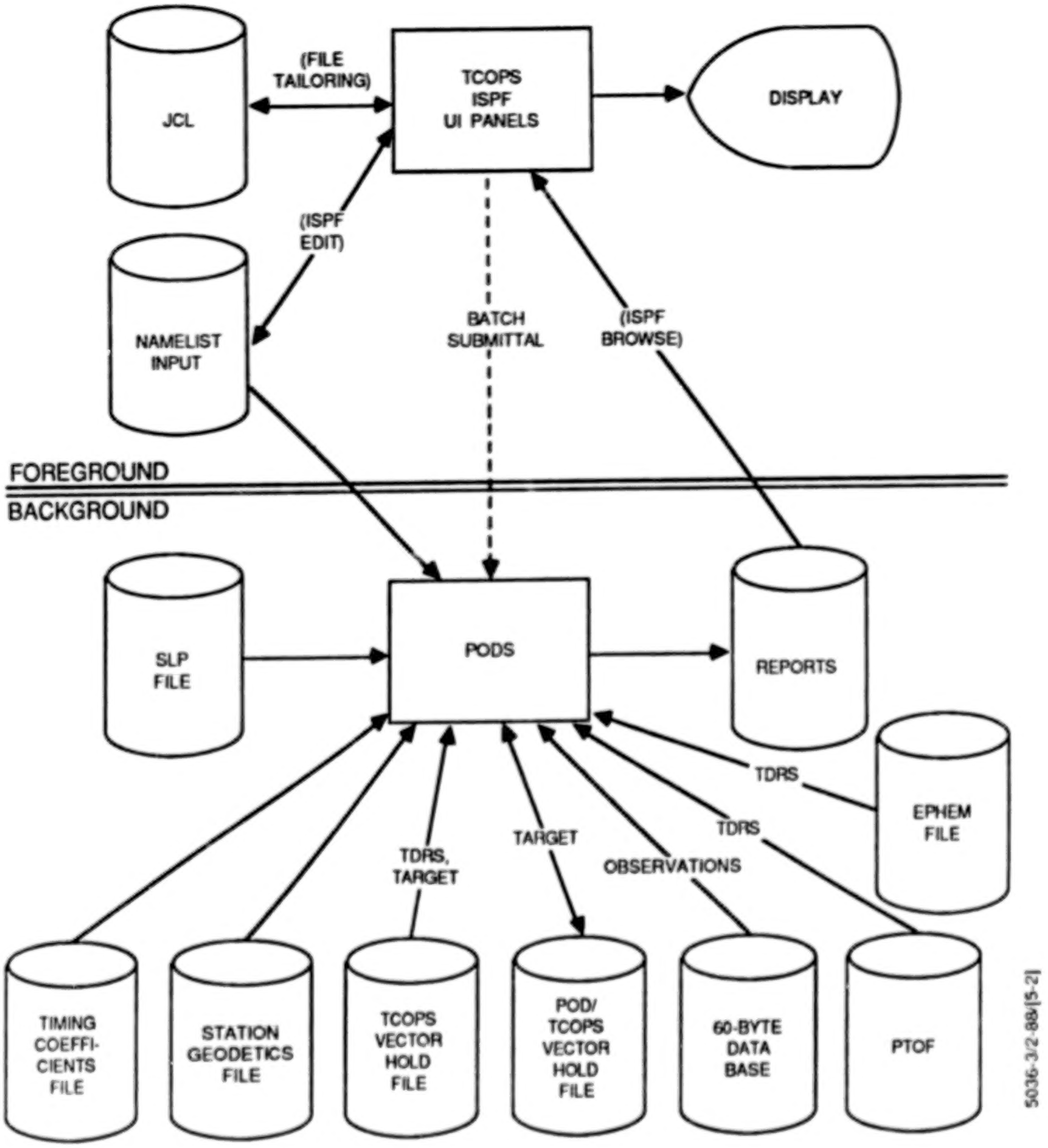
JCL
(FILE TAILORING)
TCOPS ISPF UI PANELS
DISPLAY
(ISPF EDIT)
NAMELIST INPUT
BATCH SUBMITTAL
(ISPF BROWSE)
FOREGROUND
BACKGROUND
SLP FILE
PODS
REPORTS
TDRS
EPHEM FILE
TDRS
TARGET
TDRS, TARGET
OBSERVATIONS
TIMING COEFFI-CIENTS FILE
STATION GEODETICS FILE
TCOPS VECTOR HOLD FILE
POD/ TCOPS VECTOR HOLD FILE
60-BYTE DATA BASE
PTOF
5036-3/2-88/[5-2]

Figure 3. Operational PODS Under TCOPS

3. EVALUATION STUDIES

PODS was evaluated to determine its strengths and weaknesses in calculating target states under various conditions for different targets. The following four goals formed the basis of the PODS evaluation studies:

1. Determine whether solutions can be found for a priori states of various quality, such as the following:

    a. Nearly Exact--Very close to the actual state

    b. Good--Usually extracted from the TCOPS Vector Hold File

    c. Poor--Usually degraded by long two-body propagation of a good state

    d. Generic--Typical values for the semimajor axis, eccentricity, and inclination of the orbit

2. Ascertain the limitations based on data arc length. Determine whether there is a breakdown for shorter arcs. This question is of major concern, because typical TDRSS tracking for the Landsat-4 and Landsat-5 spacecraft consists of 9- to 24-minute passes, with passes separated by at least one revolution of 99 minutes, and for the Earth Radiation Budget Satellite (ERBS) consists of 9- to 14-minute passes, with passes separated by at least two revolutions of 96.7 minutes each. This tracking schedule required PODS to succeed for short arcs. TDRSS tracking of the Solar Mesosphere Explorer (SME) spacecraft consists of 10- to 65-minute passes for a 95-minute revolution.

3. Determine how successful various combinations of data are (e.g., all range, all Doppler, mixed range and Doppler).

4. Resolve two issues for the final target state calculated in PODS:

   a. Demonstrate the effectiveness of PODS by showing that it can determine a solution for the target state from an a priori state for which the GTDS DC Program cannot obtain a solution state. Also show that this PODS solution acts as a successful a priori state in the DC Program.

   b. Determine whether screening of candidate solutions is effective by using TDRSS beam angle and physical considerations.

Several PODS executions were made to establish the feasibility of these goals; these executions are summarized in Table 1. Three target spacecraft were analyzed: COBE (using simulated data for December 21, 1987); ERBS (using real

Table 1. PODS Evaluation Executions Using the Homotopy Continuation Method

TARGET SPACECRAFT	EPOCH	ARC LENGTH (minutes)	DATA TYPE	A PRIORI STATE QUALITY	SOLUTIONS
COBE	12/21/87, 0^h	50	6D	GOOD	2 (1 GOOD)
		50	6R	GOOD	1 (NEAR D)
		30	3R (TDRS-E), 3R (TDRS-W	GOOD	1 (NEAR D, BUT TOO ECCENTRIC)
ERBS	04/10/86, 0^h	18	6R	GENERIC	4 (1 GOOD)
		18	6R, 2A, 2E	GENERIC	4 (1 GOOD)
		18	3R, 3D	POOR	4 (UNPHYSICAL)
		18	6D	GOOD	4 (1 GOOD)
ERBS	11/30/87, 0^h	11	6R	GENERIC	4 (UNPHYSICAL)
		11	6D	GENERIC	4 (NEAR R)
		11	3R, 3D	GENERIC	0
		11	4R, 2D	GENERIC	0
		11	2R, 4D	GENERIC	0
ERBS	12/16/87, 0^h	12	6R, 2A, 2E	GENERIC	4 (1 GOOD)
		12	6D	GENERIC	4 (1 GOOD)
		12	4R, 2D, 2A, 2E	GENERIC	*
SME	01/14/88, 0^h	20-50	6D	GENERIC	4 (1 GOOD)
		50	6D	GOOD	4 (1 GOOD)
		30	6R	GOOD	4 (UNPHYSICAL)
		40-50	6R, 2A, 2E	GOOD	4 (1 GOOD)
		50	6R, 2A, 2E	GENERIC	*
		50	2R, 4D	GOOD	4 (UNPHYSICAL)
		50	3R, 3D	GOOD	4 (UNPHYSICAL)
		50	4R, 2D	GOOD	4 (UNPHYSICAL)

NOTE: DATA TYPES: A = AZIMUTH, E = ELEVATION, D = DOPPLER, R = RANGE

*PROGRAM UNABLE TO COMPLETE CALCULATIONS

5036-42-88(5-2)

data for April 10, 1986; November 30, 1987; and December 16, 1987); and SME (using real data for January 14, 1988). Data arc lengths ranged from short (11 to 20 minutes) to long (30 to 50 minutes). Data types included range (R), Doppler (D), azimuth (A), and elevation (E), where azimuth and elevation are the TDRSS beam angles used to screen candidate solutions. Relay tracking was by TDRS-East (TDRS-E), except for simulated COBE data, where TDRS-West (TDRS-W) tracking is specifically noted.

The target a priori state quality (generic, poor, good, nearly exact) is also indicated in Table 1. The generic state usually consists of values for the semimajor axis (a), eccentricity (e), and inclination (i) typical of the target, as well as values of zero for the remaining classical or Keplerian elements [i.e., right ascension of the ascending node (Ω), argument of perigee (ω), and mean anomaly (M)].

A good a priori state vector can be extracted from a TCOPS Vector Hold File, where the vector was pregenerated from a GTDS DC solution. A nearly exact a priori state (although not included in the table) leads to a breakdown of the equations in the homotopy continuation method (Reference 3). A poor-quality a priori state can be established by a two-body propagation over a long period, such as 24 hours.

The last column in Table 1, SOLUTIONS, lists all unique solutions for each case in the table. Occasionally, the same solution is repeated while the solution loop is being followed, but this repetition is not indicated in the table. Typical features of unphysical (rejected) solutions noted in this column are unrealistic semimajor axis, eccentricity, inclination, apogee, or perigee.

The remainder of this section discusses the results for ERBS and SME from the perspective of the evaluation goals. The topics covered are as follows: a priori target state (Section 3.1), data arc lengths (Section 3.2), data type combinations (Section 3.3), and final target state (Section 3.4).

3.1 A PRIORI TARGET STATE

The possibility of generating solutions for various values of the a priori target state was studied. The principal example was a long SME data arc starting at 0 hours, 36 minutes, on January 14, 1988 (Figure 4). The good a priori target state vector, extracted from the TCOPS Vector Hold File, was previously generated by executing the GTDS DC Program using a good orbit propagator. Because the data arc was within 2 hours of the a priori state epoch and the final state epoch, there was no appreciable degradation from

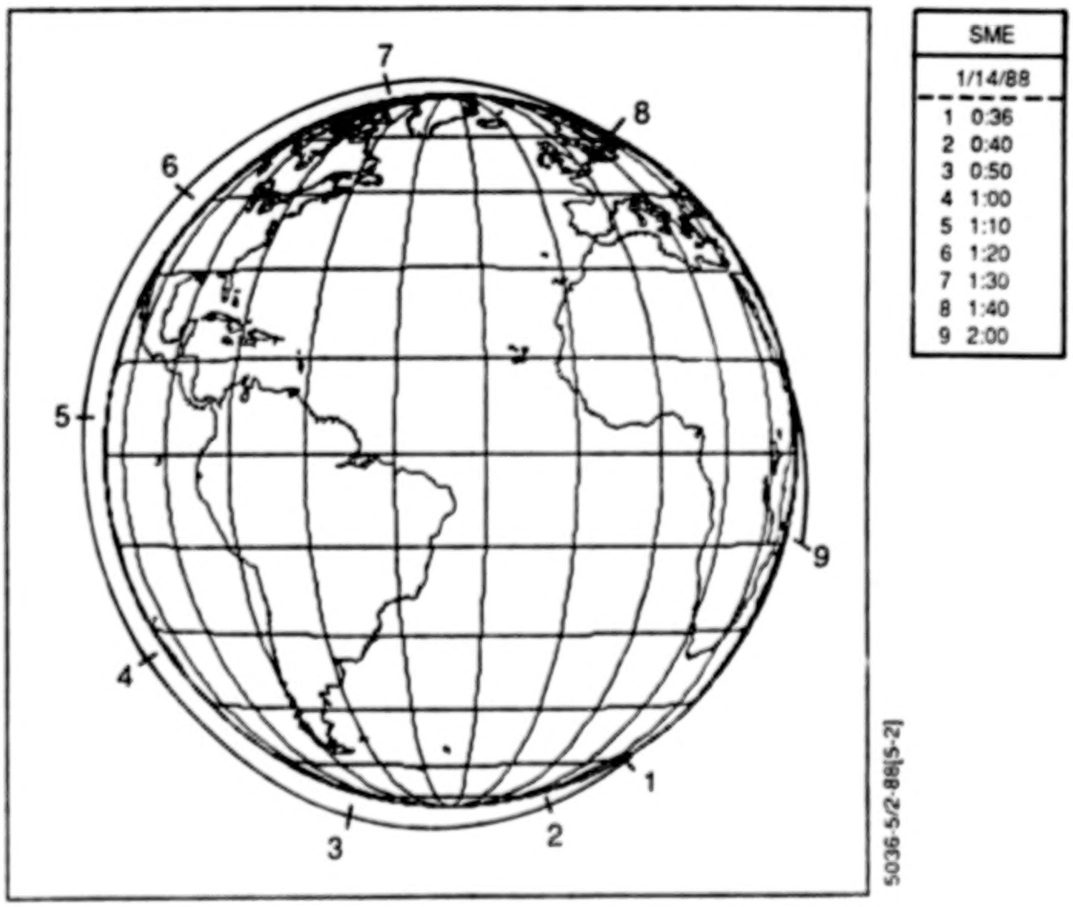
7
8
6
5
9
4
1
3
2
SME
1/14/88
1 0:36
2 0:40
3 0:50
4 1:00
5 1:10
6 1:20
7 1:30
8 1:40
9 2:00
5036-5/2-88(5-2)

Figure 4. SME Orbit as Seen From TDRS-E on January 14, 1988, From 0 to 2 Hours

using a two-body orbit propagator in PODS for the target. Values in Keplerian coordinates for both the good and generic a priori target states are given in Table 2, which summarizes the success status for PODS solutions. Both the good and generic states were successful and give identical solutions for the four Doppler data arcs given in the table. Only the good a priori target state succeeded for longer arcs of range data. Different generic values were tried for the semimajor axis, including a reduction from 8000 to 7500 kilometers, but were unsuccessful.

When an a priori target state has a value close to the solution state, the homotopy continuation algorithm breaks down (Reference 3). This effect was observed when, for a nearly exact a priori value, the correct final state was immediately determined, but the solution curve in the seven-dimensional $(\lambda, \vec{X})$ space did not close within specified tolerances.

Table 2. State of PODS Solutions for Various SME a Priori Target States on January 14, 1988, at 0 Hours

A PRIORI TARGET STATE	SUCCESS STATUS FOR PODS SOLUTIONS[a]							
	DOPPLER DATA ARC (minutes)				RANGE DATA ARC (minutes)			RANGE/DOPPLER DATA ARC (minutes)
	20	30	40	50	30	40	50	50
GOOD[b]	Y	Y	Y	Y	N	Y	Y	N
GENERIC[c]	Y	Y	Y	Y	N	N	N	N

[a] Y = SUCCESSFUL; N = NOT SUCCESSFUL

[b] GOOD A PRIORI TARGET STATE:
a = 6872 kilometers; e = 0.00079; i = 97.8 degrees;
Ω = 20.1 degrees; ω = 301.7 degrees; M = 157.6 degrees

[c] GENERIC A PRIORI TARGET STATE:
a = 8000 kilometers; e = 0.01; i = 100 degrees;
Ω = 0 degree; ω = 0 degree; M = 0 degree

5036-6/2-88[5-2]

3.2 DATA ARC LENGTHS

The continuously tracked SME data arc of 62 minutes duration on January 14, 1988, was used to study the effects of arc lengths from 20 minutes to 50 minutes in 10-minute jumps. Solutions for these data arcs are presented in Table 3 for range and Doppler tracking. The solution using Doppler data at the shortest arc studied, 20 minutes, had dropped by over 50 kilometers in its perigee from the actual value and would have been further degraded for shorter arcs. The range data solution at 40 minutes was poor, as is reflected in its very low perigee of 279 kilometers.

Short-arc studies with ERBS (see Table 1) showed that sometimes good solutions could be obtained (e.g., the 12-minute range and Doppler data arcs on December 16, 1987, and the 18-minute range and Doppler data arcs on April 10, 1986). However, at other times, poor solutions were determined (e.g., the 11-minute range and Doppler data arcs on November 30, 1987, where both solutions were slightly unphysical).

Table 3. SME Solutions for Various Data Arcs
on January 14, 1988, at 0 Hours

DATA ARC LENGTH[a] (minutes)	DATA TYPE[b]	APOGEE (kilometers)	PERIGEE (kilometers)	a (kilometers)	e	i (degrees)	Ω (degrees)	ω (degrees)	M (degrees)
20	D	499	422	6839	0.0056	96.9	20.5	85.0	14.1
30	D	516	460	6866	0.0041	97.5	20.3	78.4	20.5
40	D	566	519	6921	0.0034	98.2	20.0	8.4	91.6
40	R	485	279	6760	0.0153	98.6	19.6	150.6	299.9
50	D	569	517	6921	0.0037	98.1	20.0	9.9	90.3
50	R	558	493	6903	0.0047	99.7	19.0	214.7	240.1

[a] SELECTED DATA ARE NEARLY UNIFORMLY DISTRIBUTED WITHIN EACH ARC.

[b] DATA TYPES:
D = DOPPLER
R = RANGE

5036-7/2-88[5-2]

Previous studies (Reference 7) of SME showed that solutions became significantly degraded for data arcs of less than one-quarter of a revolution, because the equations that had to be solved became increasingly illconditioned. This limit is approximately 24 minutes for SME and ERBS. The current studies showed that in several cases accurate results were obtained for ERBS for much shorter arcs (see Section 3.4), while SME results were in general agreement with the previous findings.

3.3 DATA TYPE COMBINATIONS

The quality of solution states for various data types (all range, all Doppler, or mixed range and Doppler) varies according to the particular spacecraft conditions. For the three short arcs studied with ERBS, two arcs yielded good states for the separate Doppler and range tracking, but the third gave unphysical states. Unphysical or no solution states were found for mixed range and Doppler tracking in all three arcs. The long arc for COBE was also successful in determining good states for separate range and Doppler tracking.

SME solution states for Doppler-only data were more stable over shorter arcs than for range-only data with the January 14, 1988, arc (see Table 2); however, the reverse was found for the December 9, 1984, arc (Reference 7). In both cases, the mixed range and Doppler solutions were the least satisfactory.

3.4 FINAL TARGET STATE

A test was successfully conducted to demonstrate the primary function of PODS for handling orbit recovery when minimal data are available and the a priori target state vector is not known with certainty or with sufficient accuracy for the DC Program to perform adequately. An 18-minute data arc for ERBS on

April 10, 1986, was selected for the test. The a priori state selected had the generic value, given in Keplerian elements, as follows:

$a = 8000$ kilometers
$e = 0.01$
$i = 45$ degrees
$\Omega = \omega = M = 0$ degree

Results for all-range data are shown in Figure 5. The DC Program could not generate a solution using the generic state vector and a 4-hour arc consisting of two 18-minute passes. However, after PODS generated a state vector from the generic a priori state and an 18-minute pass, the DC program successfully used the PODS solution as an a priori target state and calculated a final target state for the 4-hour arc using all-range data. This target state, in turn, was successfully used in a differential correction over a 21-hour arc. Similar results were obtained by starting with the generic a priori target state and all-Doppler measurements over the original 18-minute arc, and then using the PODS solution for the a priori target state and 4 hours of mixed range and Doppler data in the DC Program.

A second feature that can be analyzed with this ERBS 18-minute data arc is the multiplicity of solutions and their resolutions by TDRSS beam angle screening. The four candidate solutions generated by PODS from the range data and the generic a priori target state are listed in Table 4. Each candidate solution was used to predict TDRSS beam angles for comparison with the recorded beam angles. A solution was accepted whenever the two sets of values agreed within a specified tolerance. Solutions 1 and 3 are mirror images of each other in the TDRS orbit plane, as are solutions 2 and 4. This symmetry is characteristic of TDRSS range and Doppler measurements in orbit determination (see Section 2.2). Since the TDRS orbit is inclined slightly to the Earth's equatorial

ORIGINAL PAGE IS
OF POOR QUALITY

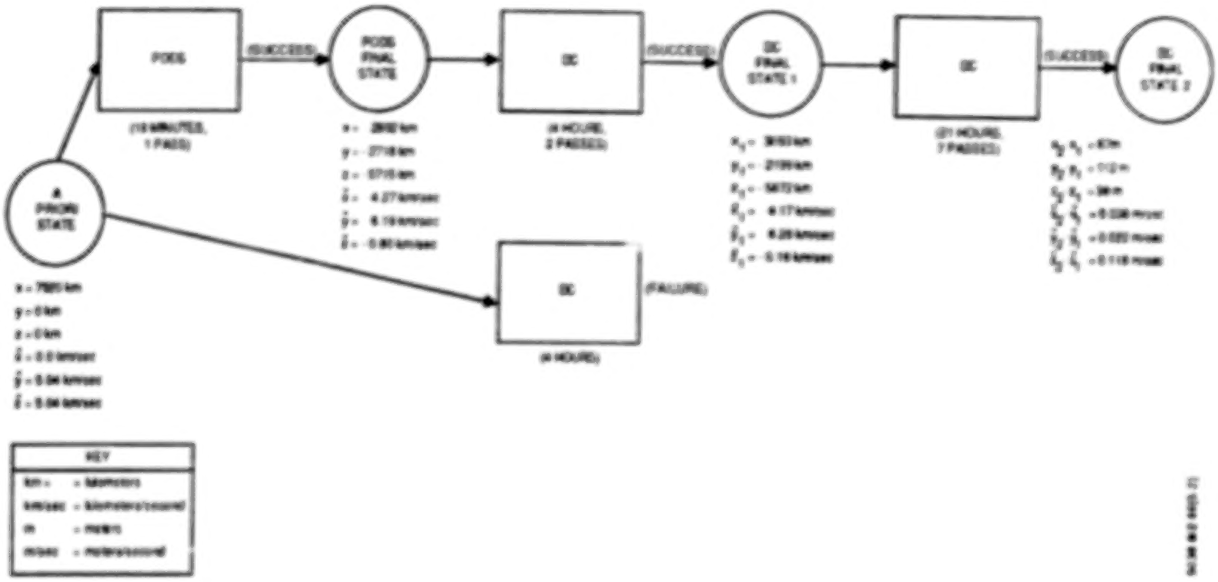
PODS
(SUCCESS)
PODS FINAL STATE
DC
(SUCCESS)
DC FINAL STATE 1
DC
(SUCCESS)
DC FINAL STATE 2
(18 MINUTES, 1 PASS)
(4 HOURS, 2 PASSES)
(21 HOURS, 7 PASSES)
A PRIORI STATE
DC
(FAILURE)
(4 HOURS)
x = 7920 km
y = 0 km
z = 0 km
ẋ = 0.0 km/sec
ẏ = 5.04 km/sec
ż = 5.04 km/sec
x = 2892 km
y = -2718 km
z = -5715 km
ẋ = 4.27 km/sec
ẏ = 6.19 km/sec
ż = -0.80 km/sec
KEY
km = kilometers
km/sec = kilometers/second
m = meters
m/sec = meters/second

Figure 5. Use of PODS To Aid in the Recovery of the TDRSS-Tracked ERBS Target on April 10, 1986

Table 4. ERBS Candidate Solutions Using Range Data on April 10, 1986

ELEMENTS	A PRIORI TARGET STATE	ERBS CANDIDATE SOLUTIONS*			
		SOLUTION 1	SOLUTION 2	SOLUTION 3	SOLUTION 4
x (kilometers)	7920	2892	5406	3047	5262
y (kilometers)	0	-2718	3269	-2824	3368
z (kilometers)	0	-5715	5219	5581	-5304
ẋ (kilometers/second)	0.0	4.27	-1.05	4.29	-1.18
ẏ (kilometers/second)	5.04	6.19	-5.23	6.18	-5.15
ż (kiloimeters/second)	5.04	-0.80	4.42	0.80	-4.49
APOGEE (kilometers)	1702	588	1825	588	1825
PERIGEE (kilometers)	1542	554	1609	554	1609
a (kilometers)	8000	6949	8095	6949	8095
e	0.01	0.00248	0.0134	0.00248	0.0134
i (degrees)	45	55.9	115.9	54.0	114.0
Ω (degrees)	0.0	59.5	54.8	239.6	234.9
ω (degrees)	0.0	142.1	247.3	322.0	67.4
M (degrees)	0.0	120.4	157.2	120.4	157.2

*SOLUTIONS ARE AT 0 HOURS FOR THE 18-MINUTE DATA ARC (0:31:30 - 0:49:50).
SOLUTION 1 WAS SELECTED BY TDRSS BEAM ANGLE SCREENING.

plane and is slightly eccentric, the mirror image solution pairs in Cartesian coordinates in Table 4 approximately obey the following:

$$z \rightarrow -z, \qquad \dot{z} \rightarrow -\dot{z}$$

$$x \rightarrow x, \qquad y \rightarrow y, \qquad \dot{x} \rightarrow \dot{x}, \qquad \dot{y} \rightarrow \dot{y}$$

When solutions 1 and 3 became the a priori states in DC Program runs with TDRSS range tracking, the corresponding DC solutions were also mirror images of each other. To resolve this ambiguity, additional information is needed for selecting the correct solution. The TDRSS beam angle screening in PODS selected solution 1. Solutions 2 and 4, easily rejected by beam angle screening, are also invalid since they are too energetic, with values for the semimajor axis that are too large (reflecting the deliberately chosen too-large a priori value).

4. CONCLUSIONS

This section summarizes the evaluation studies described in this report (Section 4.1) and discusses the conclusions drawn (Section 4.2). In addition, future enhancements to PODS are outlined (Section 4.3).

4.1 EVALUATION SUMMARY

The evaluation studies demonstrated, through various examples, the following points:

- Good and sometimes generic values for the a priori state vector led to the correct PODS solutions.

- Shorter data arcs were more unstable, but the cutoff varied on a case-by-case basis.

- Range-only and Doppler-only data were more stable than mixed range and Doppler data.

- Solution screening by TDRSS beam angles and physical considerations could select a valid solution from multiple candidates.

4.2 CONCLUSIONS

The different kinds of PODS examples given in this study reveal that PODS provides TDRSS tracking capability in preliminary orbit determination as a standalone utility under TCOPS. PODS uses the powerful homotopy continuation method with a limited number of measurements and a degraded a priori target state to determine candidate solutions from which the appropriate solution is extracted by solution screening. In addition, PODS is able to generate a solution that can be used to recover an orbit for an event when other systems such as the GTDS DC Program may fail. Some limitations that remain in PODS can be resolved through future enhancements.

4.3 FUTURE PODS ENHANCEMENTS

Future enhancements to PODS that are being developed or considered included the following:

- Improving the solution by taking the selected solution, which was generated using a two-body orbit propagator, and refining it by using a more accurate propagator along with a light-time correction algorithm (Reference 3)

- Generalizing the homotopy continuation algorithm to allow for jumping from an a priori target state loop to a solution loop, when necessary (Reference 3)

- Extending TDRSS beam angle screening from range data to Doppler data

- Allowing for ground-only and combined ground/relay tracking of the target

REFERENCES

1. Escobal, P. R., Methods of Orbit Determination. New York: John Wiley and Sons, Inc., 1965

2. Computer Sciences Corporation, CSC/SD-85/6738, Goddard Trajectory Determination System (GTDS) User's Guide, Revision 2, D. Squier and K. Byers, December 1987

3. National Aeronautics and Space Administration/Goddard Space Flight Center, Technical Memorandum 86230, Study of a Homotopy Continuation Method for Early Orbit Determination With the Tracking and Data Relay Satellite System (TDRSS), R. L. Smith and C. Huang, March 1986

4. Smith, R. L., and C. Y. Huang, "A Homotopy Continuation Method for General Preliminary Orbit Determination and Special Application to the Tracking and Data Relay Satellite System," Paper No. 85-0215, presented at the AIAA 23rd Aerospace Sciences Meeting, Reno, Nevada, January 14-17, 1985

5. Computer Sciences Corporation, CSC/SD-87/6737, System Description for the Preliminary Orbit Determination System (PODS), S. Kirschner and E. Nash, November 1987

6. Computer Sciences Corporation, CSC/SD-87/6035, Preliminary Orbit Determination System (PODS) User's Guide, S. Kirschner, E. Nash, and A. Beri, September 1987

7. Smith, R. L., and C. Y. Huang, "An Analysis of the Use of TDRSS Satellite Range and Doppler Tracking Alone for Preliminary Orbit Determination," Paper No. AAS 85-427, presented at the AAS/AIAA Astrodynamics Specialist Conference, Vail, Colorado, August 12-15, 1985

N89-15947

TRAJECTORY COMPUTATION DURING A MANEUVER: THRUST ESTIMATION WITH THE GODDARD TRAJECTORY DETERMINATION SYSTEM (GTDS)*

A. C. Beri and M. V. Samii, Computer Sciences Corporation (CSC)
C. E. Doll, Goddard Space Flight Center (GSFC)

ABSTRACT

Existing thrust modeling capabilities of the Goddard Trajectory Determination System (GTDS) have been enhanced to allow calibration of the onboard propulsion system. These enhancements provide one or more thrust scale factors, based on estimation using the batch least-squares technique, for the case of along-track thrust and the case of attitude-dependent thrust. The enhancements are evaluated using simulated tracking measurements for a test spacecraft and using actual tracking measurements for the Earth Radiation Budget Satellite (ERBS). The effects of tracking measurement noise and distribution on the accuracy of the estimation are investigated and found to be significant. Results and conclusions of the analysis are presented.

---

*This work was supported by the National Aeronautics and Space Administration (NASA)/Goddard Space Flight Center (GSFC), Greenbelt, Maryland, under Contract NAS 5-31500.

1. INTRODUCTION

The force modeling requirements for trajectory computation for spacecraft supported by the Flight Dynamics Facility (FDF) at the Goddard Space Flight Center (GSFC) are different for each mission phase (Reference 1). The forces that determine the trajectory of the spacecraft during the on-orbit phase include solar, lunar, and Earth gravitational forces; aerodynamic forces; and solar radiation effects. These forces are continuously in effect and are modeled generically for all spacecraft. Trajectory computation during maneuvers, such as transfer orbit, stationkeeping, and targeting, involves modeling the force due to thrust, which is different for different spacecraft and types of maneuvers. Two thrust models, one dealing with along-track thrust and the other with attitude-dependent thrust, have recently been implemented and tested as enhancements to the Goddard Trajectory Determination System (GTDS). These models are the subject of this paper.

The paper is organized into four sections. The remainder of Section 1 discusses the scope and goals of the paper and describes the current thrust estimation capabilities in GTDS and the current and future thrust estimation requirements. Sections 2 and 3 discuss the along-track thrust estimation model and the attitude-dependent thrust estimation model, respectively; each of these sections includes a description of the estimation method, a discussion of the estimation results, and the conclusions. Section 4 describes future developments in thrust estimation.

1.1 SCOPE AND GOALS

This paper discusses force modeling in GTDS for the case of along-track thrust and for the case of thrust with cross-track or radial components. The mathematical formulation of the thrust estimation algorithm and evaluation of the resulting enhanced GTDS are presented. The goals of the evaluation are the following:

- To establish whether a reliable postburn state can be determined

- To assess the influence of tracking measurement noise, tracking measurement distribution, and the a priori state vector on thrust estimation

1.2 CURRENT THRUST ESTIMATION CAPABILITIES IN GTDS

The inclusion of thrust forces in GTDS allows powered ephemeris generation through the Ephemeris Generation (EPHEM) Program and thrust level estimation through the Differential Correction (DC) Program. Thrust estimation is currently supported by GTDS in the form of a polynomial thrust option, which allows variation of eight or less polynomial coefficients a_i of the thrust acceleration function, A(t), written as

$$A(t) = \sum_{i=1}^{8} a_i \, t^{i-1} \qquad (1)$$

where t is the time from ignition (Reference 2). The thrust estimation can be performed in conjunction with attitude estimation (or specification). Variations in the spacecraft roll, pitch, and yaw, or in the right ascension and declination, as functions of time are each represented as polynomials of order four or less, with variable coefficients. These coefficients can also be estimated in the DC Program.

In the DC Program, the spacecraft a priori state can always be estimated. However, if the a priori state is known to be highly accurate, its variation can be suppressed, thus allowing the differential correction process to vary only the thrust scale factor. In general, this can be expected to provide a more reliable estimated thrust factor.

1.3 CURRENT AND FUTURE THRUST MODELING REQUIREMENTS

For several National Aeronautics and Space Administration (NASA) missions, such as the Cosmic Background Explorer (COBE) and Geostationary Operational Environmental Satellite (GOES), it is desirable to perform near-realtime calibration of the onboard propulsion system. Thus, If $A_{nom}(t)$ is the nominal thrust acceleration measured under controlled conditions and $A_{eff}(t)$ is the actual effective thrust acceleration during maneuvers, then a calibration factor $(1 + \tau)$ is required, such that

$$A_{eff}(t) = (1 + \tau)\, A_{nom}(t) \tag{2}$$

The polynomial thrust estimation option currently operational in GTDS potentially changes the form of the nominal thrust profile by allowing independent variation of all the coefficients. It does not allow estimation of the single calibration factor of Equation (2). A desirable enhancement would include an arbitrary profile for $A_{nom}(t)$ (e.g., thrust input in the form of a numerical table of thrust acceleration values) and the capability to estimate a calibration factor $(1 + \tau)$. Since the maneuvers are often accompanied by highly specific attitude configurations, a generalization of the attitude specification and estimation is also important. These issues are discussed further in Sections 2 and 3.

2. ESTIMATION OF ALONG-TRACK THRUST

This section presents a discussion of thrust estimation for the case of thrust entirely along the velocity direction (along-track). In GTDS, this involves the inclusion of an additional term in the force model to account for the thrust, as well as the specification of a thrust scale factor $(1 + \tau)$ to be estimated.

Several factors influence the thrust estimation process, such as the nature of the tracking measurements used for estimation (i.e., length of data arc, distribution, biases, noise), the reliability of the a priori state vector, and the number of parameters being simultaneously estimated. Functional feasibility of the enhanced GTDS can be established by evaluating the influence of these factors on the system.

The thrust estimation method is described in Section 2.1. The results of the evaluation and the conclusions of the analysis are presented in Sections 2.2 and 2.3, respectively. Further information can be found in References 3 and 4.

2.1 METHOD FOR ALONG-TRACK THRUST ESTIMATION

The enhanced GTDS thrust force model described in this section [referred to as the tabular thrust force model (TTFM)] uses the existing thrust magnitude coefficient estimation function in GTDS to enhance the capability of the polynomial thrust model. In this force model, the jth acceleration vector at time t_i, $\vec{A}_j(t_i)$, which is assumed to be aligned with the velocity of the spacecraft in the orbit plane coordinate system, can be written as follows:

$$\vec{A}_j(t_i) = (1 + \tau_j)\left[\frac{F_j(t_i)}{M_j(t_i)}\right]\hat{v} \tag{3}$$

where $\hat{v}$ = velocity unit vector

$F_j(t_i)$ = jth thrust force magnitude at time t_i

$M_j(t_i)$ = corresponding mass of the spacecraft during the jth thrust at time t_i

τ_j = thrust variation coefficient of the jth thrust

A maximum of 20 thrust forces can be modeled, each thrust being represented by a thrust table and a corresponding mass table.

One of two options, an application option or an estimation option, can be specified. If the application option is chosen for a particular thrust, for example the jth thrust, then τ_j is automatically set to zero, and the thrust and mass tables of the jth thrust are used in calculating the acceleration, $\vec{A}_j$, to be applied. If, however, the estimation option is chosen, then the best estimates of τ_j are determined by GTDS as solve-for parameters.

The TTFM is capable of applying and estimating thrust levels simultaneously. However, within this model thrust can be applied or estimated only in the spacecraft velocity direction. This limitation could be removed in several ways, one of which is discussed in Section 3 of this paper. Thrust estimation in GTDS involves the incorporation of the thrust levels in the total force function and the inclusion of the coefficients τ_i in the variational process. References 1, 3, and 4 provided detailed descriptions of the mathematical and computational procedures employed by GTDS for this estimation.

2.2 RESULTS AND DISCUSSION

In evaluating the TTFM, tests were performed to determine how well the thrust was estimated under different conditions. Specifically, the effects of the following operational conditions were studied:

- Input Thrust Level--The input thrust level can range from 0 percent to 100 percent of the "actual" thrust.
- State Estimation--Estimation of the state may or may not be performed in conjunction with thrust estimation.
- Tracking Measurement Quality--The quality of the tracking measurement can be high or low due to noise and biases.
- Tracking Measurement Distribution--The distribution of tracking measurements may be good, with a large number of passes uniformly distributed throughout the orbit determination data arc, or the distribution may be poor, with a few passes clustered together and large gaps with no tracking measurements.
- Data Arc Length--The data arc length can be small or large compared with a period during which the tracking geometry changes significantly.

Within this evaluation framework, TTFM was tested in two stages. In the first stage, the overall accuracy and reliability of TTFM was tested through thrust analysis under controlled conditions for a typical mission, called TEST, whose ascent phase includes a series of short burns, followed by longer burns. These burns were modeled by the Generalized Maneuver (GMAN) Program, which generates tables of thrust as a function of time for specified engine parameters. The tracking schedule and associated Tracking and Data Relay Satellite System (TDRSS) tracking measurements were simulated, with known thrust profiles included in the force model used by the simulation.

The single ideal thrust coefficient, τ, can be predicted exactly for this case, independently of the TTFM, and the difference between the actual estimated τ determined by the TTFM and the ideal τ provides a measure of the accuracy and reliability of the TTFM.

The second stage of TTFM testing involved performing tests to support orbit analysis for the ERBS ascent-phase maneuvers using actual Ground Spaceflight and Tracking Data Network (GSTDN) tracking measurements taken on October 7 and 8, 1984. The TTFM was applied to the 183-minute calibration burn and to the first long 376-minute burn to evaluate the performance of the TTFM using actual tracking measurements. Since the actual thrust is not known exactly for this case, these tests do not measure the accuracy of thrust estimation with the TTFM. The results for TEST and ERBS are discussed in Sections 2.2.1 and 2.2.2, respectively.

2.2.1 TEST ANALYSIS RESULTS

To evaluate the accuracy and relibility of the TTFM, GTDS was modified to include the enhanced thrust capabilities based on the TTFM. The TTFM was tested on two types of maneuvers: (1) brief (70-second) maneuvers that raise the TEST orbit by about 1 kilometer and (2) long-burn (94-minute) maneuvers that raise the TEST orbit by about 200 kilometers.

Tests of the accuracy of the thrust estimation were performed as follows:

- Simulated tracking measurements were generated with a force model containing known nominal thrust accelerations $A_j(t)$, one of which, $A_{nom}(t)$, is to be estimated [Equation (3)].

- GTDS was executed using the TTFM, with the particular input thrust level, $A_{in}(t)$, different from $A_{nom}(t)$ by a factor ϕ, i.e.,

$$A_{in}(t) = \phi A_{nom}(t) \tag{4}$$

- The thrust scale factor $(1 + \tau)$ estimated by GTDS was then examined; this scale factor defines the final estimated thrust, $A_{est}(t)$, in terms of $A_{in}(t)$, as follows:

$$A_{est}(t) = (1 + \tau) A_{in}(t) \tag{5}$$

Under ideal estimation conditions, since the tracking measurements reflect a thrust $A_{nom}(t)$, then $A_{est}(t)$ must equal $A_{nom}(t)$, i.e.,

$$A_{est}(t) = A_{nom}(t) \tag{6}$$

Or, using Equations (5) and (4),

$$(1 + \tau) A_{in}(t) = A_{nom}(t) \tag{7}$$

$$(1 + \tau) \phi A_{nom}(t) = A_{nom}(t) \tag{8}$$

Thus, for ideal thrust estimation, the following condition must be satisfied:

$$(1 + \tau) \phi = 1 \tag{9}$$

Therefore, the evaluation criterion for ideal thrust estimation is

$$\tau = \frac{1}{\phi} - 1 \qquad (10)$$

2.2.1.1 Short-Maneuver Results

The Research and Development (R&D) GTDS Program was used to generate simulated Tracking and Data Relay Satellite-East (TDRS-E) and TDRS-West (TDRS-W) tracking measurements for TEST for a total data arc span of 3 hours and 20 minutes, starting at 1 hour and 30 minutes (Figure 1). There were a total of 13 passes, eight tracked by TDRS-E and five tracked by TDRS-W. Range and Doppler data generated at 10-second intervals formed passes 8 minutes long.

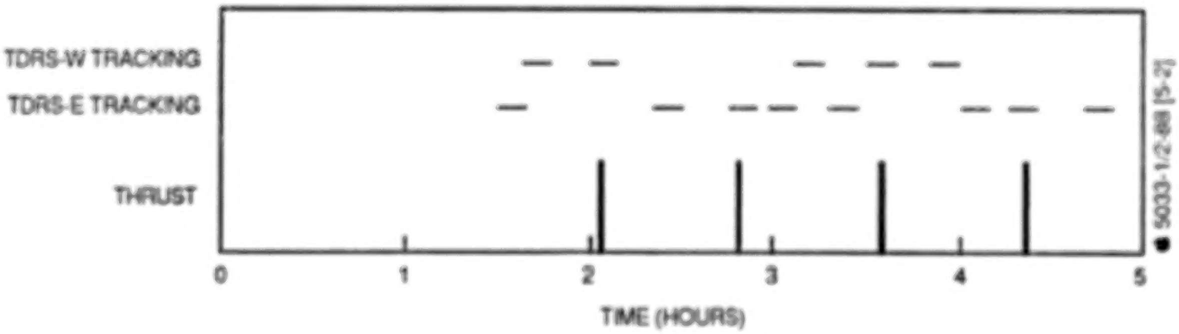

Figure 1. Simulated TDRS-W and TDRS-E Tracking Measurement Passes for TEST Short Maneuvers and the Associated Thrust Pattern

The TTFM was tested for several cases using the 70-second TEST maneuvers. Each of the four thrusts was estimated in separate executions, with 90 percent of the thrust magnitude used as input to GTDS, corresponding to $\phi = 0.9$. For each test, the remaining three thrusts were applied with $\tau_j = 0$ [Equation (3)]. From Equation (10), the value of τ expected for the case of ideal thrust estimation is 0.111111.

The results of simultaneously solving for the state and thrust for each short maneuver are given in Table 1. The estimated values of τ agree with the expected value of 0.111111 to better than 1 percent, establishing the functional reliability of the TTFM. The estimated values of the state components agree with their a priori values at epoch to within 1 meter in position and to within 10^{-3} meter per second in velocity for three of the four maneuvers. The larger differences seen for the first thrust are due to the greater cumulative effect of an early force perturbation on the overall trajectory, relative to later ones. However, the maximum 4-meter difference in position is still within quality assurance standards.

2.2.1.2 Long-Burn Results

The TEST ascent phase includes a number of long-burn, low-thrust maneuvers. Since each one of these burns typically takes more than an hour, the thrust level and state estimation during the burn can allow adjustments to the thrust that may be necessary for proper orbit raising or stationkeeping.

TEST thrust level estimation during the ascent phase was utilized to evaluate the TTFM using simulated TDRSS two-way Doppler data. The tracking schedule assumed for the first long burn of 94 minutes is depicted in Figure 2. It

Table 1. State and Thrust Estimation for TEST During Short Maneuvers

THRUST NO.	DIFFERENCE BETWEEN FINAL AND A PRIORI STATE						THRUST SCALE FACTOR, τ
	ΔX (METERS)	ΔY (METERS)	ΔZ (METERS)	$\Delta \dot{X}$ (METERS/SECOND)	$\Delta \dot{Y}$ (METERS/SECOND)	$\Delta \dot{Z}$ (METERS/SECOND)	
1	-3.6	-0.35	3.2	-0.00307	0.00093	-0.0049	0.1118
2	-0.04	0.14	-0.26	-0.00007	0.00005	0.00043	0.1112
3	0.27	0.15	-0.42	0.00015	-0.00002	0.00062	0.1112
4	0.37	0.17	-0.49	0.00026	-0.00003	0.00076	0.1117

NOTES: 1. 13 PASSES (8 TDRS-E, 5 TDRS-W) DURING 3rd 20th DATA ARC
2. RANGE AND DOPPLER OBSERVATIONS OF TEST
3. SOLVE FOR STATE AND -10% PERTURBED SINGLE THRUST

5033-16(2 88)(5-2)

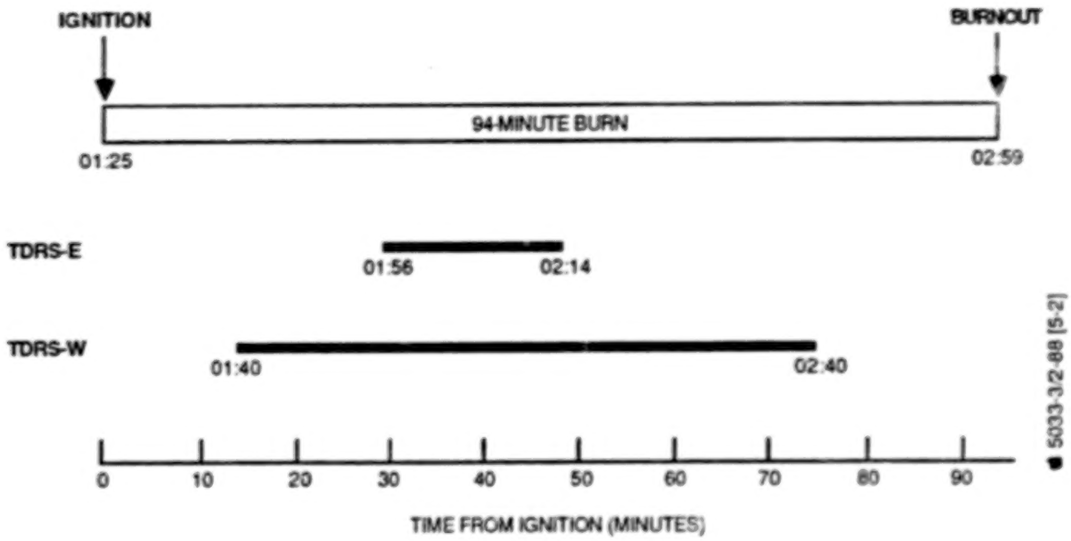

Figure 2. Simulated TDRS-E and TDRS-W Tracking Measurement Passes for the TEST Long-Burn Maneuver and the Associated Thrust

consists of one 18-minute TDRS-E pass starting from 31 minutes after ignition and one 60-minute TDRS-W pass starting from 15 minutes after ignition.

Two sets of simulated tracking measurements were generated, one with and one without measurement noise (a measurement noise standard deviation of 0.25 hertz was assumed). Initial state errors introduced in the GTDS DC Program input were assumed to be in the along-track direction (100 meters and 10 centimeters per second for the TEST spacecraft and 50 meters and 1 centimeter per second for TDRS-E and TDRS-W).

Thrust estimation was performed for the 14 tracking measurement distributions given in Figure 3. For the distributions E1(9), E1(18), W1(10), W6(10), and W16(20) shown in Figure 3, the following combinations of measurement noise and initial state error were included:

- o: No measurement noise
- a: Measurement noise

- b: Measurement noise and TEST initial state error
- c: Measurement noise, TEST initial state error, and TDRS initial state error

The results for τ and the position error at burnout and at 3 hours from burnout are presented in Tables 2 and 3. Table 2 compares the o, a, b, c results for the specific tracking scenarios and illustrates the effects of noise and TEST or TDRS initial state errors on the estimation. The results presented in Table 3 include noise and the TEST initial state error and illustrate the effects of the location of tracking measurements and the length of the measurement pass.

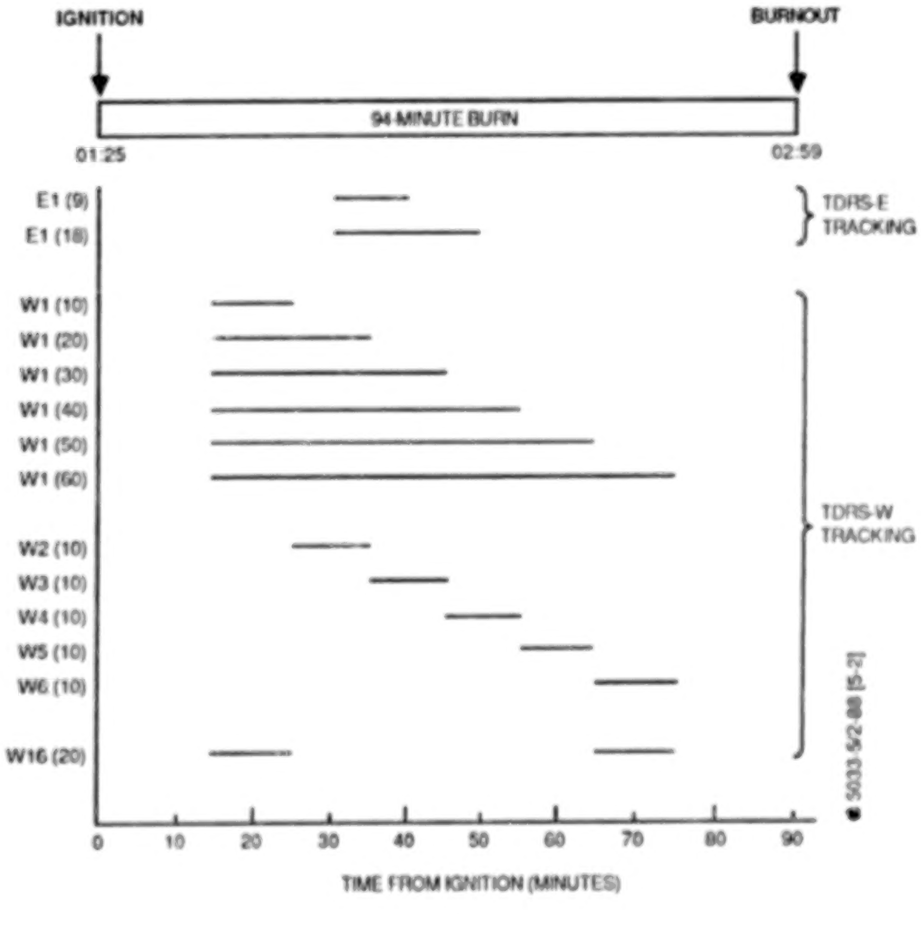

Figure 3. Tracking Measurement Distributions Used for Evaluation of TEST Long-Burn Thrust Estimation

Table 2. Effects of Noise and TEST and TDRS Initial State Errors on Thrust Estimation During the TEST Long Burn

TRACKING MEASUREMENT DISTRIBUTION*	FINAL THRUST SCALE FACTOR, τ	POSITION ERRORS (METERS)	
		AT BURNOUT	AT 3 HOURS FROM BURNOUT
E1(9)^o	0.11101	52	299
E1(9)^a	0.11143	149	1,440
E1(9)^b	0.11596	1,499	17,718
E1(9)^c	0.11624	4,243	19,508
E1(18)^o	0.11105	27	160
E1(18)^a	0.11122	42	443
E1(18)^b	0.11368	781	9,292
E1(18)^c	0.11450	2,900	13,099
W1(10)^o	0.11088	198	816
W1(10)^a	0.11219	440	4,536
W1(10)^b	0.12743	5,905	64,296
W1(10)^c	0.10451	7,064	30,604
W6(10)^o	0.11105	19	152
W6(10)^a	0.11107	11	156
W6(10)^b	0.11355	563	7,842
W6(10)^c	0.11591	3,548	16,968
W16(20)^o	0.11106	12	116
W16(20)^a	0.11109	11	69
W16(20)^b	0.11266	1,017	4,925
W16(20)^c	0.11686	4,156	20,090

5033-15/2-88[5-2]

*SEE FIGURE 3. THE NUMBERS IN PARENTHESES REPRESENT THE TOTAL DURATION MEASUREMENTS IN MINUTES. SUPERCRIPTS o,a,b,c INDICATE THE FOLLOWING:

o = NO MEASUREMENT NOISE
a = MEASUREMENT NOISE
b = MEASUREMENT NOISE AND TEST INITIAL STATE ERROR
c = MEASUREMENT NOISE, TEST INITIAL STATE ERROR, AND TDRS INITIAL STATE ERROR

Table 3. Effects of Data Arc Location and Length on Thrust Estimation During the TEST Long Burn

SOLUTION ARC*	ARC LENGTH (MINUTES)	FINAL THRUST SCALE FACTOR, τ	POSITION ERRORS (METERS)	
			AT BURNOUT	AT 3 HOURS FROM BURNOUT
W1(10)^b	10	0.12743	5,905	64,296
W1(20)^b	20	0.12328	10,282	47,336
W1(30)^b	30	0.11496	3,005	14,041
W1(40)^b	40	0.11272	1,266	5,744
W1(50)^b	50	0.11184	668	2,748
W1(60)^b	60	0.11146	444	1,538
W1(10)^b	10	0.12743	5,905	64,296
W2(10)^b	10	0.12393	10,786	49,736
W3(10)^b	10	0.11600	3,732	17,649
W4(10)^b	10	0.11398	2,099	9,965
W5(10)^b	10	0.11355	563	7,842
W6(10)^b	10	0.11326	1,045	5,801

5033-6/2-88[5-2]

*SEE FIGURE 3. THE NUMBERS IN PARENTHESES REPRESENT THE TOTAL DURATION OF MEASUREMENTS IN MINUTES. SUPERCRIPTS o, a, b, c INDICATE THE FOLLOWING:

o = NO MEASUREMENT NOISE
a = MEASUREMENT NOISE
b = MEASUREMENT NOISE AND TEST INITIAL STATE ERROR
c = MEASUREMENT NOISE, TEST INITIAL STATE ERROR, AND TDRS INITIAL STATE ERROR

As can be seen from Table 2, measurement noise does not appear to be significant in the estimation process, but the presence of TEST and/or TDRS initial state errors introduces noticeable deterioration of the quality of the orbit determination results. The overall orbital accuracy, however, is expected to satisfy the operational orbit support requirements. Table 3 shows that the observability of τ improves and, thus, the overall orbit determination accuracy improves as the length of the data arc increases or, in the case of a constant-length data arc, as the data are placed farther away from ignition.

2.2.2 ERBS ASCENT-PHASE ANALYSIS RESULTS

The TTFM was tested using real GSTDN tracking data for ERBS. The first part of the study focused on the calibration burn and on the 8.5-hour free-flight interval immediately following that burn. The second part of the study focused on the first long burn and on the subsequent 5-hour free flight. The tracking distribution for the duration of the study is shown in Figure 4. Passes C1 through C16 are used in the calibration study, and passes L1 through L10 are used in the long-burn study.

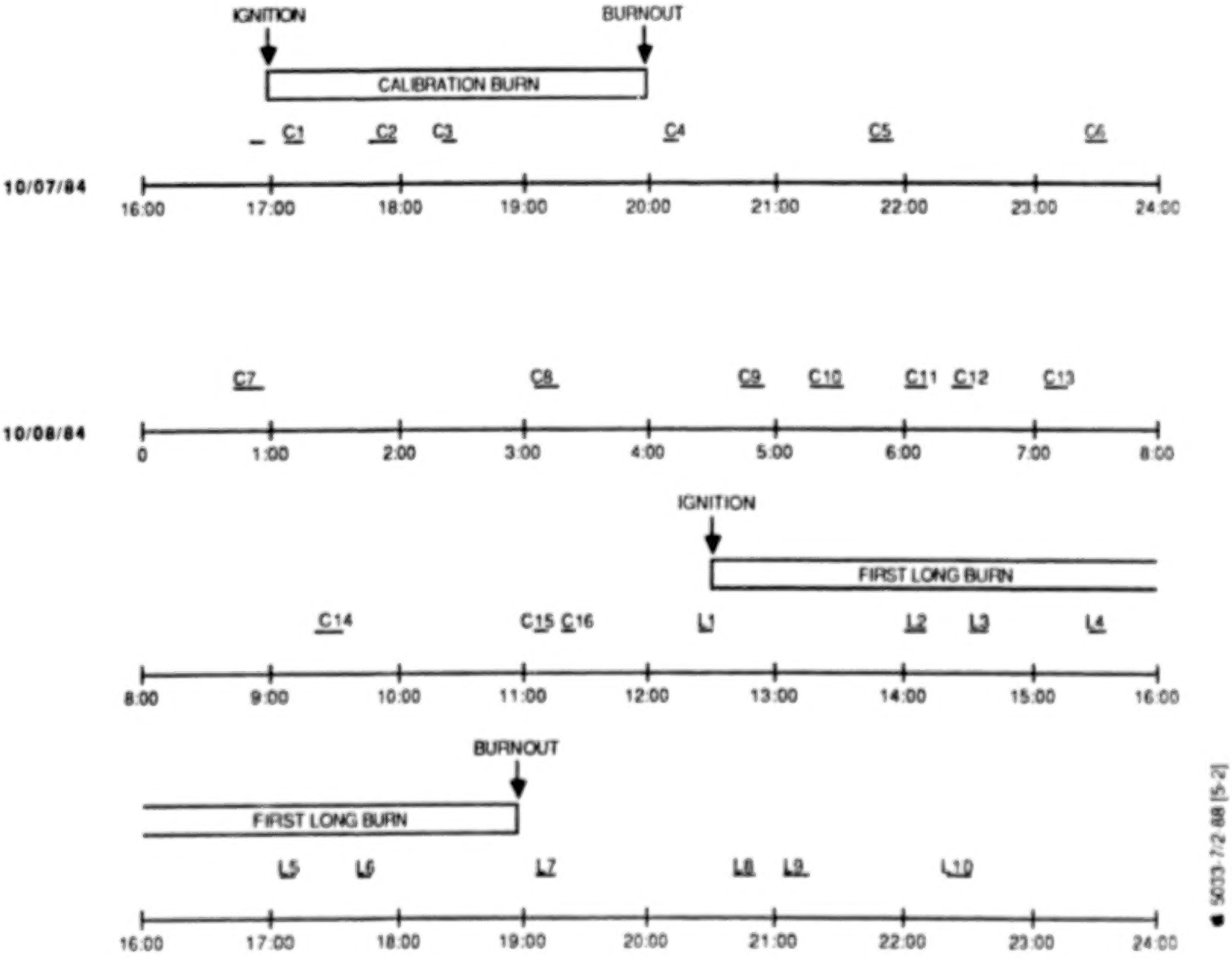

Figure 4. Tracking Measurement Distribution During the Calibration Burn and the First Long Burn of the ERBS Ascent Phase

During the ERBS analysis, thrust estimation was evaluated by comparing ephemerides [using the GTDS Ephemeris Comparison (COMPARE) Program] propagated from state vectors estimated under various conditions. These conditions included the following:

- Different distributions of tracking measurement passes.
- Different levels of constraint on the variation of the a priori state, through the state covariance matrix. (The a priori state is effectively fixed when a covariance constraint is applied, i.e., when very small values are used for the elements of the state covariance matrix.)
- Solutions based on tracking measurement taken during powered flight and those based on free-flight data.

The following evaluation criteria were used in comparing the results for the various cases:

- Consistency in the estimated value of τ
- Final value of the weighted root mean square (WRMS) of the observed-minus-computed (O-C) residuals, i.e., the differences between the actual tracking observations O and the computed (estimated) observations C
- Consistency in the differences between the ephemerides propagated from each solution and a reference ephemeris at different times on the solution arc

2.2.2.1 Calibration Burn Results

Using an epoch vector at the ignition of the calibration burn on October 7, 1984, at 16 hours, 53 minutes, a reference ephemeris (solution n) was generated using the nominal thrust level modeled by the GMAN Program. Utilizing the same epoch vector, thrust estimation was performed and the ephemeris propagated to the start of the first long burn. This was done for four cases, as follows:

1. Solution using pass C1 (with initial state covariance constraints)
2. Solution using passes C1 and C2 (with initial state covariance constraints)
3. Solution using passes C1, C2, and C3 (with initial state covariance constraints)
4. Solution using passes C1, C2, and C3 (with no initial state covariance constraints)

A fifth solution (solution 5) was a postburn, free-flight solution using passes C4 through C16 (with no initial state covariance constraints) and an epoch at 19 hours, 58 minutes.

The results for τ are summarized in Table 4. The most notable result is the convergence of τ as the number of observations increases. The value of τ from solution 3 was chosen to calculate a thrust calibration factor for the first long-burn flight segment. Solution 3 was obtained using a fixed a priori state and the greatest number of observations, thus making the corresponding thrust scale factor the most accurate. This conclusion is based on the analysis described in References 3 and 4. The larger WRMS for solutions 1, 2, and 3, compared with that for solution 4, results from poor trajectory estimation (because of the constrained initial state) for solutions 1, 2, and 3.

The GTDS COMPARE Program was used to compare solutions 1 through 4 with the reference solution and with the free-flight solution. The results are presented in Table 5. It is clear from this table that solution 1 is not acceptable. The large position error associated with this solution is due

Table 4. Results of Thrust Variation Coefficient Estimations for the ERBS Calibration Burn

SOLUTION	NO. OF PASSES	NO. OF OBSERVATIONS	FINAL THRUST SCALE FACTOR, τ	NO. OF ITERATIONS	WRMS	COVARIANCE CONSTRAINTS
1	1	31	− 0.378	3	14.166	YES
2	2	67	− 0.127	4	16.355	YES
3	3	156	− 0.117	4	12.097	YES
4	3	139	− 0.113	5	1.338	NO

5033-9/2-88 [5-2]

Table 5. Comparisons of Along-Track Position Differences for the ERBS Calibration Burn

a. COMPARISON WITH THE REFERENCE EPHEMERIS SOLUTION (SOLUTION n)

SOLUTION COMPARED	ALONG-TRACK POSITION DIFFERENCES (KILOMETERS)					
	DURING BURN		DURING FREE-FLIGHT			
	$16^h\ 58^m$	$18^h\ 28^m$	$19^h\ 58^m$	$21^h\ 18^m$	$22^h\ 38^m$	$23^h\ 58^m$
1	- 0.098209	52.23137	197.1167	357.8751	519.0224	680.5509
2	- 0.252476	13.35632	57.5685	107.1451	157.1803	207.7262
3	- 0.190235	12.83301	53.5299	98.9438	144.5701	190.5996
4	- 0.385551	12.82878	52.4604	96.6848	141.1091	185.9451

b. COMPARISON WITH THE FREE-FLIGHT SOLUTION (SOLUTION 5)

SOLUTION COMPARED	ALONG-TRACK POSITION DIFFERENCES (KILOMETERS)			
	$19^h\ 58^m$	$21^h\ 18^m$	$22^h\ 38^m$	$23^h\ 58^m$
1	139.1953	254.0555	369.3852	485.3086
2	0.0929	4.0365	8.3164	13.0124
3	- 3.9413	- 4.1571	- 4.2851	- 4.1084
4	- 4.9910	- 6.3822	- 7.7053	- 8.7258

5033-9/2-88 [5-2]

to the poor estimate of τ as discussed earlier. The other comparison results shown in Table 4 are all consistent and represent reliable estimation.

2.2.2.2 First Long-Burn Results

Thrust estimation was performed for the ERBS first long burn using the TTFM and an evaluation plan similar to that for the calibration burn. An epoch vector at the ignition of the first long burn was obtained from calibration solution 5. A reference ephemeris was generated along with a series of DC Program and EPHEM Program solutions, extending to 5 hours after the end of the burn. A value of τ equal to -0.117 (from calibration burn solution 3, see Table 4) was used to scale the input thrust used in this part of the study. The new value of τ, estimated with the calibrated thrust as input, should be close to zero.

The results of the first-long-burn study are summarized in Table 6. Solutions A through F in this table are based on the following tracking measurement distributions:

A. Solution using passes L2 and L3 (with initial state covariance constraint)

B. Solution using passes L3 and L4 (with initial state covariance constraint)

C. Solution using passes L2 through L6 (with initial state covariance constraint)

D. Solution using passes L2, L5, L6, L9 (with no initial state covariance constraint)

E. Solution using passes L2 through L10 (with no initial state covariance constraint)

F. Postburn, free-flight solution using passes L7 through L10 (with no initial state covariance constraint)

Table 6. Results of Thrust Variation Coefficient Estimations for the ERBS First Long Burn

SOLUTION	NO. OF PASSES	NO. OF OBSERVATIONS	FINAL THRUST SCALE FACTOR, τ	NO. OF ITERATIONS	WRMS	COVARIANCE CONSTRAINTS
A	2	126	−0.0166	4	3.030	YES
B	2	67	−0.0208	4	4.519	YES
C	5	231	−0.0240	5	4.358	YES
D	4	285	−0.0278	5	4.863	NO
E	9	498	−0.0277	5	14.200	NO

5033-10(2-88S-2)

The epoch vector at ignition for the long burn was propagated using the GTDS EPHEM Program to obtain a nominal ephemeris (solution N). A thrust calibration factor ($1 + \tau$) of 0.883 was used. Since the calibrated thrust was used, the magnitudes of the estimated τ in Table 6 are significantly smaller than the ones estimated during the calibration burn.

In addition to the thrust estimation, ephemeris comparisons were made analogous to those made for the calibration burn. In this case, the reference ephemeris reflects a calibrated thrust rather than the nominal thrust from the GMAN Program, so that the differences should be much smaller than those obtained for the calibration burn case. This is seen to be the case, with the position differences smaller than those observed in Table 5 by an order of magnitude or more. Detailed numerical results are available in Reference 4.

2.3 CONCLUSIONS

The conclusions from this thrust estimation study using the TTFM for the TEST and ERBS spacecraft are as follows:

- The TTFM is capable of modeling thrust application and estimation for the case of low thrust levels.
- The results for TEST establish that the thrust scale factor can be estimated to an accuracy of 1 percent.
- Measurement noise does not significantly influence thrust estimation.
- Target (TEST) or relay (TDRS) a priori state errors result in poor overall trajectory determination but adequate thrust level estimation.
- The results for TEST show that thrust estimation based on tracking measurements evenly distributed throughout the burn period or clustered away from the start of the burn period is more reliable than for other data distributions.

3. ATTITUDE-DEPENDENT THRUST ESTIMATION

This section describes the attitude-dependent thrust modeling for a spacecraft whose thrust direction maintains a fixed orientation with respect to the Sun. Specifically, the angle β between the spin axis and the spacecraft-to-Sun line is fixed, while the spin axis is perpendicular to the position vector of the spacecraft. In the scenario used for this study, the total thrust is directed along the spin axis, so that there is a substantial out-of-plane component. The purpose of this study is to examine whether the thrust variation coefficient can be estimated in the presence of a large out-of-plane component, such as in this case. The formulation of this problem is discussed in Section 3.1, and the numerical results obtained using simulated tracking measurements are presented in Section 3.2.

3.1 METHOD FOR ATTITUDE-DEPENDENT THRUST ESTIMATION

For thrust estimation in the case of out-of-plane thrust, it is necessary to determine the components of the thrust acceleration in the orbital and inertial coordinate systems. This requires the determination of the time-varying yaw angle, α, subject to the constraints mentioned previously. The resulting off-track and along-track thrusts are then estimated within GTDS, and a single calibration factor $(1 + \tau)$ is determined. The procedure for determining α is described in Reference 4.

Knowledge of α allows computation of the components of the total thrust, $A(t)$, in the orbital coordinate system. The along-track and cross-track components are $[A(t) \cos \alpha]$ and $[A(t) \sin \alpha]$, respectively. Transformation from the orbital coordinate system to the inertial coordinate system is straightforward and is described in Reference 1.

3.2 RESULTS AND DISCUSSION

The attitude-dependent thrust estimation capability was evaluated according to the plans used for along-track thrust estimation for the TEST spacecraft, with additional variation of the attitude. Simulated data were generated for the pass configuration shown in Figure 2. Range and Doppler tracking measurements were simulated for three cases, corresponding to values of β equal to 95 degrees, 89 degrees, and 85 degrees. Tables 7 and 8 present summaries of the ephemeris comparison and differential correction results, using a Sun angle of 95 degrees, for mixed (range and Doppler) and Doppler-only tracking, respectively. Results using Sun angles of 89 degrees and 85 degrees show similar trends and are not presented here.

Table 7. Attitude-Dependent Long-Burn Thrust Solutions Using Range and Doppler Tracking

PASS LENGTH (MINUTES)	COVARIANCE CONSTRAINTS	SOLUTIONS WITHOUT MEASUREMENT NOISE			SOLUTIONS WITH MEASUREMENT NOISE		
		ΔR AT TIME FROM EPOCH = $2^h\,55^m$	ΔR AT TIME FROM EPOCH = 6^h	FINAL THRUST SCALE FACTOR, τ	ΔR AT TIME FROM EPOCH = $2^h\,55^m$	ΔR AT TIME FROM EPOCH = 6^h	FINAL THRUST SCALE FACTOR, τ
10	YES	–	–	0.11082097	0.685272	3.408705	0.10916828
20	YES	–	–	0.11104922	- 0.512484	- 2.406412	0.11241663
30	YES	- 0.014102	- 0.024721	0.11110209	0.075666	0.440116	0.11803708
40	YES	- 0.008962	0.000991	0.11108741	0.014270	0.131255	0.11100793
50	YES	- 0.007407	0.008889	0.11108283	0.000376	0.062123	0.11104714
60	YES	- 0.007292	0.009374	0.11108285	- 0.003369	0.043058	0.11106740
30	NO	- 0.013935	- 0.029438	0.11110237	- 2.034615	- 20.27488	0.13113265
40	NO	- 0.014818	- 0.032377	0.11110339	- 6.832943	- 48.90036	0.15156154
50	NO	- 0.015987	- 0.037745	0.11110653	- 0.374978	- 2.113980	0.11258244
60	NO	- 0.017093	- 0.041311	0.11110714	- 0.013690	0.011517	0.11110525

5033-13/2-88 [5-2]

NOTES:

ΔR = ALONG-TRACK POSITION DIFFERENCES BETWEEN THE SOLUTION AND THE REFERENCE EPHEMERIS IN KILOMETERS.

THE "TIME FROM EPOCH" IS RELATIVE TO EPOCH 0^h ON 12/21/87.

Table 8. Attitude-Dependent Long-Burn Thrust Solutions Using Doppler Tracking

PASS LENGTH (MINUTES)	COVARIANCE CONSTRAINTS	SOLUTIONS WITHOUT MEASUREMENT NOISE			SOLUTIONS WITH MEASUREMENT NOISE		
		ΔR AT TIME FROM EPOCH = $2^h\,55^m$	ΔR AT TIME FROM EPOCH = 6^h	FINAL THRUST SCALE FACTOR, τ	ΔR AT TIME FROM EPOCH = $2^h\,55^m$	ΔR AT TIME FROM EPOCH = 6^h	FINAL THRUST SCALE FACTOR, τ
10	YES	0.089156	0.468314	0.11082982	0.700250	3.484579	0.10912462
20	YES	0.015790	0.117878	0.11102339	- 0.522313	- 2.449648	0.11244073
30	YES	- 0.014962	- 0.029045	0.11110457	0.119525	0.656298	0.11070862
40	YES	- 0.008873	0.001277	0.11108731	0.014806	0.134985	0.11100535
50	YES	- 0.007053	0.010416	0.11108205	- 0.001797	0.043368	0.11106077
60	YES	- 0.011071	- 0.010362	0.11109407	- 0.004126	0.031946	0.11106731
40	NO	- 0.014547	- 0.030515	0.11110770	- 9.1609	-74.52409	0.17437262
50	NO	- 0.017205	- 0.056732	0.11112461	- 1.099791	- 13.097040	0.12361447
60	NO	- 0.017386	- 0.060507	0.11112855	- 0.019558	- 0.68962	0.11187040

5033-14/2-88 [5-2]

NOTES:

ΔR = ALONG-TRACK POSITION DIFFERENCES BETWEEN THE SOLUTION AND THE REFERENCE EPHEMERIS IN KILOMETERS.

THE "TIME FROM EPOCH" IS RELATIVE TO EPOCH 0^h ON 12/21/87.

The tracking measurements used in evaluating the attitude-dependent thrust model (ADTM) were generated by the R&D GTDS Data Simulation (DATASIM) Program (with ADTM enhancements) for a total thrust profile determined by the GMAN Program. The estimations were performed using the GTDS DC Program, modified to include the ADTM enhancements. During the DC Program executions, the magnitude of the input thrust was scaled to 90 percent of the nominal (GMAN) thrust [$\phi = 0.9$, see Equation (10)], so that τ must have the value 0.111111 for good thrust estimation. The use of a single thrust scale factor, τ, results in uniform scaling of all components of thrust.

Comparison of the ranges of τ for noise-free data in Tables 7 and 8 shows the two to be almost identical. The differences between the estimated τ and the ideal τ range from a maximum of 0.3 percent to a minimum of 0.004 percent for noise-free data. The better comparisons are associated with the longer data arcs. The thrust scale factors are also relatively insensitive to the presence or absence of constraints on the a priori state vector for the case of noise-free data.

This is significantly different from the corresponding results for data with measurement noise. With a constrained a priori state, the differences between τ and 0.111111 range from 2 percent to 0.04 percent, but the accuracy is greatly reduced by removing the constraint. For the latter condition, the difference ranges from a maximum of 57 percent, for the smallest data arc in the series (30 minutes), to a minimum of 0.1 percent, for the 60-minute data arc.

This trend is similar to the one observed for the case of along-track thrust; i.e., for the case of data with measurement noise, the final thrust estimation accuracy is very sensitive to the data arc length when the a priori state is also being estimated. These general trends are confirmed by the ephemeris comparisons, which are very large for the shorter data arcs with no covariance constraint and are smaller and relatively insensitive to the data arc length for the case of a constrained a priori state.

3.3 CONCLUSIONS

The following conclusions can be made from the study of attitude-dependent thrust estimation presented above:

- In the case of attitude-dependent thrust, the use of a covariance matrix to fix the initial state vector ensures a reliable estimation of the thrust scale factor using a 10-minute TDRS-W tracking pass beginning 15 minutes from ignition.

- If the state vector and τ are both estimated (i.e., no a priori state covariance constraint is imposed), noise has a considerable effect on the reliability of the solution. If the initial state vector is constrained, however, noise has very little effect.

- To obtain reliable estimates of the state vector and τ, an observation timespan of at least 50 minutes is generally needed.

4. FUTURE DEVELOPMENTS IN THRUST ESTIMATION

Many future missions will make greater demands on the thrust estimation capability of trajectory determination systems. The increased sophistication of spacecraft tracking systems, stricter accuracy requirements, and more complicated attitude and thrust schedules will require thrust estimation systems to provide calibration factors on a near-realtime basis and for more general attitude acquisition scenarios. It would be desirable to have a system capable of handling attitude information from a variety of sources.

The conclusions stated here apply strictly to only the low-thrust, long-burn case. For the case of high-thrust perturbations, numerical problems, associated with the start and end of the burn period, can be anticipated. Analysis is currently being performed to determine if the status of low-burn thrust estimation in GTDS applies to the high-thrust case.

ACKNOWLEDGMENTS

The authors wish to acknowledge the assistance of the following Computer Sciences Corporation personnel: T. Lee, L. J. Bellantoni, H. L. Hooper, and E. J. Smith.

REFERENCES

1. Goddard Space Flight Center, X-582-76-77, Mathematical Theory of the Goddard Trajectory Determination System, J. O. Cappellari, Jr., C. E. Velez, and A. J. Fuchs (editors), April 1976

2. Computer Sciences Corporation, CSC/SD-85/6738, Goddard Trajectory Determination System (GTDS) User's Guide, Revision 2, D. Squier and K. Byers, December 1985

3. Computer Sciences Corporation, CSC/TM-85/6741, Study of Orbit Estimation Techniques, P. S. Lee, S. M. Kirschner, and A. S. Lyubomirsky, December 1987

4. Computer Sciences Corporation, CSC/SD-86/6724, Selected Topics in Orbit Determination, S. M. Kirschner, L. J. Bellantoni, and A. S. Lyubomirsky, January 1987

FLIGHT MECHANICS/ESTIMATION THEORY SYMPOSIUM

SESSION 3

PRECEDING PAGE BLANK NOT FILMED

N89-15948

A Gamma Ray Observatory Ground Attitude Error Analysis Study Using The Generalized Calibration System

E. Ketchum
Code 554/ Flight Dynamics Analysis Branch
Goddard Space Flight Center
Greenbelt, MD 20771

ABSTRACT

The Goddard Space Flight Center (GSFC) Flight Dynamics Division (FDD) will be responsible for performing ground attitude determination for Gamma Ray Observatory (GRO) support. The study reported in this paper provides the FDD and the GRO project with ground attitude determination error information and illustrates several uses of the Generalized Calibration System (GCS). GCS, an institutional software tool in the FDD, automates the computation of the expected attitude determination uncertainty that a spacecraft will encounter during its mission. The GRO project is particularly interested in the uncertainty in the attitude determination using Sun sensors and a magnetometer when both star trackers are inoperable. In order to examine the expected attitude errors for GRO, a systematic approach was developed including various parametric studies. The approach identifies pertinent parameters and combines then to form a matrix of test runs in GCS. This matrix formed the basis for this study.

PRECEDING PAGE BLANK NOT FILMED

I : INTRODUCTION

The Gamma Ray Observatory (GRO) is a 16,000 Kg scientific satellite that will be launched in the early part of 1990. The GRO, built by TRW, will study gamma ray sources throughout the universe. It will point inertially and fly in a circular orbit 400-450 KM from the Earth's surface. The GRO's onboard attitude sensors include two Fixed Head Star Trackers (FHST's), the NASA standard Inertial Reference Unit (DRIRU-II), an Fine Sun Sensor Assembly (FSSA), a Coarse Sun Sensor Assembly (CSSA), and a Three-Axis Magnetometer (TAM). The focus of this study will be on the FHST's, the Sun sensors, and the TAM.

This study investigates the attitude determination errors, compared to available mission requirements, that are likely to occur during the GRO mission. The various sensor combinations examined included two FHST's, a FSS and a FHST, FSSa (and TAM), and CSS (and TAM). Requirements do not exist for the contingency case involving Sun sensors and magnetometer; the study is interested in just how well the Flight Dynamics Division (FDD) can determine GRO's attitude under these circumstances. The FSS/FHST and FHST/FHST cases three sigma requirements are, respectively, 167.5 arcsec and 86.4 arcsec. This study used the Generalized Calibration System (GCS) to examine the scenarios in light of several geometrical and statistical considerations. GCS, an FDD software tool, was a well suited tool for this project because of its ability to produce large quantities of numerical data. Each sensor set up was also investigated using hand calculations (the TRIAD algorithm), which provided intuitive insight not directly seen in the numerical GCS results. These results were also compared to available mission attitude determination requirements and pre-determined capabilities.

GCS is a software tool that can predict state attitude uncertainties using a batch least squares estimator over a specified data span. GCS is generic and can be adapted to virtually any three axis stabilized or spinning spacecraft. It can model the necessary GRO attitude sensors considered in this study (FSS, CSS, TAM, and FHST). GCS is also able to solve for as well as "consider" parameters such as sensor alignment, bias, and scale factors. For a more detailed discussion of the mathematics that GCS employs, see the appendix and reference 1.

Analysis identified pertinent parameters which addressed the necessary geometric and statistical considerations of the GRO mission. Combining these parameters created a systematic GCS run work matrix. The identified parameters, considered over various sensor combinations, include: time from ascending node (spacecraft position in orbit), time of year (Sun position), data batch size (number of frames considered), as well as sensor misalignment. This study varied the time from ascending node in thirds of an orbit (smaller amounts where interesting) and time of year bi-monthly (and semi-monthly where necessary). A batch consists of one or more "frames", where a frame is a set of measurements all taken at one time. A batch size therefore represents the number of frames taken together with, in this case, approximately one minute intervals between frames. The batch

	FSS/TAM	CSS/TAM	FHST cases
STATISTICAL	batch size: single frame two frames : : 2/3 orbit	batch size: single frame two frames : : 2/3 orbit	batch size: single frame two frames : : 2/3 orbit
GEOMETRY A	s/c position time in orbit: minute intervals around orbit	s/c position time in orbit: minute intervals around orbit	
GEOMETRY B	Sun position time of year: bi-monthly	Sun position time of year: bi-monthly	
ALIGNMENT	For FSS/TAM 0 misalignment 1/2 of alignment accuracy spec full spec	for CSS/TAM 0 misalignment 1/2 of spec full spec	for 1)FHST/FSS 2)2 FHSTs 0 misalignment 1/2 of spec full spec

FIGURE 1: WORK MATRIX

size began with single frame solutions and increased in small amounts up to the point where the error is within the requirement (or within reason where no requirement is available). Sensor misalignments were varied from 0 to just over the sensor specification. This information established a GCS work matrix (fig 1); the corresponding GCS runs (using the work matrix as a guideline) identified if and when, with respect to the above parameters, the spacecraft could keep to the attitude determination requirements.

Simple hand calculations using the TRIAD algorithm (ref 2) performed on each sensor combination scenario provided a comparison with and check against the results from GCS. Certain results from the GCS runs can be explained and trusted in light of the hand computations.

The main objective of this project centers on the GRO expected ground attitude determination errors assuming both star trackers are malfunctioning, therefore assuming a sun/magnetometer solution. For comparison and an overall view, nominal scenarios (incorporating the FHST) are also investigated. Results from this study are presented below, contingency cases first followed by the nominal cases. The results are discussed in light of the GCS findings along with hand calculations using the TRIAD algorithm.

II: Attitude Determination Using Fine Sun Sensor and Magnetometer

2.1:Fine Sun Sensor/Magnetometer Configuration

All cases use a 3-2-1 Euler rotation sequence to define the spacecraft attitude. During normal operations, GRO employs at least one FHST for attitude determination. Since the FSS/TAM case is a contingency case, a strictly Sun pointing attitude was assumed which is the nominal backup control mode. Setting up the necessary sensors for the GCS study required modeling GRO's two Fine Sun Sensors as two GCS "Coarse Sun Sensors" (see the appendix), and modeling a TAM. The GCS CSS assumes the boresight to be along the sensor X axis. In order to give the appropriate alignment for GRO's sensors, the three alignment Euler angles (aligning the sensors relative to the spacecraft) used for the two Sun sensors and the TAM are, in degrees (Z,Y,X):

CSS1:(0,-60,0)   CSS2:(0,2,0)   TAM:(180,0,0)

Note that in Sun pointing mode, the Sun is only visible to CSS2. Since this sensor points roughly in the +X (roll) direction, it provides primarily pitch and yaw information and poor roll information.

The scale factors and bias for the Sun sensor measurements are assumed to be 1 and 0 respectively as this study expects these calibration constants to be known. The sensor alignment uncertainty is however considered later. Similarly, the TAM bias vector is also assumed to be 0, initially.

The observation uncertainty for the Sun sensors is 0.022 degrees (ref 3 and 4). This study used 0.4 milligauss as the observation uncertainty for the TAM (ref 3 and 4). These values represent one sigma uncertainty.

Following the work matrix described above, the GRO attitude uncertainties were examined in light of several parameters; considering Sun position, spacecraft position in orbit, batch size, and sensor alignment uncertainty.

Case 1: Variation of Attitude Uncertainty with Batch Size

This case considers several positions in orbit and times of year as the batch size varies. Varying the uncertainty over batch size for different positions in orbit showed that the uncertainty in the attitude estimation rapidly became uniform in pitch and yaw, and wavered only slightly in roll (fig 3). The only exception occurs during Sun sensor occultation, which appears at a different place in each run. During this occultation, the pitch and yaw solution does not improve, therefore creating a flat area in the graph which consequently moves with the time of the occultation. The single frame uncertainties in pitch and yaw are roughly equal to the uncertainty in the Sun sensor. This is not surprising since these sensors have a higher degree of accuracy than the magnetometer and work to determine the attitude in these directions.

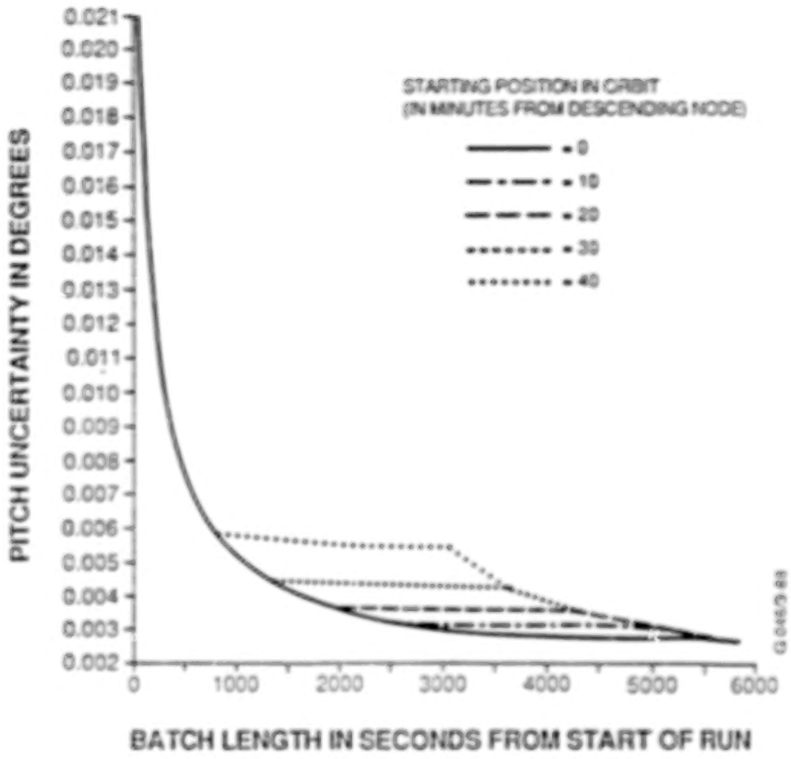

FIGURE 3a
PITCH UNCERTAINTY vs BATCH LENGTH

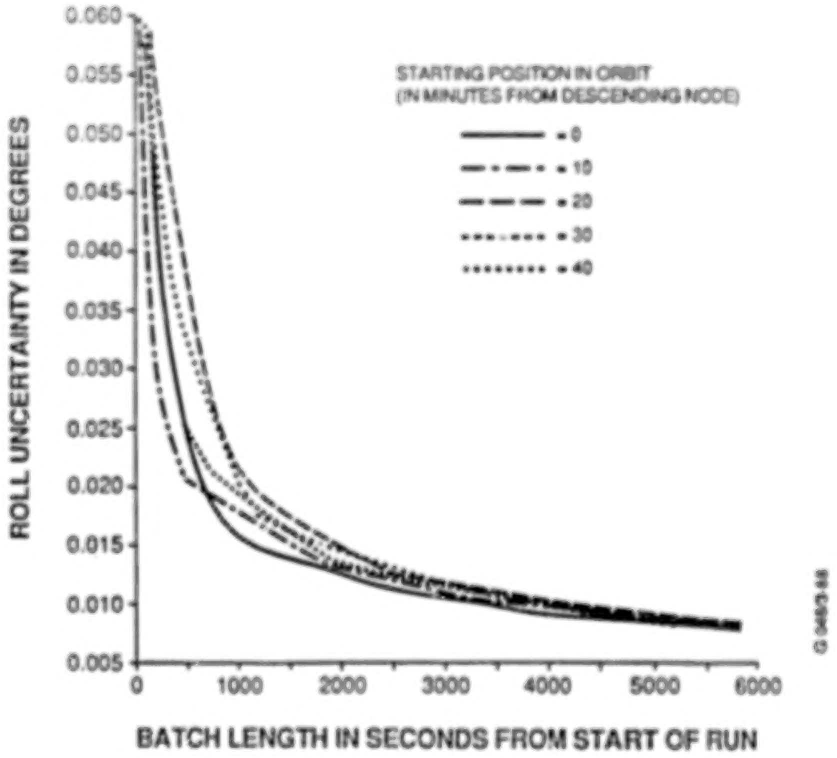

FIGURE 3b
ROLL UNCERTAINTY vs BATCH LENGTH

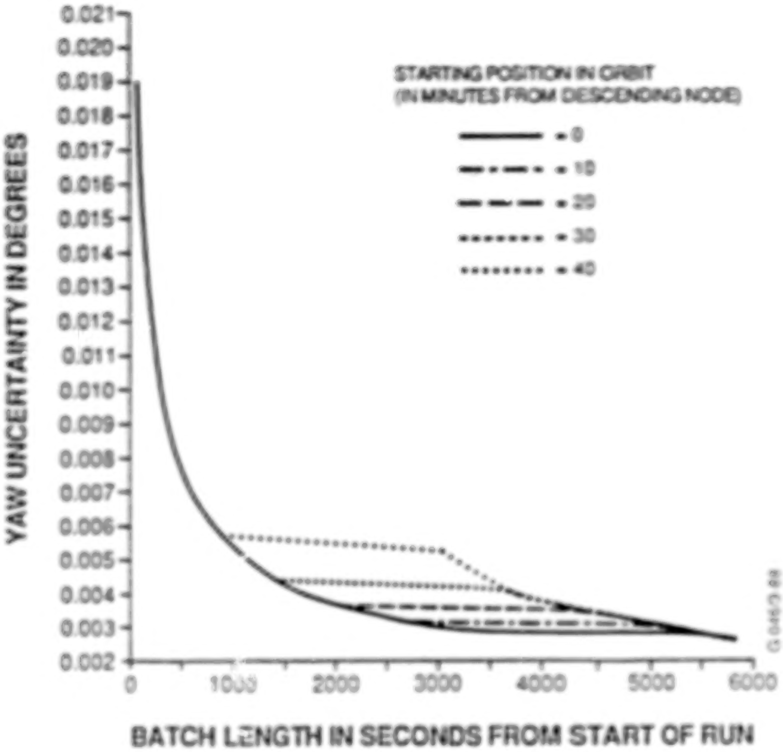

FIGURE 3c
YAW UNCERTAINTY vs BATCH LENGTH

Unfortunately, these results take into account only the random errors for the magnetometer but neglect systematic errors, particularly in the accuracy in the knowledge of the reference magnetic field. Using results obtained for the change in the magnetic field from 1965 to 1975 (ref 5), and considering that the magnetic field is well determined for 1980, (ref 5), the uncertainty of the field for 1990 can be inferred (ref 5). At the GRO altitude of 450 Km, this uncertainty has a one sigma value of 1.8 milligauss.

The incorporation of the additional magnetic field uncertainty requires careful consideration. Including the uncertainty simply as a bias consider parameter, and leaving the TAM measurement uncertainty unchanged is not satisfactory. GCS assumes that the influence of a measurement estimate is weighted inversely to the measurement's uncertainty (see appendix), creating adverse results in pitch and yaw. Maintaining the measurement uncertainty of 0.4 milligauss for the TAM means that these measurements are weighted almost half as heavily as the FSS information. As the batch gets bigger and bigger (more and more measurements included) the solution does not improve as it should but instead gets much worse in parts. Yet, in these directions attitude should be well defined in areas where Sun data is available. The deterioration of the solution exists simply because of the heavy weighting of the increasing amount of poor TAM data.

In the operational attitude determination system, measurement weighting may be specified independently of the true measurement uncertainty. To simulate this in GCS, the TAM measurement uncertainty can be adjusted to include the magnetic field uncertainty. The root-sum-square of the nominal uncertainty of 0.4 milligauss and the additional uncertainty of 1.8 milligauss produces an effective uncertainty of 1.84 milligauss. This results in the proper measurement weighting, but causes GCS to overestimate the intrinsic measurement uncertainty.

The adjusted TAM uncertainty exhibits good results in pitch and yaw (fig 4a and 4c). Note that during Sun occultation, when there is no Sun vector measurement, the poor magnetometer data does cause the solution to worsen. The new TAM uncertainty also gives a fair indication of what occurs in roll (fig 4b), especially as the batch size, and consequently the number of measurements, increases. Using the adjusted uncertainty in this manner actually creates an upper bound to the attitude uncertainty, and as the batch size increases, the bound converges upon the actual attitude accuracy. Figure 4b shows that the roll uncertainty is converging to 0.28 degrees which then implies that the minimum attitude uncertainty in roll is 0.28 degrees (one sigma). Comparing this to the pitch and roll results show that the roll uncertainty is by far the dominant component of the overall attitude uncertainty.

Case 2 : Variation of Attitude Uncertainty with Time of Year

Each of the pitch, roll, and yaw solutions gets better as the batch size increases (from single frame up to a full orbit of data containing nearly 100 measurements). Figure 5 shows the uncertainties versus different times of the year for a variety of batch sizes. These plotsuse, for the batch start time, the ascending node. Each batch on these plots start at 60 seconds from ascending node; other starting positions in the orbit display similar results.

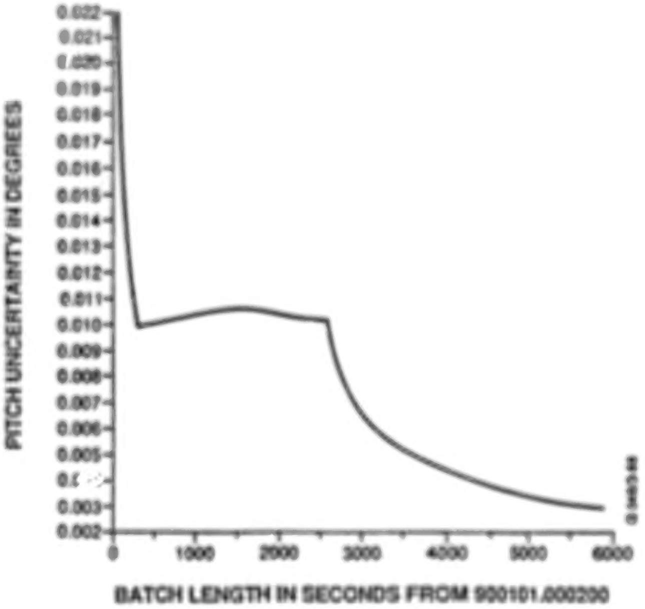

FIGURE 4a
PITCH UNCERTAINTY vs BATCH LENGTH

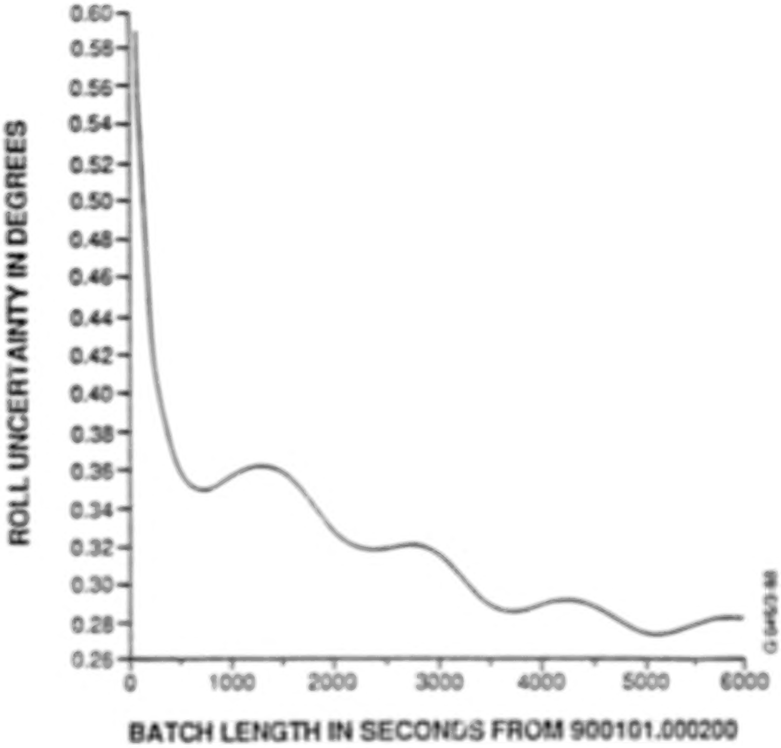

FIGURE 4b
ROLL UNCERTAINTY vs BATCH LENGTH

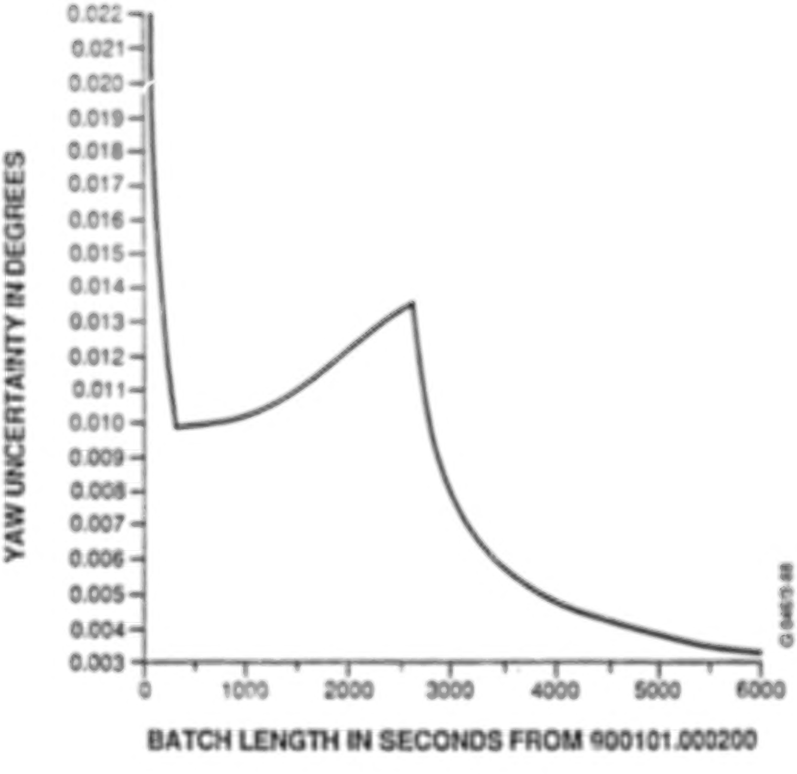

FIGURE 4c
YAW UNCERTAINTY vs BATCH LENGTH

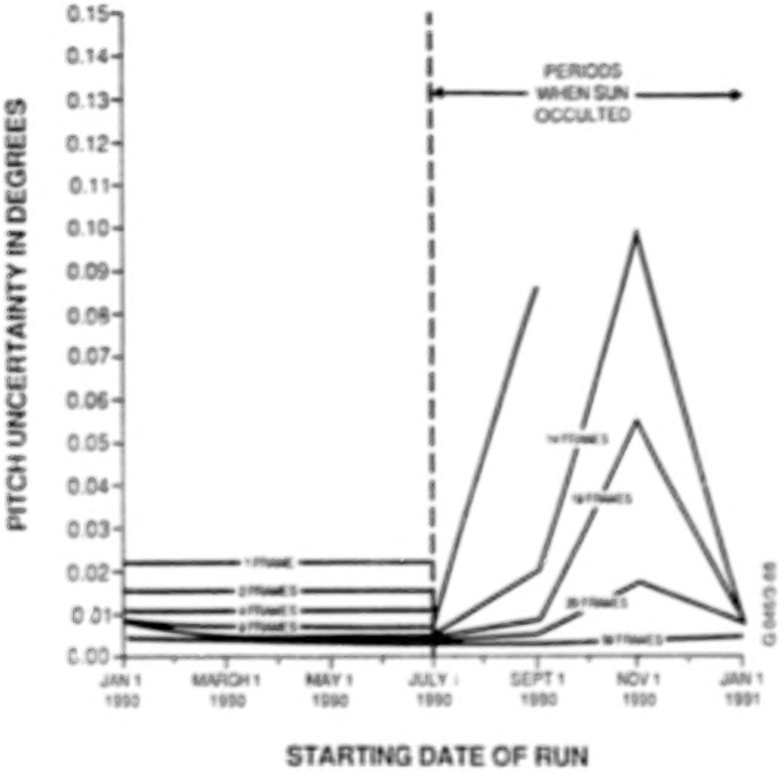

FIGURE 5a
PITCH UNCERTAINTY vs SUN POSITION
FRAMES - 61 SECONDS APART

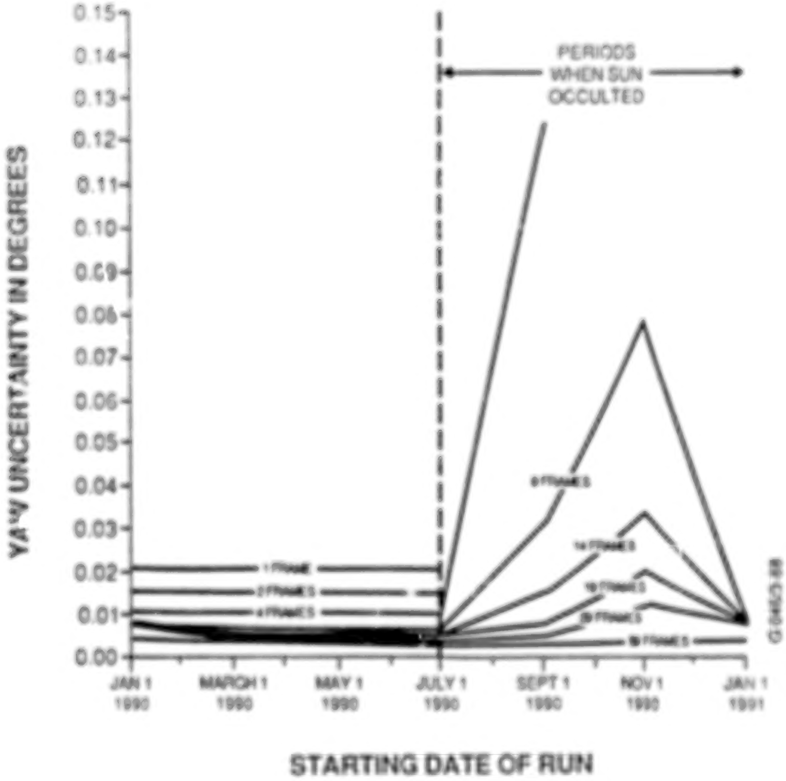

FIGURE 5b
YAW UNCERTAINTY vs SUN POSITION
FRAMES - 61 SECONDS APART

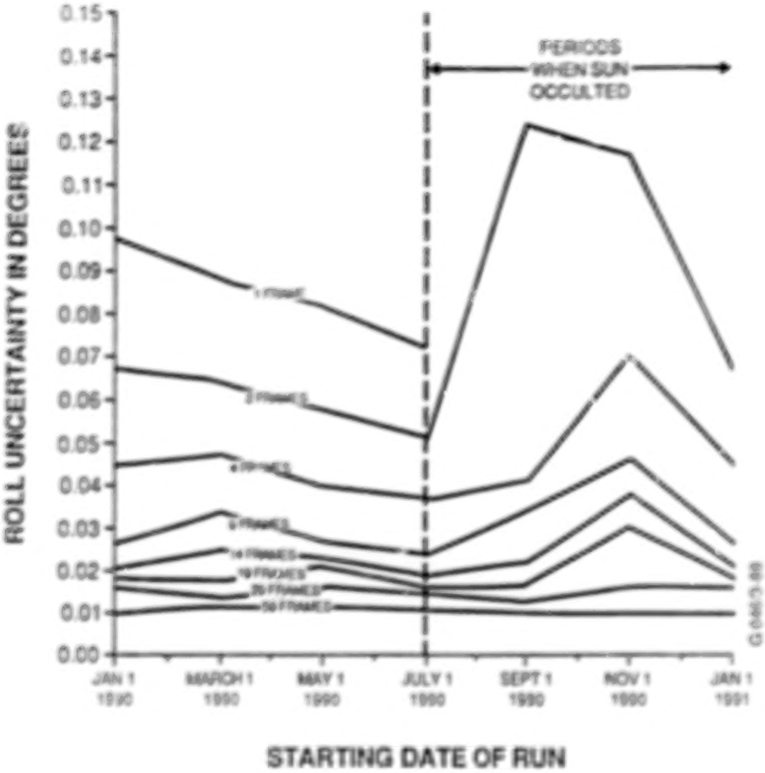

FIGURE 5c
ROLL UNCERTAINTY vs SUN POSITION
FRAMES - 61 SECONDS APART

In each of pitch, roll, and yaw the single frame solution is accurate to better than 0.1 degrees assuming that the Sun sensors receive data. In fact, pitch and yaw can be determined to 0.022 (the accuracy of the Sun sensors) single frame. After only two measurements, roll can be determined roughly as well without Sun as the single frame with Sun. Roll can be determined with Sun better than 0.07 degrees. Two frames in pitch and yaw yield 0.015 degrees uncertainty. The accuracy steadily increases in each direction to better than 0.01 degrees after 60 frames (or roughly an hour or 2/3 of an orbit in this case) with or without Sun coverage.

Again, however, the systematic errors that the magnetometer encounter need to be considered. By including the error in the uncertainty (to correct the weighting) as in Case 1, the results become more realistic. Because of the low weighting of the TAM information the pitch and yaw results remain virtually the same as without the systematic errors except in the smaller batches when there is no Sun coverage and the attitude error is exceptionally poor. The results improve as the batch size increases and Sun data is available in every batch - batches bigger than 30 minutes. However, the systematic error contributes several things to roll results. The results shift upward to give an initial uncertainty for the single frame solution of roughly 0.5 degrees. The error decreases slightly as the batch size increases, but not as significantly as when not considering the systematic error. One last impact of this new error on roll results is that it effectively puts a floor on the accuracy of 0.28 degrees, just as seen in case one.

Case 3 : Variation of Single Frame Attitude Uncertainty with Orbit Position

The single frame pitch and yaw uncertainties changed very little through the course of an orbit (except when there is earth occultation of the Sun and the uncertainty becomes infinite) and the course of the year. The pitch and yaw show 0.022 degrees uncertainty consistently, dependent only on the Sun sensor uncertainty.

However, the roll uncertainty (fig 6) varies with changes in the Sun and spacecraft position, and consequently the change in the angle between the Sun vector and the magnetic field vector. These results show that roll can be determined to 0.13 degrees at worst and about 0.055 degrees at best. When including the systematic error in the TAM, the results behave similarly but indicate larger uncertainties. The uncertainties are scaled upward, with the best results approximately 0.3 degrees and the worst roughly 0.4 degrees.

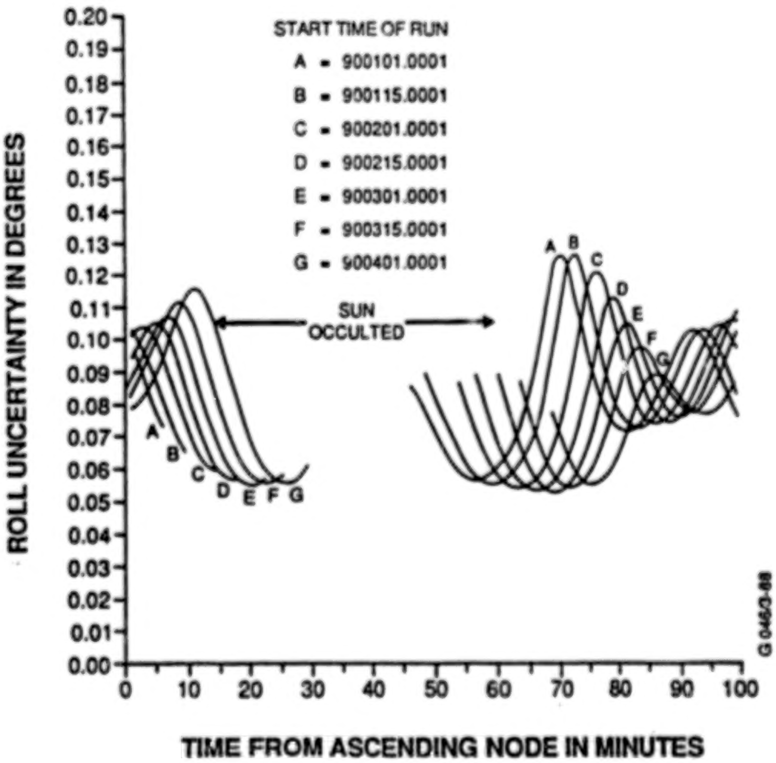

FIGURE 6
ROLL UNCERTAINTY vs SUN POSITION –
SINGLE-FRAME SOLUTION

C-4

Case 4 : Effect of Alignment Uncertainty

Combinations of several of the previous cases became benchmark runs to consider the effect of alignment uncertainty. Variation from previous cases was on the order of 10^2 degrees, roughly the order of the specification for the sensor three sigma misalignments. In general, this additional uncertainty is not of great concern.

2.2: Deterministic Attitude Estimate Study

For this contingency scenario using only a single FSS and a TAM, it is assumed that the GRO spacecraft is in Sun pointing mode. In configuring a TRIAD analysis, the FSS boresight, which GCS requires to be the X-axis (see appendix), therefore points almost directly at the Sun. Using this information, the general case of the FSS/TAM can be configured in two unit vectors (ref 7):

$$\hat{W}_1=(1,0,0)^T \qquad \hat{W}_2=(M_x,M_y,M_z)^T$$

Where $\hat{W}_1$=the Sun unit vector observed from the Sun sensor
$\hat{W}_2$=the magnetic field vector observed from the TAM

The TRIAD algorithm is a deterministic method for computing the attitude from two vector measurements (ref 2). Using the TRIAD algorithm, it can be shown that the x,y,z (roll, pitch, yaw) attitude covariance is:

$$P = \sigma_1^2 I + (1/\sin\gamma)[(\sigma_2^2-\sigma_1^2)\begin{bmatrix}1&0&0\\0&0&0\\0&0&0\end{bmatrix} + \sigma_1^2\cos\gamma\left(\begin{bmatrix}1\\0\\0\end{bmatrix}\hat{W}_2^T+\hat{W}_2[1\ 0\ 0]\right)$$

$$= \begin{bmatrix} \sigma_1^2+(1/\sin^2\gamma)(\sigma_2^2-\sigma_1^2+2\sigma_1^2\cos^2\gamma) & \sigma_1^2\tan\gamma\cos\psi & \sigma_1^2\tan\gamma\sin\psi \\ \sigma_1^2\tan\gamma\cos\psi & \sigma_1^2 & 0 \\ \sigma_1^2\tan\gamma\sin\psi & 0 & \sigma_1^2 \end{bmatrix}$$

where: γ=the angle between $\hat{W}_1$ and $\hat{W}_2$
ψ=90 degrees - γ
σ_1=the Sun sensor measurement uncertainty
σ_2=the TAM measurement uncertainty

From P, roll is the only direction that gamma effects, and only σ_1 contributes to pitch and yaw. The single frame GCS results confirm this.

Case 3 shows how the single frame solution changes around an orbit. Figure 6 displays the change in roll, the only direction affected by the changing gamma. Assuming the magnetic field model is roughly a dipole, the roll accuracy should not change much over the course of the GRO's low 28.5 degrees orbit. The GCS results, varying only 0.1 degrees around the orbit, confirm this. However, clear variations can be seen in the GCS results. Choosing the same position in orbit, different times of year yield different uncertainties. At 65 seconds from ascending node (roughly 2/3 of an orbit) for example, on January 1 in that position the uncertainty is high and on March 1 it is relatively low. The TRIAD result confirms this: Figure 7 shows that γ is larger on March 1 than on January 1, and the formula for P indicates that this will yield a smaller roll uncertainty.

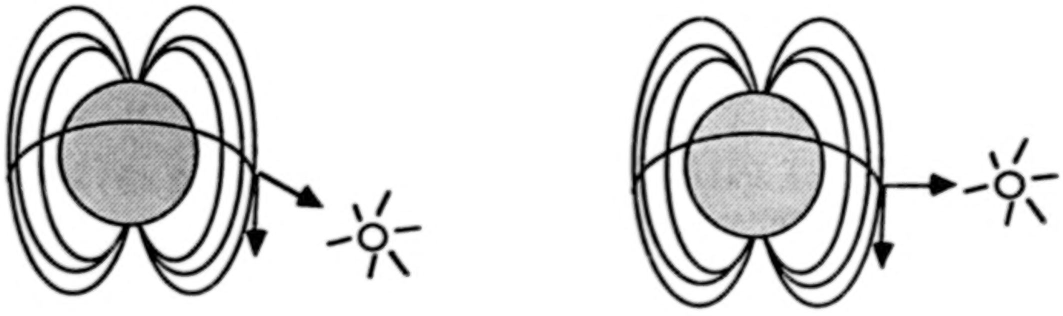

JANUARY 1

MARCH 1

FIGURE 7

3.2: Coarse Sun Sensor/Magnetometer Configuration

Spacecraft and Sensor Assumptions

Benchmark cases were run for a coarse Sun sensor and magnetometer scenario paralleling the FSS/TAM study (section 3.1). The GRO CSS's are all in the same plane, and in Sun pointing mode this plane is perpendicular to the spacecraft X axis. The four CSS measurements are combined in pairs to produce two angular Sun measurements relative to an effective boresight along the X axis. This may be modeled using a single GCS Sun sensor model aligned with the boresight along the X axis :

CSS :(0,0,0)

The effective uncertainty for the GCS model is then set to 0.707 (see appendix) times the actual analog CSS uncertainty. The actual CSS uncertainty is 0.33 degrees (one sigma). The results for each of the cases run for FSS/TAM scenario turned out to follow the results of the cases involving the FSS/TAM. Each case gave similar results qualitatively to the FSS scenario. The GRO CSS is much less accurate than the GRO FSS which results in a consistently less accurate solution.

When only considering the random error in the magnetometer model, the attitude solution is as good as 0.1 degrees in pitch and yaw and 0.25 degrees in roll after more than 20 frames of data. When including the systematic error, as in the case of the FSS, the pitch and yaw results remain unchanged. However, roll can only be determined to between 0.6 and

0.7 degrees single frame and never better than 0.5 degrees as the batch size increases (one sigma).

The similarities in the results between the FSS and the CSS case are reasonable in that they both represent one (effective) sun sensor measurement, intuitively they should only differ by a scale factor.

III: Attitude Determination Using Star Trackers

3.1: Star Tracker/Sun Sensor Configuration

For completeness and comparison purposes, this study also includes normal operation scenarios. During normal operations, the GRO is inertially pointing. A specific position in orbit, time of year, and proper FSS and FHST were selected to provide sufficient sensor coverage. The FHST was aligned and its measurement uncertainty set according to spacecraft and sensor specifications.

Results of benchmark runs (similar to those made for the contingency cases) show that GCS predicts that the spacecraft will be able to meet ground attitude requirements. Assuming some sensor coverage, an accuracy of better than 0.005 degrees one sigma can be achieved in each direction with only two or three frames of results. The three sigma requirement is 167.5 arcsec per axis which converts to roughly 0.047 degrees; the one sigma results obtained show that the attitude can be determined to 0.015 degrees three sigma with only a few measurements - well within the requirement.

The TRIAD calculations employed in the FSS/TAM scenario can be examined in a similar fashion for the FSS/FHST case. Because the spacecraft is no longer Sun pointing, the TRIAD set up must be adjusted. However the spacecraft can be simply assumed to be star pointing instead of Sun pointing. Because the FHST is the more accurate of the two sensors, it should be the first of the two vectors ($\hat{W}_1$ in section 2.2). So again, only roll will be effected by the uncertainty of both sensors, where pitch and yaw will be determined only by the FHST. The angle separating the two measurement vectors is small at roughly 135 degrees because of the relative alignment of the sensors and their fields of view. This checks out in the GCS results in that pitch and yaw show similar results where roll appears slightly worse.

3.2: Two Star Tracker Configuration

Using a setup for two FHSTs as prescribed by sensor and spacecraft specifications, benchmark cases were again examined similar to the study done for the FSS/FHST scenario. Sensor coverage is not so much a factor (except for Earth occultation) so virtually any attitude and time suffices for the study.

Results of the benchmark runs again show favorable results. Single frame solutions are as good as 0.055 in pitch and roll and 0.0035 in yaw. After roughly five frames of measurements, pitch and roll are known to 0.025

degrees and yaw to 0.002 degrees one sigma. After a short period of receiving data in both sensors, attitude can be determined to better than 0.005 degrees in pitch and roll and 0.001 in yaw. These latter results - assuming a small amount (one/two frames) of data in both sensors - compare well with the requirement. The three sigma requirement for two FHSTs is 86.4 arcsec per axis. Converting the GCS results, when there is data from at least one sensor, attitude can be determined to at best 54 arcsec per axis (yaw can be determined to 11 arcsec) three sigma.

IV: Conclusions

The GCS study for the contingency FSS/TAM scenario investigated in this paper shows that pitch and yaw can be determined quite accurately without the use of FHSTs. The three sigma result in these directions is 0.066 degrees for a single frame solution. Increasing the batch size does improve the solution, when the Sun is visible to the Sun sensors. Over a large batch of 60 frames (measurements a minute apart) or more, the three sigma pitch and yaw uncertainty improves to better than 0.009 degrees. Including geometric considerations does not alter the pitch and yaw results. As long as the Sun sensor is receiving data and/or the batch spans the eclipse, these results are valid for any time of the year or position in orbit. Although small misalignment uncertainties do not affect the results significantly, a more detailed study with larger variations outside the GRO specification could be useful.

Roll cannot be determined as well as pitch and yaw using FSS/TAM in Sun pointing mode, it can still be determined to a reasonable uncertainty. Again, geometric considerations did not change results dramatically; section 2 notes subtle changes through position in orbit and time of year. With careful handling of systematic TAM errors, a single frame solution yields a three sigma uncertainty of approximately 1 degree. Over a large batch, the three sigma uncertainty approaches 0.75 degree.

The results for CSS/TAM parallel the FSS/TAM scenario while having consistently higher uncertainty in each direction. When examining a batch of 20 frames or more, the three sigma pitch and yaw uncertainty is 0.3 degrees. In roll, the three sigma uncertainty including only random errors is 0.75 degrees. Including systematic errors, the roll single frame solution can only be determined to between 1.8 and 2.1 degrees three sigma. Over a large batch, the three sigma uncertainty in roll including systematic errors remains over 1.5 degrees.

Overall, The GRO attitude can be determined to roughly 0.75 degrees (three sigma) using FSS/TAM and to 1.5 degrees (three sigma) using CSS/TAM. It has been shown that virtually all of this error is in roll; the direction of the X axis can therefore be determined quite well but the roll rotation about this axis is difficult to determine.

GCS proved to be an excellent software tool to examine the GRO ground attitude error. GCS provided the flexibility to perform several different parametric studies. GCS also generated a large quantity of numerical results necessary for attitude error analysis. With the addition of simple hand calculations, GCS results furnished insight into the existence and growth of attitude errors.

Appendix

This appendix examines the mathematics used in GCS, including overview descriptions of the filter GCS assumes and the covariance analysis it employs. This section also describes the GCS consider parameter and its uses. GCS spacecraft sensor modeling is discussed as well. This section addresses how the Attitude Ground Support System determines attitude operationally is addressed in light of the GCS system.

A.1 Batch Least Squares Filter, Loss Function, State Estimate, and Covariance Analysis

The methods used in GCS to calculate attitude determination errors are much like those used to determine attitude near real time for GRO operationally. Both systems assume a batch least squares filter, and results can therefore be readily compared; even though the real time attitude determination system uses a different method (QUEST), results can still be compared qualitatively to GCS output. Although GCS does not actually model the filter that the fine attitude determination system does- a batch least squares filter (GCS does not use a filter at all, it never actually estimates the state parameters using real data) - the manner in which the GCS covariance analysis predicts the attitude accuracy does involve using selected observations from a batch least squares filter. So in order to clearly describe the covariance analysis performed in GCS, a brief discussion of the batch least squares filter is useful.

In general, the batch least squares filter, in computing the state vector value that best fits some data, works to minimize the residual error in the attitude estimate. Simply put, minimizing the weighted sum of the squares (of the components) of the residual error results in the best fit. The resulting loss function (to be minimized) is therefore:

$$J = 1/2\ [\vec{y} - \vec{y}_c]\ W\ [\vec{y} - \vec{y}_c] \qquad \text{(A-1)}$$

where : $\vec{y}$=real measurements made up of:

$\vec{y} = \vec{y}_c(\vec{x}_t) + \vec{v}$

$\vec{y}_c$= computed predicted sensor measurements as a function of the true state ($\vec{x}_t$)

$\vec{v}$= random measurement noise

therefore $[\vec{y} - \vec{y}_c] = \Delta\vec{y}$= residual error

W=weighting matrix

The weighting matrix used in GCS is the inverse of the measurement covariance matrix, M, which is a diagonal matrix whose diagonal elements are the expected standard deviation in the uncertainty of its corresponding measurement. So an observation with a high uncertainty gets little weight.

It is important to note that since M is a diagonal matrix, with zeros off the diagonal, GCS assumes there is no correlation between the observations. Assuming that the observations have a gaussian noise distribution and since these observations are weighted by W, the inverse of the measurement covariance matrix, this least squares fit turns out to be the Maximum Likelihood Estimate (MLE).

Lastly, GCS includes, in its filter model, some a priori knowledge of the state vector. This a priori knowledge is expressed in the form of an initial state covariance matrix and is the expectation value of $[\vec{x}_0\vec{x}_0^T]$, where $\vec{x}_0$ is the a priori estimate:

$$P_0 = E\,[\vec{x}_0\vec{x}_0^T] = \begin{bmatrix} u_1^2 & 0 & 0 \ldots\ldots\ldots\ldots 0 \\ 0 & u_2^2 & 0 \ldots\ldots\ldots\ldots 0 \\ \vdots & & \vdots \\ \vdots & & \vdots \\ 0 \ldots\ldots & \ldots\ldots & \ldots\ldots u_n^2 \end{bmatrix} \qquad \text{(A-2)}$$

Each of the diagonal elements in P_0 is the square of the standard deviation - representing the uncertainty in the corresponding state parameter. Again there is no correlation in the initial state uncertainties as seen in the off diagonal zeros. So including this a priori knowledge, $\vec{x}_0$, in the loss function to be minimized, it reads:

$$J=1/2(\vec{y}-\vec{y}_c)^T\, W(\vec{y}-\vec{y}_c) + 1/2(\vec{x}-\vec{x}_0)\; P_0^{-1}(\vec{x}-\vec{x}_0) \qquad \text{(A-3)}$$

To minimize J, the partial derivatives with respect to each state element are set equal to zero, creating simultaneous equations corresponding to each of the undetermined state vectors:

$$0=\frac{\partial J}{\partial \vec{x}} =(\vec{x}-\vec{x}_0)^T P_0^{-1}-(\vec{y}-\vec{y}_c)^T W \frac{\partial \vec{y}_c}{\partial \vec{x}} \qquad \text{(A-4)}$$

These equations are solved iteratively and are made linear about the previous estimate, $\vec{x}_k$. Begin with the a priori state estimate:

$$\vec{y}_c= \vec{y}_c(\vec{x}_k) + H(\vec{x}-\vec{x}_k) \qquad \text{(A-5)}$$

Where: H = matrix of partials evaluated at $\vec{x}_0$

The new state estimate can therefore, using equation (A-5) in equation (A-4), be expressed as:

$$\vec{x}_{k+1}= \vec{x}_k+(P_0^{-1}+H^TWH)^{-1}(H^TW(\vec{y}-\vec{y}_c(\vec{x}_k))+P_0^{-1}(\vec{x}_0-\vec{x}_k)) \qquad \text{(A-6)}$$

This equation is iterated until convergence is achieved. The expected uncertainty in the estimate can be derived in the following manner. If $\vec{e}$ is the error representing the difference in the computed state from any given state determination (using real data that contains noise), then the covariance matrix P represents the expected value of $\vec{e}\vec{e}^T$. Using equation

(A-6) and making $\vec{x}$ the new state estimate, the state can be adjusted until convergence is reached:

$$P_0^{-1}(\vec{x}-\vec{x}_0+(\vec{x}-\hat{\vec{x}}))=H^TW[\vec{y}-\vec{y}_c(\vec{x})+H\ (\vec{x}-\hat{\vec{x}})] \qquad \text{(A-7)}$$

where: $\bar{x}$=the true state
$\hat{x}$=the converged estimate

Letting $\vec{v}$ be the resulting noise in the measurements, $\vec{e}=\vec{x}-\hat{\vec{x}}$ be the difference between the true state and the converged estimate, and using equation (A-7), it can be shown that:

$$P = E(\vec{e}\vec{e}^T) = (P_0^T+H^TWH)^{-1} \qquad \text{(A-8)}$$

GCS uses this covariance equation. The final state uncertainty results that come from GCS are the standard deviations acquired by taking the square roots of the diagonal elements of the final covariance matrix.

A.2 Consider Parameters

GCS gives the user the ability to incorporate parameters that are not necessarily estimated (or "solved for"), yet whose uncertainties could still effect state uncertainties (in addition to any measurement noise effect), hence the name "consider parameter." Any parameter that GCS employs as a possible state parameter can instead be used as a consider parameter.

Let $\vec{x}_c$ represent the consider parameters. Also let H_c be the matrix containing the partials of the measurements with respect to the consider parameter. The effect of the consider parameter error, $\vec{e}_c$, on a first order estimate of the state measurement error can be shown :

$$d\vec{y}_c = H_c\ \vec{e}_c \qquad \text{(A-9)}$$

Then by adding the effect of the consider parameter to the effect of the noise the adjusted state (which is being solved for) can be computed:

$$\vec{e}=(P_0^{-1}+H^TWH)^{-1}(P_0^{-1}\vec{e}_0-H^TWH_c\vec{e}_c+H^TW\vec{v}) \qquad \text{(A-10)}$$

where: $\vec{e}_0$=a priori state error
$\vec{v}$=noise

Taking the expected value of the product of $\vec{e}\vec{e}^T$, it can be shown that :

$$P=E[\vec{e}\vec{e}^T]=P_s+P_sQ_cP_cQ_c^TP_s \qquad \text{(A-11)}$$

where: $P_s=(P_0+H^TWH)^{-1}$ for compactness
$Q_c=H^TWH_c$ for compactness
$P_c=E[\vec{e}_c\vec{e}_c^T]$=the consider parameter covariance matrix, a diagonal matrix with the diagonal elements representing the expected uncertainty in the corresponding consider parameter

$P_S Q_C P_C Q_C^T P_S$ therefore represents the consider parameter contribution to the covariance. It is this equation (A-11) that GCS uses to calculate the state covariance assuming the existence of consider parameter effects. It should also be noted that the contribution from each of the consider parameters is independent (since the covariance matrix in (A-11) is diagonal), and that GCS computes the separate as well as the total contribution.

A.3 Sensor Modeling in GCS- GRO Specific

This subsection describes how GCS models the sensors on the GRO, including the Fixed Head Star Tracker (FHST), the Fine Sun Sensor (FSS), the Coarse Sun Sensor (CSS), and the Three Axis Magnetometer (TAM). GCS models other sensors (including those for spinning spacecraft) whose models are not considered here. For the partial derivatives pertaining to these sensor models in GCS, see appendix I of reference 1.

A.3.1 Fixed Head Star Trackers

GCS models two FHST's either simultaneously or separately (and/or in conjunction with other sensor(s)). GCS defines the FHST coordinate system such that X_S is along the sensor boresight, Y_S is along the direction of the +V measurement, and Z_S is positioned so that X_S, Y_S, Z_S form a right handed coordinate system. The horizontal and vertical coordinates of the star locations in the FHST field of view, Y_H and Y_V respectively, are defined in GCS:

$$y_H = (1/S_H)\ (H + b_H) \qquad \text{(A-12)}$$

$$y_V = (1/S_V)(-V + b_V) \qquad \text{(A-13)}$$

where : $H = \tan^{-1}[F_{SZ}/F_{SX}]$ (A-14)

$V = -\tan^{-1}[F_{SY}/F_{SX}]$ (A-15)

$(F_{SX}, F_{SY}, F_{SZ}) = F_S$, the unit star vector in the FHST sensor coordinate system.

The angle H rotates from the $\hat{y}_S$-$\hat{F}$ plane to the $\hat{y}_S$-$\hat{x}_S$ plane about the $\hat{y}_S$ axis. The V angle rotates from the $\hat{z}_S$-$\hat{F}$ plane to the $\hat{z}_S$-$\hat{x}_S$ plane about $\hat{z}_S$. The state parameters are:

$$y_h = y_h(p, r, y, \phi_1, \phi_2, \phi_3, S_H, b_H) \qquad \text{(A 16)}$$
$$y_v = y_v(p, r, y, \phi_1, \phi_2, \phi_3, S_V, b_V) \qquad \text{(A 17)}$$

where p,r,y = pitch, roll, and yaw
ϕ_1, ϕ_2, ϕ_3=sensor alignment parameters
S_H, S_V=sensor scale factors
b_H, b_V=sensor biases

A.4.2 Fine Sun Sensor

Although GCS has a Fine Sun Sensor model, the GCS Coarse Sun Sensor more closely models the GRO FSS uncertainties in that the GCS CSS is a digital sensor like GRO's FSS and the GCS CSS presents the simpler model (which is sufficient to model GRO's FSS). GCS can model up to three CSS's simultaneously; when modeling GRO, only two are necessary. The sensor detects the Sun's direction (expressed as a unit vector in CSS coordinates, which can be transformed to the unit Sun vector, S_I in GCI coordinates):

$$\hat{S}_S=(S_{SX},S_{SY},S_{SZ}) \qquad \text{(A-18)}$$
$$=[M][B][A]\,\hat{S}_I \qquad \text{(A-19)}$$

where: [M], [B], [A] = matrix coordinate transforms

in terms of an α angle and a β angle (fig 8). GCS corrects these measurements using calibration coefficients, A_1,A_2,B_1,B_2:

$$N_\alpha = 1/A_2\ (\alpha - A_1) \qquad \text{(A-19)}$$
$$N_\beta = 1/B_2\ (\beta - B_1) \qquad \text{(A-20)}$$

and

$$\alpha = \tan^{-1}(S_{SY}/S_{SX}) \qquad \text{(A-21)}$$
$$\beta = \tan^{-1}(S_{SZ}/S_{SX}) \qquad \text{(A-22)}$$

This GCS model assumes that the CSS boresight is along the X_S-axis, α is the projected sun angle in the X_S-Y_S plane, and β is the projected sun angle in the X_S-Z_S plane. The state parameters for the GCS CSS are:

$$N_\alpha = N_\alpha\,(p,r,y,\phi_1,\phi_2,\phi_3,A_1,A_2) \qquad \text{(A-23)}$$
$$N_\beta = N_\beta\,(p,r,y,\phi_1,\phi_2,\phi_3,B_1,B_2) \qquad \text{(A-24)}$$

where : p,r,y = attitude parameters that define [B]
ϕ_1,ϕ_2,ϕ_3=CSS alignment parameters (defining [M])
A_1,B_1,A_2,B_2 =sensor calibration parameters

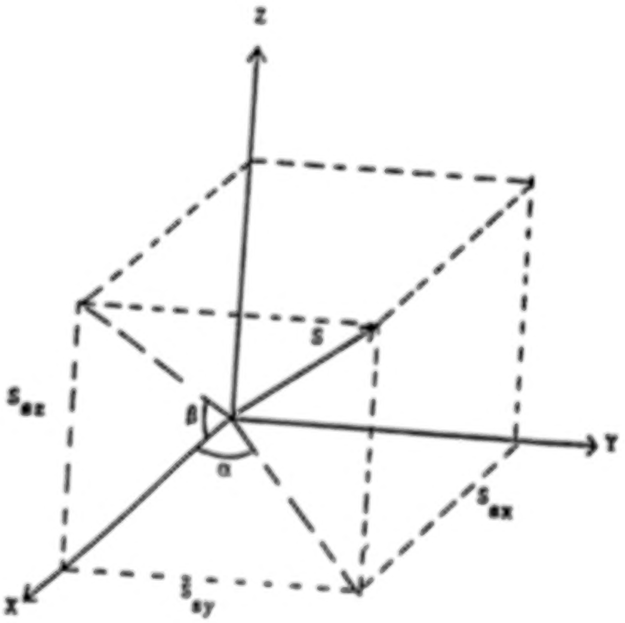

FIGURE 8. DIRECTION OF SUN VECTOR IN CBS

A.4.3 Coarse Sun Sensor

GRO's CSS is an analog sensor which is not modeled by GCS. However,a scale factor was determined so that the GCS CSS model, described in A.4.2, could be used. It can be shown that:

$$\sigma_2 = \sqrt{2}/2 \quad \sigma_1 \qquad \text{(A-25)}$$

where σ_1= uncertainty for the GRO CSS
σ_2= uncertainty for the GCS CSS

A.4.4 Three Axis Magnetometer

In GCS the TAM measurement vector in the sensor frame is in the direction of the geomagnetic vector:

$$\begin{aligned} \vec{Y} &= [M][B][A]\vec{H}_I + \vec{b} && \text{(A-25a)} \\ &= [M][B]\vec{H}_R + \vec{b} && \text{(A-25b)} \end{aligned}$$

where [M],[B],[A] =transformation matrices (see ref 1, 3.3)
$\vec{H}_I$=geomagnetic field in GCI coordinates
$\vec{H}_R$=" " reference coordinates
$\vec{b}$=bias

GCS uses the magnetic field model from the subroutine MAGFLD (ref 5). The state parameters for the GCS TAM are:

$$Y = Y(p, r, y, \Phi_1, \Phi_2, \Phi_3, \vec{b}) \qquad \text{(A-26)}$$

where: p,r,y=attitude parameters defining [B]
Φ_1, Φ_2, Φ_3=alignment parameters defining [M]
b=constant bias vector

Acknowledgement

The author would like to thank Mr. E. Seidewitz and Dr. F. L. Markley of MASA Goddard Space Flight Center for their help, guidance, and insight.

References

1. Blaisdell, Bilanow, Chen, Talukdar, and Seidewitz "Generalized Calibration System (GCS) Version 2.3 User's Guide," General Sciences Corporation, GSC-TR8713, April, 1987.

2. Shuster, M.D. and Oh, S.D. "Three Axis Attitude Determination from Vector Observations," Journal of Guidance, Control, and Dynamics, Vol. 4, No. 1, Jan/Feb 1981, pp 70-77.

3. Tracewell, D., Ketchum, E., Harman, R., "GRO Mission, Flight Dynamics Analysis Report: Review of Sensor Characteristics (Analysis Item A3.3)," May, 1988.

4. TRW, "Gamma Ray Observatory Mission Contract Critical Design Audit Package Volume II," 40420-85-231-008.

5. Wertz, J. R., *Spacecraft Attitude Determination and Control*. Dordrecht: D. Reidel Publishing Company, 1978.

N89-15949

AN ANALYSIS OF THE KALMAN FILTER IN THE GAMMA RAY OBSERVATORY (GRO) ONBOARD ATTITUDE DETERMINATION SUBSYSTEM

Frank Snow and Richard Harman
Code 554/Flight Dynamics Analysis Branch

Joseph Garrick
Code 552/Flight Dynamics Software Development Branch
Goddard Space Flight Center
Greenbelt, Maryland

ABSTRACT

The Gamma Ray Observatory (GRO) spacecraft needs a highly accurate attitude knowledge to achieve its mission objectives. Utilizing the fixed-head star trackers (FHSTs) for observations and gyroscopes for attitude propagation, the discrete Kalman Filter processes the attitude data to obtain an onboard accuracy of 86 arc seconds (3 sigma).

A combination of linear analysis and simulations using the GRO Software Simulator (GROSS) are employed to investigate the Kalman filter for stability and the effects of corrupted observations (misalignment, noise), incomplete dynamic modeling, and nonlinear errors on the Kalman filter. In the simulations, on-board attitude is compared with true attitude, the sensitivity of attitude error to model errors is graphed, and a statistical analysis is performed on the residuals of the Kalman Filter. In this paper, the modeling and sensor errors that degrade the Kalman filter solution beyond mission requirements are studied, and methods are offered to identify the source of these errors.

1. GAMMA RAY OBSERVATORY

The Gamma Ray Observatory (GRO) is a three-axis stabilized spacecraft scheduled to be launched in 1990 by the Space Transportation System (STS). The GRO science instruments study gamma ray sources between 0.1 and 30000 megaelectronvolts (MeV) before they are absorbed by the Earth's atmosphere. The spacecraft is designed to stay inertially pointed, using reaction wheel control, for 2 weeks at a time before maneuvering to the next gamma ray target. The nominal spacecraft orbit will be 350- to 450-kilometer altitude, 0.0001 eccentricity, and 28.5 degrees (deg) inclination.

GRO is equipped with two National Aeronautics and Space Administration (NASA) standard onboard computers (OBCs) of which one is used as a backup. The OBC performs sensor data processing and actuator commanding. There are five OBC control modes: Standby Mode (SM), Normal Pointing Mode (NPM), Normal Maneuver Mode (NMM), Thruster Maneuver Mode (TMM), and Velocity Control Mode (VCM). The NPM is the gamma ray inertial pointing mode.

GRO has an onboard attitude determination accuracy requirement of 86.4 arc seconds per axis (arc-sec) (3 sigma) during the normal science observation mode. This accuracy is accomplished by the use of two fixed-head star trackers (FHSTs) and an inertial reference unit (IRU). Both of these attitude sensors have been used on the Solar Maximum Mission (SMM), Landsat-4, and Landsat-5 spacecraft. The attitude is propagated using the IRU data and updated after a FHST measurement by using a Kalman filter.

1.1 FHST DESCRIPTION

The FHST is an attitude sensor that searches for, detects, and tracks stars; provides accurate position and intensity information on stars in its field of view (FOV); and generates status flags and parameters that characterize the sensor operation.

When light from the star enters the optical lens, the image of the star is focused on the photocathode of an image dissector tube (IDT), which magnetically deflects and focuses the electrons onto an aperture in a plate. The corresponding signal is amplified and processed to provide intensity and position information. The FHST functions in two operational modes: search and track mode.

In the total field of view (TFOV), a search mode consists of a horizontal scan pattern with appropriate vertical shifts at the ends (raster). Four commandable thresholds set the minimum sensitivity for acquiring a star. Position and intensity output during the search mode do not convey meaningful information.

When a star is acquired, the detector traces a small cross pattern in the form of a figure 8 centered on the star image. A star present flag is set to indicate that star position and intensity data are valid for the tracked star. The track pattern remains locked on the star during attitude changes. If the star leaves the TFOV, if its intensity falls below the commanded threshold, or if a break-track command is received, search mode resumes.

With the optional offset mode capability, a small offset raster scan can be commanded in a reduced field of view (RFOV). If a star is acquired, it will be tracked throughout the TFOV. If the star is lost, a reduced scan will begin at the original position in the RFOV. FHST parameters and values are listed in Table 1.

1.2 IRU Description

The IRU is an attitude sensor consisting of a gyro package that measures inertial vehicle rates about the sensor axis. Output consists of analog rates, accumulated angles, range status, and temperature.

The IRU contains three spinning wheels or rotors. Each rotor is mounted on two gimbals to provide 2 degrees of freedom and, therefore, rate information along two body axes (two-channel output). The

Table 1. FHST Parameters and Values

Parameter	Value
TFOV	8 by 8 deg
RFOV	1.5 by 1.5 deg
Range of star visual magnitude	+5.7 to -7.0
Number of threshold settings	4
Maximum tolerable vehicle rate	0.3 deg/second (sec)
Search mode:	
Scan type	Raster
Number of lines in TFOV	70
Maximum acquisition time	10 sec (TFOV), 1.5 sec (RFOV)
Track mode:	
Scan type	Unidirectional cross-scan
Scan period	100 milliseconds
Output rate	10/sec (each axis)
Accuracy	10/arc-sec (1 sigma) calibrated over 8-deg diameter circular FOV
Nominal data resolution	7 arc-sec

six-channel IRU configuration provides dual redundancy along each body axis. The IRU assembly is fixed in the spacecraft (strapdown). The current required to magnetically torque a gimbal to maintain null deflection (torque rebalancing) is proportional to the accumulated rotation angle (rate integrating) about the corresponding body axis. Torque current is differenced after small intervals of time to generate analog rates. The IRU can operate in either high-rate or low-rate mode (range status). IRU parameters and values are listed in Table 2.

Table 2. IRU Parameters and Values

Parameter	Value
Scale factor stability	±0.01 percent/month (low rate) ±0.1 percent/month (high rate)
Acceleration-insensitive drift rate (AIDR)	±0.04 arc-sec/sec for 30 days of start-stop operation (low rate), ±0.003 arc-sec/sec for 6 hours of continuous operation (low rate), ±0.001 deg/sec for 30 days (high rate)
Nominal data resolution	0.8 arc-sec/count (high rate), 0.05 arc-sec/count (low rate)
High-rate range	±2.0 deg/sec
Low-rate range	±400 arc-sec/sec

1.3 KALMAN FILTER

A Kalman filter combines all available measurement data, plus prior knowledge about the system and measuring devices, to produce an estimate of the state vector such that the error is statistically minimized. The Kalman filter of the GRO flight software uses the error state space formulation method in which the state vector contains the errors in the spacecraft attitude and the gyroscope biases. The state vector is updated whenever there is a measurement by the FHSTs or the fine Sun sensor (FSS).

From the dynamic modeling of the state vector, the Kalman filter computes a noise covariance matrix and then propagates the state covariance matrix from the last filter update. Propagation of this covariance matrix requires the computation of the state transition matrix for the dynamic equations. After propagation of the covariance matrix, the Kalman filter uses the measurement model and the propagated covariance matrix to compute the Kalman gain matrix. From this gain matrix and the measurement residuals, the Kalman filter computes the updated state vector to correct the attitude and gyro drift biases. The last processing in the Kalman filter is to update the covariance matrix to reflect the effects of sensor measurement processing.

2. GRO SOFTWARE SIMULATOR

The primary tool used in this analysis was the GRO Software Simulator (GROSS) developed in the Flight Dynamics Division. GROSS is a closed-loop GRO Attitude Control System (ACS) simulator, which for this analysis consisted of two major functions: the Truth Model (TM) and the functional OBC.

The TM models spacecraft dynamics, environmental torques, and hardware. The environmental models take into account four torques that act to perturb the dynamics. These are the solar radiation, residual magnetic dipole, aerodynamic, and gravity gradient torques. The hardware model reflects a detailed functional description of the actuators, sensors, and moving parts. These models include not only nominal performance, but also biases, noises, misalignments, and failures. The actuators modeled include four reaction wheels, eight attitude control thrusters (ACTs), four orbit adjust thrusters (OATs), and two magnetic torquer assemblies (MTAs). The sensors modeled include two (FSSs), four coarse Sun sensors (CSSs), four reaction wheel tachometers, two FHSTs, an IRU consisting of three gyros and dual-output capabilities per axis, and two three-axis magnetometers (TAMs). The moving parts are the High-Gain Antenna (HGA) and solar arrays, which respond to ground pointing commands. The movement of these create a momentum component to be used in the dynamics. The dynamics modeling uses a fourth-order, variable-step, Adams-Moulton-Bashforth (AMB) numerical integrator.

The functional OBC is GROSS's FORTRAN representation of GRO's onboard flight software. The OBC processes sensor data from the TM, determines the spacecraft attitude, and generates the appropriate control commands based on the control laws for the current mode. The functional OBC and the GRO attitude flight software were coded from the same software specifications. In an attempt to model the spacecraft flight software as closely as possible, the functional OBC executes the same algorithms including the same approximations for trigonometric functions. The Attitude Estimation function in the GROSS OBC is shown in Figure 1.

2.1 GROSS MODELING OF FHST

The FHST model generates the star camera data. The camera is commanded by the OBC to search an RFOV for a guide star. Once a star is acquired by the FHST, and it meets the prescribed restraints, the star is tracked. Output from a star tracker consists of a (u, v) coordinate measured in the camera's focal plane, along with the star's intensity. The camera will continue to track the star until a break-track command is received from the OBC or from the ground, or until the star proceeds to exit the TFOV.

GROSS simulates the search mode by ordering the stars found in the RFOVs associated with the current pointing in the same fashion as would be encountered in a normal search mode. When a star is determined to be the guide star for that RFOV by the OBC, the FHST will hold on that star and do all the processing in the model with this star's position and intensity data. The FHST model will also determine if the line of sight (LOS) is occulted by the Earth, Sun, or Moon and will take the appropriated action by closing the shutter and issuing the appropriate status flag to the OBC, indicating that it is currently inhibited. After the true data are generated, the FHST model will employ a decalibration scheme to corrupt the values sent to the OBC.

In the OBC, the FHST processing routine uses a calibration scheme to correct for temperature, flat field, magnetic fields, and star intensity variations.

GROSS provides the capabilities to operate the FHSTs in other than a nominal condition. The following user-changeable parameters are associated with the star trackers:

- Misalignment of cameras
- Noises per camera per axis
- Biases per camera per axis
- Failures of individual cameras
- Guide stars per RFOV

- Additional stars per RFOV
- Number of RFOV per TFOV
- Number of scan lines per TFOV
- Methods for determining guide stars
- Size of TFOV per camera
- Size of RFOV per camera
- Star magnitude acceptability range
- Responds to normal ground commands

2.2 GROSS MODELING OF IRU

The IRU consists of three rate-integrating gyros and has six channels to measure angular displacement along the three spacecraft body axes. For each axis, one channel is primary and one is backup. For each channel, gyro data generation involves the following two steps: (1) calculating angular displacement and (2) modeling gyro noise to add onto the angular displacement. Angular displacement is calculated as follows:

1. Input angular spacecraft velocity vector, w.
2. Project w along channel input axis, G, to get rate, r, measured by that channel ($r = G * w$) in radians (rad)/sec.
3. Calculate angular displacement by integrating rate.

Gyro noise in GRO comes from two sources:

1. Noise on angular rate. This noise is modeled as Gaussian, zero mean, and white.
2. Noise on the rate of change of the gyro bias. This is noise modeled as Gaussian, zero mean, and white.

These noises are then added to the calculated gyro measurement and sent to the OBC as gyro data.

User-changeable parameters associated with the IRU are as follows:

- Misalignment of IRU
- Gyro rate bias
- Gyro drift

- Gyro drift rate
- Gyro and gyro channel failures

2.3 KALMAN FILTER

The Kalman filter is implemented in two steps. First, the propagation of the internal statistics based on the Dynamics Model and second, updating the state vector based on the Observation Model and the internal statistics.

2.3.1 DYNAMICS MODEL

The Dynamics Model for the GRO flight software Kalman filter is found in References 1 and 2. The gyro rate measurement is assumed to have the following form:

$$\dot{\theta} = w - b_o - b + \eta_v \qquad (1)$$

$$\dot{b} = \eta_u$$

where $\dot{\theta}$ = gyro rate measurement
w = true spacecraft rate
b_o = gyro bias
b = gyro drift bias
η_v = float torque noise (Gaussian white noise)
η_u = float torque derivative noise (Gaussian white noise)

Since b is the integral of a white noise, it becomes a random walk. The attitude rate error $\dot{\psi}$ is formed in the following manner:

$$\dot{\psi} = -b_o - b + \eta_v \qquad (2)$$

The gyro bias b_o is assumed to be known and can be derived from Equation (2). The Dynamics Model is then reduced to the following form:

$$\begin{aligned} \dot{\psi} &= -b + \eta_v \\ \dot{b} &= \eta_u \end{aligned} \qquad (3)$$

If these two equations are put into a linear state space formulation, Equation (4a), Equation (4b) is derived:

$$\dot{X}(t) = F\ X(t) + W(t) \tag{4a}$$

$$\dot{X}(t) = \begin{bmatrix} \dot{\psi} \\ \dot{b} \end{bmatrix} = \begin{bmatrix} 0_{3x3} & -I_{3x3} \\ 0_{3x3} & 0_{3x3} \end{bmatrix} \begin{bmatrix} \psi \\ b \end{bmatrix} + \begin{bmatrix} \eta_{v(3x1)} \\ \eta_{u(3x1)} \end{bmatrix} \tag{4b}$$

where ψ = attitude error

b = gyro drift bias

η_v = float torque noise (Gaussian)

η_u = float torque derivative noise (Gaussian)

$$E[W(t)] = 0$$

$$E[W(t)\ W^T(t')] = \begin{bmatrix} vI_{3x3}\ \delta(t-t') & 0_{3x3} \\ 0_{3x3} & uI_{3x3}\ \delta(t-t') \end{bmatrix} \tag{5}$$

$$Q(t) = E[W(t)\ W^T(t')]$$

where $Q(t)$ is the spectral density matrix.

From Equation (4b) the state transition matrix $\Phi_k = \Phi(t_k, t_{k-1})$ is obtained, which allows one to solve for the dynamic noise covariance matrix, Q_k.

$$Q_k = \int_{t_{k-1}}^{t_k} \Phi(t_k,\tau)\ Q(\tau)\ \Phi^T(t_k,\tau)\ d\tau \tag{6}$$

$$P_k(-) = \Phi_k\ P_{k-1}(+)\ \Phi_k^T + Q_k \tag{7}$$

where $P_k(-)$ = propagated covariance matrix at time k

$P_{k-1}(+)$ = updated covariance matrix at time k-1

2.3.2 OBSERVATION MODEL

In the GRO flight software, the FHST measurements are used to create an observed star unit vector, OS, in the sensor coordinate frame. The identified star position in the star catalog is used to create an expected or computed unit star vector, CS, in the sensor coordinate frame. Then,

$$Z(i) = OS(i) - CS(i) \quad \text{for } i = 1 \text{ to } 2$$

where i = ith coordinate of the vectors

Z = measurement residuals

From this definition of Z, H is shown to be (Reference 3)

$$H_k = \begin{bmatrix} \left(\bar{X} \times \bar{S}_k\right)^T & 0 \\ \left(\bar{Y} \times \bar{S}_k\right)^T & 0 \end{bmatrix} \tag{8}$$

where S_k = observed star in spacecraft body frame

X = X coordinate of FHST in the spacecraft body frame

Y = Y coordinate of FHST in the spacecraft body frame

In the Observation Model

$$Z_k = H_k X_k + V_k \tag{9}$$

where Z_k = observation

V_k = sensor noise (Gaussian)

For sensor noise characteristics,

$$E[V_k] = 0 \tag{10}$$

$$E\left[V_k\ V_1^T\right] = \begin{bmatrix} R_{11} & 0 \\ 0 & R_{22} \end{bmatrix} \tag{11}$$

It is further assumed that the initial state vector X_0 is Gaussian and X_0, W, and V_k are independent of each other. They all are assumed to be Gaussian, which is equivalent to assuming they are uncorrelated.

2.3.2 UPDATE ALGORITHMS

The state vector is updated by processing the following equation with the inputs $P_k(-)$ (Equation (7)), H (Equation (8)), R_k (Equation (11)), and the observation vector Z_k (Equation (9)).

$$K_k = P_k(-)\left[H_k^T\ \ H_k\ P_k(-)\ H_k^T + R_k\right]^{-1} \tag{12}$$

where K_k is the Kalman gain matrix.

$$P_k(+) = (I - K_k H_k)\ P_k(-) \tag{13}$$

where $P_k(+)$ is the updated covariance matrix.

$$X_k(+) = X_k(-) + K_k(Z_k - H_k X_k(-)) \tag{14}$$

where $X_k(+)$ is the updated state vector.

The GRO flight software employs a scaler implementation method that requires the sequence of Equations (12), (13), and (14) to be executed twice. In the first pass

$$\begin{aligned} H_k &= H_{k,1} = \left[\left(\bar{X} \times \bar{S}_k\right)^T \quad 0\right] \\ R_k &= R_{k,1} = R_{11} \end{aligned} \tag{15}$$

The resulting Kalman gain matrix $K_{k,1} = K_k$ is used to update the covariance matrix (Equation (13)) where $P_{k,1} = P_k$ and update the state (Equation (14)) where $X_k\,(-) = 0$. The equations are as follows:

$$K_{k,1} = P_k(-)\, H^T_{k,1} \Big/ \left[H_{k,1}\, P_k(-)\, H^T_{k,1} + R_{k,1}\right] \qquad (16)$$

$$P_{k,1}(+) = [I - K_{k,1}\, H_{k,1}]\, P_k(-) \qquad (17)$$

$$X_{k,1}(+) = K_{k,1}\, Z_1 \qquad (18)$$

In the second pass, there are the following substitutions:

$$H_k = H_{k,2} = \left[(\bar{Y} \times \bar{S}_k)^T \quad 0\right]$$

$$R_k = R_{k,2} = R_{22}$$

$$K_k = K_{k,2} \qquad (19)$$

$$P_k(-) = P_{k,1}$$

$$X_k(-) = X_{k,1}(+)$$

where $X_{k,1}(+)$ is the state vector update from the first pass.

The final Kalman gain matrix $K = K_{k,2}$ is used to update the covariance matrix $P_k(+) = P_{k,2}(+)$ and to update the state $X(+) = X_{k,2}(+)$. The equations are as follows:

$$K_{k,2} = P_{k,1}(+)\, H^T_{k,2} \Big/ \left[H_{k,2}\, P_{k,1}(+)\, H^T_{k,2} + R_{k,2}\right] \qquad (20)$$

$$P_{k,2}(+) = [I - K_{k,2}\, H_{k,2}]\, P_{k,1}(+) \qquad (21)$$

$$X_{k,2}(+) = X_{k,1}(+) + K_{k,2} [Z_2 - H_{k,2} X_{k,1}(+)] \tag{22}$$

$$X_k(+) = X_{k,2}(+), \quad P_k(+) = P_{k,2}(+) \tag{23}$$

3. CASE STUDY OBJECTIVES AND IDENTIFICATION

There are three primary objectives in the case studies. First, the short-term stability and covariance of the Kalman filter are studied for a nominal baseline case. Second, the covariance and short-term stability of four cases involving sensor noise and misalignments are studied and compared with the baseline. Lastly, the short-term stability and covariance are studied for two anomalous cases.

The cases studied are as follows:

- Case 1: Baseline Simulation
- Case 2: Noise and Misalignment
  - 2A: Normal run with excessive gyro noise
  - 2B: Normal run with gyro unit misalignment
  - 2C: Normal run with excessive FHST noise
  - 2D: Normal run with FHST misalignment
- Case 3: Anomalous Simulations
  - 3A: One FHST with one and two guide stars
  - 3B: Convergence using one and two FHSTs

4. CASE STUDY RESULTS

The results described for each case were attained using two primary forms of data: statistical and Kalman error. A running mean and variance of the residuals from the OBC as well as other Kalman filter information were output to an analysis file that was read by a post-processor that produced plots and tabular data used for statistical analysis. The Kalman error is the error quaternion that represents the difference between the Truth Model state quaternion and the OBC state quaternion.

4.1 CASE 1: BASELINE SIMULATION

The nominal baseline case represents the expected on-orbit conditions for the spacecraft. Noises for this test case are based on latest values received from the manufacturers. The stability and statistics for the Kalman filter are based on a simulation of 90 minutes. The nominal noises for the sensor data are as follows:

●	IRU float torque	0.20×10^{-6} radians (rad)/sec$^{3/2}$
	IRU float torque derivative	0.21×10^{-9} rad/sec$^{5/2}$
●	FHST measurement noise	0.49×10^{-4} rad (10 arc-sec)

The Kalman error for this case is seen in Figure 2. The maximum error is in the roll axis, (R), where a bias of approximately 20 arc-sec can be observed. Both the pitch axis (P) and yaw axis (Y) show differences of less than 10 arc-sec. All three are well within the specified attitude determination requirement of 86 arc-sec (3 sigma).

Statistics for the baseline case measurement residuals are as follows:

Mean X (arc sec)	Mean Y (arc sec)
1.8	7.8

Mean X (rad)	Mean Y (rad)	Var X	Var Y
0.86×10^{-5}	-0.38×10^{-4}	0.23×10^{-8}	0.23×10^{-8}

The expected values for the residuals are zero. The baseline case shows the expected values of the measurements to be less than 10 arc-sec, which is the "zero reference" used for comparisons with other case studies.

4.2 CASE 2: NOISE AND MISALIGNMENT

4.2.1 CASE 2A: EXCESSIVE GYRO NOISE

The objective of this case is to identify unmodeled dynamic errors. Simulations were ran with the gyro noise of 5, 10, 20, and 50 times greater than the statistics modeled in the flight software Kalman filter. The excessive float torque and float torque derivative noise (Equation (4)) causes the filter to place too much weight on the Dynamics Model and eventually results in a divergence.

The Kalman errors shown in Figure 3 represent the worst case scenario (i.e., 50 times the nominal). It reveals no evidence of instability with the filter over the 90-minute simulation. However, the initial values of the Kalman error are larger than the baseline case but are quickly damped to within accepted values. This suggests that the Kalman filter is accurately accounting for the noise. The residual analysis (see Table 3), however, shows the divergence of the data with increasing noise. The mean of the X and Y residuals are approximately the same as the reference expected value in the baseline case. The variances though show an increased amount of excursion from the mean as the noise increases.

Table 3. Excessive Gyro Noise for Case 2A

Noise (X nominal)	Mean X (rad)	Mean Y (rad)	Var X	Var Y
1	0.86×10^{-5}	-0.38×10^{-4}	0.23×10^{-8}	0.23×10^{-8}
5	0.61×10^{-5}	-0.41×10^{-4}	0.37×10^{-8}	0.30×10^{-8}
10	0.82×10^{-5}	-0.43×10^{-4}	0.56×10^{-8}	0.43×10^{-8}
20	0.51×10^{-5}	-0.40×10^{-4}	0.16×10^{-7}	0.82×10^{-8}
50	0.12×10^{-5}	-0.38×10^{-4}	0.95×10^{-7}	0.39×10^{-7}

4.2.2 CASE 2B: MISALIGNMENT OF GYROS

In this case, the gyro assembly was misaligned 5 and 10 arc-sec. Table 4 lists the residual statistical results of this simulation, and the Kalman errors are plotted on Figure 4. Statistically, there is no observable difference. This is because the misalignment acts as a bias on the system that is too small to affect the system.

Table 4. Residual Statistical Results for Case 2B

Misalignment (arc sec)	Mean X (rad)	Mean Y (rad)	Var X	Var Y
5	0.68×10^{-5}	-0.41×10^{-4}	0.22×10^{-8}	0.27×10^{-8}
10	0.65×10^{-5}	-0.41×10^{-4}	0.22×10^{-8}	0.27×10^{-8}

4.2.3 CASE 2C: OBSERVATION NOISE

In this case, observation noise was added to one FHST and to both FHSTs. Tables 5 and 6 list the tabular statistical output for one FHST and two FSHTs, respectively. Figures 5 and 6 plot the Kalman errors for one FHST and two FHSTs, respectively. It can be seen from Figures 5 and 6 that the roll and pitch axis are biased when compared with the baseline simulation. Since the measurement data is being corrupted and the Kalman filter cannot extract the noise to produce a better measurement, the statistical data reflect the bias and divergence with increasing noise.

Table 5. Observation Noise With One FHST

Noise (X nominal)	Mean X (rad)	Mean Y (rad)	Var X	Var Y
5	0.76×10^{-5}	-0.73×10^{-4}	0.13×10^{-7}	0.17×10^{-7}
10	0.11×10^{-4}	-0.19×10^{-3}	0.51×10^{-7}	0.96×10^{-7}

Table 6. Observation Noise With Two FHSTs

Noise (X nominal)	Mean X (rad)	Mean Y (rad)	Var X	Var Y
5	0.27×10^{-4}	-0.21×10^{-3}	0.28×10^{-7}	0.66×10^{-7}
10	0.57×10^{-4}	-0.39×10^{-3}	0.11×10^{-6}	0.23×10^{-6}

4.2.4 CASE 2D: MISALIGNMENT OF FHST

This case simulated misaligning one FHST and both FHSTs. The effects did not show up in the residual statistics (Table 7), but they did appear in the Kalman filter errors (Figure 7).

Since the measurements were only biased, and misalignment is equivalent to biasing the measurement data, it is expected that the system would converge on the observed data with the same statistics as for the baseline. Also, with a bias in measurement data, it is expected that the Kalman error would converge to the biased value. From Figure 7, it can be seen that the roll-and-pitch-axes data converge to a biased point, whereas the yaw axis is equivalent to the baseline simulation. The roll axis and yaw axes data are 0.18×10^{-3} and 0.20×10^{-4} rad, respectively. A misalignment of 30 arc-sec in the FHST pitch axis is equivalent to 0.14×10^{-3} rad. Thus, the misalignment can be seen as a bias in the roll and pitch axes.

Table 7. Misalignment of FHST for Case 2D

Misalignment (arc sec)	Mean X (rad)	Mean Y (rad)	Var X	Var Y
One FHST 30	0.67×10^{-5}	-0.43×10^{-4}	0.17×10^{-8}	0.23×10^{-8}
Two FHSTs 30	0.4×10^{-5}	-0.37×10^{-4}	0.16×10^{-8}	0.23×10^{-8}

4.3 CASE 3: ANOMALOUS SIMULATIONS

4.3.1 CASE 3A: ONE FHST WITH ONE AND TWO GUIDE STARS

In this case, two subcases were studied: one FHST with one guide star and one FHST with two guide stars. The spacecraft did not maintain requirements with one FHST and one guide star. However, the spacecraft did maintain requirements for one FHST and two guide stars. Table 8 gives the residual statistics for both subcases, and Figures 8 and 9 give the Kalman filter attitude errors with one and two guide stars, respectively.

Table 8. Residual Statistics for Case 3A

Subcase	Mean X (rad)	Mean Y (rad)	Var X	Var Y
One Guide Star	0.12×10^{-4}	-0.51×10^{-5}	0.16×10^{-8}	0.11×10^{-8}
Two Guide Stars	0.21×10^{-4}	-0.91×10^{-5}	0.18×10^{-8}	0.12×10^{-8}

In the one-guide-star simulation, a large roll and pitch error divergence can be seen, whereas there is not a large yaw error divergence. An explanation can be found in looking at the LOS of the star being observed. No error will be detected if the spacecraft were to spin about this axis. Components of this revolution are in the roll and pitch axes of the spacecraft. However, a small movement in the yaw axis can be detected immediately.

In the two-guide-star simulation, the stars have an angular separation of 4.4 deg. If each star LOS is looked at separately, the preceding analogy is valid. However, since a break-track command is being sent every few minutes, the measurement data being used are alternated between the two stars. Thus, two observation vectors are available. This system is similar to the two-FHST configuration. The small angular separation between the star LOSs, as compared with the angular separation of the two FHSTs, requires a larger rotation angle to register a measurement error than does the two-FHST system.

4.3.2 CASE 3B: CONVERGENCE

This case tests the capability of recovering from a large error and converge within a required accuracy, providing the guide star is still within the TFOV. The case initializes the pointing error to 2.0 deg in the spacecraft body pitch axis. Initially, the spacecraft was at a -90-deg pitch. Two subcases are simulated for comparison. The first uses the normal configuration of two FHSTs, with one guide star per RFOV. The second involves one FHST and two guide stars. The convergence requirement for both cases is a Kalman error of ≤ 60 arc-sec (3 sigma). Figures 10 and 11 show the results of these two simulations for one guide star and two guide stars, respectively. With the nominal configuration, the 2.0-deg error was removed in approximately 22 minutes. The single FHST case took approximately 39 minutes to converge. The longer convergence time for the single FHST case was expected because of the small angular separation between star LOSs.

5. CONCLUSIONS

Five primary conclusions are derived from this study. First, the baseline simulation that contained expected on-orbit conditions performed within spacecraft specifications. Second, excessive dynamics noise (gyros) is picked up by the measurement residual statistics but not by the Kalman errors. Third, increasing observation noise is picked up by the measurement residual statistics and the Kalman errors are biased. These two results indicate that sensor failures can be picked up in the measurement residual statistics long before they show up in the Kalman errors. Fourth, misalignments for the gyros and FHSTs are picked up only in the Kalman errors. Lastly, convergence has been proven for the anomalous case of one FHST with two guide stars. The convergence required longer than the nominal two FHST with one guide star each simulation due to the small angles between observation vectors in one FHST.

REFERENCES

1. James W. Murrell, "Precision Attitude Determination for Multimission Spacecraft", AIAA Paper No. 78-1248, 1978

2. R. Farrenkopf, "Generalized Results for Precision Attitude Reference Systems Using Gyros," AIAA Paper No. 74-903, AIAA Mechanics and Control of Flight Conference, Anaheim, California, August 5-9, 1974

3. TRW, GRO Operations Data Book Part 3 - ACAD Subsystem, Volume II, 40420-86-322-001, September 2, 1986.

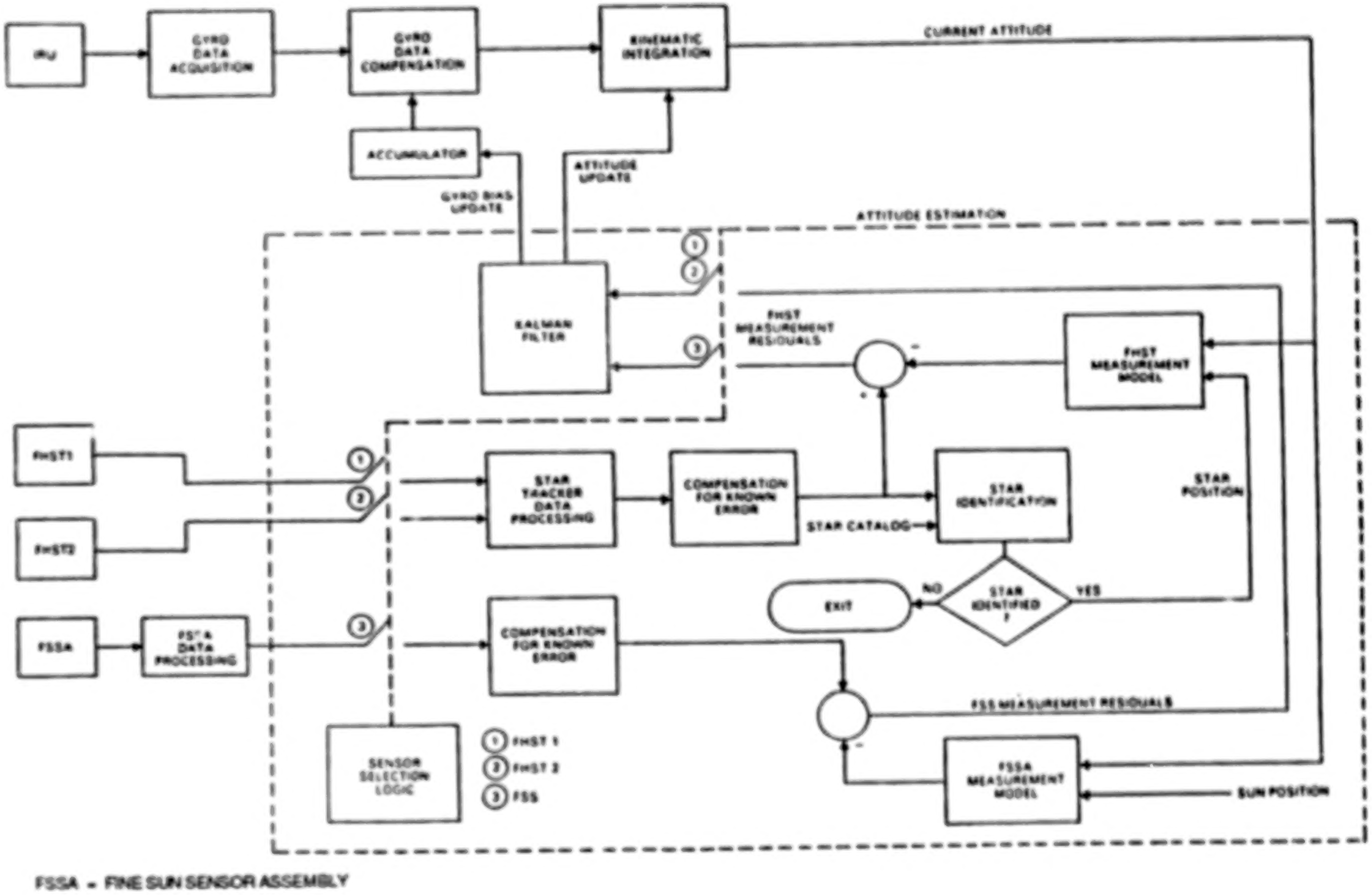
IRU
GYRO DATA ACQUISITION
GYRO DATA COMPENSATION
KINEMATIC INTEGRATION
CURRENT ATTITUDE
ACCUMULATOR
GYRO BIAS UPDATE
ATTITUDE UPDATE
ATTITUDE ESTIMATION
KALMAN FILTER
FHST MEASUREMENT RESIDUALS
FHST MEASUREMENT MODEL
FHST1
FHST2
FSSA
FSSA DATA PROCESSING
STAR TRACKER DATA PROCESSING
COMPENSATION FOR KNOWN ERROR
STAR IDENTIFICATION
STAR CATALOG
STAR POSITION
STAR IDENTIFIED ?
YES
NO
EXIT
COMPENSATION FOR KNOWN ERROR
FSS MEASUREMENT RESIDUALS
FSSA MEASUREMENT MODEL
SUN POSITION
SENSOR SELECTION LOGIC
① FHST 1
② FHST 2
③ FSS
FSSA - FINE SUN SENSOR ASSEMBLY

Figure 1. Attitude Estimation Algorithm Functional Block Diagram

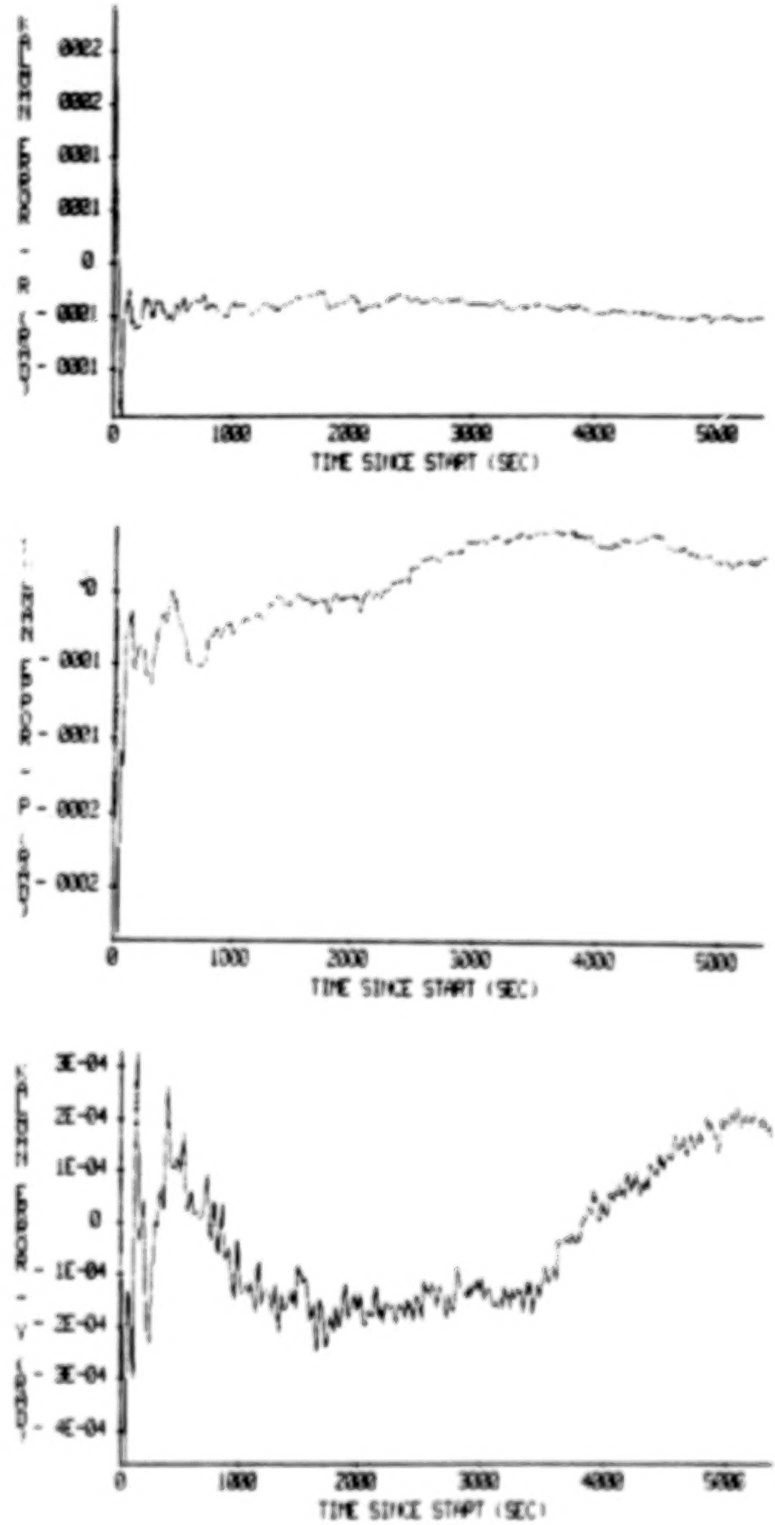

Figure 2. Baseline Nominal Performance

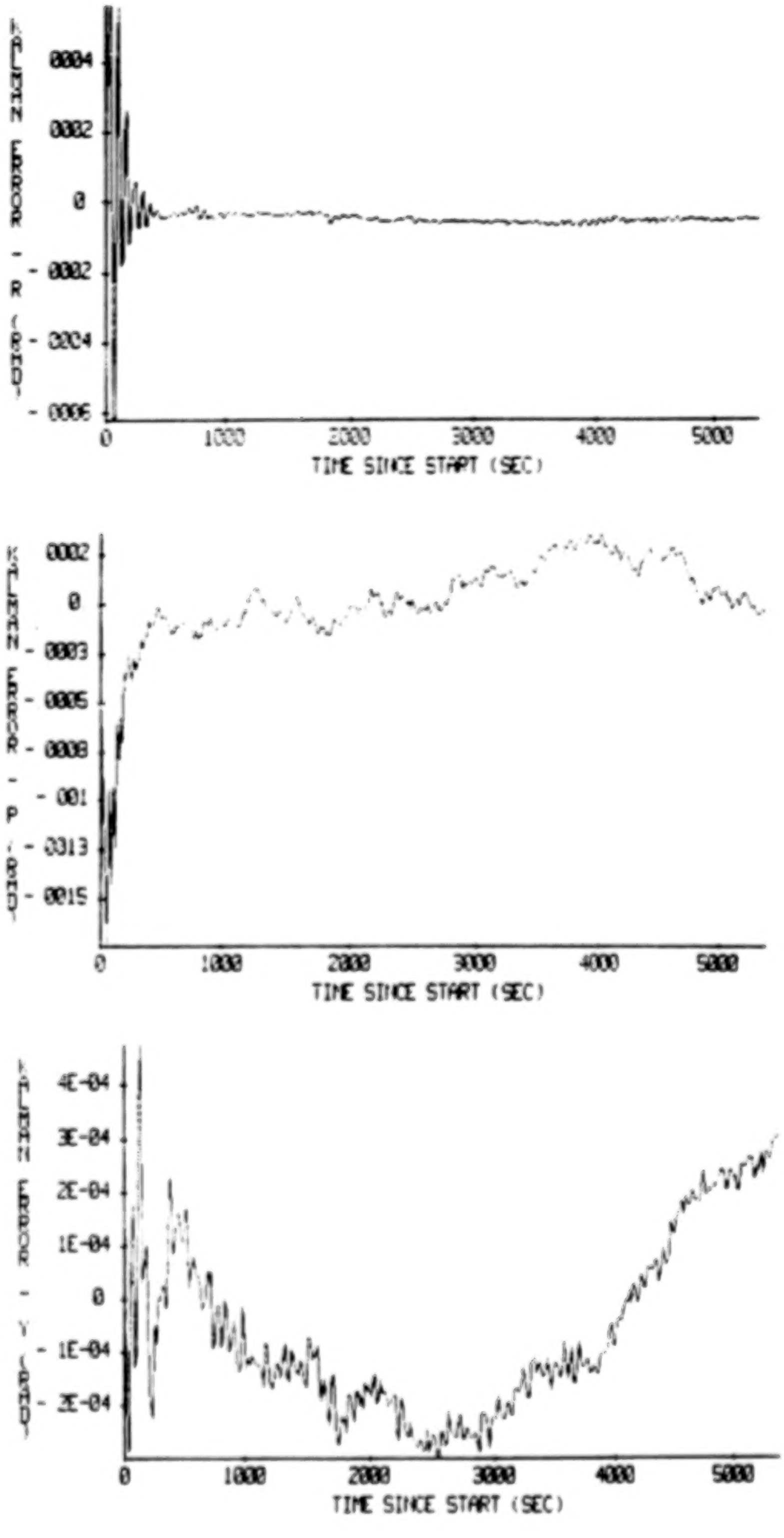

Figure 3. Modeling Noise on IRU

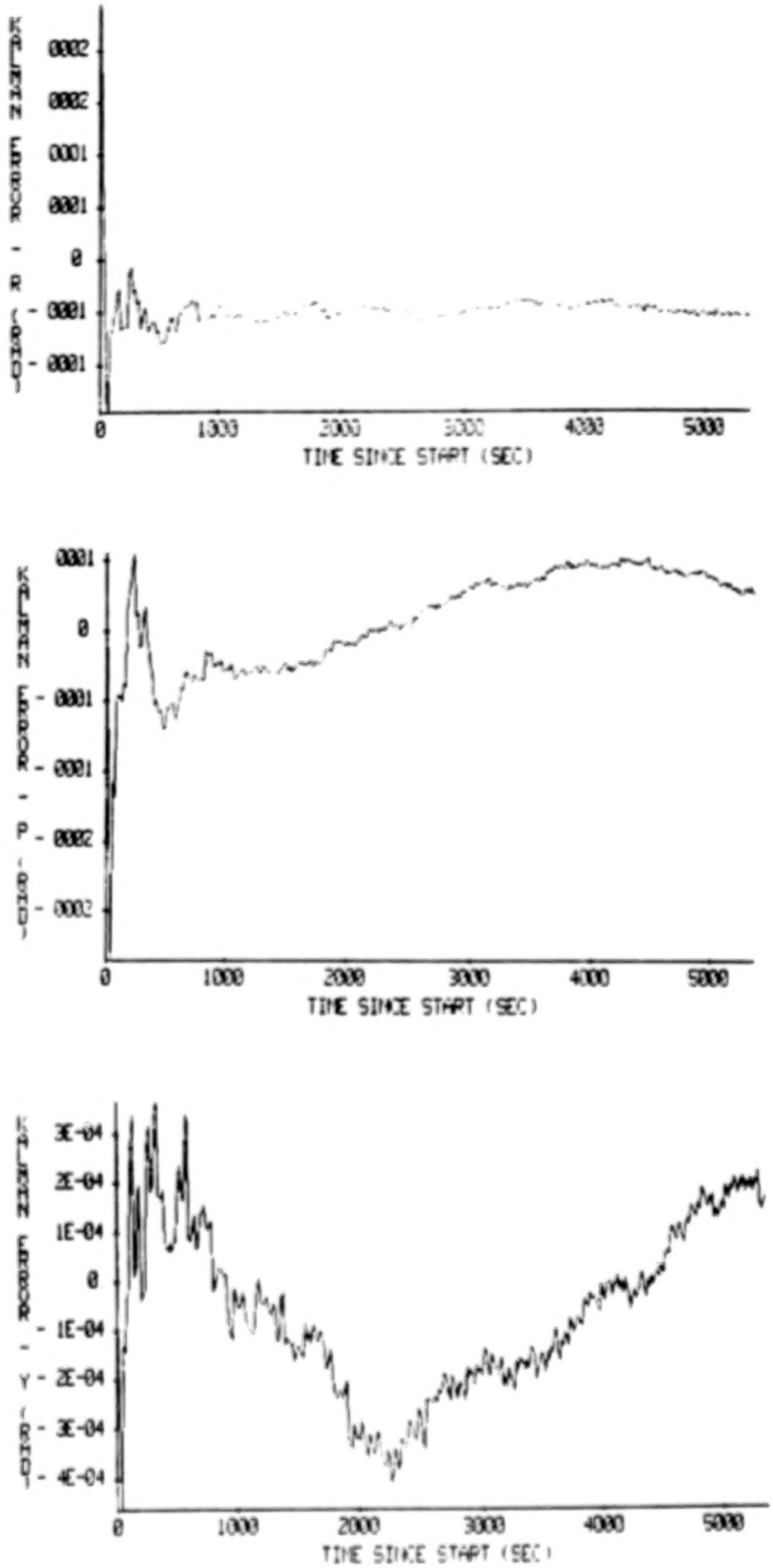

Figure 4. Misalignment of IRU

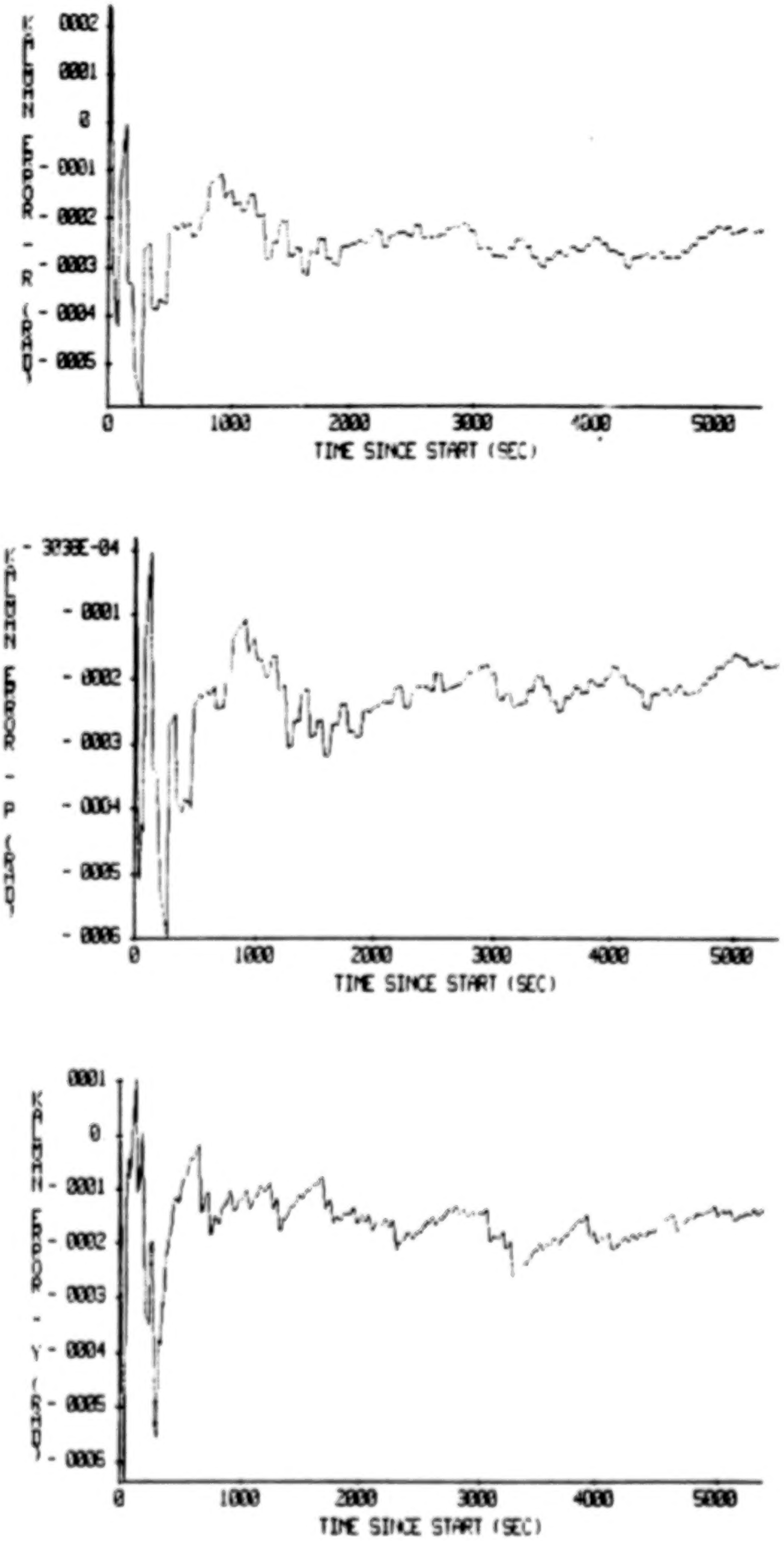

Figure 5. Observation Noise, One FHST

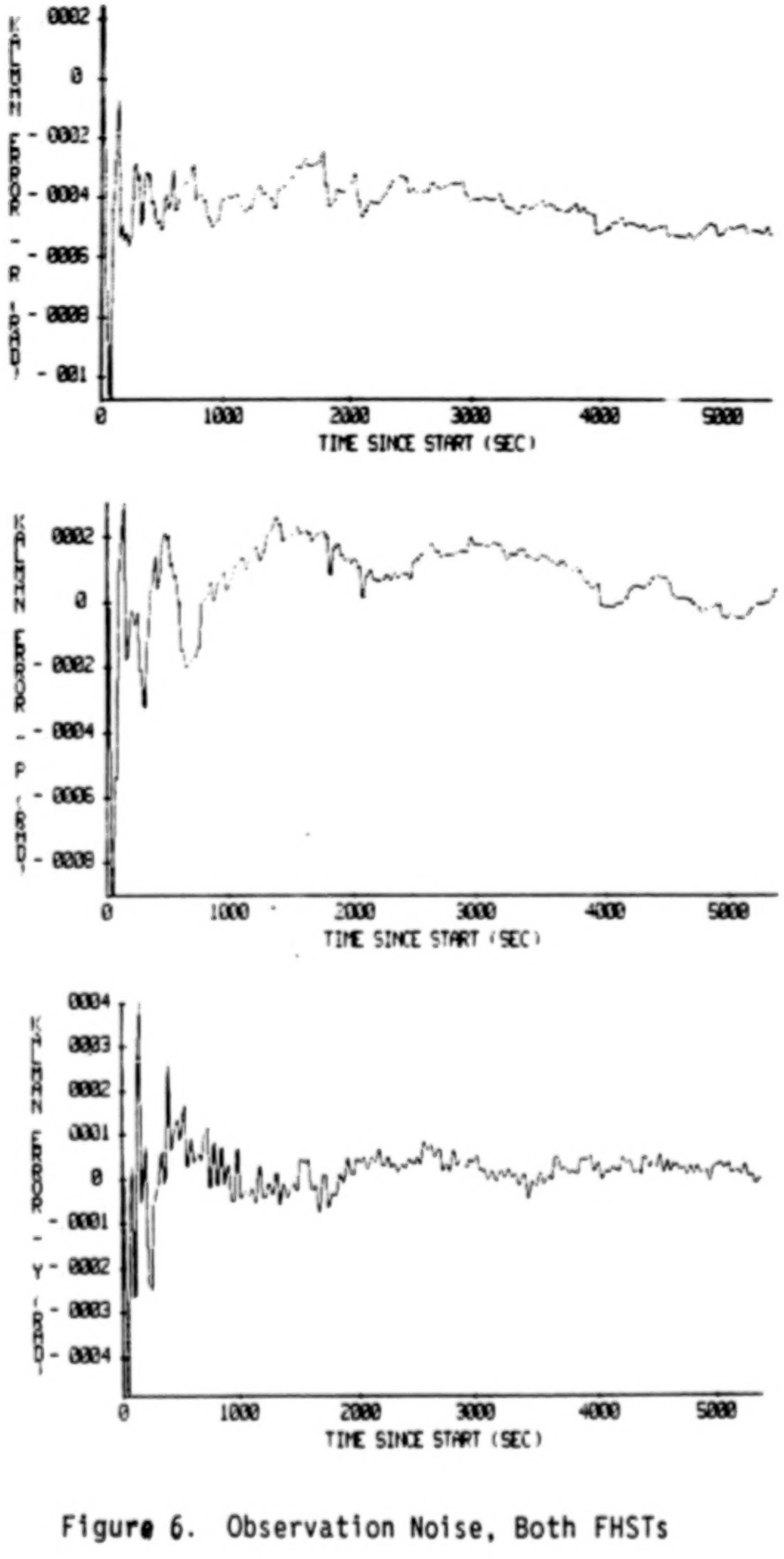

Figure 6. Observation Noise, Both FHSTs

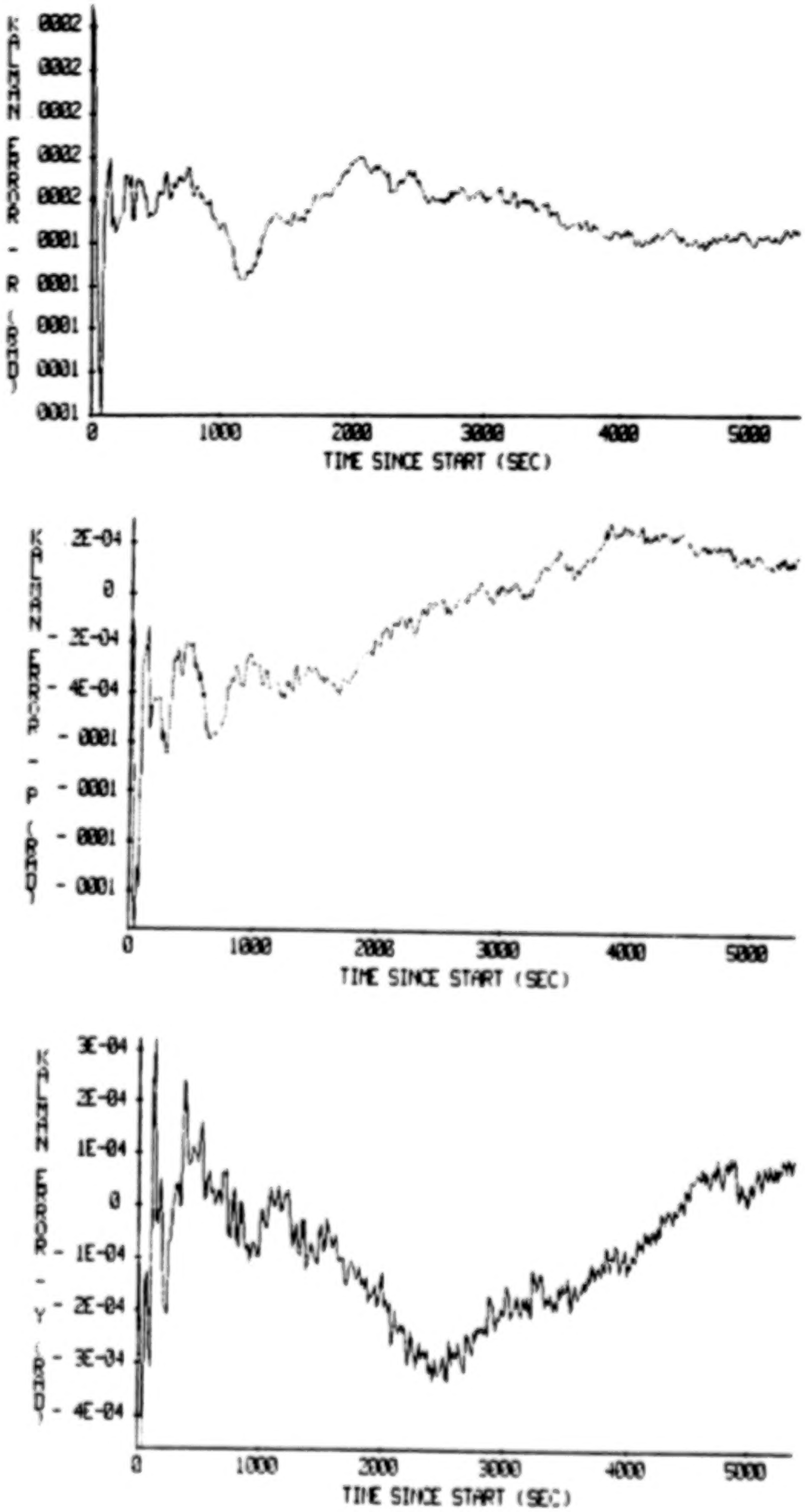

Figure 7. Misalignment, Both FHSTs

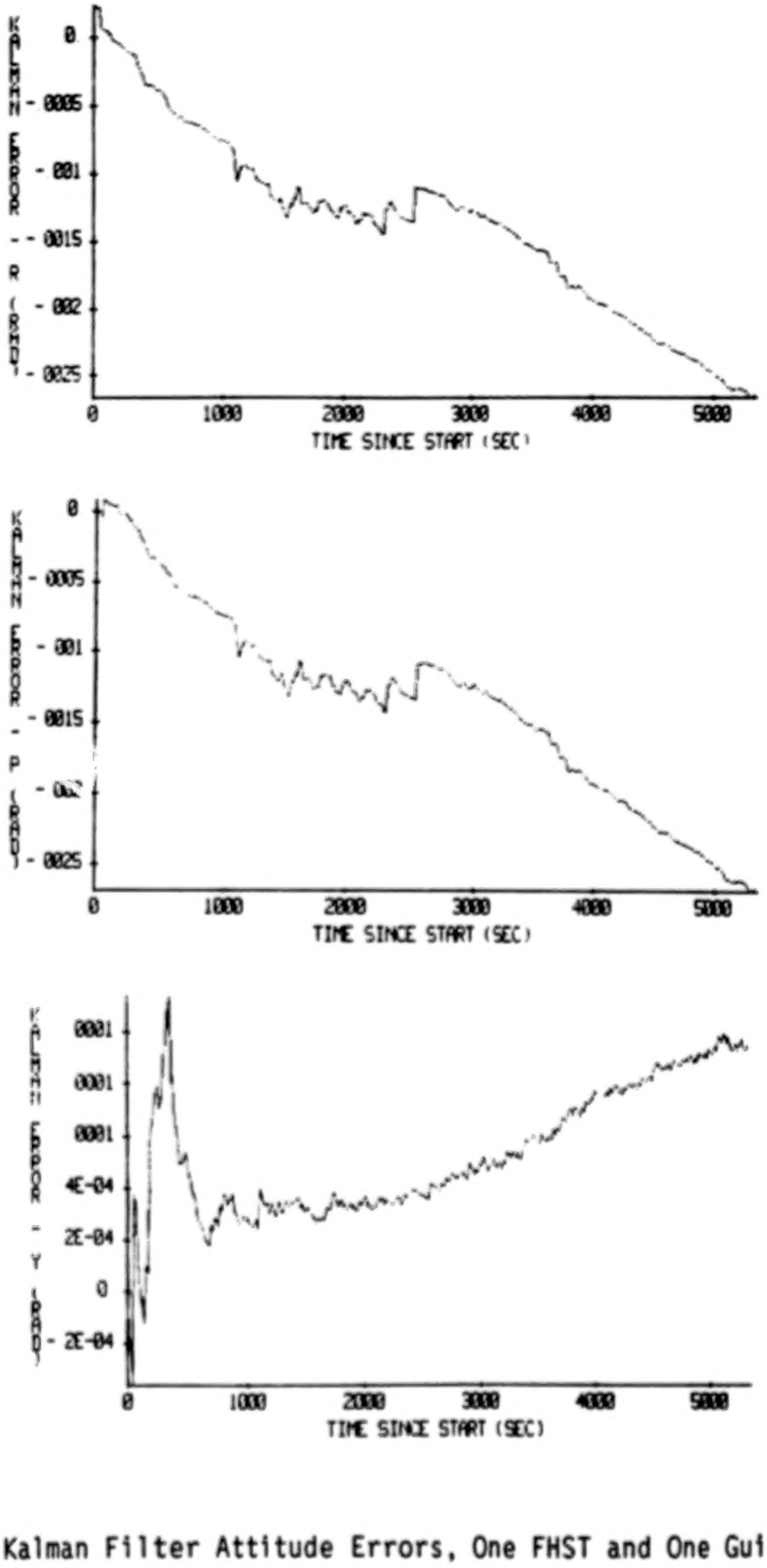

Kalman Filter Attitude Errors, One FHST and One Guide Star

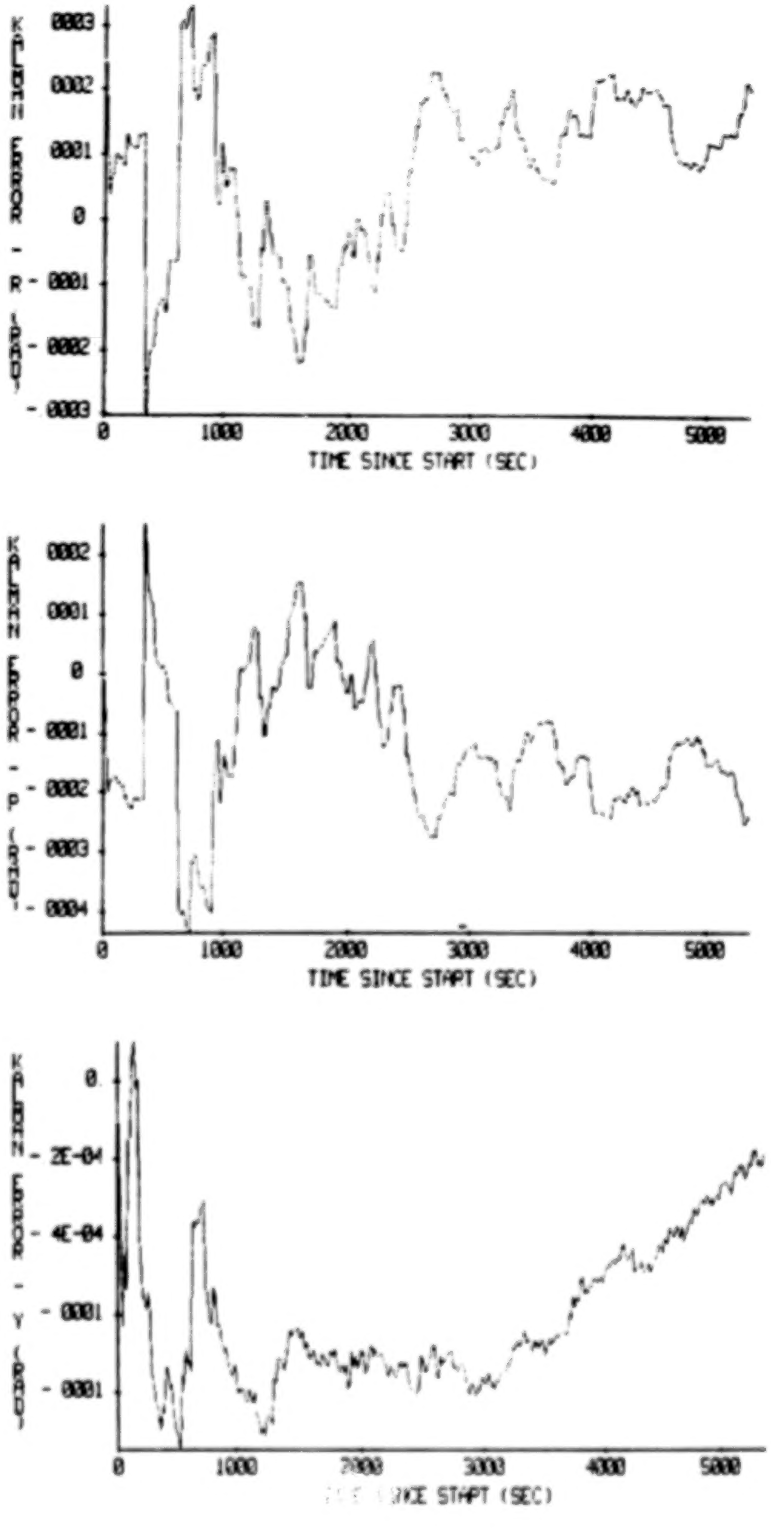

Figure 9. Kalman Filter Attitude Errors, One FHST and Two Guide Stars

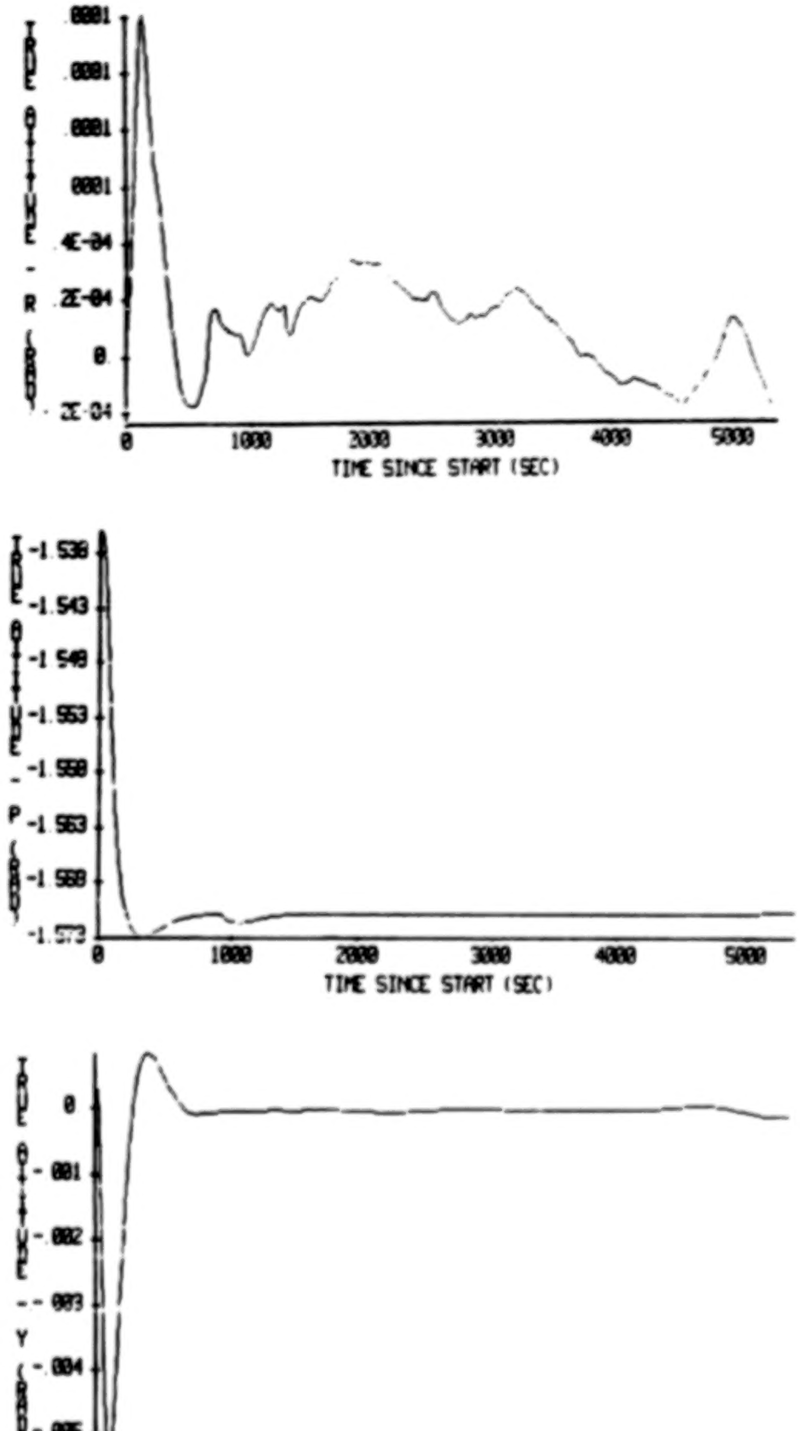

Figure 10. Both FHSTs, One Guide Star per FHST, and 2-deg Error in Pitch Axis

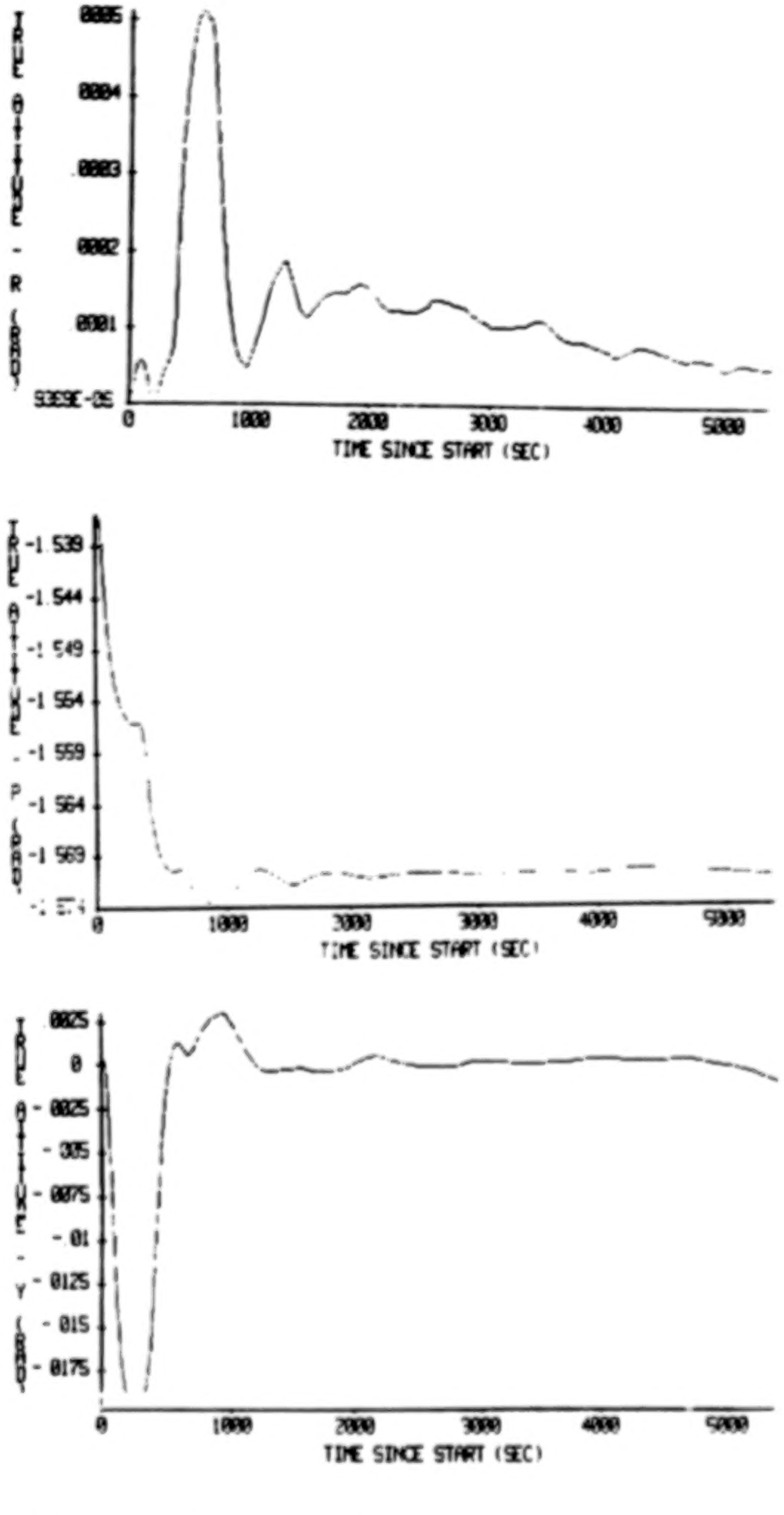

11. One FHST, Two Guide Stars, and 2-deg Error in Pitch Axis

N89-15950

IN-FLIGHT DETERMINATION OF SPACECRAFT MAGNETIC BIAS INDEPENDENT OF ATTITUDE

by
P. B. Davenport
Goddard Space Flight Center
and
W. M. Rumpl and G. L. Welter
Computer Sciences Corporation

ABSTRACT

A simple algorithm for the in-flight determination of the magnetic bias of a spacecraft is presented. The algorithm, developed for use during the Hubble Space Telescope mission, determines this bias independently of any attitude estimates and requires no spacecraft sensor data other than that from the spacecraft magnetometer(s). Estimates of the algorithm's accuracy and results from a number of numerical studies on the use of this algorithm are also presented.

I. INTRODUCTION

The determination of the magnetic bias of a spacecraft before launch can be quite difficult, particularly if the spacecraft is fairly large. The lack of such a bias determination can severely restrict the usefulness of onboard magnetometers in measuring the ambient magnetic field and thus also in determining spacecraft attitude. Attitudes based on magnetometer data are often the first to be determined during a spacecraft's mission. Having an algorithm that can determine the spacecraft magnetic bias at the location of each magnetometer without requiring knowledge of the spacecraft attitude is therefore desirable. We present here a simple algorithm that fulfills this need. The algorithm, developed specifically for the Hubble Space Telescope (HST) mission, requires no spacecraft sensor data other than that from the spacecraft magnetometer(s). The only other required input data are magnetic field values from a data base geomagnetic field model. Section II of this article presents the algorithm; Section III, an analytical error model; Section IV, numerical examples of the use of the algorithm; and Section V, our conclusions.

II. MAGNETIC BIAS DETERMINATION ALGORITHM

The spacecraft magnetic bias, **D**, at the location of an onboard magnetometer is related to the measured magnetic field, **M**, and the local geomagnetic field, **B**, as follows:

$$\mathbf{M} - \mathbf{D} = A\,\mathbf{B}\,, \qquad (1)$$

where **M** and **D** are defined in spacecraft coordinates and **B** in geocentric coordinates, and *A* is the (unknown) spacecraft attitude transformation matrix. The bias **D** is assumed to be time independent in the spacecraft reference frame. The value of **B** is to be obtained from a geomagnetic field model. Obtaining **B** from the model requires both a spacecraft ephemeris and the magnetometer measurement times. The final accuracy of the determination of **D** will depend on the accuracies of the magnetometer calibration and the geomagnetic field model (including differential errors introduced by spacecraft ephemeris errors and timing errors), as well as noise in the magnetometer readings. Taking the scalar product of each side of equation (1) with its transpose (noting that $A^{T} = A^{-1}$) results in

$$M^2 - 2\,\mathbf{M}^{T}\mathbf{D} + D^2 = B^2 \qquad (2)$$

Equation (2) is independent of spacecraft attitude because B^2 is invariant under rotation. We have, however, reduced a three-component vector equation to a scalar equation. Because **D** has three components, measurements must be taken in such a way as to provide at least three linearly independent versions of equation (2). This can be done either by taking measurements at a number of positions in the orbit or by changing the spacecraft attitude. With the latter approach, it is still not necessary to know what the various attitudes are -- only that they are distinct from one another.

Equation (2) may be used as the basis for constructing a least-squares loss function for use in solving for **D**. The loss function is constructed using an error variable, e_i, defined by

$$e_i = (M_i^2 - 2\,\mathbf{M}_i^{T}\mathbf{D} + D^2) - B_i^2\,, \qquad (3)$$

where the subscript i indicates measurement number. The corresponding least-squares loss function, J, is given by

$$J = 1/2 \, \Sigma \, w_i \, (e_i - < e_i >)^2 \tag{4a}$$

$$= 1/2 \, \Sigma \, w_i \, [\, (M_i^2 - 2 \, \mathbf{M}_i^T \mathbf{D} + D^2) - B_i^2 - < e_i >]^2 \, , \tag{4b}$$

where w_i is a weight, inversely proportional to the variance of e_i, associated with the ith measurement, and $< e_i >$ is the expectation value of e_i. The implicit assumption made in selecting equation (4a) as the loss function is that each e_i is an independent random variable with Gaussian (or nearly Gaussian) distribution. If this assumption is true, then the value of **D** that minimizes J is the optimal estimate for the true spacecraft bias. Specification of the values for w_i and $< e_i >$ is not necessarily a trivial matter. The simplest approach, of course, is to assume $w_i = 1$ and $< e_i > = 0$ for all i. We present in Section III a simple analytic model from which more exact expressions for w_i and $< e_i >$ can be derived. It is worth bearing in mind, of course, that because of the uncertainties involved in modeling errors (both in their magnitude and the form of their distribution), the concept of an "optimal" solution for **D** becomes a bit fuzzy. All solutions for **D** within a small error window about the value that minimizes J will be essentially equally valid.

We now construct an algorithm to determine the value of **D** that minimizes J. Equation (3) is quadratic in the unknowns, i.e., in the components of **D**. This is awkward because it prevents simply applying the standard tools of linear algebra to construct a least-squares solution for the problem. We note, however, that if the quantity D^2 on the right-hand side of equation (3) were a constant, then standard linear techniques would be applicable. We therefore construct a modified version, J_C, of the loss function:

$$J_C = 1/2 \, \Sigma \, w_i \, [\, (M_i^2 - 2 \, \mathbf{M}_i^T \mathbf{D} + D_C^2) - B_i^2 - < e_i >]^2 \, , \tag{5}$$

where the term D_c^2 is to be considered an adjustable parameter rather than a function of the components of **D**. Standard linear least-squares techniques (e.g., see Reference 1) may be used to find the value of **D** that minimizes J_c for any specified value of D_c^2; the solution is

$$\mathbf{D} = 1/2\,(\Sigma\, w_i\, \mathbf{M}_i\, \mathbf{M}_i^T)^{-1}\,[\,\Sigma\, w_i\,(M_i^2 - B_i^2 - \langle e_i \rangle)\,\mathbf{M}_i + D_c^2\,\Sigma\, w_i\,\mathbf{M}_i] \,. \tag{6}$$

We may now select the value of **D** that simultaneously satisfies equation (6) and the constraint

$$D^2 = D_c^2 \,. \tag{7}$$

A solution for **D** selected in this manner is not guaranteed to be a minimum for the loss function J. We do expect, however, that a vector $\mathbf{D}_c$ chosen to satisfy equations (6) and (7) simultaneously will be both a good estimate for the solution that would minimize J and a good estimate for the true bias. In particular, we note that in the limit of noise-free data, there exists a value of **D** (namely, the true bias) that simultaneously zeroes J and J_c while also satisfying the constraint of equation (7). Because J and J_c are by definition nonnegative, a solution that zeroes them both is a minimum for both. It follows, therefore, that $\mathbf{D}_c$ will be the exact solution for **D** in the limit of zero noise.

With the constraint of equation (7) applied, equation (6) can be rewritten as

$$\mathbf{D}_c = \mathbf{U} + D_c^2\,\mathbf{V} \,, \tag{8}$$

where

$$\mathbf{U} = 1/2\,(\Sigma\, w_i\, \mathbf{M}_i\, \mathbf{M}_i^T)^{-1}\,\Sigma\, w_i\,(M_i^2 - B_i^2 - \langle e_i \rangle)\,\mathbf{M}_i \,, \tag{9}$$

$$\mathbf{V} = 1/2\,(\Sigma\, w_i\, \mathbf{M}_i\, \mathbf{M}_i^T)^{-1}\,\Sigma\, w_i\,\mathbf{M}_i \,. \tag{10}$$

Solving equation (8) for $\mathbf{D}_c$ first requires a solution for D_c^2. This can be found as follows.

Multiplying each side of equation (8) with its transpose results in

$$D_c^2 = \mathbf{D}_c^T \mathbf{D}_c = \mathbf{U}^T \mathbf{U} + 2\,\mathbf{U}^T \mathbf{V}\, D_c^2 + \mathbf{V}^T \mathbf{V}\,(D_c^2)^2 . \tag{11}$$

This can be written as a simple quadratic in D_c^2:

$$y = a\,(D_c^2)^2 + b\,D_c^2 + c = 0 , \tag{12}$$

where

$$a = \mathbf{V}^T \mathbf{V} , \tag{13}$$

$$b = (2\,\mathbf{U}^T \mathbf{V} - 1) , \tag{14}$$

$$c = \mathbf{U}^T \mathbf{U} . \tag{15}$$

The solutions of equation (12) are

$$D_c^2 = [\, -b \pm (b^2 - 4ac)^{1/2}\,] / 2a . \tag{16}$$

That the negatively signed solution is the proper solution can be demonstrated in the following manner. Any real solution for D_c^2 must have $b^2 \geq 4ac$. Parameters a and c are nonnegative because **V** and **U** are real vectors. From this it follows that $|b| \geq (b^2 - 4ac)^{1/2}$. In order that D_c^2 be nonnegative, it follows in turn that $b \leq 0$. Both solutions for D_c^2 are therefore nonnegative. For cases in which neither bias nor measurement error exists, $c = 0$ and $b = -1$. The negatively signed solution is clearly required to give $D_c^2 = 0$ for such cases. The parabola $y(D_c^2)$ defined in equation (12) remains the same in form (i.e., open upwards, with two nonnegative crossings of the D_c^2-axis) for cases of nonzero bias and error. Any physically realizable measurement situation may be imagined as achieved by a continuous change through a family of situations that starts with zero bias and zero error. During this change, the function y, and therefore the two solutions for equation (16), change smoothly. The negatively and positively signed solutions of equation (16) do not merge (and therefore cannot switch places) with each other unless the family of situations contains a "point" having $b^2 = 4ac$. An incremental shift in the family to a neighboring one having $b^2 > 4ac$ everywhere is equally acceptable and removes the conceptual possibility of sign switching for the true solution. The negatively signed solution is therefore always the correct solution for equation (16). Equations (16) and (8) can thereby be solved to obtain $\mathbf{D_C}$.

The value of $\mathbf{D_C}$ may be used either as an acceptable estimate of the magnetic bias or as an initial estimate in an iterative algorithm to find the value of **D** that minimizes the loss function J. The iterative algorithm is as follows. **D** is expressed as

$$\mathbf{D} = \mathbf{D}_0 + \mathbf{d}\,, \tag{17}$$

where $\mathbf{D}_0$ is an estimate (initially set to $\mathbf{D_C}$) of **D**, and **d** is a correction to this estimate. Equation (3) may then be written as

$$e_i = (M_i^2 + D_0^2 - 2\,\mathbf{M}_i^T \mathbf{D}_0 - 2\,\mathbf{M}_i^T \mathbf{d} + 2\,\mathbf{D}_0^T \mathbf{d} + d^2) - B_i^2\,. \tag{18}$$

The loss function J becomes

$$J = 1/2\, \Sigma\, w_i\, [\, (M_i^2 - B_i^2 + D_0^2 - 2\,\mathbf{M}_i^T \mathbf{D}_0 + d^2 - \langle e_i \rangle) - 2\,(\mathbf{M}_i - \mathbf{D}_0)^T \mathbf{d}\,]^2\,. \tag{19}$$

Taking the gradient of J with respect to the components of **d** yields

$$\begin{aligned}\nabla J = \Sigma\, w_i\, [\, (M_i^2 - B_i^2 + D_0^2 - 2\,\mathbf{M}_i^T \mathbf{D}_0 + d^2 - \langle e_i \rangle) - 2\,(\mathbf{M}_i - \mathbf{D}_0)^T \mathbf{d}\,] \\ [\, 2\,\mathbf{d} - 2\,(\mathbf{M}_i - \mathbf{D}_0)\,]\,.\end{aligned} \tag{20}$$

Neglecting the terms in equation (20) that are quadratic or cubic in **d** yields

$$\begin{aligned}\nabla J = 2\, \Sigma\, w_i\, \{\, (M_i^2 - B_i^2 + D_0^2 - 2\,\mathbf{M}_i^T \mathbf{D}_0 - \langle e_i \rangle)\, \mathbf{d} \\ - [\, (M_i^2 - B_i^2 + D_0^2 - 2\,\mathbf{M}_i^T \mathbf{D}_0 - \langle e_i \rangle) - 2\,(\mathbf{M}_i - \mathbf{D}_0)^T \mathbf{d}\,]\, (\mathbf{M}_i - \mathbf{D}_0)\, \}\,,\end{aligned} \tag{21}$$

which may be rearranged to read

$$\nabla J = 2\,(\boldsymbol{Y}\,\mathbf{d} - \mathbf{Z})\,, \tag{22}$$

where

$$\boldsymbol{Y} = \Sigma\, w_i\, [\, 2\,(\mathbf{M}_i - \mathbf{D}_0)\,(\mathbf{M}_i - \mathbf{D}_0)^T + (M_i^2 - B_i^2 + D_0^2 - 2\,\mathbf{M}_i^T\mathbf{D}_0 - \langle e_i \rangle)\,\boldsymbol{I}\,]\,, \tag{23}$$

$$\mathbf{Z} = \Sigma\, w_i\, [\,(\, M_i^2 - B_i^2 + D_0^2 - 2\,\mathbf{M}_i^T\mathbf{D}_0 - \langle e_i \rangle\,)\,(\mathbf{M}_i - \mathbf{D}_0)\,]\,, \tag{24}$$

and $\boldsymbol{I}$ is the 3-by-3 identity matrix. The desired solution for **d** is found by setting ∇J to zero and multiplying both sides of the resulting equation by $\boldsymbol{Y}^{-1}$:

$$\mathbf{d} = \boldsymbol{Y}^{-1}\,\mathbf{Z}\ . \tag{25}$$

The loop is closed by adding **d** to $\mathbf{D}_0$, thus obtaining a new estimate for **D**. The process continues until **d** is made arbitrarily close to zero. As noted above, we expect that a solution for **D** obtained using this iterative technique should not differ significantly from $\mathbf{D}_C$.

The uncertainty, $\Delta\mathbf{D}$, associated with the estimated value of **D** should be of order $\sigma/N^{1/2}$, where σ is the root-mean-square (rms) magnetometer measurement error, and N is the total number of measurements made. A more accurate estimate of the uncertainty of **D** can be made as follows. If equation (25) had resulted from a "standard" least-squares problem, i.e., one in which all measurement errors were associated with the vector **Z** while the matrix $\boldsymbol{Y}$ was composed of known constants or model parameters, then the uncertainty $\Delta\mathbf{D}$ would be given by

$$\Delta\mathbf{D} = [\, 2\, J(\mathbf{D}) \,/\, (N-1)\,]^{1/2}\,\mathbf{W}\ , \tag{26}$$

with **W** defined as the vector with components equal to the square root of the diagonal components of $\boldsymbol{Y}^{-1}$. If all measurement errors are "extracted" from $\boldsymbol{Y}^{-1}$, it reduces to a matrix $\boldsymbol{X}$ defined as

$$X = [\, \Sigma\, w_i\, 2\, (\mathbf{M}_i - \mathbf{D})\, (\mathbf{M}_i - \mathbf{D})^T\,]^{-1} \tag{27a}$$

$$= [\, \Sigma\, w_i\, 2\, (\, \boldsymbol{A}_i\, \mathbf{B}_i\,)\, (\, \boldsymbol{A}_i\, \mathbf{B}_i\,)^T\,]^{-1}\ . \tag{27b}$$

We therefore take our estimate of $\Delta\mathbf{D}$ to be as given by equation (26), with $\mathbf{W}$ defined as the square root of the diagonal of $\boldsymbol{X}$. In Section III we give an evaluation of $\Delta\mathbf{D}$ more directly comparable with the simple estimate $\sigma/N^{1/2}$.

III. ANALYTICAL ERROR MODEL

In this section we present a simple analytical model for the magnetometer errors and use it to derive expressions for the parameters w_i and $< e_i >$. We further apply this model to a simple observing scenario and calculate the corresponding uncertainty $\Delta\mathbf{D}$. In principle, errors associated with both $\mathbf{M}_i$ and $\mathbf{B}_i$ exist, the latter resulting from errors both in the geomagnetic field model and the spacecraft ephemeris. For simplicity, we assume here that the total error is sufficiently dominated by the error in $\mathbf{M}_i$ that the error in $\mathbf{B}_i$ can be neglected. We define $\mathbf{r}_i$ as the error vector associated with $\mathbf{M}_i$ and assume it to be composed of three independent random variables, each having Gaussian distribution with mean zero and variance σ^2. The full variance of $\mathbf{r}_i$ is $3\sigma^2$. Using this model, the variable e_i is related to $\mathbf{r}_i$ by the relation

$$\begin{aligned} e_i &= (\, \mathbf{M}_i - \mathbf{D}_i\,)^2\ -\ B_i^2 \\ &= (\, \mathbf{B}_i + \mathbf{r}_i\,)^2\ -\ B_i^2 \\ &= 2\, \mathbf{B}_i^T\, \mathbf{r}_i\ +\ r_i^2\ . \end{aligned} \tag{28}$$

The expectation value of e_i is given by

$$
\begin{aligned}
< e_i > &= \int G(\mathbf{r}_i)\, e_i \, dv_r \\
&= \int G(\mathbf{r}_i) \left(2\, \mathbf{B}_i^T \mathbf{r}_i + r_i^2 \right) dv_r \\
&= \int G(\mathbf{r}_i) \left(2\, B_i\, r_i \cos(\theta) + r_i^2 \right) dv_r \\
&= 3\sigma^2 ,
\end{aligned} \tag{29}
$$

where $G(\mathbf{r}_i)$ is the Gaussian distribution function (proportional to $\exp(-r_i^2/2\sigma^2)$), dv_r is a volume element in r-space, and θ is the angle between $\mathbf{B}_i$ and $\mathbf{r}_i$. (The integral $\int f \cos(\theta)\, dv_r$ yields zero for any $f(\mathbf{r}_i)$ that is spherically symmetric.) The variance, s_i^2, of e_i is in turn given by

$$
\begin{aligned}
s_i^2 &= \int G(r_i) \left(e_i - < e_i > \right)^2 dv_r \\
&= \int G(r_i) \left[2\, B_i\, r_i \cos(\theta) + r_i^2 - 3\sigma^2 \right]^2 dv_r \\
&= \int G(r_i) \left[4\, B_i^2\, r_i^2 \cos^2(\theta) + 2\, B_i\, r_i \cos(\theta)\, (r_i^2 - 3\sigma^2) \right. \\
&\qquad \left. + \; r_i^4 - 2\, r_i^2\, (3\sigma^2) + (3\sigma^2)^2 \right] dv_r \\
&= 4/3\, B_i^2\, (3\sigma^2) + 5\, \sigma^2\, (3\sigma^2) - 2\, (3\sigma^2)^2 + (3\sigma^2)^2 \\
&= 2\, \sigma^2 \left(2\, B_i^2 + 3\sigma^2 \right) .
\end{aligned} \tag{30}
$$

The weight w_i may be set equal to s_i^{-2}. We assumed for the derivation of equations (29) and (30) that the error in $\mathbf{M}_i$ dominated that in $\mathbf{B}_i$. This was done for simplification and is in no way essential. Allowing an error in $\mathbf{B}_i$ having components with Gaussian distribution of variance σ_b^2 yields the following expressions for $< e_i >$ and s_i^2:

$$
< e_i > = 3\sigma^2 - 3\sigma_b^2 , \tag{31}
$$

$$
s_i^2 = 2\, \sigma^2 \left(2\, B_i^2 + 3\sigma^2 \right) + 2\, \sigma_b^2 \left(2\, B_i^2 + 3\sigma_b^2 \right) + 2 \left(3\sigma^2\, 3\sigma_b^2 \right) . \tag{32}
$$

$$\begin{aligned} <e_i> &= \int G(\mathbf{r}_i)\, e_i\, dv_r \\ &= \int G(\mathbf{r}_i)\, (\, 2\, \mathbf{B}_i^T\, \mathbf{r}_i \;+\; r_i^2\,)\, dv_r \\ &= \int G(\mathbf{r}_i)\, (\, 2\, B_i\, r_i \cos(\theta) + r_i^2\,)\, dv_r \\ &= 3\sigma^2\, , \end{aligned} \tag{29}$$

where $G(\mathbf{r}_i)$ is the Gaussian distribution function (proportional to $\exp(-r_i^2/2\sigma^2)$), dv_r is a volume element in r-space, and θ is the angle between $\mathbf{B}_i$ and $\mathbf{r}_i$. (The integral $\int f \cos(\theta)\, dv_r$ yields zero for any $f(\mathbf{r}_i)$ that is spherically symmetric.) The variance, s_i^2, of e_i is in turn given by

$$\begin{aligned} s_i^2 &= \int G(r_i)\, (\, e_i - <e_i>\,)^2\, dv_r \\ &= \int G(r_i)\, [\, 2\, B_i\, r_i \cos(\theta) + r_i^2 - 3\sigma^2\,]^2\, dv_r \\ &= \int G(r_i)\, [\, 4\, B_i^2\, r_i^2 \cos^2(\theta) \;+\; 2\, B_i\, r_i \cos(\theta)\, (r_i^2 - 3\sigma^2) \\ &\qquad + \; r_i^4 \;-\; 2\, r_i^2\, (3\sigma^2) \;+\; (3\sigma^2)^2\,]\, dv_r \\ &= 4/3\, B_i^2\, (3\sigma^2) \;+\; 5\, \sigma^2\, (3\sigma^2) \;-\; 2\, (3\sigma^2)^2 \;+\; (3\sigma^2)^2 \\ &= 2\, \sigma^2\, (\, 2\, B_i^2 \;+\; 3\sigma^2\,)\; . \end{aligned} \tag{30}$$

The weight w_i may be set equal to s_i^{-2}. We assumed for the derivation of equations (29) and (30) that the error in $\mathbf{M}_i$ dominated that in $\mathbf{B}_i$. This was done for simplification and is in no way essential. Allowing an error in $\mathbf{B}_i$ having components with Gaussian distribution of variance σ_b^2 yields the following expressions for $<e_i>$ and s_i^2:

$$<e_i> \;=\; 3\sigma^2 \;-\; 3\sigma_b^2\, , \tag{31}$$

$$s_i^2 \;=\; 2\, \sigma^2\, (\, 2\, B_i^2 \;+\; 3\sigma^2\,) \;+\; 2\, \sigma_b^2\, (\, 2\, B_i^2 \;+\; 3\sigma_b^2\,) \;+\; 2\, (\, 3\sigma^2\, 3\sigma_b^2\,)\; . \tag{32}$$

For illustration, we present here typical values of B, σ, and σ_b for the specific case of the HST mission. The rms noise level associated with the HST magnetometers has been determined to be approximately 0.01 gauss (Reference 2). The geomagnetic field model to be used is the International Geomagnetic Reference Field (IGRF) for 1975 (Reference 3). A typical value for B at an altitude of 445 kilometers is about 0.3 gauss. Typical errors to be associated with the reference field can be estimated on the basis of the work by Trombka and Cain (Reference 4), wherein the IGRF for 1975 was compared with that for 1965. The rms error at 445 kilometers was found to be approximately 0.002 gauss. Launch date for the HST mission is currently scheduled for June 1989, 15 years after the completion of the 1975 IGRF. Assuming linear error growth with time, the error to be associated with the reference field at HST launch should be about 0.003 gauss. The error in the estimate of the local geomagnetic field value due to spacecraft position error can be estimated as $|(\nabla \cdot \mathbf{B})|\,|(\Delta \mathbf{R})|$, where $\nabla \cdot \mathbf{B}$ is the divergence of $\mathbf{B}$, and $\Delta \mathbf{R}$ is the ephemeris error for the spacecraft. The definitive ephemeris for the HST is expected to have an rms accuracy of 0.2 kilometer (Reference 5). Given that the near-Earth dipole field falls off approximately as R^{-3}, the magnitude of $\nabla \cdot \mathbf{B}$ can be estimated as $3\,B / R_0$, where R_0 is the semimajor axis of the spacecraft orbit. Together these yield a field error of approximately 0.03 milligauss. The error in $\mathbf{B}_i$ is dominated by the error in the field model. The ratio σ^2 / σ_b^2 is approximately 10, indicating that neglecting σ_b^2 in equations (31) and (32) would be a reasonable approximation.

We now use equations (26), (27b), and (30) to provide a simple expression for $\Delta \mathbf{D}$ for an idealized observing scenario. We consider a situation in which the geomagnetic field is constant and the spacecraft changes attitude in such a way as to have the field aligned with each of the principal spacecraft axes for one-third of the measurements. For this scenario the variance s_i^2 is the same for all i, and w_i may be set to 1. The loss function $J(\mathbf{D})$ and matrix $\boldsymbol{X}$ are then for large N given by

$$J(\mathbf{D}) = 1/2\, N\, s^2 = N\, \sigma^2 (\, 2\, B^2 + 3\sigma^2 \,)\,, \qquad (33)$$

$$\boldsymbol{X} = (\, 2/3\, N\, B^2\, \boldsymbol{I}\,)^{-1}\,, \qquad (34)$$

from which it follows that each component of $\Delta\mathbf{D}$ is given by

$$\begin{aligned}\Delta D &= [\,2\,J(\mathbf{D})\,/\,N\,]^{1/2}\,W \\ &= [\,2\,\sigma^2\,(\,2\,B^2 + 3\sigma^2\,)\,]^{1/2}\,(\,2/3\,N\,B^2\,)^{-1/2} \\ &= \sigma/N^{1/2}\;6^{1/2}\;[\,1 + (\,3\sigma^2/\,2\,B^2\,)\,]^{1/2}\;. \qquad (35)\end{aligned}$$

The estimate specified above indicates that, for situations in which the measurement errors are small compared with the field strength, the algorithm described in this article will provide an estimate for the spacecraft bias that is about a factor of $6^{1/2}$ (i.e., ~ 2.5) less accurate than that which could be obtained with the same measurements if attitude information were independently available.

In situations where the use of the algorithm described in this article is intended as a preliminary calibration of the spacecraft bias, many of the details of algorithm may be neglected. As mentioned earlier, setting $< e_i > = 0$ and $w_i = 1$ is the simplest approach in practice. If B^2 is fairly constant, as should be roughly true (to within a factor of about 4) for a spacecraft at constant altitude, then taking the weights for all variables e_i to be equal would not be a bad approximation. It would be inappropriate, however, for spacecraft with highly eccentric orbits. Intuitively, it might be expected that neglecting $< e_i >$ could introduce errors in the solution for **D** of perhaps as much as σ. (Our numerical examples actually show this estimate to be too high.) Errors of this order are probably not significant for preliminary estimates. In the HST mission, for example, for which final spacecraft bias calibration will be performed using high-accuracy attitude information, the algorithm described here will be used with $< e_i > = 0$ and $w_i = 1$ and without iteration.

IV. NUMERICAL EXAMPLES

In this section we present the results of a number of numerical simulations that illustrate the use of the algorithm and verify its accuracy. After verifying that the algorithm obtains the exact solution when no noise is added to the measurements, we ran six test scenarios using noisy data. Each scenario comprises K bias determinations for each of two magnetometers, with each determination based upon N data points. Both K and N have the value 100 for all of the scenarios. The strength of the geomagnetic field is ~ 0.35 gauss in all cases, i.e., typical of that experienced by a spacecraft in near-Earth orbit, and the true values for spacecraft bias at the two magnetometer locations are

$$\mathbf{D}_1 = (\ 0.005,\ -0.015,\ 0.010\ )^T \text{ gauss} , \tag{36}$$

$$\mathbf{D}_2 = (\ -0.170,\ 0.280,\ 0.220\ )^T \text{ gauss} . \tag{37}$$

We selected these values to test the algorithm with bias values substantially below and approximately equal to the ambient field strength. For each scenario, we calculated the average error in the estimated bias (for both $\mathbf{D}_C$ and $\mathbf{D}$) and the standard deviation of these errors for each magnetometer. For calculating $\mathbf{D}$, we defined convergence as $|\mathbf{d}| < 0.001\ \sigma/N^{1/2}$.

We divide the six scenarios into two groups. The scenarios in the first group (scenarios 1, 2, and 3) all use a constant geomagnetic field. We are therefore able to compare the results of these scenarios directly with the analytic calculations presented in Section III. The scenarios in the second group (scenarios 4, 5, and 6) use a geomagnetic field constructed to simulate that which could be experienced by a spacecraft in near-Earth orbit. The height of the simulated orbit is 522 kilometers; the inclination is 28.5 degrees; and the right ascension of ascending node, argument of perigee, and latitude at epoch time (i.e., time of the first data point) are all 0 degrees. The geomagnetic field experienced by a spacecraft with this orbit is reasonably simulated (at least for our purposes) using the following parameterization:

$$B_{1,i} = 0.01 + 0.17\cos(\theta_i) \text{ gauss} , \tag{38}$$

$$B_{2,i} = -0.19 + 0.15\sin(\theta_i) \text{ gauss} , \tag{39}$$

$$B_{3,i} = 0.20 + 0.07\sin(\theta_i) \text{ gauss} , \tag{40}$$

where $\theta_i = 7.2\ (\ i - 1)$ degrees. The sample spacing corresponds roughly to one data point per minute over a single orbit. We present details for the individual scenarios in the following paragraphs and the principal numerical results in Table 1 (for scenarios 1, 2, and 3) and Table 2 (for scenarios 4, 5, and 6) at the end of this section. The specific entries in the tables are average error, standard deviation of the errors, estimated uncertainty based on equation (26), and for scenarios 1 and 2 the "theoretical" uncertainty calculated using equation (35).

Scenario 1. This scenario is a numerical execution of the idealized case described in Section III. It is designed to demonstrate the algorithm's accuracy for situations where the magnetometer measurements are uniformly distributed. The values for the parameters B and σ are 0.35 gauss and 0.01 gauss, respectively. As can be seen from Table 1, the magnetic bias estimates are equally accurate for both magnetometers, and no significant difference exists between the estimates **D** and $\mathbf{D}_C$. Typically, only two iterations are required to obtain the estimate **D** after $\mathbf{D}_C$ has been determined. The standard deviation for each of the error components is ~ 0.0018 gauss, in contrast to the "theoretical" value of ~ 0.0025 gauss predicted by both equations (26) and (35). This difference may be attributable to the qualitative nature of the concept of "extracting" the measurement errors from the matrix Y^{-1} that was used in deriving equation (27b). The average error in the estimated bias for each component of **D** (or $\mathbf{D}_C$) is zero to within plus or minus about twice $1.8\ \sigma / (N\ K)^{1/2}$ (i.e., ~ twice 0.00018 gauss), which is what would be expected given the standard deviation of the errors.

Scenario 2. This scenario is a repetition of scenario 1, except that in this case the parameter $< e_i >$ is set to zero. This scenario is designed to determine whether the algorithm with this simplification provides results of essentially the same accuracy as does the full algorithm. This, in fact, proves to be the case. The standard deviation of the errors is essentially the same as for scenario 1 (i.e., ~ $1.8\ \sigma / N^{1/2}$), and the average of the errors for any given component of **D** or $\mathbf{D}_C$ is shifted only slightly (~ 0.0006 gauss) from zero. This offset, though statistically significant, is small compared with the typical uncertainty of ~ 0.002 gauss for any single determination. It appears that a user of the algorithm can apply the simplification of neglecting both $< e_i >$ and the steps of iterating between $\mathbf{D}_C$ and **D** without substantially corrupting the results of the calculation.

Scenario 3. This scenario is designed to investigate the observability problems that the algorithm encounters if an observing run with insufficient variation of the geomagnetic field is used. The field strength and noise levels are the same as for scenario 1, but the three attitudes used are all within 14 degrees of one another. Specifically, the right ascension, declination, and roll for the three attitudes are, in degrees, (0, 0, 0), (10, 0, 0), and (0, 10, 0); and the geomagnetic field is directed toward sky coordinates (0, 0). As shown in Table 1, component 1 of the standard deviation vector for the errors of **D** is substantially smaller (by a factor of between 7 and 9) than components 2 and 3. Furthermore, the same kind of ratio between components applies for the uncertainty estimate derived using equation (26). Despite this basic agreement (i.e., proportionality) between the standard deviation vector and the uncertainty estimate, the average errors of the components of **D** are larger in size (i.e., offset from zero) by amounts that are statistically significant when compared with their expected rms size of $K^{-1/2}$ times the standard deviation. This is true in particular for component 1 for magnetometer 1 and components 2 and 3 for magnetometer 2. Although the offsets are statistically significant, they are all still smaller than the corresponding standard for the given component of **D**. The calculation of **D** remains basically good, but significantly degraded, for this scenario. In contrast to these results for **D**, the bias estimate $\mathbf{D}_C$ is a poor estimate of the true bias (particularly in the case of magnetometer 2, for which the true bias is large). For the scenario presented here, the averages of the errors for components 2 and 3 of $\mathbf{D}_C$ for magnetometer 2 are nearly 10 times as large as the rms error of a single measurement. These results emphasize the need for the user to arrange for data acquisition in a manner that guarantees substantial field variation in the spacecraft's frame. They further indicate that if such uniform data acquisition is for some reason not possible, then application of the full algorithm (i.e., continuing on to calculate **D** after $\mathbf{D}_C$) is imperative.

Scenario 4. This scenario, as well as the next two, is designed to test the algorithm using the more realistic geomagnetic field model described at the beginning of this section (i.e., as specified by equations (38) through (40)). The parameters w_i and $< e_i >$ are set in accordance with equations (29) and (30), with σ again equal to 0.01 gauss. As can be seen in Table 2, the results for scenario 4 with respect to accuracy of the solution are essentially the same as those for scenario 1 (component 3 of the error for both **D** and $\mathbf{D}_C$ for magnetometer 2 is just slightly greater than three times the expected rms value). These results demonstrate that the algorithm works well for realistic ambient magnetic field values, as well as for the idealized cases such as scenario 1.

Scenario 5. This scenario is a repetition of scenario 4, but with w_i set to 1 and $< e_i >$ set to 0. This scenario is designed with the same purpose as scenario 2, i.e., to check the accuracy of the algorithm when it is applied with the indicated simplifications. Comparing the results of this scenario and those of scenario 4 indicates (as was noted for scenario 2) that a mild degradation of results occurs when the simplified algorithm is used, but that this degradation is quite small. In actual operations, use of the simplified algorithm would almost certainly be acceptable. For the realistic error estimate being used in these scenarios (i.e., $\sigma \sim 0.01$ gauss), the final uncertainty in the bias estimate (using either **D** or $\mathbf{D}_C$) is of order 0.003 gauss.

Scenario 6. This scenario is a repetition of scenario 4, but with σ set to 0.1 gauss. The purpose is to test the robustness of the algorithm when used with very noisy data; the noise level used is about one-third of the ambient field strength. The algorithm requires approximately six iterations to converge and yields estimates for the bias with errors of order 0.04 gauss. In one case the algorithm failed to converge even after 10 iterations. As is clear in Table 2, the components of the vector of average errors are offset from zero by as much as 10 times the expected rms value. There is no indication that the estimate **D** is any better determined than is $\mathbf{D}_C$.

The basic conclusions to be the drawn from the six scenarios are that (1) the algorithm works very well for cases in which magnetometer noise levels are like those expected for actual spacecraft operations, (2) results obtained using the simplifications of setting w_i to 1 and $< e_i >$ to 0 and not iterating beyond the first estimate $\mathbf{D}_C$ are very nearly as good as those obtained using the full algorithm, and (3) the user of the algorithm should make every effort to arrange that magnetometer data acquisition be done in a way that provides substantial variation in all components. The results of scenarios 4 and 5 indicate that the kind of magnetic variation that a spacecraft with constant attitude in near-Earth orbit automatically experiences over a single orbit is adequate to the needs of the algorithm.

Table 1. Statistical Results from Scenarios 1 through 3

Magnetometer:		1			2		
Component:		1	2	3	1	2	3
Scenario 1							
	Average Error	0.00038	0.00038	0.00000	0.00008	0.00033	0.00027
D:	Standard Deviation	0.00179	0.00184	0.00182	0.00166	0.00190	0.00181
	Estimated Uncertainty	0.00242	0.00242	0.00239	0.00246	0.00246	0.00242
	Average Error	0.00037	0.00042	-0.00002	0.00029	-0.00001	-0.00001
D_c:	Standard Deviation	0.00178	0.00183	0.00181	0.00165	0.00188	0.00182
	Estimated Uncertainty	0.00242	0.00242	0.00239	0.00246	0.00246	0.00242
	Theoretical Uncertainty	0.00246	0.00246	0.00243	0.00246	0.00246	0.00243
Scenario 2							
	Average Error	0.00081	0.00081	0.00043	0.00051	0.00076	0.00070
D:	Standard Deviation	0.00179	0.00184	0.00182	0.00166	0.00190	0.00181
	Estimated Uncertainty	0.00242	0.00242	0.00238	0.00245	0.00245	0.00242
	Average Error	0.00080	0.00085	0.00041	0.00072	0.00041	0.00042
D_c:	Standard Deviation	0.00178	0.00183	0.00181	0.00165	0.00188	0.00181
	Estimated Uncertainty	0.00242	0.00242	0.00238	0.00245	0.00245	0.00242
	Theoretical Uncertainty	0.00246	0.00246	0.00243	0.00246	0.00246	0.00243
Scenario 3							
	Average Error	0.00093	0.00000	-0.00127	0.00018	-0.00807	-0.00955
D:	Standard Deviation	0.00209	0.01530	0.01677	0.00149	0.01342	0.01386
	Estimated Uncertainty	0.00242	0.01958	0.01943	0.00235	0.01899	0.01885
	Average Error	0.00077	0.00146	-0.00150	0.01664	-0.09821	-0.09171
D_c:	Standard Deviation	0.00178	0.01265	0.01405	0.00552	0.01369	0.01398
	Estimated Uncertainty	0.00242	0.01959	0.01944	0.00295	0.02386	0.02368

Note: All values are in gauss.

Table 2. Statistical Results from Scenarios 4 through 6

Magnetometer:			1			2	
Component:		1	2	3	1	2	3
Scenario 4							
D:	Average Error	-0.00003	0.00035	0.00032	0.00047	-0.00023	0.00077
	Standard Deviation	0.00272	0.00240	0.00212	0.00285	0.00243	0.00220
	Estimated Uncertainty	0.00375	0.00317	0.00292	0.00373	0.00315	0.00290
$\mathbf{D}_c$:	Average Error	-0.00006	0.00045	0.00023	0.00097	-0.00050	0.00076
	Standard Deviation	0.00270	0.00239	0.00211	0.00282	0.00241	0.00219
	Estimated Uncertainty	0.00375	0.00317	0.00292	0.00373	0.00315	0.00290
Scenario 5							
D:	Average Error	-0.00008	0.00056	0.00087	0.00054	0.00003	0.00128
	Standard Deviation	0.00270	0.00243	0.00216	0.00285	0.00244	0.00220
	Estimated Uncertainty	0.00378	0.00306	0.00323	0.00376	0.00304	0.00321
$\mathbf{D}_c$:	Average Error	-0.00011	0.00066	0.00077	0.00102	-0.00016	0.00122
	Standard Deviation	0.00269	0.00241	0.00215	0.00283	0.00242	0.00219
	Estimated Uncertainty	0.00378	0.00306	0.00323	0.00376	0.00304	0.00321
Scenario 6							
D:	Average Error	0.00086	0.02297	0.04112	0.00856	0.01891	0.04873
	Standard Deviation	0.03783	0.03083	0.03081	0.04478	0.03685	0.04229
	Estimated Uncertainty	0.03798	0.03188	0.02992	0.03749	0.03146	0.02953
$\mathbf{D}_c$:	Average Error	-0.00252	0.02606	0.02527	0.03283	-0.00035	0.02891
	Standard Deviation	0.02238	0.01896	0.01700	0.02563	0.02270	0.02359
	Estimated Uncertainty	0.03817	0.03203	0.03007	0.03847	0.03228	0.03031

Note: All values are in gauss.

V. CONCLUSIONS

We have presented a simple algorithm for the in-flight determination of the magnetic bias of a spacecraft. The algorithm, developed for use during the HST mission, is independent of any attitude estimates and requires no telemetry from spacecraft sensors other than the magnetometers at the locations where the bias is being determined. We have presented an analytical model for the errors in a typical observing scenario, as well as the results from a number of numerical studies demonstrating the general stability and accuracy of the algorithm. The algorithm works well and should be a useful tool for preliminary spacecraft magnetic bias determination for a variety of spacecraft missions.

The work reported in this article was supported in part by NASA contract NAS 5-26685 for the development of ground support software for the Hubble Space Telescope mission.

REFERENCES

1. K. A. Brownlee, Statistical Theory and Methodology in Science and Engineering. New York: John Wiley & Sons, Inc., 1960
2. H. Dougherty, *Effect of Magnetometer Noise on System Performance*, Memorandum LMSC/F227860 0/64-20, B/579, Lockheed Missiles & Space Company, Inc., 1988
3. B. R. Leaton, *International Geomagnetic Reference Field 1975*, Transactions of the American American Geophysical Union, 1976, vol. 57, no. 3, p. 120
4. B. T. Trombka and J. C. Cain, Computation of the IGRF I. Spherical Expansions, NASA X-922-74-303, National Aeronautics and Space Administration, Goddard Space Flight Center, August 1974
5. E. Zavaleta, Operations Support Computing Facility (OSCF) to Space Telescope (ST) Payload Operations Control Center (POCC) Interface Control Document, ST-ICD-32, CSC/TM-82/6152, Computer Sciences Corporation, May 1983, Section 3.2.4

N89-15951

Three-Axis Attitude Determination via Kalman Filtering of Magnetometer Data

by François Martel†, Parimal K. Pal*, and Mark L. Psiaki**

Abstract

A three-axis Magnetometer/Kalman Filter attitude determination system for a spacecraft in low-altitude Earth orbit is developed, analyzed, and simulation tested. The motivation for developing this system is to achieve light weight and low cost for an attitude determination system.

The extended Kalman filter estimates the attitude, attitude rates, and constant disturbance torques. Accuracy near that of the International Geomagnetic Reference Field model is achieved. Covariance computation and simulation testing demonstrate the filter's accuracy. One test case, a gravity-gradient stabilized spacecraft with a pitch momentum wheel and a magnetically-anchored damper, is a real satellite on which this attitude determination system will be used.

This work is similar to that of Heyler [5]. The application to a nadir pointing satellite and the estimation of disturbance torques represent the significant extensions contributed by this paper. Beyond its usefulness purely for attitude determination, this system could be used as a part of a low-cost three-axis attitude stabilization system.

---

† Vice President, Spacecraft Instruments Div., Ithaco Inc.

* Attitude Control Analyst, Ithaco Inc.

** Assistant Professor, Mechanical and Aerospace Engineering, Cornell University

Paper No. 17 for the Flight Mechanics/Estimation Theory Symposium, NASA/Goddard Space Flight Center, Greenbelt Maryland, May 10 & 11, 1988.

Three-Axis Attitude Determination via Kalman Filtering of Magnetometer Data

by François Martel, Parimal K. Pal, and Mark L. Psiaki

1 Introduction

1.1 Objective

The objective of this work has been to develop a low-cost system for estimation of 3-axis spacecraft attitude information based solely on 3-axis magnetometer measurements from one satellite orbit. Such a system will be useful for missions that operate in an inclined, low-Earth orbit and require only coarse attitude information. It can also serve as the sensor part of a low-cost 3-axis closed-loop attitude control system, or as a back-up attitude estimator.

A single 3-axis magnetometer measurement can give only 2-axes worth of attitude information and no attitude rate or disturbance torque information. Therefore, this attitude determination system must use a sequence of magnetometer measurements. It processes these measurements recursively in a Kalman filter. This paper, then, describes the design, development, analysis, and simulation testing of a Kalman filter and reports its expected performance. A follow-on, post-launch paper is planned to report actual performance.

1.2 Background/Prior Work

Kalman filters have been widely applied to the problem of spacecraft attitude determination [1-7]. Everything from star sensors [2,3] to sun sensors [4], gyroscopes [2], and magnetometers [4,5] have been used for filter inputs, and accuracies as fine as 2 arc sec. are possible [3].

Very few attitude determination systems have attempted to use only magnetometer data to estimate attitude. Perhaps this is because of the low accuracy of the measurements; even with perfect magnetometer measurements, inaccuracy of the knowledge of the Earth's magnetic field may introduce errors of 0.4° per axis. Perhaps such systems are rare because of the complexity of computing the Earth's magnetic field from spherical harmonic models [6]. In at least one case the benefits (low cost and low weight) have outweighed the costs and such a system has been developed. Heyler reports the use of such a system on the NOVA program [5]. That system was able to estimate spin axis attitude with a 2° accuracy as well as spin rate. These estimates were based on one eighth of an orbit's worth of magnetometer readings.

The Kalman filter reported in this paper uses 50 to 300 magnetometer samples distributed evenly over an orbit to estimate 3-axis attitude, attitude rate, and disturbance torques for a gravity-gradient-stabilized spacecraft. It is similar to the filter described by Heyler in that 3-axis information is derived purely from magnetometer measurement time histories. It differs from Heyler's filter in two respects; it estimates the attitude and rates for a different type of spacecraft, and it estimates disturbance torques. Also presented is a detailed accounting of the various contributions to estimation error, including the effects of spacecraft dynamic modeling error.

1.3 Outline of Approach

The remainder of this paper contains descriptions of the dynamic model of the spacecraft under consideration, the filter design, and the filter evaluation criteria and procedures. It concludes with the results of the filter evaluation. The spacecraft description discusses the type of spacecraft for which this filter will work and presents notation and equations necessary to the remaining sections. The filter design section presents the overall filter structure and two different gain selection techniques. The section on evaluation methodology describes the filter accuracy and stability performance criteria and the tools that were used to gauge these properties. The results of the accuracy and stability evaluations are presented in the final section, which includes examples of simulation time histories as well as numerical measures of performance.

2 Spacecraft Dynamic Model

2.1 Mission/Orbit Characteristics

The Kalman filter discussed in this work is applicable to nadir pointing Earth satellites operating at low altitudes in inclined orbits. The inclination and low altitude of the orbit are necessary to the proper functioning of the filter. The orbit must stay close enough to the Earth, within about 4 Earth radii [6], so that a spherical harmonic approximation of the Earth's magnetic field gives a reliable attitude reference. Some inclination of the orbit is necessary to make the attitude of all three axes sufficiently observable. Pitch information in a 1-orbit magnetometer time history gets poor for low inclinations, although theoretically, there is still some pitch information even in equatorial orbits; the Earth's magnetic poles do not coincide with its rotational poles. This study considers spacecraft in nearly circular orbits at 1.1 to 1.2 Earth radii. Filter analysis and testing has been done for the inclinations 43° and 57°.

2.2 Spacecraft Attitude Dynamics Model

The generic spacecraft (S/C) under consideration is a gravity gradient stabilized spacecraft. One model also has a pitch momentum wheel for passive yaw stiffening and a magnetically anchored damper for passive libration damping. The following equations of motion model the spacecraft attitude dynamics for purposes of filter state propagation:

$$\dot{\underline{\omega}} = \mathbf{I}_{inrt}^{-1}[\mathbf{n} - \underline{\omega} \times (\mathbf{I}_{inrt}\underline{\omega} + \mathbf{h}_w)] \tag{1}$$

$$\dot{\boldsymbol{q}} = \frac{1}{2}\begin{bmatrix} 0 & \omega_{SC/E_3} & -\omega_{SC/E_2} & \omega_{SC/E_1} \\ -\omega_{SC/E_3} & 0 & \omega_{SC/E_1} & \omega_{SC/E_2} \\ \omega_{SC/E_2} & -\omega_{SC/E_1} & 0 & \omega_{SC/E_3} \\ -\omega_{SC/E_1} & -\omega_{SC/E_2} & -\omega_{SC/E_3} & 0 \end{bmatrix}\boldsymbol{q} \tag{2}$$

$$\dot{\mathbf{n}}_d = \mathbf{0} \tag{3}$$

where $\underline{\omega}$ is the S/C's inertial angular velocity vector, $\mathbf{I}_{inrt}$ is the moment and product of inertia matrix, $\mathbf{n}$ is the total external vector torque acting on the S/C, $\mathbf{h}_w$ is the constant vector angular momentum of the pitch wheel, $\boldsymbol{q}$ is a quaternion that represents the orientation of the S/C-fixed coordinate system with respect to an Earth-fixed coordinate system, $\underline{\omega}_{SC/E}$ is the S/C's Earth-relative angular velocity, and $\mathbf{n}_d$ is the disturbance torque (the net unmodeled external torque). All of the above are expressed in S/C-fixed coordinates except the quaternion. It is expressed in Earth-fixed coordinates. Equation 1 is Euler's equation for rigid body rotational dynamics, and eq. 2 is the kinematic equation for a quaternion [6]. Equation 3 is special to the filter. It represents the unmodeled disturbance torques.

The net external torque acting on the S/C, $\mathbf{n}$, has been divided into three components, gravity gradient torque, $\mathbf{n}_{gg}$, passive magnetically-anchored damper torque, $\mathbf{n}_{damp}$, and all other unmodeled disturbance torques, $\mathbf{n}_d$:

$$\mathbf{n} = \mathbf{n}_{gg} + \mathbf{n}_{damp} + \mathbf{n}_d \tag{4}$$

The first two of these torque components, when present, have been explicitly modeled for purposes of filter state and covariance propagation.

The gravity gradient torque depends on the attitude quaternion, the ephemeris, and the moments and products of inertia:

$$\mathbf{n}_{gg} = \mathbf{n}_{gg}(\boldsymbol{q}, t; \mathbf{I}_{inrt}) \tag{5}$$

where t is the time. The gravity gradient model used in this study neglects J_2 effects [6].

The magnetically-anchored damper torque depends on the S/C-fixed magnetic field unit vector and its time rate of change, which in turn, depend on the attitude quaternion, the Earth-relative S/C angular velocity, and the ephemeris [6]:

$$\mathbf{n}_{damp} = c_{damp}\left[\hat{\mathbf{b}}(\boldsymbol{q}, t) \times \frac{d\hat{\mathbf{b}}}{dt}\bigg|_{(\boldsymbol{q},\, \underline{\omega}_{SC/E},\, t)}\right] \tag{6}$$

where c_{damp} is the damping factor, $\hat{\mathbf{b}}$ is the magnetic field unit vector in S/C-fixed coordinates, and the derivative with respect to time is the total derivative ($\boldsymbol{q}$ is time varying).

The unmodeled disturbance torque, $\mathbf{n}_d$, may include the effects of atmospheric drag, solar radiation pressure, residual magnetic dipole moment, S/C dynamics modeling errors, or any other unmodeled external torques. No explicit physical model of any of these torques is included. Rather, this term is retained in an effort to estimate these torques in the filter by modeling them as a random walk process.

The coordinate systems used in this study are a S/C-fixed coordinate system, an Earth-fixed coordinate system,

Table 1

Attitude Dynamics Parameters of Two Spacecraft

Spacecraft No.	I_{xx}	I_{yy}	I_{zz}	I_{xy}	I_{xz}	I_{xz}	c_{damp}	h_{w_2}
	(kg-m^2)						(N-m-s)	(kg-m^2/s)
1	200,000	300,000	70,000	200	2,000	-60	1	-70
2	250	250	10	0	0	0	0	0

and an orbit-following coordinate system. The S/C-fixed coordinate system is a Roll-Pitch-Yaw coordinate system; the x axis is nominally* parallel to the velocity vector, the y axis is nominally anti-parallel to the orbit normal, and the z axis is nominally along nadir. This reference frame is used to define the equations of motion and related equations, eq. 1-6, the inertia matrix, $\mathbf{I}_{inrt}$, and the pitch wheel angular momentum, $\mathbf{h}_w$.

The orbit-following coordinate system defines the nominal orientation of the gravity-gradient-stabilized S/C. Its z axis is exactly along nadir, its y axis is exactly anti-parallel to orbit normal, and its x axis is approximately parallel to velocity (exactly parallel in the case of circular, nondecaying orbits). Its only purpose in this study is as a point of reference for measuring roll, pitch, and yaw angles in reporting attitude results.

The Earth-fixed coordinate system has its origin at the Earth's center. Its x axis passes through the equator at the Greenwich meridian, its y axis passes through the Equator at 90° East Longitude, and its z axis passes through the North Pole. It is used to calculate the S/C ephemeris and the Earth's magnetic field, which are used in torque modeling and filter update calculations. Because this reference frame rotates with the Earth, there is a difference between the S/C's inertial angular velocity, $\underline{\omega}$, and its angular velocity with respect to this reference frame, $\underline{\omega}_{SC/E}$:

$$\underline{\omega}_{SC/E} = \underline{\omega} - \mathbf{A}\begin{bmatrix} 0 \\ 0 \\ \omega_e \end{bmatrix} \quad (7)$$

where $\mathbf{A}$ is the coordinate transformation matrix from Earth-fixed to S/C-fixed coordinates defined by $\boldsymbol{\varphi}$, and ω_e = $7.29\text{x}10^{-5}$ rad/sec is the Earth's rotational angular velocity. The angular velocity of the Earth as its revolves about the Sun has been neglected in this transformation.

Table 1 lists the nominal values of the attitude dynamics parameters for two S/C examples. Spacecraft 1 is stabilized by a long gravity gradient boom with a tip mass, a constant momentum pitch wheel, and a magnetically-anchored damper. Spacecraft 2 has a gravity-gradient boom, but it is left neutrally stable in yaw. The tabulated parameter values (sometimes with deliberately introduced perturbations) apply to the analyses and simulations described below.

2.3 Attitude Determination Hardware

The only attitude determination sensor used by this filter is a 3-axis magnetometer. It measures the magnetic field vector in S/C-fixed coordinates:

$$\mathbf{b} = \mathbf{A}\,\mathbf{b}_{E/F} \quad (8)$$

where $\mathbf{b}_{E/F}$, the magnetic field in the Earth-Fixed coordinate system, depends only on the S/C ephemeris. The $\mathbf{A}$ matrix depends on $\boldsymbol{\varphi}$, so eq. 8 defines the nonlinear measurement equation used by the extended Kalman filter.

---

* In the absence of orbital eccentricity, librational motion, disturbance torques, or product of inertia terms.

2.4 A Linearized Attitude Dynamics Model

Linearized equations of motion and sensor equations are useful for filter analysis and design. This involves linearization of eq. 1, 2, 4, 5, 6, and 8. They are linearized about the nominal S/C attitude time history: z axis along nadir, y axis along negative orbit normal, and y-axis angular velocity equal to the orbital rate. The orbit is assumed circular and J_2 effects are neglected. As a further simplification, a dipole model of the Earth's magnetic field is used [6], and the field at the S/C is assumed periodic with the orbital period (the rotation of the field with the Earth is ignored).

The attitude quaternion has been linearized in a special way. Instead if expressing $\boldsymbol{q}$ in terms of the sum of a nominal value plus a perturbation, it is expressed in terms of a perturbation quaternion times the nominal quaternion using quaternion multiplication:

$$\boldsymbol{q} = \boldsymbol{q}_{\mathrm{nom}} \bullet \begin{bmatrix} \Delta q_1 \\ \Delta q_2 \\ \Delta q_3 \\ 1 \end{bmatrix} = \boldsymbol{q}_{\mathrm{nom}} \bullet \begin{bmatrix} \Delta \mathbf{q} \\ 1 \end{bmatrix} \tag{9}$$

where, by definition of the nominal attitude time history, $\boldsymbol{q}_{\mathrm{nom}}$ defines the attitude of the orbit-following coordinate system. The perturbational quaternion is already normalized to within first order in the Δq_i. This perturbational expression of the attitude has just three unknowns; the fourth is not needed because the angles are small, the equations are linear, and no attitude singularity occurs.

The linearized equations are

$$\Delta \dot{\underline{\omega}} = \mathbf{I}_{\mathrm{inrt}}^{-1} [\Delta \mathbf{n} - \Delta \underline{\omega} \times (\mathbf{I}_{\mathrm{inrt}} \underline{\omega}_{\mathrm{orb}} + \mathbf{h}_w)$$

$$- \underline{\omega}_{\mathrm{orb}} \times (\mathbf{I}_{\mathrm{inrt}} \Delta \underline{\omega})] \tag{10}$$

$$\Delta \dot{\mathbf{q}} = \frac{1}{2} \Delta \underline{\omega} \tag{11}$$

$$\Delta \mathbf{n} = \Delta \mathbf{n}_{gg} + \Delta \mathbf{n}_{\mathrm{damp}} + \mathbf{n}_d \tag{12}$$

$$\Delta \mathbf{n}_{gg} = \frac{3\mu}{r_{S/C}^3} \left\{ \begin{bmatrix} -I_{23} \\ I_{13} \\ 0 \end{bmatrix} + 2 \begin{bmatrix} I_{33}-I_{22} & I_{12} & 0 \\ I_{12} & I_{33}-I_{11} & 0 \\ -I_{13} & -I_{23} & 0 \end{bmatrix} \Delta \mathbf{q} \right\} \tag{13}$$

$$\Delta \mathbf{n}_{\mathrm{damp}} = c_{\mathrm{damp}} \Big[(-\mathbf{I} + \hat{\mathbf{b}}_{\mathrm{orb}} \hat{\mathbf{b}}_{\mathrm{orb}}^T) \Delta \underline{\omega} + \hat{\mathbf{b}}_{\mathrm{orb}} \times \frac{d\hat{\mathbf{b}}_{\mathrm{orb}}}{dt}$$

$$+ 2 \left(\hat{\mathbf{b}}_{\mathrm{orb}} \times \frac{d\hat{\mathbf{b}}_{\mathrm{orb}}}{dt} \right) \times \Delta \mathbf{q} \Big] \tag{14}$$

$$\mathbf{b} = \mathbf{b}_{\mathrm{orb}} - 2 \Delta \mathbf{q} \times \mathbf{b}_{\mathrm{orb}} \tag{15}$$

where $\Delta \underline{\omega}$ is the perturbational S/C angular velocity expressed in S/C-fixed coordinates, $\underline{\omega}_{\mathrm{orb}}$ is the orbital angular velocity expressed in orbit-following coordinates (its only nonzero element is its y element), μ is the geocentric gravitational constant, $r_{S/C}$ is the S/C geocentric radius, I_{ij} is the i,j element of $\mathbf{I}_{\mathrm{inrt}}$, $\mathbf{I}$ is the identity matrix, and $\mathbf{b}_{\mathrm{orb}}$ is the Earth's magnetic field vector at the S/C expressed in orbit-following coordinates.

These equations can be combined in standard state vector format to yield a 9th-order system of the form

$$\Delta \dot{\mathbf{x}} = \mathbf{F}(t) \Delta \mathbf{x} + \mathbf{z}(t) \tag{16}$$

$$\mathbf{y} = \mathbf{H}(t) \Delta \mathbf{x} \tag{17}$$

where the state is defined as $\Delta \mathbf{x}^T = (\Delta \underline{\omega}^T, \Delta \mathbf{q}^T, \mathbf{n}_d^T)$ and where the observation is $\mathbf{y} = \hat{\mathbf{b}} \times \hat{\mathbf{b}}_{\mathrm{orb}}$. This definition of $\mathbf{y}$ retains all of the attitude information in the magnetometer measurements and gives an $\mathbf{H}(t)$ matrix consistent with the innovation definition given below (eq. 21). The 9x9 $\mathbf{F}(t)$ and matrix and the 9-element $\mathbf{z}(t)$ vector are derived from eq. 3, 10-14 and the definition of $\Delta \mathbf{x}$. The 3x9 $\mathbf{H}(t)$ matrix is derived from eq. 15 and the definition of $\mathbf{y}$. $\mathbf{F}(t)$, $\mathbf{H}(t)$, and $\mathbf{z}(t)$ are all periodic at the orbital period because the magnetic field has been assumed periodic at the orbital period. The periodicity of this linear system can be used to advantage in filter design and analysis.

The presence of $\mathbf{z}$ indicates that linearization has not been done about the nominal motion. As can be seen from eq. 13 and 14, the nonhomogeneous terms result from product of inertia terms (a gravity gradient effect) and from the time variation of the Earth's magnetic field as experienced in the orbit following reference frame (a magnetically-anchored damper effect). Nonzero $\mathbf{z}$ means that the S/C is not exactly trimmed at its nominal orientation. This out-of-trim condition is not vary large ($\leq\sim 1°$), and the linearized model is a good approximation for small perturbations from trim.

3 Filter Design

3.1 Filter Mission

The filter's mission is to estimate 3-axis attitude, attitude rate, and disturbance torque. The accuracy goal of the attitude estimates is on the order of ± 1°. This information may be required to run experiments off of a passively stabilized S/C or to provide feedback signals for active stabilization. For the former mission, the attitude estimation may be done in a ground station in batch mode once per orbit. When part of a feedback control loop, the filter will operate on board the S/C, recursively updating the attitude, rate, and torque estimates.

The filter computer program must execute quickly for such missions. When operating in a ground station there is only a short time window for magnetometer data transmission, one orbit's worth of filtering, and subsequent experimentation. Less time spent filtering leaves more time for the primary mission experiments. When operating on board, the filter has more time to filter one orbit's worth of data, but filtering will be only one of many tasks for the on-board computer. Less time spent filtering means more computer time left for primary mission usage.

3.2 Filter Structure and Gain Computation

The basic filter structure is that of the typical sampled-data extended Kalman Filter: a state/covariance propagation phase alternating with a state/covariance update phase once for each sensor sample time. Figure 1 gives a block diagram of this basic structure and the associated information flow. In the figure, t_k and t_{k+1} are sample times, $\mathbf{b}_{meas}$ is the vector of magnetometer measurements, $\tilde{\mathbf{x}}$ is the state estimate, $\mathbf{P}$ is the state estimate covariance matrix (not always used), and the (-) and (+) superscripts on $\tilde{\mathbf{x}}$ and $\mathbf{P}$ refer to pre- and post-update values, respectively, at a given magnetometer sample instant.

The state propagation portion of the filter is the usual nonlinear simulation of the system equations of motion, eq. 1-3. Therefore, the state estimate in the extended Kalman filter is a 10-dimensional vector:

$$\tilde{\mathbf{x}} = \begin{bmatrix} \tilde{\boldsymbol{\omega}} \\ \tilde{\mathbf{q}} \\ \tilde{\mathbf{n}}_d \end{bmatrix} \tag{18}$$

where the (~) overstrike indicates an estimate. The state propagation algorithm computes $\tilde{\mathbf{x}}^-(t_{k+1})$ as a function of $\tilde{\mathbf{x}}^+(t_k)$ by numerically integrating eq. 1-3 from time t_k to time t_{k+1} starting from the initial conditions:

$$\begin{bmatrix} \tilde{\boldsymbol{\omega}}(t_k) \\ \tilde{\mathbf{q}}(t_k) \\ \tilde{\mathbf{n}}_d(t_k) \end{bmatrix} = \tilde{\mathbf{x}}^+(t_k) \tag{19}$$

Formally, one may consider this procedure the definition of a vector function, $\boldsymbol{f}$, and a discrete-time system:

$$\tilde{\mathbf{x}}^-(t_{k+1}) = \boldsymbol{f}[\tilde{\mathbf{x}}^+(t_k),k] \tag{20}$$

Filter state propagation and evaluation of the function $\boldsymbol{f}$ are equivalent.

The state update calculation in this filter is slightly different from the traditional extended Kalman filter update in several respects. The filter innovations, the method of updating the quaternion estimate, and the method of calculating the filter gain are all slightly different from standard extended Kalman filter practice. Each of these differences has been introduced in order to handle the nonlinearities in a manner better than brute force linearization.

The cross product of the measured magnetic field unit vector with its pre-update estimate has been chosen for the innovation:

$$\underline{y}(t_{k+1}) = \hat{\mathbf{b}}_{meas}(t_{k+1}) \times \tilde{\hat{\mathbf{b}}}^-(t_{k+1}) \tag{21}$$

where $\underline{y}$ is the innovation and where the (^) overstrike indicates a unit vector. The standard extended Kalman filter would simply take the difference between $\mathbf{b}_{meas}$ and its pre-update estimate to form the innovation. The formula in eq. 21 essentially throws out all of the length information in the measured magnetic field. Nothing is lost as there is no attitude information in the length. In the linear analysis, either innovation formula would give the same update, but the eq. 21 formula is to be preferred in the nonlinear case because its magnitude and direction both are physically significant; they define the magnitude and direction of the known angular error.

The update formulas for the attitude rate and disturbance torque estimates take the usual form:

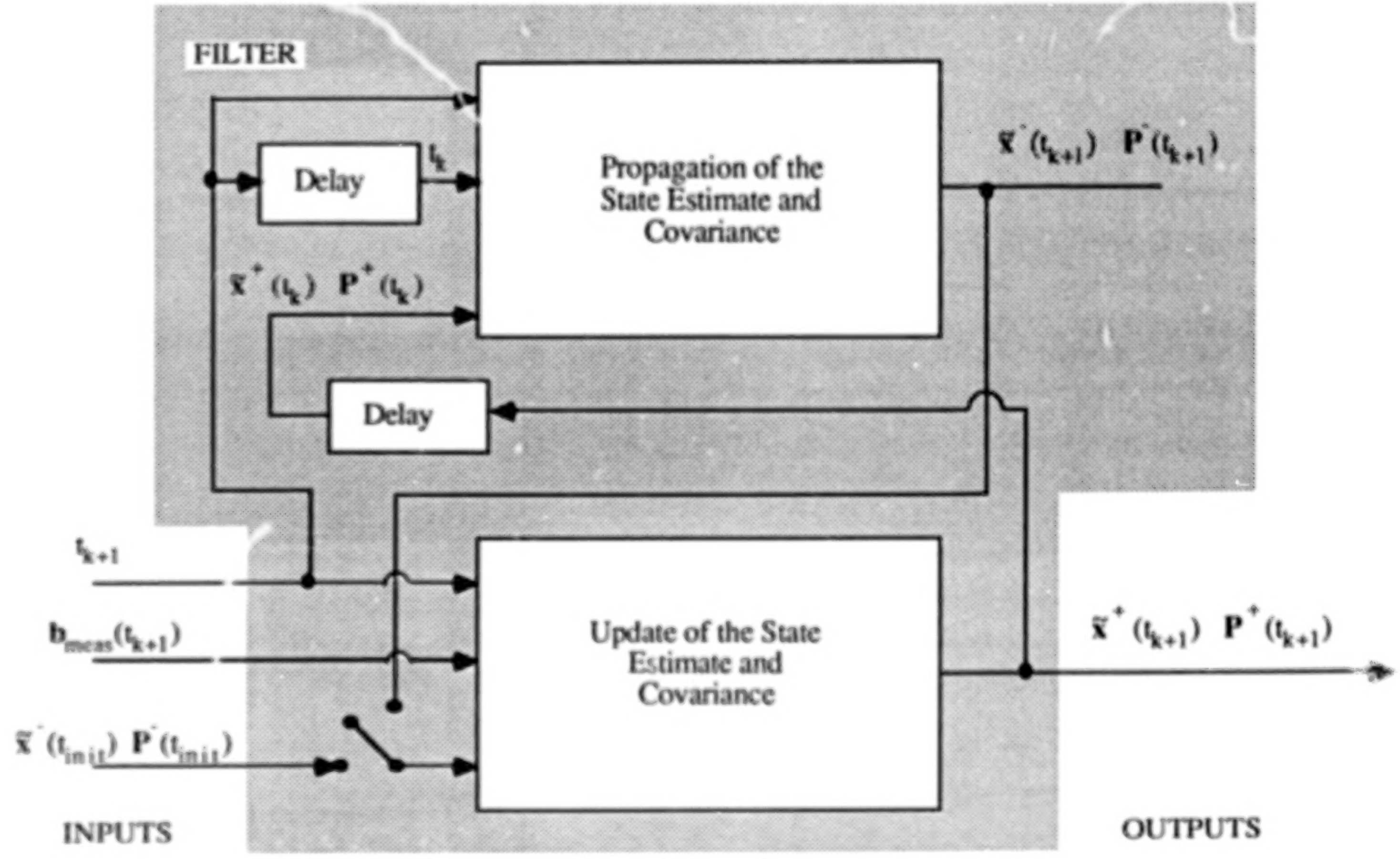
FILTER
Delay
t_k
Propagation of the State Estimate and Covariance
$\tilde{\mathbf{x}}^-(t_{k+1})$ $\mathbf{P}^-(t_{k+1})$
$\tilde{\mathbf{x}}^+(t_k)$ $\mathbf{P}^+(t_k)$
Delay
t_{k+1}
$\mathbf{b}_{meas}(t_{k+1})$
$\tilde{\mathbf{x}}^-(t_{init})$ $\mathbf{P}^-(t_{init})$
Update of the State Estimate and Covariance
$\tilde{\mathbf{x}}^+(t_{k+1})$ $\mathbf{P}^+(t_{k+1})$
INPUTS
OUTPUTS

Figure 1. Block Diagram of Kalman Filter Structure and Information Flow.

$$\vec{\hat{\omega}}^{+}(t_{k+1}) = \vec{\hat{\omega}}^{-}(t_{k+1}) + \mathbf{K}_{\omega_{k+1}}\underline{y} \qquad (22)$$

$$\vec{\hat{n}}_g^{+}(t_{k+1}) = \vec{\hat{n}}_g^{-}(t_{k+1}) + \mathbf{K}_{n_{k+1}}\underline{y} \qquad (23)$$

but the quaternion update uses quaternion multiplication instead of addition:

$$\vec{\bar{q}}^{+}(t_{k+1}) = \vec{\bar{q}}^{-}(t_{k+1}) \bullet \left[\frac{\Delta \mathbf{q}_{ud}}{\sqrt{1 - |\Delta \mathbf{q}_{ud}|^2}} \right] \qquad (24)$$

with

$$\Delta \mathbf{q}_{ud} = \mathbf{K}_{q_{k+1}}\underline{y} \qquad (25)$$

This form of the quaternion update explicitly recognizes that there are only three free variables in the quaternion and updates it accordingly. The $\Delta \mathbf{q}_{ud}$ vector elements constitute the three free variables as in the quaternion update method described by Lefferts *et.al.* [1]. The update preserves the quaternion's normalization.

The three **K** matrices in eq 22, 23, and 25 are the Kalman filter gain matrices. Because of the form of the innovation and the attitude update, the magnitude of the $\mathbf{K}_q$ gain matrix takes on physical significance. If the attitude determination system attempted to eliminate all of the measured attitude error at each measurement, $\mathbf{K}_q$ would be 1/2 times the 3x3 identity matrix. This is because $\underline{y}$ and $\Delta \mathbf{q}_{ud}$ are both in the direction of the measured attitude error, but the magnitude of $\underline{y}$ is proportional to the sine of the error while the magnitude of $\Delta \mathbf{q}_{ud}$ is proportional to the sine of half the error.

Two Kalman filter gain selection schemes have been tried. One uses, with a few necessary modifications, the standard extended Kalman filter covariance propagation, gain calculation, and covariance update formulas. The other uses fixed gains. The traditional extended Kalman filter was used in order to get the best possible filter performance. The fixed gain filter was used in the hope of achieving acceptable performance at a greatly reduced computational load.

The extended Kalman filter gain and covariance equations perform the necessary bookkeeping to derive 3-axis attitude information from the sequence of single-vector observations available to this filter. Modifications to these equations are necessitated by the nonstandard quaternion update, eq. 24 and 25, and by the nonstandard innovation, eq. 21. In addition, a discrete-time form of the covariance propagation equation is used in the interest of reducing the programming complexity; the continuous-time update would involve programming covariance differential equations; the discrete-time update involves only matrix arithmetic and calculation of the state transition matrix via numerical differentiation of the *f*[ ] function (eq. 20).

The discrete-time covariance propagation equation is

$$\mathbf{P}^{-}(t_{k+1}) = \Phi(t_{k+1},t_k)\mathbf{P}^{+}(t_k)\Phi^{T}(t_{k+1},t_k) + \mathbf{Q} \qquad (26)$$

where **P** is the 9x9 covariance matrix for the perturbation vector $\Delta \mathbf{x}^T = (\Delta \underline{\omega}^T, \Delta \mathbf{q}^T, \Delta \mathbf{n}_g^T)$, $\Phi(t_{k+1},t_k)$ is the state transition from $\Delta \mathbf{x}(t_k)$ to $\Delta \mathbf{x}(t_{k+1})$, and **Q** is the discrete-time disturbance input covariance matrix. The $\Delta \mathbf{q}$ perturbation is defined in the same way as the $\Delta \mathbf{q}_{ud}$ perturbation in eq. 24. This use of the 3-element $\Delta \mathbf{q}$ instead of the 4-element Δq simplifies the filter because there is no normalization constraint on the elements of $\Delta \mathbf{q}$. Thus, the 9x9 covariance is nonsingular, and the standard Kalman filter equations for gain computation and covariance update can be used [1].

The use of $\Delta \mathbf{q}$ affects the computation of the state transition matrix. Normally, it would simply be the 10x10 matrix $\partial f/\partial \mathbf{x}$. The expression of quaternion perturbations in terms of three independent components makes the state transition matrix

$$\Phi(t_{k+1},t_k) =$$

$$\begin{bmatrix} \mathbf{I} & 0 & 0 \\ 0 & \left.\frac{\partial q}{\partial \Delta q}\right|^{T}_{\vec{\bar{q}}^{-}(t_{k+1})} & 0 \\ 0 & 0 & \mathbf{I} \end{bmatrix} \left.\frac{\partial f}{\partial \mathbf{x}}\right|_{[\vec{\hat{\mathbf{x}}}^{+}(t_k),k]} \begin{bmatrix} \mathbf{I} & 0 & 0 \\ 0 & \left.\frac{\partial q}{\partial \Delta q}\right|_{\vec{\bar{q}}^{+}(t_k)} & 0 \\ 0 & 0 & \mathbf{I} \end{bmatrix} \qquad (27)$$

which is a 9x9 matrix. The derivative of the quaternion with respect Δq is just

$$\left.\frac{\partial q}{\partial \Delta q}\right|_{\vec{\bar{q}}} = \begin{bmatrix} \bar{q}_4 & -\bar{q}_3 & \bar{q}_2 \\ \bar{q}_3 & \bar{q}_4 & -\bar{q}_1 \\ -\bar{q}_2 & \bar{q}_1 & \bar{q}_4 \\ -\bar{q}_1 & -\bar{q}_2 & -\bar{q}_3 \end{bmatrix} \qquad (28)$$

where the $\bar{q}_i$ are the elements of $\vec{\bar{q}}$. This completes the covariance propagation formula. The approach of Lefferts *et. al.* is essentially the same [1].

The gain computation and covariance update formulæ are the usual Kalman filter formulæ [8]:

$$\begin{bmatrix} \mathbf{K}_{\omega_{k+1}} \\ \mathbf{K}_{q_{k+1}} \\ \mathbf{K}_{\eta_{k+1}} \end{bmatrix} = \mathbf{K}_{k+1}$$

$$= \mathbf{P}^{-}(t_{k+1})\mathbf{H}^{T}(t_{k+1})\left[\mathbf{R} + \mathbf{H}(t_{k+1})\mathbf{P}^{-}(t_{k+1})\mathbf{H}^{T}(t_{k+1})\right]^{-1} \tag{29}$$

$$\mathbf{P}^{+}(t_{k+1}) = \mathbf{P}^{-}(t_{k+1}) - \mathbf{K}_{k+1}\mathbf{H}(t_{k+1})\mathbf{P}^{-}(t_{k+1}) \tag{30}$$

where $\mathbf{R}$ is the measurement noise covariance matrix and $\mathbf{K}_{k+1}$ is the 9x3 filter gain matrix. The calculation of the observation matrix, $\mathbf{H}(t_{k+1})$ (as in eq. 17), accounts for the nonstandard innovation and the nonstandard quaternion update. The following formula gives the true $\mathbf{H}$ in the spirit of the extended Kalman filter:

$$\mathbf{H}(t_{k+1}) = -\frac{\partial \underline{\mathbf{y}}(t_{k+1})}{\partial \Delta \mathbf{x}(t_{k+1})}$$

$$= \left[\mathbf{0},\quad -2\tilde{\hat{\mathbf{b}}}^{-}(t_{k+1})\hat{\mathbf{b}}^{T}_{meas}(t_{k+1}),\quad \mathbf{0}\right] \tag{31}$$

which is a 3x9 matrix.

The fixed-gain extended Kalman filter avoids the complexity of eq. 26-31 and the considerable computational burden of calculating the state transition matrix via numerical differentiation of *f*[ ]. It can do this because fixed gains can stabilize the periodic observer associated with the periodic linearized system in eq. 16 and 17. Floquet analysis confirms this assertion. These gains have been calculated using a sub-optimal periodic observer theory that is similar to the sub-optimal control theory found in Anderson and Moore [9]. The algorithm for calculating such gains is very complicated and slow, but executes off line. Discussion of its theory is omitted, but results using this filter are presented below.

3.3 Filter Tuning

Filter tuning has two goals, timely convergence to an accurate estimate and maximum accuracy of the estimate. Filter tuning is possible through the selection of $\mathbf{Q}$, $\mathbf{R}$, and $\mathbf{P}^{-}(t_0)$. $\mathbf{Q}$ and $\mathbf{R}$ determine the trade-off between the filtering of measurement noise and the rapid tracking of disturbance noise-induced state variations. $\mathbf{P}^{-}(t_0)$ determines the rapidity of the initial filter convergence. In steady state, $\mathbf{Q}$ and $\mathbf{R}$ also determine the filter stability as a by-product of the measurement noise/disturbance noise trade-off. $\mathbf{P}^{-}(t_0)$ has no effect on the steady state performance of the filter.

The filter needs to have a rapid initial convergence because its mission is to accurately determine attitude with one orbit's worth of magnetometer data and poor initial attitude estimates. This means either a large $\mathbf{P}^{-}(t_0)$ compared to $\mathbf{R}$ or a large $\mathbf{Q}$ compared to $\mathbf{R}$. For the extended Kalman filter, which is inherently a time-varying filter, the former method has been used to achieve rapid initial convergence. The latter method has been used for the fixed-gain filter because it is a steady-state filter; it has no $\mathbf{P}^{-}(t_0)$. This points to one advantage of time-varying filters: they allow rapid convergence without sacrifice of steady state filtering optimality.

Optimal steady-state tuning of the filter is important to achieving the accuracy goal of ± 1°. The levels of measurement noise and disturbance torque that are present in a real S/C system make this a challenging goal. For the extended filter, this tuning is achieved by setting $\mathbf{Q}$ and $\mathbf{R}$ to magnitudes representative of the expected disturbance inputs and measurement noise. For the one case where detailed error analysis has been done, the disturbance torque level has been based on models of atmospheric drag torque and solar radiation pressure torque. The measurement noise has been based on magnetometer digitization error. The measurement error is actually much larger due to analog magnetometer noise and field model errors, so the filter is somewhat over sensitive to measurement noise in this case.

4 Evaluation of Filter Performance: Objectives and Tools

4.1 Filter Performance Criteria

There are two criteria for satisfactory filter performance: Does it converge? How accurate are its estimates of the S/C attitude? Because the system is nonlinear, filter stability is not guaranteed for large initial errors in the state estimate. Furthermore, the rate of convergence of stable filters is important because of the mission requirements; convergence must be achieved within one orbit. The importance of estimation accuracy is self evident. To evaluate the filter with respect to these two criteria is the objective of the test procedures that are outlined below. Results are reported in Section 5.

4.2 Analytical Tools for Performance Evaluation

The linearized model of the S/C's attitude dynamics, eq. 16 and 17, provides a valuable tool for analyzing filter stability and accuracy. The corresponding discrete-time model takes the form

$$\mathbf{x}_{k+1} = \Phi(t_{k+1},t_k)\mathbf{x}_k + \zeta_{wk} \quad \text{for } k = 0,\ldots,N-1 \tag{32}$$

$$\mathbf{y}_k = \mathbf{H}(t_k)\mathbf{x}_k \quad \text{for } k = 1,\ldots,N \tag{33}$$

where N is the number of magnetometer samples per orbit. Because the system in eq. 16 and 17 is periodic with the orbital period, the above discrete-time system is periodic with period N.

System observability from one orbit's worth of data can be analyzed by computation of the 1-orbit observability Gramian [10]. This Gramian is

$$\mathcal{O} = \sum_{k=1}^{N} \Phi^T(t_k,t_0)\mathbf{H}^T(t_k)\mathbf{H}(t_k)\Phi(t_k,t_0) \tag{34}$$

If this 9x9 matrix is nonsingular, then the system is observable from one orbit's worth of data and there is hope for constructing a filter that converges in one orbit. One would expect this matrix to approach singularity with decreasing orbital inclination. A study of this dependence would map out the inclinations where the filters under consideration can be applied. The only observability Gramians computed for this study, however, were for the two orbital inclinations mentioned in Section 2, 43° and 57°.

Filter stability can be analyzed by applying Floquet theory to the discrete-time model of the steady-state filter. The steady-state, linear-model filter gains, $\mathbf{K}_k$ for $k = 1\ldots N$, are periodic with period N; so, the filter itself is periodic. The one-orbit state transition matrix of the filter becomes:

$$\begin{aligned}\Phi_{CL}(t_N,t_0) &= [\mathbf{I} - \mathbf{K}_N\mathbf{H}(t_N)]\Phi(t_N,t_{N-1})\ldots[\mathbf{I} - \mathbf{K}_1\mathbf{H}(t_1)]\Phi(t_1,t_0)\\ &= \prod_{k=0}^{N-1}[\mathbf{I} - \mathbf{K}_{k+1}\mathbf{H}(t_{k+1})]\Phi(t_{k+1},t_k)\end{aligned} \tag{35}$$

where the CL subscript means closed-loop in the sense that the open-loop system state transition matrix and the filter gains are factored into this expression to give the 1-orbit observer error state transition matrix. The eigenvalues of $\Phi_{CL}(t_N,t_0)$ must all have magnitudes less than unity for filter stability, and the smallness of the eigenvalue magnitudes indicates the rate of convergence.

Accuracy of the filter can also be studied with the linearized, steady-state filter model. Given measurement and disturbance noise covariance matrices, **R** and **Q**, the periodic linear-filter covariance, $\mathbf{P}^+(t_k)$ for $k = 0\ldots N$, can be determined from the following linear system of equations:

$$\begin{aligned}\mathbf{P}^+(t_{k+1}) = {}&[\mathbf{I} - \mathbf{K}_{k+1}\mathbf{H}(t_{k+1})][\Phi(t_{k+1},t_k)\mathbf{P}^+(t_k)\Phi^T(t_{k+1},t_k)\\ &+ \mathbf{Q}][\mathbf{I} - \mathbf{K}_{k+1}\mathbf{H}(t_{k+1})]^T\\ &+ \mathbf{K}_{k+1}\mathbf{R}\,\mathbf{K}^T_{k+1} \qquad \text{for } k = 0,\ldots,N-1\\ \mathbf{P}^+(t_N) = {}&\mathbf{P}^+(t_0)\end{aligned} \tag{36}$$

The **Q** and **R** matrices used here must be the best estimates of the actual disturbance and noise covariances, whereas those used in determining the $\mathbf{K}_{k+1}$ in an optimal or sub-optimal filter calculation may differ from the best estimates for various reasons. The 1-orbit average of the covariance yields the mean square filter accuracy:

$$\mathbf{P}_{MS} = \frac{1}{N}\sum_{k=0}^{N-1} \mathbf{P}^+(t_k) \tag{37}$$

which is a good measure of the effects of random disturbances and measurement noise on the filter accuracy.

4.3 Simulation Testing

Simulation testing is an important complement to analysis for purposes of filter evaluation. Nonlinearities may cause the filter to diverge for large initial attitude errors. Systematic errors such as parameter uncertainty or biases may degrade stability or accuracy or both. Linear analysis cannot evaluate these effects, but simulation can.

Each simulation test has two parts, a simulation and a filter. The simulation starts with an "actual" initial state, $\mathbf{x}(t_0)$, and integrates the S/C attitude dynamics equations, eq. 1-3 or eq. 16, to produce a simulated "actual" state time history, $\mathbf{x}(t_k)$ for $k = 0,1,2,\ldots$ It also simulates the magnetometer measurements to produce a measurement time history, $\mathbf{b}_{meas}(t_k)$ for $k = 0,1,2,\ldots$ The filter takes these simulated magnetometer measurements, combined with initial estimates of the state and covariance, and produces an estimate of the state time history, $\hat{\mathbf{x}}^+(t_k)$ for $k = 0,1,2,\ldots$ Evaluation of the filter is accomplished by comparing the

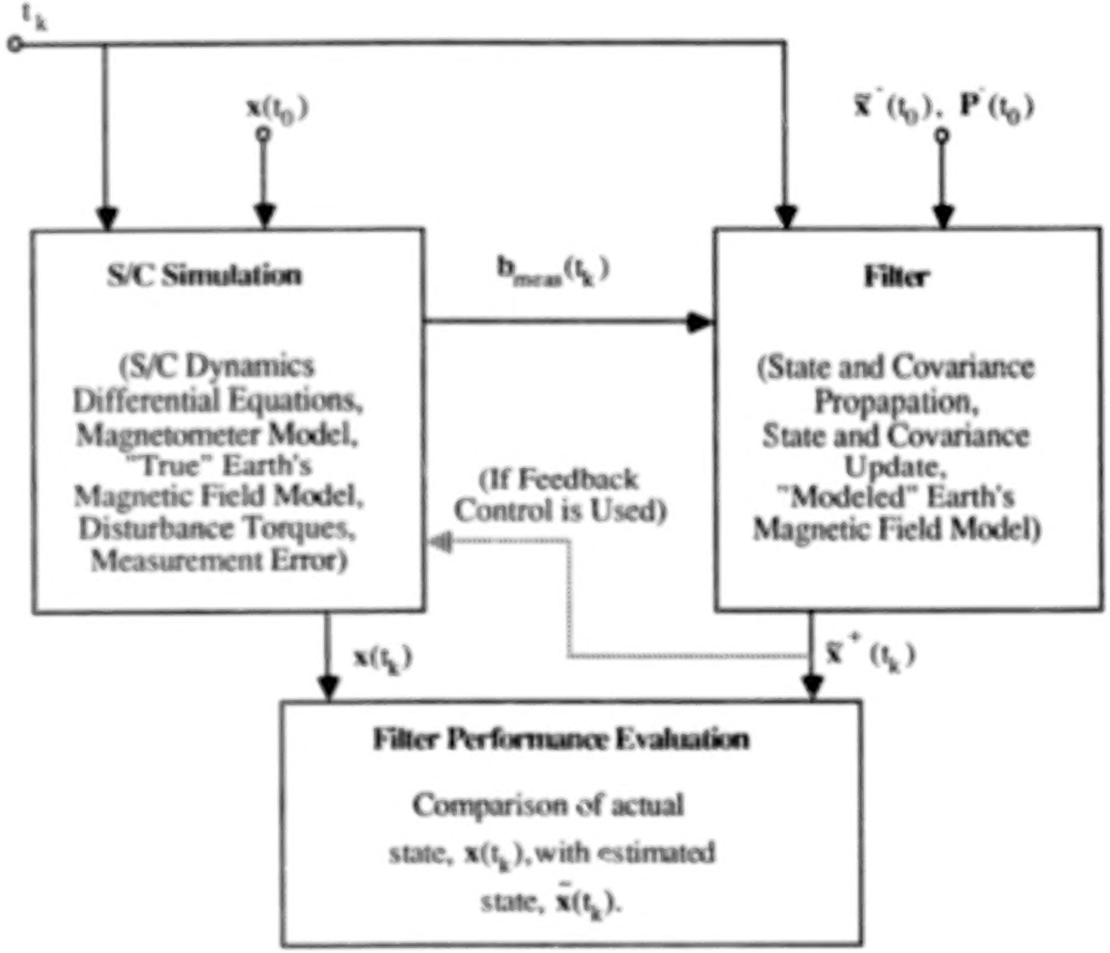
t_k
$\mathbf{x}(t_0)$
$\bar{\mathbf{x}}^-(t_0)$, $\mathbf{P}^-(t_0)$
S/C Simulation
(S/C Dynamics Differential Equations, Magnetometer Model, "True" Earth's Magnetic Field Model, Disturbance Torques, Measurement Error)
$\mathbf{b}_{meas}(t_k)$
Filter
(State and Covariance Propagation, State and Covariance Update, "Modeled" Earth's Magnetic Field Model)
(If Feedback Control is Used)
$\mathbf{x}(t_k)$
$\bar{\mathbf{x}}^+(t_k)$
Filter Performance Evaluation
Comparison of actual state, $\mathbf{x}(t_k)$, with estimated state, $\bar{\mathbf{x}}(t_k)$.

Figure 2. Block Diagram of Simulation Test Structure and Information Flow.

"actual" state time history with the estimated state time history. Figure 2 depicts this two-part process, the flow of information between the parts, and the information used in evaluating the filter. For a good filter $\hat{\mathbf{x}}^{+}(t_k)$ will converge quickly to $\mathbf{x}(t_k)$ and stay near it despite large discrepancies between $\hat{\mathbf{x}}^{-}(t_0)$ and $\mathbf{x}(t_0)$ and despite disturbance torques, measurement noise, and modeling error.

Several properties of the filter have been evaluated with this simulation test scheme: the ability of the filter to converge from large initial attitude or rate errors, the ability of the filter to estimate constant disturbance torques, filter accuracy in the face of random disturbance torques and measurement noise, filter accuracy in the face of parameter errors in the S/C attitude dynamics model, and filter accuracy in the face of magnetometer biases. The attitude, rate, and torque estimation capabilities have been tested simply by running the nonlinear simulation and the filter starting each with different initial conditions (remember, disturbance torque is treated as a state). Filter accuracy in the face of random inputs has been evaluated by linear analysis, and for verification purposes, by simulation. The latter has been done by using time-varying measurement noise and disturbance torque models in appropriate parts of the simulation.

Attitude-dynamics parameter errors and measurement biases are systematic errors. Evaluation of their effects is tricky. They may or may not affect filter stability. They will certainly affect accuracy. The method used to evaluate these effects has been to simulate with one attitude dynamics/measurement process model and filter with a different model, the difference being the particular systematic error under consideration. The filter's stability and accuracy are then evaluated by comparison of the simulated "actual" state time history with the estimated state time history. Convergence is evaluated by comparing these two time histories for the first orbit. Accuracy is evaluated by taking the root mean square value of the difference between the estimated state and the "actual" state for all subsequent orbits. Convergence and accuracy are both dependent on the magnitude of the modeling errors. They may also be dependent on the magnitude of the S/C librations. Therefore, correct sizing of the errors and of the S/C libration amplitude is critical to correct analysis of these effects.

5 Filter Performance Results

5.1 Convergence

Filter convergence can be achieved if the 9x9 1-orbit observability Gramian (eq. 34) is nonsingular. This has been found to be the case for low Earth orbits at both 43° and 57° inclination. For S/C 1 of Table 1 in the 43° orbit, the 50-samples-per-orbit Gramian has a ratio of minimum eigenvalue to maximum eigenvalue of 8×10^{-7}. If the constant disturbance torque columns and rows are omitted, then the ratio increases to 3×10^{-4} for the resulting 6x6 sub-Gramian. For S/C 2 operating in the 57° orbit, a full Gramian has a minimum to maximum eigenvalue ratio of 6×10^{-13} (still nonzero in double precision arithmetic); whereas, the sub-Gramian for observing just the angles and the rates has an eigenvalue ratio of 6×10^{-4}. Thus, the filter can be made to converge in one orbit. The torques are less observable than the angles and rates. All cases are observable, but the second S/C case is less observable than the first, probably due more to the difference in S/C dynamic properties than to the difference in orbit.

The magnitudes of the eigenvalues of the one-orbit filter state transition matrix (eq. 35) are direct measures of stability. These have been computed for the time-varying filters in steady-state and for the fixed-gain filters. The fixed gain filter case that has been analyzed in detail involves S/C 1 operating in the 43° orbit at 50 magnetometer samples per orbit. The lowest achievable maximum eigenvalue magnitude for the fixed-gain 1-orbit state transition matrix has been 0.32, which indicates adequate stability but slow convergence. The time-varying extended Kalman filters do better, even in steady state. Their 1-orbit state transition matrices have maximum eigenvalue magnitudes typically less than 0.20. The initial convergence of these time-varying filters is even better than this steady-state result indicates because of the high values selected for the initial covariance matrix, $\mathbf{P}^{-}(t_0)$.

This rapid initial convergence is indicated clearly in Fig. 3 and 4 for S/C 2 in the 57° orbit. The time-varying filter used in this case operates on about 300 magnetometer samples per orbit; all of the S/C-1 cases used 50 samples per orbit. In these figures as in most of the remaining figures, the "actual" value, the estimated value, and the estimation error for a particular quantity are all plotted together on a single graph. The orbital period is a little over 5,000 sec, so

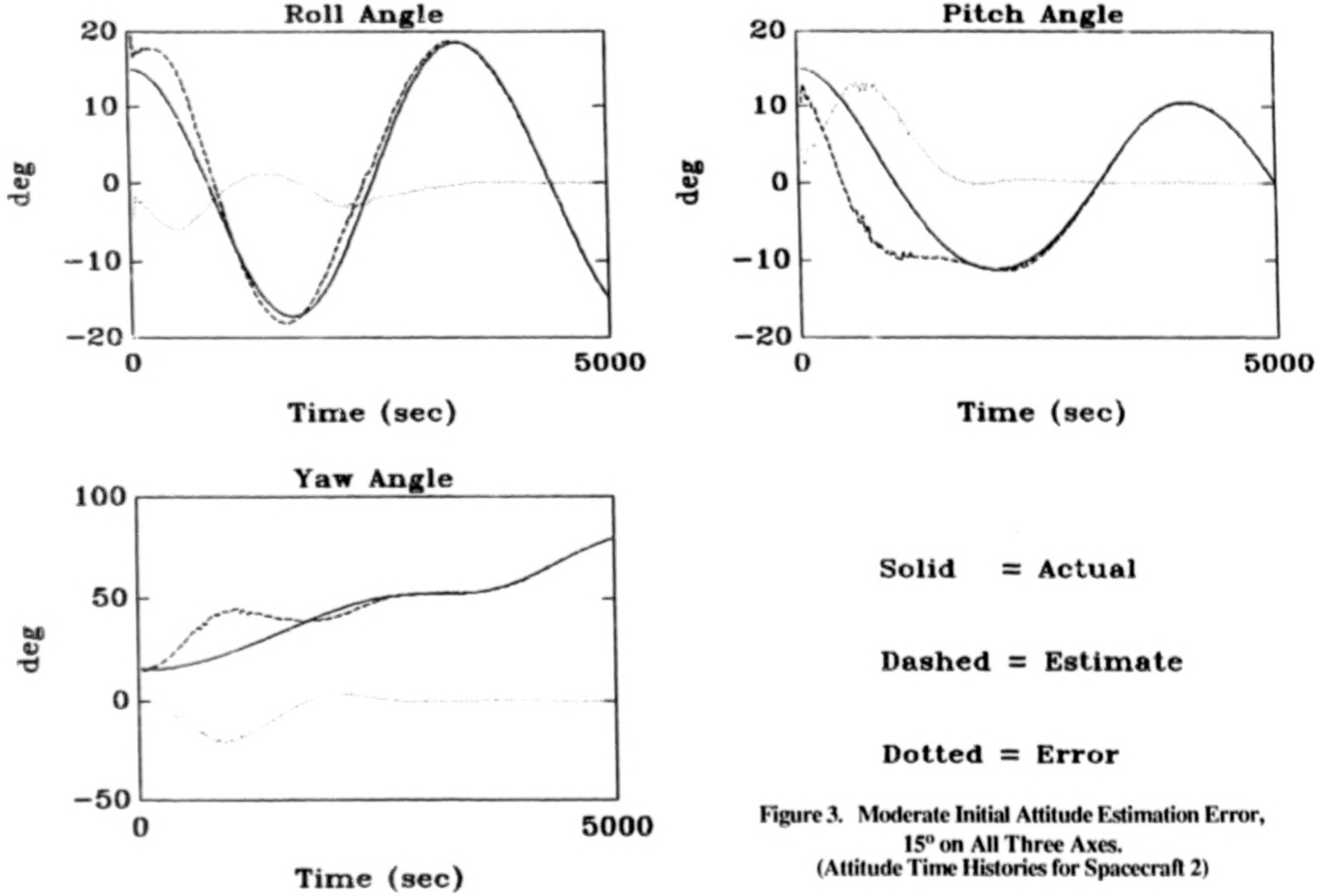

Figure 3. Moderate Initial Attitude Estimation Error, 15° on All Three Axes. (Attitude Time Histories for Spacecraft 2)

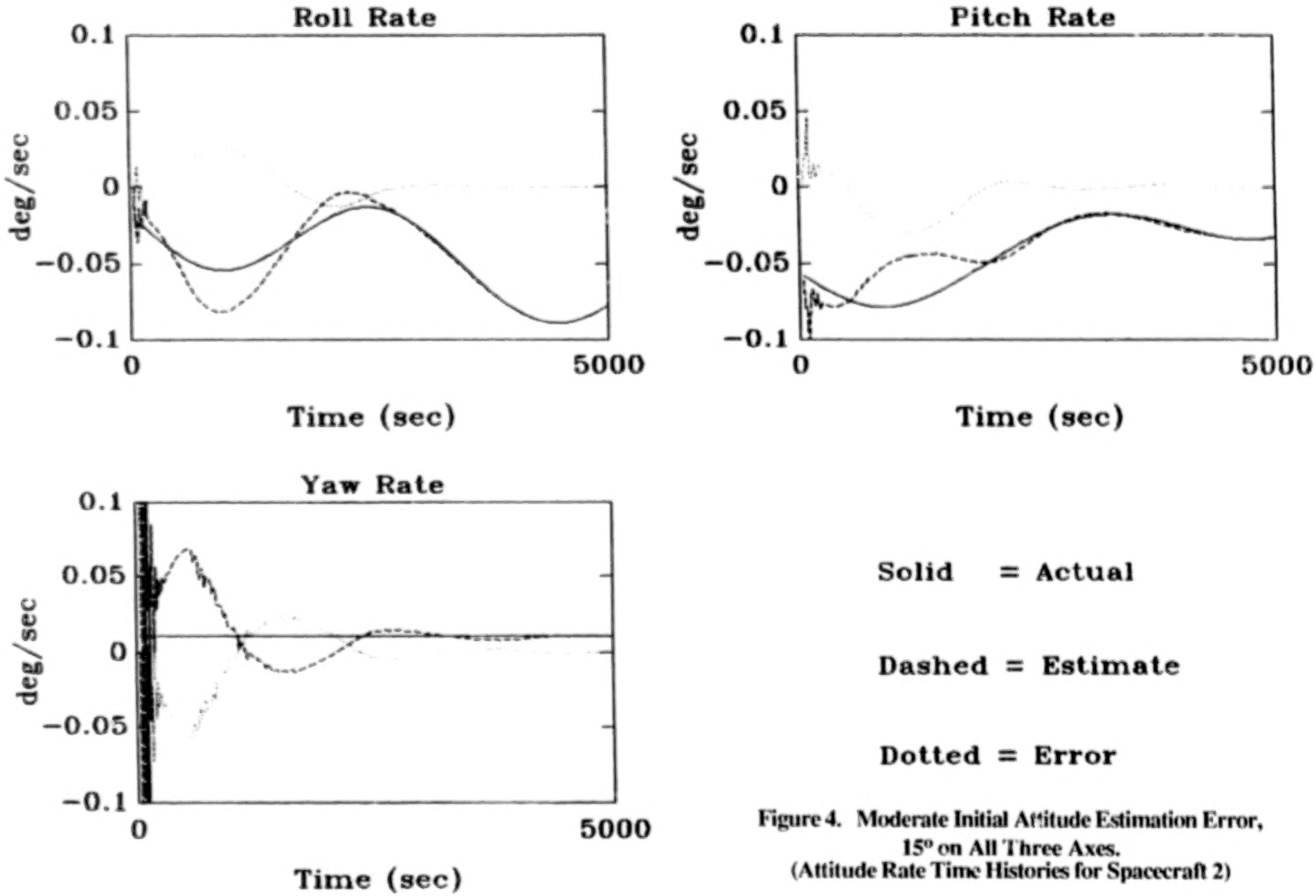

Figure 4. Moderate Initial Attitude Estimation Error, 15° on All Three Axes. (Attitude Rate Time Histories for Spacecraft 2)

convergence takes place within about half an orbit. The initial error is 15° each in roll, pitch, and yaw with no initial rate errors. The initial filter jitter in the rate estimates (Fig. 4) arises because of the high initial filter gains. Perhaps these are too high. Essentially, the filter is trying to take first and second derivatives to get rate and torque information.

Figures 5 and 6 further demonstrate the ability of the time-varying extended Kalman filter to converge. In the case of Fig. 5, a 0.017 N-m aerodynamic pitch torque is acting on S/C 1, which is in the 43° orbit. The filter converges to a correct estimate of this disturbance torque in just about one orbit (5,700 sec). Figure 6 corresponds to the same S/C-orbit case with large initial errors in the attitude estimate; the total initial rotational error is 45°. The filter successfully converges in about one orbit, despite the increased significance of nonlinearities.

Figure 7 also depicts estimation of the attitude of S/C 1 in the 43° orbit, but the estimates have been generated by a fixed-gain filter. These estimates converge from moderate initial errors (11° in all three axes), but convergence is slow. After almost two orbits errors on the order of 1° still persist. This makes sense in light of the large maximum filter eigenvalue. This convergence rate is too slow for the filter's intended purpose. Time-varying filters are preferable to fixed gain filters because of the ability to achieve faster initial convergence by increasing $\mathbf{P}^{-}(t_0)$.

5.2 Steady-State Error Analysis

Error analysis has been done for S/C 1 operating in the 43° orbit. This error analysis combines the linear analysis technique described in Section 4.2 with the simulation technique described in section 4.3. The linear technique has been used for random errors, the simulation technique for systematic errors. The final error budget combines the two in a square-root-of-the-sum-of-the-squares (RSS) sense.

The random effects considered are time varying solar and atmospheric drag disturbance torques (constant disturbance torques do not affect the error because they are estimated as part of the filter state vector), random magnetometer measurement error and digitization error, and random or high-order International Geomagnetic Reference Field (IGRF) model error. The disturbance covariance matrix magnitude is based on the results of a solar torque and aerodynamic torque analysis for the S/C. The magnetometer random error is based on a 5 mGauss spec for its accuracy and a 12-bit digitization. The field error was set at 0.41° rms per axis based on experience with the IGRF model data [6].

Figure 8 depicts a simulation of the effects of one of the random errors, magnetometer digitization error. Initial convergence is hardly affected by this random process; convergence to within 0.5° still occurs within one orbit. Afterwards, random effects dominate the error signal. This calls for proper selection of the **Q** and **R** filter matrices for optimal steady state filter performance.

The systematic error magnitudes have been derived from typical S/C 1 specifications. Errors of 2% in the magnitudes of the principal moments of inertia were used. This number is based on the possible variability of the boom lengths and tip mass weights. Errors of 1.5° for the principal axis orientations were used to generate the cross product of inertia errors. This magnitude is based on angular accuracy specifications for the booms. A 5% error for the pitch wheel angular momentum was used, based on hardware specifications. A 1.4 N-m-sec error for the magnetically-anchored damping constant was assumed, a typical level of variability on orbit. A 3 mGauss bias error per axis for the magnetometer was used based on a typical magnetometer spec.

Representative libration magnitudes were used for the error budget simulations: 0.4° peak-to-peak roll angle oscillations, 4.0° peak-to-peak pitch angle oscillations, and 1.6° peak-to-peak yaw angle oscillations. These libration magnitudes are based on analysis of typical S/C 1 motions on orbit.

Figures 9 and 10 are typical of the simulation/filter time histories that have been used to evaluate the effects of systematic errors. The simulation in Fig.9 corresponds to discrepancies between the filter model and the simulation model of 1.5° in all three principal axes. The discrepancy corresponding to Fig. 10 is 1.4 N-m-sec in the passive damping constant. The filter converges in both these cases. As per the analysis description at the end of Section 4.3, the steady state error contributions have been taken to be the post-one-orbit rms error values.

Table 2 summarizes the error budget for this case. According to this analysis the filter meets the 1° attitude

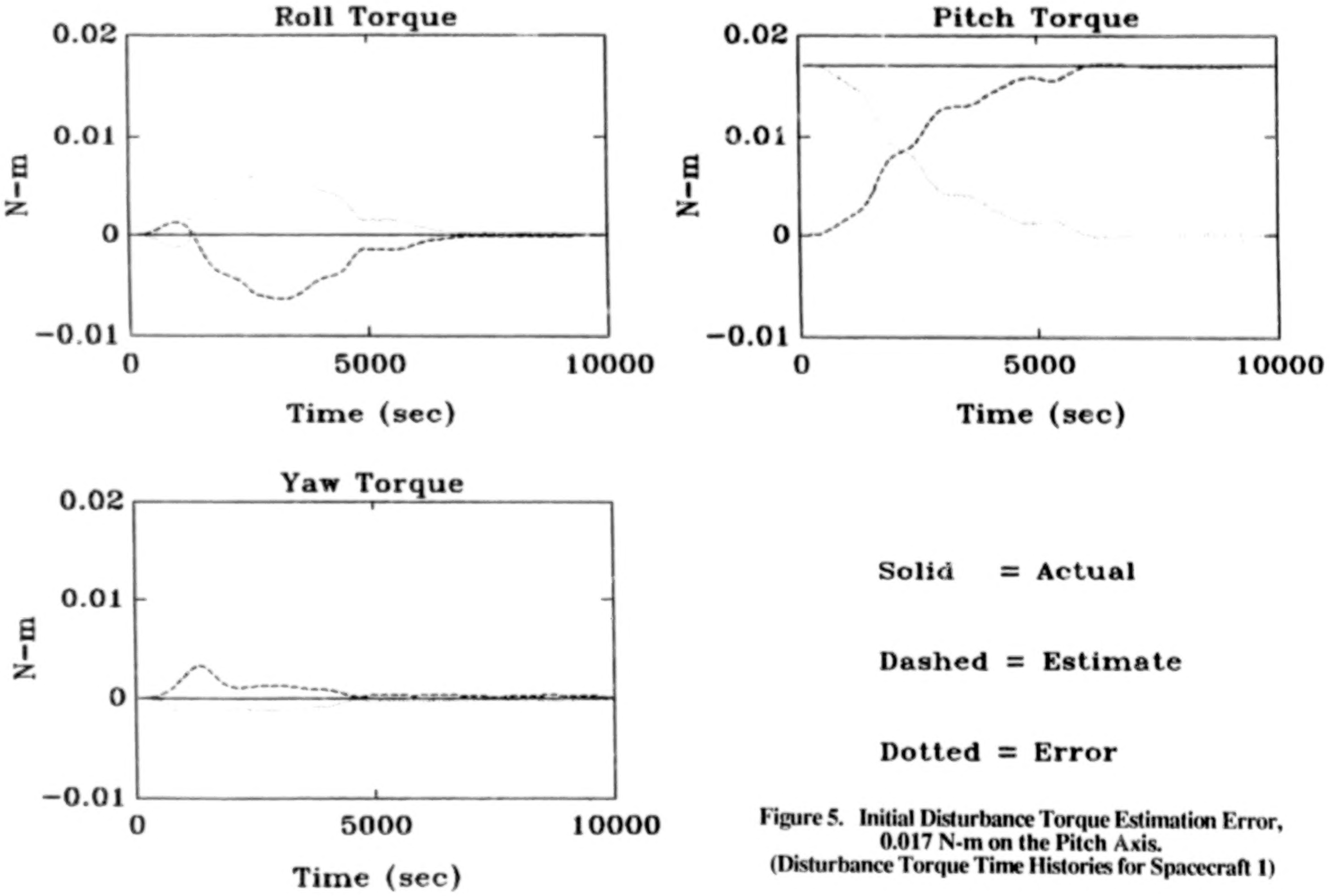

Figure 5. Initial Disturbance Torque Estimation Error, 0.017 N-m on the Pitch Axis. (Disturbance Torque Time Histories for Spacecraft 1)

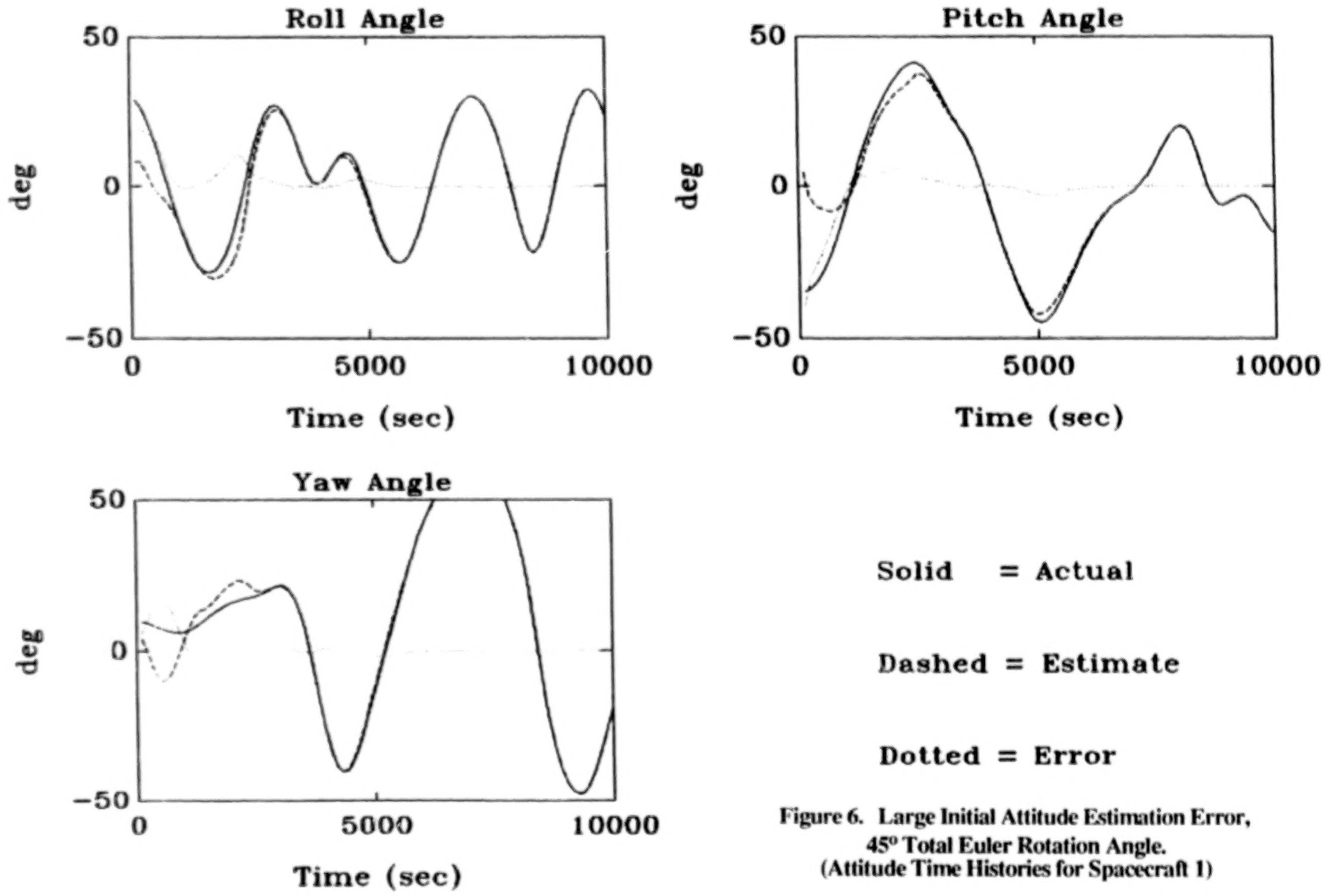

Figure 6. Large Initial Attitude Estimation Error, 45° Total Euler Rotation Angle. (Attitude Time Histories for Spacecraft 1)

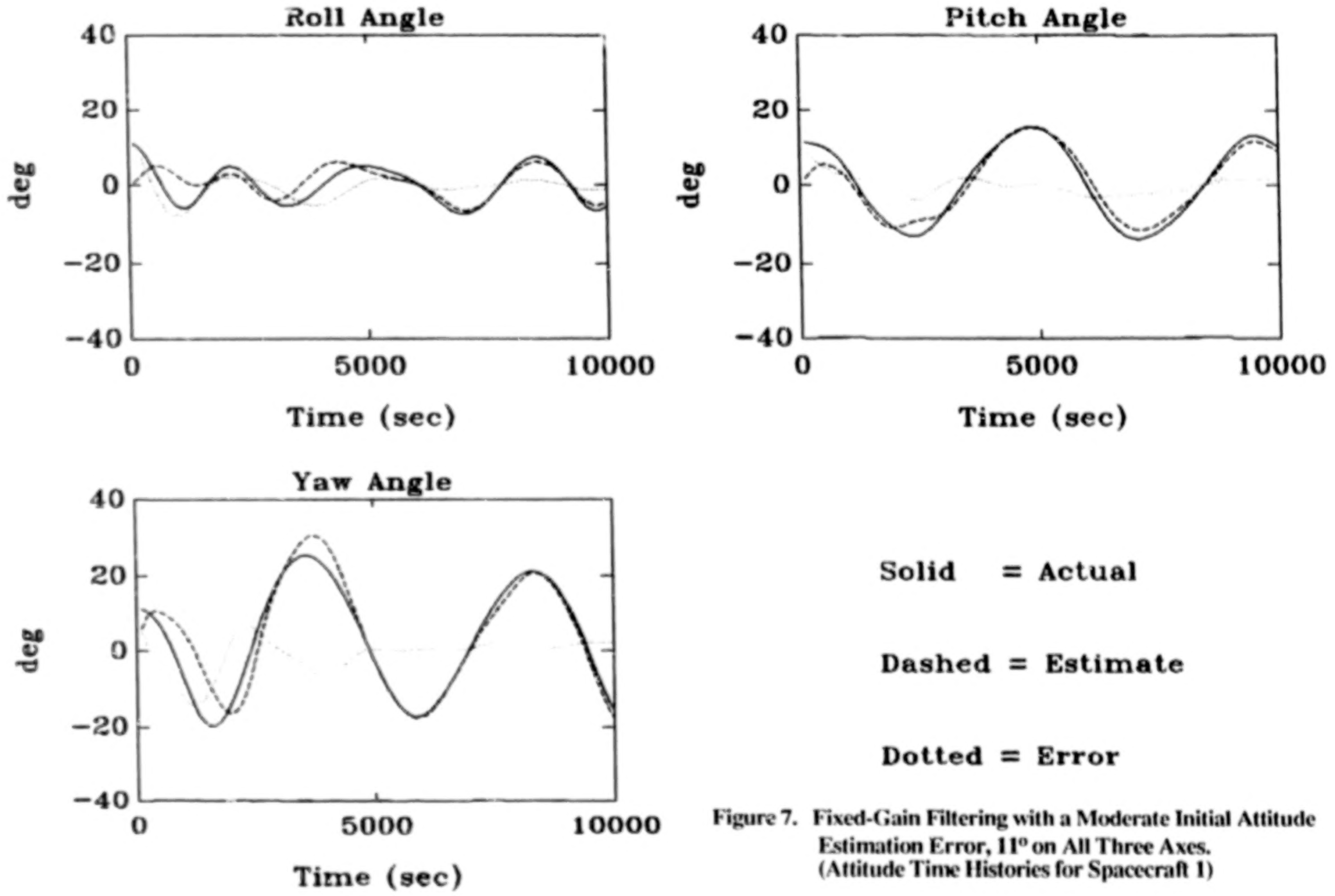

Figure 7. Fixed-Gain Filtering with a Moderate Initial Attitude Estimation Error, 11° on All Three Axes. (Attitude Time Histories for Spacecraft 1)

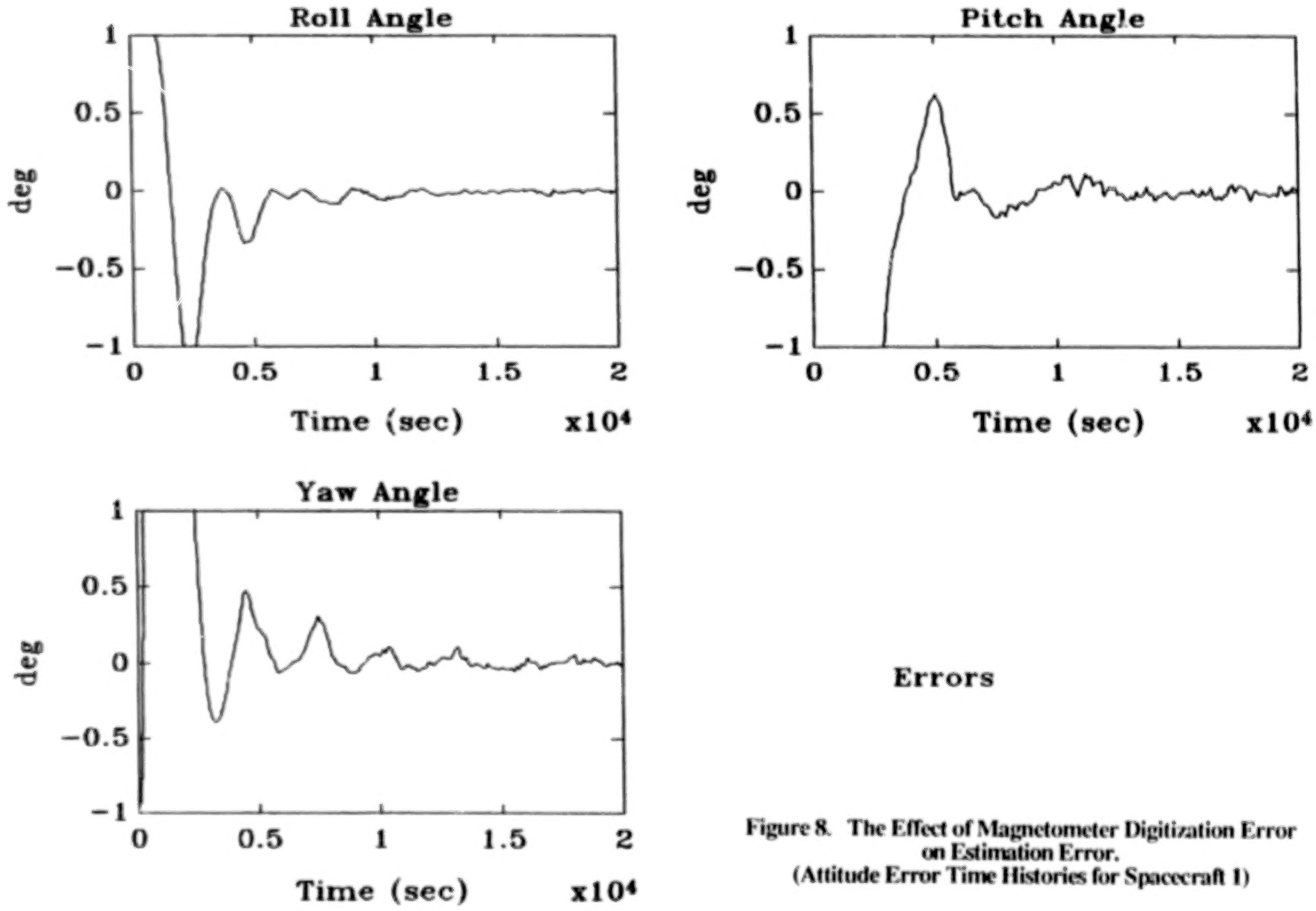

Figure 8. The Effect of Magnetometer Digitization Error on Estimation Error.
(Attitude Error Time Histories for Spacecraft 1)

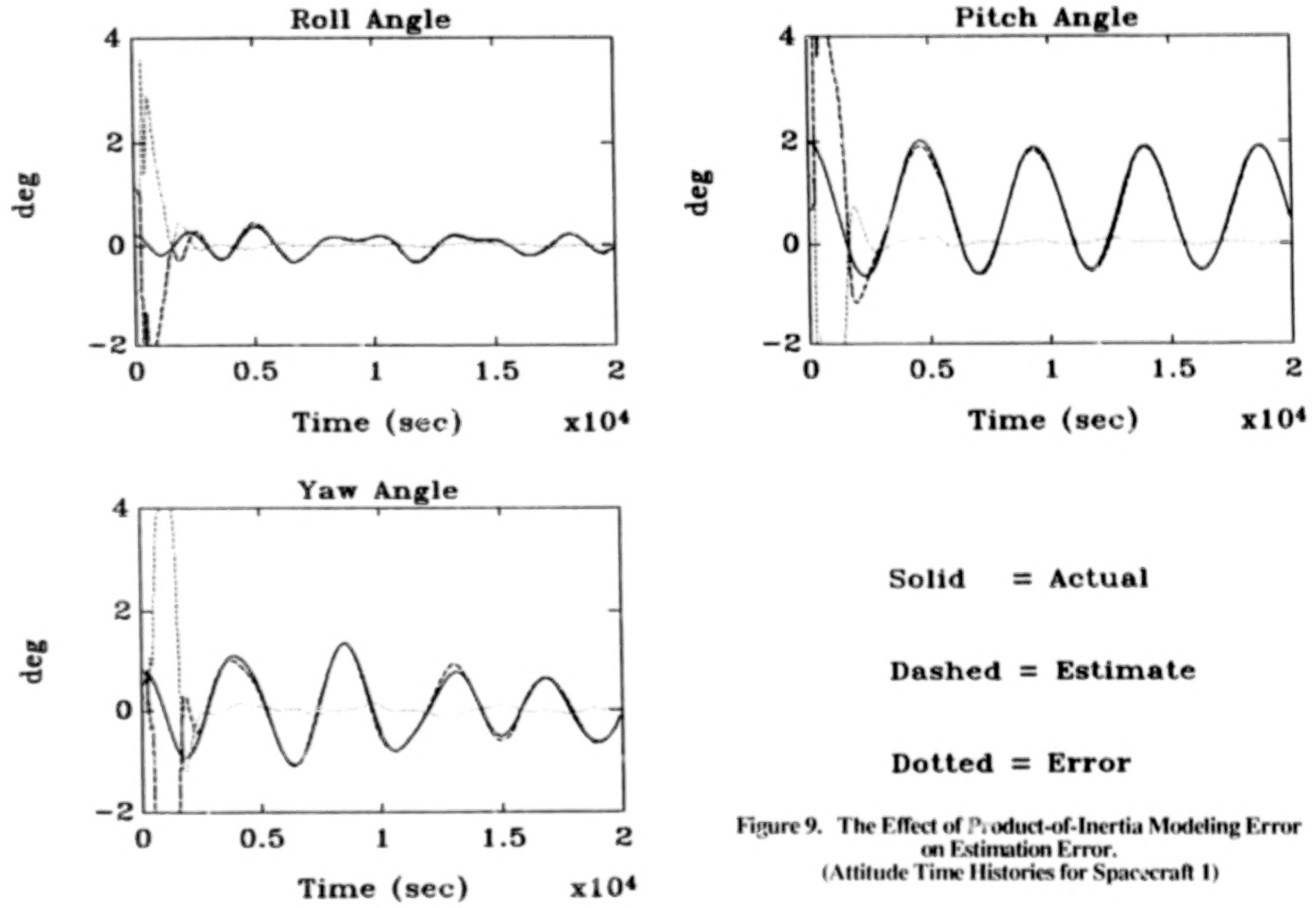

Figure 9. The Effect of Product-of-Inertia Modeling Error on Estimation Error.
(Attitude Time Histories for Spacecraft 1)

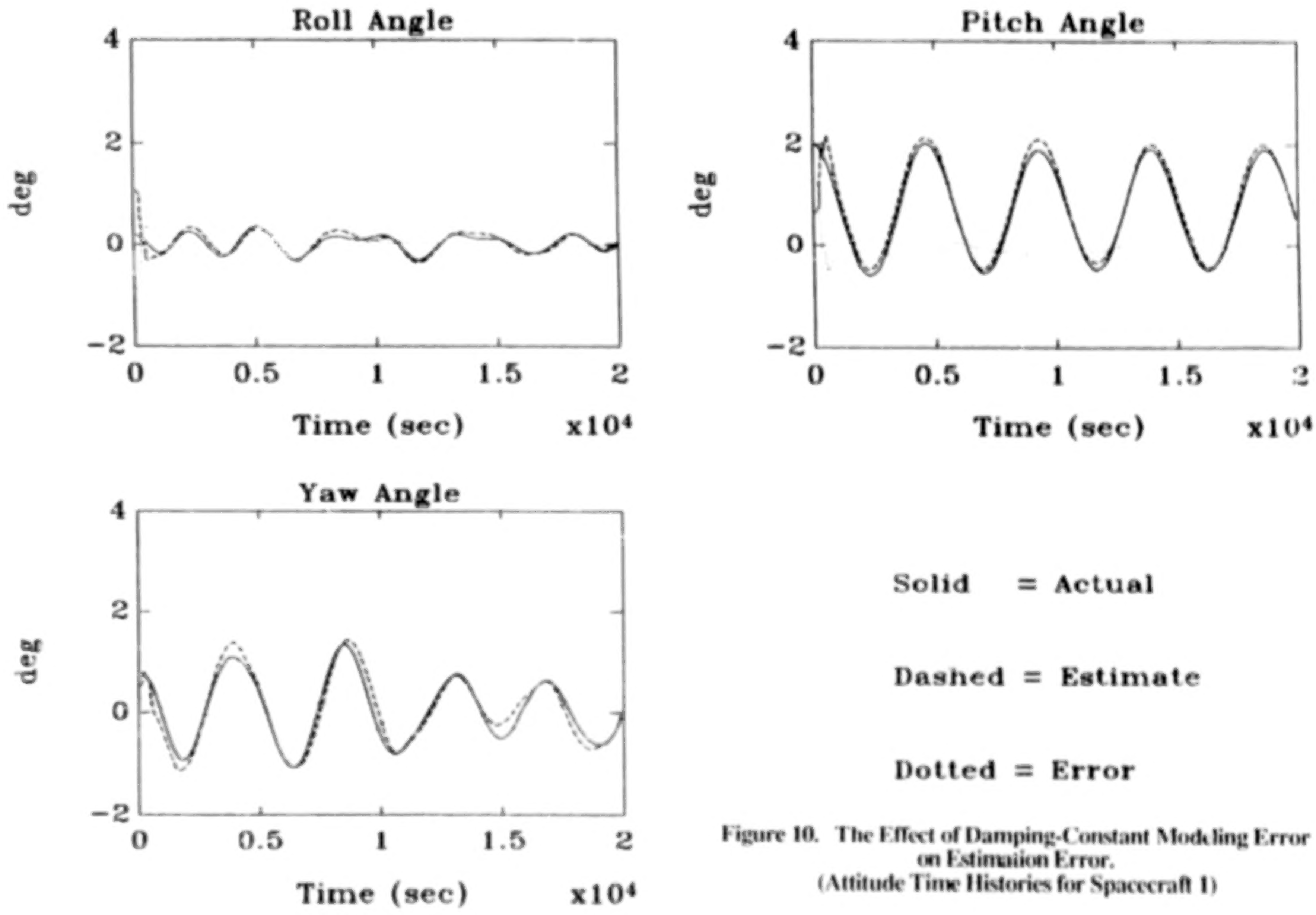

Figure 10. The Effect of Damping-Constant Modeling Error on Estimaiion Error.
(Attitude Time Histories for Spacecraft 1)

Table 2

Error Analysis Results for S/C 1

Error Source	RMS Value (deg)		
	Roll	Pitch	Yaw
2% Roll-Axis Moment of Inertia Error	0.015	0.021	0.026
2% Pitch-Axis Moment of Inertia Error	0.016	0.027	0.033
2% Yaw-Axis Moment of Inertia Error	0.006	0.011	0.013
1.5° Principle Axes Skew Error (in all three axes)	0.017	0.041	0.063
1.4 N-m-sec Magnetically-Anchored Damping Error	0.056	0.112	0.159
5% Pitch Wheel Momentum Error	0.008	0.014	0.017
3 mGauss Magnetometer Bias Error	0.231	0.369	0.568
Random Measurement and Field Model Error	0.345	0.789	0.816
Random Disturbance Torque Error	0.009	0.016	0.023
RSS Error	0.420	0.880	1.010

knowledge goals in roll and pitch, but misses slightly in yaw. These are 1-σ numbers.

The main contributors to the errors are uncertainty in the IGRF model and magnetometer accuracy limitations. Increasing the magnetometer accuracy by a factor of 5 would decrease the RSS error by 40 %. Increasing the field model accuracy would also have a significant beneficial impact on the error budget. Decreasing the error in the knowledge of the magnetically-anchored damping constant would further improve the filter accuracy. Increasing the **R** weighting in the filter might also improve things. The current low **R** value causes the filter to rely too heavily on each magnetometer measurement, hence the large effects on accuracy of measurement-type errors and the small effects of disturbance torque errors and modeling errors.

A significant result of this analysis is the relative insensitivity of the filter to angular shifts in the S/C principal axes. The filter identifies these as disturbance torques and continues to achieve attitude accuracy on the order of 0.06° or better (neglecting other contributions to error), despite the 1.5° bias in the spacecraft attitude from that predicted by gravity gradient analysis and the modelled products of inertia.

5.3 Notes on Filter Performance

This filter runs relatively fast. It is able to perform one orbit's (50 samples) worth of filtering in about 3 minutes when operating on an INTEL 8088/8087-based personal computer with an 8 MHz clock rate. This time does not include the time to compute the IGRF model from a spherical expansion. In this particular filter implementation, the field calculation is done offline and the filter gets the resulting data from a table look-up.

Several problems having to do with convergence occur with this filter. One problem occurs in covariance initialization. For the case of "large" diagonal $\mathbf{P}(t_0)$ and "small" **R**, if the initial magnetometer measurement occurs at t_0, then $\mathbf{P}(t_0)$ is immediately updated to yield $\mathbf{P}^+(t_0)$ before the first covariance propagation, and the filter converges. If the first magnetometer measurement occurs at t_1, on the other hand, then propagation to $\mathbf{P}(t_1)$ occurs first, and the filter sometimes fails to converge. This is because $\Phi(t_1,t_0)$ has some large elements for long sampling periods, which makes $\mathbf{P}(t_1)$ very high and results in very high filter gains. These cause divergence due to nonlinearities.

Another convergence problem occurs because of the quaternion update scheme in eq. 24 and 25. The argument of the square root in eq. 24 becomes negative for very large initial attitude errors. This occurs because the linear update in eq. 24 does not recognize when it is asking for more angular correction than makes physical sense. This problem occurred for an initial angular error of 90° (the filter did converge for a 60° initial error). It also can occur when filter gains are too high -- $\mathbf{P}(t_0)$ or $\mathbf{Q}$ or both are too large relative to $\mathbf{R}$. A way to avoid this would be to add a further nonlinearity to the quaternion update to scale down updates that are physically unrealizable.

6 Conclusions

The modified extended Kalman filter described and analyzed in this paper can estimate 3-axis S/C attitude, attitude rate, and constant disturbance torques solely from 3-axis magnetometer measurements distributed over one orbit. The filter works for gravity-gradient stabilized S/C operating in inclined, low-Earth orbits. The filter can converge from initial attitude errors as large as 60° and can achieve a 1-σ attitude accuracy of 1° or better on all three axes.

Filter performance has been evaluated in two ways: by linear analysis of small perturbations from the nominal gravity-gradient orientation and by filtering of magnetometer data generated by a nonlinear S/C simulation. The linear analysis has confirmed the observability of the system and the stability of the filter. Also, it has predicted the inaccuracy induced by random disturbances and measurement noise. The nonlinear simulation has demonstrated the filter's ability to converge from large initial errors and has predicted the contributions of systematic errors to inaccuracy.

For one of the S/C-orbit cases considered, the most significant contributors to filter inaccuracy are magnetometer inaccuracy and inaccuracy of the knowledge of the Earth's magnetic field. Reduction of the filter's 3-σ attitude uncertainty to 1° could be achieved by use of a magnetometer with 1 mGauss 1-σ accuracy in combination with a model of the Earth's magnetic field that is accurate to 0.1° 1-σ. The necessary accuracy increases are about 3 times for the magnetometer and about 4 times for the field model. More accurate predictions of the passive magnetically-anchored damping factor would also improve filter accuracy.

7 Recommendations and Planned Follow-Up Work

Comparison of these accuracy and convergence results with flight test results is planned. There are plans to launch a satellite using this filter in the ground station as a back-up attitude determination system. The S/C will also carry optical attitude determination instruments, which are more accurate than the magnetometer. Comparison of filter attitude with the attitude determined by the more accurate system will provide a bench mark for its evaluation. A post-launch action that will be considered for improvement of the filter accuracy is on-orbit magnetometer calibration and bias determination similar to what was done in Ref. 4.

A related application for magnetometer data filtering could be made on the autonomous satellite navigation problem. The observability of the attitude/trajectory system should be checked, this time retaining length information for the field vector. The system may be observable. In that case, a navigation system based solely on magnetometer measurements or on a combination of horizon sensor and magnetometer measurements would be theoretically possible.

The filter described in this paper coupled with a magnetometer and sufficient computer capacity can be used when a low-cost, light-weight, low-accuracy system for attitude determination is required.

Acknowledgements

This work was supported in part by the Naval Research Laboratory and by Fairchild Industries under contract numbers N00014-87-C-2092 and SC00150.

References

1. Lefferts, E.J., Markley, F.L., and Shuster, M.D., "Kalman Filtering for Spacecraft Attitude Estimation," **Journal of Guidance, Control, and Dynamics**, Vol. 5, No. 5, Sept.-Oct. 1982, pp. 417-429.

2. Potter, J.E., and Vander Velde, W.C., "Optimum Mixing of Gyroscope and Star Tracker Data," **Journal of Spacecraft and Rockets**, Vol. 5, May 1968, pp. 536-540.

3. Gai, E., Daly, K., Harrison, J., and Lemos, L., "Star-Sensor Based Satellite Attitude/Attitude Rate Estimator," **Journal of Guidance, Control, and Dynamics**, Vol. 8, No. 5, Sept.-Oct. 1985, pp. 560-565.

4. Thompson, R.H., Neal, G.F., and Shuster, M.D., "Magnetometer Bias Determination and Spin Axis Attitude

Estimation for the AMPTE Mission," **Journal of Guidance, Control, and Dynamics**, Vol. 7, No. 4, July-Aug. 1984, pp. 505-507.

5. Heyler, G.A., "Attitude Determination by Enhanced Kalman Filtering Using Euler Parameter Dynamics and Rotational Update Equations," AIAA Paper No. A81-45832, AAS/AIAA Astrodynamics Specialist Conference, Lake Tahoe, Nevada, Aug. 3-5, 1981.

6. Wertz, J.R. ed., **Spacecraft Attitude Determination and Control**, D. Reidel Pub. Co., (Boston, 1978).

7. Bar-Itzhack, I.Y., and Oshman, Y., "Attitude Determination from Vector Observations: Quaternion Estimation," **IEEE Trans. on Aerospace and Electronic Systems**, Vol. AES-21, No.1, Jan. 1985, pp. 128-135.

8. Stengel, R.F., **Stochastic Optimal Control**, J. Wiley and Sons, (New York, 1986).

9. Anderson, B.D.O., and Moore, J.B., **Linear Optimal Control**, Prentice-Hall, (Englewood Cliffs, N.J., 1971).

10. Kailath, T. **Linear Systems**, Prentice-Hall, (Englewood Cliffs, N.J., 1980).

N89-15952

ATTITUDE ANALYSIS OF THE EARTH RADIATION BUDGET SATELLITE (ERBS)

YAW TURN ANOMALY

J. Kronenwetter and M. Phenneger, Computer Sciences Corporation (CSC)

W. Weaver, National Aeronautics and Space Administration/Langley Research Center (NASA/LRC)

ABSTRACT

The July 2 Earth Radiation Budget Satellite (ERBS) hydrazine thruster-controlled yaw inversion maneuver resulted in a 2.1 degree per second (deg/sec) attitude spin. This mode continued for 150 minutes (min) until the spacecraft was inertially despun using the hydrazine thrusters. The spacecraft remained in a low-rate Y-axis spin of .06 deg/sec for 3 hours until the B-DOT control mode was activated. After 5 hours in this mode, the spacecraft Y-axis was aligned to the orbit normal, and the spacecraft was commanded to the mission mode of attitude control.

This work presents the experience of real-time attitude determination support following analysis using the playback telemetry tape recorded for 7 hours from the start of the attitude control anomaly. For the high-spin-rate mode, sunlit portions of the orbit, the Sun data are used with dynamic interpolation of the gaps to derive the path of the Sun through the light-sensitive science instrument sensor and solar array fields of view. During the despun mode, results from ERBS Attitude Determination System (ADS) processing of the magnetometer data show graphically the alignment and slow rotation of the body coordinate system in the geocentric inertial (GCI) reference frame. These data provide an evaluation and explanation of the marginal power condition during the despun recovery period. Comparisons of the attitude results with science sensor output are provided to illustrate the impact of the attitude control anomaly on the science instruments. The paper concludes with an assessment of the experience gained and suggestions for additional procedures and software to provide spacecraft attitude maneuver and contingency support.

1. INTRODUCTION

On July 2, 1987, a thruster actuated, yaw inversion test maneuver with a disabled X-axis inertial reference unit (IRU) resulted in an uncontrolled tumble of the Earth Radiation Budget Satellite (ERBS) at approximately 2.1 degrees per second (deg/sec). The cause was a command sequence error that prematurely activated instead of disabled a roll thruster without roll-axis rate input. The large pitch and roll angles experienced during the tumble resulted in periodic loss of contact with the Tracking and Data Relay Satellite (TDRS) and loss of Earth contact by the horizon scanners, causing erroneous input into the magnetic control loop (MCS). Also, the rates achieved during the tumble exceed the telemetry limits for the IRU, resulting in saturated gyro data. Thus, only magnetometer and occasional Sun sensor data were available to derive attitude information during the tumble.

Analysis of the attitude sensor data from the tumble was conducted to derive continuous pointing information during the period of the tumble since both ERBE scientific instruments remained in their normal operating modes during most of the period. The analysis also included verifications of the effects of the Earth limb and the Sun on the science sensor output. The analysis and results are believed an important example and guideline for planning spacecraft support in the future.

Following a brief overview of the ERBS spacecraft, the analysis of the sensor data during the spacecraft tumble is presented. The presentation begins with a narrative description of the playback and real-time data and continues with the analysis and the results of an attempt to provide continuous ground-determined attitude solutions using playback data. A dynamic model was developed for this part of the analysis to provide continuous rate data required by the ERBS fine attitude determination system (FADS). The solutions are compared with data output from the ERBS nonscanner instrument. Finally, the application of the tools developed in this study to ERBS real-time and future mission attitude support are examined. A major portion of the work, data, and analysis presented in this paper is based on material presented more comprehensively in an October 15, 1987, memorandum prepared for the ERBS project by the FDD (Reference 1). The science sensor performance is similarly treated in more detail in a memorandum to the ERBS project written by W. Weaver, Langley Research Center (LRC) (Reference 2).

2. ERBS SPACECRAFT AND INSTRUMENT OVERVIEW

The ERBS is an Earth-pointing, momentum-biased spacecraft carrying scientific instruments to map the absorption and emission of thermal energy by the Earth. Two of the instruments, the Earth Radiation and Budget Experiment (ERBE) nonscanner and scanner, measure outgoing radiation in three broad spectral bands. The ERBE scanner is a three-channel radiometer that scans from horizon-to-horizon in a plane normal to the orbit plane. The ERBE nonscanner has two wide field-of-view (WFOV) and two medium field-of-view (MFOV) Earth-viewing channels and a Solar channel for viewing the Sun periodically. Each WFOV detector has a total conical FOV of about 140 deg and views the entire disk of the Earth, and a MFOV detector has a conical FOV of 90 deg. In the normal operating mode, the optical axes of the Earth-viewing detectors are aligned with the spacecraft Z-axis, and thus have their FOVs centered on the Earth at the nadir. A third science instrument is the Stratospheric Aerosol and Gas Experiment (SAGE), which views the Sun on the Earth limb to measure absorption spectra at sunrise and sunset yielding the mixing ratios of atmospheric aerosols. ERBS utilizes two analog attitude control methods, the Magnetic Control System (MCS) and the Reaction Control System (RCS) during scientific sensor operations, and orbit and attitude adjust maneuvers, respectively.

The MCS sensors and actuators are two Earth IR horizon scanners, one momentum wheel, two Scanwheels,[1] and four electromagnets. The MCS maintains the ERBS pointing to within 1.0 deg of the nominal null reference attitude on all three axes.

The RCS sensors and actuators are two redundant Inertial Reference Units (IRUs) containing three single-axis gyros for rate information to control eight 2.2 Newton hydrazine thrusters.

Attitude information for use with the science data is derived from the analog output of the onboard gyrocompass subsystem of the RCS. These data are periodically verified on the ground using the FADS, which utilizes the IRU rate, Earth infrared (IR), and Sun sensor data.

3. ATTITUDE DATA ANALYSIS AND DESCRIPTION

Three distinct phases of the yaw turn anomaly are

- The initial phase, starting at the beginning of the yaw maneuver at 15:17:08 during the action of the anomalous and constant roll thruster firing, and command execution of the still active stored yaw turn commands and occasional real-time commands
- The approximately torque-free tumble phase, which begins at 15:32:58 and continues until the initiation of the G-RATE mode to despin the spacecraft at 18:45:28 (when the thruster auto cutoff was disabled in the G-RATE mode)
- The post G-RATE mode when the spacecraft is nearly inertially despun except for a 0.06-deg rate around the +Y-axis and a switch by real-time command to the B-DOT mode at 22:08:15 universal time coordinated (UTC).

3.1 PLAYBACK DATA DESCRIPTION

The attitude sensor data used for the nominal attitude determination support are from the Sun sensors, the IR scanners, and the three-axis IRU. During the high-rate (2 deg/sec) tumble, the IRU data were saturated and of limited use except as rate polarity and rate transition time indicators. The IR scanner data were also confused with valid data occurring occasionally when the Earth scan geometry was near the geometry of the planned operation of the scanners. The data that are most illustrative of the spacecraft attitude motion during the yaw turn tumble are the data from the three-axis magnetometer and Sun sensors. The magnetometer data plotted for the duration of the playback tape are illustrated in Figure 1. The data show the beginning of the control anomaly when the thrusters were on (15:17:08 to 15:32:58) and the motion is torque driven. Next is a period of relatively constant angular momentum with no thrusting at an instantaneous spin rate of 2.1 deg/sec (15:32:58 to 18:45:28). During this period the spacecraft body is spinning around an angular momentum vector that is approximately constant in the GCI reference frame. However, the angular velocity vector moves in the body reference frame as a result of precession and nutation and in response to momentum exchange between the wheel and the body. After this high-spin period, the G-RATE mode drives the spacecraft into a near despun mode, with rates that are typically less than .1 deg/sec on all three axes. It is in this interval that the B-DOT mode is commanded, but no obvious change occurs in the magnetometer or Sun data to delineate this event.

---

[1] Scanwheel is a registered trademark of ITHACO Corp.

3.1.1 MAGNETOMETER DATA

The magnetometer data in the torque-driven, torque-free, and low-rate intervals illustrated in Figure 1 show

- Oscillations at an approximate period of 2 to 3 min
- Occasional periods when the amplitude of the magnetic field oscillations goes to zero at a near-constant value on all three axes simultaneously at 16:11, 16:59, 17:48, and 18:37
- The transition in the spin rate from the nominal pre-yaw turn 1-RPO mode to the tumble and the return to the low-rate mode after the G-RATE action at 18:45:28

The four periods of low amplitude magnetic field oscillation are times when the spacecraft spin axis is closely aligned with the local magnetic field. The field at each of these times is within 10 deg of 70-deg latitude and 252-deg right ascension. The sign and magnitude of each of the three field components at these times thus gives an approximate indication of the location of the spin axis in the body reference frame and in the GCI frame. It should be noted that the Y component is always positive, the X component is zero to negative, and the Z component switches sign.

3.1.2 SUN SENSOR DATA

The Sun sensor data throughout the playback period are illustrated in Figure 2. The major feature in these data is the rapid motion of the Sun through the full range (64 deg) of the sensor field of view at approximately 2.5-min intervals. The long intervals with no Sun data correspond to spacecraft night. The period from sunrise at 16:37 to the first Sun data at 16:51 is an interval where the geometry of the spin vector keeps the Sun out of the sensor field of view for

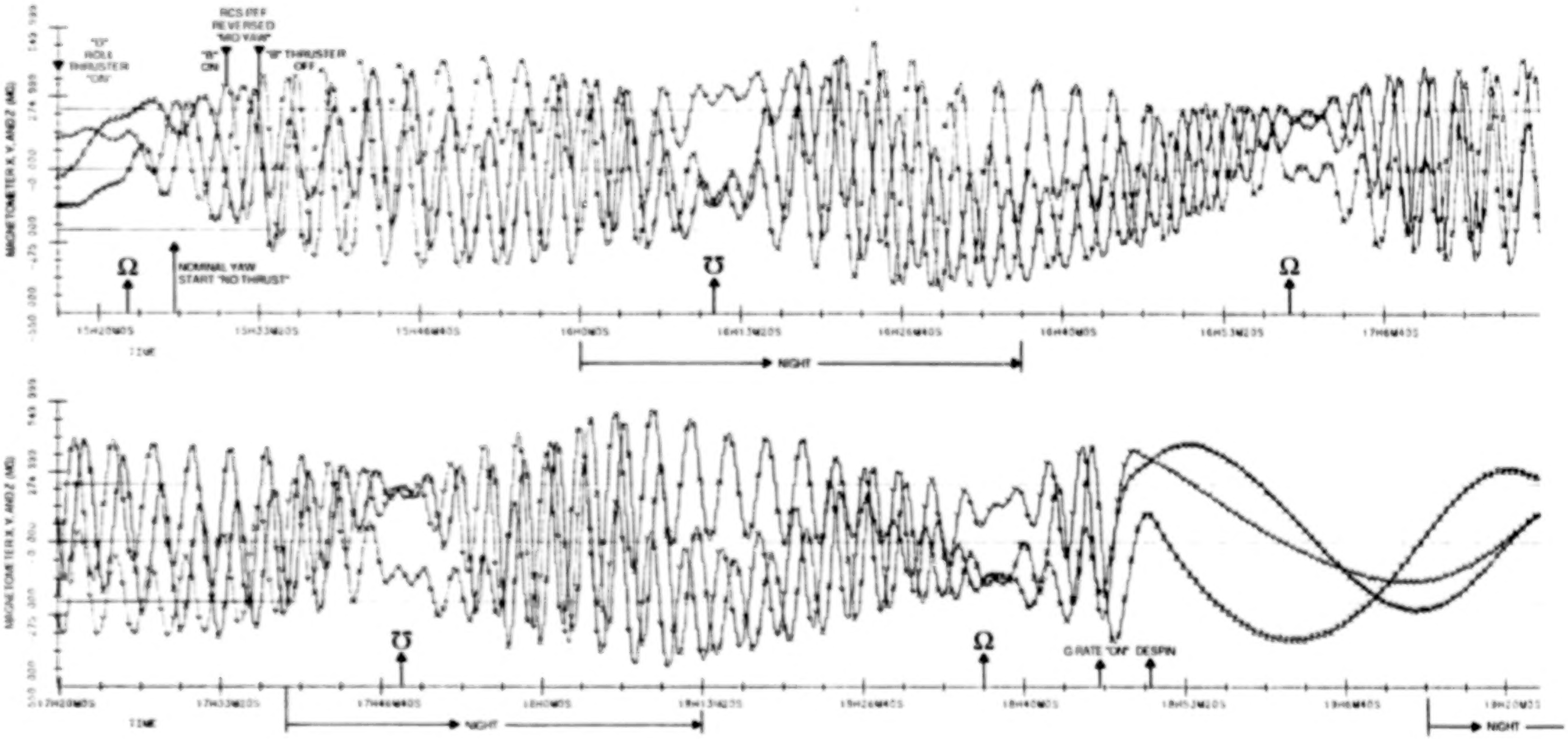

Figure 1. Magnetometer Playback Data During the ERBS Yaw Turn Tumble (1 of 2)

ORIGINAL PAGE IS
OF POOR QUALITY

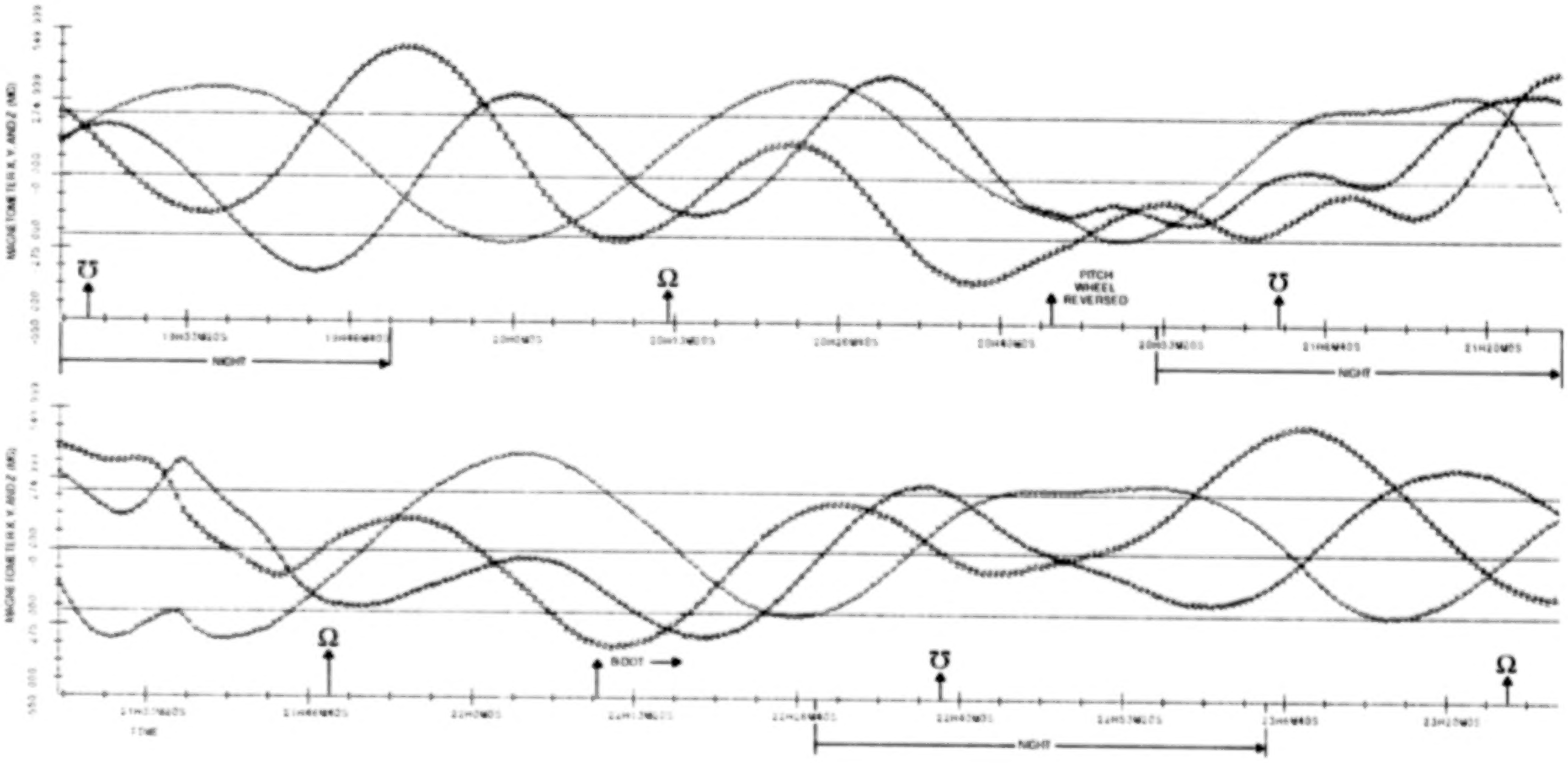

Figure 1. Magnetometer Playback Data During the ERBS Yaw Turn Tumble (2 of 2)

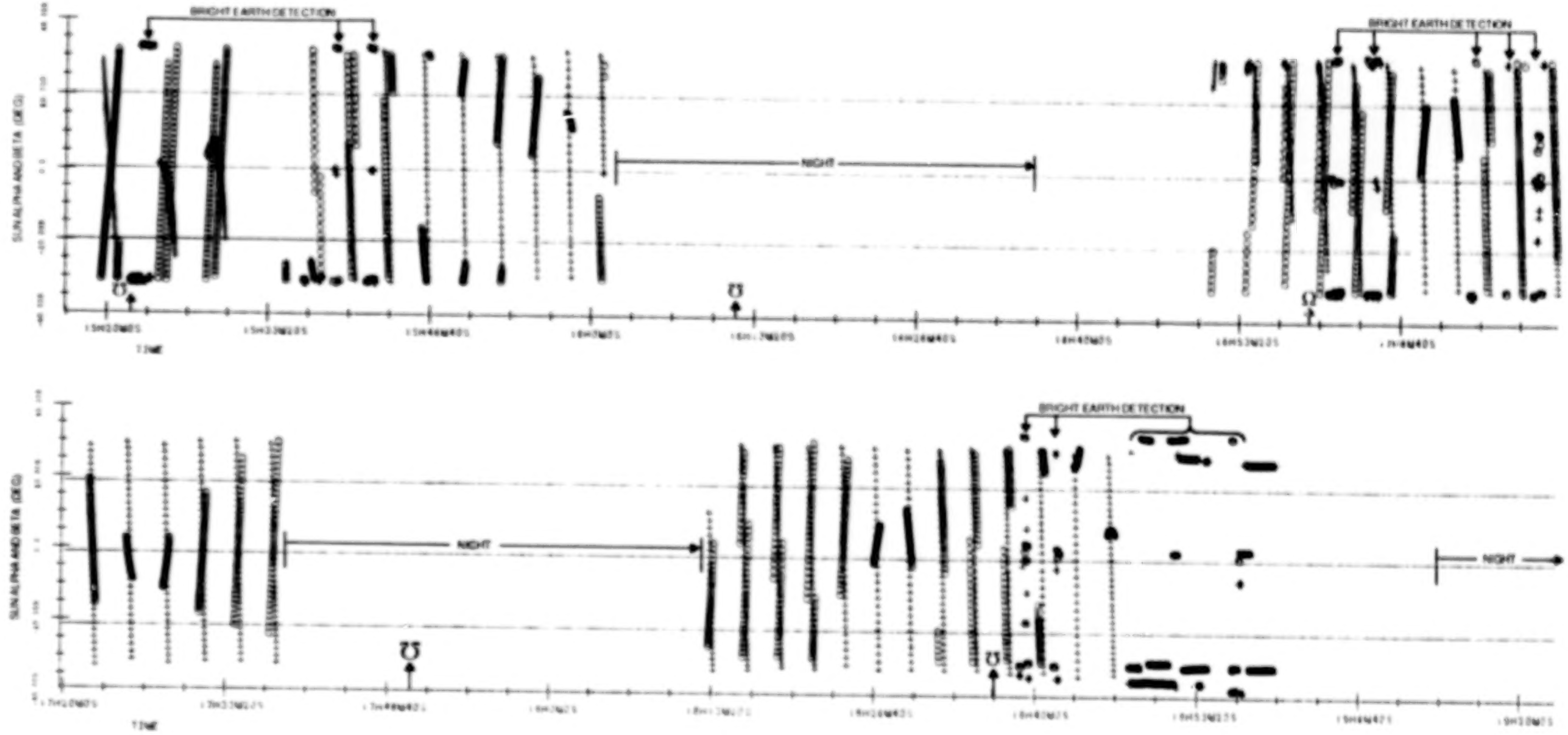

Figure 2. Sun Sensor Playback Data (15:16 through 19:20 UTC) Alpha Angles (O), Beta Angles (+)

three to four spin cycles. The corner of sensor 2 begins to encounter Sun at 16:51. Another feature in the Sun data is the stimulation of the fine reticle and coarse Gray code by reflected light off the Earth. These data can be seen at 17:17 and 18:38. Other intervals of Earth light stimulation of the Sun sensor are primarily fine reticle events with the Gray code at midrange or at the all ones or all zeros limits; these are the data at 17:01 and 15:39.

In the low-spin-rate mode, after the G-RATE mode despin, the spacecraft is aligned with the -Y-axis close to the Sun (<20 deg). In this orientation, the Sun sensor views the Earth during the orbit day and space during orbit night; also for this orientation the solar array normal is near-orthogonal to the Sun vector. The fine and coarse reticle, Earth-stimulated Sun sensor data occur at orbital positions that are about 10 min (40 deg) from spacecraft noon.

3.1.3 INFRARED SCANNER DATA

The IR scanner data are illustrated in the upper half of Figure 3. To be useful for the attitude processor, in the high-rate tumble mode, the data would require extensive filtering beyond what is available in the ERBS ADS Data Adjuster Subsystem. For this reason the data were not used in this analysis except for an attempt to select only data that could be verified as originating from near nominal Earth viewing geometry during the spacecraft nighttime period. The results from this were deemed unacceptable.

3.1.4 GYRO DATA

The gyro-rate data, illustrated in the lower half of Figure 3, are presented to illustrate the characteristics of these data during the high-rate tumble. For the nominal attitude processing, the design of the ERBS ADS could not accommodate these data. The information contained is an accurate measure of the polarity and duration of polarity for rates on the body axes; also apparent is a record of the time at which the rates are switching sign. For this analysis, these data were used to verify the dynamic modeling (described later in Section 3) of the first 5 min of the high-torque interval, and for dynamic state initialization. Approximate agreement was obtained for the polarity switch in the X-gyro rate at 15:24.

3.2 REAL-TIME DATA DESCRIPTION

The real-time data received during the ERBS yaw turn anomaly requires attention in this review because it is an example of the type of data that will be relied on in future spacecraft emergency recovery support. Also, for future preparedness, it is a useful exercise for spacecraft attitude control analysts to review these data to translate the experience to other missions. During the real-time monitoring of the yaw turn maneuver, the data that most vividly illustrated the onset of the problem were the Sun sensor data. These data, illustrated in Figure 4, are from two real-time passes. The 15:16 to 15:30 pass is from TDRS; the 17:02 to 17:13 is from Merritt Island (MIL). Sun data were not expected at the time of the maneuver. The occurrence of Sun sensor data near 15:18 was, therefore, a strong indicator of the problem. The characteristics of the real-time data reveal the complexities of real-time support

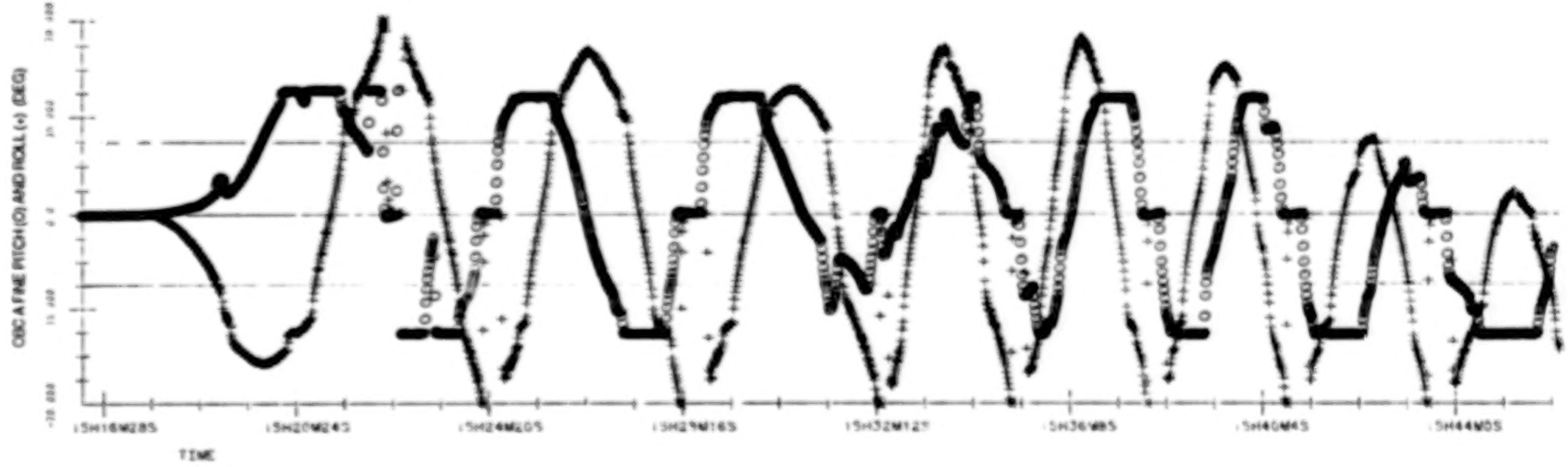

Figure 3(a). IR Scanner

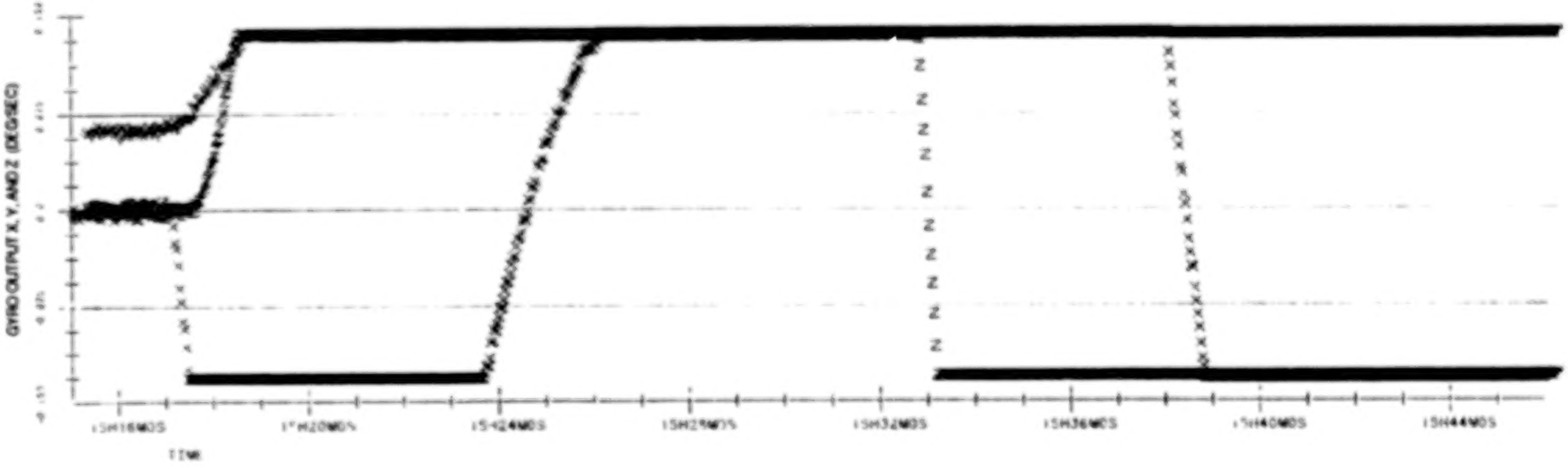

Figure 3(b). IRU Rate

ORIGINAL PAGE IS
OF POOR QUALITY

ORIGINAL PAGE IS
OF POOR QUALITY

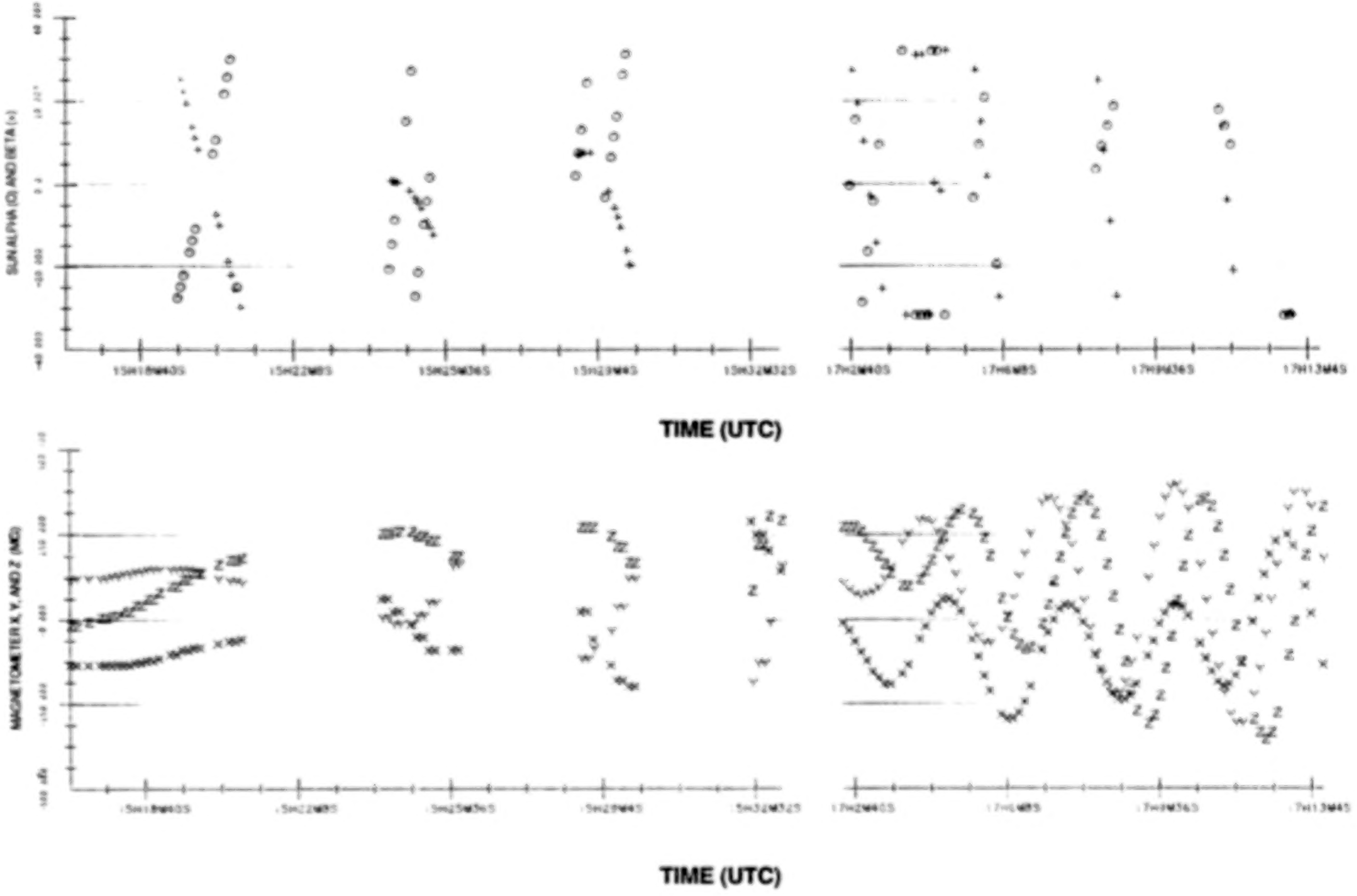

Figure 4. Real-Time Data From the First Two Passes (TDRS and Merrit Island) Sun Sensor α and β Angles (Upper) Magnetometer x, y, z (Milligauss) (Lower)

with these data. The first feature is that the telemetry during the TDRS contact data are periodic at approximately the tumble period, as expected from a sensor with a wide field of view periodically scanning the Sun at the spacecraft spin rate. However, the geometry of the MIL pass and omni RF beam does not cause obvious strobing. Not immediately obvious, however, was the fact that the TDRS contact data were being strobed by the telemetry downlink interruptions caused by the rotation of the omni antenna hemispherical radio frequency (RF) beam. Had the control center support been performed for this maneuver or similar command load events using a TDRSS high-gain antenna, the availability of the data and command RF link following the control error would have been severely limited. The strobing of the data by the RF was not noticed immediately in the Flight Dynamics Facility (FDF). It became apparent when an attempt to plot the Sun trace in the sensor field of view showed that it occasionally started or ended in the middle of the field of view on consecutive spin rotations. The telemetry strobing is more obvious in the magnetometer and IRU data from the TDRSS pass illustrated in the lower portion of Figure 4 and Figure 5, respectively. For a real-time contact, these data should be contiguous throughout. The IR scanner data are illustrated for completeness in the upper half of Figure 5.

4. ATTITUDE DETERMINATION WITH DYNAMICS

The FDF ERBS Attitude Ground Support System (AGSS) includes two attitude estimation methods: the quaternion estimator (QUEST) for the coarse attitude determination system (CADS) and the batch least-squares routine for the FADS. The QUEST algorithm requires at least two sensor observation vectors per frame to derive the optimal attitude quaternion. The batch least-squares algorithm uses the IRU as a motion model to propagate the attitude from a solution at an epoch. Sun and IR horizon data are used to determine the epoch attitude and the gyro biases.

The data from the anomaly cannot be used directly in either technique for continuous attitude determination. QUEST cannot provide continuous solutions due to the lack of two valid observation vectors when Sun data are not present. The FADS could not be used because it requires contiguous, unsaturated IRU telemetry data. Therefore, a dynamic model was developed to fill in the intervals of saturated IRU telemetry. Previous attempts at this procedure had shown substantial errors for long periods of modeling (Reference 3). For the tumble, however, only short segments of modeling are required due to the presence of Sun data every 2 min.

4.1 THE DYNAMIC MODEL

The dynamic model uses Euler equations of motion to determine the spacecraft body rates in the saturated intervals. This is followed by an application of the FADS, which fills the 3-min periods between Sun data for up to 6 minutes of propagation. The differential corrector was applied to the model to determine a constant torque bias for each axis. The objective of the corrector was to achieve body rates within .01 deg/sec of the known rates during Sun periods.

ORIGINAL PAGE IS
OF POOR QUALITY

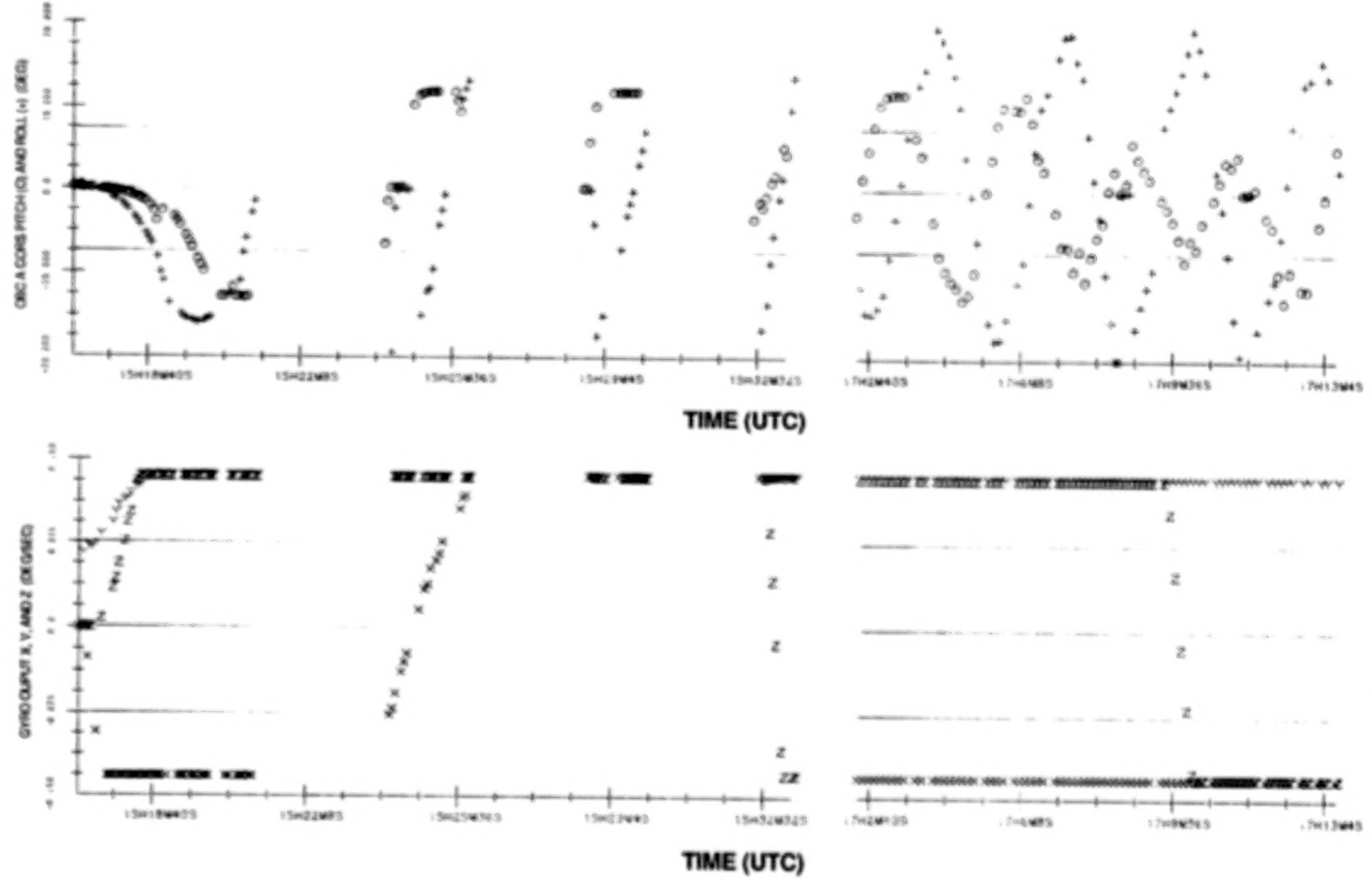

Figure 5. Real-Time Data From TDRSS (Left) and MIL (Right); IR Scanner Pitch and Roll (Upper); IRU x, y, and z Body Rates (Lower)

The dynamic motion model from the Euler equations of motion is

$$I\frac{d\tilde{\omega}}{dt} = \tilde{N} - \frac{d\tilde{h}}{dt} - \tilde{\omega}x(I\tilde{\omega} + \tilde{h})$$

where I = 3 x 3 moment of inertia matrix
$\tilde{\omega}$ = body angular rate vector
$\tilde{h}$ = sum total angular momentum of the wheels in the body frame
$\tilde{N}$ = external torque vector (thruster and environmental)

The equations of motion are integrated numerically using the fourth order Runge-Kutta method. The quantities $\tilde{h}$ and $\frac{d\tilde{h}}{dt}$ are determined from the wheel speeds in the playback data, where $\frac{d\tilde{h}}{dt}$ is taken to be constant between wheel speed samples.

The Gauss-Newton least-squares estimator is employed to estimate the initial state vector from the intervals of valid data. The state vector is composed of the following parameters:

- Initial spacecraft body angular rates
- Scale factors for each resultant thruster torque
- External torque bias

The batch least-squares method requires the comparison of the observation data to a sensor data model which is based on the state vector which evolves according to the dynamic motion model. The observations used are valid IRU rate data during the occasional nonsaturated transition intervals and Sun sensor data. A Sun sensor data model is derived by letting the model vector equal the observed at the first occurrence of a valid observation. At time Δt (= 1 sec) the Sun vector model is calculated from

$$\tilde{S}_{mt2} = \frac{\tilde{S}_{mt1} + \tilde{S}_{mt1} \times \tilde{\omega}_B \Delta t}{|\tilde{S}_{mt1} + \tilde{S}_{mt1} \times \tilde{\omega}_B \Delta t|}$$

The gyro rate ($\tilde{w}_B$) is taken directly from the integrated equations of motion.

The state vector is determined iteratively using

$$\tilde{x}^0_{K+1} = \tilde{x}^0_K + \left[S_0 + G_K^T W G_K\right]^{-1} \left[G_K^T W(\tilde{y}-\tilde{g}_K) + S_0\left(x^0_A - \tilde{x}^0_K\right)\right]$$

which is a result of minimizing the loss function, (J), where

$$J = \frac{1}{2} (y - g)^T W(\tilde{y} - \tilde{g}) + \frac{1}{2}\left(\tilde{X}^0 - \tilde{X}^0_A\right)^T S_0 \left(\tilde{X}^0 - \tilde{X}^0_A\right)$$

and $\tilde{x}^0_K$ = Kth estimate of the state vector at the epoch

x^0_A = a priori estimate of the state vector at the epoch

S_0 = diagonal state weight matrix

W = diagonal observation weight matrix

G_k = matrix of model partial derivative of the form $\frac{\partial \tilde{y}}{\partial \tilde{x}^0_K}$

$\tilde{y}$ = observation vector

$\tilde{g}_K$ = sensor observation model vector

To replace the saturated gyro data, the dynamic iteration model is employed in the following manner. The playback data are processed in the AGSS, flagging all saturated gyro and invalid Sun data. These data are written to a data file that can be accessed by other software.

The dynamic model uses these data for a user-specified time segment. This time segment is usually the interval from the middle of one Sun occurrence to the middle of the next. The a priori estimate for the angular rates is determined from the final rates of the previous batch. When the previous batch is not available, the initial rates are determined by processing a small segment of time through the dynamic model. By weighting the a priori estimate of the torque biases, the dynamic model will converge on an accurate estimate of the body rates. These rates are then used for the a priori estimate of the entire time interval.

The body rates resulting from the solved-for state vector are used to replace the IRU rates in the data file read by the FADS. The FADS is then used to determine continuous attitude solutions over the high-spin rate interval by propagating from an epoch attitude and rate bias using attitude variation from the dynamically interpolated rates.

4.2 ATTITUDE RESULTS

An example of the pitch, roll, and yaw angle results from the dynamic interpolation is shown in Figure 6. Since the dynamic motion model used was not accurate enough to span time gaps exceeding 6 min, this technique was not applied to the night periods.

ORIGINAL PAGE IS
OF POOR QUALITY

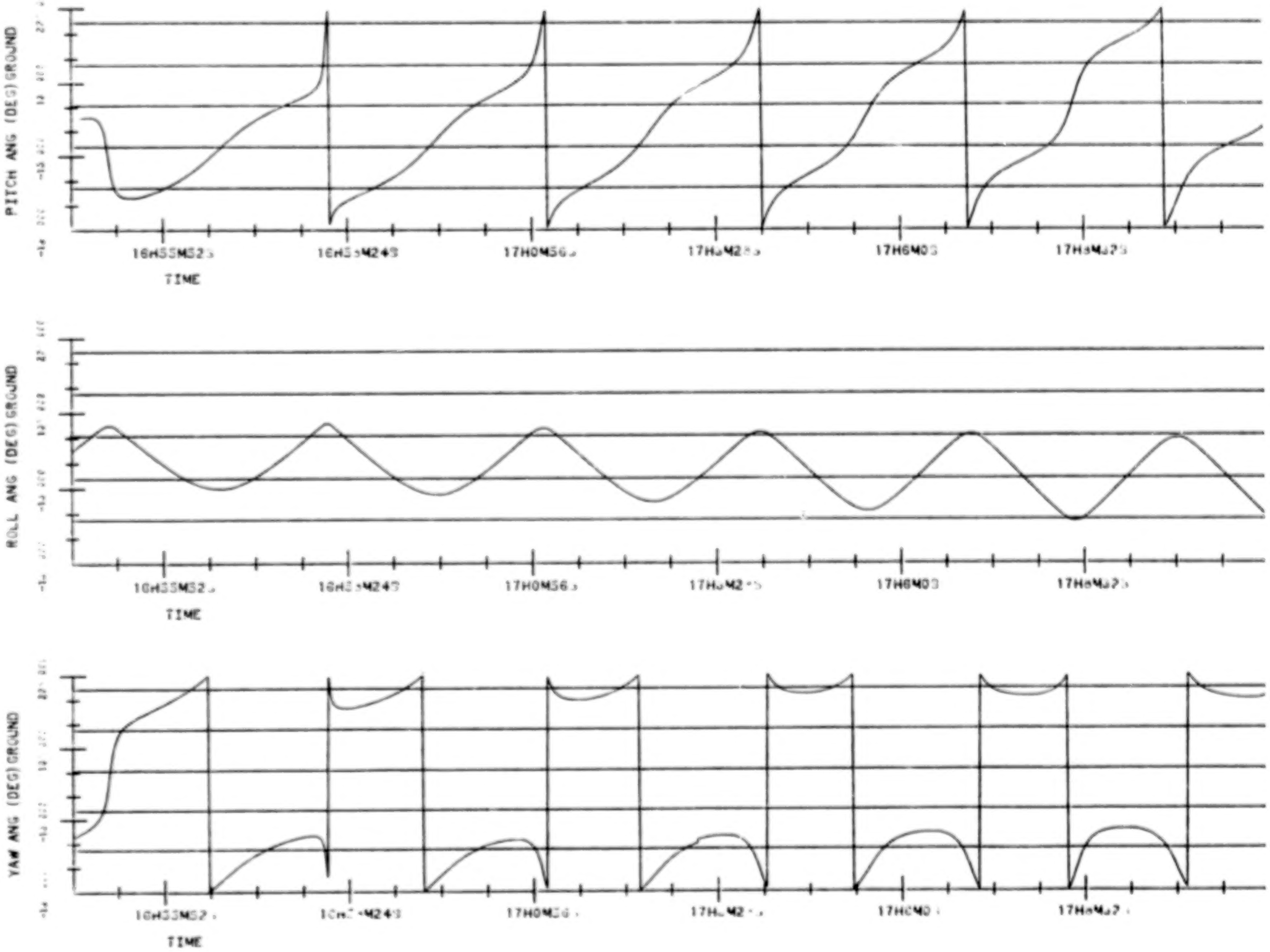

Figure 6. The Pitch, Roll, and Yaw Attitude From Dynamic Interpolation of the Sun Sensor Data

For the period after the tumble was halted, the IRU data returned to nominal, and the attitude could be calculated directly using FADS with magnetometer data.

The attitude solutions obtained from the dynamic interpolation of the IRU data during the high-rate tumble and from the FADS for the despun mode were used to plot the motion of the Sun on the unit sphere of the body reference frame (BCS). Figure 7 covers two intervals of high-spin rate and low-spin rate data. The low-rate data are from the time immediately following the command to the G-RATE mode when the spacecraft is despun using thrusters. The two spheres on each page of the figure show the BCS frame oriented with the +Z-axis downward as in the ERBS configuration of nominal flight. The +Y-axis side of the BCS is the left-hand sphere with the Sun sensor field of view inscribed on the sphere to allow correlation of these data with the Sun sensor data displayed in Figure 7. The left-hand sphere is the -Y-axis side of the BCS viewed from slightly below the X-Y plane. The Sun traces on the sphere are labeled with numbered tick marks at 30-sec intervals for the data corresponding to the high-spin-rate mode. The ERBE science sensor 45-deg and 70-deg fields of view are also delineated as cones around the +Z-axis. The solar array field of view, which is depicted here as a 2π steradian field 11 deg off the -Z-axis, is also illustrated to show when the Sun was shining on the array. The sphere-plot representations of the despun Sun traces, such as those in Figure 7(b) for the whole recorded interval, indicate that for all but 50 min of the daytime periods between 18:43 UTC and 23:00 UTC, the Sun was off the solar array.

5. COMPARISON OF CALCULATED SPACECRAFT POINTING DATA WITH ERBE NONSCANNER INSTRUMENT DATA

Both ERBE instruments remained in their normal operational modes from the beginning of the yaw anomaly on July 2 until after the primary rotation of the spacecraft was stopped. The nonscanner detectors were pointed along the spacecraft positive Z-axis, and the scanner detectors were scanning in a plane that is normal to the spacecraft X-axis. Data indicate that the fields of view of both instruments were exposed to direct solar radiation. The scanner detectors respond erratically when exposed to the strong solar radiation, making it difficult to accurately resolve when the exposure begins and ends. Thus, only nonscanner instrument data acquired during spacecraft rotation are described.

Figure 8 shows the raw output (one measurement every 16 sec) of the wide field of view total radiation detector for the period on July 2, starting before the yaw maneuver began and ending a few minutes after the rapid motion of the spacecraft was stopped. The period of the data begins with the detectors viewing the Earth in full darkness. The raw output of the detector is a maximum for zero input radiation and decreases with increased input radiation. The first isolated spike seen in the detector data of Figure 8 indicates when the detector viewed the Sun at the spacecraft horizon as the spacecraft passed from darkness into sunlight. This spike is normal in the nominal mission mode, occurring twice each orbit. Comparing this Sun spike to data obtained during

ORIGI...
OF POOR QUALITY

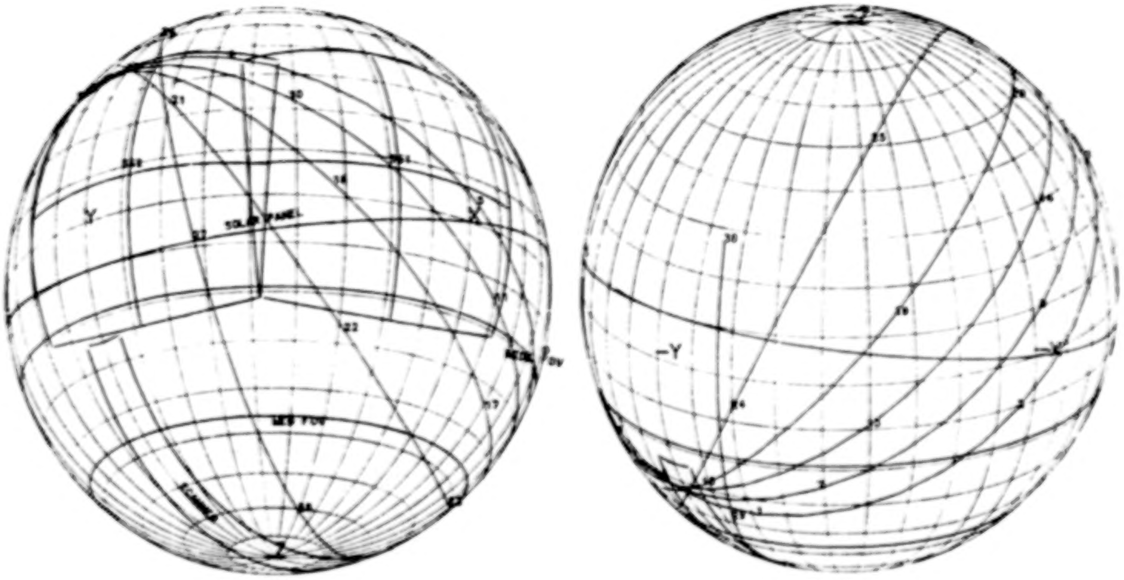
Y
SOLAR PANEL
X
SES FOV
SCANNER
-Y
-X

Figure 7(a). Sun Traces in the Body Frame From 1655 to 1710 (Tick Marks Every 30 sec)

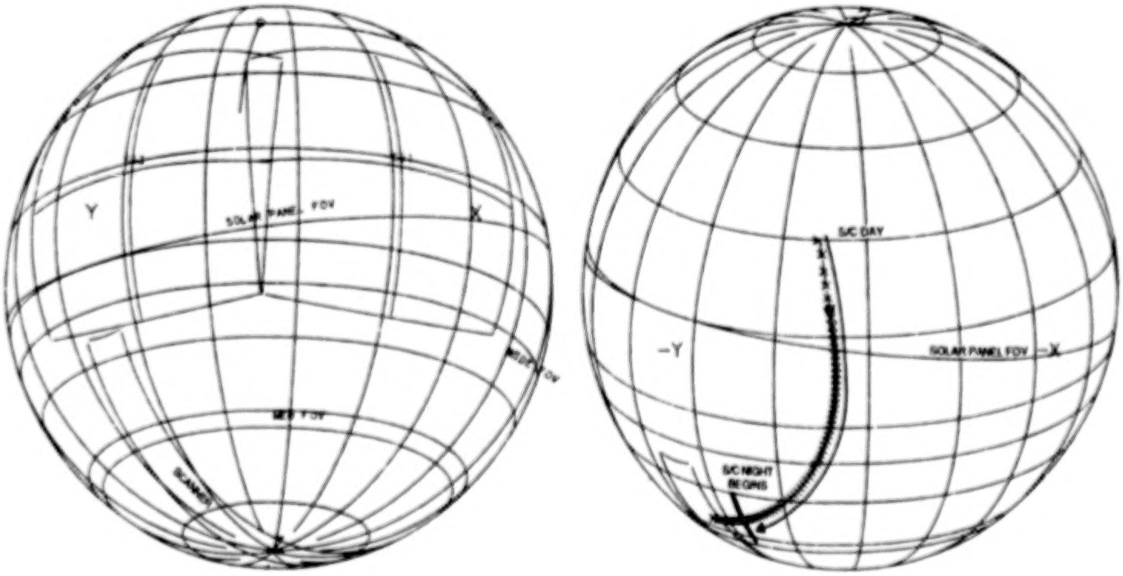
Y
SOLAR PANEL FOV
X
SES FOV
SCANNER
S/C DAY
-Y
SOLAR PANEL FOV
-X
S/C NIGHT BEGINS

Figure 7(b). Sun Traces in Body Frame From 870702.184301 to 870702.192101 (0 = Start Time, X at Every 30 sec)

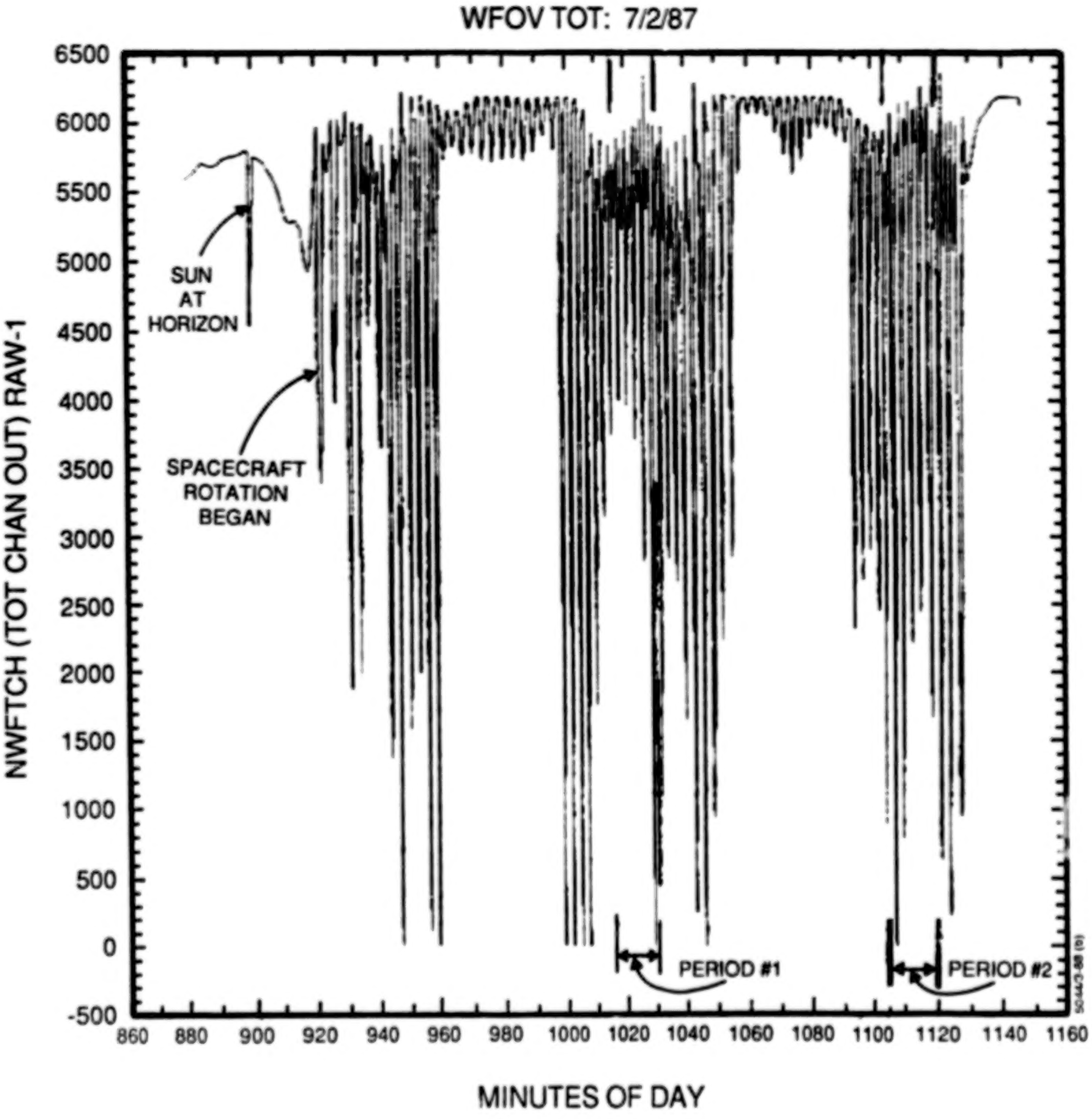

Figure 8. Raw Radiance Signal From the Wide Field of View ERBE Nonscanner from 15:00 UTC to 19:00 UTC

the period of spacecraft rotation, it appears that the wide field of view detectors sensed some solar input about every 3 min during the sunlight portions of the three orbits that the spacecraft was rotating.

Raw radiometric data from the wide and medium fields of view total detectors for the two 15-min periods identified in Figure 8 are presented on enlarged time scales in Figures 9 and 10 along with corresponding plots from the calculations of the angular separation of the detector fields of view from the Earth nadir and Sun vectors using attitude results based upon the dynamic interpolation.

From the attitude angles, the angles from the edges of the field of view of both a wide angle (70 deg) and medium angle (45 deg) nonscanner to the nadir vector and the Sun vector were calculated. These values correspond to the data in the upper sphere plot of Figure 7. The solid line indicates the wide angle nonscanner limits, and the dashed line indicates medium angle nonscanner field of view limits. From the graphs, the time when either experiment viewed the Sun or the Earth can be determined. To view the Sun, the edge of the field of view must include the Sun line, which is the zero angle in the upper graph. To view the Earth, the field of view edge must include the Earth edges, which are the lines of constant value ±70 deg in the lower graph.

The calculated field of view envelope data indicate that the wide field of view detector received solar radiation during every spacecraft rotation cycle from 16:55 to 17:10 and that the medium field of view detector sensed the Sun only during the last two cycles. These calculations are verified by the corresponding detector output data of Figure 9. The increasing Solar exposure predicted for the wide field-of-view detector can also be seen clearly during the last two rotation cycles in Figure 9. The Earth-view predictions and comparisons with detector output data are not as interesting. However, the calculations, which predict Earth views every cycle for both detectors, are confirmed by the raw radiometric data of Figure 9. Two features of the calculated field of view envelope data for the period from 18:25 to 18:40 (Figure 10) are confirmed by the ERBE instrument radiometric data for that period. Solar exposure was greatest during the second rotation cycle (about 18:27), and Earth radiation exposure was greatest during the last cycle (about 18:40).

6. CONCLUSION

A description of the characteristics of the ERBS yaw turn attitude control anomaly, which occurred during an in-flight test of the X-gyro disabled yaw inversion maneuver plan, has been presented. Processed attitude sensor data from playback data augmented by a dynamics model has provided a complete description of the attitude history throughout the sunlit period of the control anomaly covered by the playback data. Verification of the method applying the dynamic model to interpolate the IRU data was performed by direct comparison of calculated science sensor boresight to Sun and Earth angles with raw IR intensity data from the ERBE nonscanner. Examples of the attitude sensor data received in the real-time telemetry data illustrated the complication that

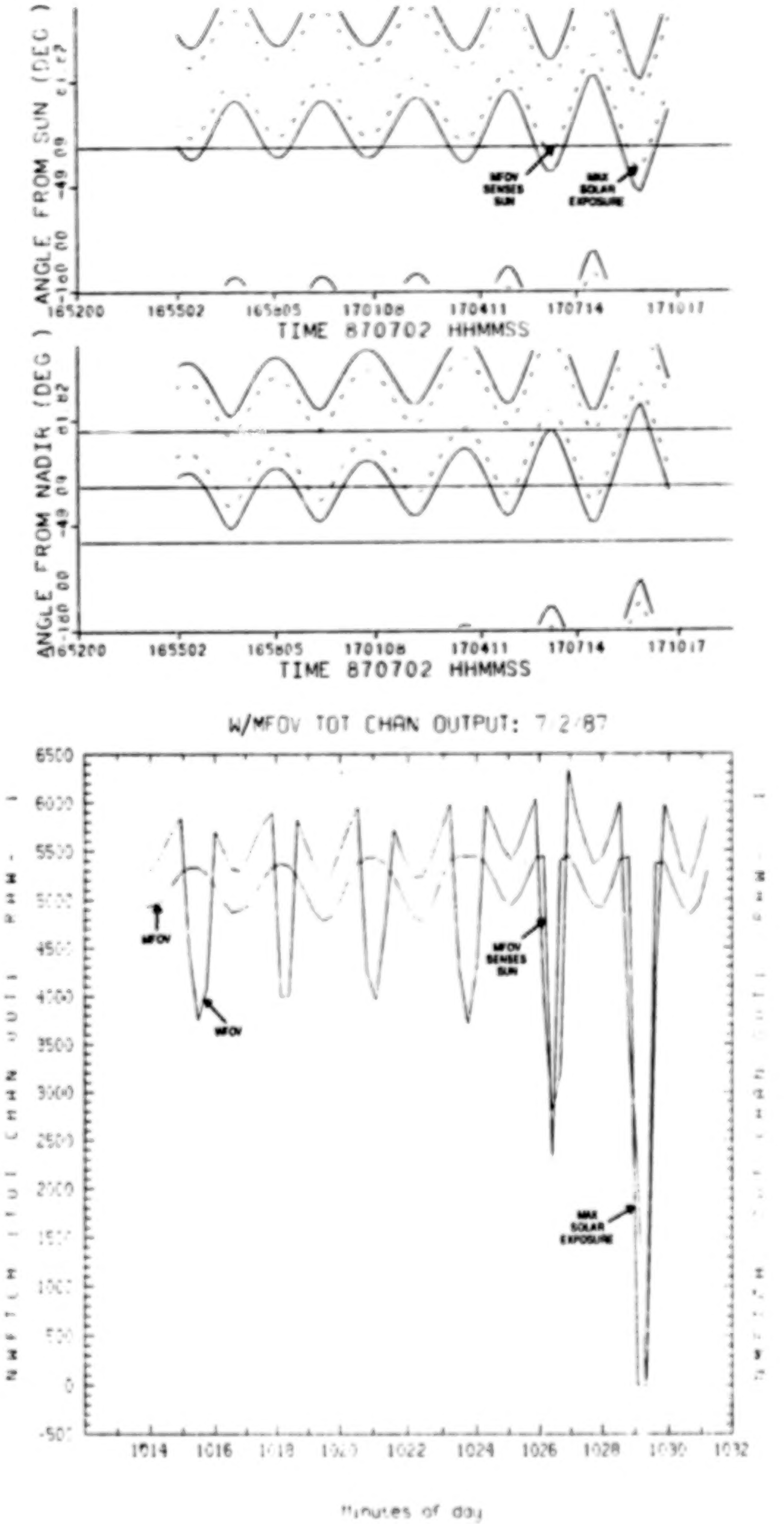

Figure 9. A Comparison of the ERBE Nonscanner Sun and Nadir Angle Computations (Upper) With the ERBE Nonscanner Raw Radiometric Output From 16:55 UTC and 17:10 UTC

ORIGINAL PAGE IS
OF POOR QUALITY

ORIGINAL PAGE IS
OF POOR QUALITY

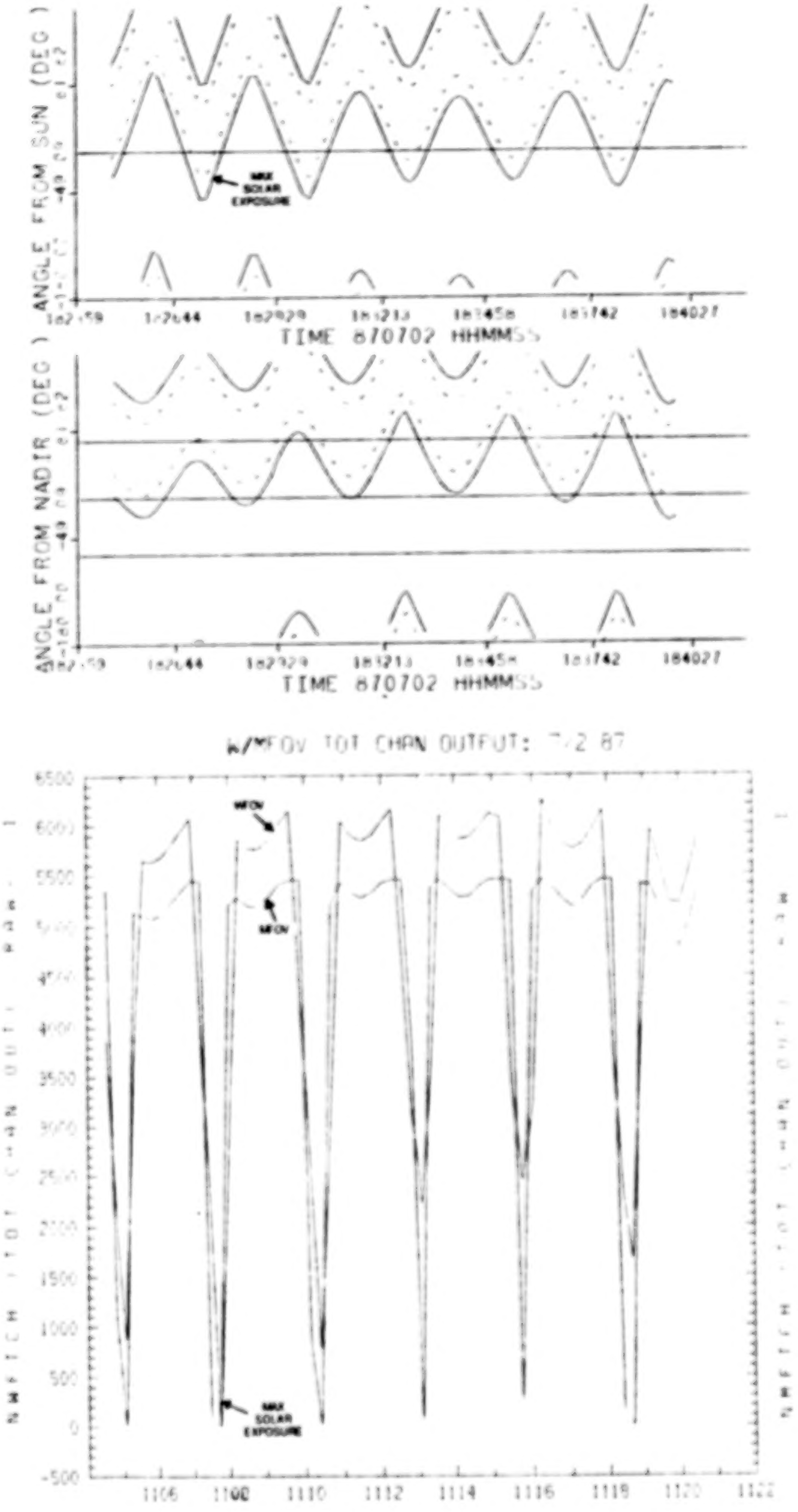

Figure 10. A Comparison of the ERBS Nonscanner Sun and Nadir Angle Computation With the Raw Radiometric Output From 18:24 UTC to 18:40 UTC

telemetry strobing imposes on real time commanding and attitude telemetry interpretation. The playback data revealed the phenomenon of stimulation of the fine Sun sensor by the Earth albedo at orbital locations approximately 40 deg on either side of the subsolar point. The analysis of the July 2, 1987, ERBS yaw turn anomaly has provided an opportunity to assess the software and procedures requirements for support of spacecraft emergencies in the FDF.

In retrospect, the following observations can be made about the experience pertaining to the contingency support procedures and software. The point of view is taken relative to the real-time event, and, therefore, it is imperative not to assume that data quality and diagnostic resources are near those provided by the playback data analyzed and presented in this work.

1. Real-time telemetry was useful for the initial problem diagnostics, including the tumble state and a rough estimate of the spacecraft body rate. These data also provided the Sun sensor data for the early hand-drawn versions of the Sun traces in the BCS frame field-of-view plots. These plots were then instrumental in demonstrating the telemetry strobing and providing crude estimates of the evolution of the spin axis in the BCS frame. Beyond this, the real-time attitude telemetry was of limited use with the software and procedures that were in place at the time.

2. Later, after the entry into the despun mode and even later during the activation of the B-DOT control mode, occurrences of unflagged (Sun presence "on") Sun sensor data led to incorrect conclusions about the despun orientation, which if acted upon could have further complicated the situation. These were subsequently (days later) determined to have been caused by the bright Earth light.

3. Valid solutions to the attitude in the periods of high-spin rate were possible using the ERBS CADS; however, the attitude representation of pitch, roll, and yaw was not suited for the spinning and nutating condition. This suggests that the availability of alternative representation, such as the spin-axis right ascension and declination, BCS spin unit vector, and angular momentum vector representations, may have contributed to a more rapid resolution of the detailed attitude and spacecraft spin state from the limited real-time data.

4. Reliable spacecraft dynamics simulation in conjunction with attitude determination using Sun sensor and magnetometer data could contribute significantly to the real-time attitude estimation process in the contingency mode.

5. An attitude algorithm relying only on the magnetometer data with initialization during periods of valid Sun sensor and gyro data or during those special periods of coalignment of the spin axis and the geomagnetic field, in addition to optional choices for the attitude state representation would probably have been the most useful tool. The usefulness of such a software tool would have been directly proportional to the graphics capabilities and the ability to quickly generate hardcopy versions of attitude results in some of the optional representations presented in this work.

REFERENCES

1. CSC Memorandum Analysis of the ERBS Attitude Motion During the July 2, 1987, Control Anomaly, J. A. Kronenwetter and M. C. Phenneger (CSC), October 1987

2. Langley Research Center Memorandum, Analysis of the ERBE Instrument Data Around Time of ERBS Yaw Maneuver Anomaly on July 2, 1987, W. Weaver (NASA/LRC) and M. G. Payton, (STX Corporation), September 4, 1987

3. E. J. Lefferts (GSFC) and F. L. Markley (CSC), Dynamic Modeling for Attitude Determination 76-1910 AIAA Guidance and Control Conference, San Diego, California, August 16-18, 1976

N89-15953

EVALUATION OF ERBE SCANNER POINTING ACCURACY BASED UPON A COASTLINE DETECTION ALGORITHM

William L. Weaver, Lawrence H. Hoffman, and James F. Kibler
Atmospheric Sciences Division
NASA Langley Research Center
Hampton, Virginia 23665-5225

ABSTRACT

Measurements from the Earth Radiation Budget Experiment (ERBE) scanning radiometers must be accurately located at the top of the Earth's atmosphere for proper interpretation of derived longwave and shortwave components of the Earth radiation field. The accuracy of the location calculations is affected by the orbit characteristics and attitude control systems of the three spacecraft, ERBS, NOAA-9, and NOAA-10. A technique was developed which makes use of the longwave scanner measurements to detect the thermal gradients at the boundaries of ocean and land masses. By analyzing many such coastline boundaries, estimates of the overall accuracy of the scanner measurement location calculations have been derived for the three satellites. The resulting measurement location errors are found to be smaller than the resolution of the radiometers, and this accuracy is well within the required location knowledge for useful science analysis of the ERBE scanner data.

EVALUATION OF ERBE SCANNER POINTING ACCURACY BASED UPON A COASTLINE DETECTION ALGORITHM

William L. Weaver, Lawrence H. Hoffman, and James F. Kibler
Atmospheric Sciences Division
NASA Langley Research Center
Hampton, Virginia 23665-5225

INTRODUCTION

The Earth Radiation Budget Experiment (ERBE) instruments are operating on three Earth-orbiting spacecraft. The Earth Radiation Budget Satellite (ERBS) operated by the National Aeronautics and Space Administration (NASA) at the Goddard Space Flight Center (GSFC), is in a 600-km, 57° inclination orbit with a precessional period of about 2 months. The National Oceanic and Atmospheric Administration (NOAA) satellites NOAA-9 and NOAA-10, launched in December 1984 and September 1986, respectively, are in about 860- and 825-km Sun-synchronous orbits, each with a different local time for its nodal crossing. Each ERBE instrument set consists of fixed field-of-view (non scanning) and cross-track scanning radiometers. The overall ERBE mission concept and design is described in reference 1, and the ERBE scanner and non scanner instruments are described in references 2 and 3, respectively.

In deriving Earth radiation fields from the ERBE radiation measurements, both the surface characteristics at the measurement location on the Earth and the satellite-Earth-Sun geometry play important roles. The task of accurately calculating the Earth locations for the ERBE measurements is complicated by the fact that there is no imaging system associated with the ERBE measurements, and thus, landmark identification is difficult. Therefore, a concerted effort was made to understand the process by which the Earth locations of measurements are calculated, and a technique was developed for verifying the accuracy of the calculations. Because of the more rigorous accuracy requirements of the scanner instruments, this paper is concerned only with the measurements from the scanners. The scanner instruments make instantaneous radiance measurements in three broad spectral bands: shortwave, longwave, and total as the scan head traverses a path normal to the orbit ground track every 4 seconds.

The Earth-location verification technique developed makes use of the scanner radiometric measurements to detect sharply contrasting thermal regions on the Earth which occur at the boundaries of water and land masses. This paper describes the steps in computing the measurement locations and the development of the verification technique and its application to assessing the accuracy of the ERBE measurement locations.

CALCULATION OF EARTH LOCATIONS OF ERBE SCANNER INSTRUMENT MEASUREMENTS

The primary objective of the ERBE experiment is to determine the monthly average radiant exitances at the top of the atmosphere (TOA) over the Earth with a resolution of 250 km. Figure 1, which is an example of a typical monthly product, is the map of the average longwave exitance for April 1985 derived from ERBE scanner measurements made from the ERBS spacecraft. The production of this end product, starting with computing the radiances from the individual scanner measurements at the spacecraft, inverting the radiances to flux densities at the TOA, and then averaging over time and space, is discussed in reference 4.

The accuracy of these derived exitances depends on correctly calculating the locations on the Earth of the source of each of the individual scanner radiometric measurements. This calculation is done in two major steps. The first major step is to transform a pointing vector in the detector coordinate system to one in a local geodetic system. Figure 2 is a schematic of the scanner instrument which illustrates its coordinate systems, and figure 3 illustrates the instantaneous local geodetic (or horizon) system at the spacecraft. The X-axis of the local geodetic system is along the component of the velocity vector in the geodetic plane (V_x), the Y-axis is normal to the orbit plane, and the Z-axis is along the local geodetic nadir. The pointing vector for the scanner measurement is derived as follows: The unit vector along the optical axis of the detector is transformed from detector coordinates into pedestal coordinates by rotating through the instrument elevation and azimuth angles; the resulting vector is transformed into the coordinates of the specific spacecraft; and finally, this vector is transformed into the local geodetic system by rotating through the spacecraft orientation or attitude angles. Some salient points in this process are given here, and the details are described in reference 5.

Special attention was given at each stage of instrument manufacturing and buildup and in the process of mating the instruments with their respective spacecraft to ensure proper alignment of components which affect the calculation of detector pointing vectors. The decision was made to use the actual values of the instrument elevation and azimuth beam angles for calculating the location of each measurement instead of deriving these angles by modeling the motion of the instrument elevation angles. This, we believe, significantly increased the accuracy of the measurement locations. The instrument azimuth and elevation beam angles are edited during processing to ensure correct values before calculating the pointing vector. The frequency of occurrence of the instrument azimuth beam angles in the telemetry data stream is much lower than that of the radiometric measurements, and pointing vectors are not computed if the azimuth beam is in motion.

Both the ERBS and NOAA spacecraft use a combination of horizon sensors, inertial gyros, and Sun sensors to keep the spacecraft aligned with the local geodetic system of figure 3. The three spacecraft attitude angles are provided in the telemetry data as deviations from these instantaneous coordinate axes, and the attitude angles are used in the final transformation of the pointing vector into the local geodetic coordinates. The quantities required to define the local geodetic system of figure 3 and to transform the scanner pointing vector from that system into an Earth-fixed system are derived from orbit ephemeris data. The ephemeris data for both the ERBS and the NOAA spacecraft are calculated by GSFC, and these ephemeris data have been found to be very accurate.

The second major step in calculating the Earth location of a scanner measurement starts by transforming the pointing vector from the local geodetic system to Earth-fixed coordinates using the spacecraft heading angle. The associated spacecraft ephemeris data are transformed from the inertial frame to the same Earth- fixed coordinate system and are interpolated to the time of the scanner measurement. The details of these transformations are described in reference 5.

The final task is to determine the intersection of the pointing vector with the Earth's surface. The Earth's surface is modeled by an ellipsoid, and the geometry of the pointing vector intersection with the ellipsoid is illustrated in figure 4. In this figure, R_e and R_p are the equatorial and polar radii of the Earth and h is the altitude of the TOA above the Earth's surface. Given a vector from the center of the Earth to the spacecraft ($\mathbf{P}$) and a detector unit pointing vector ($\hat{\mathbf{V}}$) the magnitude of the vector from the spacecraft to the intersection with the ellipsoid ($\mathbf{V}$), is determined using relationships described in reference 5. The final result is the estimated latitude and longitude of the center of the measurement point on the surface of the Earth.

METHOD OF ASSESSING MEASUREMENT LOCATION ACCURACY

The method described above is used in the ERBE processing system to calculate the Earth location of every scanner radiometric measurement. Now, a technique is needed to evaluate how successfully the method locates the scanner measurements. One way to assess the accuracy is to identify Earth features using the scanner radiometric measurements. The shortwave radiometric measurements are not used because they have large variations due to clouds and are not useful at night. When there are large thermal contrasts, the longwave measurements show thermally interesting features such as desert adjacent to an ocean. Points on this thermal boundary between the desert and ocean can be identified making use of multiple scan cycles of scanner radiometric data. The points on the coastline determined by this method can then be compared to an actual map, and errors in the latitude and longitude of the estimated location point can be estimated. Coastline identification results for many days and several sites are then accumulated in scatter plots which illustrate both the random errors and biases in the locations of the detected coastlines.

In selecting suitable coastlines for use in applying the coastline detection algorithm, the following characteristics were considered important to its successful application:

(a) Probable high thermal contrast between land and water.
(b) Infrequent cloud cover.
(c) No unusual terrain features, such as lakes and mountains, next to the coastline.
(d) Interesting coastline. An absolutely straight coastline is not adequate for detecting errors along the coastline. A coastline with regular curves, peninsulas, and bays is most useful.

The following coastline sites were selected, and together they provide a range of useful and desirable conditions:

(a) Baja, California. This site is a desert-like peninsula surrounded by water.
(b) The northwest coast of Australia. This site has an irregular coastline with desert immediately adjacent to ocean.
(c) The coast of Libya. The Gulf of Sidra intrudes into desert regions at this site.
(d) The southeast coast of the Arabian peninsula. This site is an irregular coastline roughly parallel to the ERBS orbit ground track.

Figure 5 shows a typical plot of longwave radiance measurements as the scan track crosses a coastline. Each point represents one scanner measurement. Measurements with the higher radiance values are assumed to be land in daytime or water at night, and those with the lower radiance values are assumed to be the reverse. Thus, if there is a homogeneous land region bounded by water, a scan across the coastline boundary yields a measurement pattern similar to that shown in figure 5.

A cubic equation in latitude and longitude is fitted to each set of four consecutive points in a scan cycle. The inflection point for the equation is calculated for each of these sets of points. An inflection point is considered a coastal crossing (or boundary) if it falls between the two center points and if the total change in the values of the four measurements is larger than a threshold value. The threshold value is used to eliminate spurious inflection points caused by normal variations in the measurements. Once a coastal crossing point has been selected, its location is determined by interpolating between the latitude and longitude of adjacent measurement locations.

A collection of calculated coastal crossing points during a spacecraft pass is fitted to a digitized map of the corresponding coastline. Figure 6 shows two typical sets (one for ERBS, one for NOAA-9) of these calculated crossing points plotted on maps. The circles represent the calculated coastline crossing points, and the squares represent the subsatellite ground track during the overpass. Shown also is the spacecraft identification, the date of the data, the scan direction, and whether data period is during ascending or descending part of orbit. The rotation direction of the scan motion is clockwise as one looks down the spacecraft velocity vector of both the ERBS and NOAA-9 spacecraft in figure 6. This is always the case for the NOAA-9 spacecraft and the case for the ERBS spacecraft when configured with its X-axis pointed backward. The opposite is the case when ERBS is configured with its X-axis pointed forward. The data error information is discussed in the next paragraph. Data from most spacecraft passes over the selected coastlines do not produce useful information because of the presence of clouds or poor thermal contrast at the time of satellite passage. However, by examining many days of data for each site, a large number of useful passes can be accumulated.

A figure-of-merit is needed to assess how well the estimated coastline matches the actual map coastline. The figure-of-merit selected is the least-squares distance between the calculated coastal crossing points and the map coordinates of the coastline. A latitude and longitude correction is applied to each crossing point in a manner which minimizes the sum of the squares of the distances from the crossing points to the map. This correction is then defined as the location error, in latitude and longitude, for the spacecraft pass. Values for this correction are shown on figure 6. It is also useful to consider the measurement location errors in a coordinate system at the Earth surface in which one axis is along the direction of scan and the other is perpendicular to the scan direction. Figure 6a shows that the least-squares latitude and longitude errors for this pass map into errors of −0.0478° (approximately 5 km) in the direction of the scan (cross-track or normal to orbit ground track) and 0.0271° (approximately 3 km) perpendicular to the scan direction (along the orbit ground track).

Errors from a number of coastline detection passes can be plotted to depict a statistical distribution of the errors. Figure 7 presents a scatter plot for data from the ERBS spacecraft for November 1984 in which each point is the result of analyzing the coastline crossing points for a single coastline pass. The ellipse is the 95-percent probability region, computed assuming that the data have a Gaussian distribution with mean and covariance equal to that of the data. The random errors include uncertainties in calculating actual Earth locations of the radiometric measurements; but they also include uncertainties in the technique used in calculating the coastline crossing points. The random errors in the actual Earth location of the measurements, which include spacecraft position and attitude errors and instrument angle and misalignment errors, should, therefore, be bounded by such an error ellipse. The center of the ellipse in figure 7 suggests that there is a bias in the calculations of −0.026° (about 3 km) in the cross-track direction and a much smaller bias of 0.0048° (about 0.5 km) in the along-track direction. This bias is discussed in the next section.

RESULTS AND DISCUSSION

The method presented earlier for calculating ERBE scanner measurement locations on the Earth has been implemented in the data processing software to calculate the latitude and longitude of every scanner radiance measurement. The coastline detection technique described in the last section has been applied to large numbers of coastline crossings to evaluate how accurately the calculations of Earth locations are being made. Figure 6, introduced in the previous section, shows comparisons in coastline crossing points between actual map values and values computed using the coastline detection technique. The estimated coastline crossing points are seen to follow the actual coastlines of the California Baja peninsula and Libya quite well.

The figure-of-merit errors computed for the pass of figure 6a of 0.027° along-track and −0.048° cross-track result in errors in distance at the Earth surface of about 3 and 5 km respectively. The largest difference in distance between an individual actual and calculated crossing point for the ERBS and NOAA-9 data of figure 6 was found to be about 15 km. Since the scanner field-of-view is about 30 km at nadir, the calculated Earth locations are well within this field of view.

The distribution of errors in the calculations of the coastline crossing points for the ERBS spacecraft for November 1984 (figure 7) shows a small cross-track bias. This bias of −0.03° represents a constant error of about 3 km along the scan track in a direction which is opposite to the direction of the scan beam motion. The plot of figure 7 includes data from passes over all four different coastlines, and it includes data from cases when the ERBS spacecraft was flying X-axis forward and cases when it was flying X-axis backward. With this range of conditions, it is unlikely that the bias is caused by errors in spacecraft ephemeris or attitude data or in the method of calculating the coastline detection errors. Instead, the bias may be caused by a detector misalignment, errors in instrument elevation angles, or by the method used to account for the response of the instrument as it views a changing scene. The effect of the bias has been removed in the production processing for both the ERBS and NOAA-9 spacecraft by subtracting a constant from the value of the elevation angle before calculating each pointing vector.

Figure 8 is a plot of the measurement location errors for ERBS and NOAA-9 for April 1985. The Earth location calculations for the scanner radiometric measurements include use of the bias correction described above. The data show that the bias correction works a little better for the ERBS measurement calculations than those of NOAA-9 during this period, but the bias errors for both spacecraft are small. The error ellipses show that 95 percent of all coastline detection calculations are less than 10 km in error from the true coastline location.

Figure 9 is a plot of the measurement location errors for ERBS for December 1986. The random errors appear to be about the same as they were 2 years earlier. The data also show that the bias in calculating the scanner measurement locations on ERBS, which was discovered during the analysis of data for November 1984 is not much different than it was over 2 years ago. The agreement would be even better except for the single large error in the upper right quadrant of figure 9. This location error is caused by large errors in some of the individual coastline crossing points in the upper right corner of figure 10. These individual errors could be caused by the unusually irregular coastline or clouds in the area. This problem suggests that certain calculated coastline crossing points need to be eliminated before deriving the figure- of-merit coastline location error for some of the coastline passes.

The first coastline location error calculations for NOAA-10, which was launched in September 1986 were made for data from November and December 1986, and the data are presented in figure 11. The random errors are larger than those seen for ERBS and NOAA-9, and there is an apparent location bias of about 12 km, most of which is along the scan axis of the instrument. This bias, however, is not normal to the ground track like the bias for ERBS and NOAA-9, because the scanner instrument on NOAA-10 normally scans in a plane which is 35° from the cross-track azimuth position. This off-normal scan mode is necessary to prevent the scanner detectors from viewing the Sun, which remains above the spacecraft horizon during most orbits. The bias shown in figure 11 is along the same axis (scan axis) and in the same direction as the bias for the ERBS and NOAA-9 spacecraft.

Sluggishness of the scan beam on NOAA-10 was observed in the data for early January 1987 and the problem became severe later in January and lasted well into February. There were times in January and February that the scan beam would come to a complete stop during the Earth scan portion of a scan cycle. The problem may have been worse than originally thought in December 1986, and this problem may account for the larger bias seen in figure 11. The problem needs further study, and it may be necessary to use biases with different values at different times, depending on the severity of the scan beam problem.

CONCLUDING REMARKS

The steps in calculating the Earth locations of the ERBE instrument scanner measurements have been described, and a coastline detection algorithm has been developed and applied to assessing the accuracy of the calculated locations. The results presented demonstrate that the ERBE scanner measurements are located within a region on the surface of the Earth which is much smaller than the field-of-view of the scanner detectors.

Most of the bias in the scanner measurement locations for all three spacecraft is aligned with the instrument scan axis and is probably not caused by errors in ephemeris and attitude data or in the method of calculating the location errors. The value of the bias for the measurements on the ERBS spacecraft appears to have remained nearly constant for the first 2 years of operation. The measurement location estimates for ERBS and NOAA-9 imply that the spacecraft ephemeris and on-board attitude data are accurate and are correctly merged with the radiation measurements. The larger bias in the location estimates for the NOAA-10 spacecraft for November and December 1986 may be caused by an observed scan beam problem and needs further investigation.

For the ERBS and NOAA-9 data analyzed, figure-of-merit coastline location errors for a coastline pass are less than 10 km, and individual location errors during a pass are less than 15 km. The average figure-of-merit coastline location error for ERBS and NOAA-9 for a month of data is less than 5 km in the cross-track and down-track direction. These errors include uncertainties in the coastline detection technique as well as errors in calculating the scanner measurement locations.

Users of the ERBE data can rely on the geographical locations of the measurements on the archival data products. The coastline detection technique presented should have application to other remote sensing instruments which scan in a cross-track plane and which can sense thermal differences between land and ocean. The technique might also be extended to a 2-dimensional method to allow coastline detection for instruments which provide nearly simultaneous measurements in both along-track and cross-track directions.

REFERENCES

1. Barkstrom, Bruce R., 1984: The Earth Radiation Budget Experiment (ERBE). *Bulletin of the American Meteorological Society*, Vol. 65, No. 11, pp. 1170-1185.
2. Kopia, L. P., 1986: The Earth Radiation Budget Experiment Scanner Instrument. *Rev. Geophys. and Space Physics*, Vol. 24, pp. 400-406.
3. Luther, M. R., 1986: The Earth Radiation Budget Experiment Non-Scanner Instrument. *Rev. Geophys. and Space Physics*, Vol. 24, pp. 391-399.
4. Smith, G. L., Barkstrom, B. R. and Harrison, E. F., 1987: The Earth Radiation Budget Experiment: Early Validation Results. *Adv. Space Res*, Vol 7, No. 3, pp. (3)167-(3)177.
5. Hoffman, L. H., Weaver, W. L. and Kibler, J. F., 1987: Calculation and Accuracy of ERBE Scanner Measurement Locations, NASA Technical Paper 2670.

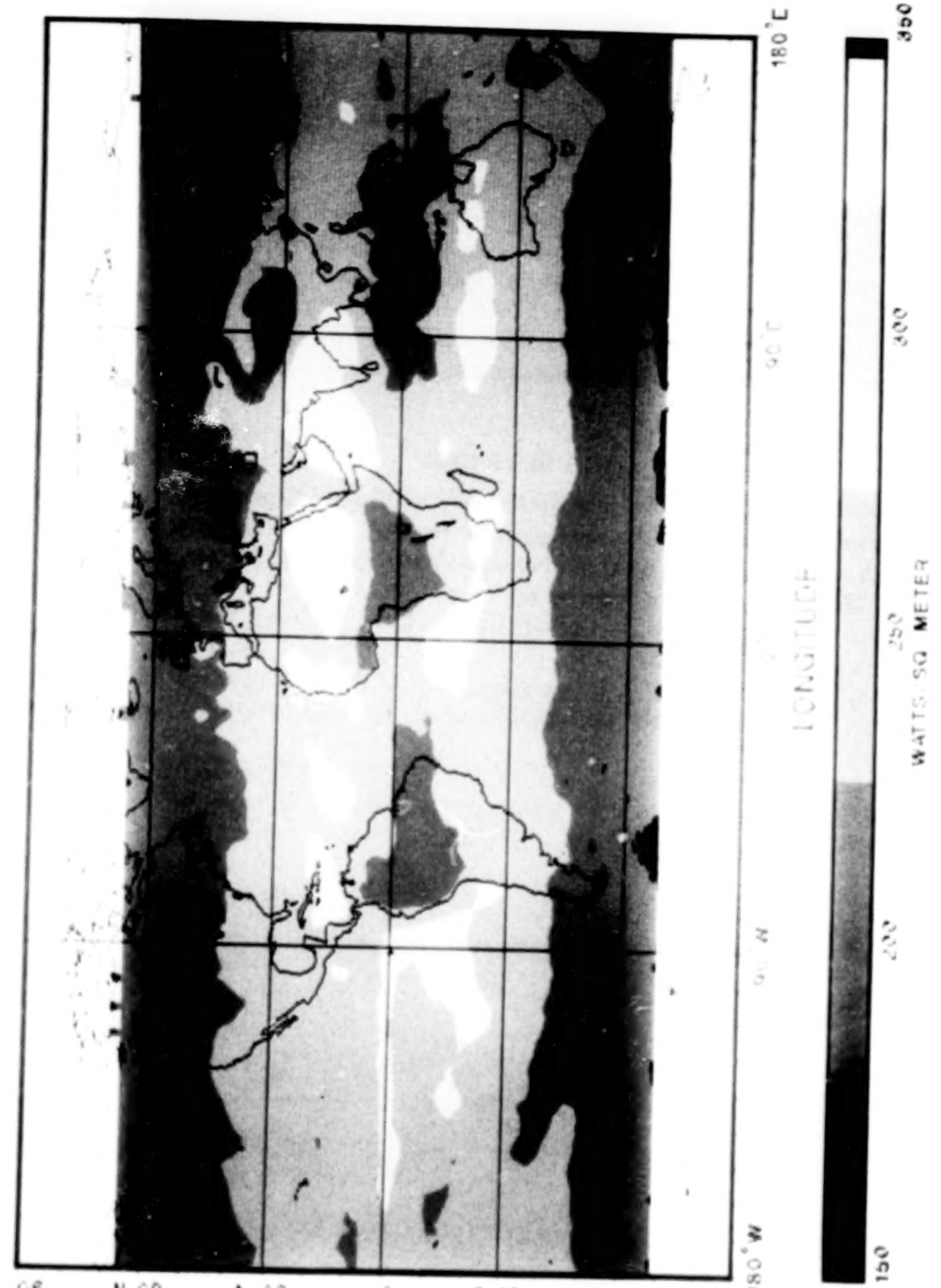
90°N
60°N
30°N
0°
30°S
60°S
90°S
LATITUDE
180°W
90°W
0°
90°E
180°E
LONGITUDE
150
200
250
300
350
WATTS/SQ METER

Figure 1.- Average longwave exitance for April 1985 from the ERBS spacecraft.

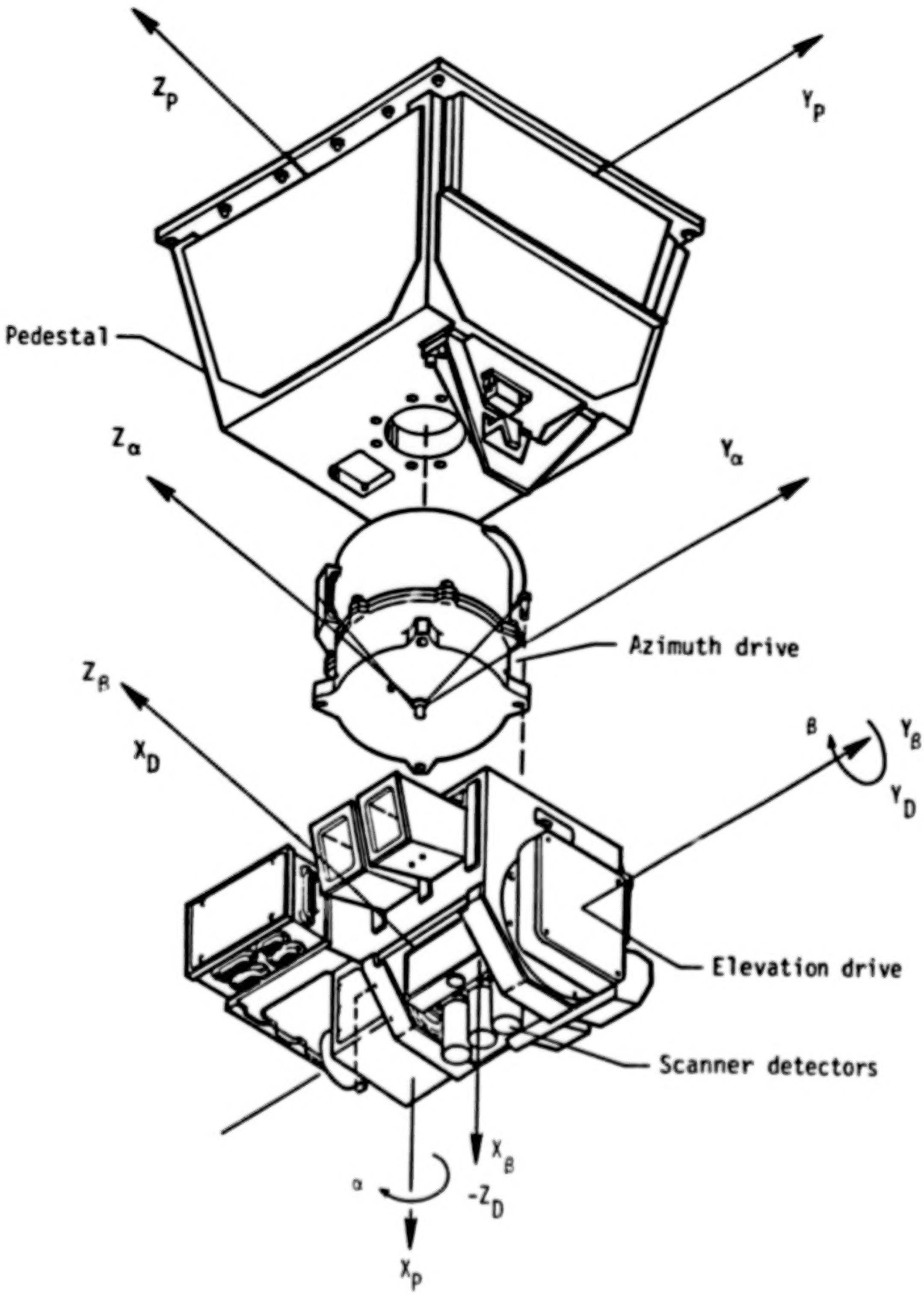
Z_P
Y_P
Pedestal
Z_α
Y_α
Azimuth drive
Z_β
X_D
β
Y_β
Y_D
Elevation drive
Scanner detectors
X_β
α
$-Z_D$
X_P
X_α

Figure 2.- Coordinate systems of ERBE scanner instrument

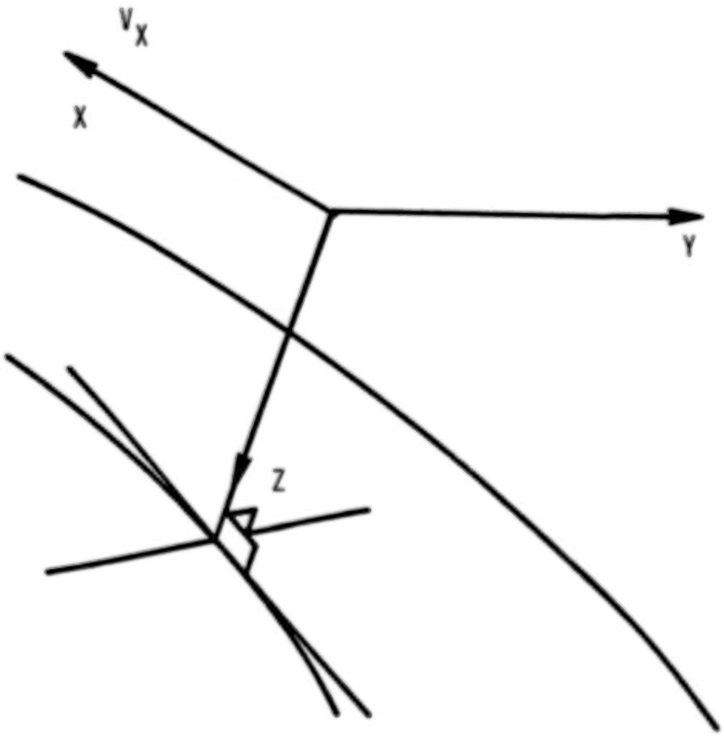

Figure 3.- Local geodetic coordinates

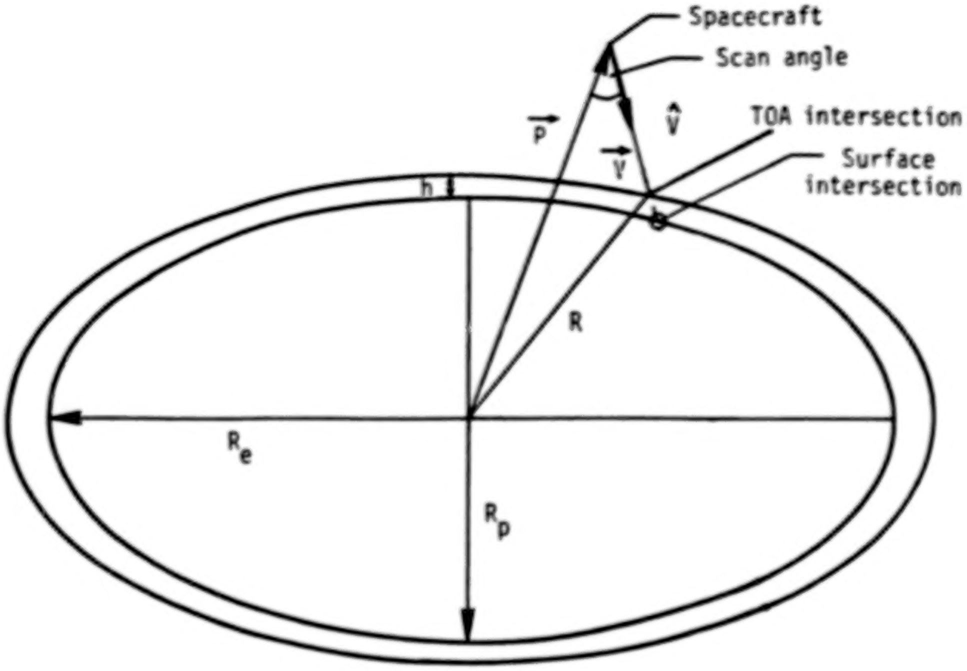
Spacecraft
Scan angle
$\vec{P}$
$\hat{V}$
TOA intersection
$\vec{V}$
Surface intersection
h
R
R_e
R_p

Figure 4.- Intersection of pointing vector with Earth ellipsoid.

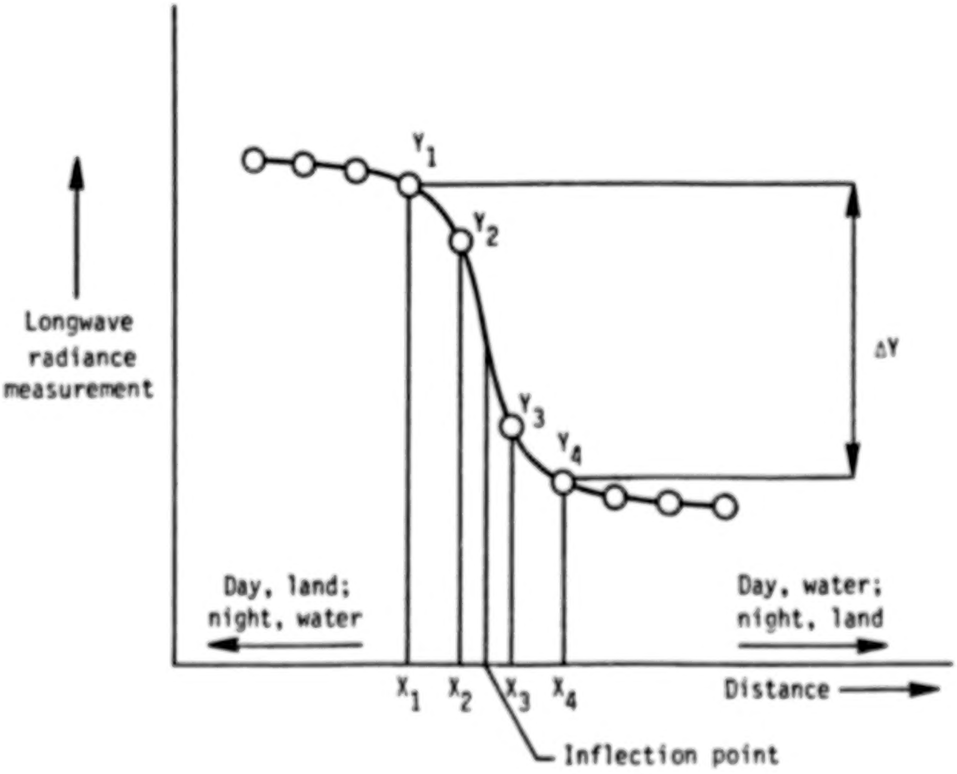
Longwave radiance measurement
Y_1
Y_2
Y_3
Y_4
ΔY
Day, land; night, water
Day, water; night, land
X_1
X_2
X_3
X_4
Distance
Inflection point

Figure 5.- Cubic fit for coastline detection.

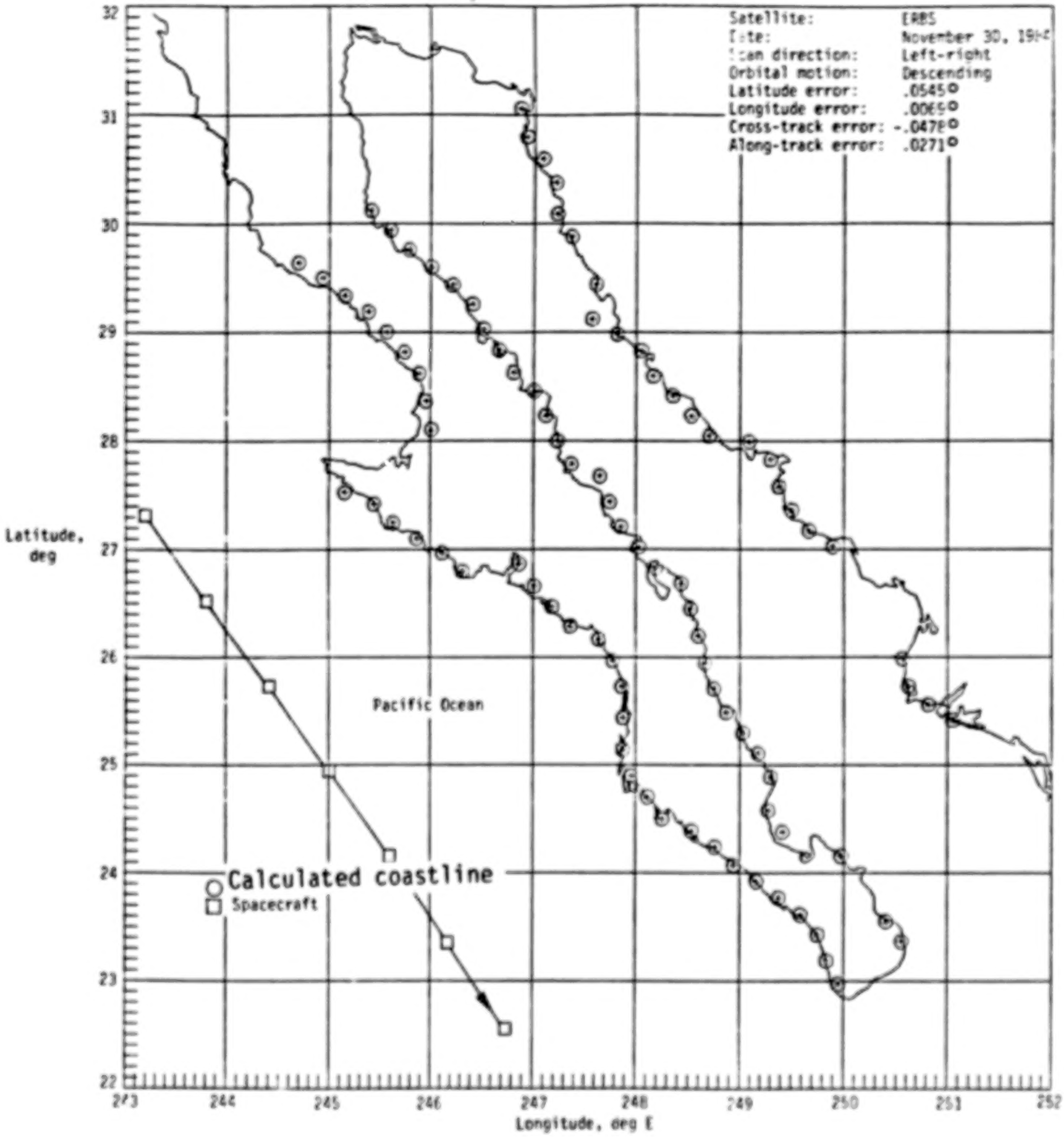

(a) ERBS over Baja California.

Figure 6.- Coastline detection results.

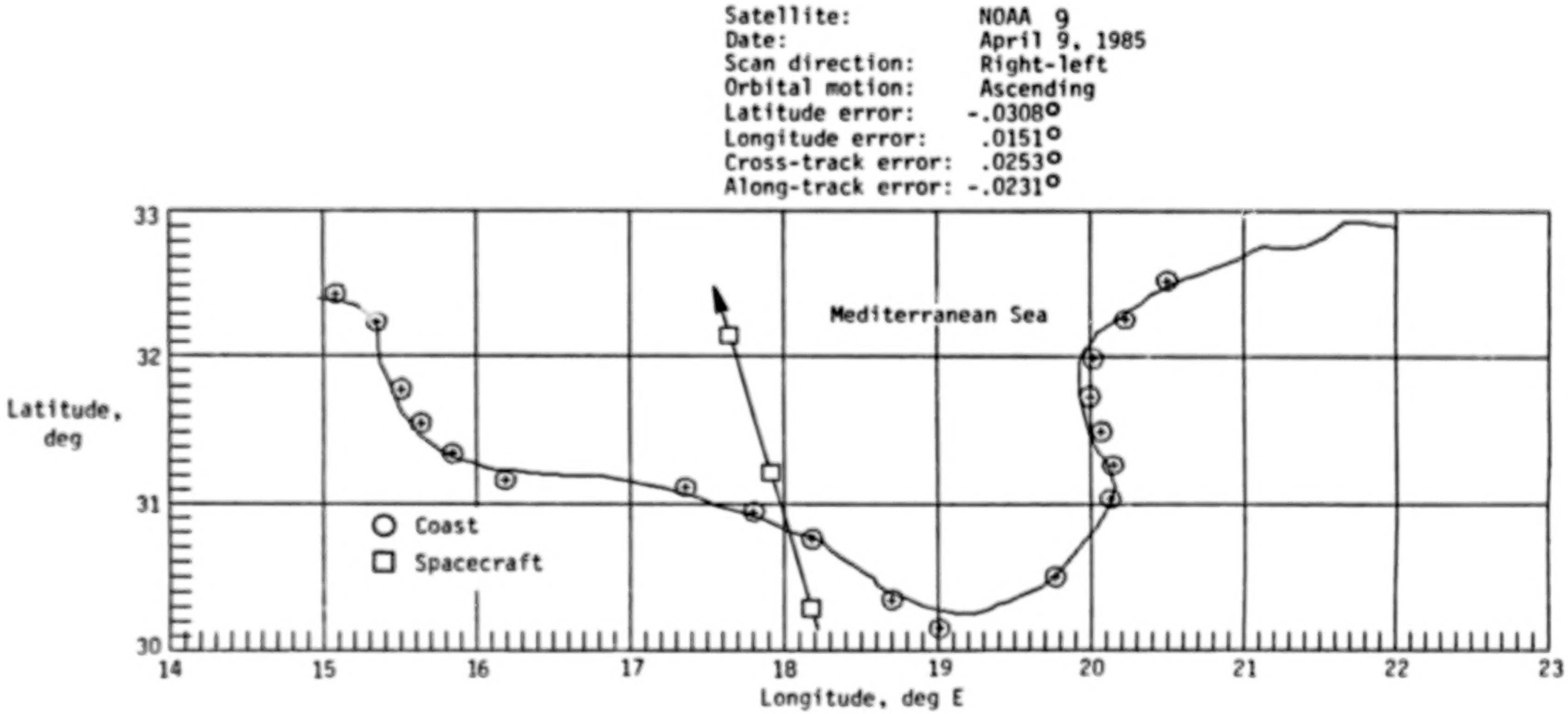

(b) NOAA-9 over Libya.

Figure 6.- Concluded.

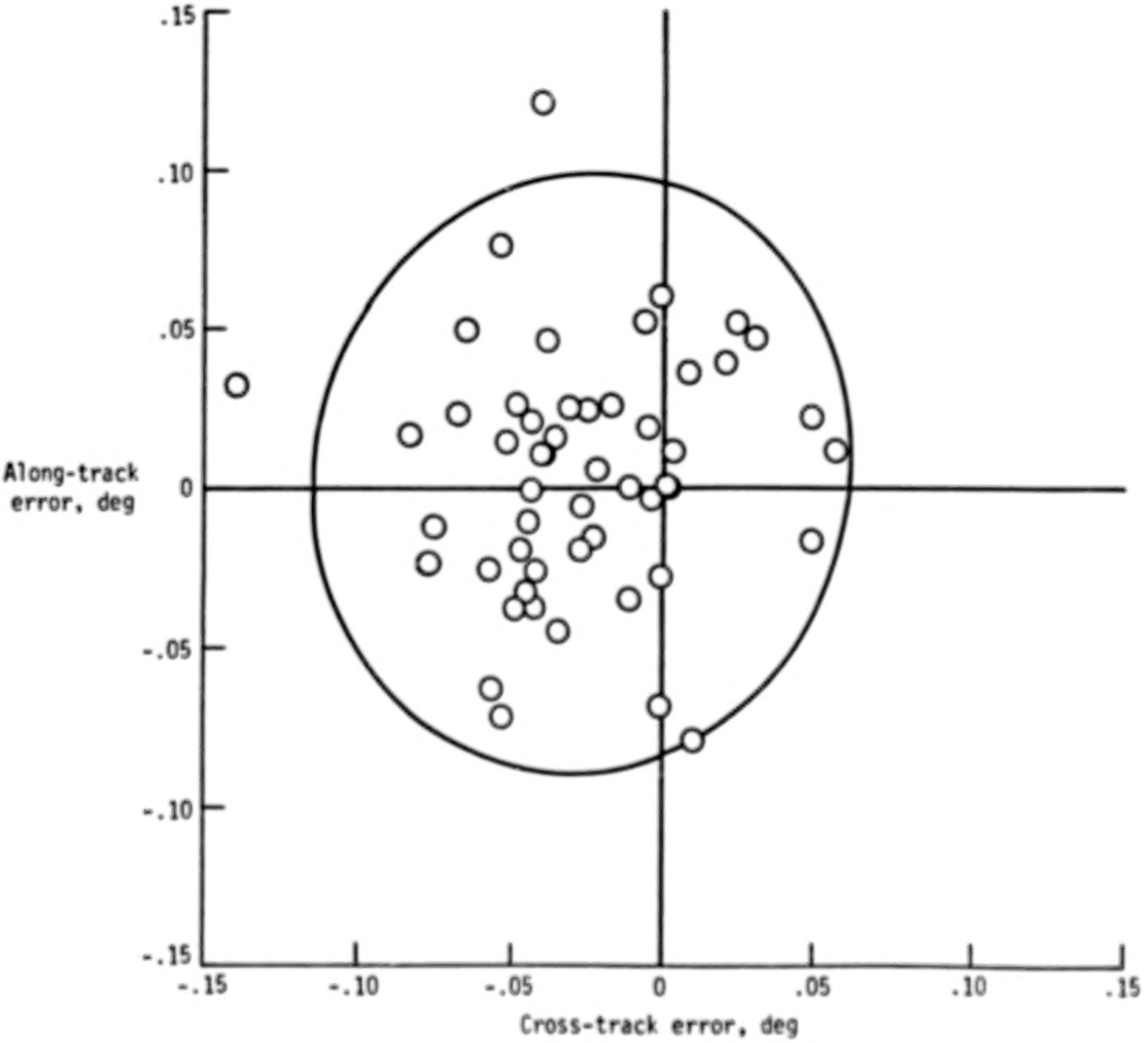

Figure 7.- Scanner measurement location errors for ERBS November 1984 showing bias.

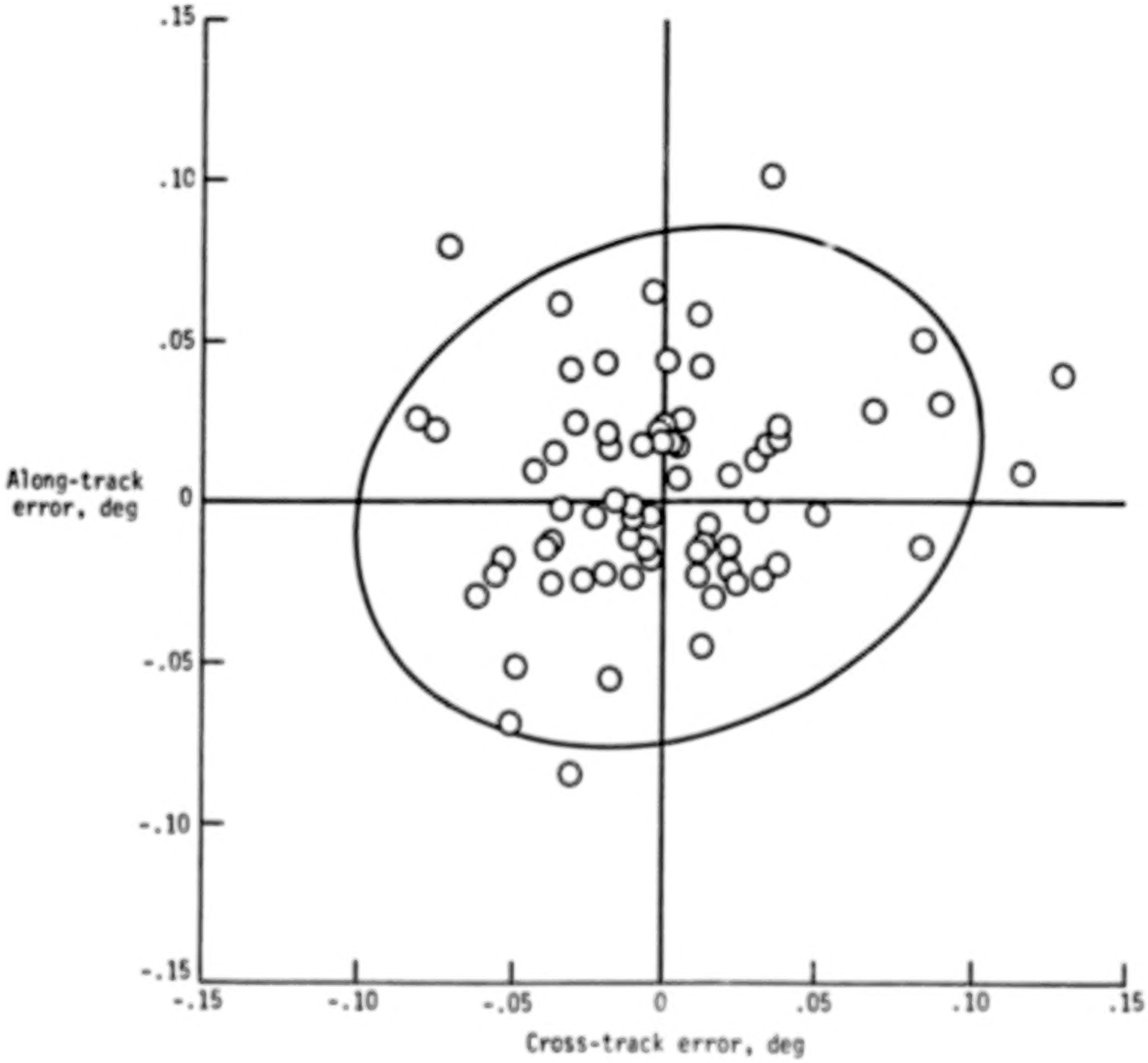

(a) ERBS.

Figure 8.- Scanner measurement location errors for April 1985.

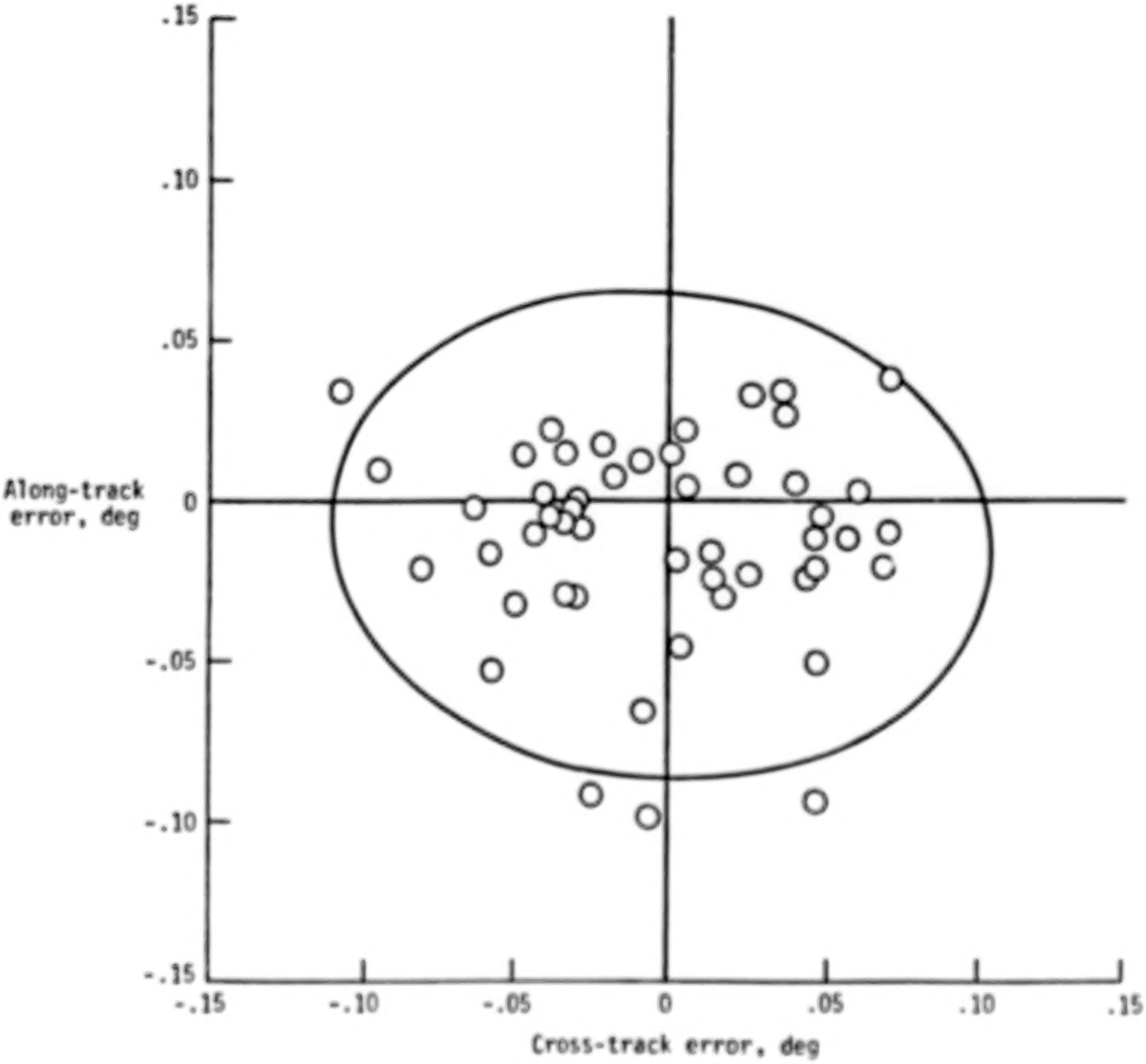

(b) NOAA 9.

Figure 8.- Concluded.

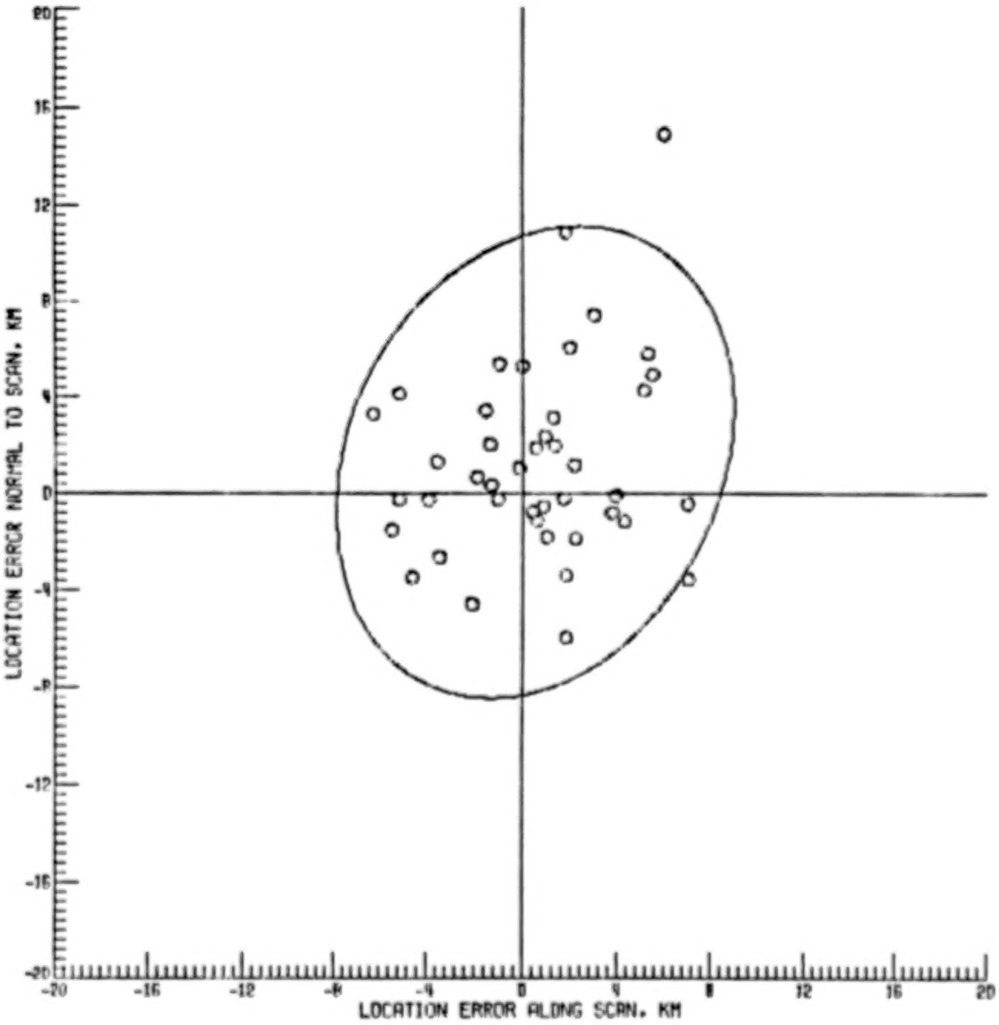

Figure 9.- Scanner measurement location errors for ERBS December 1986.

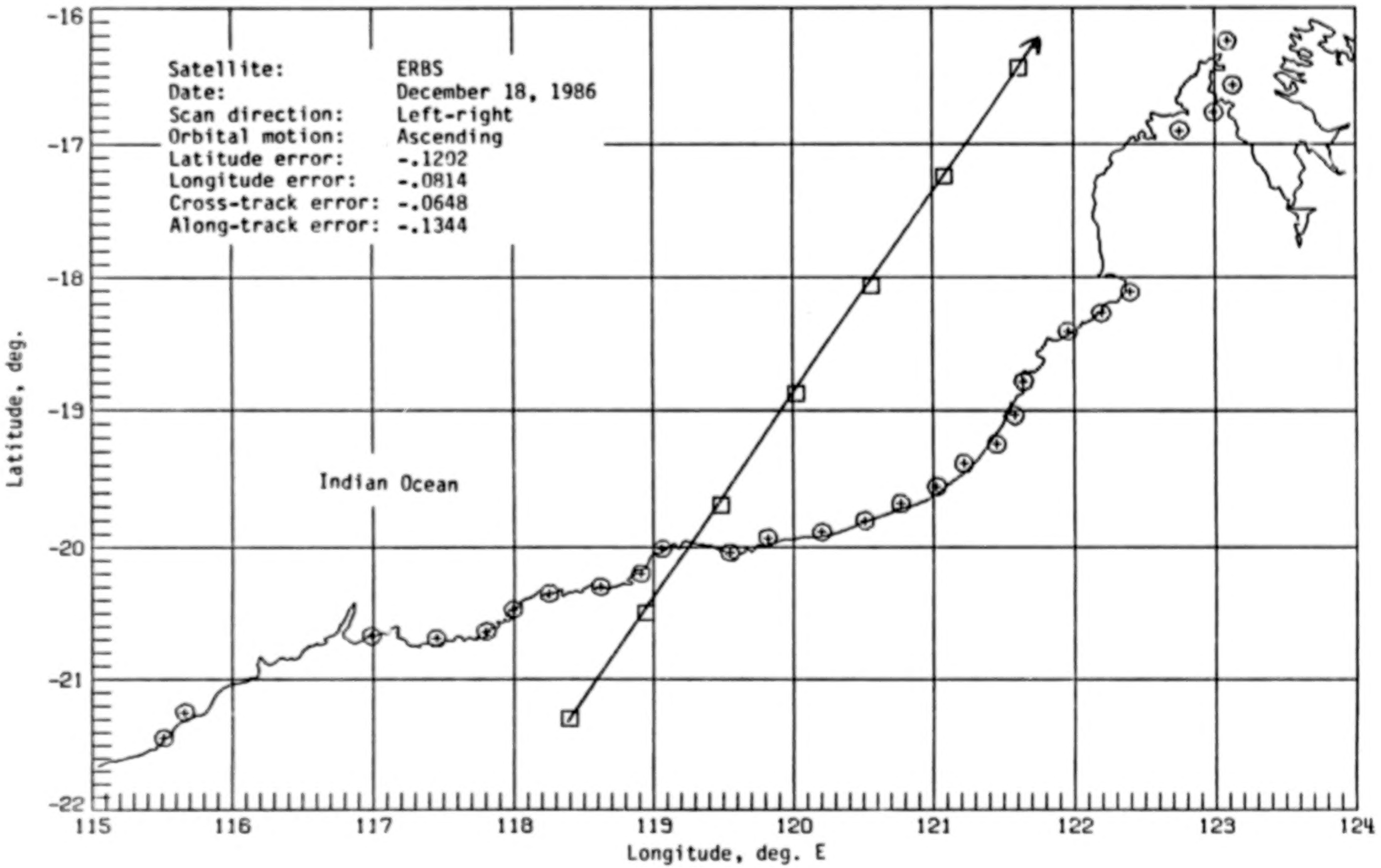
Satellite: ERBS
Date: December 18, 1986
Scan direction: Left-right
Orbital motion: Ascending
Latitude error: -.1202
Longitude error: -.0814
Cross-track error: -.0648
Along-track error: -.1344
Indian Ocean
-16
-17
-18
-19
-20
-21
-22
Latitude, deg.
115
116
117
118
119
120
121
122
123
124
Longitude, deg. E

Figure 10.- Scanner measurement location errors for ERBS over Australia.

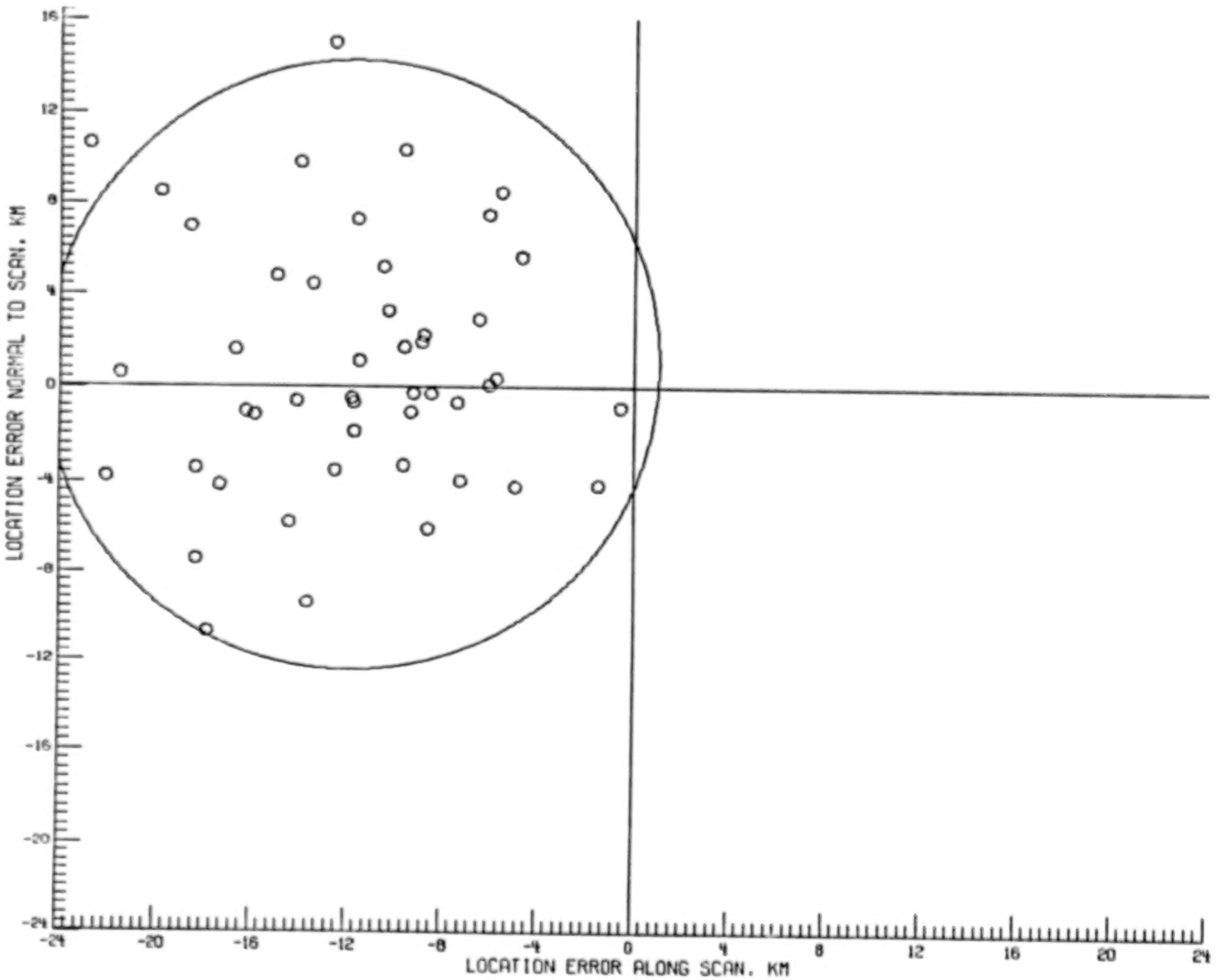

Figure 11.- Scanner measurement location errors for NOAA-10.

N89-15954

ATTITUDE MOTION OF A NON-ATTITUDE-CONTROLLED CYLINDRICAL SATELLITE *

C. K. WILKINSON †

ABSTRACT

In 1985, two non-attitude-controlled satellites were each placed in a low earth orbit by the Scout Launch Vehicle. The satellites were cylindrical in shape and contained reservoirs of hydrazine fuel. Three-axis magnetometer measurements, telemetered real time, were used to derive the attitude motion of each satellite. Algorithms are generated to deduce possible orientations (and magnitudes) of each vehicle's angular momentum for each telemetry contact. To resolve ambiguities at each contact, a force model was derived to simulate the significant long-term effects of magnetic, gravity gradient, and aerodynamic torques on the angular momentum of the vehicles. The histories of the orientation and magnitude of the angular momentum are illustrated.

---

* *This work was performed in conjunction with Contract F04701-78-C-0125 for the United States Air Force, Space Division*

† *Principal Engineer, Flight Dynamics Department, Textron Defense Systems*

INTRODUCTION

The Scout Launch Vehicle placed the two satellites into a low earth orbit inclined at 37° to the equator. Approximately one minute after orbit insertion, the Scout-4th-Stage/Satellite-System was despun to about 90 deg/s and the two satellites were separated sequentially. The separation event imparted lateral rates to the vehicles which modified their angular momentums and coning angles. The coning angles just after the separation event were predicted to be approximately 10° and 50° for the respective satellites. Each satellite contained a reservoir of hydrazine fuel amounting to 15% of the total mass. It was expected that energy dissipation from the sloshing fuel would cause the satellites to quickly attain a 90° coning angle, i.e. a flat spin about the maximum inertia axis. The satellites are essentially axisymmetric with the minimum inertia axis being the axis of symmetry (see Fig. 1). The maximum inertia axis should be located very close to the $\vec{Y}_G - \vec{Z}_G$ plane.

PROBLEM STATEMENT

The problem is to derive each satellite's motion characteristics which are needed to validate and interpret satellite system and mission performance.

ATTITUDE RELATED DATA

Three-axis magnetometer data are telemetered real time, during contacts, at the rate of 8 samples/second. Fig. 2 illustrates the magnetometer data histories (MAGX, MAGY and MAGZ along the X, Y and Z axes) for a 7 minute contact with vehicle 2 on revolution (Rev) 20.4, approximately 1.3 days after launch. The dropouts and wild points have not been removed from the illustrated data. The equal periodicity on each axis, and the small amplitude in the MAGZ data, indicate that the satellite is indeed in a flat spin about an axis very near the Z-axis of the satellite. Both vehicles achieved a flat spin prior to the first telemetry contact which occurred approximately one hour after launch.

The telemetry data is a) processed real time for CRT display and associated hardcopy output, and b) stored on an analog tape for optional post-pass processing. Both processing methods convert the raw magnetometer data to engineering units using calibration curves derived on the ground prior to launch. The quantization interval, in engineering units, is $0.472\,\mu$T. Real-time hardcopy output of the magnetometer data at a rate of 1 sample/second is routinely available. Since post-pass analog tape processing is expensive, a ground-rule was established that the analysis process be compatible with use of the real-time hardcopy output.

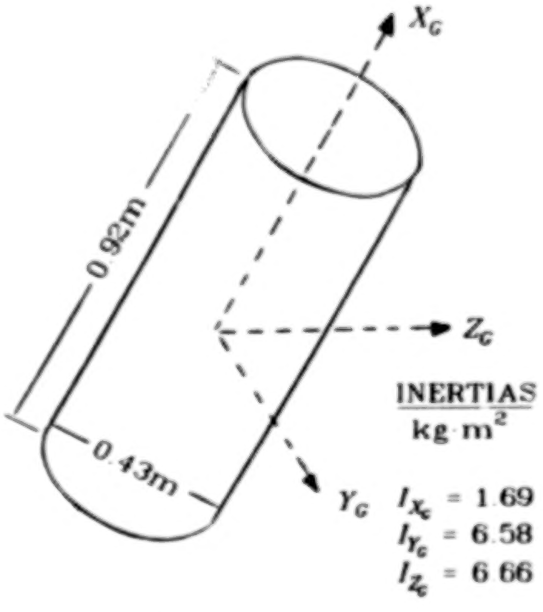
X_G
Z_G
Y_G
0.92m
0.43m
INERTIAS
kg·m²
$I_{X_G} = 1.69$
$I_{Y_G} = 6.58$
$I_{Z_G} = 6.66$

Fig. 1 Satellite Configuration

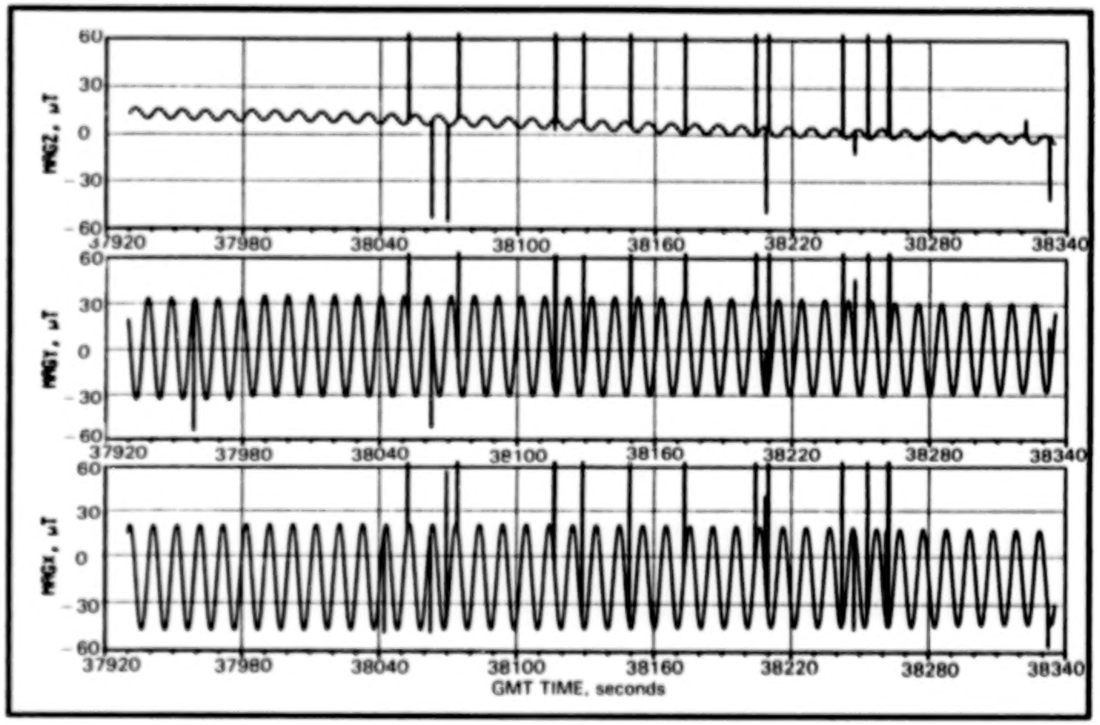

Fig. 2 Magnetometer Histories for Rev 20.4, Vehicle 2

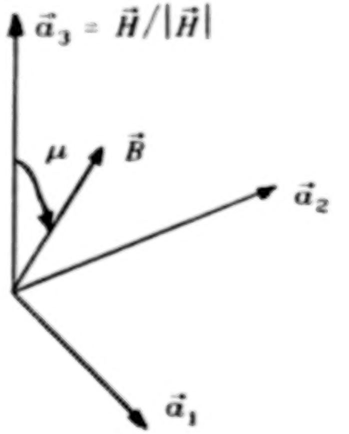
$\vec{a}_3 = \vec{H}/|\vec{H}|$
μ
$\vec{B}$
$\vec{a}_2$
$\vec{a}_1$

Fig. 3 Instantaneous Coordinate System

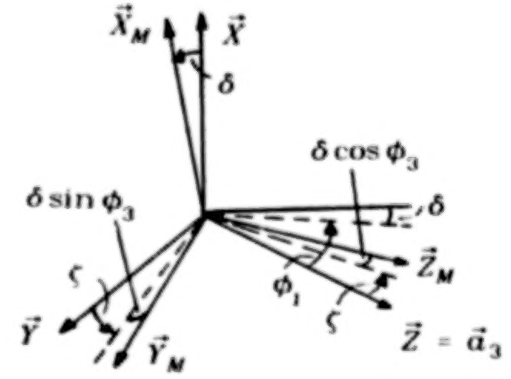
$\vec{X}_M$
$\vec{X}$
δ
$\delta \cos \phi_3$
$\delta \sin \phi_3$
δ
ζ
ϕ_1
ζ
$\vec{Z}_M$
$\vec{Y}$
$\vec{Y}_M$
$\vec{Z} = \vec{a}_3$

Fig. 4 Relationship Between Principal and Magnetometer Coordinates

ORIGINAL PAGE IS
OF POOR QUALITY

ANGULAR MOMENTUM, SINGLE CONTACT

External torques acting on the orbiting satellites are small. Thus, during a short contact, the angular momentum $\vec{H}$ (referenced to an inertial Newtonian frame) may be assumed to be constant. At a given time t, let $\vec{B}(t)$ be the magnetic induction vector, and establish a coordinate system $\vec{a}_1(t), \vec{a}_2(t)$, and $\vec{a}_3$ of mutually perpendicular unit vectors satisfying:

$\vec{a}_3$ is parallel to $\vec{H}$,
$\vec{a}_2(t)$ is parallel to $\vec{a}_3 \times \vec{B}(t)$, and
$\vec{a}_1(t) = \vec{a}_2(t) \times \vec{a}_3$.

The geometry at a given instant in time is illustrated in Fig. 3. Let $\mathcal{P} = (\vec{X}\ \vec{Y}\ \vec{Z})$ be the principal axes coordinate system of the vehicle with $\vec{Z}$ the maximum inertia axis and $\vec{X}$ the minimum inertia axis. For flat spin motion, $\vec{Z}$ is parallel to $\vec{H}$, i.e. $\vec{Z} = \vec{a}_3$. The relationship between the vehicle magnetometer coordinate system $\mathcal{M} = \left(\vec{X}_M\ \vec{Y}_M\ \vec{Z}_M\right)$ and $\mathcal{P}$ is illustrated in Fig. 4. The magnetometer axes are designed to be mutually orthogonal and oriented along the vehicle geometric, $\mathcal{G}$, frame. The magnetometer data gives no information on the $\mathcal{G}$ frame. We thus work with the $\mathcal{M}$ frame and assume it is an orthogonal system.

The vehicle motion in principal axes is described by:

$$\begin{aligned}
\vec{X}(t) &= \vec{a}_1(T_o)\cos(\Omega_p t + \psi_o) + \vec{a}_2(T_o)\sin(\Omega_p t + \psi_0) \\
\vec{Y}(t) &= -\vec{a}_1(T_o)\sin(\Omega_p t + \psi_0) + \vec{a}_2(T_o)\cos(\Omega_p t + \psi_0) \qquad (1) \\
\vec{Z}(t) &= \vec{a}_3
\end{aligned}$$

where

Ω_p	is the precession rate,
ψ_o	is the initial precession angle,
T_o	is the initial time,
T	is the current time, and
t	$= T - T_o$.

In the $\mathcal{M}$ frame, making the small angle approximation for δ and setting $\cos\delta$ to 1:

$$\begin{aligned}
\vec{X}_M(t) &= \vec{X}(t) + \delta\sin\phi_1\,\vec{Y}(t) - \delta\cos\phi_1\,\vec{Z}(t) \\
\vec{Y}_M(t) &= \delta\sin\phi_3\,\vec{X}(t) + \cos\zeta\,\vec{Y}(t) + \sin\zeta\,\vec{Z}(t) \qquad (2) \\
\vec{Z}_M(t) &= \delta\cos\phi_3\,\vec{X}(t) - \sin\zeta\,\vec{Y}(t) + \cos\zeta\,\vec{Z}(t)
\end{aligned}$$

where

ϕ_1, δ and ϕ_3 are the Euler angle rotations about the X, Y and X axes, respectively, and
$\zeta = \phi_1 + \phi_3$. (See Fig. 4.)

The vehicle's spin period is short relative to its translational motion. Thus we assume that $\vec{B}$, and therefore $\vec{a}_1$ and $\vec{a}_2$, are constant over one spin cycle. Then the magnetometer history over one cycle satisfies:

$$\begin{aligned}
\vec{X}_M \cdot \vec{B} &= |\vec{B}|\,[-\,\delta\cos\mu\cos\phi_1 - \delta\sin\mu\sin\phi_1\sin(\Omega_p t + \psi_o) + \sin\mu\cos(\Omega_p t + \psi_o)] \\
\vec{Y}_M \cdot \vec{B} &= |\vec{B}|\,[\cos\mu\sin\zeta - \sin\mu\cos\zeta\sin(\Omega_p t + \psi_o) + \delta\sin\mu\sin\phi_3\cos(\Omega_p t + \psi_o)] \qquad (3) \\
\vec{Z}_M \cdot \vec{B} &= |\vec{B}|\,[\cos\mu\cos\zeta + \sin\mu\sin\zeta\sin(\Omega_p t + \psi_o) + \delta\sin\mu\cos\phi_3\cos(\Omega_p t + \psi_o)]
\end{aligned}$$

The extrema, $\vec{E}^{\pm}$, in (3) are:

$$E^{\pm}_{X_M} = |\vec{B}|\,[\pm\sin\mu - \delta\cos\mu\cos\phi_1] \qquad (4a)$$

$$E^{\pm}_{Y_M} = |\vec{B}|\,[\pm\sin\mu\cos\zeta + \cos\mu\sin\zeta] \qquad (4b)$$

$$E^{\pm}_{Z_M} = |\vec{B}|\,[\pm\sin\mu\sin\zeta + \cos\mu\cos\zeta] \qquad (4c)$$

The extrema, $\tilde{E}^{\pm}$, in the observed values, assuming no scaling errors, are:

$$\tilde{E}^{\pm} = \vec{E}^{\pm} + \vec{D} \qquad (5)$$

where

$\vec{D} = \begin{pmatrix} D_{X_M} \\ D_{Y_M} \\ D_{Z_M} \end{pmatrix}$ are the biases along the magnetometer axes.

The derivatives of (3) are:

$$\begin{aligned}
\frac{d\,\vec{X}_M \cdot \vec{B}}{dt} &= -\,\Omega_p\,|\vec{B}|\sin\mu\,[\,\delta\sin\phi_1\cos(\Omega_p t + \psi_o) + \sin(\Omega_p t + \psi_o)\,] \\
\frac{d\,\vec{Y}_M \cdot \vec{B}}{dt} &= -\,\Omega_p\,|\vec{B}|\sin\mu\,[\,\cos\zeta\cos(\Omega_p t + \psi_o) + \delta\sin\phi_3\sin(\Omega_p t + \psi_o)\,] \qquad (6) \\
\frac{d\,\vec{Z}_M \cdot \vec{B}}{dt} &= \Omega_p\,|\vec{B}|\sin\mu\,[\,\sin\zeta\cos(\Omega_p t + \psi_o) - \delta\cos\phi_3\sin(\Omega_p t + \psi_o)\,]
\end{aligned}$$

The occurrences of the extrema are summarized below:

$$\vec{X}_M \cdot \vec{B} : \tan(\Omega_p t + \psi_o) = -\,\delta\sin\phi_1 \qquad (7a)$$

$$\vec{Y}_M \cdot \vec{B} : \tan(\Omega_p t + \psi_o) = -\,\cos\zeta / \delta\sin\phi_3 \qquad (7b)$$

$$\vec{Z}_M \cdot \vec{B} : \tan(\Omega_p t + \psi_o) = \sin\zeta / \delta\cos\phi_3 \qquad (7c)$$

Equation 7c is particularly useful in determining δ when ζ and ϕ_3 are small. In this case $\zeta \approx \phi_1$. Note that Equation 7a is ≈ 0.

Procedure

1) Obtain μ from the amplitude in $\vec{X}_M \cdot \vec{B}$ (Equation 4a).
2) Obtain ς from either $\vec{Y}_M \cdot \vec{B}$ or $\vec{Z}_M \cdot \vec{B}$, whichever has the smaller amplitude (Equation 4b or 4c).
3) Equations 7b and 7c yield approximations to δ and ϕ_3 from inexact values of t determined from the magnetometer data.
4) Determine $\vec{E}^{\pm}$ from Equation 4.
5) Determine $\vec{D}$ from Equation 5.

If $\sin\mu \approx 1$, then an accurate value of μ or $\vec{D}$ cannot be obtained. The best procedure here is to assume $\sin\mu = 1$, perform steps 2) and 3), and use an average value of $\vec{D}$ from other contacts to solve for $\cos\mu$ from either of Equations 4b or 4c. With the exception of this case, the magnetometer biases need not be a priori known to solve for μ and ς.

Determination of Quadrant

The following rules resolve the quadrants of ς and μ:

$$\begin{aligned}
\operatorname{sgn}(\sin\varsigma) &= \operatorname{sgn}\left(\frac{d\,\vec{X}_M \cdot \vec{B}}{dt}\right) \text{ at } t \text{ maximizing } \vec{Y}_M \cdot \vec{B}. \\
\operatorname{sgn}(\cos\varsigma) &= \operatorname{sgn}\left(\frac{d\,\vec{X}_M \cdot \vec{B}}{dt}\right) \text{ at } t \text{ maximizing } \vec{Z}_M \cdot \vec{B}. \\
\operatorname{sgn}(\cos\mu) &= \operatorname{sgn}\left(\overline{\vec{Z}_M \cdot \vec{B}}\right)\operatorname{sgn}(\sin\varsigma).
\end{aligned} \tag{8}$$

Effect of $\vec{B}$ Variation with Time

In practice, fixing $\vec{B}$ has little effect on the solutions for μ, ς and δ. The variation in $\vec{B}(t)$ is important in the determination of Ω_p:

$$\Omega_p = \tilde{\Omega}_p + \frac{d\,\vec{a}_2(t)}{dt} \tag{9}$$

Specifically, the observed precession rate, $\tilde{\Omega}_p$, can be quite different from Ω_p if $\vec{H} \cdot \vec{B}$ is small. Further, the values of $\vec{a}_2(t)$ for the two solutions of $\vec{H}$ are opposite in sign.

Example 1: $\sin\mu$ is Small

Table 1 gives results for the contact on Rev 164 with vehicle 2. The telemetered magnetometer histories are illustrated in Fig. 5. The $\vec{B}$ values were obtained from an orbit simulation code using a 12 degree spherical harmonic expansion for the geomagnetic potential. The algorithms are used to compute ζ, μ, $(\vec{E}^{+} + \vec{E}^{-})/2$, $\vec{D}$ and δ. Independent estimates, $\hat{D}$, for the biases, for comparison purposes, were obtained by an estimation scheme which minimizes, in a least squares sense, the difference between the magnitudes of the bias-adjusted measured vector and the modelled magnetic induction vector. The value of the biases vary with the operating configuration of the satellite which is slightly different for each of the three times. The accuracy in δ is poor because of the small variation in $\vec{Z}_M \cdot \vec{B}$ and the large quantization interval. The offset in the extrema of $\vec{Z}_M \cdot \vec{B}$ from $\vec{X}_M \cdot \vec{B}$ and $\vec{Y}_M \cdot \vec{B}$ is illustrated in Fig. 6 for Rev 20.4 which gives a larger variation in $\vec{Z}_M \cdot \vec{B}$. The satellite rotates about 64° between the occurrences of the $\vec{X}_M \cdot \vec{B}$ and $\vec{Z}_M \cdot \vec{B}$ maxima. This angle was used in Equation 7c to solve for δ assuming ϕ_3 is 0. Analysis of several contacts indicated that the values for ζ and δ were close to 5° and 2°, respectively. When used in Equations 4 and 5, these yield a value of $\vec{D}$ which agrees very closely with $\hat{D}$.

Example 2: $\sin\mu \approx 1$

It is difficult to determine μ accurately when $\sin\mu \approx 1$. Table 2, pertaining to the contact on Rev 20.4 of vehicle 2, illustrates the procedure described above. (Refer to Fig. 2 for the magnetometer histories.) First obtain estimates, $\hat{\mu}$ and $\hat{D}$, of μ and D. Equation 4a is used to determine $\hat{\mu}$. In general, $\hat{D}$ is an average over several selected contacts. (The value of $\hat{D}$ used in Table 2 was obtained using the aforementioned bias estimation code since the analog tape for that contact was processed post-pass.) Then $\vec{E}^{\pm}$ is determined from Equation 5 and μ is computed more accurately from (4c) in the form:

$$\cos\mu = \frac{\vec{E}^{+} + \vec{E}^{-}}{2\,|\vec{B}|\cos\zeta}$$

where ζ is obtained by the usual procedure, but using $\hat{\mu}$. The other components of $\vec{D}$ now agree fairly well with those of $\hat{D}$.

TABLE 1 COMPUTATIONS FOR REV 164.2, VEHICLE 2

	T = 82849s, GMT			T = 83029s, GMT			T = 83179s, GMT		
	X	Y	Z	X	Y	Z	X	Y	Z
$\tilde{\vec{E}}^{+}$	-5.2	10.6	38.2	-10.3	7.4	43.0	-6.6	11.3	45.3
$\tilde{\vec{E}}^{-}$	-22.8	-7.0	36.3	-17.0	0.7	42.3	-20.6	-2.6	44.0
$\lvert\vec{B}\rvert$		27.62			30.39			32.92	
ζ		6.2			6.0			5.3	
δ		3.0			2.9			2.6	
μ		18.6			6.3			12.3	
$\overline{\vec{E}^{\pm}}$	-1.36	2.82	26.02	-1.52	3.16	30.04	-1.46	2.97	32.03
$\vec{D}$	-12.64	-1.02	11.23	-12.13	0.89	12.61	-12.15	1.38	12.62
$\hat{D}$	-13.17	0.15	11.30	-12.62	1.61	12.55	-12.62	1.61	12.55

TABLE 2 COMPUTATIONS FOR REV 20.4, VEHICLE 2

	T = 37941s, GMT			T = 38147s, GMT			T = 38327s, GMT		
	X	Y	Z	X	Y	Z	X	Y	Z
$\tilde{\vec{E}}^{+}$	20.4	33.7	16.1	20.3	34.6	8.5	17.0	30.7	0.8
$\tilde{\vec{E}}^{-}$	-47.4	-33.3	9.8	-45.7	-30.8	2.3	-42.7	-28.4	-4.8
$\lvert\vec{B}\rvert$		34.09			33.92			33.32	
$\hat{D}$	-13.53	0.17	12.48	-13.08	2.64	13.47	-13.20	2.32	13.05
$\hat{\mu}$		90.			103.4			116.4	
$\overline{\vec{E}^{\pm}}$	0.03	0.03	0.47	0.38	-0.74	-8.07	0.45	-1.17	-15.05
ζ		5.3			5.4			5.3	
δ		2.6			2.6			2.6	
μ		89.2			103.8			117.0	
$\vec{D}$	-13.47	0.15	12.48	-13.09	2.66	13.47	-13.43	2.55	-15.05

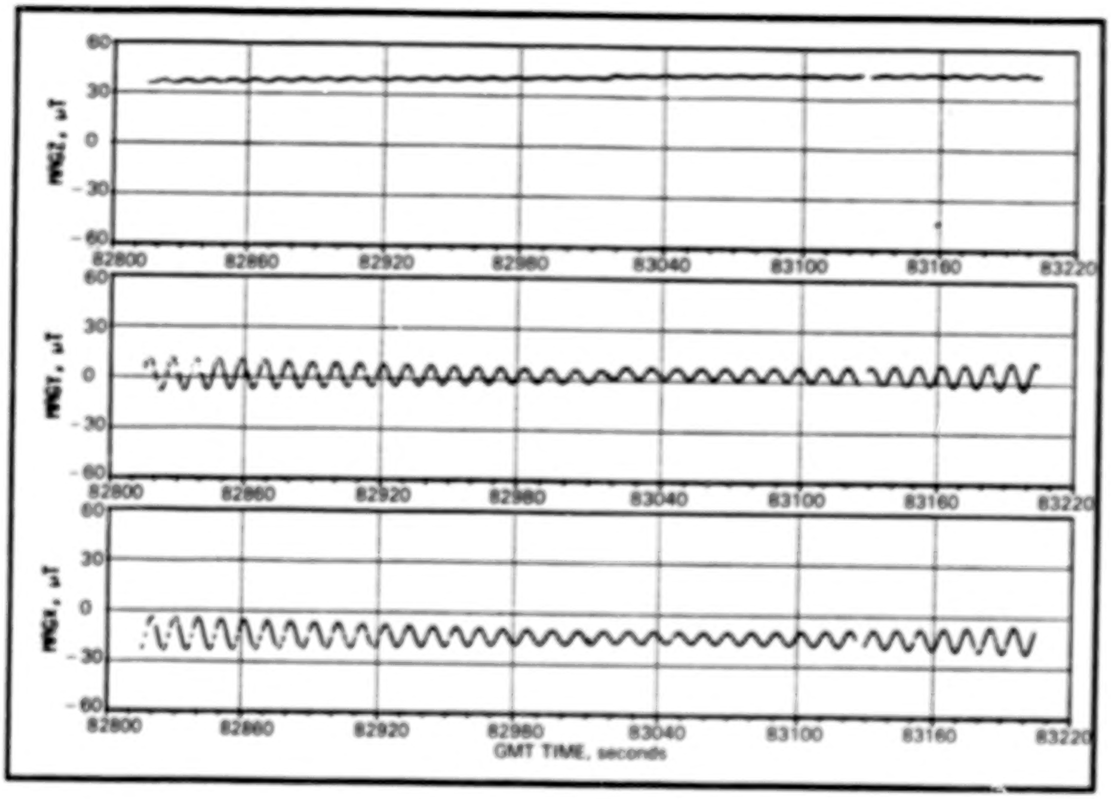

Fig. 5 Magnetometer Histories for Rev 164.2, Vehicle 2

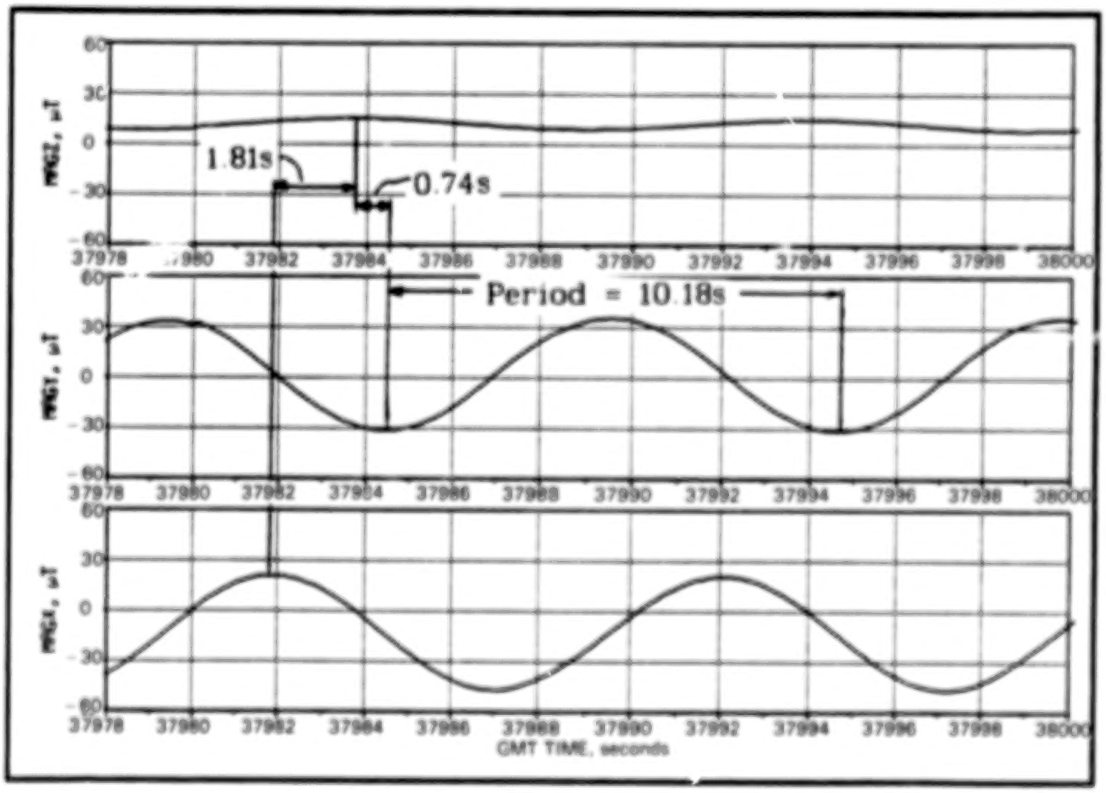

Fig. 6 Magnetometer Cycle Offset for Rev 20.4, Vehicle 2

Ambiguity in $\vec{H}$

The procedure described above resolves $\vec{H}$ to lie on a cone of angle μ about $\vec{B}$. As the geometry, specifically $\vec{B}$, varies with time due to satellite orbital motion, $\vec{H}$ can be resolved to two points: the intersection of two cones. Over a short contact, the magnetic induction vectors are essentially co-planar. The two possible $\vec{H}$ vectors are the true $\vec{H}$ and its mirror image relative to the '$\vec{B}(t)$ plane'. The key point is that $\vec{H}$ cannot be uniquely determined over a short contact. This can be observed very readily in Fig. 7 which illustrates the loci of possible $\vec{H}$ (minor circles of radius μ_i about point Bi which is the intersection of $\vec{B}_i$ with the unit sphere) in right ascension and declination at the three times in Table 1. (A Kalman filter estimation technique designed specifically for this problem could not, in general, decide which of the two possibilities was the correct $\vec{H}$ orientation.)

The geometry of the two possible $\vec{H}$ solutions will vary with the orientation of the actual $\vec{H}$ with respect to the $\vec{B}$ vectors during the contact. For Rev 21.4, vehicle 1 (Fig. 8), $\vec{H}$ is quite far from the 'plane' of the $\vec{B}(t)$ vectors so that the two $\vec{H}$ possibilities are widely separated. This contact is sufficiently long - 7 minutes - for $\vec{B}(t)$ to be non-planar which allows the correct $\vec{H}$ to be resolved. On Rev 20.1, vehicle 2 (Fig. 9), $\vec{H}$ is many degrees from $\vec{B}$ but is close to the $\vec{B}(t)$ plane so that, with the uncertainties associated with μ, the possible $\vec{H}$ values lie along an arc of $\approx 30^\circ$ encompassing declinations from -20° to -45^0. Rev 1.1 for vehicle 1 (see Fig. 10) has similar geometry.

Since the satellite contacts are short, on the order of 3 to 5 minutes, and may be separated by about 30 days, other methods must be employed to resolve the ambiguity in the angular momentum orientation. The next section discusses how this issue is resolved.

ANGULAR MOMENTUM RESOLUTION

Resolution of the correct angular momentum orientation between the two possibilities requires a) an initial orientation for $\vec{H}$, and b) a torque model from which a long-term history of $\vec{H}$ can be derived.

Initial Orientation of $\vec{H}$

There were frequent contacts with the satellites during the first few days in orbit. Fig. 10 illustrates a resolved orientation for the $\vec{H}$ of vehicle 1 at the intersection of the loci for contacts on Revs 1 and 2. This solution is essentially

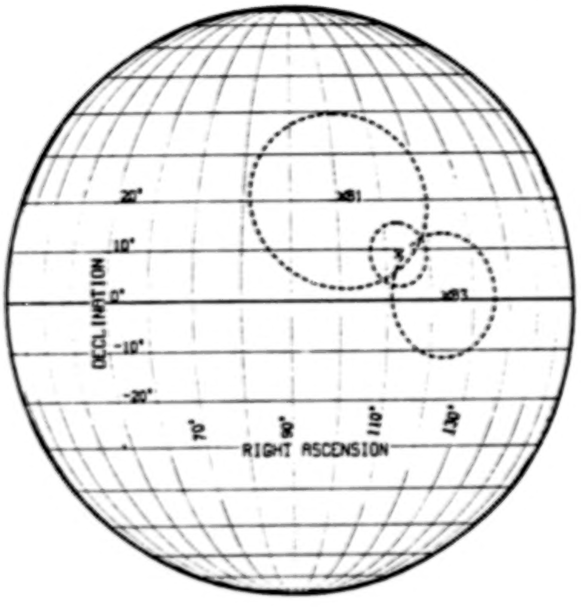

Fig. 7 Potential $\vec{H}$ Orientations:
Rev 164.2, Vehicle 2

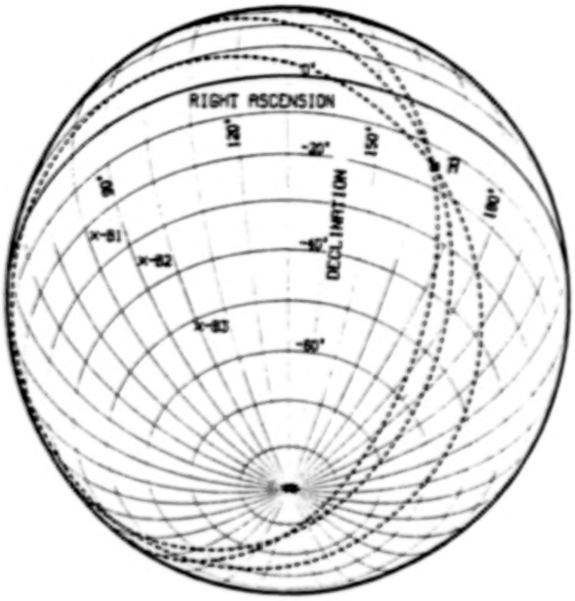

Fig. 8 Resolved $\vec{H}$ Orientation:
Rev 21.4, Vehicle 1

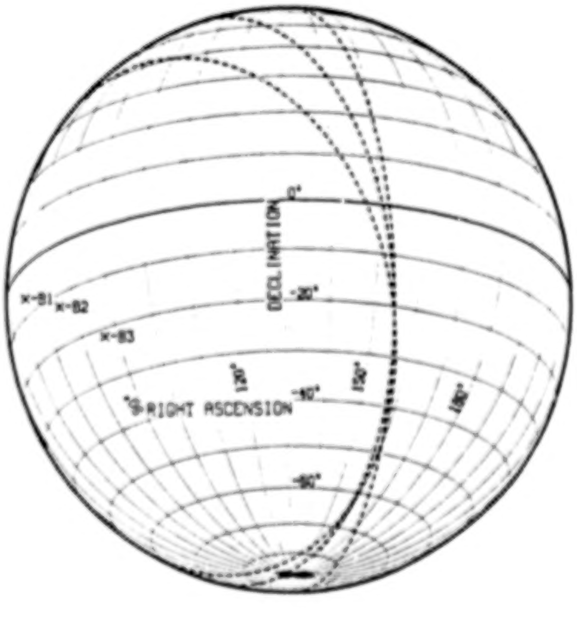

Fig. 9 Potential $\vec{H}$ Orientations:
Rev 20.4, Vehicle 2

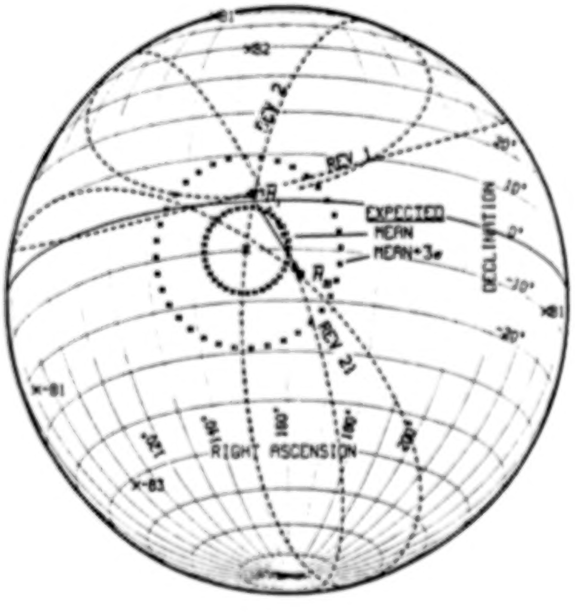

Fig. 10 Resolved $\vec{H}$ Orientations:
Days 1-2, Vehicle 1

on the mean of the expected loci determined by a statistical analysis, conducted pre-launch, of the separation of the satellites from the 4th Stage of the launch vehicle. Fig. 10 illustrates a likely $\vec{H}$ path from this solution to the $\vec{H}$ solution on Rev 21. This corresponds to a precession in $\vec{H}$ of $\approx 15^\circ/\text{day}$.

The initial orientation of $\vec{H}$ for vehicle 2 was established at a right ascension of 162° and a declination of -30°

Torque Model

Torques acting on the orbiting satellites originate from magnetic, gravity gradient, aerodynamic, and solar radiation pressure effects. The approach taken was to obtain expressions, available in the published literature, for the effect, on $\vec{H}$, of each significant torque over one satellite revolution. These expressions, along with a dipole model of the earth's magnetic field[5] were incorporated into a semi-anlytic orbit generation code using a 1-rev step-size. The torque expressions are described briefly below. Because of the small size of the satellites, solar radiation pressure was judged to be a relatively insignificant contributor and was not included in the model.

Magnetic Torques: - Magnetic torques result from the interaction between the magnetic properties of a spacecraft and the ambient magnetic field of the earth. The primary magnetic disturbance torques are:

1. Dipole moment from the permanent magnetism in the spacecraft;
2. Eddy currents induced when a conducting body moves in a magnetic field;
3. Spacecraft generated current loops; and
4. Hysteresis damping.

Because of the limited amount of spacecraft operating time and the specific amount and properties of permeable material present on the spacecraft, items 3. and 4. were judged to have small contributions to total vehicle torque and were not included in the model.

The torque, $\vec{T}_D$, due to the dipole moment is normal to $\vec{a}_3 = \vec{H}/|\vec{H}|$, and hence has only a precession component. It satisfies[2,3,5]:

$$\vec{T}_D = m_d \vec{a}_3 \times \vec{B} \tag{10}$$

where

m_d is the satellite's dipole moment along its Z-axis.

Making the assumption that the satellite Z-axis is inertially fixed for an orbital period, the average torque over one orbit rev satisfies:

$$\left(\vec{T}_D\right)_{av} = m_d \vec{a}_3 \times (\vec{B})_{av} \tag{11}$$

$(\vec{B})_{av}$ can be integrated with respect to time over an orbital period[2] to give an average induction vector.

The total torque due to eddy current effects satisfies[5]:

$$\vec{T}_E = k_e\left(\vec{\omega}_Z \times \vec{B}\right) \times \vec{B} \tag{12}$$

where

k_e is a constant which depends on the geometry and conductivity of the rotating object, and

$\vec{\omega}_Z$ is the angular velocity vector of the satellite.

Equation (12) can be separated into despin, T_{EZ}, and precession, $T_{E\perp}$, components of torque:

$$T_{EZ} = -k_e(B_\perp)^2\omega_Z \tag{13}$$

$$T_{E\perp} = k_e B_Z B_\perp \omega_Z \tag{14}$$

where

$B_\perp$ is the component of $\vec{B}$ orthogonal to $\vec{Z}$,

B_Z is the component of $\vec{B}$ parallel to $\vec{Z}$, and

ω_Z is the angular velocity.

These equations are conceptually simple. The complication arises in finding the average values for $(B_\perp)^2$ and $B_Z B_\perp$ over one revolution of the satellite. Reference 3 derived equations for $B_\perp$ and B_Z and then integrated the resulting products. It is easier to a) resolve $\left(\vec{\omega}_Z \times \vec{B}\right) \times \vec{B}$ into its three components, b) integrate, and then c) compute the despin and orthogonal components, $(T_{EZ})_{av}$ and $(T_{E\perp})_{av}$, of torque. Since the orbit eccentricity is small, terms of $o(e^3)$ and $o(e^4)$ can be deleted.

Gravity Gradient Torque - The average torque over one orbit due to the effect of the earth's gravitation on the satellite is[1,2,3,4]:

$$\left(\vec{T}_G\right)_{av} = 1.5\frac{\mu_E}{a^3(1-e^2)^{1.5}}\left(I_Z - \frac{I_X + I_Y}{2}\right)\left(\vec{a}_3 \cdot \vec{N}\right)\left(\vec{a}_3 \times \vec{N}\right) \tag{15}$$

where

μ_E is the earth's gravitational constant,

a is the semi-major axis of the orbit,

e is the eccentricity of the orbit, and

$\vec{N}$ is the unit normal to the orbit plane.

Aerodynamic Torque: - The average aerodynamic torque over one satellite spin cycle satisfies:

$$\vec{T}_A = \frac{1}{2}\rho v^2 S C_D d\left(\vec{I}_v \times \vec{a}_3\right) \tag{16}$$

where

ρ is the density of the atmosphere,
v is the velocity of the satellite,
S is the projected area in the direction of motion averaged over one satellite rotation,
C_D is the drag coefficient,
d is the distance from the center of mass of the satellite to its aerodynamic center of pressure along $\vec{Z}$ averaged over one satellite rotation, and
$\vec{I}_v$ is the unit velocity vector of the satellite.

The average torque over one orbit was determined using a relatively common procedure[3] for somewhat elliptical orbits.

Spin-axis Rate Change in One Orbit Revolution: - Assuming that the vehicle is in a pure spin motion about the body Z-axis, i.e. the principal inertia axis, the change in the spin rate in one orbit revolution caused by the eddy current torque is:

$$\Delta\omega_Z = -\left|(T_{EZ})_{\text{av}}\right|\omega_Z P / I_Z \tag{17}$$

where

I_Z is the moment of inertia about the body Z-axis, and
P is the satellite orbital period.

Spin-axis Precession in One Orbit Revolution: - Over one orbit rev, the angular momentum vector, $\vec{H}$, precesses by the angle $\left|\vec{T}_{\text{av}}\right| / \omega_Z I_Z$ from $\vec{H}$ towards $\vec{T}_{\text{av}}$ where $\vec{T}_{\text{av}}$ is the sum of the individual torque contributors normal to $\vec{H}$.

RESULTS

With the incorporation of the torque model into the orbit generation code, the determination of approximate values for the key torque-related vehicle-unique properties proceeded rapidly using an iterative simulation process. The inertia properties given in Fig. 1 and an aerodynamic lever arm, d, of 0.75 cm, equal to the pre-flight measured c.g.-offset along the Z_G-axis, were used initially for both vehicles. Though they were varied to determine sensitivities, these values were used in the final simulation. The derived magnetic properties are summarized in Table 3.

TABLE 3 DERIVED MAGNETIC PROPERTIES

VEHICLE	DIPOLE MOMENT, m_d A - m^2	k_e m^4/ohm
1	+0.543	465
2	-0.230	465

The dipole moment values are within expectations since satellite magnetic properties were minimally controlled during the design process. The k_e constant should be the same for both vehicles. The derived value is reasonably close to the 600 m^4/ohm value computed pre-flight. The histories of the orientation of $\vec{H}$ over the first six months in orbit are illustrated in Figures 11 and 12 for vehicles 1 and 2 respectively. Over this period, the maximum differences between the simulated and calculated $\vec{H}$ orientations were one day ($\approx$15 revs) in-track (parallel to the trace of $\vec{H}$), and $\approx 10^\circ$ cross-track (normal to the trace of $\vec{H}$). Generally the agreement was much better. Fig. 13 illustrates, for Rev 3056 of vehicle 2, typical agreement between the simulation and computations for the orientation of $\vec{H}$.

The simulated spin rate histories are summarized in Figures 14 and 15. They match the 'observed' data very well except for the first few days where the differences are attributed to residual angular momentum in the hydrazine fuel. There appears to be no significant hysteresis in the material magnetization cycle. This would be manifested as a constant component to the primarily exponential spin decay rate.

Figures 16 and 17 illustrate the histories of the angles between $\vec{H}$ and $\vec{N}$. For vehicle 1, $\vec{H}$ is never more than 20° out of the orbit plane. Its projected area along the flight path, averaged over a spin cycle, is essentially constant. For contrast, the $\vec{H}$ for vehicle 2 is at times nearly normal to the orbit plane. Thus, its average projected area along the flight path is smaller than that for vehicle 1. This correlates with observed periods of $\approx$ 5% smaller effects of drag on vehicle 2.

Finally, Figures 18 and 19 illustrate the dynamic history of the sun aspect angle. This, along with the eclipse history, are necessary inputs to an assessment of the thermal performance of the vehicles. The long thermal time constant ($\approx$9 days) of the well insulated vehicles, combined with the rapid fluctuation in the sun aspect angle, led to a very uniform internal temperature history.

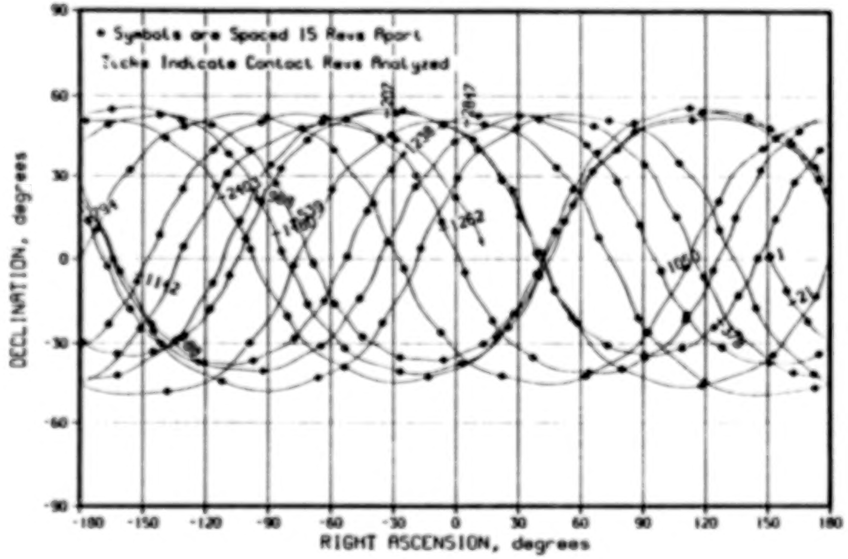

Fig. 11 Evolution of the Orientation of $\vec{H}$ for Vehicle 1

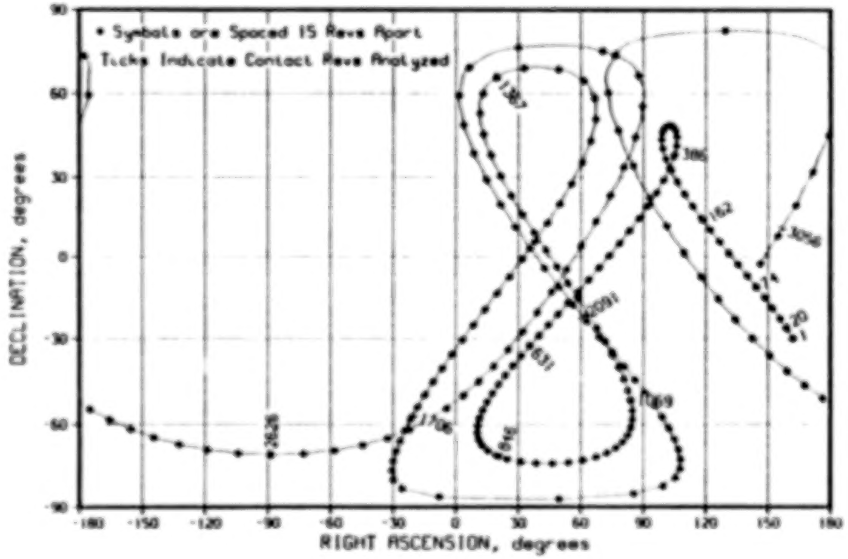

Fig. 12 Evolution of the Orientation of $\vec{H}$ for Vehicle 2

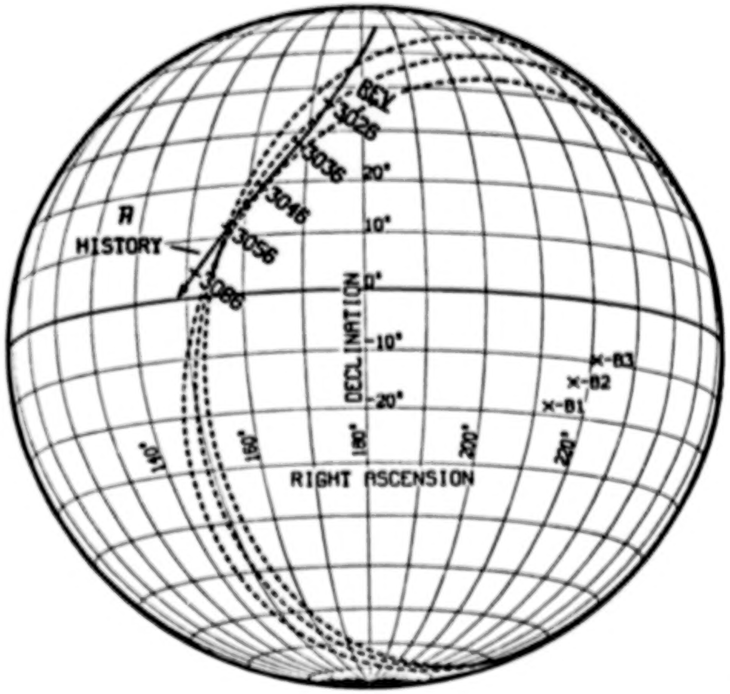

Fig. 13 Simulated vs. Resolved $\vec{H}$:

Rev 3056.2, Vehicle 2

R QUALITY

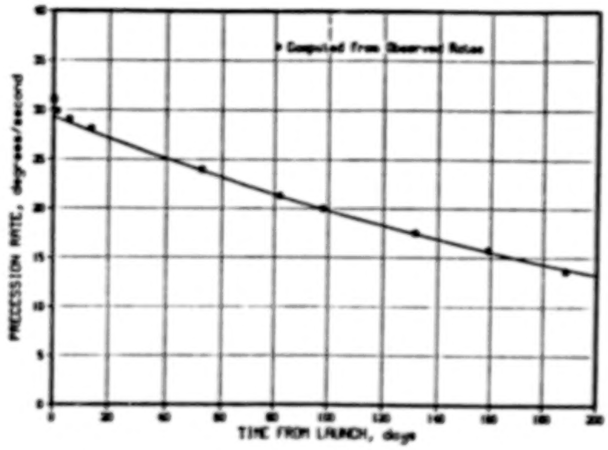

Fig. 14 Precession Rate History for Vehicle 1

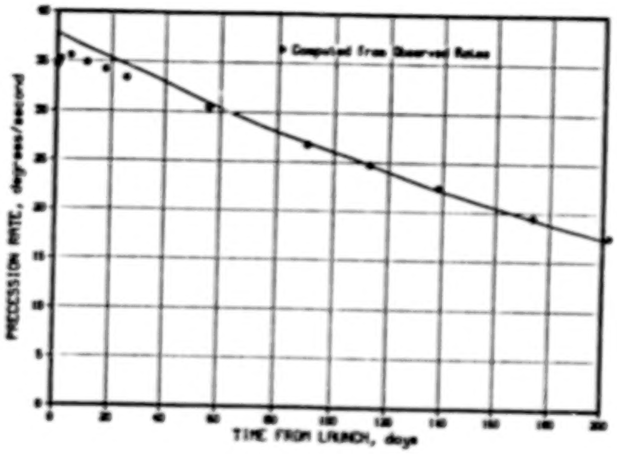

Fig. 15 Precession Rate History for Vehicle 2

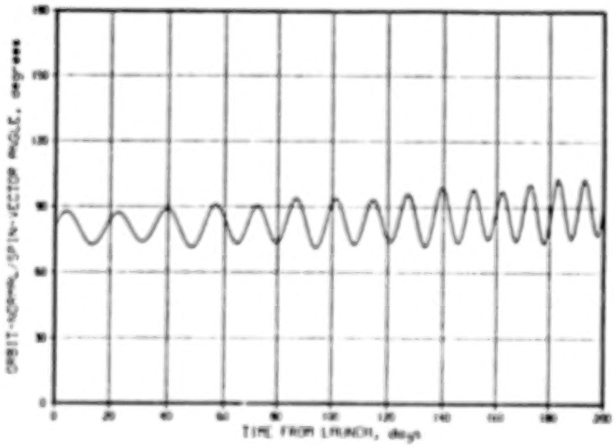

Fig. 16 Angle from $\vec{H}$ to Orbit Normal, Vehicle 1

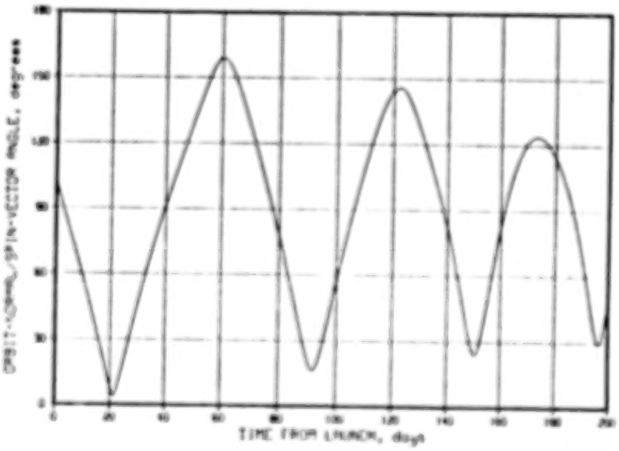

Fig. 17 Angle from $\vec{H}$ to Orbit Normal, Vehicle 2

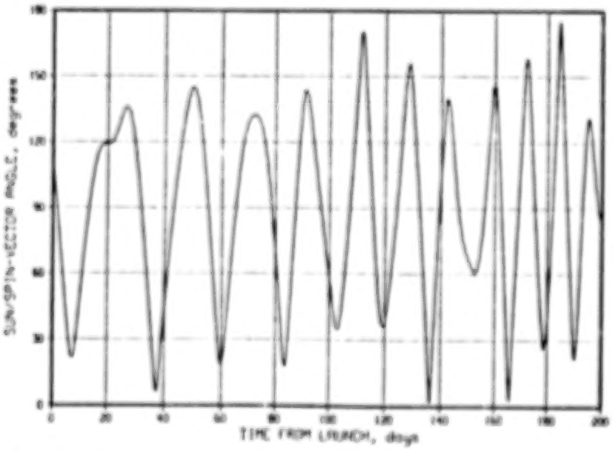

Fig. 18 Solar Aspect Angle to $\vec{H}$ for Vehicle 1

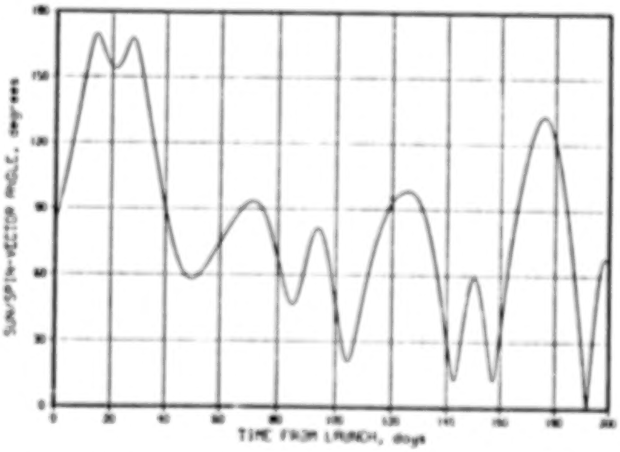

Fig. 19 Solar Aspect Angle to $\vec{H}$ for Vehicle 2

ORIGINAL PAGE IS
OF POOR QUALITY

ACKNOWLEDGEMENT

The author is indebted to Mr. Richard Heldt of Synetics Corp. (formerly of Textron Defense Systems) for generating, coding, and exercising the bias estimation and Kalman filter codes.

REFERENCES

1. Hughes; Peter C. *Spacecraft Attitude Dynamics*, John Wiley & Sons, New York, 1986

2. Patapoff, H. "Attitude Drift of a Spin-Stabilized Satellite due to the Earth's Magnetic and Gravitational Fields", *Proceedings*, *XIVth International Astronautical Congress*, Paris, 1963

3. Renard, Marc L. "Attitude Perturbations and Magnetic Control of a Spin-Stabilized Satellite", ESRO TR-1 (ESTEC), January,1966

4. Sample, E. C. "A Study of the Spin-Axis Precession Characteristics to be Expected of the S53/UK3 Satellite", RAE Technical Note No. Space 62, April, 1964

5. "Spacecraft Magnetic Torques", NASA SP-8018, March, 1969

N89-15955

GOES DYNAMIC PROPAGATION OF ATTITUDE

F. Landis Markley and Ed Seidewitz, Goddard Space Flight Center

Don Chu and John N. Rowe, Computer Sciences Corporation

ABSTRACT

The spacecraft in the next series of Geostationary Operational Environmental Satellites (GOES-Next) are Earth pointing and have 5-year mission lifetimes. Because gyros can be depended on only for a few years of continuous use, they will be turned off during routine operations. This means attitude must, at times, be determined without benefit of gyros and, often, using only Earth sensor data. To minimize the interruption caused by dumping angular momentum, these spacecraft have been designed to reduce the environmental torque acting on them and incorporate an adjustable solar trim tab for fine adjustment. A new support requirement for GOES-Next is that of setting the solar trim tab. Optimizing its setting requires an estimate of the unbalanced torque on the spacecraft. These two requirements, determining attitude without gyros and estimating the external torque, are addressed by replacing or supplementing the gyro propagation with a dynamic one, that is, one that integrates the rigid body equations of motion. By processing quarter-orbit or longer batches, this approach takes advantage of roll-yaw coupling to observe attitude completely without Sun sensor data. Telemetered momentum wheel speeds are used as observations of the unbalanced external torques. GOES-Next provides a unique opportunity to study dynamic attitude propagation. The geosynchronous altitude and adjustable trim tab minimize the external torque and its uncertainty, making long-term dynamic propagation feasible. This paper presents the equations for dynamic propagation, an analysis of the environmental torques, and an estimate of the accuracies obtainable with the proposed method.

1. INTRODUCTION

Accurate attitude determination typically requires a large amount of data taken at different times. This takes advantage of averaging to reduce the effects of sensor noise but requires a means of attitude propagation. Three-axis stabilized spacecraft usually carry gyros that measure how much the spacecraft rotates over short time intervals. For the next series of Geostationary Operational Environmental Satellites (GOES-Next), however, the gyros will be turned off when the spacecraft is on-station, making the usual method of attitude determination impossible.

GOES-Next has Earth and Sun sensors, and when both provide data, it is possible to compute a "single-frame" attitude solution. The Earth sensors provide pitch and roll data; the Sun sensors provide pitch and yaw data. However, the Sun is visible to the Sun sensors for only two-thirds of the day-long orbit, causing an 8-hour period each day when yaw cannot be observed directly. Having an alternative to gyro propagation would make it possible to compute the yaw when the Sun is visible and then predict it for later times when the Sun is out of view. The obvious candidate for this role is the dynamic equation for rigid body rotation, or Euler's equation.

Using Euler's equation to propagate for attitude estimation is not a new idea. In 1976, Lefferts and Markley (Reference 1) and Markley and Wood (Reference 2) applied dynamic propagation to Nimbus-6. The estimator included detailed torque and dynamic modeling and, in addition to solving for attitude and angular velocity, allowed the estimation of torque model parameters. It worked well with simulated data but was unable to duplicate real Nimbus-6 attitude histories. This difficulty seemed due to imperfectly known environmental torques, unmodeled control system activity, and uncertainty about the mass properties of the spacecraft.

Fein (Reference 3) concentrated on the idea of estimating environmental torques from wheel speeds and sensor data. He attributed short-term variations in the speed to the control system and long-term variations to the environmental torques. Based on the knowledge that the attitude remained close to nominal, he was able to model the torques with low-order polynomial functions. Sensor observations served to correct the propagated attitude. Although only time spans up to 22 minutes were considered, agreement with observed attitude histories was good.

Because GOES-Next is at the much higher geosynchronous altitude, environmental torques are expected to be much smaller and correspondingly less uncertain. This should make dynamic propagation more feasible for GOES-Next than for Nimbus-6. Prospects for GOES-Next are further encouraged by its large pitch momentum bias, which stabilizes the spacecraft yaw and roll by keeping the pitch axis aligned with the orbit normal (Reference 4).

This paper describes an attitude estimator that uses Euler's equation, adapts it to the GOES-Next mission, and estimates its accuracy for yaw determination.

2. GOES-NEXT ATTITUDE

The attitude of GOES-Next is defined relative to a rotating reference coordinate system with its z-axis pointing to the center of the Earth; y-axis in the direction of the negative orbit normal; and x-axis oriented so that x, y, and z form a right-handed orthogonal triad. The spacecraft attitude relative to the reference system is defined by a 3-1-2 Euler axis sequence with the three rotation angles referred to as yaw (y), roll (r), and pitch (p) (Reference 5).

The spacecraft roll, pitch, and yaw axes (x, y, and z, respectively) are close to the principal axes of the spacecraft moment-of-inertia tensor. The diagonal components of this tensor in the roll, pitch, yaw frame are $I_x = 3364.376$ kilogram-meters squared (kg-m^2), $I_y = 954.936$ kg-m^2, and $I_z = 3461.393$ kg-m^2, and all of the off-diagonal elements (the products of inertia) are less than 30 kg-m^2 in magnitude.

Estimated attitude uncertainty is due to sensor noise, sensor visibility, and propagation noise. The standard deviation of the sensor noise is a measure of the accuracy of the sensors. Visibility, in this case, involves only Sun visibility since the Earth is assumed to be in view at all times. Propagation noise includes errors in the models of environmental and control torques and unmodeled contributions to these torques.

2.1 SENSORS AND SUN VISIBILITY

GOES-Next has Earth sensors that measure pitch and roll and Sun sensors that measure pitch and yaw; these measurements are telemetered at 0.512-second intervals (Reference 6). Under normal conditions, the Earth sensors provide continuous measurements. The Sun sensors, however, do not cover the spacecraft z-axis and so do not see the Sun around local midnight.

There are two Earth sensors that scan east-west across the Earth disk and combine their measurements to give pitch and roll. Because of the high altitude, horizon height uncertainty contributes little to sensor error, and the standard deviation of these observations is given as 0.01 degree (1σ). The quantization is also 0.01 degree.

There are two types of Sun sensor. The digital Sun sensor (DSS) is the more accurate of the two, having standard deviation of 0.0042 degree (1σ) and quantization of 0.125 degree. There are also two coarse analog Sun sensor (CASS) systems. These are less accurate, having unspecified noise characteristics and quantization of 0.039 degree. The error for these sensors is on the order of 1 degree on the boresight and increases away from the boresight.

GOES-Next rotates once a day about its y-axis, which is roughly 67 degrees from the ecliptic plane. The percentage of each orbit having Sun coverage is approximately the fraction of the spacecraft x-z plane in the Sun sensor fields of view. As seen from Figure 1, this leaves about one-third of each day without coverage

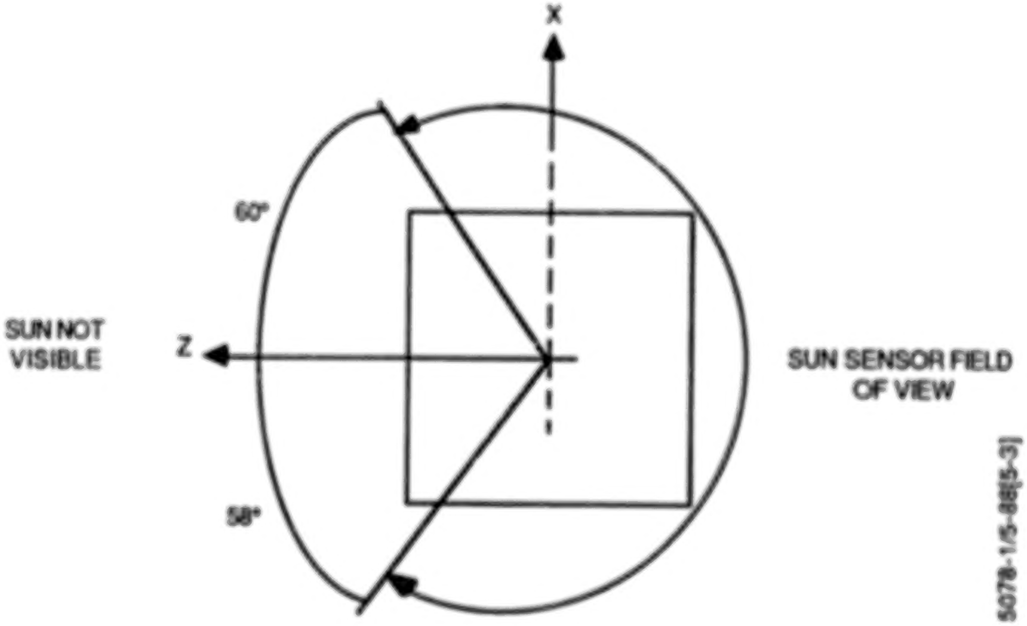

Figure 1. Sun Sensor Field of View

and without yaw observations. It is the more accurate DSS that sees the Sun just before the loss of coverage.

2.2 TORQUES

The torques acting on a spacecraft arise both naturally and from the control system. Natural disturbances include solar radiation, gravity gradient, residual magnetic dipole, and aerodynamic torques. For GOES-Next, which is at geosynchronous altitude, atmospheric torques are negligible. The torques caused by the control system include those due to the magnetic torquers, changing wheel speeds, and thruster activity. Because the thrusters are not expected to be used more than once a day, they are not modeled here.

Solar radiation causes the largest environmental torques on GOES-Next (Reference 7). There is a controllable flap at the end of the solar array that is commanded from the ground to minimize the solar torque. Proper setting of the trim tab can reduce the solar torque to 10^{-7} newton meters (N•m), but the residual torques may be as large as 10^{-5} N•m. The solar torque is approximately a constant scalar times the cross product of the vector from the center of pressure of the solar array to the center of pressure of the solar sail, which is closely aligned with the spacecraft pitch axis, and the Sun-to-spacecraft vector. Thus, the solar torque vector is nearly constant in inertial space and is mostly in the spacecraft roll/yaw plane. In the spacecraft body frame, the largest components of the solar torque are the roll and yaw components, which have sinusoidal time dependence with the orbit period (one sidereal day) with nearly equal magnitudes, and a 90-degree difference in phase. Figure 2 illustrates this dependence of the roll and yaw torques.

Gravity gradient torques depend only on the spacecraft attitude and moment-of-inertia tensor, so they are easily modeled. The largest errors in the gravity gradient torque model come from uncertainty about the inertia tensor for the spacecraft.

Magnetic torques come from residual and control magnetic dipoles (References 8 and 9). The residual dipoles are due to electric currents, magnetized material in the spacecraft, and commanded torquer biases. They are considered to be almost constant in the spacecraft body frame and to have magnitudes of about 8 ampere-meters squared (A-m^2). At geosynchronous altitude, this can produce a torque of at most

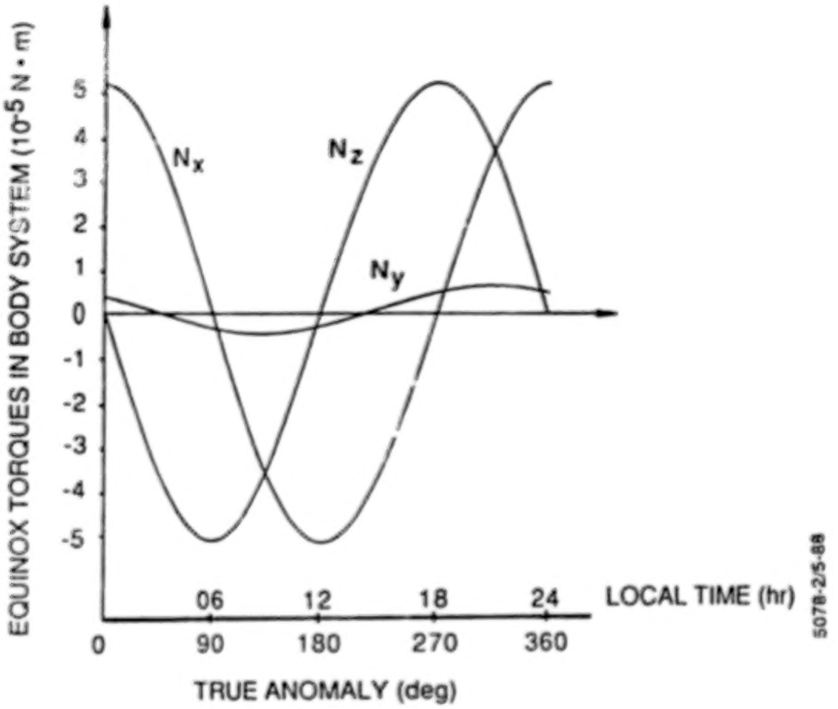

Figure 2. Solar Radiation Torques

10^{-7} N•m. Because of the equatorial orbit of GOES-Next, the Earth's magnetic field is mainly along its pitch axis. Therefore, the torque due to residual dipoles is approximately constant in the body frame. The control dipoles vary slowly over time, producing torques as large as 10^{-6} N•m.

2.3 MOMENTUM WHEELS

GOES-Next is equipped with two momentum wheels with their axes in the pitch-yaw plane, canted at an angle of 1.656 degrees from the pitch axes. These produce a pitch angular momentum bias of

$$H = -I_w(\omega_1 + \omega_2) \cos (1.656^\circ) \tag{1}$$

and a yaw angular momentum of

$$h = I_w(\omega_1 - \omega_2) \sin (1.656^\circ) \tag{2}$$

where ω_1 and ω_2 are the angular velocities of the two wheels in radians per second (rad/sec) and $I_w = 0.1082$ kg-m^2 is the moment of inertia of each momentum wheel. The nominal on-orbit wheel speeds are 5485 revolutions per minute (rpm) for both wheels, giving $H = -124.2$ Nms and $h = 0$. Commanding the wheels in the same direction gives a pitch control torque, and commanding them in opposite directions gives a yaw control torque. The dominant error contribution of the momentum wheels is the torque ripple, which has a maximum spectral density of 6×10^{-7} $(N \cdot m)^2$/hertz (Hz) for each wheel (Reference 10). The momentum wheel speed is measured by a tachometer, sampled at 0.512-second intervals, with a quantization of 0.0163 rpm and a noise level of 0.0978 rpm (3σ) (Reference 11).

Should one momentum wheel fail, the other wheel is operated with a smaller reaction wheel (moment of inertia = 0.008626 kg-m^2) whose axis is along the yaw axis. The speeds of these wheels are nominally set to give a smaller pitch angular momentum bias and zero net angular momentum along the yaw axis, as before. The present analysis is easily extended to this backup situation, but it will not be considered further.

3. DYNAMIC MODEL

For an Earth-pointing spacecraft in a circular orbit, Euler's equation and the kinematic attitude equations can be expressed in terms of roll, pitch, and yaw; the resulting equations can be linearized for small deviations from nominal attitude (e.g., pages 608-610 of Reference 5). The resulting equations for GOES-Next, taking into account the rotation of the reference frame (at one revolution per sidereal day, or $\omega_0 = 7.29 \times 10^{-5}$ rad/sec) are

$$I_x\ddot{r} - \omega_0[H - 4(I_y - I_z)\,\omega_0]\,r - [H + (I_x - I_y + I_z)\,\omega_0]\,\dot{y} = N_x + \omega_0 h \qquad (3a)$$

$$I_y\ddot{p} + 3\omega_0^2(I_x - I_z)\,p = N_y - \dot{H} \qquad (3b)$$

$$I_z\ddot{y} - \omega_0[H - (I_y - I_x)\,\omega_0]\,y + [H + (I_x - I_y + I_z)\,\omega_0]\,\dot{r} = N_z - N_w \qquad (3c)$$

where r, p, and y are the spacecraft roll, pitch, and yaw in radians; a dot denotes a time derivative; I_x, I_y, and I_z are the diagonal components of the spacecraft moment-of-inertia tensor (the off-diagonal elements have been neglected); H and h are the internal pitch and yaw angular momentum (as defined in Section 2.3); N_x, N_y, and N_z are the external torques on the spacecraft (excluding the gravity gradient torque, which is included on the left-hand sides of the equations); and N_w is the yaw component of the momentum wheel control torque, so that

$$\dot{h} = N_w \tag{4}$$

Equations (3a), (3b), and (3c) exhibit the well-known fact that the spacecraft pitch motion is independent of the coupled roll/yaw motion, to within the accuracy of the linear approximations used to derive these equations. The GOES-Next pitch is well determined by continuous Earth sensor measurements, as discussed in Section 2.1, so this paper will concentrate on the roll/yaw motion.

The numerical values for I_x and I_z given in Section 2 establish the validity of the approximation

$$I_x = I_z = I \equiv (I_x I_z)^{1/2} = 3412.54 \text{ kg-m}^2 \tag{5}$$

The differences of the principal moments of inertia can be ignored in the coefficients containing the bias momentum in Equations (3a) and (3c) since

$$\omega_o (I_y - I) \approx 0.0015 \text{ H} \tag{6}$$

With these approximations, Equations (3a) and (3c) can be written

$$\ddot{r} = \omega_o \omega_n r + (\omega_n + \omega_o)\, \dot{y} + (N_x + \omega_o h)/I \tag{7a}$$

$$\ddot{y} = \omega_o \omega_n y - (\omega_n + \omega_o)\, \dot{r} + (N_z - N_w)/I \tag{7b}$$

where the nutation frequency ω_n is given by

$$\omega_n = H/I = 0.0364 \text{ rad/sec} \tag{8}$$

This corresponds to a nutation period of 173 seconds.

Precise attitude estimation will require simultaneous estimation of unmodeled torques, in view of the difficulty of accurately modeling the disturbance and control torques. As discussed in Section 2.2, the principal torque modeling errors have both a constant term $\overline{N}_c$ and a sinusoidal term $\overline{N}_p$ with angular frequency ω_o. Thus, the torques are

$$N_x = N_x^* + N_{cx} + N_{px} + w_x \tag{9a}$$

$$N_z = N_z^* + N_{cz} + N_{pz} + w_z \tag{9b}$$

$$N_w = N_w^* + w_w \tag{9c}$$

where N_x^*, N_z^*, and N_w^* are the modeled roll, yaw, and wheel torques, respectively, and w_x, w_z, and w_w are independent white noise processes. The estimated values of $\overline{N}_c$ and $\overline{N}_p$ will include all the unmodeled torques with the prescribed time dependence.

A nine-component state vector containing all the parameters to be estimated is

$$\overline{x} \equiv [r,\ \dot{r}/\omega_n,\ y,\ \dot{y}/\omega_n,\ h,\ N_{px},\ N_{pz},\ N_{cx},\ N_{cz}]^T \tag{10}$$

where superscript T denotes the matrix transpose. For GOES-Next, variations in H, and therefore in ω_n, are very small and can be ignored. Then, combining Equations (4), (7), (9), and (10) with the assumed sinusoidal dependence of $\overline{N}_p$ gives the dynamic equation

$$\dot{\overline{x}} = F\ \overline{x} + \overline{u} + \overline{w} \tag{11a}$$

where

$$F = \left[\begin{array}{c|c} A & B \\ \hline 0 & C \end{array}\right] \tag{11b}$$

with

$$A = \begin{bmatrix} 0 & \omega_n & 0 & 0 \\ \omega_o & 0 & 0 & \omega_n + \omega_o \\ 0 & 0 & 0 & \omega_n \\ 0 & -(\omega_n + \omega_o) & \omega_o & 0 \end{bmatrix} \tag{11c}$$

$$B = \frac{1}{H} \begin{bmatrix} 0 & 0 & 0 & 0 & 0 \\ \omega_o & 1 & 0 & 1 & 0 \\ 0 & 0 & 0 & 0 & 0 \\ 0 & 0 & 1 & 0 & 1 \end{bmatrix} \tag{11d}$$

$$C = \omega_o \begin{bmatrix} 0 & 0 & 0 & 0 & 0 \\ 0 & 0 & 1 & 0 & 0 \\ 0 & -1 & 0 & 0 & 0 \\ 0 & 0 & 0 & 0 & 0 \\ 0 & 0 & 0 & 0 & 0 \end{bmatrix} \tag{11e}$$

and O is a 5-by-4 matrix of zeros.

The nine-component vectors $\bar{u}$ and $\bar{w}$ are given by

$$\bar{u} = [0,\ N_x^*/H,\ 0,\ (N_z^* - N_w^*)/H,\ N_w^*,\ 0,\ 0,\ 0,\ 0]^T \tag{12a}$$

and

$$\bar{w} = [0,\ w_x/H,\ 0,\ (w_z - w_w)/H,\ w_w,\ w_{px},\ w_{pz},\ w_{cx},\ w_{cz}]^T \tag{12b}$$

where w_{px}, w_{pz}, w_{cx}, and w_{cz} are independent (of each other and of w_x, w_z, and w_w) random noise processes. If w_{cx} and w_{cz} are not zero, $\overline{N}_c$ will not be truly constant but will behave as a random walk. Nonzero w_{px} and w_{pz} will give random walk dependence to the phase and amplitude of $\overline{N}_p$.

Equation (11a) has the formal solution

$$\bar{x}(t) = \Phi(t, t_o)\, \bar{x}(t_o) + \int_{t_o}^{t} \Phi(t, t')[\bar{u}(t') + \bar{w}(t')]\, dt' \tag{13}$$

where the state transition matrix $\Phi(t, t_o)$ is a solution of

$$\dot{\Phi}(t, t_o) = F\, \Phi(t, t_o) \tag{14a}$$

with the initial condition

$$\Phi(t_o, t_o) = I_9 \equiv \text{the } 9 \times 9 \text{ identity matrix} \tag{14b}$$

To avoid confusion, capital I denoting an identity matrix will always have a numerical subscript, and capital I denoting moment of inertia will have either a literal subscript or no subscript. The state transition matrix has a partitioning similar to Equation (11b):

$$\Phi(t, t_o) = \left[\begin{array}{c:c} \phi(t, t_o) & \theta(t, t_o) \\ \hdashline 0 & \psi(t, t_o) \end{array}\right] \tag{15}$$

Substituting Equation (15) into Equations (14a) and (14b) gives

$$\dot{\phi}(t, t_o) = A\, \phi(t, t_o) \qquad \text{with } \phi(t_o, t_o) = I_4 \tag{16a}$$

$$\dot{\psi}(t, t_o) = C\, \psi(t, t_o) \qquad \text{with } \psi(t_o, t_o) = I_5 \tag{16b}$$

and

$$\dot{\theta}(t, t_o) = A\, \theta(t, t_o) + B\, \psi(t, t_o) \qquad \text{with } \theta(t_o, t_o) = 0 \tag{16c}$$

The solution of Equation (16c) is

$$\theta(t, t_o) = \int_{t_o}^{t} \phi(t, t') B \psi(t', t_o) dt' \tag{17}$$

so $\theta(t, t_o)$ is determined when $\phi(t, t_o)$ and $\psi(t, t_o)$ are determined. The solution of Equation (16b) is easily seen to be

$$\psi(t, t_o) = \begin{bmatrix} 1 & 0 & 0 & 0 & 0 \\ 0 & c_o & s_o & 0 & 0 \\ 0 & -s_o & c_o & 0 & 0 \\ 0 & 0 & 0 & 1 & 0 \\ 0 & 0 & 0 & 0 & 1 \end{bmatrix} \tag{18}$$

where

$$c_o \equiv \cos \omega_o(t - t_o) \tag{19a}$$

and

$$s_o \equiv \sin \omega_o(t - t_o) \tag{19b}$$

It is thus seen that the structure of the matrix C gives the desired sinusoidal dependence of $\overline{N}_p$.

Equation (16a) is more difficult to solve. Since A is constant,

$$\phi(t, t_o) = \exp [A(t - t_o)] \tag{20}$$

The characteristic equation of A is

$$0 = \det [A - \lambda I_4] = \left(\lambda^2 + \omega_o^2\right) \left(\lambda^2 + \omega_n^2\right) \tag{21}$$

so the eigenvalues of this matrix are $\pm\, i\omega_o$ and $\pm\, i\omega_n$. With Equation (20), this shows that $\phi(t, t_o)$ comprises sinusoidal terms with angular frequencies ω_o and ω_n. This is the justification for referring to ω_n as the nutation frequency. Note that the characteristic equation is intractable without the assumptions leading from Equations (3a) and (3c) to Equations (7a) and (7b). With the periodic nature of $\phi(t, t_o)$ known, it is not too difficult to show that the solution of Equation (16a) is

$$\phi(t, t_o) = \phi_o(t, t_o) + \phi_n(t, t_o) \tag{22a}$$

where

$$\phi_o(t, t_o) = \frac{1}{\omega_n - \omega_o} \begin{bmatrix} \omega_n c_o & -\omega_n s_o & \omega_n s_o & \omega_n c_o \\ -\omega_o s_o & -\omega_o c_o & \omega_o c_o & -\omega_o s_o \\ -\omega_n s_o & -\omega_n c_o & \omega_n c_o & -\omega_n s_o \\ -\omega_o c_o & \omega_o s_o & -\omega_o s_o & -\omega_o c_o \end{bmatrix} \tag{22b}$$

with c_o and s_o defined by Equations (19a) and (19b), and

$$\phi_n(t, t_o) = \frac{1}{\omega_n - \omega_o} \begin{bmatrix} -\omega_o c_n & \omega_n s_n & -\omega_o s_n & -\omega_n c_n \\ \omega_o s_n & \omega_n c_n & -\omega_o c_n & \omega_n s_n \\ \omega_o s_n & \omega_n c_n & -\omega_o c_n & \omega_n s_n \\ \omega_o c_n & -\omega_n s_n & \omega_o s_n & \omega_n c_n \end{bmatrix} \tag{22c}$$

with

$$c_n \equiv \cos \omega_n(t - t_o) \tag{23a}$$

and

$$s_n \equiv \sin \omega_n(t - t_o) \tag{23b}$$

Substituting Equations (18) and (22a), (22b), and (22c) into Equation (17) gives integrals that are convolutions of trigonometric functions and can be evaluated without too much difficulty. The terms in $\Theta(t, t_o)$ have only six kinds of time dependence: $1-c_n$, s_n, $1-c_o$, s_o, $\omega_o(t - t_o)c_o$, and $\omega_o(t - t_o)s_o$.

4. OBSERVABILITY

Before proceeding to detailed treatment of the attitude estimation algorithms, it is useful to establish that the attitude state defined in Section 3 is observable. To discuss observability in a more general sense, consider an n-dimensional state vector and an m-dimensional vector of measurements of $\overline{x}$:

$$\overline{g} = G\,\overline{x} \tag{24}$$

where G is an m-by-n matrix. Then the state is observable if and only if the nm-by-n observability matrix

$$M \equiv \begin{bmatrix} G \\ GF \\ GF^2 \\ \cdot \\ \cdot \\ \cdot \\ GF^{n-1} \end{bmatrix} \tag{25}$$

has full rank n, where F is the dynamic matrix defined by Equation (11a) for the n-component state $\overline{x}$.

Consider first the full nine-component state, with F given by Equations (11b) through (11e). If roll, yaw, and wheel tachometer measurements are available, m = 3 and

$$G = \begin{bmatrix} 1 & 0 & 0 & 0 & 0 & 0 & 0 & 0 & 0 \\ 0 & 0 & 1 & 0 & 0 & 0 & 0 & 0 & 0 \\ 0 & 0 & 0 & 0 & 1 & 0 & 0 & 0 & 0 \end{bmatrix} \tag{26}$$

A computation of M shows that the state is observable in this case; in fact, computing G, GF, GF^2, and GF^3 achieves full rank. Thus, the roll/yaw attitude, attitude rates, wheel speed, and torques are all observable with roll, yaw, and tachometer measurements.

The observability when yaw measurements are not available is also of interest, as discussed in Section 2.1. With only roll and tachometer measurements, m = 2 and

$$G'' = \begin{bmatrix} 1 & 0 & 0 & 0 & 0 & 0 & 0 & 0 & 0 \\ 0 & 0 & 0 & 0 & 1 & 0 & 0 & 0 & 0 \end{bmatrix} \tag{27}$$

The observability matrix computed with this has rank eight, so the nine-component state is not observable.

To ascertain which parameters are observable and which are not, consider the eight-component state vector obtained by deleting the constant yaw torque from $\overline{x}$:

$$\overline{x}' \equiv [r,\ \dot{r}/\omega_n,\ y,\ \dot{y}/\omega_n,\ h,\ N_{px},\ N_{pz},\ N_{cx}]^T \tag{28}$$

This obeys the state equation

$$\dot{\overline{x}}' = F'\ \overline{x}' + \overline{U}' + \overline{W}' \tag{29a}$$

where

$$F = \left[\begin{array}{c|c} A & B' \\ \hline 0 & C' \end{array}\right] \tag{29b}$$

with

$$B' = \frac{1}{H}\begin{bmatrix} 0 & 0 & 0 & 0 \\ \omega_0 & 1 & 0 & 1 \\ 0 & 0 & 0 & 0 \\ 0 & 0 & 1 & 0 \end{bmatrix} \tag{29c}$$

and

$$C' = \omega_o \begin{bmatrix} 0 & 0 & 0 & 0 \\ 0 & 0 & 1 & 0 \\ 0 & -1 & 0 & 0 \\ 0 & 0 & 0 & 0 \end{bmatrix} \qquad (29d)$$

With only roll and tachometer measurements

$$G' = \begin{bmatrix} 1 & 0 & 0 & 0 & 0 & 0 & 0 & 0 \\ 0 & 0 & 0 & 0 & 1 & 0 & 0 & 0 \end{bmatrix} \qquad (30)$$

Forming the observability matrix from products $G'(F')^k$ for power k up to six gives full rank, establishing that the attitude, attitude rates, wheel speed, periodic torque and constant roll torque are observable with only roll and tachometer measurements. It is more difficult to observe the reduced state without yaw measurements than to observe the full state using yaw measurements along with the roll and tachometer measurements, as indicated by the need for higher powers of F in the former case.

The preceding computations establish that the full nine-component state is observable with roll, yaw, and tachometer measurements, but the constant yaw torque is unobservable in the absence of yaw measurements, the other eight components of the state remaining observable from roll and tachometer measurements. This indicates that the constant yaw torque must be estimated during periods with yaw measurements, and that the errors in this torque must not grow too rapidly in periods without Sun sensor visibility. This is equivalent to the assumption that the error source w_{cz} is small.

5. KALMAN FILTER

In principle, the GOES-Next attitude estimation could be carried out using either a batch least-squares estimator or a Kalman filter. The Kalman filter is preferred because it is more straightforward to account for process noise with this method. The observability analysis of Section 4 shows that yaw data are needed to estimate the constant yaw torque. Thus, a batch estimator must use at least one-third of an orbit, or 8 hours, of data to estimate the GOES-Next yaw across the period of yaw data outage. It is very likely that the dynamic models are not accurate enough to propagate across this interval without accounting for process noise. Thus, only the Kalman filter will be considered in this paper.

The Kalman filter propagates estimates of the state $\hat{x}_{k-1}(+)$ and covariance matrix $P_{k-1}(+)$ immediately after the $(k-1)^{st}$ measurement to the time t_k of the k^{th} measurement by means of the following equations:

$$\hat{x}_k(-) = \Phi(t_k, t_{k-1})\, \hat{x}_{k-1}(+) + \int_{t_{k-1}}^{t_k} \Phi(t_k, t')\, \bar{u}(t')\, dt' \tag{31}$$

and

$$P_k(-) = \Phi(t_k, t_{k-1})\, P_{k-1}(+)\, \Phi^T(t_k, t_{k-1}) + \int_{t_{k-1}}^{t_k} \Phi(t_k, t')\, Q\, \Phi^T(t_k, t')\, dt' \tag{32}$$

where the transition matrix Φ is given by Equation (15) and the process noise spectral density matrix Q is defined by

$$E[\bar{w}(t)\, \bar{w}^T(t')] = Q\, \delta(t - t') \tag{33}$$

E denotes the expectation value, $\bar{w}$ is defined by Equation (12b), and $\delta(t - t')$ denotes the Dirac delta (unit impulse) function. Equation (31) is simply Equation (13) without the unknown process noise term, $\bar{w}$. The explicit form for the process noise spectral density matrix is

$$Q = \left[\begin{array}{c:c} Q_{5x5} & 0 \\ \hdashline 0 & Q_{4x4} \end{array}\right] \tag{34a}$$

with

$$Q_{5x5} = \begin{bmatrix} 0 & 0 & 0 & 0 & 0 \\ 0 & q_x/H^2 & 0 & 0 & 0 \\ 0 & 0 & 0 & 0 & 0 \\ 0 & 0 & 0 & (q_z + q_w)/H^2 & -q_w/H \\ 0 & 0 & 0 & -q_w/H & q_w \end{bmatrix} \tag{34b}$$

and

$$Q_{4x4} = \text{diag}\ [q_{px}, q_{pz}, q_{cx}, q_{cz}] \tag{34c}$$

where the latter notation means that Q_{4x4} is a diagonal matrix with the indicated arguments as the elements on the main diagonal. The scalar spectral density q_x is defined by

$$E[w_x(t)\ w_x(t')] = q_x \delta(t - t') \tag{35}$$

and similar relations hold for q_z, q_w, q_{px}, q_{pz}, q_{cx}, and q_{cz}. The results of Section 3 allow closed form evaluation of the integral in Equation (32), giving a very efficient means of covariance propagation.

When a measurement is processed, the state estimate and covariance matrix are updated as follows:

$$\hat{x}_k(+) = \hat{x}_k(-) + K_k[\bar{g}_k - G_k\hat{x}_k(-)] \tag{36}$$

and

$$P_k(+) = (I_9 - K_kG_k)\, P_k(-)\, (I_9 - K_kG_k)^T + K_kR_kK_k^T \tag{37}$$

where $\bar{g}_k$ is the vector of measured values at time t_k, G_k is the matrix relating the measurement to the state as in Section 4, R_k is the measurement covariance and K_k is the Kalman gain:

$$K_k = P_k(-)\, G_k^T\left[G_kP_k(-)G_k^T + R_k\right]^{-1} \tag{38}$$

If the attitude estimates are not needed in near-real time, an optimal filter-smoother may be preferable to a Kalman filter (Reference 12), but that option will not be considered in this paper.

6. ACCURACY ESTIMATES

In the absence of detailed simulations, quantitative estimates of the accuracy attainable with the proposed estimation procedure require the use of approximate models. This paper will consider the accuracy during periods when no yaw measurements are available, because these periods test the attitude estimation process more severely than periods containing yaw data. The observability analysis of Section 4 shows that the external torques are not completely observable without yaw data; the model will therefore be simplified here by eliminating the torques from the state vector. The remaining five-component state has an estimation error represented by a 5-by-5 covariance matrix, and the accuracy estimates will be obtained by computing an approximation to this matrix. The computation can be further simplified by averaging the covariance propagation Equation (32) over a nutation period, using the results of Section 3 for the transition matrix, and then considering the limit at which the orbit rate is negligible compared to the nutation rate. This permits the deletion of the roll rate and yaw rate from the state, resulting in an effective 3-by-3 covariance matrix. The steady-state covariance can then be found by solving a quartic equation, which is possible in principle but inconvenient in practice. However, the simplified approach presented below gives equivalent results for the steady-state covariance.

The validity of the approximate steady-state covariance analysis rests on two quantitative aspects of the GOES-Next attitude determination. First, the orbit rate is much less than the nutation rate, by a factor of 2×10^{-3}. Second, the wheel tachometer measurements are so accurate that the yaw component of the internal angular momentum, which is a component of the state vector, is essentially determined by tachometer measurements alone; the correlation between its errors and the attitude errors is thus effectively zero.

Consider the dynamic Equations (7a) and (7b) in the limit that ω_n becomes infinite. The resulting equations will describe motion on time scales large compared to the nutation period, with nutation averaged out. The second derivative terms in Equations (7a) and (7b) are seen to be negligible if nutation is ignored. The factor $1/I$ is replaced by ω_n/H using Equation (8), and H is held at its physical value as ω_n is taken to infinity. This means that the rotational inertia of the spacecraft body is dominated by the bias angular momentum on time scales larger than the nutation period. The limits of Equations (7a) and (7b) are

$$0 = \omega_o r + \dot{y} + (N_x + \omega_o h)/H \tag{39a}$$

$$0 = \omega_o y - \dot{r} + (N_z - N_w)/H \tag{39b}$$

The two-component state

$$\tilde{x} \equiv [r + h/H,\ y]^T \tag{40}$$

obeys the dynamic equation

$$\dot{\tilde{x}} = \tilde{F}\,\tilde{x} + \tilde{u} + \tilde{w} \tag{41a}$$

with

$$\tilde{F} = \omega_o \begin{bmatrix} 0 & 1 \\ -1 & 0 \end{bmatrix} \tag{41b}$$

$$\tilde{u} = H^{-1} \begin{bmatrix} N_z^*, & -N_x^* \end{bmatrix}^T \tag{42a}$$

and

$$\tilde{w} = H^{-1} [w_z, -w_x]^T \tag{42b}$$

Equation (4) was used in deriving these equations. With the assumption that q_x and q_z, defined in Equation (35), are equal, the process noise spectral density matrix, defined by an equation analogous to Equation (33), is

$$\tilde{Q} = (q/H^2) I_2 \tag{43}$$

where q denotes the common value of q_x and q_z.

In this derivation, q is the spectral density of the process noise representing unmodeled external torques. The more rigorous method of averaging over a nutation period, as discussed at the beginning of this section, shows that a contribution 1/2 q_w from the momentum wheels should be added to q, the factor of 1/2 arising from the time average of $\sin^2 \omega_n t$ and $\cos^2 \omega_n t$. Since q_w arises from torque ripple, as discussed in Section 2, its numerical value can be estimated as

$$q_w = 2(\sin 1.656^o)^2(6 \times 10^{-7}/2\pi)(N{\cdot}m)^2 \text{ s} = 1.3 \times 10^{-10}(N{\cdot}m)^2 \text{ s} \tag{44}$$

where the factor of 2 appears because two wheels contribute to h, and 2π is the conversion from hertz to radians per second. The environmental torque errors are not well approximated by a white noise process, but the spectral density of these errors can be estimated by multiplying the mean square torque errors by a correlation time. The maximum expected torque errors are about 10 percent of the amplitude of equinox torques shown in Figure 2. The quarter-orbit period, which also gives the filter memory span required to estimate yaw, is a reasonable estimate of the correlation time. Thus, an upper limit of the spectral density of external torques is

$$q = \left(5 \times 10^{-6}\ \mathrm{N{\bullet}m}\right)^2 (21541\ \mathrm{s}) = 5.4 \times 10^{-7}\ (\mathrm{N{\bullet}m})^2\ \mathrm{s} \qquad (45)$$

The wheel torque ripple spectral density, q_w, is negligible compared to this. The speed of each momentum wheel is measured at 0.512-second intervals with error variance:

$$R_{tach} = [(0.0163)^2/12 + (0.0978/3)^2](2\pi/60)^2(\mathrm{rad/s})^2 = 1.2 \times 10^{-5}\ (\mathrm{rad/s})^2 \qquad (46)$$

where the factor of 12 converts quantization error to variance and 2π/60 converts revolutions per minute to radians per second. The roll is also measured at 0.512-second intervals with error variance:

$$R_{roll} = [(0.01)^2/12 + (0.01)^2](\pi/180)^2\ \mathrm{rad}^2 = 3.3 \times 10^{-8}\ \mathrm{rad}^2 \qquad (47)$$

where π/180 converts degrees to radians. These measurements can be combined to give a measurement of the first component of $\tilde{x}$ with error variance

$$R_k = R_{roll} + 2\left(I_w \sin 1.656^\circ/H\right)^2 R_{tach} \cong R_{roll} \qquad (48)$$

since the tachometer errors are negligible.

Since the measurement interval Δt is much less than the nutation period, which has already been neglected in deriving Equation (41a), the measurements can be treated as continuous rather than discrete. This leads to a first-order differential equation for the covariance (Reference 12):

$$\dot{\tilde{P}} = \tilde{F}\tilde{P} + \tilde{P}\tilde{F}^T + \tilde{Q} - \tilde{P}\tilde{G}^T R^{-1} \tilde{G}\tilde{P} \tag{49}$$

where

$$\tilde{G} = [1 \ \ 0]^T \tag{50}$$

and

$$R = R_k \Delta t = 1.7 \times 10^{-8} \text{ rad}^2\text{s} \tag{51}$$

Writing

$$\tilde{P} = \begin{bmatrix} p_{11} & p_{12} \\ p_{12} & p_{22} \end{bmatrix} \tag{52}$$

and using Equations (41b) and (43) gives the three scalar equations:

$$\dot{p}_{11} = 2\,\omega_o p_{12} + q/H^2 - p_{11}^2/R \tag{53a}$$

$$\dot{p}_{22} = -2\,\omega_o p_{12} + q/H^2 - p_{12}^2/R \tag{53b}$$

$$\dot{p}_{12} = \omega_o(p_{22} - p_{11}) - p_{11}\, p_{12}/R \tag{53c}$$

Solving Equations (53a), (53b), and (53c) for the covariance for which the time derivatives vanish gives the following steady-state covariance:

$$p_{11} = \omega_o R[(\alpha + 3)(\alpha - 1)]^{1/2} \tag{54a}$$

$$p_{22} = \omega_o R\ \alpha[(\alpha + 3)(\alpha - 1)]^{1/2} \tag{54b}$$

$$p_{12} = \omega_o R(\alpha - 1) \tag{54c}$$

where

$$\alpha \equiv \left[1 + q/\left(\omega_o^2 H^2 R\right)\right]^{1/2} \tag{54d}$$

Taking α equal to the negative of the square root in Equation (54d) also gives a steady-state solution, but this is unacceptable because it gives a negative value for p_{22}, which must be nonnegative.

The principal quantity of interest for this analysis is the variance of the yaw estimate, or p_{22}. For GOES-Next, $q/(\omega_o^2 H^2 R) = 3.9 \times 10^5 \gg 1$, so to an excellent approximation:

$$p_{22} \simeq \omega_o R\alpha^2 \simeq q/\left(\omega_o H^2\right) \tag{55}$$

It is remarkable that the yaw variance is independent of the measurement error R in this limit. Equation (55) provides a general parameterization of the yaw accuracy as a function of the torque modeling errors. Inserting the GOES-Next values for the parameters gives

$$\sigma_{yaw} = (p_{22})^{1/2} \simeq 6.9 \times 10^{-4} \text{ rad} = 0.040 \text{ deg} \tag{56}$$

This is very close to the performance expected by the spacecraft contractor (Reference 10).

7. CONCLUSIONS

Dynamic propagation promises to be a valuable complement to gyro propagation for GOES-Next, permitting observation of yaw during Sun sensor data gaps and estimation of environmental torques for setting the trim tab. Provided the attitude remains close to Earth pointing, the propagation equations are nearly linear. The added assumption that the body angular momentum is much smaller than that of the momentum wheels allows closed-form solution of those equations. The solution has terms that vary at the orbital rate and at the much higher nutation rate. Neglecting errors with greater than the nutation frequency allows closed-form expressions for the yaw accuracy, also.

Error enters the propagation through imperfectly modeled environmental torques, control torques that are ignored because of lack of information, and random fluctuations in the wheel-bearing torque. The largest sources of error are expected to be the solar torque modeling and the neglected magnetic control torques. The stabilizing pitch momentum bias, the accurate wheel tachometer data, and the relatively small torques at geosynchronous altitude permit propagation in the presence of these errors.

Since the error propagation equations are linear, the Kalman filter proposed here is also linear and should be easier to develop than a general extended Kalman filter. With the transition matrices calculated in closed form, the filter should also be efficient to operate. In practice, this filter would process full orbits of data to estimate torque parameters and propagate the yaw during Sunless periods. The process and sensor noise levels expected for GOES-Next yield an estimated yaw accuracy of 0.040 deg following the gap in Sun coverage. This number is consistent with manufacturer estimates of yaw drift over that period. Successfully applying dynamic propagation to GOES-Next operations support would break new ground for the Flight Dynamics Division of the Goddard Space Flight Center and would provide a much needed backup to the usual gyro propagation.

REFERENCES

1. E. J. Lefferts and F. L. Markley, "Dynamic Modeling for Attitude Determination," AIAA Guidance and Control Conference, San Diego, California, August 1976, paper no. 76-1910

2. Computer Sciences Corporation, CSC/TM-76/6235, Nimbus-G Attitude Determination Feasibility Study Utilizing the Attitude Dynamics Generator (ADGEN), F. L. Markley and J. W. Wood, December 1976

3. --, CSC/TM-77/6115, Evaluation of Wheel Rate Data for LANDSAT Attitude Modeling, J. Fein, April 1977

4. Ford Aerospace and Communications Corporation, DRL 302-01, GOES IJK/LM Attitude/Orbit Control Analysis, January 15, 1987

5. J. R. Wertz, ed., Spacecraft Attitude Determination and Control. D. Reidel: Dordrecht, Holland, 1978

6. Ford Aerospace and Communications Corporation, DRL 300-03, GOES IJK/LM Fields of View Analysis, December 17, 1986

7. Computer Sciences Corporation, "Notes on GOES-Next Solar Torque Analysis," unpublished, J. Rowe, October 1977

8. Ford Aerospace and Communications Corporation, PCC-TM-0733, ODC-86-053, "Compensation of S/C Magnetic Dipole Using the Magnetic Torquers," C. Weyandt, November 11, 1986

9. --, PCC-TM-0966, ODC-87-059, "Need for Magnetic Torquers," C. Weyandt, February 18, 1987

10. --, "Dynamics and Controls Analysis CDR Data Package," Book 2, March 8-9, 1988

11. T. Kailath, Linear Systems. Prentice-Hall: Englewood Cliffs, New Jersey, 1980

12. A. Gelb, ed., Applied Optional Estimation. M.I.T. Press: Cambridge, Massachusetts, 1974

FLIGHT MECHANICS/ESTIMATION THEORY SYMPOSIUM

SESSION 4

PRECEDING PAGE BLANK NOT FILMED

N89-15956

CONTROLLED REENTRY
OF THE GAMMA RAY OBSERVATORY (GRO)

EVETTE R. BROWN
FLIGHT DYNAMICS DIVISION
TRAJECTORY & TRACKING ANALYSIS
SECTION/Code 554.2

PRECEDING PAGE BLANK NOT FILMED

1. ABSTRACT

Reentry of the GRO satellite must be controlled because it is expected that a great portion of the massive spacecraft would survive the reentry into the earth's atmosphere with the debris possibly causing harm to human life and property. The intent of this paper is to present a technique, results, and conclusion for a controlled reentry scenario for GRO. The planned impact would occur in an uninhabited portion of the South Pacific Ocean.

Two major areas were analyzed. First, targeting analysis examined conditions under which the orbital maneuver study was done. Finally, the debris scatter involved analyzing effects of the breakup of the spacecraft on the impact area. These two areas were the basis from which the controlled reentry study was accomplished.

2. BACKGROUND INFORMATION

The Gamma Ray Observatory (GRO) satellite is scheduled to be launched in the first quarter of 1990 by the Space Transportation System out of the Eastern Test Range. GRO is a relatively large spacecraft with weight of approximately 34,500 lbs. GRO's mission is to study cosmic gamma ray sources. This satellite is equipped with four detectors to obtain the gamma ray science. They are: the Oriented Scintillation Spectrometer Experiment (OSSE), the Imaging Compton Telescope (COMPTEL), the Energetic Gamma Ray Experiment Telescope (EGRET), and the Burst and Transient Source Experiment (BATSE).

GRO will be transported by the shuttle to an initial parking orbit. The onboard propulsion system will be used to raise it to its final mission orbit. Mission life time, that period where science data will be obtained, is required to extend at least 27 months. The first year will take the form of a full sky survey, viewing gamma ray sources for two week periods of time. The second year, not yet confirmed, may consist of concentrated viewing of a few targets. If sufficient orbit maintenance fuel remains the mission life may be extended. At the end of mission life, a controlled GRO reentry is required into a relatively unpopulated region of the earth, since it is expected that major portions of the structure will survive the intense heat and forces during its flight back to earth.

The relatively unpopulated region of the earth used in this study was taken from TRW GRO Mission Contract "Observatory Reentry Plan (Final)" (July 1985).[1] The area, noted as the nominal impact area, is outlined by the following islands:

Nominal Impact Area

Place	Latitude	Longitude
South Point of Hawaii	18.95 N	155.73 W
Christmas Island	1.87 N	157.33 W
Hiva Oa Island	9.75 S	139.00 W
Ducie Island	24.75 S	124.77 W
Easter Island	27.12 S	109.37 W
Isla Sala-y-Gomez	26.47 S	105.47 W
Isla San Felix	26.28 S	80.08 W
Lima Peru	12.05 S	77.05 W
Isla Isabela	0.63 S	91.45 W
Clipperton Island	10.28 N	109.22 W
Ocean Location	18.28 N	123.00 W

See Figure A-1 for pictorial representation of the impact region. For reference purposes the length for descending groundtracks measured from the southern point of Hawaii to Isla San Felix is approximately 9,500 kilometers, and the length measured form Hiva Oa Island to the coordinate (25 S latitude, 100 W longitude) is approximately 4,500 kilometers. This impact location is desirable because: it is the largest location within the +/- 28.5 latitudes that is comparatively uninhabited and consists mainly of open ocean; also, it is a location that is achievable without the additional fuel penalty of a plane change. The most favorable targeting will produce an impact that is centrally positioned within the impact region and therefore farthest from the islands tabulated above.

As a result of the location of the nominal impact box, Tracking Data Relay Satellite System (TDRSS) coverage was a concern. TDRSS is the environment with which contact with the GRO satellite will be maintained. The two TDRS's (East and West) positioned at 41 degrees West longitude and at 171 degrees West longitude respectively, resulting in each having an exclusion region in which contact can not be established between that particular TDRS and a user spacecraft. The inter-section between each TDRS's exclusion region is known as the TDRSS Zone of Exclusion (ZOE). The TDRSS ZOE for a spacecraft at an altitude of 300 km has East longitudes between approximately 58 degrees and approximately 95 degrees. The GRO maneuvers are initiated approximately between 55 to 100 degrees East longitude which contain the region where TDRSS coverage is not readily available. In addition, the lower the altitude of the spacecraft the larger the ZOE region gets. As a result, some maneuver burns will have to be initiated with stored commands and communication will have to resume when GRO is out of the ZOE region.

The following pages represent the analysis performed and the results obtained using the above information as a basis for the GRO controlled reentry.

3. TARGETING ANALYSIS

Reentry Targeting Analysis was done to investigate a feasible technique for a controlled GRO reentry into an unpopulated region of the earth. Three areas were be addressed under this analysis item. They are: assumptions, methodology, and TDRSS coverage. Each of the above items played a significant role in the targeting analysis and is discussed below.

3.1 Assumptions

The starting reentry orbit used was circular, approximately (315 km x 315 km). This is assumed to be the altitude where an STS rendezvous would take place and the remaining usable fuel on board is at least 1000 pounds to be used for the controlled reentry. The orbital conditions chosen for the controlled reentry were obtained from Code 554 GRO Lifetime Studies. This orbit represents a likely candidate for GRO at the end of life phase of the mission. To model the atmospheric conditions, solar flux obtained from the 97th percentile Marshall Flight Center Prediction Table August 1987, was used. Listed below are the assumed orbital elements and solar flux that were used for this study:

OSCULATING ELEMENTS

Epoch	April 1, 1992	11 hr. 19 min. 43 sec. GMT
semimajor axis	6695.389	km
eccentricity	0.000143	
inclination	28.51771	deg.
node	0.000013	deg.
argument of perigee	19.60527	deg.
mean anomaly	340.3947	deg.
solar flux	200.0	W/M sq. * Nt.-M

The major software tools that were used for this analysis were the General Maneuver (GMAN) program and the Goddard Mission Analysis System (GMAS) program. GMAN was used to compute the orbital maneuvers. GMAS was used for propagating from the post-burn state vector. For this analysis GMAS was equipped with an atmospheric density model that took into consideration the increased drag effect of near earth conditions.

In order to perform burn simulations, GRO-unique spacecraft parameters (especially the propulsion system) were modeled. The GMAN program, in modeling the GRO satellite at the beginning of controlled reentry, was given the following spacecraft parameters:

Spacecraft Parameters

Total Weight	31182.0 lbs
Total Expendable	1000.0 lbs
Fuel Weight	1040.0 lbs (260.0 lbs per tank)
Fuel Pressure	105 lbs per square inch absolute
Fuel Temperature	24.0 degrees Celsius
Cross Sectional Area	46.0 square meters
Drag Coefficient	2.2

The combined effects of these two mission analysis programs, GMAN and GMAS, provided good estimations of the orbital maneuvers and the orbital evolution.

The fuel considerations for each phase of the mission were obtained from TRW Gamma Ray Observatory Mission Contract based on a 34,500 lbs spacecraft at liftoff with 40 lbs of residual fuel.

Phase	Fuel (lbs.)
Ascent	1315
Orbit Maintenance	445
Reentry	1000
Rendezvous	1040
Attitude Control	400
Total	4200

It will be assumed that the fuel load at the onset of reentry will be 1,040 lbs; 1000 lbs usable fuel and 40 lbs of residual. The predicted fuel to be expended for maneuvers was obtained by transforming the Rocket equation:

$$\text{Delta-V} = g * Isp * \ln (Mo / (Mo - \text{Delta-M}))$$

to $$\text{Delta M} = Mo * (1 - e^{k}), \quad k=-(\text{Delta-V}) / g * Isp$$

where Delta-V is the velocity change, g is the gravitational constant (9.8 m/sec sq.), Isp is the specific impulse of the propulsion system, Mo is the total weight of the spacecraft at the start of the burn, Delta-M is the fuel weight expended. The results were verified by GMAN after each maneuver.

3.2 Methodology

The next tasks were to determine: what will be the maneuvering guidelines leading to the desired impact location; and what would be the best staging deboost altitudes. The combination of these two items established the methodology which was taken.

Addressing the latter of the two above items, it was obvious that an infinite number of staging altitudes are possible. However, to provide the fundamental procedures needed to handle this task, three scenarios were analyzed. A single maneuver, a 2-burn maneuver sequence, and a classical two and half Hohmann transfer were examined. Lowering only perigee was the approach for both the single maneuver and the two maneuver sequences. The single maneuver and the 2-burn maneuver sequences were the plans selected because of the tremendous fuel saving when compared to circularizing the orbit when deboosting. If the classical two and one half burn Hohmann transfer for circular orbits were used, a negative delta-V would be applied at apogee, which causes perigee to be lowered. A second, similar negative delta-V would be applied at perigee which causes the lowering of apogee, and the circularization of the orbit. The final maneuver would cause the spacecraft to impact. In comparison to the standard two and one half burn Hohmann, the lowering only of perigee entails applying a single negative Delta-V equal to the first burn in the two burn Hohmann case. Comparing the two methods, the lowering of only perigee has these advantages over the standard two and one half burn Hohmann transfer: there is a tremendous fuel saving (factor of 2, except for the terminal burn) which could be allocated to extend the mission life and operationally, it is simpler in that only one burn operation must be carried out per targeted deboost altitude, thus less risk. Hence, the Hohmann transfer will not be utilized for the controlled reentry.

Derived Maneuver Constraints:

1. Perigee altitude must be selected such that the spacecraft will reenter less than 1/2 revolution after the terminal burn.
2. All maneuvers were to be made approximately 1/2 orbit away from the impact location region as determined from debris scatter study.
3. A minimum of 24 hours will be allotted between multiple burns for orbit calibration and generating command loads.
4. The longitude and latitude at 50 kilometers altitude will be considered the longitude and latitude at impact which is based on GMAS test cases that produced tenths of a degree difference at 1 kilometer as compared to the 50 kilometers; there is practically a vertical drop.

Also, all terminal burns were targeted for an altitude of 50 km because it is well within the critical altitude span where the spacecraft will not skip out. A spacecraft with a perigee altitude above 90 kilometers may not reenter within the 1/2 revolution after the completion of the maneuver because the accumulated drag force may not be great enough to deplete the kinetic energy within the 1/2 orbit constraint. Thus, the risk factor is increased because the depletion of the kinetic energy from the orbit can occur anywhere and the spacecraft could impact in an unfavorable location. At the completion of the burn the satellite will not have reached a 50 kilometer altitude, however the earth's atmosphere will provide the needed drag to cause the remaining loss of kinetic energy for the spacecraft to be pulled in.

A tool was developed to aid in selecting the appropriate delta-V that causes the spacecraft to impact. This was achieved by manual estimations followed by fine tuning with the GMAN and GMAS programs. Several initial altitudes were examined targeting for the following perigee altitudes: 75, 50, 25, and 1 kilometers. The range from impact to the midpoint of the burn was computed. Delta-V and range were graphed for each case. Also, groundtrack plots of the initial orbit were produced. The groundtrack plots were used to determine which descending passes fell in the desired impact box and to back out a time for the maneuver to begin. When the desired groundtracks were chosen, usually there were three candidates, the placement of the maneuver was derived by backing away approximately 180 degrees. The range vs. delta-V graph was used as an indicator of how much change in velocity was needed. The combination of delta-V vs. range graph and the groundtrack plots gives a fairly good estimation of where the burn should begin to produce an impact in the desired impact region.

3.3 TDRSS Coverage

Analysis was done for each maneuver to determine if a line of sight contact could be established and sufficiently maintained between GRO and TDRSS during the burn. It was assumed for this analysis that the average maneuver for the first burn of the 2-burn multiple case will be a maximum of 7 minutes long and approximately 15 minutes long for the second of the 2-burn case; 22 minutes will be the burn duration for the single burn case. Analysis has shown that it may not always be possible to maintain TDRSS communications throughout a maneuver while performing the maneuver at the most opportunistic time to achieve the desired impact region. Due to the positions of the spacecraft at the time of the scheduled maneuver it may be mandatory to maneuver, without TDRSS coverage at all. Earlier analysis showed that an altitude of 315 kilometers is too high to affect controlled reentry with 1000 pounds of fuel. Thus, it was necessary to await orbital decay to 276 km or less. The analysis performed was based on maneuvering from altitudes ranging from 276 kilometers to 215 kilometers.

4. DEBRIS SCATTER

The area over which GRO debris is expected to scatter upon impact was studied. Knowledge of the scatter is required to determine the safe targeting range to ensure that all pieces impact within the designated region. The altitude assumed where the spacecraft will begin to break up is 83 kilometers; this is based upon TRW's Gamma Ray Observatory Mission Contract Observatory Reentry Plan (Final) July 1985.[2] Two areas of concentration were addressed, effects of the ballistic coefficients (BC) and calibration errors. Each was thought to cause some effect on the scatter.

One way of estimating the scatter was by computing the impact points over a range of ballistic coefficients (BC):

$$\text{Ballistic Coefficient} = (Cd*A)/(2*m)$$

where m is the mass of a particular object, Cd is the dimensionless drag coefficient, and A is the average cross-sectional area perpendicular to the velocity vector. "The BC is the measure of the spacecraft to overcome air resistance."[3] To put this in perspective, a satellite with a large BC (large area to mass ratio) will impact earlier than one with a small BC.

In addition to the ballistic coefficient, the efficiency of the thrusters was thought to play a significant role in the area over which the debris is scattered. Targeting errors are the effects of thruster calibration errors on the terminating reentry orbit. This was analyzed by inducing a +/- 10 percent calibration error using the GMAN targeting tool. The net result, as compared to the nominal, showed displacements. The +10 percent calibration error (firing hot) produced an impact further up track from the nominal; and the -10 percent (firing cold) produced an impact further down track from the nominal. Firing hot caused a 10% increase in the fuel consumed and the converse was true for the cold firing. Combining the thruster inefficiencies with the ballistic coefficients factors (hot with maximum and cold with minimum) also increased the scatter range. As expected, the hot firing and maximum BC impacted furthest up track in comparison to all of the previous cases, and conversely for the cold and minimum BC. Therefore, the determination of the maximum range over which the debris is expected to be scattered was based upon a range of ballistic coefficients in conjunction with thruster inefficiencies.

The BC range consisting of a maximum (135 x 10 -1 lbs/ft. **2) and a minimum (0.5 x 10 -1 lbs/ft. **2) corresponds to the high gain antenna and EGRET respectively. These coefficients were derived from TRW's study on potential spacecraft breakage. They are representative bounds for determining the range over which the debris is expected to scatter. The minimum BC causes a later impact and the maximum BC causes an earlier impact. Results obtained using the minimum BC and the maximum BC determined the lower and upper bounds over which the GRO will be scattered upon impact. The actual length of this scatter along the groundtrack is the arc distance along the surface of the earth formed by the vectors that extend from the center of the earth to the spacecraft impact points corresponding to the cold/minimum and hot/maximum BCs. The arc-length distance was computed using the following equations:

$$\cos = \sin\delta_1 \sin\delta_2 + \cos\delta_1 \cos\delta_2 \cos(\alpha_1 - \alpha_2), \quad 0 < \theta_i < 180 \qquad \text{(A-1)}$$ [4]

where (α_i, α_i) are the longitude and latitude points on a unit sphere and θ_i is the angle between them

$$S = \theta * Re \qquad \text{(A-2)}$$

where S is the arc-length distance of angle θ and Re is the earth's radius. This is consideted to be the along track scatter. Previous studies have shown that the cross track scatter is considered to be negligible.

5. STUDY CASES

5.1 Single Burn Scenario

A single burn scenario consists of one long burn that is applied to the spacecraft to lower perigee far enough so that the accumulated drag forces would deplete its kinetic energy sufficiently to cause it to impact. Analysis was performed for several single deboost maneuvers; however, only one will be presented. It is for an approximate (250 km x 250 km) circular orbit targeting to a perigee altitude of approximately 50 kilometers, this assumes a nominal spacecraft area, mass, and thruster efficiency. This orbit was achieved by allowing the spacecraft to drag down from the previously stated 315 km circular orbit for approximately 2 months. The reason for the desirable decay of the orbit was that the allotted reentry fuel of 1000 pound could not accommodate a controlled reentry to impact. There simply is not enough fuel to cause a designated impact from that altitude. Therefore, a lower altitude was required. The Delta-V needed to go from 250 km to 50 km was estimated by using the Vis-Via equation for the initial and final orbits and taking the difference between the two orbit velocities to find the impulsive delta between the two. The equations are as follows:

$$V1 = \sqrt{Mu\ (2/R1 - 1/A1)}, \qquad V2 = \sqrt{Mu\ (2/R1 - 1/A2)},$$

$$\text{Delta-V} = V2 - V1$$

where V1 and V2 are the velocities of the initial orbit and final orbit respectively, Mu is the gravitational constant, A1 and A2 are the semimajor axes of the initial and final orbits, R1 is the radius of apogee of both initial and final orbits. Once the Delta-V was calculated it was applied at a specific ignition time and direction for this single deboost maneuver which would take place approximately 1/2 orbit away from the desired impact point. In addition to the 1/2 orbit requirement for burn placement, the Delta-V was applied near an ascending node such that the spacecraft reentered near a descending node. Reentry near a descending node is important in order to achieve a groundtrack pass along the length of the impact area region, as opposed to reentering near an ascending node along the shorter width of the impact region.

Table A-1 lists the effects of the nominal, +/- 10 percent calibration, and the maximum and minimum BC cases in terms of ignition and impact coordinate points for opportunities 1, 2, and 3.

Table B-1 is a list of the debris scatter.

Figure A-2 show the groundtracks for the three consecutive opportunities. Impacts are recorded for firing 10% hot and cold, with a maximum and minimum BC, and the combination of the cold/minimum and hot/maximum are displayed.

In essence it appears that the size and weight of the spacecraft and the efficiencies of the thrusters are important factors to look at in determining the area over which the debris is scattered. The total length of the debris scatter measured from the hot/max impact to the cold/min impact is approximately 3,100 kilometers long. The fuel consumption for all of the cases fell marginally within the fuel allotment of 1000 pounds. Orbital conditions achieved were suitable to drive the spacecraft well below the critical skip altitude. Finally, the lengths of the burns were approximately twenty-two minutes initiating very close to the ZOE region. Thus controlled reentry is feasible with one long single burn.

5.2 Two-Burn Scenario

The 2-burn reentry scenario entails progressively reducing the perigee altitude by dividing the maneuver over two separate orbits over 24 hours until perigee is lowered well below the critical skip-out attitude. This two burn strategy was considered since the burn error produced by sequential retargeting should be smaller. Any number of burns could be made, however the goal is to obtain a degree of accuracy but yet be efficient. The 2-burn maneuver sequence does this. The 2-burn maneuver sequence, as the single burn maneuver sequence begins at an altitude lower than 315 km. The 2-burn maneuver sequence was started at a near circular (288 km x 276 km) orbit. It took a little over one month to decay down from 315 km. Establishing where to begin the burns for each of the two deboost orbits was based upon the alignment of the line of apsides (the diameter from the apogee point to the perigee point) with the impact box. The placement of the burn was also near an ascending node. The natural precession of the orbit was taken into account for placement of the first burn so that reentry could occur approximately 24 hours later. The orbit precessed approximately 7 degrees per day. Therefore, the first burn was performed approximately 7 degree away from the desired location for apogee. One of the maneuvering guidelines states there will be at least 24 hours between burns. The first burn was targeted for a perigee height of approximately 215 km. The Flight Dynamics Division has performed studies showing that below 200 km altitude there is a possibility that nominal attitude control of the spacecraft may be lost. It is imperative to maintain good attitude control before, during and after the maneuver especially since another maneuver is needed to drive in the spacecraft. A perigee altitude of 215 km has a padding to allow for a one day decay of the orbit and other complications that may occur. From 215 km there are approximately seven days before a portion of the orbit slips below 200 km. The second burn, which causes the spacecraft to impact was performed one day after the first burn. Also, the second burn is performed at apogee, near an ascending node. As stated earlier there are three consecutive orbital opportunities for impact into the nominal impact region and the same logistics apply. This second burn was targeted for a perigee altitude of approximately 50 kilometers. Like in the single maneuver scenario, analysis was performed using +/- 10% calibrations. However, after performing the +10% calibration case the results indicated that a lower perigee altitude was achieved on the first burn and more fuel was expended. The second burn could not achieve the total burn time desired because the fuel ran out. Therefore, all of the cases were tempered by the delta burn time (minutes) that was needed for the hot case to achieve a low enough perigee altitude which would result in an impact within 1/2 revolution and not run out of fuel before the completion of the maneuver. This delta burn time affected the nominal targeted perigee altitude of 50 kilometers. The perigee altitude for the nominal case was approximately 20 kilometers higher and the cold was even higher. However, all of the cases resulted in the designated area impacts within 1/2 of a revolution.

Table A-2.1 and A-2.2 list the effects of the nominal, +/- 10 percent calibration, and the maximum and minimum BC cases in terms of ignition and impact coordinate points for opportunities 1, 2, and 3.

Table B-2 is a list of the debris scatter.

Figure A-3 shows the terminating groundtracks for the three consecutive opportunities. Impacts are recorded for firing 10% hot and cold, with a maximum and minimum BC, and the combination of the cold/minimum and hot/maximum.

Figuure A-4 is an altitude vs time graph showing apogee and perigee decay against time.

5.3 Evaluation of cases

The two cases represent two slightly different methods. The 2-burn case allows for the calibrating of the thrusters and setting up the spacecraft for the optimal orbital conditions required for accurate targeting. Also, during the actual mission the errors due to targeting at impact will be somewhat smaller because the second burns can take into account the error caused by the first burn. The objective for this study was to see if a worst case scenario would provide for a controlled reentry where all the debris would fall in the box; the results did show this. However, there are uncertainties associated with any burn case. The thrusters could fail during a maneuver, unanticipated torque on the spacecraft could throw off the attitude control and misalign the direction of the thrust, or there could be any number of unexpected phenomena. However, after examining the results of these two cases the two burn appears to be better. The two burn case allows for the error in the first burn to be removed during targeting for the second burn, thus cutting the error down significantly from the single burn scenario. The single burn scenario does not allow for the calibration of the thrusters. Therefore, the 2-burn maneuver sequence is recommended as the most effective way of performing the controlled reentry of GRO.

6. CONCLUSION

The controlled reentry analysis of the 34,500 pound, Gamma Ray Observatory is a dynamic task filled with many subtle uncertainties and technical lessons. The paper represents a basis from which more detailed analysis will be done. In performing this analysis several other areas to investigate surfaced; e.g using another impact region located in the Indian Ocean, what affect will lift have on the spacecraft's deboost, as well as the flight path angle. As a result, this study has served as a catalyst by stimulating questions which will help further complete development of a controlled reentry program for the GRO spacecraft. Several of the assumptions made at the onset of the study have changed, and undoubtedly, some will even change as late as two years into the mission. However, the lowering of perigee technique presented here is a viable one (the 2-burn maneuver sequence is the recommended scenario). It is based on normal orbital occurrences; therefore, it is believed that the uncertainties about the orbit, spacecraft, and atmospheric conditions should not affect the foundation on which the analysis is based in providing a controlled GRO reentry.

If the reentry phase begins with GRO's altitude greater than 276 km, it is necessary to allow the orbit to decay to less than or equal to 276 km to accomplish the controlled reentry with less than or equal to 1000 pounds of fuel during a 2-burn scenario. Also, the reentry area is approximately 180 degrees away from the TDRSS ZOE. It will be necessary to sacrifice TDRSS coverage during the maneuvers to accomplish the controlled reentry into the designated region.

9. FOOTNOTES

1. TRW, "Observatory Reentry Plan (Final)", (July, 1985), 15.

2. ibd.

3. Wertz, James R., "Spacecraft Attitude Determination & Control", (Boston: D. Reidel Publishing Co., 1980), 64 .

4. ibd.

10. REFERENCES

1. Bate, Mueller, White. "Fundamental of Astrodynamics", NY: Dover Publications, Inc., 1971.

2. Jensen, Townsend, Kork, and Kraft. "Design Guide to Orbital Flight", New York: McGraw-Hill Book Co., 1980.

3. Wertz, James R. "Spacecraft Attitude Determination & Control", Boston: D. Reidel Publishing Co., 1980.

4. Computer Science Corporation/Contract NAS5-27888/64600, "Gamma Ray Observatory (GRO) Compendium Of Flight Dynamics Analysis Reports", R. McIntoch, December 1986.

5. TRW, "Mass Properties Status Report Gamma Ray Observatory", June, 1985.

6. TRW, "Observatory Reentry Plan (Final)", July, 1985.

ORIGINAL PAGE IS
OF POOR QUALITY

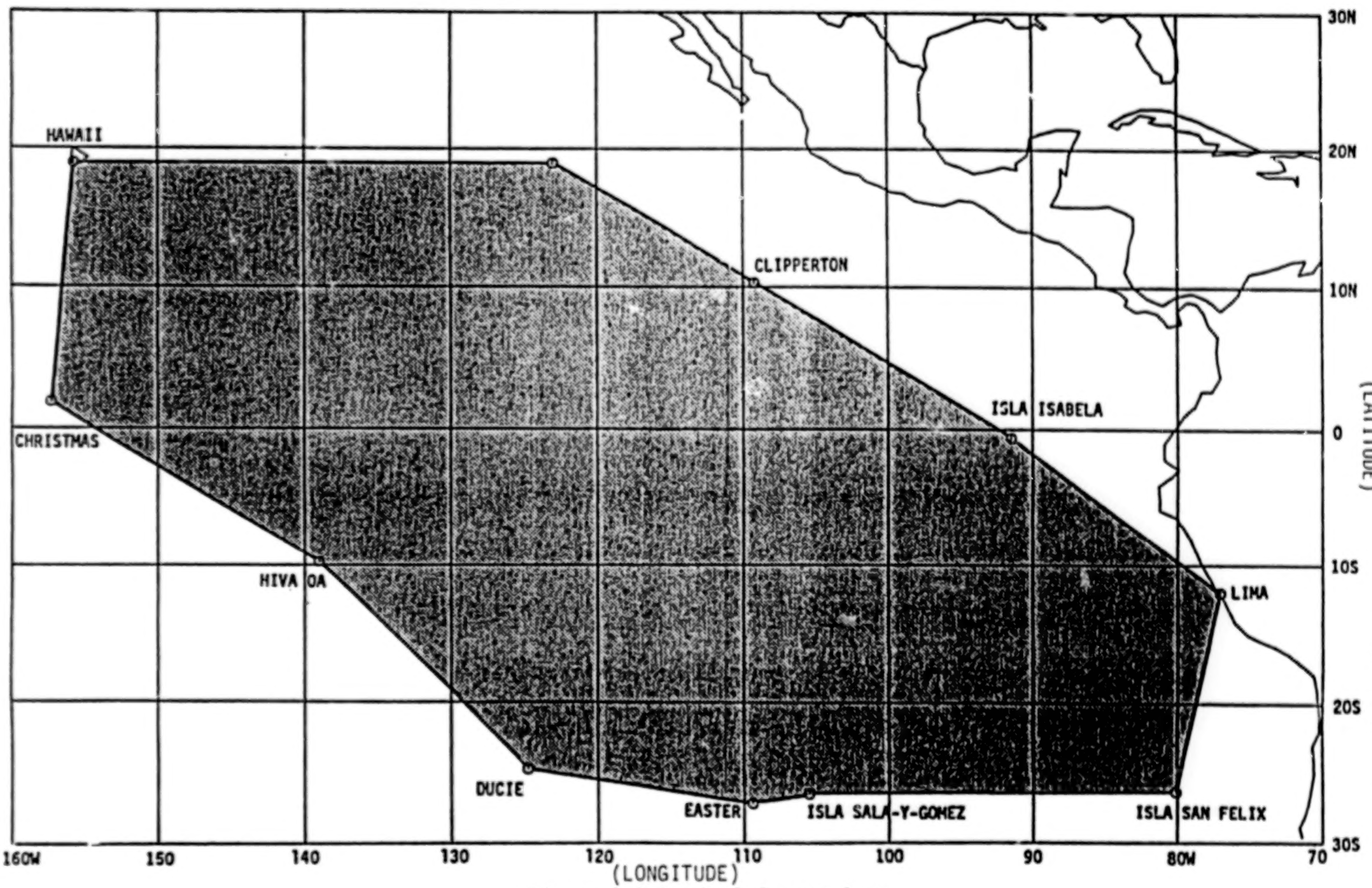
30N
20N
10N
0
10S
20S
30S
(LATITUDE)
160W
150
140
130
120
110
100
90
80W
70
(LONGITUDE)
HAWAII
CHRISTMAS
HIVA OA
DUCIE
EASTER
ISLA SALA-Y-GOMEZ
ISLA SAN FELIX
LIMA
ISLA ISABELA
CLIPPERTON

Figure A-1 Nominal Impact Area

Table A-1. Single Maneuver Sequence

POST MANEUVER CONDITIONS

OPPORTUNITY		COLD/ MIN BC	MIN BC	COLD	NOMINAL	HOT	MAX BC	HOT/ MAX BC
1	FUEL(LBS)	811	895	811	895	977	895	977
	BURN TIME (MIN)	22	22	22	22	22	22	22
	DELTA-V (FT/SEC)	193	213	193	213	233	213	233
	APOGEE(KM)	229	228	229	228	227	228	227
	PERIGEE(KM)	64	46	64	46	26	46	26
2	FUEL(LBS)	811	895	811	895	977	895	977
	BURN TIME (MIN)	22	22	22	22	22	22	22
	DELTA-V (FT/SEC)	193	213	195	213	233	213	233
	APOGEE(KM)	229	228	229	228	227	228	227
	PERIGEE(KM)	64	45	64	45	26	45	26
3	FUEL(LBS)	811	895	811	895	977	895	977
	BURN TIME (MIN)	22	22	22	22	22	22	22
	DELTA-V (FT/SEC)	193	213	193	213	233	213	233
	APOGEE(KM)	229	228	229	228	227	228	227
	PERIGEE(KM)	66	47	66	47	28	47	28

Table B-1.

SINGLE MANEUVER SEQUENCE	DEBRIS SCATTER (KM)
NOMINAL TO HOT/MAXIMUM BC	1700
NOMINAL TO MAXIMUM BC	900
NOMINAL TO HOT	1100
NOMINAL TO COLD	1300
NOMINAL TO MINIMUM BC	150
NOMINAL TO COLD/MINIMUM BC	1400
*HOT/MAXIMUM TO COLD/MINIMUM BC	3100

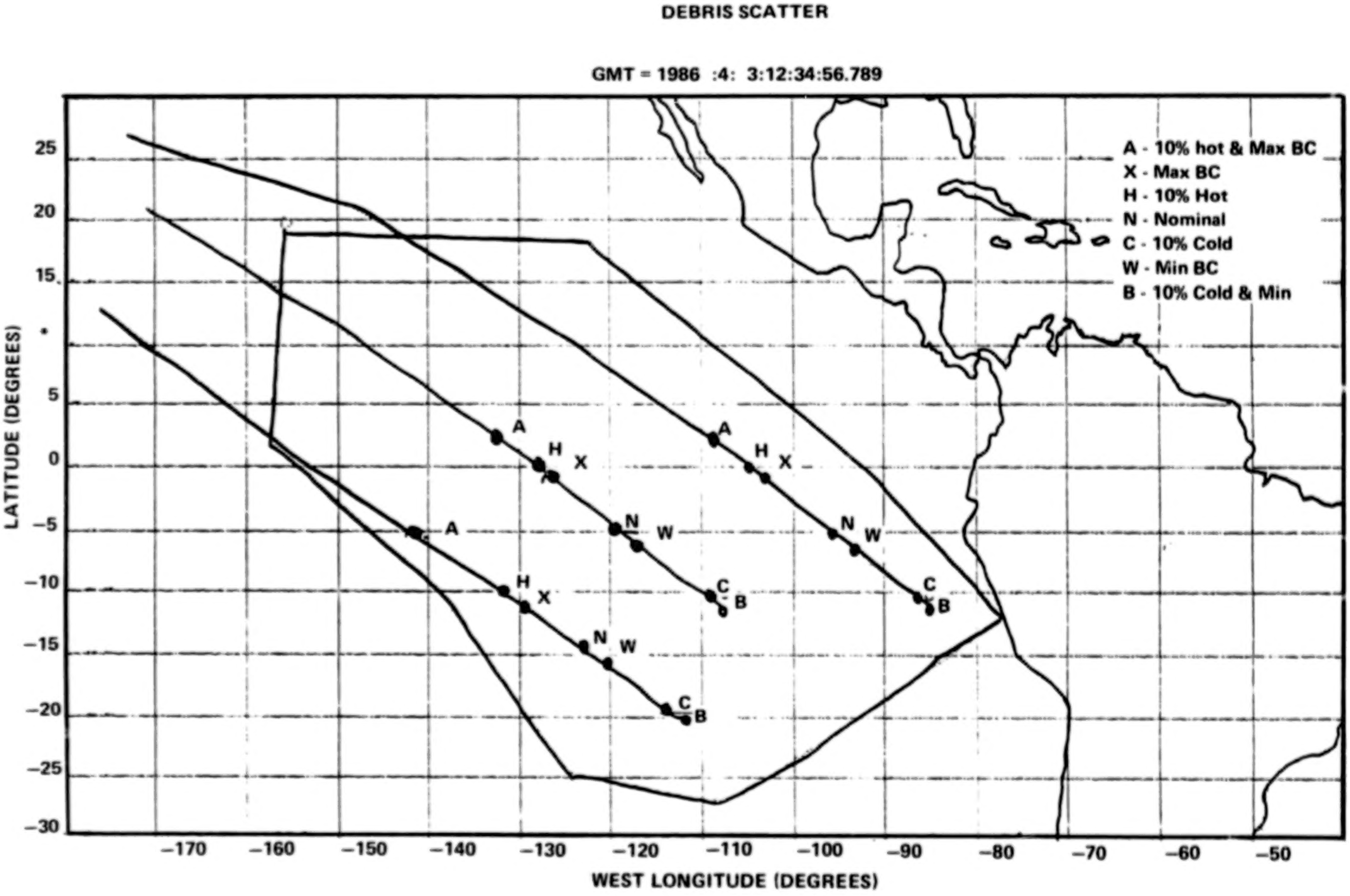
DEBRIS SCATTER
GMT = 1986 :4: 3:12:34:56.789
A - 10% hot & Max BC
X - Max BC
H - 10% Hot
N - Nominal
C - 10% Cold
W - Min BC
B - 10% Cold & Min
A
H
X
N
W
C
B
LATITUDE (DEGREES)
25
20
15
5
0
−5
−10
−15
−20
−25
−30
−170
−160
−150
−140
−130
−120
−110
−100
−90
−80
−70
−60
−50
WEST LONGITUDE (DEGREES)

Figure A-2. Single Burn Maneuver

Table A-2.1 2-Burn Maneuver Sequence

FIRST OF TWO POST MANEUVER CONDITIONS

OPPORTUNITY		COLD/ MIN BC	MIN BC	COLD	NOMINAL	HOT	MAX BC	HOT/ MAX BC
1	FUEL(LBS)	270	298	270	298	326	298	328
	BURN TIME (MIN)	7	7	7	7	7	7	7
	DELTA-V (FT/SEC)	64	70	64	70	77	70	77
	APOGEE(KM)	276	276	276	276	276	276	276
	PERIGEE(KM	222	215	222	215	208	215	208
2	FUEL(LBS)	270	298	270	298	327	298	327
	BURN TIME (MIN)	7	7	7	7	7	7	7
	DELTA-V (FT/SEC)	64	70	64	70	77	70	77
	APOGEE(KM)	276	276	276	276	276	276	276
	PERIGEE(KM	222	215	222	215	208	215	208
3	FUEL(LBS)	270	298	270	298	327	298	327
	BURN TIME (MIN)	7	7	7	7	7	7	7
	DELTA-V (FT/SEC)	64	70	64	70	77	70	77
	APOGEE(KM)	276	276	276	276	276	276	276
	PERIGEE(KM)	222	215	222	215	208	215	208

Table A-2.2 2-Burn Maneuver Sequence

SECOND OF TWO POST MANEUVERS CONDITIONS

OPPORTUNITY		COLD/ MIN BC	MIN BC	COLD	NOMINAL	HOT	MAX BC	HOT/ MAX BC
1	FUEL(LBS)	528	578	528	578	630	578	630
	BURN TIME (MIN)	14.7	14.7	14.7	14.7	14.7	14.7	14.7
	DELTA-V (FT/SEC)	126	138	126	138	151	138	151
	APOGEE(KM)	264	261	264	261	256	261	256
	PERIGEE(KM)	89	72	89	72	54	72	54
2	FUEL(LBS)	528	578	528	578	630	578	630
	BURN TIME (MIN)	14.7	14.7	14.7	14.7	14.7	14.7	14.7
	DELTA-V (FT/SEC)	126	138	126	138	151	138	151
	APOGEE(KM)	263	260	263	260	256	260	256
	PERIGEE(KM)	89	72	89	72	54	72	54
3	FUEL(LBS)	528	578	528	578	630	578	630
	BURN TIME (MIN)	14.7	14.7	14.7	14.7	14.7	14.7	14.7
	DELTA-V (FT/SEC)	126	138	126	138	151	138	151
	APOGEE(KM)	263	260	263	260	256	260	256
	PERIGEE(KM)	89	71	89	71	53	71	53

Table B-2.

2-BURN MANEUVER SEQUENCE	DEBRIS SCATTER (KM)
NOMINAL TO HOT/MAXIMUM BC	2300
NOMINAL TO MAXIMUM BC	800
NOMINAL TO HOT	1500
NOMINAL TO COLD	2100
NOMINAL TO MINIMUM BC	150
NOMINAL TO COLD/MINIMUM BC	2300
*HOT/MAXIMUM TO COLD/MINIMUM BC	4600

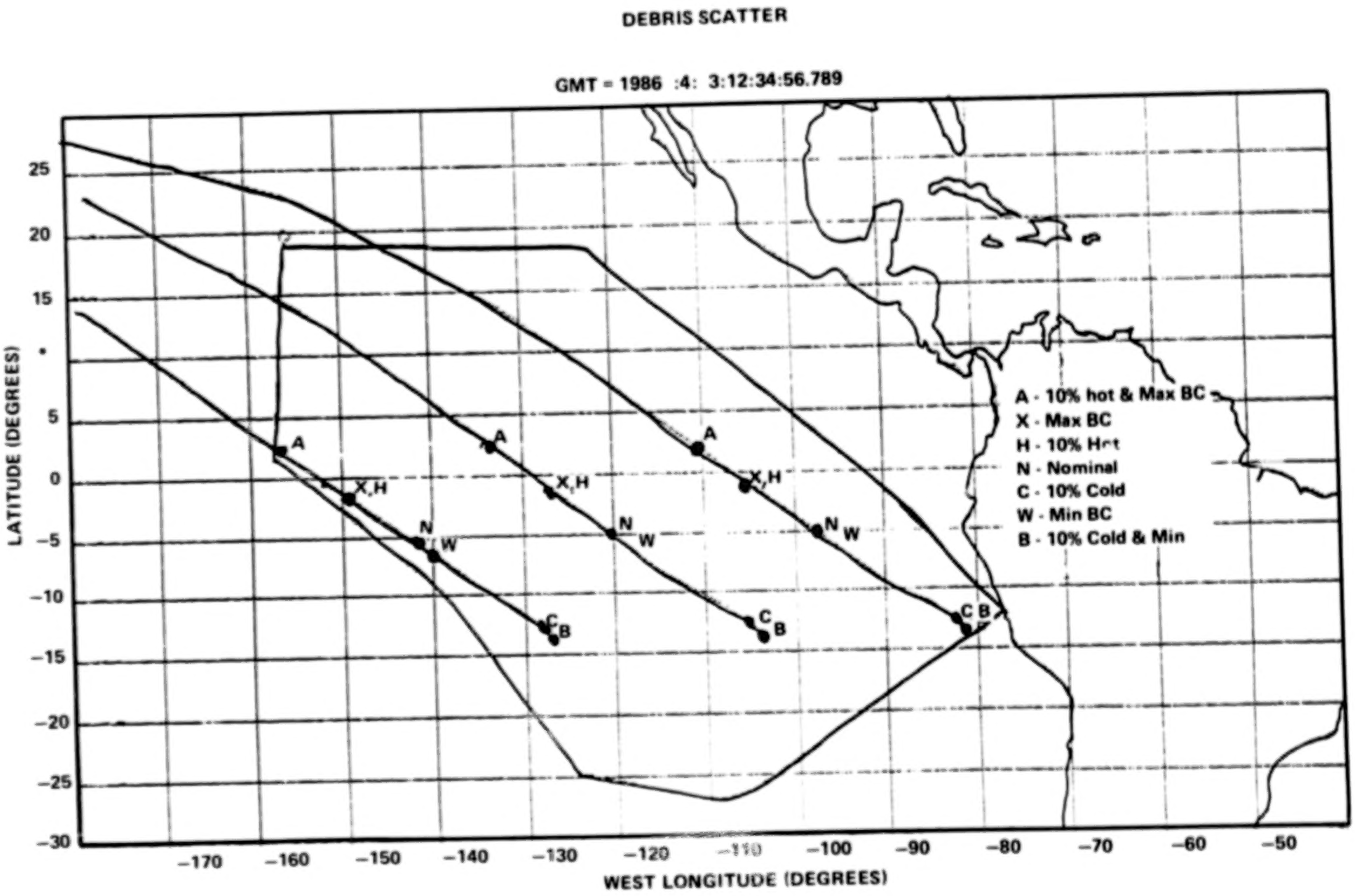
DEBRIS SCATTER
GMT = 1986 :4: 3:12:34:56.789
LATITUDE (DEGREES)
25
20
15
5
0
−5
−10
−15
−20
−25
−30
WEST LONGITUDE (DEGREES)
−170
−160
−150
−140
−130
−120
−110
−100
−90
−80
−70
−60
−50
A
X,H
N
W
C
B
A - 10% hot & Max BC
X - Max BC
H - 10% Hot
N - Nominal
C - 10% Cold
W - Min BC
B - 10% Cold & Min

Figure A-3. 2-Burn Maneuver Sequence

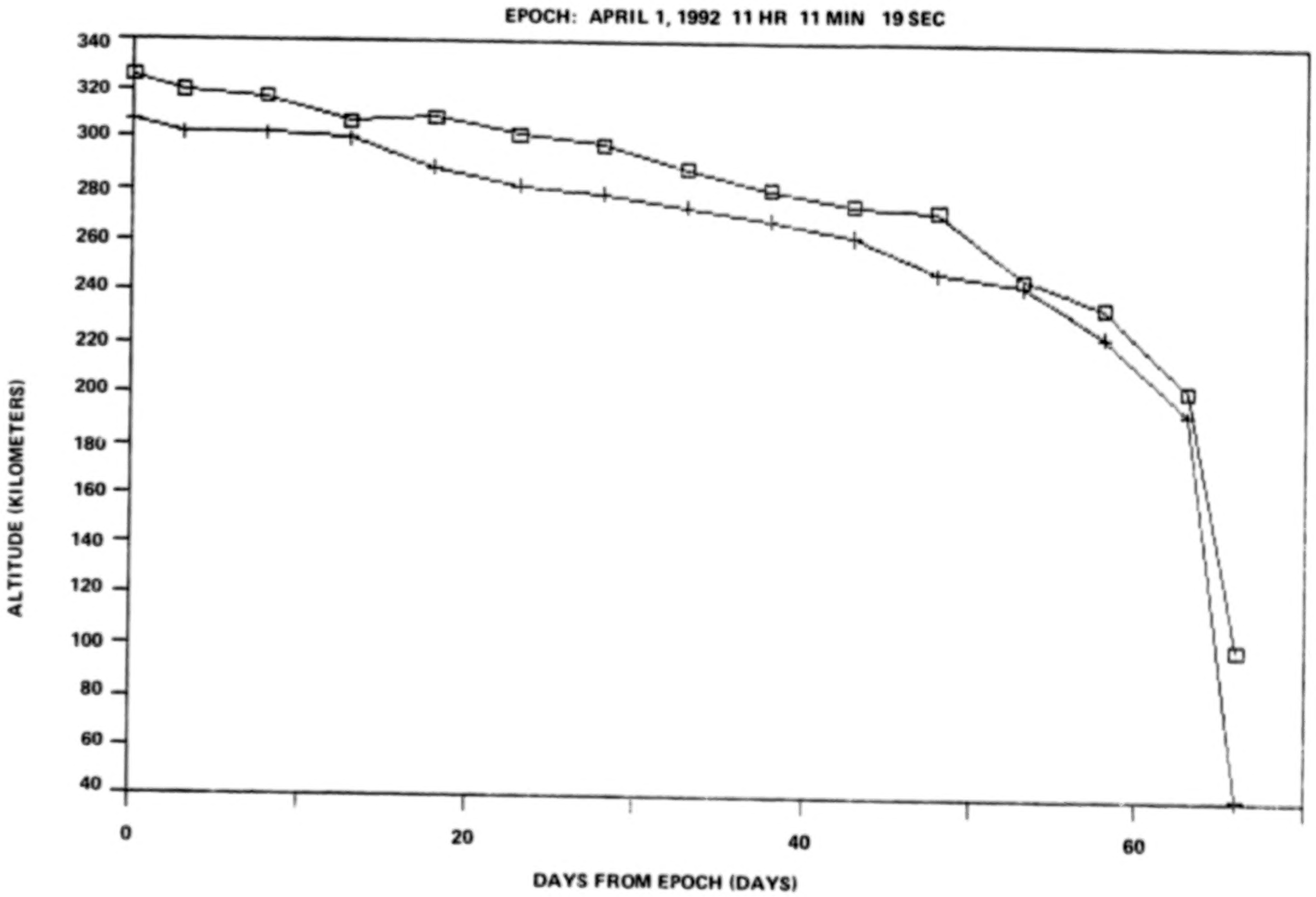

Figure A-4. Altitude vs Time Decay (315 km cir.)

N89-15957

EUVE/XTE ORBIT DECAY STUDY

K. Richon, Goddard Space Flight Center

J. Hashmall, M. Lambertson, and T. Phillips, Computer Sciences Corporation

ABSTRACT

The Explorer Platform (EP) program currently comprises two missions, the Extreme Ultraviolet Explorer (EUVE) and the X-ray Timing Explorer (XTE), each of which consists of a scientific payload mounted to the EP. The EP has no orbit maintenance capability. The EP with the EUVE payload will be launched first. At the end of the EUVE mission, the spacecraft will be serviced by the Space Transportation System (STS), and the EUVE instrument will be exchanged for the XTE. The XTE mission will continue until reentry or reservicing by the STS.

Because the missions will be using the EP sequentially, the orbit requirements are unusually constrained by orbit decay rates. The initial altitude must be selected so that, by the end of the EUVE mission (2.5 years), the spacecraft will have decayed to an altitude within the STS capabilities. In addition, the payload exchange must occur at an altitude that ensures meeting the minimum XTE mission lifetime (3 years) because no STS reboost will be available.

Studies were performed using the Goddard Mission Analysis System to estimate the effects of mass, cross-sectional area, and solar flux on the fulfillment of mission requirements. In addition to results from these studies, conclusions are presented as to the accuracy of the Marshall Space Flight Center solar flux predictions.

1.0 INTRODUCTION

The Extreme Ultra-Violet Explorer (EUVE) will be housed on the Explorer Platform (EP) and launched in August 1991. This study is based on the following mission scenario:

> After a nominal 2.5-year mission, the Space Transportation System (STS) will rendezvous with the EP and replace the EUVE payload with the X-ray Timing Experiment (XTE). It is assumed that XTE will remain in orbit for at least an additional 3 years.

During the 5.5-year combined EP lifetime, the spacecraft altitude will gradually decrease, primarily because of the effects of atmospheric drag. This gradual decrease in altitude over time is called orbit decay.

The EP has no propulsion system and, thus, no capability of boosting to a higher altitude. No plans currently exist to raise its orbit during the payload exchange; therefore, the EP orbit over the entire 5.5 years will be determined by the initial EUVE altitude and by the rate of orbit decay.

To ensure that the second payload, XTE, remains in orbit for its nominal mission lifetime, EUVE must be placed in an initial orbit that is high enough to prevent the EP from reentering for at least 5.5 years after launch. Because the current maximum rendezvous altitude for the STS is 500 kilometers (km), the EP orbit must decay to 500 km or less by the end of 2.5 years to allow for payload changeout. The purpose of this study was to determine the constraints placed on the initial EUVE altitude by the combined mission requirements. The study was performed by modeling the orbit decay over a range of conditions to determine initial altitudes (EUVE epoch altitudes) that would meet all altitude requirements.

2.0 ANALYSIS

The rate of decay of a spacecraft's orbit is approximately proportional to the deceleration due to aerodynamic drag, F_D/m, where F_D is the aerodynamic drag force and m is the spacecraft mass. F_D/m is given by

$$F_D/m = (C_DA/2m)\ \rho V^2$$

where the ratio in parentheses is generally referred to as the ballistic coefficient, ß. C_D is the drag coefficient, A is the cross-sectional area, ρ is the atmospheric density, and V is the spacecraft velocity relative to the atmosphere. For a spacecraft in a given orbit, the factors influencing the rate of orbit decay will be mass, area, drag coefficient, and atmospheric density. The first three of these are conveniently combined into the ballistic coefficient.

Atmospheric density depends on altitude and solar flux. During periods of high solar flux, the upper atmosphere absorbs energy and the atmospheric density increases. The Goddard Mission Analysis System (GMAS) uses the initial orbit, spacecraft parameters, and monthly values of the solar flux to compute and integrate the equations of motion and to predict the orbit decay over a specified period. The Harris-Priester atmospheric density model was used.

The study was performed using three spacecraft cross-sectional areas, three spacecraft mass combinations, and two solar flux levels. In all cases, the drag coefficient was assumed to be 2.2. The mass and area values used are listed in Table 1. These values were used to bound the problem until specific design data become available. This table defines the nine cases arising from combinations of mass and cross-sectional area.

The mass values used are based on each mission's nominal mass and contingency mass. For each mission, the nominal mass was used as a low-mass case, the nominal mass plus the contingency mass was used as a high-mass case, and the mean of these two was used as a median-mass case. Whenever one mass case (high, low, or median) was used for the EUVE portion of the mission, the corresponding mass case was used for the XTE portion of the mission.

The three spacecraft areas used were computed as the estimated spacecraft area and areas 20-percent higher and 20-percent lower than this value. EUVE and XTE were assumed to have the same average cross-sectional area. The masses and areas used to form the nine cases are listed below.

EUVE Mass (kg)	XTE Mass (kg)	Spacecraft Area (m^2)
2601.4	2844.0 (low mass)	14.9 (nominal - 20%)
2814.5	3114.4 (median mass)	18.6 (nominal)
3028.2	3387.4 (high mass)	22.3 (nominal + 20%)

Table 1. Parameters for Each Case Definition

Case No.	Cross-Sectional Area (m^2)	EUVE		XTE	
		Mass (kg)	Ballistic Coefficient $(m^2/kgx10^{-3})$	Mass (kg)	Ballistic Coefficient $(m^2/kgx10^{-3})$
1	14.9	2601.4	6.30	2844.0	5.76
2	18.6	2601.4	7.87	2844.0	7.12
3	22.3	2601.4	9.43	2844.0	8.63
4	14.9	2814.5	5.82	3114.4	5.26
5	18.6	2814.5	7.27	3114.4	6.57
6	22.3	2814.5	8.71	3114.4	7.88
7	14.9	3028.2	5.41	3387.4	4.84
8	18.6	3028.2	6.75	3387.4	6.04
9	22.3	3028.2	8.35	3387.4	7.24

The solar flux levels used were based on the August 21, 1987, Marshall Space Flight Center (MSFC) 97.7-percent and 50-percent solar flux predictions. These predictions are based on a statistical model using data from all previous solar cycles. In principle, there is a 50-percent chance that the actual solar flux will be below the 50-percent prediction, and a 97.7-percent chance that it will be below the 97.7-percent prediction. Figure 1 plots the solar flux prediction levels used as functions of time.

The assumptions made in this analysis are as follows:

- The total EUVE/XTE mission lasts 5.5 years.
- The EUVE mission duration is 2.5 years, from August 31, 1991, to March 1, 1994.
- The XTE mission duration is 3 years, from March 1, 1994, to March 2, 1997.
- The EUVE spacecraft is placed in a circular orbit with an inclination of 28.5 degrees on August 31, 1991.
- The payload changeout occurs on March 1, 1994, and must be performed at or below a 500-km altitude by the STS. The EP orbit remains unchanged.
- The EP has no boost capability and receives no boost from the STS.
- The XTE mission must be at or above 300 km at the end of the mission (5.5 years after launch). This is the altitude at which reentry was considered imminent.

The first part of this analysis consisted of determining the maximum and minimum EUVE launch epoch altitudes for each combination of mass, area, and solar flux. The maximum initial altitude was determined by searching for the highest EUVE launch altitude that would decay to 500 ± 1 km at the end of 2.5 years (the end of the EUVE mission).

The minimum initial altitude was determined by searching for the lowest EUVE epoch altitude that would decay to 300 ± 2 km at the end of 5.5 years. The spacecraft mass was changed to the XTE value during the propagation at 2.5 years from epoch, and restarted for an additional 3-year period.

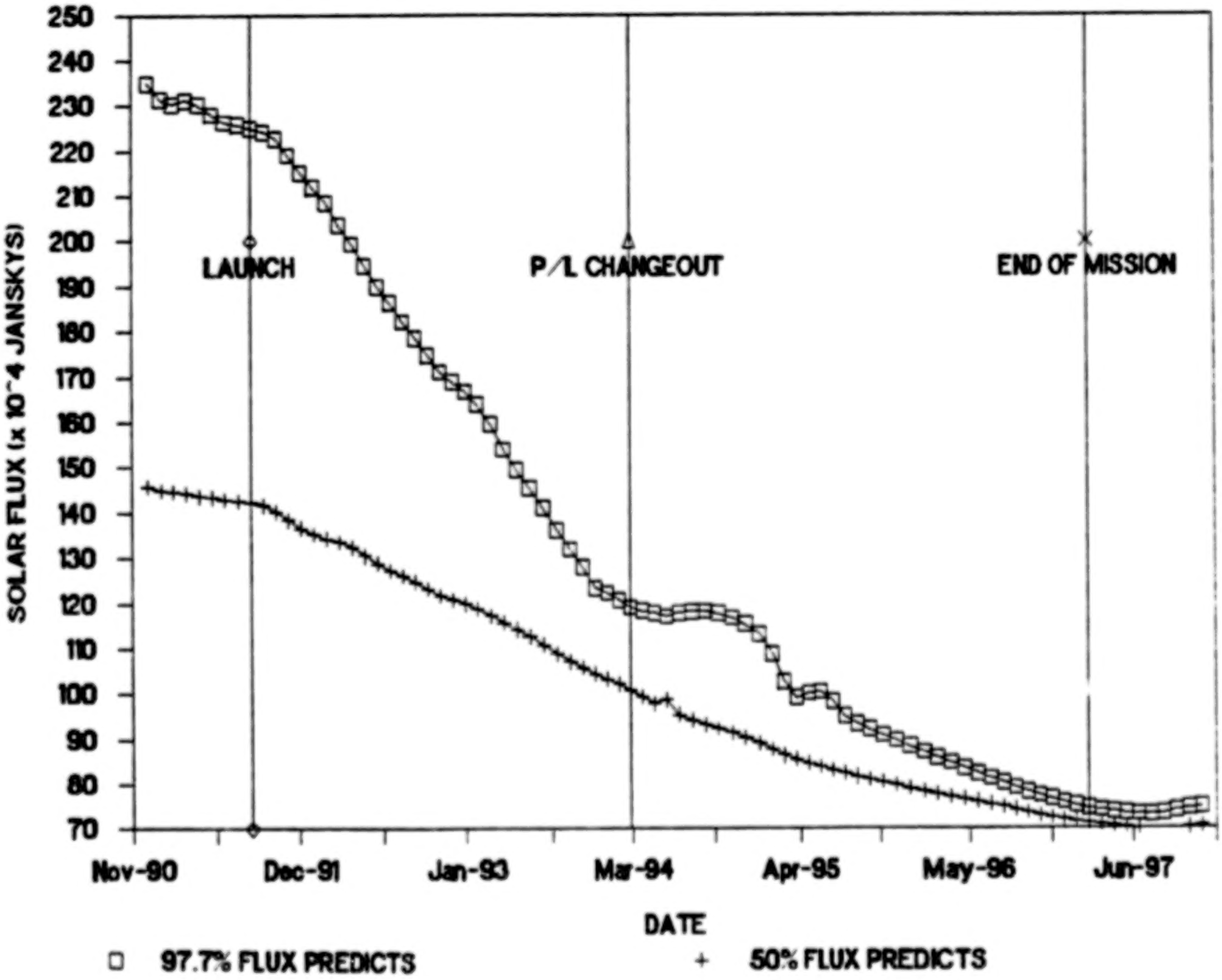

Figure 1. MSFC Solar Flux Predictions as of August 21, 1987

The maximum and minimum altitudes define an altitude band for each mass-area-flux combination; any altitude within the band will meet the mission requirements for the flux level used.

The 97.7-percent solar flux level is commonly used for mission planning as a worst-case scenario because the orbit decays faster at a higher flux level, and thus the mission life is shorter. However, because one EUVE/XTE mission requirement is that the EUVE spacecraft altitude be 500 km or less after 2.5 years, planning with the 97.7-percent solar flux level can mean that this goal is not met. If the flux level is actually much lower, 50-percent for example, the atmosphere will be less dense than predicted, and the orbit decay will be slower. Thus, the satellite would be above the 500-km maximum payload changeout altitude after 2.5 years. For this reason, two sets of altitude bands, corresponding to the 97.7-percent and the 50-percent solar flux levels, were determined for use in mission planning for each mass and area combination.

The second part of the study consisted of recomputing all the previous cases, using the exact same parameters including the initial altitudes, except that the flux level was changed to the alternate level. That is, all runs made at the 97.7-percent solar flux level were remade using the 50-percent solar flux level, and vice versa. The purpose of this half of the analysis was to illustrate the effects on planning with potential solar flux prediction error levels. These cases are the "what if" cases; they show what happens if the mission is planned using too high or too low a solar flux level and indicate the critical nature of the solar flux in mission planning, particularly near launch time, when commitment to a final launch altitude will be made.

The purpose of the third section of the analysis was to examine the accuracy of the MSFC solar flux predictions and, in particular, to determine whether the difference in predicted and actual values can be as great as between the 97.7- and 50-percent solar flux profiles used in the first two parts of this study. This was accomplished by examining MSFC predictions and actual data for the previous solar cycle. Using a 97.7-percent prediction and actual data from solar cycle 21, maximum and minimum initial altitudes were determined using the same method outlined above, assuming a launch on May 1, 1982. This launch date was chosen so that it occurred at the same place in relation to the cycle 21 solar peak as the current EUVE launch date is to the predicted solar peak. Then, as in the second half of the analysis, the orbit from both initial altitudes was propagated using the actual solar flux data.

3.0 RESULTS

The results of the study are summarized in Tables 2 and 3. In each table, the first column indicates the case number, corresponding to one mass-area-flux combination. Cases with the same mass and area have the same numerical part of the case number (e.g., 1 in 1A), while those with the same flux level have the same letter.

The second column contains the cross-sectional area for both spacecraft in square meters. The third and fifth columns contain the masses of the EUVE and XTE spacecraft, respectively, in kilograms. The fourth and sixth columns contain the ballistic coefficients, ß, of the two spacecraft in square meters per kilogram.

The seventh column contains the EUVE epoch initial altitude in kilometers. The maximum altitude is on the top line for each case, and the minimum altitude is on the second line. The eighth and ninth columns contain the altitudes after 2.5 years and 5.5 years, respectively, in kilometers. The tenth and eleventh columns contain the altitudes reached using the same initial altitude but the alternate flux level.

Figure 2 illustrates the initial altitude band as a function of area and mass for both solar flux levels. The bands shown represent the acceptable altitude range for each of the nine cases at each flux level.

The effect of area on the altitude range can be seen by comparing consecutive cases that have the same spacecraft mass, such as 1A, 2A, and 3A. For this mass, an increase in cross-sectional area from 14.9 to 22.3 m^2 causes a 16-km difference in the maximum initial altitude required and a 28-km difference in the minimum initial altitude. The larger the area, the higher the altitude band must be. The range, or the size of the altitude band, is also affected by the area; it can be seen for the same cases that the smallest area allows a 29-km acceptable altitude band but the largest area decreases the acceptable altitude band to 17 km.

ORIGINAL PAGE IS
OF POOR QUALITY

Table 2. Upper and Lower Initial EUVE Altitudes at 97.7-Percent Flux Level

Spacecraft Parameters							97.7% Solar Flux		50% Solar Flux	
Case No.	X-Sect Area (m^2)	EUVE		XTE		EUVE Epoch Altitude (km)	2.5 Yr Altitude (km)	5.5 Yr Altitude (km)	2.5 Yr Altitude (km)	5.5 Yr Altitude (km)
		Mass (kg)	β $(m^2/kg$ $x10^{-3})$	Mass (kg)	β $(m^2/kg$ $x10^{-3})$					
1A	14.9	2601.4	6.30	2844.0	5.76	547.10* **518.13**	499.99 434.47	479.88 301.34	532.25 494.49	524.30 479.16
2A	18.6	2601.4	7.87	2844.0	7.12	555.68 533.54	500.05 445.96	473.78 301.51	538.98 509.79	529.96 494.89
3A	22.3	2601.4	9.43	2844.0	8.63	563.44 546.44	500.00 455.58	466.81 301.46	545.22 522.63	535.33 508.09
4A	14.9	2814.5	5.82	3114.4	5.26	544.31* **512.54**	499.97 429.82	481.89 300.93	530.12 488.86	522.64 473.50
5A	18.6	2814.5	7.27	3114.4	6.57	552.41 527.82	499.83 441.20	476.23 301.55	536.34 504.02	527.79 489.10
6A	22.3	2814.5	8.71	3114.4	7.88	559.98 540.61	500.02 450.74	470.54 301.55	542.42 516.75	533.02 502.18
7A	14.9	3028.2	5.41	3387.4	4.84	541.85* **507.42**	499.99 425.63	483.58 301.70	528.26 483.72	521.21 468.34
8A	18.6	3028.2	6.75	3387.4	6.04	549.66* **522.56**	499.95 436.87	478.67 301.26	534.22 498.73	526.13 483.78
9A	22.3	3028.2	8.35	3387.4	7.24	556.89 535.25	500.04 446.32	473.54 301.88	539.94 511.35	531.00 496.75

* These initial altitudes satisfy requirements at both flux levels.

ORIGINAL PAGE IS
OF POOR QUALITY

Table 3. Upper and lower Initial EUVE Altitudes at 50-Percent Flux Level

Spacecraft Parameters							50 % Solar Flux		97.7% Solar Flux	
		EUVE		XTE						
Case No.	X-Sect Area (m^2)	Mass (kg)	β (m^2/kg $x10^{-3}$)	Mass (kg)	β (m^2/kg $x10^{-3}$)	EUVE Epoch Altitude (km)	2.5 Yr Altitude (km)	5.5 Yr Altitude (km)	2.5 Yr Altitude (km)	5.5 Yr Altitude (km)
1B	14.9	2601.4	6.30	2844.0	5.76	**522.09*** 476.36	499.98 422.06	486.12 299.92	445.92 r 1.55yr	373.80
2B	18.6	2601.4	7.87	2844.0	7.12	526.66 489.25	499.97 432.76	482.11 301.39	421.15 r 1.47yr	r 4.19yr
3B	22.3	2601.4	9.43	2844.0	8.63	530.98 500.00	499.99 441.70	477.86 300.31	380.21 r 1.40yr	r 3.07yr
4B	14.9	2814.5	5.82	3114.4	5.26	**520.63*** 471.64	499.97 417.83	487.45 300.43	451.91 r 1.56yr	401.31
5B	18.6	2814.5	7.27	3114.4	6.57	524.97 484.41	500.00 428.38	483.92 301.78	431.78 r 1.48yr	r 4.99yr
6B	22.3	2814.5	8.71	3114.4	7.88	529.04 495.07	499.98 437.22	400.11 301.02	402.23 r 1.42yr	r 3.48yr
7B	14.9	3028.2	5.41	3387.4	4.84	**519.73*** 467.24	500.47 413.82	489.16 299.19	457.53 r 1.59yr	418.97
8B	18.6	3028.2	6.75	3387.4	6.04	**523.46*** 479.94	499.99 424.34	485.38 301.19	439.65 r 1.51yr	330.55
9B	22.3	3028.2	8.35	3387.4	7.24	527.33 490.50	499.98 433.04	481.98 300.67	416.46 r 1.44yr	r 4.00yr

* These initial altitudes satisfy requirements at both flux levels.

NOTE: r x.xx yr means reentry after x.xx years

The effect of mass on the altitude band is also shown in Figure 2. Comparison of cases 1A, 4A, and 7A shows that an increase in mass (from lowest to highest) causes a difference of 5.25 km in maximum altitude required and a difference of 10.71 km in minimum altitude. An increase in mass also causes a slight increase in the range of acceptable altitudes. The total effect of the mass is about half that of the total effect of the area. The figure shows a uniformly increasing epoch altitude with increasing ballistic coefficient.

The effect of solar flux is also indicated in Figure 2. A cursory glance shows that the 97.7-percent solar flux level causes the altitude band to be higher than that defined for the 50-percent level. This is simply because the satellite will decay faster at a higher flux level, and thus the band needs to be higher to compensate. The altitude range is also shorter for the 97.7-percent flux level. Altitude selection is less flexible if the 97.7-percent solar flux level is used, and less room exists for orbit injection error.

Figures 3 and 4 illustrate orbital decay using the 97.7-percent and 50-percent solar flux levels for the median mass and nominal area cases (5A and 5B). The two solid lines in Figure 3 show the orbit decay from the maximum and minimum altitudes determined using the 97.7-percent solar flux (case 5A). The lines defined by the symbols correspond to the 50-percent flux level and show the orbit decay from the same altitudes if the solar flux is actually at the 50-percent prediction level. The mission constraints cannot be met using this maximum altitude if the flux level is 50-percent, because the satellite orbit does not decay to 500 km in the 2.5-year requirement; the minimum altitude shown almost meets the 500-km constraint with a 50-percent solar flux level (within 4 km). The minimum altitudes indicated with an asterisk in Table 2 meet the mission constraints ($\leq$500 km at 2.5 years and $\geq$300 km at 5.5 years) at both flux levels. No maximum altitudes determined using the 97.7-percent flux level will satisfy the mission requirements if the 50-percent flux level occurs.

Figure 4 is identical to Figure 3, except that the mission planning and the altitude band definition were made using the 50-percent flux level (case 5B). The maximum and minimum altitudes are depicted by the two solid lines, and the lines defined by the symbols correspond to the orbit decay if a 97.7-percent solar flux

ORIGINAL PAGE IS
OF POOR QUALITY

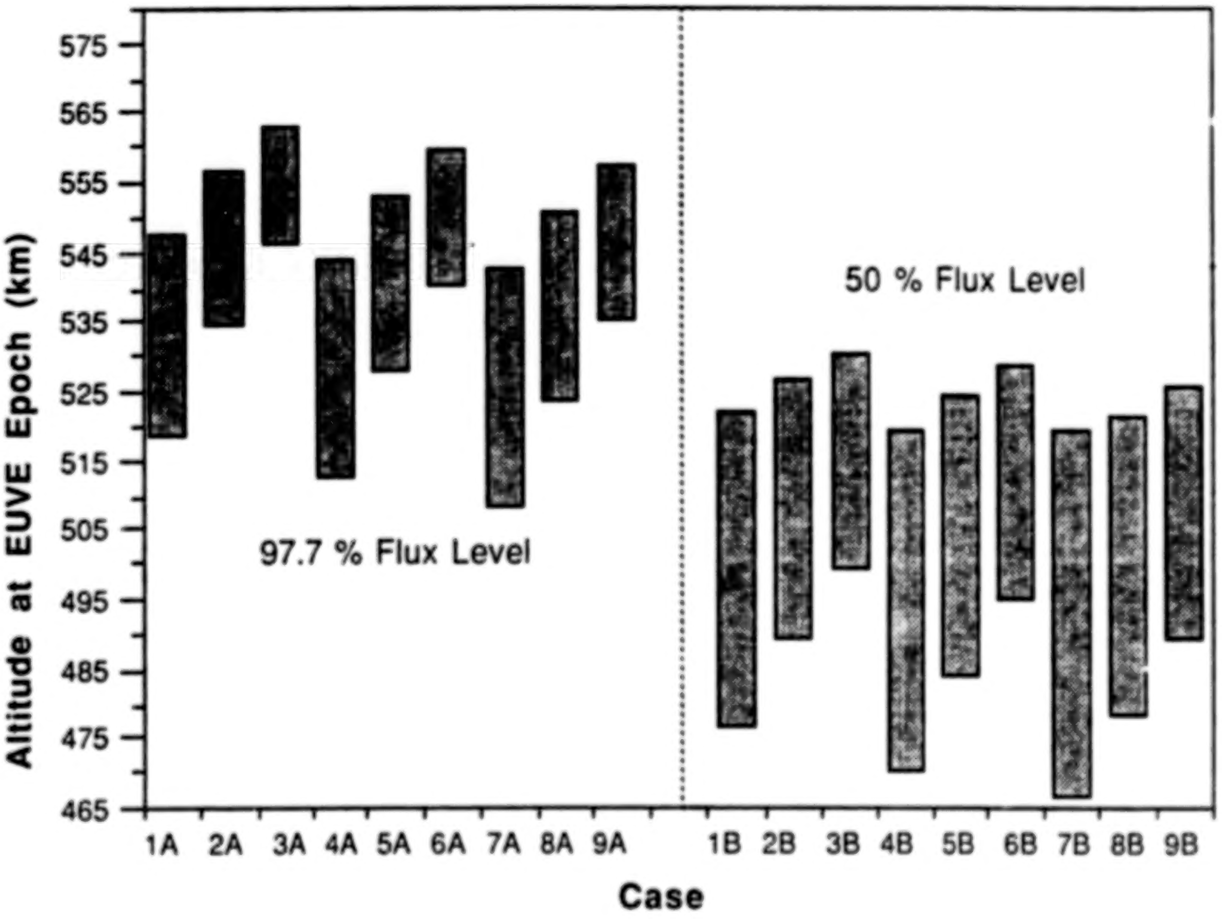

Figure 2. Altitude Ranges at Two Flux Levels (Altitudes in the Shaded Regions Meet Mission Requirements)

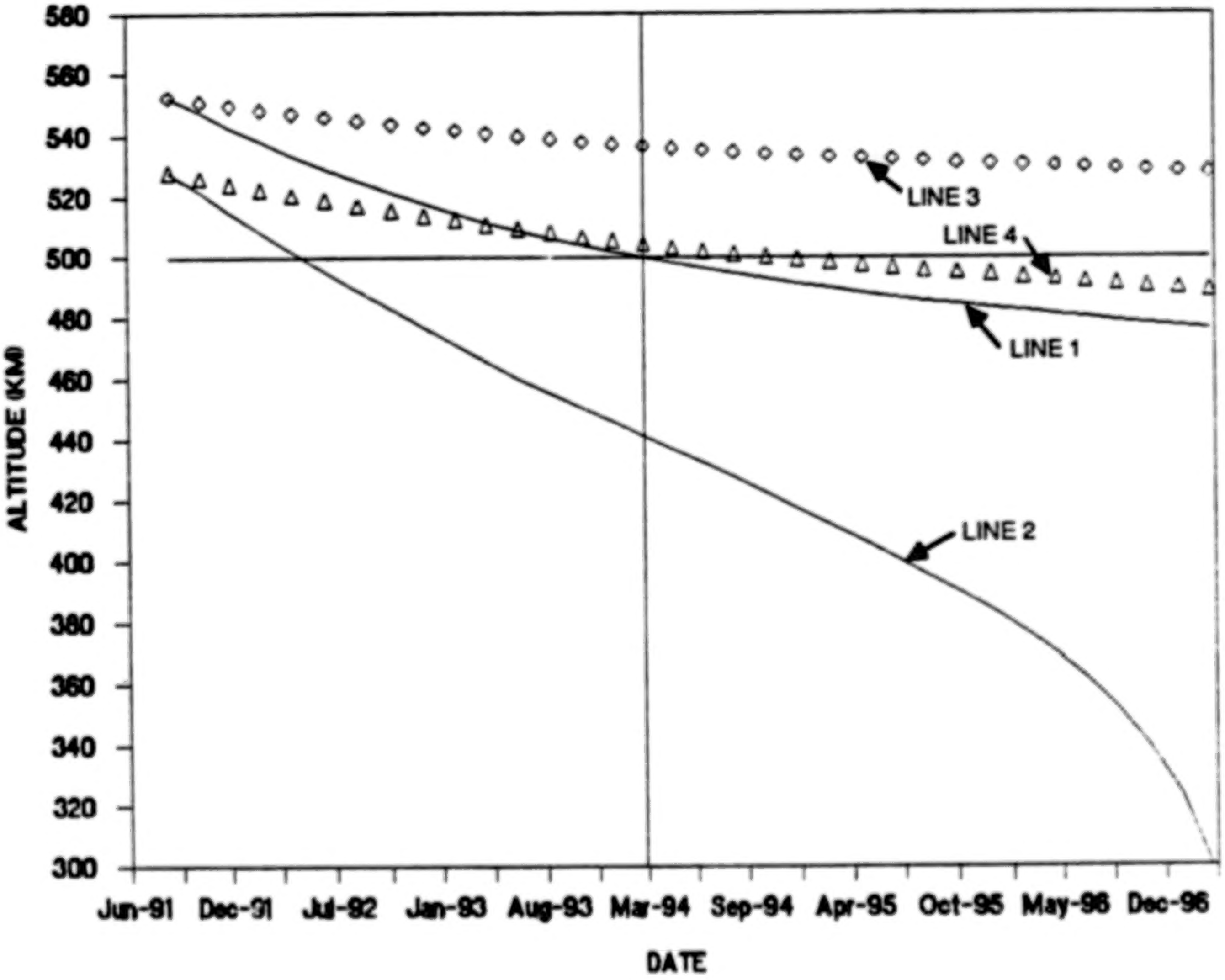

Figure 3. EUVE/XTE Orbit Decay Using 97.7-Percent Solar Flux

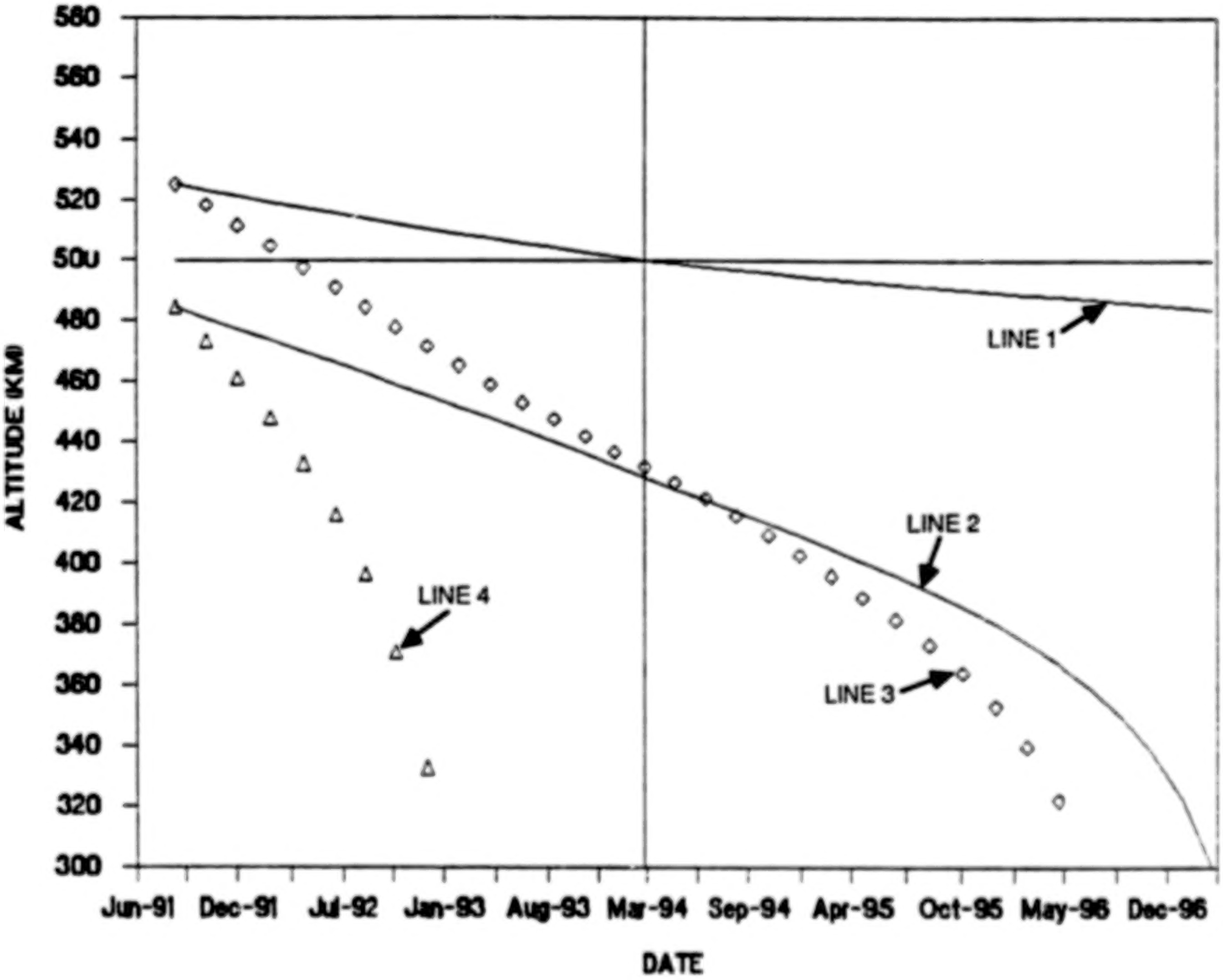

Figure 4. EUVE/XTE Orbit Decay Using 50-Percent Solar Flux

level is realized. If the actual flux level is 97.7-percent, the minimum EP lifetime (5.5 years) may not be met for the entire altitude band. The maximum altitudes in Table 3 that can satisfy both mission constraints are marked with an asterisk; no minimum altitudes calculated for the 50-percent flux level meet the mission requirements if the flux level is 97.7 percent. These graphs indicate what may happen if the solar flux level is not well known when final mission planning occurs.

The final altitude, at the end of 5.5 years, is extremely sensitive to the initial altitude, which can be seen by referring to Tables 2 and 3. For the median mass and nominal area (cases 5A and 5B), a comparison of the orbit decay from the maximum altitude for case 5B and the minimum altitude for case 5A, both with a 97.7-percent solar flux level, shows that a difference in initial altitude of 2.85 km can cause a 6-month difference in mission life. This can be seen graphically by comparing line 2 from Figure 3 to line 3 of Figure 4. This sensitivity is due in part to the end altitude of 300 km; if the satellite reaches 300 km too early, it will reenter very rapidly, in approximately 2 months. This sensitivity to initial altitude must be given serious consideration in planning the mission, and the area, mass, drag coefficient, and solar flux must be as well known as possible. It should be noted, however, that the sensitivity is decreased when the 50-percent solar flux level is used (only 4.02 km difference for the maximum altitude and 5.18 km for the minimum altitude in cases 5A and 5B).

Figure 5 shows the minimum and maximum EUVE launch epoch altitudes as a function of the EUVE ballistic coefficient at both flux levels. Because the XTE ballistic coefficients used in this study are linearly related to the corresponding EUVE ballistic coefficients, the arbitrary choice of EUVE parameters does not affect the results. The two bands shown in this figure represent the launch epoch altitude ranges at which mission requirements are met for the two flux levels. The bands overlap only in a small region. Only ballistic coefficients less than 0.0068 m^2/kg will meet the requirements at both flux levels, and then only launch epoch altitudes of approximately 496 to 518 km can be used. Outside this region, a deviation of flux level from the predicted level by the amount corresponding to the difference between the 97.7- and 50-percent levels will result in a failure to meet one or both of the mission requirements.

ORIGINAL PAGE IS
OF POOR QUALITY

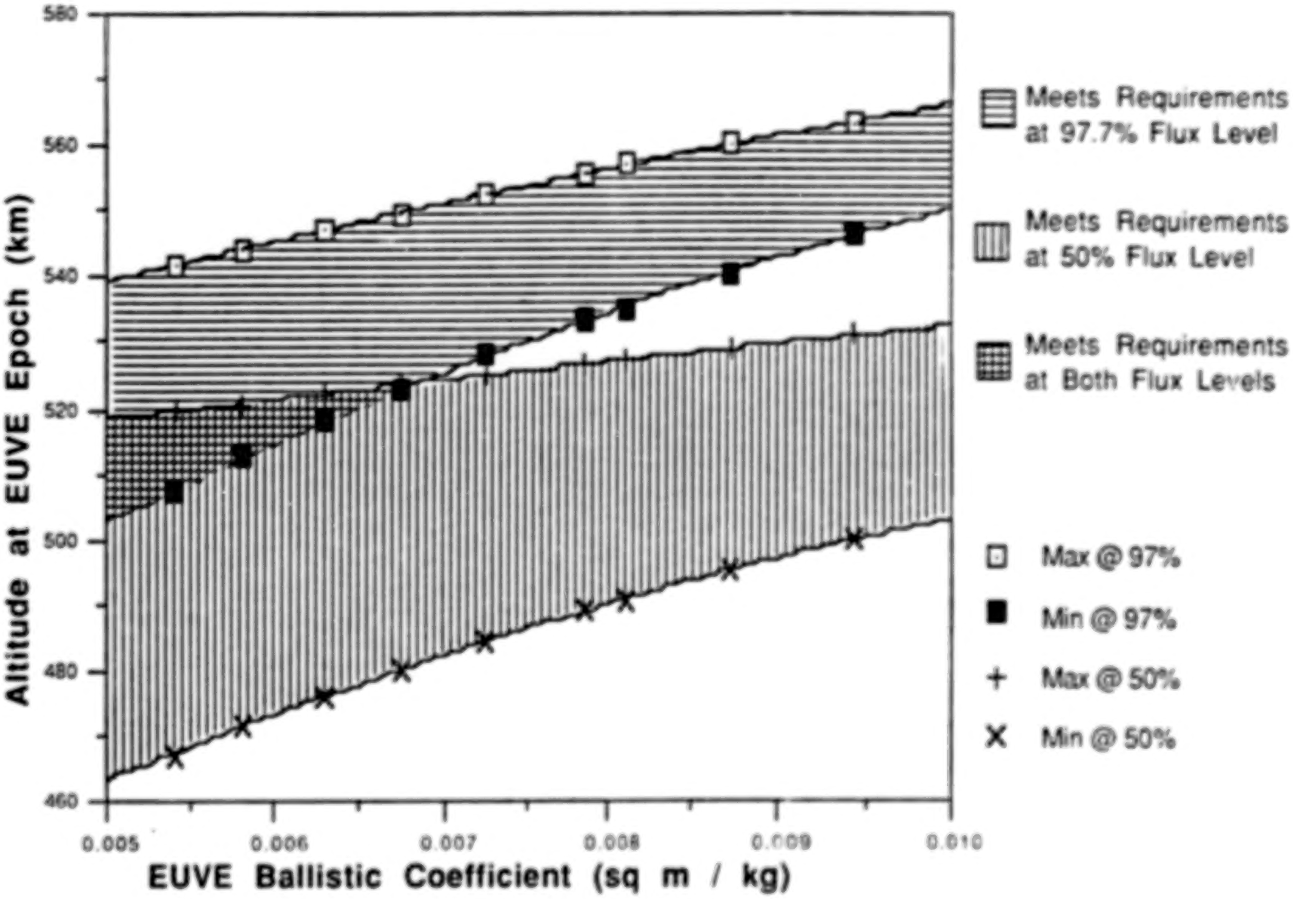

Figure 5. Range of EUVE Epoch Altitudes as a Function of Ballistic Coefficient

Figure 5 shows clearly that successful planning for the EP mission requires an uncertainty in flux-level predictions that is smaller than the difference between the 50- and 97.7-percent predictions used in this study for ballistic coefficients less than 0.0068. For this reason, the third part of the study was performed, to analyze the accuracy of MSFC predictions in the past, and to determine whether the difference in the 97.7- and 50-percent flux levels used above is realistic; that is, is it possible that MSFC predictions used for mission planning can have an error as great as that between the August 1987 97.7- and 50-percent prediction values.

Figure 6 illustrates the previous solar flux cycle (cycle 21) and two sets of MSFC predictions made for that cycle. The jagged line indicates the actual measured monthly values, and the dark line shows the 13-month smoothed data. The two thin lines above the smoothed data line are the 97.7- and 50-percent predictions made in April 1982. The two thin lines below the smoothed data are the 97.7- and 50-percent predictions made in September 1980. In both sets of predictions, the 97.7-percent predictions are higher than the 50-percent predictions. For cycle 21, the solar peak occurred in March 1981. A launch made in May 1982 occurs 14 months after the peak, the same time difference as between the EUVE launch and the predicted solar flux peak (cycle 22).

As shown in Figure 6, predictions made 2.5 years before a May 1982 launch would have underestimated the solar flux level; the results of a mission planned using the September 1980 97.7-percent solar flux predictions would be similar to those shown in Table 3 (the total mission lifetime would be shortened considerably). A more realistic scenario for a May 1982 launch would be to plan the mission using solar flux predictions made as close as possible to launch, in this instance, the April 1982 MSFC 97.7-percent predictions. Table 4 shows the initial altitudes determined for a May 1982 launch using the April 1982 97.7-percent prediction data, for the area and mass cases 2, 5, and 8. After the initial altitudes were determined, the cases were rerun using the actual 13-month smoothed solar flux data. The results are very similar to those shown in Table 2 for the same cases, although the minimum altitude always meets all mission requirements in the cycle 21 analysis. This suggests that the difference between the April 1982 97.7-percent predictions and the actual solar flux is close to the difference between the August

ORIGINAL PAGE IS
OF POOR QUALITY

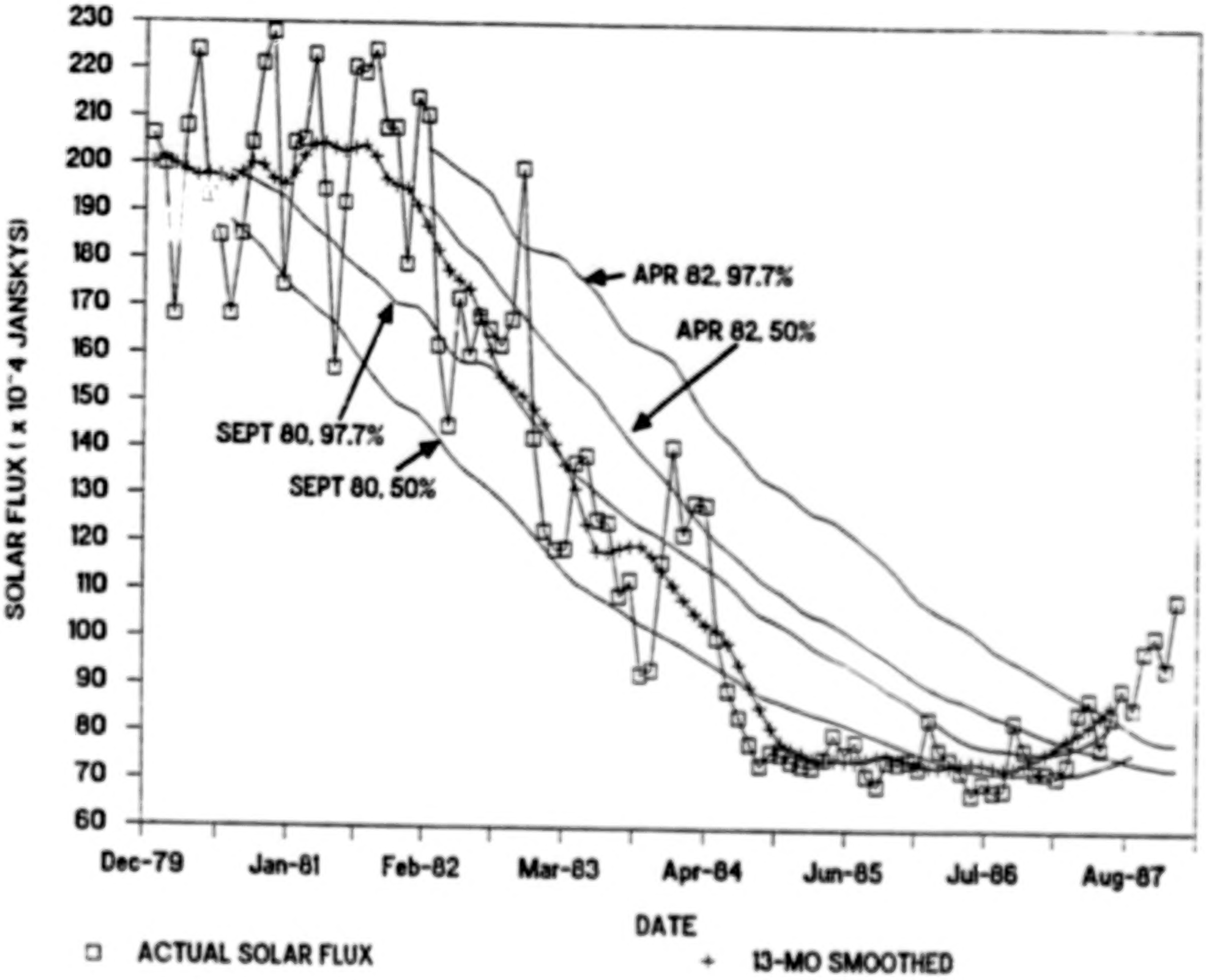

Figure 6. MSFC Solar Flux Prediction Comparison of Actual Data to 97.7- and 50-Percent Predictions

Table 4. Upper and Lower Initial EUVE Altitudes at April 1982 97.7-Percent Flux Level

Spacecraft Parameters							97.7% Solar Flux		Actual Solar Flux	
Case No.	X-Sect Area (m²)	EUVE		XTE		EUVE Epoch Altitude (km)	2.5 Yr Altitude (km)	5.5 Yr Altitude (km)	2.5 Yr Altitude (km)	5.5 Yr Altitude (km)
		Mass (kg)	β (m²/kg $\times 10^{-3}$)	Mass (kg)	β (m²/kg $\times 10^{-3}$)					
2C	18.6	2601.4	7.87	2844.0	7.12	552.08 **531.16** *	500.84 453.43	468.57 299.51	530.16 500.40	521.10 485.09
5C	18.6	2814.5	7.27	3114.4	6.57	548.81 **525.50** *	500.24 448.46	471.19 299.30	527.77 494.79	519.22 479.46
8C	18.6	3028.2	6.75	3387.4	6.04	546.06 **520.33** *	500.03 444.03	473.78 300.72	525.90 489.69	517.83 474.34

* These initial altitudes satisfy requirements at both flux levels.

1987 97.7- and 50-percent predictions. The MSFC predictions close to launch can be as inaccurate as the difference between these two flux-prediction levels.

4.0 CONCLUSIONS

The nominal GSFC Flight Dynamics Division (FDD) scenario for orbit lifetime early mission planning uses the 97.7-percent solar flux predictions. The result of using 97.7-percent solar flux predictions for mission planning while only a 50-percent solar flux level is realized is that the spacecraft may take longer than 2.5 years to reach the 500-km payload changeout altitude; therefore, either the XTE payload changeout will have to be delayed, or the STS will have to rendezvous with the EP at altitudes above 500 km, ranging from 545.22 to 502.18 km. If 50-percent solar flux predictions are used for mission planning and the flux is actually at the 97.7-percent flux level, the lifetime of both payloads will be severely jeopardized and, in some cases, the total lifetime of the EP would be shortened to 1.4 years. In such a case, the STS might have to rendezvous earlier than 2.5 years for payload changeout, and perhaps boost the EP spacecraft to a higher orbit to achieve the XTE mission objectives.

Because the goal of maintaining the spacecraft above 300 km for 5.5 years (and thus preventing early reentry) is more critical than reaching the changeout altitude after 2.5 years, the 97.7-percent solar flux level scenario should be used for early mission planning. In particular, the minimum altitude as determined using the 97.7-percent solar flux level should be used for mission planning because, in all cases, such an altitude can meet or can almost meet the midmission objective (500 km after 2.5 years) regardless of whether the solar flux level is at 50 percent or 97.7 percent.

However, as shown by Figure 6, even MSFC predictions made a month before launch can contain great uncertainties. The uncertainty in the MSFC solar flux predictions can be as great as the difference between the August 1987 97.7- and 50-percent levels used in this study. Any mission planning should accommodate such an uncertainty; an initial altitude selected would need to meet the 97.7- and 50-percent prediction levels to ensure meeting the mission goals. The GSFC FDD is currently investigating the use of solar flux predictions, made by GSFC Code 600, Sciences Directorate, which are based on models of physical phenomena as opposed to the statistical estimations made by MSFC. In the future, the FDD plans to use GSFC solar activity predictions for lifetime studies.

The solar flux level has the greatest effect on the EP mission lifetime, but the spacecraft cross-sectional area and mass also have significant effects. If the solar flux level uncertainty is as great as that indicated in this study, the ballistic coefficient plays a large role in determining an altitude to meet mission objectives. It may be necessary to add mass to adjust the ballistic coefficient to minimize the effects of uncertainty in solar flux predictions. The EP lifetime study should be updated as close as possible to launch, when the flux levels, the area, and the masses are better known. At that time, commitment to a final launch altitude will be made.

REFERENCES

1. Computer Sciences Corporation, CSC/SD-85/6019UD2, Goddard Mission Analysis System (GMAS) User's Guide, Revision 2, Update 2, December 1987

2. Marshall Space Flight Center, Solar Activity Inputs for Upper Atmospheric Models Used in Programs to Estimate Spacecraft Orbital Lifetimes, W. W. Vaughan, September 21, 1980

3. --, Solar Activity Inputs for Upper Atmospheric Models Used in Programs to Estimate Spacecraft Orbital Lifetimes, W. W. Vaughan, April 9, 1982

4. --, Solar Activity Inputs for Upper Atmospheric Models Used in Programs to Estimate Spacecraft Orbital Lifetimes, W. W. Vaughan, August 21, 1987

5. Fairchild Spacecraft Company, presentation material from the Explorer Platform System Concept Review, July 8, 1987

6. Goddard Space Flight Center, presentation material from the Extreme Ultra-Violet Explorer Mission System Concept Review, July 7-8, 1987

N89-15958

REMOTE CHANCE OF RECONTACT?

D. Elkin and S. Abeyagunawardene, Computer Sciences Corporation

R. DeFazio, NASA/Goddard Space Flight Center

ABSTRACT

The ejection of appendages with uncertain drag characteristics presents a concern for eventual recontact. Recontact shortly after release can be prevented by avoiding ejection in a plane perpendicular to the velocity. For ejection tangential to the orbit, the likelihood of recontact within a year is high in the absence of drag and oblateness. The optimum direction of ejection of the thermal shield cable and an overestimate of the recontact probability are determined for the Cosmic Background Explorer (COBE) mission when drag, oblateness, and solar/lunar perturbations are present. The probability is small but possibly significant.

1. INTRODUCTION

The Cosmic Background Explorer (COBE) thermal shield cable is scheduled to be ejected before the Delta second-stage separation, 101 seconds (sec) after the second-stage cutoff (3699 sec after lift-off), near the first ascending node. Determining the optimum direction of ejection to prevent recontact and estimating the risk of recontact with the cable (within the constraints specified by the COBE Project Office) are the aims of this study.

Background information is presented in Section 2, the methods used are briefly described in Section 3, and the analysis is given in Section 4. Ejection for a spherical Earth without drag will be studied first to provide insight (Section 4.1). The optimum direction of ejection in this case will be determined, and the probabilities of recontact for optimum and tangential ejections will be calculated. A trajectory simulation having a near recontact with drag and oblateness will be presented and examined, and the probability of recontact will then be estimated (Section 4.2). An extremely large cross-sectional area was chosen to provide high drag so that the recontact could be obtained easily. This choice does not affect the generality of the result. The conclusions are summarized in Section 5.

In this paper, computations have a 60-sec integration step. This limitation was imposed to conserve computer time. Sixty seconds represents a relatively low level of resolution because, for example, a separation of over 1/3 kilometer (km) is possible in this time for an ejection speed of 20 feet per second (ft/sec).

The calculated probability is expected to be an overestimate. Radial separation due to drag can be greater than the minimum separation required for recontact. An otherwise possible recontact can thereby be prevented, or a new recontact can become possible. The former is much more likely than the latter because the separation required to break a recontact is small. This effect should be minor, since drag is small, and it is not included in the analysis.

2. BACKGROUND

In accordance with guidelines set by the COBE Project Office, the following constraints on the ejection are assumed. The ejection speed is between 8 and 20 ft/sec. The direction of the ejection is determined by the position of the cable cutter, which can be located at any point around the body of the spacecraft. This direction is known to within ±20 degrees (deg) in the plane perpendicular to the nadir and is assumed to have no radial component.

2.1 SPHERICAL EARTH, NO DRAG

Ejection in the direction of the positive or negative orbit normal (or in a radial direction) leaves the tangential component of the cable's velocity unchanged. Since the ejection speed is small compared to the orbital velocity, the cable's orbital velocity is nearly identical to the spacecraft's. The orbital periods are therefore almost equal, and recontact occurs within the first revolution.

For example, an 8-ft/sec ejection speed in either the radial or orbit normal direction results in a separation of only 7.5 meters (m) in one revolution. Recontact can occur at the ejection point because the radius is unchanged by the ejection. Recontact occurs in half an orbit for ejection along the orbit normal.

To prevent this form of recontact, a tangential component is required. The tangential component increases as the ejection direction moves from the orbit normal toward the tangential direction or as the ejection speed increases. The larger the tangential component, the greater the separation after one revolution. For ejection along the positive spacecraft velocity direction, the cable orbit period is greater than that of the spacecraft, and the cable will follow the spacecraft after one revolution. Ejection along the negative velocity direction produces the converse effect. After sufficiently many revolutions, an opportunity for recontact will occur because the cable makes exactly one revolution more or less than the spacecraft. Several opportunities for recontact may occur in a year. The smaller the tangential component of the ejection velocity, the fewer the number of possible recontacts within a year.

2.2 EFFECT OF DRAG

The drag on the cable cannot be determined accurately because of the cable's extremely long and thin shape. Concern arises because there is doubt about whether the drag on the cable will be greater than or less than that on the spacecraft. If the ejection is along the positive orbital velocity vector, recontact can occur only if drag on the cable is greater than on the spacecraft. For ejection along the negative velocity, drag on the cable must be less than on the spacecraft for recontact to occur.

Drag changes the time of recontact because the semimajor axis of each orbit changes. The difference in drag is small. The along-track separation produced by drag can be canceled by an appropriate change in ejection speed. As mentioned in the introduction, the radial separation could either prevent an otherwise possible recontact or create a new one. An overestimate of the probability results from neglecting this effect. There are still several opportunities for recontact in the year.

2.3 EFFECT OF OBLATENESS

Oblateness causes precession of the line of nodes and rotation of the line of apsides. The ejection gives the cable orbit a semimajor axis and inclination that may differ from those of the spacecraft, resulting in a nodal precession rate different from the spacecraft's. The COBE orbit is nearly polar (99-deg inclination). The only chance of recontact after the first orbit is therefore at the northernmost or southernmost points of the orbit (except in one rare case). For any given angle of ejection, the difference in node upon recontact is independent of the ejection speed because the increasing nodal rate is canceled by the decreasing time to recontact as ejection speed increases.

The difference in rate of change of the argument of perigee of the spacecraft and cable orbits is negligible. The rate of change of the argument of perigee is 2.75 deg/day. This rate places the apsis initially at the ascending node at the southernmost point in the orbit in 32 days, and at the northernmost point in 98 days. The worst case occurs in 65 days, when this apsis is at the descending node, as happens for a tangential ejection at 8.9 ft/sec. The distance between orbits at the northernmost or southernmost points is then 5.3 km. Variations in semimajor axis of ±9 km are typical, but it is expected that the spacecraft and cable orbits will vary in the same fashion. Recontact is therefore not possible when the line of apsides is along the line of nodes. Recontact is only possible when the appropriate apsis is near the northernmost or southernmost point. The fraction of time spent in an orientation in which the distance between orbits at these points is within the required minimum separation distance for recontact will be determined and used to estimate the probability of recontact.

3. METHOD AND SOFTWARE USED

3.1 ANALYTICAL CALCULATIONS

The analytical calculations shown here are strictly valid in the absence of drag, oblateness, and solar/lunar perturbations. Standard equations for two-body circular and elliptical orbits are used. These equations permit separation distances to be calculated by determining the orbital periods from knowledge of the ejection velocity.

3.2 SOFTWARE USED

The EPHGEN program was used to generate the ephemeris of COBE with given epoch elements and that of the ejected cable with epoch elements calculated when the magnitude and direction of the velocity of ejection relative to COBE are known. The EPHCMP and GTDS-COMPARE programs were run to compare the COBE and the cable ephemerides. The output contains the spacecraft separation at specified time intervals from epoch. An 3-by-8 model of the geopotential zonal and tesseral harmonics and the Goddard Trajection Determination System (GTDS) Atmospheric Density Model No. 3 were used. A 60-sec integration step was used to provide efficiency with adequate accuracy.

3.3 METHODS FOR CALCULATING PROBABILITY

An empirical method for determining the probability was devised. It involves counting all the ways in which recontact can occur and determining the extent of the dispersions in ejection velocity for each, such that a maximum separation distance is not exceeded. A close encounter will be said to occur in one synodic period.

3.3.1 NO DRAG OR OBLATENESS

When drag and oblateness are not considered, the method is as follows. Values of ejection velocity that give a recontact on the first close encounter are obtained. Dispersions about these values are found that produce the maximum tolerance in separation distance, conservatively assumed to be 20 m. An average value of the dispersions is determined over the specified velocity range. The average dispersion is divided by the magnitude of the range of velocities and multiplied by the number of possible revolutions consistent with the range of velocities to obtain the probability. An equivalent method, which can also be used with drag and oblateness, equates the probability of recontact for a given ejection velocity with the fraction of a revolution in which the minimum separation occurs. The different ways in which recontact can occur in a year on subsequent close encounters are enumerated so that the probability can be determined for the year. The probability of recontact is the same for all close encounters for a given ejection velocity.

3.3.2 DRAG AND OBLATENESS

When drag and oblateness are considered, the method is as follows. The COBE orbit is nearly polar (99-deg inclination). Precession of the nodes therefore prevents recontact except at the northernmost or southernmost points of the orbit (except in one rare case). The probability for recontact is estimated as above. An additional factor related to the orientation of the cable orbit is needed. This is the only place where radial separation is taken into account. The result is an overestimate, as explained in the introduction, since radial separation due to drag is ignored.

4. CALCULATIONS AND RESULTS

4.1 ANALYTICAL CALCULATIONS

In this section, ejection will be considered in the absence of drag and oblateness. Recontact must occur at or near the ejection point. The orbits are coplanar throughout. The probability of recontact for the first close encounter and for the first year will be calculated. The optimum angle of ejection will be determined, and the associated probability of recontact will be calculated.

The COBE and cable orbits are characterized by the following parameters:

Radius of circular COBE orbit	7278.14 km
Period of circular COBE orbit	102.98887 minutes (min)
Velocity of COBE	7.40046 km/sec
Assumed maximum cable ejection speed	20 ft/sec
Assumed minimum cable ejection speed	8 ft/sec
Uncertainty in the angle of ejection	±20 deg
Cable length and diameter	25 ft x 3/32 inches (in.)
Area/mass COBE (ft^2/kilogram (kg))	160/2260 = 0.07
Nominal area/mass cable* (ft^2/kg)	0.154/1 = 0.15
Rate of change of COBE semimajor axis	0.5 km/year (yr)
Rate of change of cable semimajor axis	1.0 km/yr

The control parameters, in order of increasing importance for recontact, are the angle of ejection Θ (Figure 1), the speed of ejection, and the coefficient of drag/area-to-mass ratio. Only the first can be influenced by design. It is assumed that the ejection produces no radial component. The ejection speed and direction are assumed to be random within the specified limits.

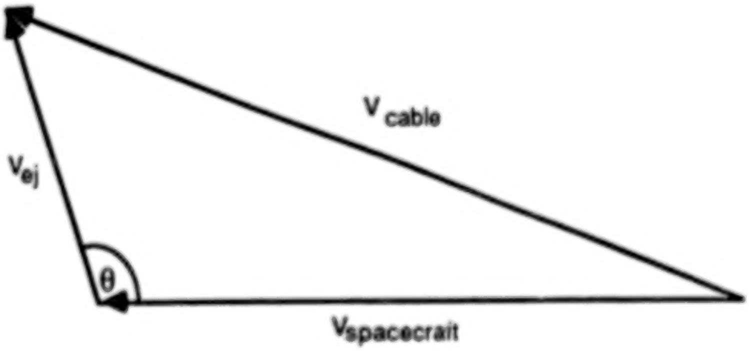

Figure 1. Definition of Angle of Ejection (Θ)

---

*Based on an effective length of 20 ft calculated by assuming a random orientation over a solid angle of 4π.

4.1.1 TANGENTIAL EJECTION

Spacecraft and cable orbits are shown in Figure 2 for ejection in the direction of the velocity. Drag and oblateness are not considered here. The numbers shown in the figure refer to the order in which the close encounters occur. The meeting point is at the point of ejection. Recontact occurs for a close encounter at or near the meeting point.

Let the first close encounter occur in x_1 cable orbits. A convenient approximation from which cable velocity can be determined with satisfactory accuracy is

$$x_1 \; t_{cable} = (x_1 + 1) \; t_{s/c}$$

where t is the orbital period.

Therefore,

$$x_1 = t_{s/c}/(t_{cable} - t_{s/c})$$

The nth close encounter is given by

$$x_n = n \; x_1$$

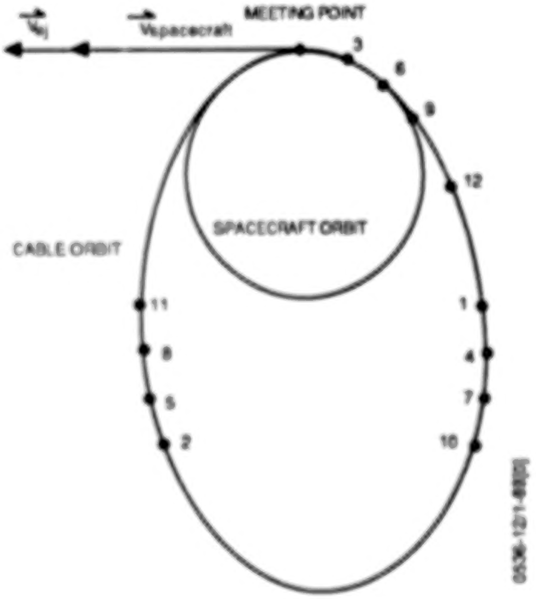

$\vec{V}_{ej}$
$\vec{V}_{spacecraft}$
MEETING POINT
3
6
9
12
SPACECRAFT ORBIT
CABLE ORBIT
11
8
5
2
1
4
7
10
0536-121-89[illegible]

Figure 2. Close Encounters for Ejection Along the Spacecraft Velocity

Table 1 shows values of x_1 for four cases: ejection at 20 or 8 ft/sec in the direction of the plus or minus spacecraft velocity vector.

Table 1. x_1 for Various Cases

V_{ej} (ft/sec)	+ OR -	V_{CABLE} (km/sec)	τ_{CABLE} (min)	$\tau_{CABLE} - \tau_{S/C}$ (sec)	PER-ORBIT SEPARATION (km)	x_1
20	+	7.406556023	103.2440093	15.31	113.3	403.667
20	-	7.394364023	102.7349948	15.23	112.7	404.662
8	+	7.402898423	103.0907762	6.11	45.2	1010.655
8	-	7.398021623	102.8871713	6.10	45.1	1011.655

0536-2/1-88[0]

The first close encounter will occur at the meeting point when $x_1 = 404$, if $V_{ej} = 19.983$ ft/sec. Recontract takes place about 29 days after ejection. All subsequent close encounters will also occur at the meeting point. For $x_1 = 405$, $V_{ej} = 19.934$ ft/sec. Clearly, numerous close encounters occur between 8 and 20 ft/sec.

4.1.2 WINDOW OF NO RECONTACT

Recontact is possible for either ejection along the orbit normal or for a tangential ejection. An intermediate region of ejection directions exists for which no recontact is possible within a year.

Approximately 5100 spacecraft orbits occur per year. The circumference of the orbit is 45,730 km. A per-orbit separation of greater than 20 m or less than 8.95 km will guarantee that no recontact will occur in the first year. For $V_{ej} = 8$ ft/sec, a separation of 20 m occurs in half an orbit for $\Theta = 89.96$ deg or $\Theta = 90.11$ deg. A per-orbit separation of 8.95 km occurs for tangential ejection at 1.59 ft/sec. For $V_{ej} = 20$ ft/sec, the 8.95-km per-orbit separation therefore occurs for $\Theta = 94.52$ deg or $\Theta = 85.43$ deg.

These limits on Θ define regions II and II' in Figure 3. Hence, if Θ is in region II or II', no recontact is possible within a year because no close encounters can occur. Unfortunately, Θ cannot be placed in regions II and II' because the uncertainty in the angle of ejection then extends to the orbit normal direction. In regions I and I', recontact occurs in half an orbit. In regions III and III', at least one close encounter occurs in the year. The number of possible close encounters in a year increases as Θ approaches 0 or 180 deg.

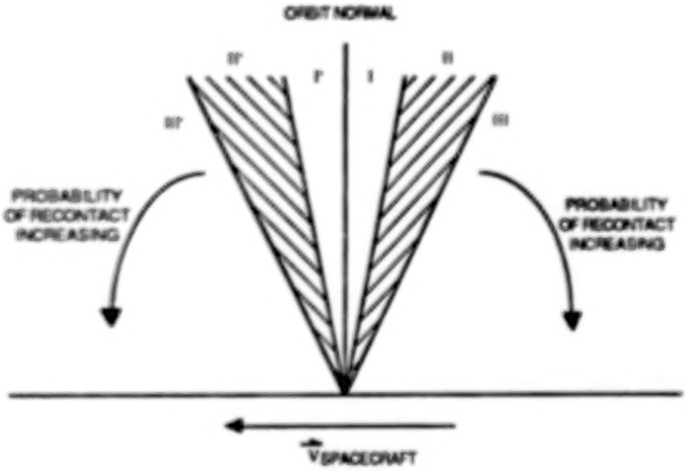
ORBIT NORMAL
II'
I'
I
II
III'
III
PROBABILITY OF RECONTACT INCREASING
PROBABILITY OF RECONTACT INCREASING
$\vec{V}_{SPACECRAFT}$

	REGION	ANGULAR WIDTH (DEG)	PROBABILITY OF RECONTACT
RECONTACT IN 1 ORBIT	I I'	0.04 0.11	1.0
NO RECONTACT	II II'	4.53 4.41	0
RECONTACT POSSIBLE	III III'	85.43 85.48	NONZERO

Figure 3. Regions of Recontact; No Drag or Nodal Precession

4.1.3 TANGENTIAL EJECTION, NO DRAG AND OBLATENESS

Consider ejection along the negative spacecraft velocity vector. Defining recontact to be a close approach of 20 m and assuming it occurs in about 404 spacecraft revolutions (V_{ej} = 20 ft/sec), the approximate positions of the spacecraft and cable for which a minimum separation of 20 m occurs (i.e., r = 7278.12) are shown in Figure 4 and determined by the angle γ. For the cable orbit, a = 7266.15458722, e = 0.0016495, and c = ae = 11.9855. At point p, r = 7278.12 and γ is 3.3009 deg. This is ±0.0091692 revolution. In 1011 spacecraft revolutions (V_{ej} = 8 ft/sec), γ is 5.225 deg; in 2023 revolutions (V_{ej} = 4 ft/sec), γ is 7.394 deg.

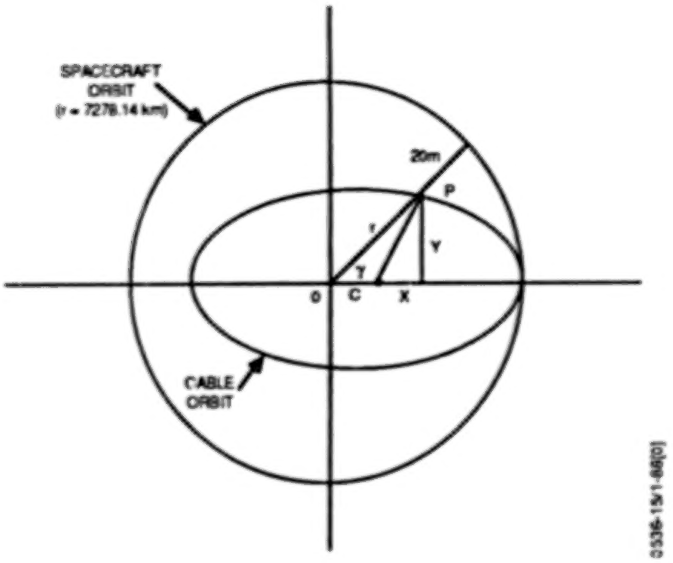
SPACECRAFT ORBIT (r = 7278.14 km)
20m
P
r
Y
γ
o
C
X
CABLE ORBIT
3336-15/1-88[0]

Figure 4. Cable and Spacecraft Orbits

Selected values relating x_1, which is here the number of spacecraft orbits until the first close encounter, to the ejection velocity are shown in Table 2. Some variations in ejection speed that still result in recontact (as given by γ) can be

Table 2. V_{ej}* for Various Values of x_1

x_1	V_{ej}
403	20.0824947
404	20.0327856
404.6622675	20
404.9908308	19.9837743
405	19.9833218
405.0091692	19.9828694
406	19.9341018
1011	8.0051852
1011.6552847	8
1012	7.9972750

* V_{ej} = 8 AND 20 ft/sec, APPROXIMATELY.

5046-1/2-88[5-2]

seen in this table. They correspond to x_1 = integer ±0.0091692 (V_{ej} = 20 ft/sec). A few values of V_{ej} are shown graphically in Figure 5. In the darkened intervals, recontact (i.e., a separation of 20 m or less) occurs.

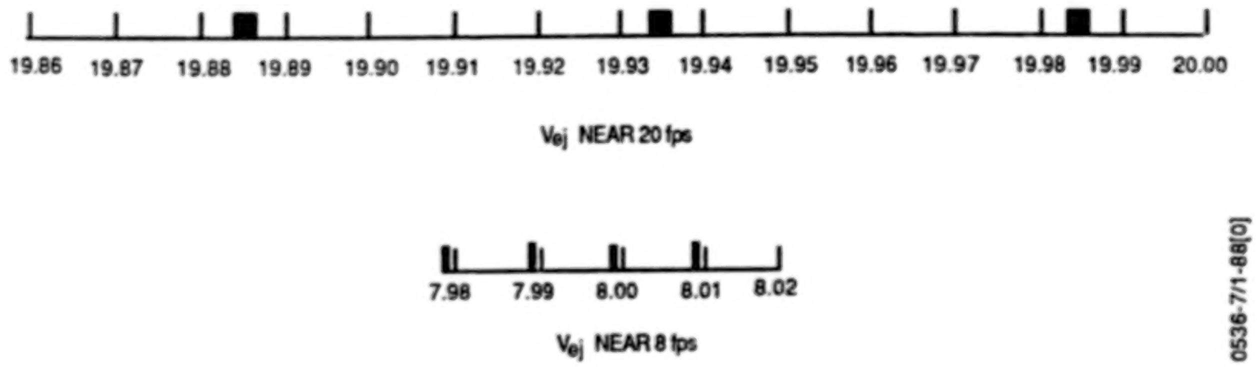

Figure 5. Some Values of V_{ej} Resulting in Recontact in 1 Year

The number of intervals is 1012 - 405 = 607. The width of the interval for x_1 = 405 is ±0.0004524, and for x_1 = 1012 it is ±0.000115. The average width is (0.0009048 + 0.00023)/2 = 0.00057. The separation between intervals is 0.049 and 0.008, respectively. The width of the total domain is (20 - 8) = 12 ft/sec. Therefore, the probability (P) of recontact on the first close encounter is

$$P = \frac{(607)(0.00057)}{12} = 2.88\%$$

This remarkably large probability is obtained because the spacecraft and cable orbits are coplanar upon recontact.

The probability of recontact for any close encounter in the absence of drag will now be calculated. In 1 year, as many as 12 close encounters can occur. The various values for the fractional part of x_1 giving recontact on a specified close encounter are shown in Table 3. The distribution of values is approximately uniform, except for a gap from 0 to 1/12. Referring to Table 3, a close encounter can occur in 10 ways at the meeting point when there are 5 close encounters in the year ($V_{ej} \approx 8$ ft/sec and $x_1 \approx 1011$), and a close encounter can occur in 46 ways when there are 12 close encounters in the year ($V_{ej} \approx 20$ ft/sec and $x_1 \approx 405$).

Table 3. Fractional Part of x_1 Giving Recontact on Various Close Encounters

CLOSE ENCOUNTER NUMBER											
1	2	3	4	5	6	7	8	9	10	11	12
0	1/2	1/3	1/4	1/5	1/6	1/7	1/8	1/9	1/10	1/11	1/12
		2/3	3/4	2/5	5/6	2/7	3/8	2/9	3/10	2/11	5/12
				3/5		3/7	5/8	4/9	7/10	3/11	7/12
				4/5		4/7	7/8	5/9	9/10	4/11	11/12
						5/7		7/9		5/11	
						6/7		8/9		6/11	
										7/11	
										8/11	
										9/11	
										10/11	

0536-4/1-88[0]

The probability of recontact (P) in the vicinity of any value of x_1 is now

$$P = \frac{\text{(number of ways) x (width of recontact interval)}}{\Delta V}$$

where ΔV is the difference in ejection velocity between possible recontacts on successive orbits.

For $x_1 = 405$ ($V_{ej} \approx 20$ ft/sec), separation within 20 m occurs when the width of the recontact interval is 0.0009 (as shown above) and $\Delta V = 0.049$. Therefore,

$$P(V_{ej} \approx 20) = 46(0.0009)/0.049 = 84\%$$

For x_1 = 1012 ($V_{ej} \approx 8$ ft/sec), separation within 20 m occurs when the width of the recontact interval is 0.00015 and ΔV = 0.008. Therefore,

$$P(V_{ej} \approx 8) = 10(0.00023)/0.008 = 29\%$$

The average value for x_1 = 405 to 1012 is 56 percent. The possibility of more than one recontact in a year is ignored. It can also be shown that

$$P_{(V_{ej} \approx 4 \text{ ft/sec})} = 4\%$$

4.2 NUMERICAL COMPUTATIONS

The preceding results apply to the case without drag and oblateness. When these effects are considered for ejection at the ascending node, the circumstances of the problem change. The knowledge gained in the idealized problem will be used to obtain an estimate of the probability of recontact in the actual problem.

To demonstrate the possibility of recontact in the presence of drag, oblateness, and solar/lunar perturbations, the case was considered in which drag on the cable is very much larger than that on COBE, so that recontact could be obtained easily. A tangential ejection of about 20 ft/sec in the positive velocity direction was assumed. The cross-track, radial, and along-track separations needed to be minimized simultaneously. Variation of the speed of ejection and coefficient of drag enabled this to be done, albeit tediously.

A value of the area that gave near-zero values of the cross-track and radial separations at the time of the closest approach of the cable and spacecraft was found iteratively to be 4.2×10^{-7} km^2. Drag on the cable was then 60 times larger than on the spacecraft. The best value of the ejection velocity giving the minimum separation for this area was then found iteratively.

4.2.1 RECONTACT WITH EXTERNAL PERTURBATIONS

The minimum separation was found to decrease linearly with decreasing ejection speed until a minimum value of 0.294 km was obtained at 19.79433 ft/sec (Figure 6). The minimum occurred as expected at the southernmost point. Figure 7 shows the

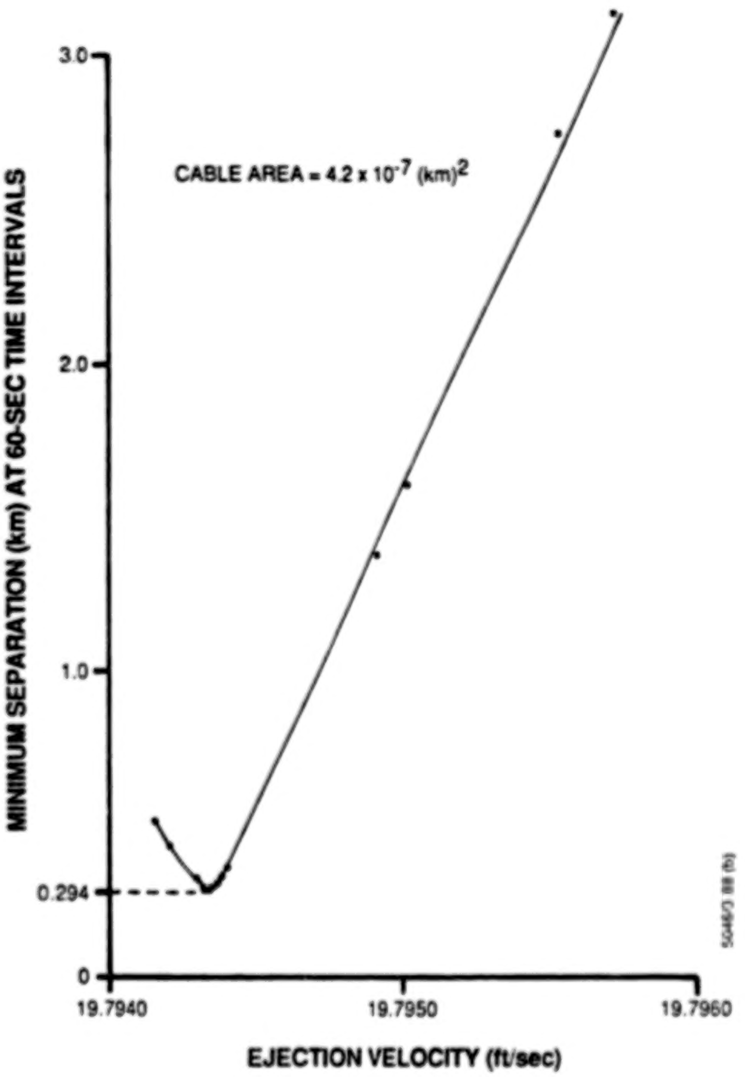

Figure 6. COBE/Cable Separation: Variation of Minimum Separation With Cable Ejection Velocity

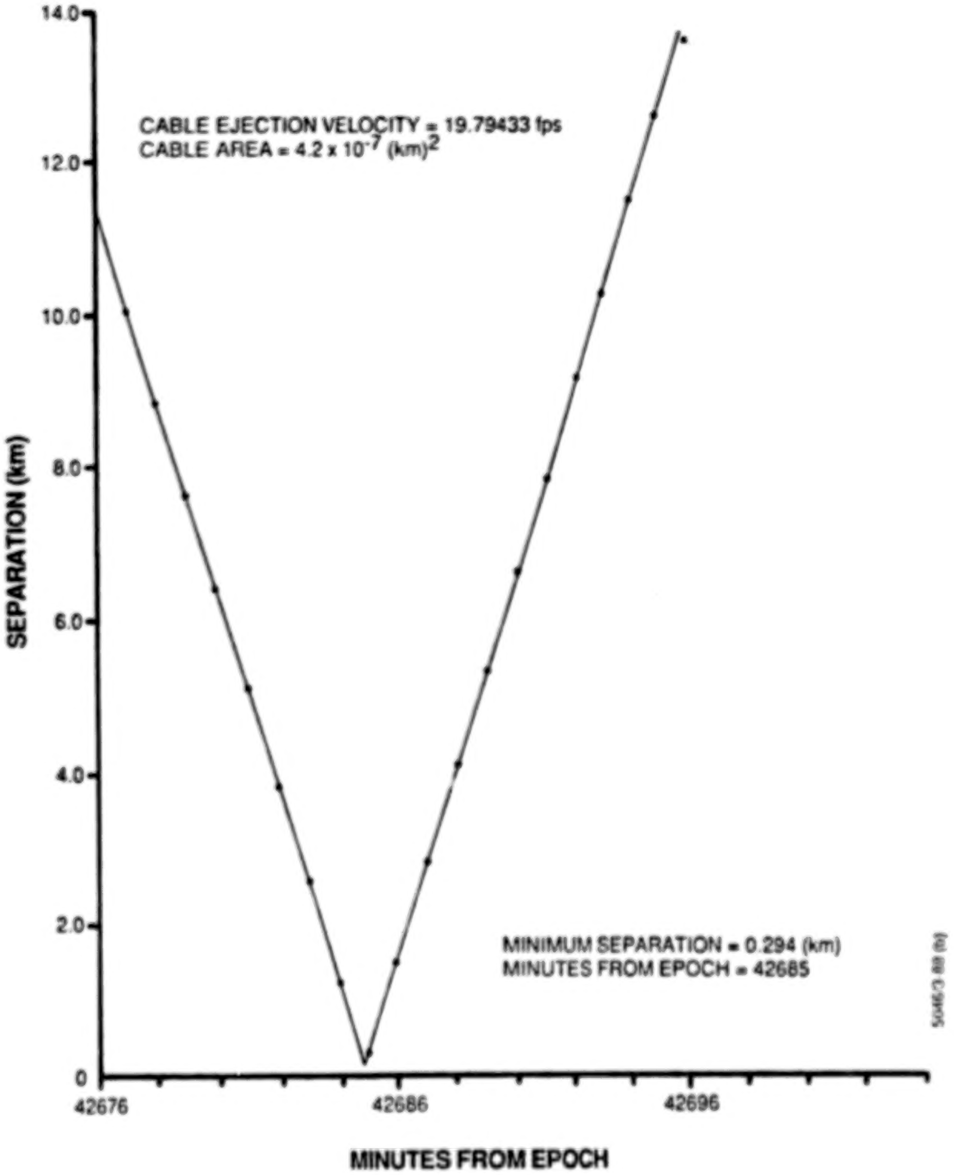

Figure 7. COBE/Cable Separation: Variation of Separation With Time for Case of Closest Approach With Realistic Drag and Geopotential Models

change in the separation with time when the ejection speed is 19.79433 ft/sec and the cable area is 4.2×10^{-7} km^2. For an ejection speed of 19.79435 ft/sec, the variation of the minimum separation with area is shown in Figure 8.

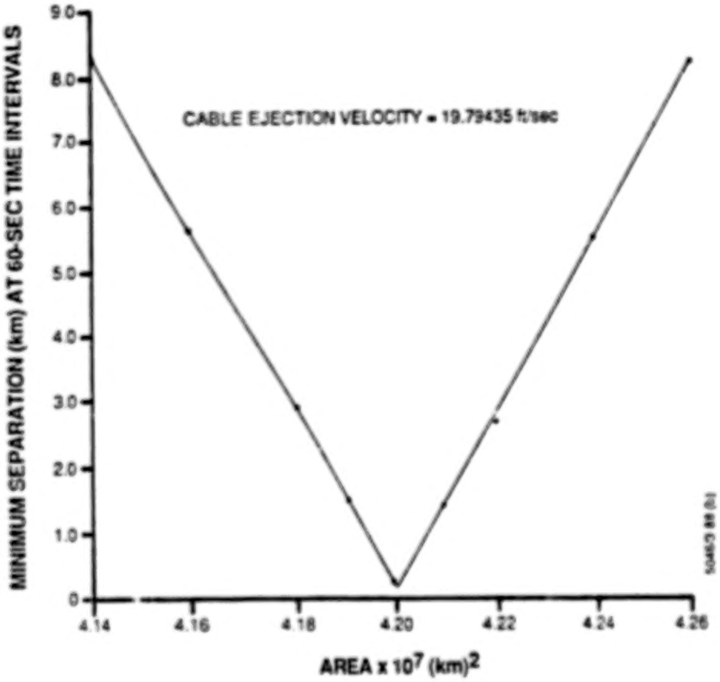

Figure 8. COBE/Cable Separation: Variation of Minimum Separation With Area of Cable

4.2.2 ESTIMATE OF PROBABILITY FOR RECONTACT WITHIN 1 YEAR WITH ALL EXTERNAL PERTURBATIONS - TANGENTIAL EJECTION

The minimum separation criterion for the numerical simulation of a recontact was 1/3 km. A minimum separation distance of 0.294 km was obtained for an ejection along the spacecraft velocity vector with

$$V_{ej} = 19.79433 \text{ ft/sec}$$

$$\text{area} = 4.2 \times 10^{-7} \text{ km}^2$$

A smaller minimum separation could be obtained for a smaller integration step. The recontact occurred about 30 days after epoch, when perigee was at the southernmost point. The variations in ejection speed and area separately that produce an increase of 1/3 km in the minimum separation distance are

$$\Delta V_{ej} = \pm\ 0.00027 \text{ ft/sec}$$

$$\Delta \text{area} = \pm\ 0.00273 \times 10^{-7} \text{ km}^2$$

These values are interpolated from the data (not shown) used to generate Figures 6 and 8.

The variation in ejection speed that produces an increase of 20 m in the along-track separation is given by interpolation (data not shown):

$$\Delta V_{ej} = \pm\ 0.0000085 \text{ ft/sec}$$

Using this value for ΔV_{ej}, the probability of recontact is obtained by dividing by 0.049 ft/sec (the velocity difference for recontact on orbit numbers 404 and 405). The probability is 0.035 percent. An analytical result will be given in Section 4.3.2 for comparison.

4.3 CALCULATING THE PROBABILITY OF RECONTACT

4.3.1 TANGENTIAL EJECTION

The angle between the orbit planes upon recontact is 0.165 deg (see below). The minimum separation occurs very near the meeting point at this angle. Using the equations in Section 4.1.1, an along-track separation of 20 m for recontact on orbit 404 can be shown to result from the value of

$$\Delta V_{ej} = \pm\ 0.000008761 \text{ ft/sec}$$

This is in agreement with the numerical result. The probability of recontact is 0.036 percent.

4.3.2 OPTIMUM DIRECTION OF EJECTION

Tangential ejection was considered above. It remains to consider a nontangential ejection. The maximum difference in inclination of the cable orbit from the spacecraft orbit is 0.044 deg, which occurs for a 20-ft/sec ejection at ±70 deg. This produces a 5.6-km displacement of the northernmost points of the orbits, or the southernmost points. Although recontact can no longer occur exactly at the northernmost or southernmost points, the displacement is small and recontact remains possible at some nearby point. The dihedral angle between the orbit planes is therefore largely composed of the difference in the right ascensions of the ascending nodes. It will be assumed that the difference in inclination is negligible and that the dihedral angle between the orbit planes is equal to the difference in node between the two orbits.

An ejection in the negative spacecraft velocity direction will be considered since the area-to-mass ratio of the cable is nominally greater than that of the spacecraft. In Table 4, the dihedral angle is calculated for ejection angles between -70 and 70 deg from the negative spacecraft velocity vector. For these limits, the ejection is at least 20 deg away from the orbit normal. The probability of recontact for a 20-m minimum separation criterion is calculated only for angles near 47.9 deg. This is a special case. The calculation uses the dihedral angle to determine the angle γ required for a 20-m cross-track separation. Minimum separation occurs away from the meeting point. Below 44.4 deg and above 51.0 deg, minimum separation occurs in the vicinity of the meeting point. The probability in this case is calculated below. A dihedral angle of 0.164 deg was derived from the numerical results for a 180-deg angle of ejection. This agrees with the result of 0 deg shown in Table 4.

A positive dihedral angle indicates that the cable orbit leads the spacecraft orbit in the nodal precession, while a negative dihedral angle indicates that the cable orbit lags the spacecraft orbit. There is a singular point at 47.9 deg for which the probability is relatively high. At this angle, the rates of precession of the spacecraft and cable orbits are equal and the orbits are coplanar upon recontact. Calculation of the probability is analogous to that in Section 4.1.3. If the small difference in inclination is not neglected, the orbits are never perfectly coplanar. The location of a possible recontact is no longer at the northernmost or southernmost points, but the probability remains high, though not as high as for the coplanar case. The angle of 47.9 deg should be avoided.

When the angle of ejection is between 44.4 and 51.0 deg, the magnitude of the dihedral angle is less than or equal to 0.019 deg. The minimum separation is then the cross-track separation, which may be several kilometers away from the meeting point. However, when the magnitude of the dihedral angle is less than or equal to 0.0027 deg, the orbits are virtually coplanar. The minimum separation becomes the radial separation, which is greater than the cross-track separation. The probability of recontact then becomes large, as shown in Section 4.1.3. Above 51.0 deg, the uncertainty of ±20 deg in the angle of ejection will make avoidance of both the orbit normal and the angle of 47.9 deg almost impossible to guarantee.

Table 4. Dihedral Angle Between Orbit Planes for Various Angles of Ejection

ANGLE OF EJECTION (deg)	DIHEDRAL ANGLE (deg)	PROBABILITY OF RECONTACT (%)
70	-0.243	–
60	-0.093	–
51.0	-0.019	0.264
47.9	-0.0001	6.140*
44.4	0.019	0.264
35	0.060	–
15	0.124	–
0	0.165	–
-15	0.204	–
-35	0.268	–
-60	0.422	–
-70	0.571	–

5046-4/4-88 [5-3]

* AVERAGED OVER EJECTION SPEEDS OF 8 TO 20 ft/sec. A FACTOR OF 2 IS INCLUDED BECAUSE DRAG CREATES A SECOND MEETING POINT. THE CALCULATION IS ANALOGOUS TO THAT IN SECTION 4.1.3 FOR COPLANAR ORBITS.

The probability of recontact will now be determined for ejection angles outside the above range (Table 5). The case of a tangential ejection was discussed above. The calculation required finding the magnitude of ΔV_{ej} that produced a 20-m along-track separation at the meeting point. Minimum separation does not occur exactly at the meeting point. For ejection angles between -70 and 20 deg, the dihedral angle is greater than 0.1 deg, and the minimum separation occurs sufficiently close to the meeting point to make a negligible difference in this calculation. The

Table 5. Probability of Recontact in 1 Year for Various Ejection Angles for a 20-Meter Minimum Separation Criterion

Θ (deg)	V_{ej} (ft/sec)	V_{ej} TANGENTIAL COMPONENT (ft/sec)	X_i	P (%)	NUMBER OF CLOSE ENCOUNTERS	$P_{1\ YEAR}$	P_{av} (%)	FRACTION OF TIME*	P_{final} (%)
+20	20	18.79	431	0.038	42	1.596	1.080	0.05	0.054
+20	8	7.52	1076	0.094	6	0.564			
0	20	20.00	404	0.036	46	1.656	1.273	0.05	0.064
0	8	8.00	1012	0.089	10	0.890			
-35	20	16.38	494	0.043	32	1.376	1.012	0.06	0.060
-35	8	6.55	1235	0.108	6	0.648			
-70	20	6.84	1183	0.104	6	0.624	0.442	0.07	0.031
-70	8	2.74	2958	0.259	1	0.259			

5046-5/4-88 [5-3]

* REFERS TO THE FRACTION OF TIME THE ORBITS ARE SEPARATED BY 20 METERS OR LESS AT THE NORTHERNMOST OR SOUTHERNMOST POINTS. THE VALUE IS $2\gamma/\pi$.

change in ejection speed needed to shift the recontact by one revolution is also required. This is divided into ΔV_{ej} to obtain the probability of recontact on any close encounter (P). Ejection speeds of 20 ft/sec and 8 ft/sec are considered. The number of close encounters possible is enumerated by reference to Table 3, and the probability for the year is determined by multiplication. A simple average is then calculated. To obtain an estimate of the probability of recontact (P_{final}) from this, a factor is needed that takes into account the orientation of the cable orbit with respect to the northernmost or southernmost points. The value of this factor is available from calculating the angle γ (Figure 4). The fraction of time that the relevant apsis spends within a domain of $\pm\gamma$ from the northernmost or the southernmost point is then $2\ \gamma/\pi$. This fraction is typically less than 0.1. The probability of recontact can be seen to be a decreasing function of $|\Theta|$. Notice for $\Theta = 0$ deg, $V_{ej} = 20$ ft/sec, that $P = 0.036$ percent, in agreement with the numerical result.

A minimum separation criterion of 20 m was used. For a more realistic criterion of 10 m, P is half as large, but γ is also smaller. For example, the probability of recontact within 10 m for a tangential ejection is 0.022 percent.

5. CONCLUSIONS

Recontact of the COBE thermal shield cable is inevitable for ejection in the positive or negative orbit normal directions. A relatively high probability of recontact exists for ejection at or near 47.9 deg, because the cable and spacecraft orbits would be nearly coplanar upon recontact. It is then possible for recontact to occur at a node. Ejection in the vicinity of the above directions should be avoided.

Recontact in the presence of drag and oblateness is possible only at the northernmost or southernmost points of the orbits, provided that ejection does not take place along the orbit normal or near 47.9 deg. The probability depends upon the dihedral angle subtended between the orbit planes upon recontact, for angles of ejection between 44.4 and 51.0 deg. For all other angles, the probability depends upon the along-track separation at the meeting point for dispersions about a recontact velocity.

A numerical simulation provided an example of a near recontact for a tangential ejection. An analytical determination of the probability of recontact agreed with the numerical results.

The optimum direction of ejection is the one that minimizes the number of close encounters within a year, maximizes the dihedral angle between orbit planes upon recontact (i.e., avoids 47.9 deg), but guarantees that ejection will not take place along the orbit normal. For an uncertainty of ±20 deg in ejection angle, the recommended angle is therefore -69.96 deg. The direction of this ejection is such as to increase the inclination. The probability of having a separation of 20 m or less at this value was calculated to be 0.031 percent. The probability of recontact for a tangential ejection was found to be 0.064 percent. These values are overestimates.

ACKNOWLEDGMENTS

The authors wish to thank L. Hooper and R. Pendley of Computer Sciences Corporation for their many helpful suggestions.

N89-15959

COMPARISON OF CIRCULAR ORBIT AND FOURIER POWER SERIES EPHEMERIS REPRESENTATIONS FOR BACKUP USE BY THE UPPER ATMOSPHERE RESEARCH SATELLITE ONBOARD COMPUTER

J. R. Kast, Computer Sciences Corporation

ABSTRACT

The Upper Atmosphere Research Satellite (UARS) is a three-axis stabilized Earth-pointing spacecraft in a low-Earth orbit. The UARS onboard computer (OBC) uses a Fourier Power Series (FPS) ephemeris representation that includes 42 position and 42 velocity coefficients per axis, with position residuals at 10-minute intervals. New coefficients and 32 hours of residuals are uploaded daily. This study evaluated two backup methods that permit the OBC to compute an approximate spacecraft ephemeris in the event that new ephemeris data cannot be uplinked for several days: (1) extending the use of the FPS coefficients previously uplinked and (2) switching to a simple circular orbit approximation designed and tested (but not implemented) for Landsat-D. The FPS method provides greater accuracy during the backup period and does not require additional ground operational procedures for generating and uplinking an additional ephemeris table. The tradeoff is that the high accuracy of the FPS will be degraded slightly by adopting the longer fit period necessary to obtain backup accuracy for an extended period of time. The results for UARS show that extended use of the FPS is superior to the circular orbit approximation for short-term ephemeris backup.

1.0 INTRODUCTION

The Upper Atmosphere Research Satellite (UARS) will use a Fourier Power Series (FPS) ephemeris representation (Hall and Long, 1978; Long and Folta, 1986) similar to that used by Landsat for normal onboard computation of the spacecraft ephemeris. The nominal procedure will be to uplink a new set of FPS coefficients daily along with 32 hours of residuals. Precision FPS results are required for this 32 hour timespan.

The term "ephemeris representation" is understood to include the entire process of supplying ephemeris information to the spacecraft. It includes ground-based computer generation of the spacecraft ephemeris coupled with data compression techniques, data transmission to the spacecraft, and onboard algorithms for computing the required data. Interest in a backup ephemeris representation capability for times beyond the normal 32-hour timespan led to a study in which two approaches were evaluated: (1) continuing to compute an ephemeris using the FPS coefficients without residuals, or (2) switching to a simple circular orbit approximation.

The emphasis of the study was on the fit errors introduced by substituting the FPS or circular orbit approximations as models of the predicted reference ephemeris. Although uncertainty in the predicted ephemeris itself introduces additional errors, these are the same for both FPS and circular orbits. While the effect of fit period on possible overflow of FPS coefficients and residuals (using the Landsat-D scaling parameters) was evaluated, errors introduced by overflow in onboard computer (OBC) intermediate computations were ignored. Miller (1987, p. 9) has shown that, for the FPS fits to the nominal UARS orbit used in this study, there was a sufficient cushion to avoid overflow.

The existing Landsat OBC software permits the continued use of the FPS calculation at reduced accuracy beyond the timespan of the residuals. Because the accuracy of the FPS algorithm degrades rapidly when it is evaluated at times beyond the fit period, an extended fit period for the normal FPS uplink must be considered. For this study, effects of 3-day and 7-day fits were evaluated. Lengthening the fit period extends the time period for which the FPS can be used as a backup ephemeris, but at the cost of possibly decreasing the accuracy during the normal 32-hour period of use.

The accuracy of 3-day and 7-day fits of the circular orbit approximation were evaluated and compared to FPS results. Accuracies for both techniques were computed in terms of nadir-pointing errors; along-track, cross-track, and radial position differences; velocity errors in the spacecraft body frame; and yaw, pitch, and roll errors.

The UARS OBC controls pointing of the UARS high-gain antenna (HGA) toward the Tracking and Data Relay Satellite (TDRS) by computing the required HGA gimbal angles using UARS and TDRS ephemeris results and the OBC attitude solution. Thus, extended use of the TDRS ephemeris representation would be required if UARS tracking of TDRS were to continue during the backup period. For this reason, 3-day and 7-day fits of the TDRS ephemeris representation were generated, and the Earth (nadir)-pointing errors (which can serve as a measure of the contribution of TDRS ephemeris error to the spacecraft-to-TDRS tracking error) were computed. Errors were small for either fit period.

2.0 BACKGROUND

2.1 FPS

In studies reported by Hall and Long (1978), a number of possible ephemeris representations for Earth-orbiting spacecraft with near-circular (eccentricities less than 0.02) orbits and both low-Earth (550 to 950 kilometers (km) altitude) and geosynchronous orbits were considered. Algorithms were evaluated for usefulness when computational time, data storage, and data transmission were all limited, and accuracies of 1 meter (m) to 10 km root-mean-square (rms) position error were required for timespans of up 4 days. The FPS was selected as the spacecraft ephemeris representation to be used for onboard computation by the Solar Maximum Mission (SMM), which used the first National Aeronautics and Space Administration (NASA) Standard Spacecraft Computer (NSSC-1) OBC. The predicted ephemeris was first generated on the ground; then, using a truncated FPS, the coefficients and residuals were determined and uplinked to the OBC, where the FPS was evaluated to provide the Cartesian elements at specified time intervals.

To represent the Cartesian spacecraft ephemeris data at equispaced grid points for Landsat and for UARS, an FPS of the following form was chosen:

$$\sum_{i=1}^{N=3} \sum_{j=0}^{M=5} \left[a_{ij} t^j \sin (i\omega t) + b_{ij} t^j \cos (i\omega t) \right]$$

$$+ \sum_{k=0}^{1} [\sin (\omega t) + \cos (\omega t)]^k \, [c_k \sin (2\omega_e t) + d_k \cos (2\omega_e t)]$$

where ω is the orbital frequency and is assumed to be the same for each Cartesian coordinate. The Earth's sidereal rotation frequency, ω_e, is assumed to have a value of

$$\omega_e = 2\pi/[23.934467 \ (3600)] \text{ radians/second}$$

In operational programs, the series is used in a nested form as follows:

$$\begin{aligned}
x(t) = {} & A_1 + t\{A_2 + t(A_3 + t(A_4 + t(A_5 + tA_6)))\} \\
& + \{A_7 + t[A_8 + t(A_9 + t(A_{10} + t(A_{11} + tA_{12})))]\} \sin (\omega t) \\
& + \{A_{13} + t[A_{14} + t(A_{15} + t(A_{16} + t(A_{17} + tA_{18})))]\} \cos (\omega t) \\
& + \{A_{19} + t[A_{20} + t(A_{21} + t(A_{22} + tA_{23}))]\} \sin^2 (\omega t) \\
& + \{A_{24} + t[A_{25} + t(A_{26} + t(A_{27} + tA_{28}))]\} \sin (\omega t) \cos (\omega t) \\
& + \{A_{29} + t[A_{30} + t(A_{31} + tA_{32})]\} \sin^3 (\omega t) \\
& + \{A_{33} + t[A_{34} + t(A_{35} + tA_{36})]\} \sin^2 (\omega t) \cos (\omega t) \\
& + \{A_{37} + A_{39} \sin (\omega t) + A_{41} \cos (\omega t)\} \sin (2\omega_e t) \\
& + \{A_{38} + A_{40} \sin (\omega t) + A_{42} \cos (\omega t)\} \cos (2\omega_e t)
\end{aligned}$$

where $x(t)$ = any position or velocity component

ω = mean orbital frequency of the spacecraft for the data span

ω_e = Earth's sidereal rotation frequency

t = spacecraft clock time relative to a spacecraft clock reference time for the data span, modeled as follows (from Lee, 1981, p. 3-1; NASA, 1987, Section 3205.2.2):

$$t = t_0 + (1 + R)(T - T_0) + R_d\ (T - T_0)^2$$

where T = true ephemeris time

t_0, T_0 = spacecraft clock time and corresponding true time at the FPS reference time (TREF)

R = spacecraft clock drift rate

R_d = rate of change of R

For the TDRS ephemeris representation in the UARS OBC, residuals are not used and only the A_1, A_2, A_7, A_8, A_{13}, A_{14}, A_{19}, and A_{24} terms are fit (NASA, 1987, Section 3205.2.3).

Although some rough analogies can be made with such factors as J_2 perturbations, the individual terms of the FPS should not be thought of as having physical significance. The FPS is simply a convenient method using a limited number of terms to compute near-circular, low-Earth orbits to a suitable degree of accuracy for limited time periods.

To accurately determine the orbital frequency, ω, the maximum entropy method (MEM) is used. This method provides superior frequency resolution to Fourier analysis for short data spans; MEM can locate periodicities in the data that are of the order of the length of the data span itself without quantizing them. The MEM analysis is followed by a least squares fit of the coefficients of a truncated FPS to a precise ephemeris file generated by numerical integration. Residuals are then computed at specific grid-point times. In the OBC, these residuals can be added to the position and velocity generated by evaluating the coefficients at selected grid-time intervals to obtain Cartesian elements nearly identical to the initial precise ephemeris. A four-point Hermite interpolator is then used to obtain Cartesian elements between grid-time intervals.

2.2 CIRCULAR ORBIT APPROXIMATION

The circular orbit approximation was originally designed for use by Landsat-4 at a time when the solar panels appeared to be undergoing progressive failure (Quinn, 1984). The requirements were to provide a coarse (on the order of 1 degree) ephemeris algorithm that would need to be updated from the ground no more frequently than once per week and, if necessary, could be used for 1 month. The circular orbit algorithm uses an average nodal period, average nodal precession, and orbit radius to compute the position and velocity. For UARS, the circular orbit parameters would be fitted on the ground and uplinked as an additional OBC table each time the FPS ephemeris was uplinked.

The circular orbit model was defined by Quinn (1984, p. 4). Position and velocity are computed in GCI coordinates as follows:

$$x = R\,(\cos\Omega\cos\Theta - \sin\Omega\cos i\sin\Theta)$$
$$y = R\,(\sin\Omega\cos\Theta + \cos\Omega\cos i\sin\Theta)$$
$$z = R\,(\sin i\sin\Theta)$$
$$\dot{x} = -V\,(\cos\Omega\sin\Theta + \sin\Omega\cos i\cos\Theta)$$
$$\dot{y} = -V\,(\sin\Omega\sin\Theta - \cos\Omega\cos i\cos\Theta)$$
$$\dot{z} = V\,(\sin i\cos\Theta)$$

where Ω = right ascension of ascending node:

$\Omega = \Omega\ (\text{at } T = 0) + T * \dot{\Omega}$

$\dot{\Omega}$ = nodal precession rate

T = time elapsed since reference time

Θ = orbit angle (linear function of time): $\Theta = (2\pi/P)T$

P = average nodal period

R = radius at first ascending node

V = velocity at first ascending node

i = inclination of UARS orbit

2.3 EFFECT OF EPHEMERIS ERRORS ON SPACECRAFT OPERATION

It is accepted that the OBC-computed backup ephemeris may not be accurate enough for the spacecraft to meet the nadir-pointing control requirements for normal science measurements. Two coarse control requirements remain: (1) The spacecraft line-of-sight direction to TDRS must be computed to an accuracy of 1 deg (NASA, 1987, Section 3205.2.2, p. 4) to maintain TDRS contact. (2) The spacecraft nadir-pointing error must be maintained below approximately 5 deg to avoid a transition to a safehold mode triggered by off-null Earth sensor measurements.

The UARS spacecraft will have a component of nadir-pointing error due to ephemeris representation error when it is measuring an inertial attitude and controlling to a local vertical frame computed using the onboard ephemeris. This nadir-pointing error is computed as the angle between the GCI spacecraft positions obtained from the onboard ephemeris representation and from the reference ephemeris.

When UARS is flying forward at normal attitude, the yaw axis (Z) is in the nadir direction. The pitch axis (Y) is in the direction of the negative orbit normal. The roll axis (X) is orthogonal and positive in the direction of flight. The mathematical formulation of the errors in spacecraft attitude due to errors in the OBC ephemeris representation was given by Folta (1987, Appendix A).

The nadir-pointing error is simply the root-sum-square (rss) of the pitch and roll errors, and these all depend only on position error. However, the yaw error depends on errors in the direction of the negative orbit normal, which is computed as the cross product of the spacecraft position and the velocity. Since the UARS FPS includes position but not velocity residuals, pitch and roll errors should be reduced when residuals are used, but yaw error should be relatively unaffected.

The component of spacecraft attitude error perpendicular to the spacecraft line of sight to TDRS contributes directly to error in pointing the spacecraft's high-gain antenna (HGA) at TDRS. The individual contributions from roll, pitch, and yaw depend on the geometry, but as an upper bound on error, their rss value can be used. However, the spacecraft position error also contributes to TDRS pointing error, and this error is highly correlated with pitch and roll error.

The effect of this correlation is shown in Figure 1. The normal UARS attitude control algorithm is indicated by a subscript I (applicable when the spacecraft is measuring an inertial referenced attitude and controlling to a computed nadir-pointing attitude based on the OBC ephemeris) and a possible backup control mode by a subscript E (applicable when the spacecraft is controlling to a nadir-pointing attitude based on Earth sensor measurements). UARS and TDRS actual positions are indicated by S and T; a prime (') indicates the OBC computed position. The UARS

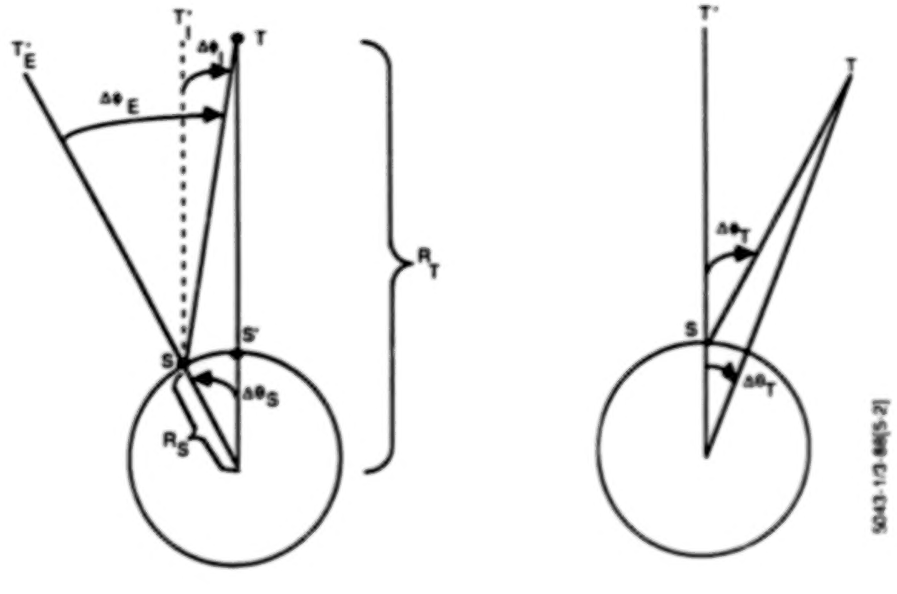

(a) UARS EPHEMERIS ERROR

(b) TDRS EPHEMERIS ERROR

Figure 1. TDRS Pointing Error Geometry

and TDRS "computed nadir-pointing" error due to ephemeris error is indicated by $\Delta\Theta_S$ and $\Delta\Theta_T$.

The contribution from $\Delta\Theta_S$ to spacecraft-to-TDRS pointing error is $\Delta\Phi_I$ or $\Delta\Phi_E$, depending on the spacecraft control mode; the contribution from $\Delta\Theta_T$ is $\Delta\Phi_T$. Letting S and T also represent spacecraft (6,978 km) and TDRS (42,164 km) distance from the Earth's center, it can be seen for the geometry shown that

$$\Delta\Phi_I = \frac{S}{T - S}\,\Delta\Theta_S = 0.20\,\Delta\Theta_S$$

$$\Delta\Phi_E = \Delta\Theta_S + \Delta\Phi_I = 1.20\,\Delta\Theta_S$$

$$\Delta\Phi_T = \frac{T}{T - S}\,\Delta\Theta_T = 1.20\,\Delta\Theta_T$$

The equation for $\Delta\Phi_I$ seems to indicate that (for normal inertial-referenced attitude control) correlations reduce the effect of ephemeris errors on TDRS pointing errors. However, when the UARS and TDRS positions are 90 deg apart, it is clear that UARS yaw errors transform directly to TDRS pointing errors. The equation for $\Delta\theta_T$ indicates that the contribution of TDRS ephemeris errors to UARS-to-TDRSS pointing error may be approximated as the equivalent TDRS nadir-pointing error. We will therefore consider the UARS-to-TDRS pointing error to be approximated as the sum of UARS attitude error and TDRS nadir-pointing error.

3.0 PROCEDURES

Orbits generated by the FPS and the circular orbit approximation were fit and compared to a predicted ephemeris generated by the Goddard Trajectory Determination System (GTDS). The Ephemeris Representation Ground Support System (ERGSS) and a modified version of the Ephemeris Representation Ground Support Quality Assurance (ERGSQA) programs were used to compute coefficients and to generate ephemeris files past the length of time used to fit the coefficients. These programs are discussed by Boland and Lee (1982) and Boland (1982).

The circular orbit fit uses the numerical average of the nodal period over the timespan desired. The FPS fit is performed over a selected timespan of the predicted ephemeris to determine the orbital frequencies, coefficients, and residuals. Current Landsat operations use 3 days as the data span for fitting coefficients. The extended fit length used in this report was arbitrarily selected as 7 days, the largest fit length that is currently supported by the ERGSS program. Accuracies for both approximations are given for nadir-pointing angles; yaw, pitch, and roll angles; along-track, cross-track, and radial positions; and velocity components.

4.0 RESULTS

4.1 FPS AND CIRCULAR ORBIT ACCURACIES

Table 1 compares the length of time until the nadir-pointing error (defined here as the combination of pitch and roll errors) exceeds a 1-deg or 5-deg angle. These angles are as suggested by the General Electric Company for maintaining TDRS pointing and for avoiding transition to the safehold mode, respectively. As seen in the table, a 1.0-deg nadir-pointing accuracy can be maintained by either the FPS or circular orbit approximation for about the same time period if a 7-day fit

Table 1. Comparison of Length of Time From Beginning of Fit Until Nadir-Pointing Errors Exceed 1 or 5 Degrees

Representation	Days From Beginning of Fit	
	1-Degree Error	5-Degree Error
Circular		
3-day fit	9.8	21.4
7-day fit	12.7	23.5
FPS		
3-day fit	5.3	6.8
7-day fit	13.1	16.9

is used. Figures 2 and 3 present these results for 3-day and 7-day fits, respectively. Each figure shows the errors for the FPS orbit and the circular orbit when compared to a predicted ephemeris. As shown in Figure 3, from 7 days to approximately 11 days from the start of the data fit, both FPS and circular orbits give similar results for a 7-day fit. However, the FPS orbit degrades after 11 days.

Tables 2 and 3 present the position differences for both the circular orbit and FPS orbit. Maximum values are given for 3-day and 7-day fits. The significant position difference is in the along-track direction and agrees with the previous nadir-pointing result. An improvement in using the FPS instead of the circular orbit was especially noted over the first several days even after the residuals have been exhausted.

Figures 4 and 5 present the yaw errors for a 3-day fit and a 7-day fit when the FPS and circular orbit approximations are compared to a predicted ephemeris. As shown in the figures, the FPS accuracy is superior to the circular orbit accuracy during the time interval used for fitting coefficients and for a short time after for a 7-day FPS fit. Although the circular orbit has initially larger errors than the FPS orbit, it will degrade at a slower rate than the FPS orbit when significantly past the end of the time interval used for fitting coefficients. Tables 4, 5, and 6 present the yaw, pitch, roll, and velocity errors for 1-, 3-, and 7-day periods, respectively. Results represent the maximum angle or velocity errors over the stated period. During the fit period, the FPS errors are much smaller

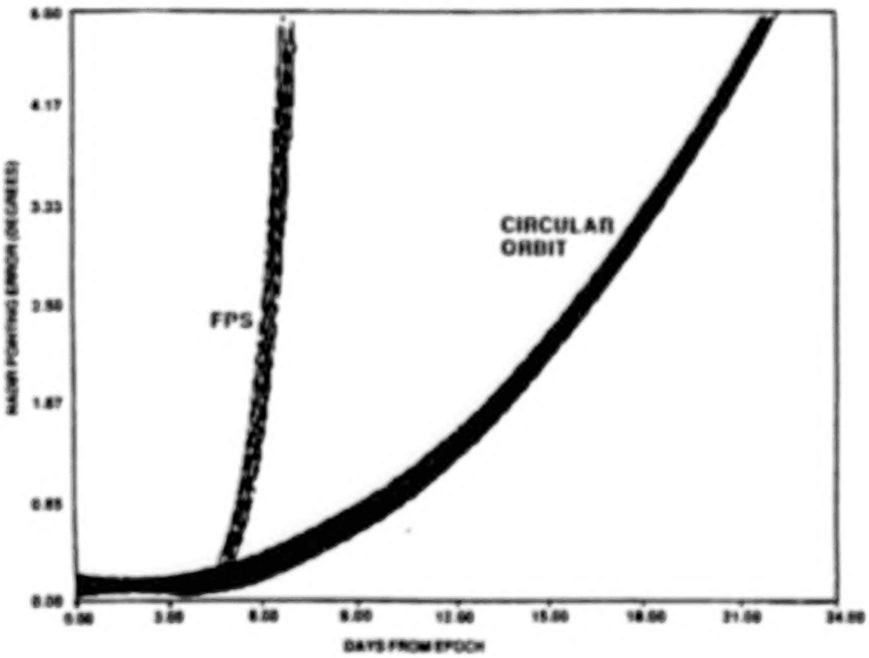

Figure 2. UARS Nadir-Pointing Error for a 3-Day Fit: FPS (No Residuals) and Circular Ephemeris Representations

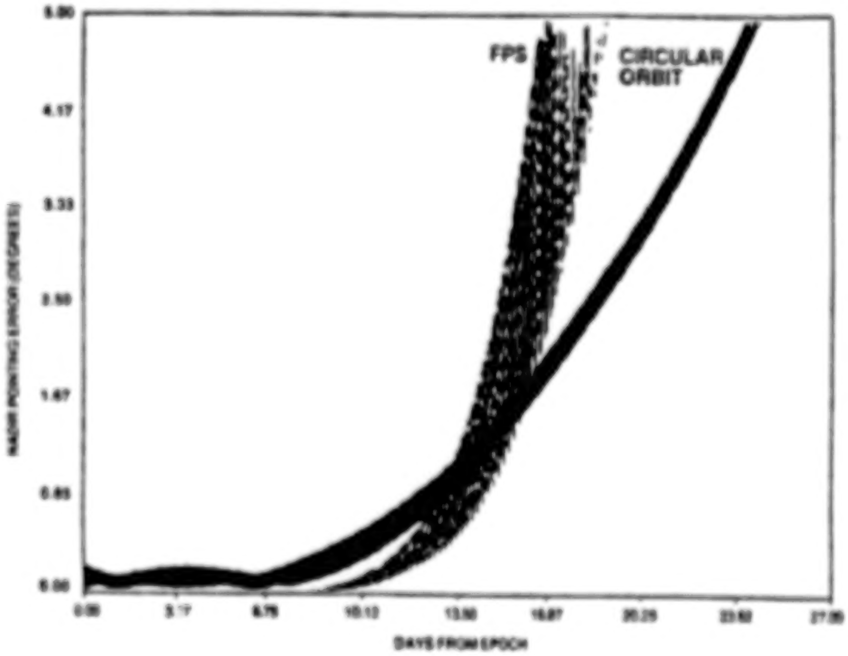

Figure 3. UARS Nadir Pointing Error for a 7-Day Fit: FPS (No Residuals) and Circular Ephemeris Representations

Table 2. Maximum Position Difference (km) During First Day of Fit

Direction	3-Day Circular	7-Day Circular	3-Day FPS		7-Day FPS	
			No Residuals	With Residuals	No Residuals	With Residuals
Along-track	-29.8	-29.8	0.47	0.05	0.80	0.06
Cross-track	2.7	2.9	0.13	-0.01	0.21	-0.02
Radial	11.3	11.4	0.17	-0.05	0.19	-0.05

Table 3. Maximum Position Difference (km) During First 7 Days of Fit

Direction	3-Day Circular	7-Day Circular	3-Day FPS		7-Day FPS	
			No Residuals	With Residuals	No Residuals	With Residuals[a]
Along-track	-65.7	-29.8	795.	-	0.89	-
Cross-track	9.7	9.7	272.	-	0.27	-
Radial	11.3	11.5	146.	-	0.19	-

---

[a] Only 32 hours of residuals are uplinked.

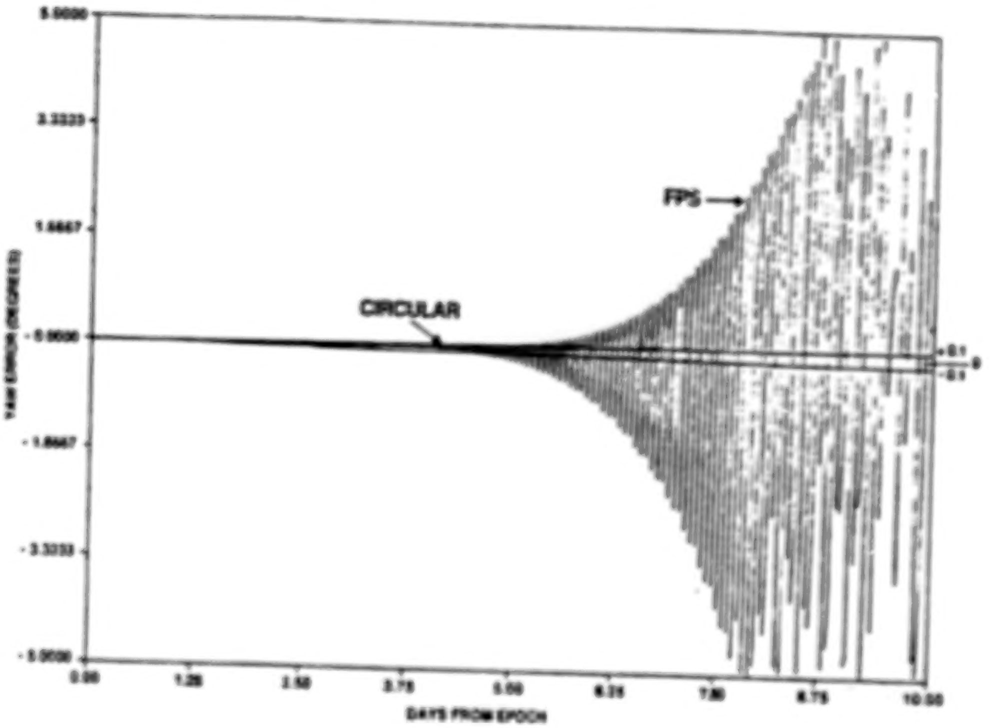

Figure 4. UARS Yaw Error for a 3-Day Fit: FPS (No Residuals) and Circular Ephemeris Representations

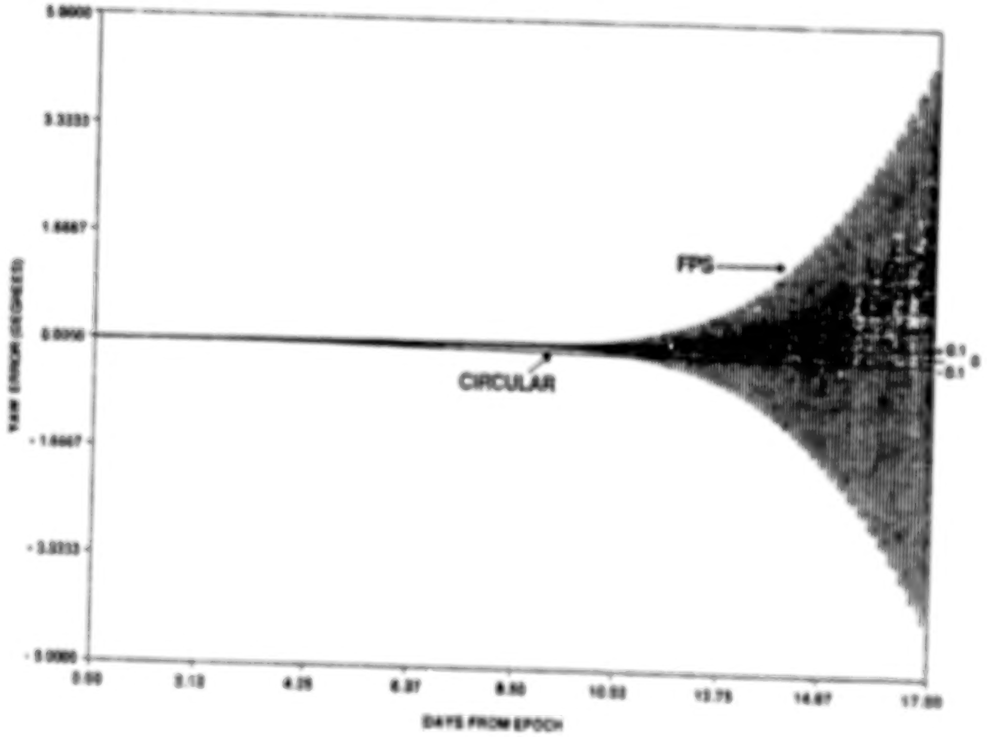

Figure 5. UARS Yaw Error for a 7-Day Fit: FPS (No Residuals) and Circular Ephemeris Representations

Table 4. Maximum Yaw, Pitch, Roll, and Velocity Errors During First Day of Fit

Errors	3-Day Circular	7-Day Circular	3-Day FPS No Residuals	3-Day FPS With Residuals	7-Day FPS No Residuals	7-Day FPS With Residuals
Pointing Errors (deg)						
Yaw	±0.0189	±0.0189	±0.0012	±0.0012	±0.0018	±0.0016
Pitch	+0.2467	+0.2451	±0.0060	±0.0003	-0.0065	±0.0005
Roll	±0.0238	±0.0232	±0.0013	±0.0001	±0.0014	±0.0001
Velocity errors (km/sec)						
X-axis	-0.0146	-0.0147	+0.0003		±0.0003	
Y-axis	±0.0025	±0.0025	±0.0002		±0.0002	
Z-axis	+0.0227	+0.0225	-0.0007		-0.0007	
Magnitude[a]	0.0246	0.0246	0.0007		0.0008	

---

[a] Magnitude at a given epoch and not magnitude of maximum values at different epochs.

Table 5. Maximum Yaw, Pitch, Roll, and Velocity Errors During First 3 Days of Fit

Errors	3-Day Circular	7-Day Circular	3-Day FPS No Residuals	3-Day FPS With Residuals	7-Day FPS No Residuals	7-Day FPS With Residuals
Pointing Errors (deg)						
Yaw	±0.0338	±0.0338	±0.0014	±0.0014	±0.0022	±0.0022
Pitch	+0.2671	+0.2451	±0.0062	±0.0004	-0.0065	±0.0004
Roll	±0.0402	±0.0401	±0.0013	±0.0001	±0.0014	±0.0001
Velocity errors (km/sec)						
X axis	±0.0147	±0.0147	±0.0003		+0.0003	
Y axis	±0.0046	±0.0036	±0.0007		±0.0008	
Z axis	+0.0227	+0.0225	-0.0007		-0.0008	
Magnitude[a]	0.0243	0.0268	0.0007		0.0008	

---

[a] Magnitude at a given epoch and not magnitude of maximum values at different epochs.

than the circular orbit errors. For both the circular orbit and the FPS orbit without residuals, yaw error is comparable to roll error, and pitch error is larger. The FPS pitch and roll errors are reduced by a factor of 10 by adding residuals, since computation of these angles depends only on the position. Velocity error comparisons for FPS and circular orbit again show the FPS to be superior to the circular orbit.

Table 6. Maximum Yaw, Pitch, Roll, and Velocity Errors During First 7 Days of Fit

			3-Day FPS		7-Day FPS	
Errors	3-Day Circular	7-Day Circular	No Residuals	With Residuals	No Residuals	With Residuals
Pointing Errors (deg)						
Yaw	±0.0802	±0.0801	-2.4100	-	±0.0022	±0.0022
Pitch	+0.5505	+0.2451	-6.4389	-	±0.0073	±0.0004
Roll	±0.0804	±0.0801	-2.3000	-	±0.0018	±0.0001
Velocity errors (km/sec)						
X axis	-0.0147	-0.0147	-0.1028		±0.0003	
Y axis	±0.0107	±0.0107	+0.3204		±0.0002	
Z axis	+0.0606	+0.0247	-0.7925		-0.0009	
Magnitude[a]	0.0638	0.0243	0.8139		0.0009	

---

[a] Magnitude at a given epoch and not magnitude of maximum values at different epochs.

Yaw accuracy degradation over the first 3 days due to switching from a 3-day fit to a 7-day fit was analyzed. Table 7 and Figures 6 and 7 show that some slight degrading does occur. The result of extending fit lengths is to increase the yaw error from 0.0014 deg to 0.0022 deg over the first 3 days of use, which is still better than the corresponding value of 0.0338 deg for the circular orbit. Pitch and roll accuracies are not significantly affected over the first 3 days by extending the fit length, as shown in Table 5. Adding position residuals does not significantly improve the yaw accuracy.

Table 7. Results of Yaw Error Comparison During First 3 Days

Representation	Maximum Yaw Error Observed Over First 3 Days 3-Day Fit (Degrees)	7-Day Fit (Degrees)
FPS (with residuals)	0.0014	0.0022
FPS (without residuals)	0.0015	0.0022
Circular orbit	0.0338	0.0338

4.2 EVALUATION OF SCALING AND SIZING OF FPS COEFFICIENTS AND RESIDUALS FOR OBC USE

An analysis was performed comparing the FPS coefficients to the largest and smallest values that can be uplinked when scale factors are used to convert them for uplink to the OBC.

The UARS OBC is structured for double-precision, 36-bit double words for position and velocity coefficients and single-precision, 18-bit words for position residuals. The double-precision words do not use the sign bit of the low-order, 18-bit word; thus, only 35 bits are used. From the scale factor and number of bits used, the largest and smallest possible values of the uplink parameters can be computed from the following equations:

$$\text{Largest coefficient} = (2^N - 1)/(2^{N-S})$$

$$\text{Smallest coefficient} = 1/(2^{N-S})$$

where N = one less than the number of bits used (i.e., N = 34 for position and velocity coefficients; N = 17 for single-precision residual coefficients)

S = scale factor of OBC data taken from Landsat-D System Tables (Shirey, 1983) one for each coefficient used

These equations were used to evaluate the largest and smallest values that can be uplinked when the scale factor is taken into account. The units of the coefficients were changed from meters per $(\text{second})^P$ to meters per $(\text{millisec})^P$, where P represents the power of time used in generating the coefficient. This was done to match the units used by the OBC. Each coefficient computed by the ERGSS program was found to be between the largest and smallest values that could be uplinked.

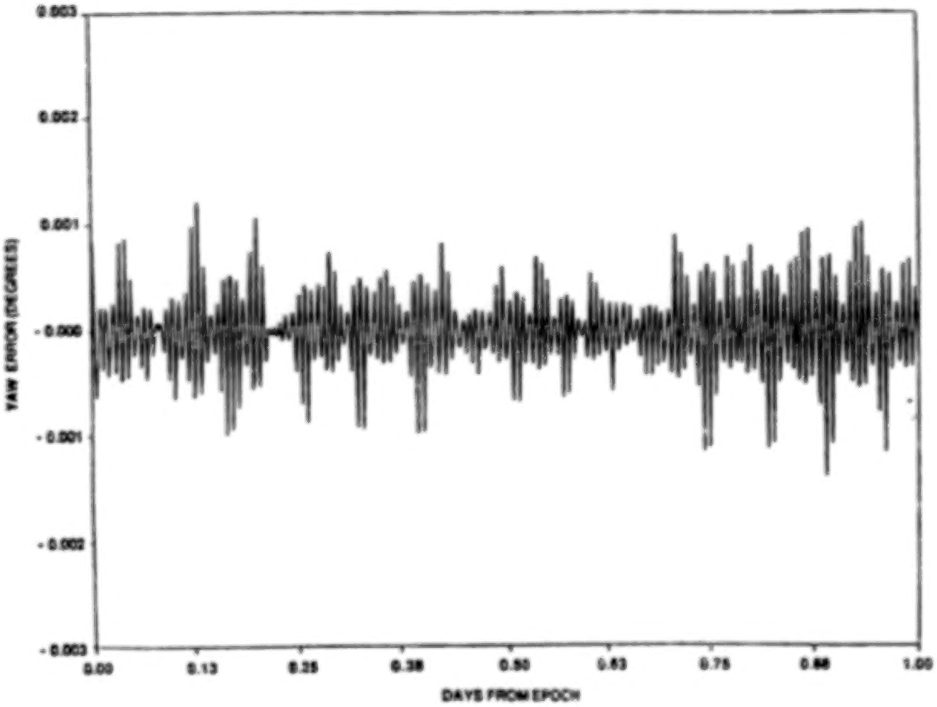

Figure 6. UARS Yaw Error During First Day for a 3-Day Fit of FPS (With Residuals)

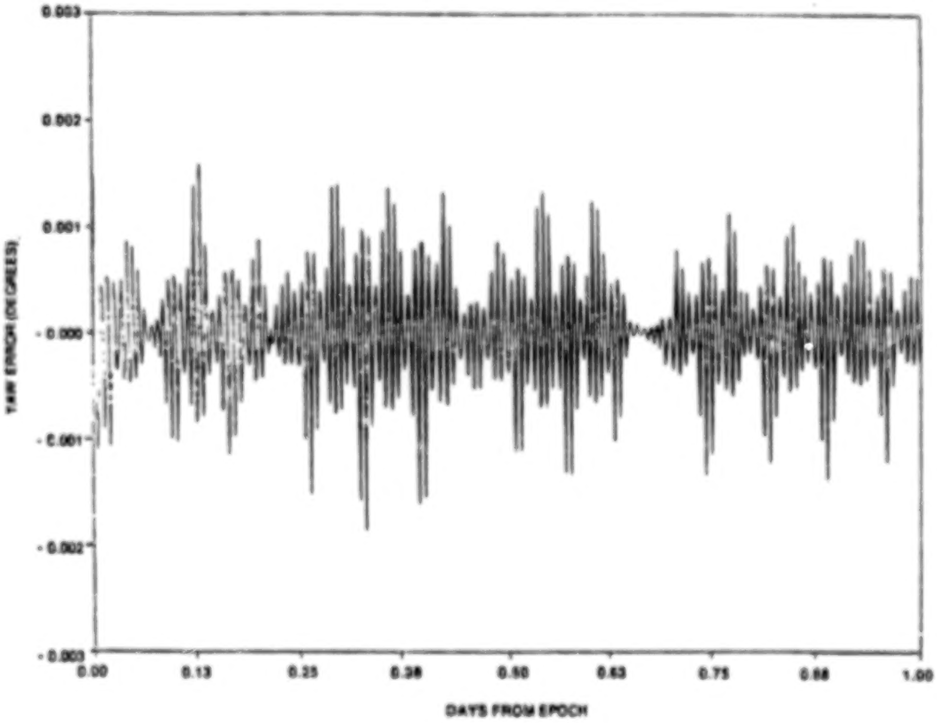

Figure 7. UARS Yaw Error During First Day for a 7-Day Fit of FPS (With Residuals)

Overflow or underflow was not encountered for the nominal eccentricity, e = 0.001486.

A study was next carried out (Hashmall, 1987) to determine if the Landsat scaling parameters would produce overflows using nonnominal orbital parameters. In this study, a worst-case orbit was assumed to be one with an eccentricity (e) of 0.05. Both 7-day and "standard" 3-day FPS fits were considered. The programs and procedures previously used were modified slightly to improve processing efficiency, and a search was done to determine the largest eccentricity before an overflow would occur. Most of the orbit generation runs were performed with the standard set of input orbital elements, other than eccentricity.

Additional 3-day orbit generation runs were performed for e = 0.05 with several values of the right ascension of the ascending node. The 172.035-deg value was reduced by 45 deg in 7.5-deg steps. Additionally, one run was done with a 90-deg decrement of the right ascension of the ascending node.

Computations of FPS coefficients were performed with a reference time (TREF) of 21 hours after the start time (as in the original study) and repeated with a TREF of 36 hours after the start time.

For the 3-day fits, overflow first occurred at e = 0.066, where one position coefficient, three velocity coefficients, and one residual overflowed. At e = 0.065, there were no overflows. For the 7-day fits, the first overflow occurred at e = 0.049, where a single residual overflowed. At e = 0.048, there were no overflows. These results were unaffected by changing the FPS reference time from 21 to 36 hours after the start of the computation interval.

FPS coefficients for 3-day fits at e = 0.05 showed no overflows in cases where the right ascension of the ascending node was set to values differing from the standard value by up to 45 deg.

The 3-day fit results indicated that the FPS ephemeris table scaling used for Landsat will not produce scaling problems for UARS. Even if a 7-day fit were used, an eccentricity greater than 0.048 is probably quite unlikely.

4.3 EVALUATION OF UNCERTAINTIES IN THE UARS PREDICTED ORBIT

The different scenarios for tracking passes and expected error sources, such as daily uncertainty in the solar flux or geopotential fields, result in an uncertainty in predicting the UARS orbit. Schanzle (1985, 1987) analyzed this uncertainty and reported the expected results for UARS. Figure 8 indicates a possib total nadir-pointing error when the uncertainty in the UARS orbit is added to an FPS nadir-pointing error from a 7-day fit of coefficients (from Folta, 1987). Even though the circular orbit long-term accuracy is better than the FPS orbit accuracy, the predicted orbit uncertainty becomes the dominant error source and may exceed TDRS pointing requirements within 2 weeks.

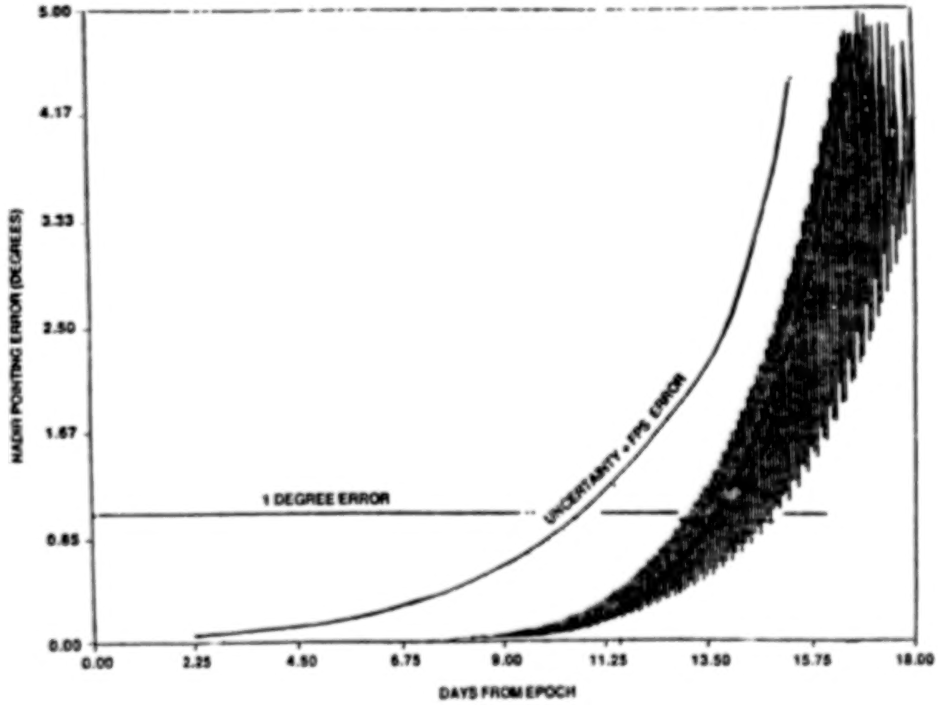

Figure 8. UARS Nadir-Pointing Error (Prediction Uncertainty Added) for a 7-Day Fit of FPS (No Residuals)

4.5 TDRS FPS ACCURACIES

UARS requires a predicted TDRS orbit to allow onboard computation of the HGA pointing angles. The TDRS orbit will be represented by FPS coefficients as described in Section 2.1, with eight coefficients uplinked to represent the position.

To determine the accuracy of this representation, an analysis was performed using 3-day and 7-day FPS fit intervals. The results, presented in Figure 9, compare the TDRS nadir-pointing error to elapsed time using the same methods described in Sections 3 and 4.1. Both fit intervals yield small nadir-pointing errors over the first 3 days, with the 7-day fit interval superior for longer periods. As indicated in Section 2.3, the contribution to spacecraft-to-TDRS pointing error, $\Delta\phi_T \approx 1.2\ \Delta\Theta_T$ (the computed nadir pointing error).

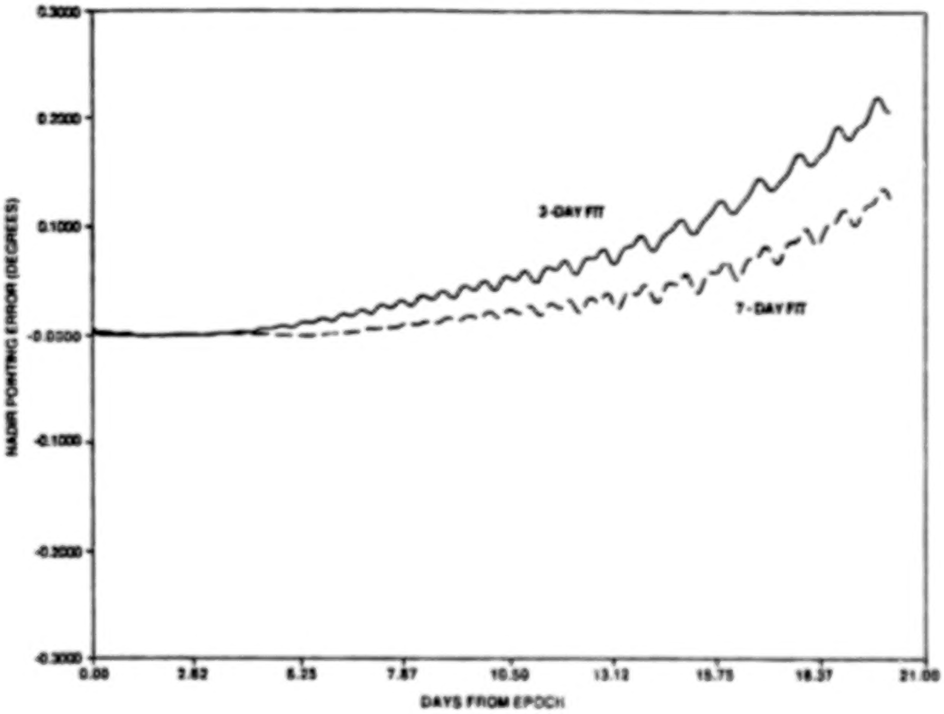

Figure 9. TDRS Nadir-Pointing Error for 3- and 7-Day Fits of FPS (No Residuals)

5.0 CONCLUSIONS

The UARS orbit can best be represented for short periods (1 week after residuals are exhausted), with coefficients generated from an FPS fit to a 7-day predicted ephemeris. Even without residuals added, the FPS orbit is superior to the circular orbit representation and should be considered for backup instead of the circular orbit technique. The results of this analysis confirmed the following:

- In general, for short-term backup (1 week), orbits generated from the FPS approximation are more accurate than those using the circular orbit approximation. Circular orbits are initially less accurate than FPS orbits but degrade more slowly over long timespans.

- A 1-deg nadir-pointing fit error and a 0.1-deg yaw fit error can be maintained by both the FPS orbit and circular orbit representations for approximately 11 days when using a 7-day fit interval.

- During the nominal uplink period, pitch and roll errors are not significantly increased by extending the fit interval from 3 days to 7 days. The maximum yaw error over the first 3 days increased from 0.0014 deg to 0.0022 deg when extending the fit length.

- Roll errors are comparable in magnitude to yaw errors for circular orbits, and for FPS orbits when position residuals are not used.

- Yaw, pitch, and roll errors, when using the FPS approximation with or without residuals, are significantly smaller then those for circular orbits over the length of the fit. When the time of comparison exceeds the timespan of the fit, the FPS accuracies degrade rapidly.

- Coefficients generated for the 7-day fit using Landsat scaling factors do not violate OBC word size requirements.

- Any increased fit accuracy in using circular orbits for long-term backup may be irrelevant because of the uncertainty in predicting the UARS orbit.

- TDRS ephemeris representation fit errors remain small (<0.1 deg) over the 1- to 2-week timespan considered in this report and do not pose a problem for spacecraft-to-TDRS pointing.

ACKNOWLEDGMENTS

A. Long provided background information on the ephemeris representations. Most of the work reported in this paper was performed by D. Folta. J. Hashmall extended the study of scaling and sizing of FPS coefficients to include nonnominal orbits.

APPENDIX - ELEMENTS USED FOR INPUT INTO EPHEMERIS GENERATION

The nominal osculating elements used in this analysis are as follows:

Epoch	October 1, 1989
a	6978.0653 km
e	0.0014860
i	57.017788 deg
Ω	172.03500 deg
ω	60.937802 deg
M	299.16207 deg

The propagation parameters used in this analysis are as follows:

Drag coefficient	2.2
UARS spacecraft area	0.000028 km^2
UARS spacecraft weight	5500.0 kg
Solar flux ($F_{10.7}$)	200×10^{22} watt/(m^2Hz)
Geopotential	15 by 15
Propagator	12th order Cowell, 60-second stepsize
Solar perturbations	Included
Lunar perturbations	Included

REFERENCES

1. Boland, D., *System Description and Users Guide for the Ephemeris Representation Ground Support System Quality Assurance Program (ERGSQA)*, Computer Sciences Corporation, CSC/TM-82/6085, April 1982

2. Boland, D. and Y. Lee, *Users Guide and Mathematical Description of the Ephemeris Representation Ground Support System (ERGSS)*, Computer Sciences Corporation, CSC/TM-82/6111, April 21, 1982

3. Folta, D., "Evaluation of the Accuracies of Circular Orbit and Fourier Power Series (FPS) Approximations for Backup Use by the UARS Onboard Computer (OBC)," *Upper Atmosphere Research Satellite (UARS) Compendium of Flight Dynamics Analysis Reports*, Computer Sciences Corporation, CSC/TM-87/6020, Mission Report 87001, April 1987

4. Hall, D. L. and A. C. Long, "Spacecraft Ephemeris Representation for Onboard Computation," Paper 78-1402, AIAA/AAS Astrodynamics Conference, Palo Alto, California, August 7-9, 1978

5. Hashmall, J., "Fourier Power Series Coefficient Size as a Function of Orbit Eccentricity (an Addendum to Report 87001)," Upper Atmosphere Research Satellite (UARS) Compendium of Flight Dynamics Analysis Reports, Computer Sciences Corporation, CSC/TM-87/6020, Mission Report 87002, October 1987

6. Lee, Y. M., User's Guide and Mathematical Description of the Ephemeris Representation Ground Support System (ERGSS), Computer Sciences Corporation, CSC/TM-81/6111, June 1981

7. Long, A., and D. Folta, Spacecraft Ephemeris Representation for Onboard Computation, presentation to Code 554.1, November 20, 1986 (unpublished)

8. Miller, J., OBC Ephemeris Software Requirements, General Electric Company, Astro Space Division, PIR No. U-1K20-UARS-927, September 2, 1987

9. NASA/General Electric Company, [UARS] Systems and Operations Requirements Document (baseline version 0), SVS-11118, December 1987

10. Quinn, R., Landsat-4 Repair Mission Flight Software Requirements, General Electric Company, PIR 1250-lsd-1541, November 5, 1984

11. Schanzle, A. F., Prelaunch Orbital Error Analysis for the Upper Atmosphere Research Satellite (UARS), EG&G Washington Analytical Services Center, Inc., November 1985

12. --, Additional Prelaunch Orbital Error Analysis for the Upper Atmosphere Research Satellite (UARS), EG&G Washington Analytical Services Center, Inc., March 1987

13. Shirey, R., Landsat-D Prime Flight Software System Tables, General Electric Company, Space Division, PIR-1D30-LSD-1415, February 25, 1983

N89-15960

GOES-NEXT NAVIGATION OPERATIONS

John L. Fiorello, Jr., and In-Hwan Oh, Computer Sciences Corporation

C. Lee Ranne, National Oceanic and Atmospheric Administration

ABSTRACT

The next generation of Geostationary Operational Environmental Satellites, GOES-I through -M (hereafter referred to as GOES-Next), begins a new era in the operation of weather satellites by the National Oceanic and Atmospheric Administration (NOAA). With a new spacecraft design, three-axis attitude stabilization, new ground support equipment, and improved methods of image navigation and registration that use on board compensation techniques to correct images for satellite motion, NOAA expects improved performance over the current series of dual-spin spacecraft. To meet these expectations, planning is currently underway for providing the complex and intensive operational environment that will meet the challenge of operating the GOES-Next spacecraft. This paper describes that operational environment.

1.0 INTRODUCTION

The Geostationary Operational Environmental Satellites-I through -M (hereafter referred to as GOES-Next), expected to be first launched in the early 1990s, will continue the GOES tradition as our Nation's primary weather monitoring system. It will have a different attitude stabilization system, a new ground support system, and improved image-processing techniques over its ancestors. This paper presents an overview of the National Oceanic and Atmospheric Administration's (NOAA's) current plans for providing navigational support for the operations of GOES-Next. It describes the GOES-Next mission, the GOES-Next ground equipment, and the operational requirements for the mission. It also provides an overview of the navigation and image navigation and registration (INR) support that will be provided, which includes orbit and attitude determination, star measurements, data monitoring, stationkeeping, housekeeping, and image motion compensation (IMC), which is the method used to correct image pixels for satellite motion.

1.1 MISSION DESCRIPTION

The purpose of the GOES mission is to provide meteorological, scientific, and communications services. Its meteorological services include providing visible and infrared images of clouds and of the Earth's surface. It also obtains water vapor field data and soundings of the Earth's atmosphere. Scientifically, the GOES-Next mission measures solar X-rays in 2 bands, low-energy particle flux in 14 bands, and high-energy flux of protons and alpha particles. The GOES-Next communication services include a data collection platform service to relay environmental data to the ground, a weather facsimile service to relay weather-related data, and a search-and-rescue service to relay data from emergency transmitters.

Figure 1 shows the spacecraft configuration. The structure consists of a main body that houses the instruments and the attitude and orbit control system, a solar array connected to the south face of the main body, and a solar sail connected to the north face of the main body. The primary instruments are the imager and the sounder, which are located on the Earth-pointing face of the main body. The imager provides 4 infrared channels and 1 visible channel for images of the Earth; the sounder provides 18 infrared channels and 1 visible channel for soundings of the Earth's atmosphere. The imager and the sounder provide the data for the meteorological services of the GOES mission.

ORIGINAL PAGE IS
OF POOR QUALITY

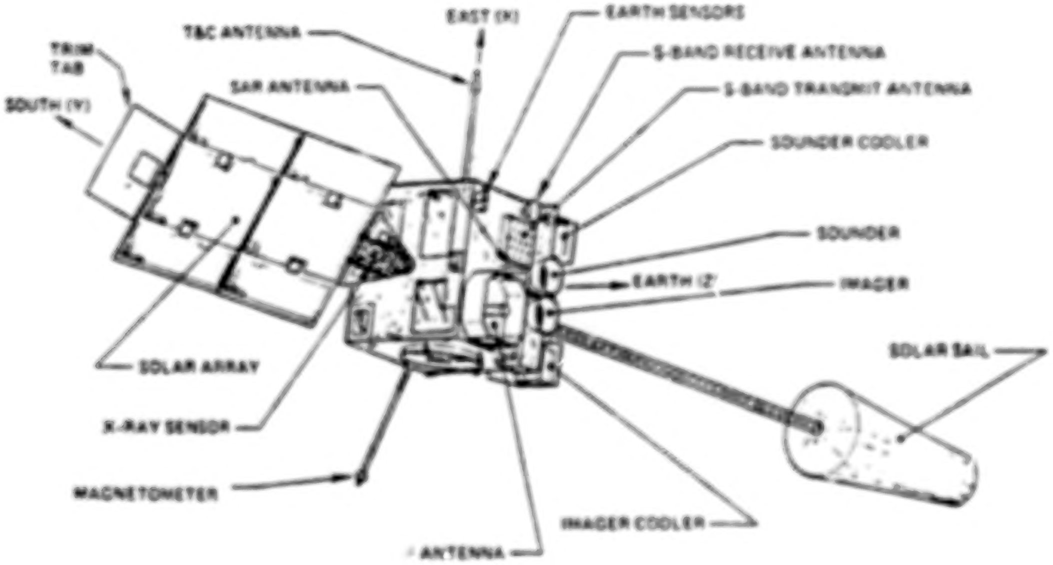
TRIM TAB
SOUTH (Y)
T&C ANTENNA
SAR ANTENNA
EAST (X)
EARTH SENSORS
S-BAND RECEIVE ANTENNA
S-BAND TRANSMIT ANTENNA
SOUNDER COOLER
SOUNDER
EARTH (Z)
IMAGER
SOLAR SAIL
SOLAR ARRAY
X-RAY SENSOR
MAGNETOMETER
IMAGER COOLER
ANTENNA

Figure 1. GOES-Next Spacecraft Configuration

There are six types of sensors and five types of actuators on the spacecraft (Figures 1 and 2) that are used for attitude and orbit control. The sensors include two sets of coarse analog Sun sensors (CASSs), redundant digital Sun sensors (DSSs), redundant Digital Integrating Rate Assemblies (DIRAs), redundant Earth sensors, a magnetometer, and two Sun analog sensors (located on the solar array yoke). The CASS orients the spacecraft with respect to the Sun during transfer orbit. The DSS calibrates the DIRA during the transfer orbit. The DIRA is a system of three mutually perpendicular rate integrating gyros that monitors attitude drift throughout the transfer orbit and during stationkeeping maneuvers. The Earth sensor provides pitch and roll data and is the primary sensor for on-orbit attitude control. The magnetometer senses the ambient magnetic field in the space environment. The Sun analog sensors provide information about the Sun's position relative to the solar array.

The configuration of the actuators is shown in Figure 2. The actuators include six redundant pairs of 5-pound thrusters, two momentum wheels, a reaction wheel, two magnetic torquer coils (not shown in the figure), and a solar array trim tab panel. The thruster pairs are located on the east, south, and west faces of the spacecraft. They are used by the onboard Attitude and Orbit Control System (AOCS)

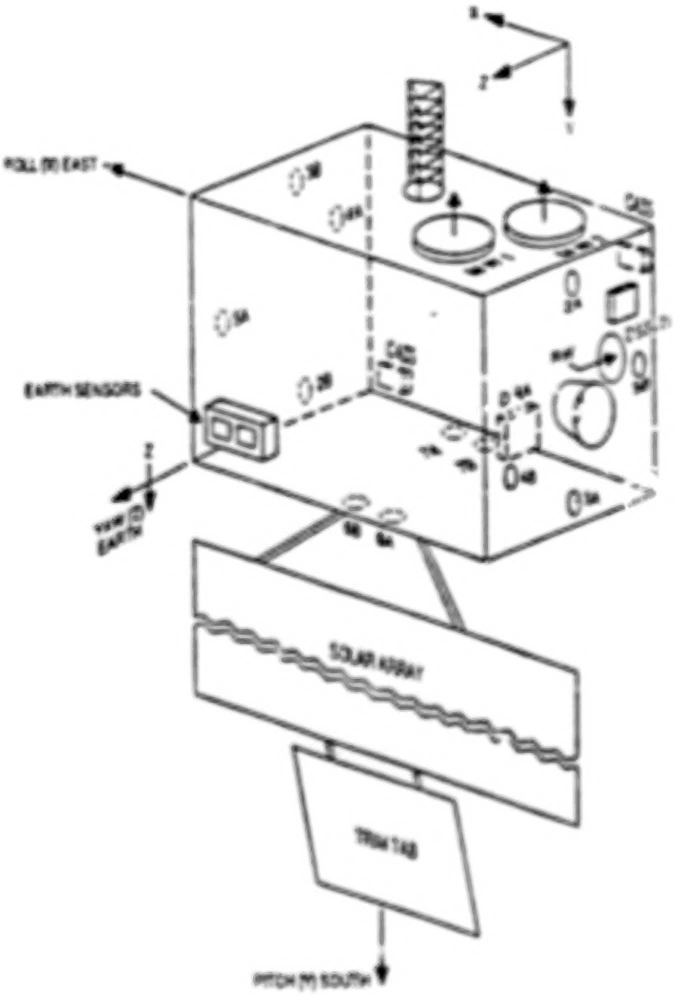

Figure 2. GOES-Next Attitude and Orbit Control System

for autonomous attitude control and by ground command for orbit control. The momentum wheels are used for primary attitude stabilization, with the reaction wheel as a backup. The magnetic torquer coils are located on the anti-Earth and east faces of the spacecraft; they are used for yaw control. The trim tab panel is located at the end of the solar array and is used for compensating the solar radiation torque on the solar array. The solar array is continuously rotated by a stepper motor to expose all solar cells to the Sun.

The two operational GOES-Next spacecraft will fly in geosynchronous orbit with designated stations of 75 degrees and 135 degrees west longitude. Their nominal

ORIGINAL PAGE IS
OF POOR QUALITY

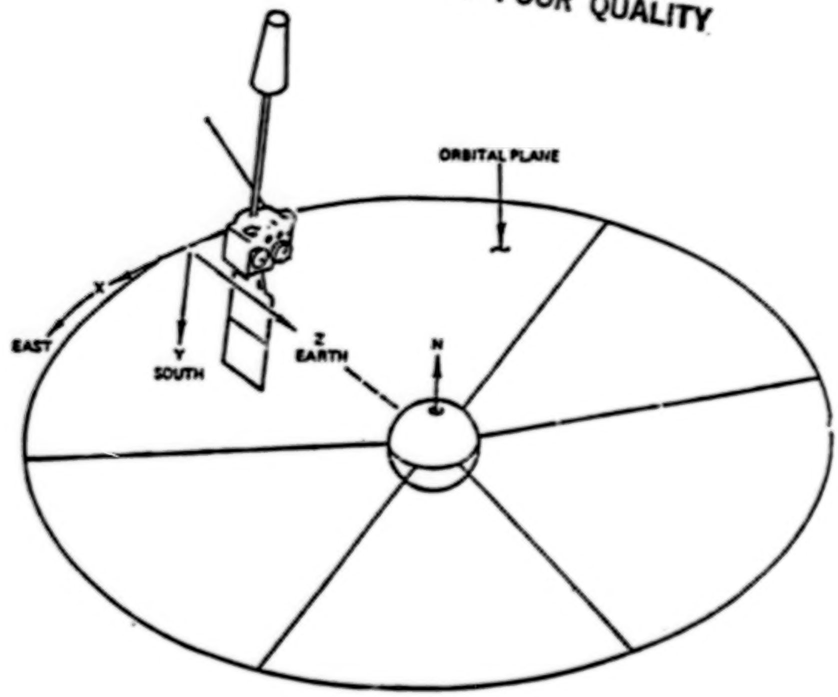

Figure 3. Nominal GOES-Next Orientation

inclination is ±0.1 degree about the Equator. Their attitude is three-axis stabilized, spinning at one revolution per orbit to maintain Earth pointing for the imager and the sounder. Figure 3 shows the nominal GOES-Next attitude orientation.

1.2 OPERATIONS GROUND EQUIPMENT (OGE) DESCRIPTION

On-orbit ground support for the GOES-Next spacecraft will be provided by the Operations Ground Equipment (OGE) located at the Satellite Operations Control Center (SOCC) (currently in Suitland, Maryland) and at a command and data acquisition (CDA) station at Wallops Island, Virginia. The OGE components at the SOCC include the Product Monitor (PM) and the Orbit and Attitude Tracking System (OATS). The PM performs data quality monitoring, system troubleshooting, landmark identification, and image navigation and registration (INR) data capture and distribution. The latter two functions are performed in support of the OATS, which is the key tool for navigation operations. The CDA station OGE components include the OGE Data Acquisition and Patching Subsystem (ODAPS), the Sensor Processing System (SPS), the OGE Input Simulator (OIS), and the PM. The ODAPS performs demodulation, bit synchronization, and patching functions. The SPS performs processing of imager and

C-7

sounder raw data. The OIS simulates data in support of OGE integration and testing and serves as a diagnostic tool. During mission operations, the OIS will be a backup for the OATS. The PM at the CDA station is used for backup quality monitoring and testing. Figure 4 is a diagram of the OGE at both locations.

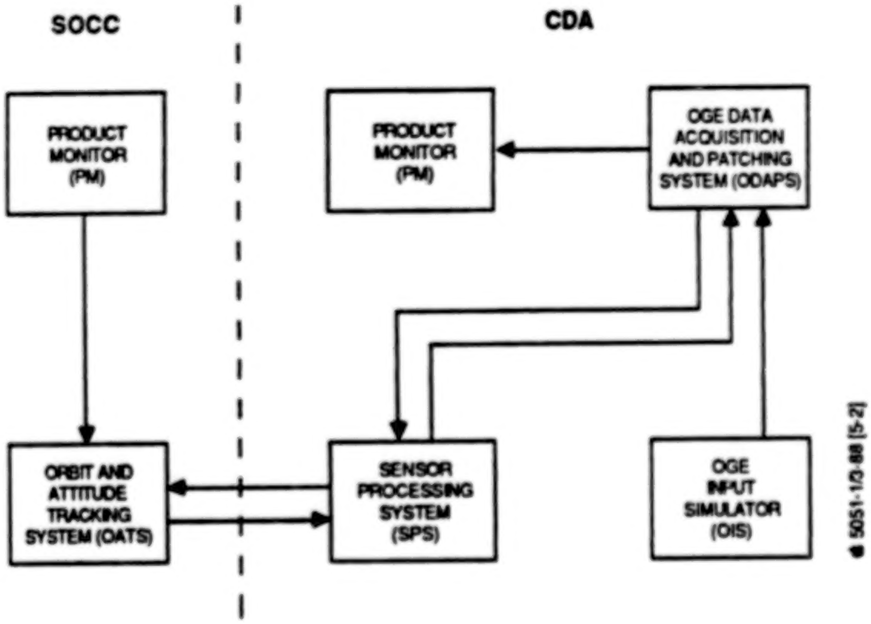
SOCC
CDA
PRODUCT MONITOR (PM)
PRODUCT MONITOR (PM)
OGE DATA ACQUISITION AND PATCHING SYSTEM (ODAPS)
ORBIT AND ATTITUDE TRACKING SYSTEM (OATS)
SENSOR PROCESSING SYSTEM (SPS)
OGE INPUT SIMULATOR (OIS)
5051-1/3-88 [5-2]

Figure 4. OGE Components at SOCC and CDA Station

The OATS is the primary tool for performing all the navigation operations functions. It is composed of both hardware and software. The hardware includes a Gould CONCEPT 32/6751 central processing unit (CPU) with a 4-megabit (Mb) random access memory (RAM) and a hardware floating-point accelerator as the central processor. There are also two 160-Mb disk drives, one 800/1600-bit-per-inch (bpi) magnetic tape drive, seven input/output (I/O) devices, and two communication multiplexers. The system software includes a Gould MPX-32 Operating System, a macro assembler, a FORTRAN 77+ compiler, control software, and analysis and planning software. The control software provides a multitasking environment and support for multiple spacecraft for the analysis and planning software.

The analysis and planning software includes modules that perform the major functions for navigation operations. It estimates the spacecraft orbit state and the spacecraft attitudes for the imager and the sounder. It generates predictions of star availability, sensor conflicts, eclipses, and the spacecraft ephemeris. Using the orbit and attitude states, it generates coefficients for uplink to the spacecraft that will be used to compensate the images for orbit and attitude motion. It also generates orbit and attitude parameters that are used for gridding and Earth location. It uses star availability predictions to generate commands for uplink to the spacecraft to view stars. It also generates commands for changing the trim tab angle and for calibrating the DIRA. It plans stationkeeping maneuvers and generates the thruster firing commands for these maneuvers. It also analyzes thruster firing telemetry for calibrating the thrusters and for monitoring fuel use.

1.3 OPERATIONAL REQUIREMENTS

The primary purpose of navigation operations is to monitor and maintain the accuracy of image navigation and registration (INR). Image navigation is the process of determining the Earth longitude and latitude corresponding to each pixel in an image. Image registration is the process of maintaining the image so that each pixel points to the same corresponding Earth location. The INR accuracy requirements are currently being defined. They are stated in terms of Earth location and image registration accuracy. Furthermore, all images and soundings taken within a 24-hour period must meet the Earth location accuracy requirements with reference to a common grid.

The Earth location accuracy requirements apply to the instantaneous geometric field of view for every pixel in any image. The central Earth angle is the angle between the subsatellite point at the center of the image and the pixel that is being Earth located.

Image registration requirements are specified in three categories: image registration between pixels in the same image, image registration between corresponding pixels in any two images taken within a 90-minute period not interrupted by a disturbance interval, and image registration between corresponding pixels in any two images taken within a 24-hour period interrupted by up to three 10-minute housekeeping intervals.

Maintaining the attitude and geostationary orbit constraints is also the responsibility of navigation operations. The orbital requirements are a spacecraft inclination in the range of ±0.1 degree and a spacecraft longitude maintained within ±0.5 degree of its nominal station.

Navigation operation activities focus on providing INR support for maintaining the INR requirements and on maintaining the spacecraft orbit and attitude through stationkeeping and housekeeping support.

2.0 INR SUPPORT

Navigation operation activities that support the effort of maintaining the INR requirements include orbit and attitude determination, star measurements, IMC coefficient generation, and data monitoring. All these activities are performed using the OATS.

2.1 ORBIT AND ATTITUDE DETERMINATION

The orbit and attitude determination process for GOES-Next uses range, star, and landmark data to obtain the best estimate of the spacecraft orbit and attitude. The estimated orbit and attitude states are then used to generate IMC coefficients to be uplinked to the spacecraft. These coefficients are used on board to correct each pixel in the image corresponding to the true orbit and attitude to produce an image corresponding to the ideal orbit and attitude.

Spacecraft range measurements are the primary observable for orbit determination and are taken from the CDA station. Landmark observations are primarily obtained by the imager visible channel. Each operational spacecraft has a separate landmark list, although several landmarks are common to both operational spacecraft. Star observations are performed by the imager and the sounder with commands generated by the OATS for observing them. Star measurements are discussed in detail in the next section.

The orbit and attitude determination process involves the nonlinear estimation of the orbit and attitude state vectors such that the weighted sum of the squares of the residual errors of the observables,

$$\sum_{i} \delta \vec{M}^{T} \cdot W \delta \vec{M} \qquad (1)$$

is minimized. The data weighting matrix, W, is the inverse of the covariance matrix for measurement noise and $\delta\vec{M}$ is the residual error.

The observation data used are the slant range and star and landmark scan angles. The slant range is the distance from the CDR tracking station to the spacecraft. The scan angle observables, E and N (designated in Figure 5), are transformed from raw star and landmark observations. E is the complement of the angle between the instrument X_B axis and the line of sight to the star or landmark, $\hat{S}$, in the scan plane. This is approximately in the east-west direction. N is the angle between the instrument X_B-Z_B plane and the scan plane. This is approximately in the north-south direction.

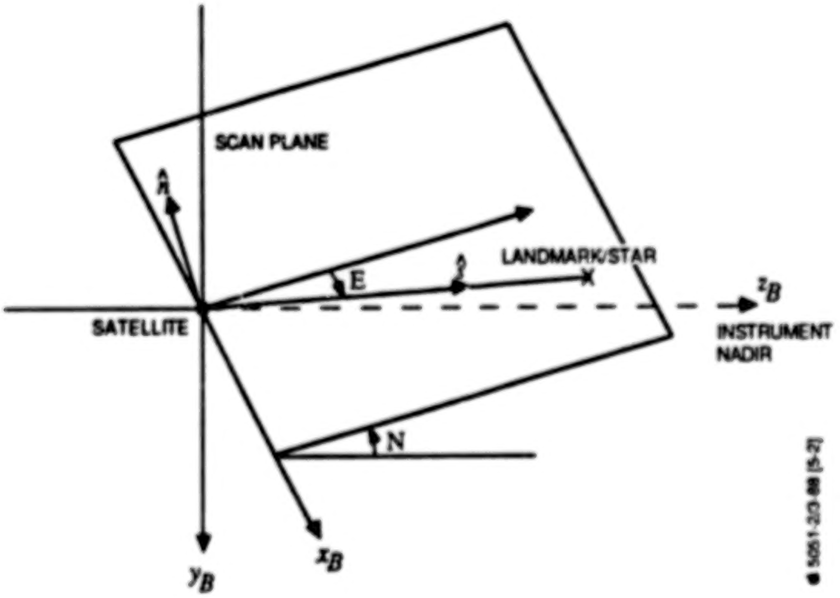

Figure 5. Scan Angle Observables

The scan angles are affected by detector misalignment and small attitude changes. Detector misalignment shifts the center of the image when the instrument is at an angle N in the north-south direction. This causes the following corrections in the scan angles:

$$\delta E = \Theta_{ma} \cos N + \Phi_{ma} \sin N \qquad (2)$$

$$\delta N = \phi_{ma} \cos N - \Theta_{ma} \sin N \tag{3}$$

where Θ_{ma} and ϕ_{ma} are the pitch misalignment and roll misalignment, respectively. Small changes in roll, pitch, and yaw ($\delta\phi$, $\delta\Theta$, $\delta\psi$) also cause corrections to the scan angles:

$$\delta E = -\cos N\delta\Theta - \sin N\delta\psi \tag{4}$$

$$\delta N = -\delta\phi - \tan E \sin N\delta\Theta - \tan N \cos N\delta\psi \tag{5}$$

The observable model, $\vec{M}$, is a function of the state vector, $\vec{g}(\vec{\mu},\vec{\beta})$, which includes the orbital state vector, $\vec{\mu}$, consisting of the orbital elements, and the attitude/misalignment state vector, $\vec{\beta}$, which consists of the roll, pitch, and yaw attitude angles (ϕ, Θ, ψ) and the roll and pitch instrument misalignment angles (ϕ_{ma}, Θ_{ma}). The attitude model used is an empirical model that fits each angle with a linear combination of Fourier, exponential, and B-Spline basis functions:

$$\beta^k(t) = \sum_{j=1}^{n} C_j^k \; B_j(t): \quad \text{generalized attitude state vector} \tag{6}$$

where the superscript k indicates the attitude state vector angle (ϕ, Θ, ψ, ϕ_{ma}, Θ_{ma}) indexed from 1 to 5. $B_j(t)$ are the basis functions, and C_j^k are their associated coefficients. These coefficients are part of the solve-for parameters and are the IMC coefficients for attitude. From a finite element analysis, the expected attitude variation over one day is as shown in Figure 6. Caused mainly by instrument thermal distortions, this variation should be repeatable approximately every 24 hours, lending itself to a natural periodic fit with a Fourier series. Exponential basis functions are used to model the attitude during eclipse season. However, some erratic behavior in the attitude is expected even after the Fourier and exponential fit has been made. B-spline functions are available to fit this erratic behavior, if necessary.

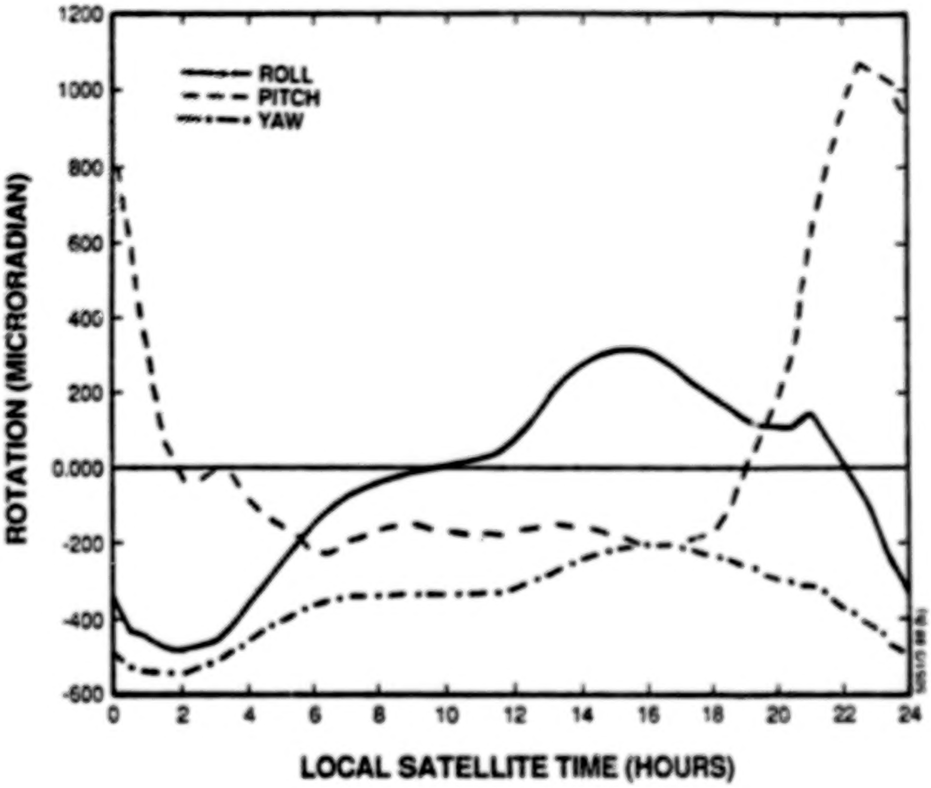

Figure 6. Expected Daily Attitude Variation

2.2 STAR MEASUREMENTS

Predicting star windows and generating star viewing commands are navigation operation functions that support the orbit and attitude determination process in OATS. The GOES-Next star catalog consists of approximately 500 stars of 6th magnitude and brighter, including some variable and multiple stars. Star observations are made in the imager and sounder fields of view around the Earth. Stars are selected for observation only if they are observed uniformly throughout the day and are separated geometrically within an image. It is currently planned to observe approximately three stars in the interval following each imaging interval (every half-hour). This provides approximately 150 stars per day for use in attitude determination. Navigation operation responsibilities include investigating and taking corrective action for anomalies such as missed star observations and large star measurement residuals.

2.3 IMAGE MOTION COMPENSATION

IMC is the process of correcting the pixels in an image for orbital and attitude motion effects and for instrument thermal distortions. This is performed in the attitude and orbit control electronics by the control system processor. The east-west and north-south shift in each pixel is based on the IMC coefficients that are computed in the OATS. As a result, the scan lines in the image seen by the user appear as a perfect image. Figure 7 is a diagram of the IMC system. The top of Figure 7 shows the scan lines that would result from no pixel shifts due to satellite motion. This would occur in an ideal orbit and attitude. However, in the actual motion of the satellite, scan lines trace a path that deviates from the ideal path (shown at the bottom of Figure 7). The IMC system will correct the azimuth and elevation of each image pixel so that the scan line seen by the user is ideal.

The field of view of the imager is 23 degrees in azimuth by 21 degrees in elevation. There are 1480 scan lines from top to bottom. Each visible scan line contains a series of pixel arrays that are 1 pixel wide by 8 pixels high. Individual pixels are 1 kilometer in both azimuth and elevation. The number of pixel arrays contained in an image depends on the scan field. Scan fields range from a full Earth scan down to an intensive region scan covering 1000 kilometers in both azimuth and elevation.

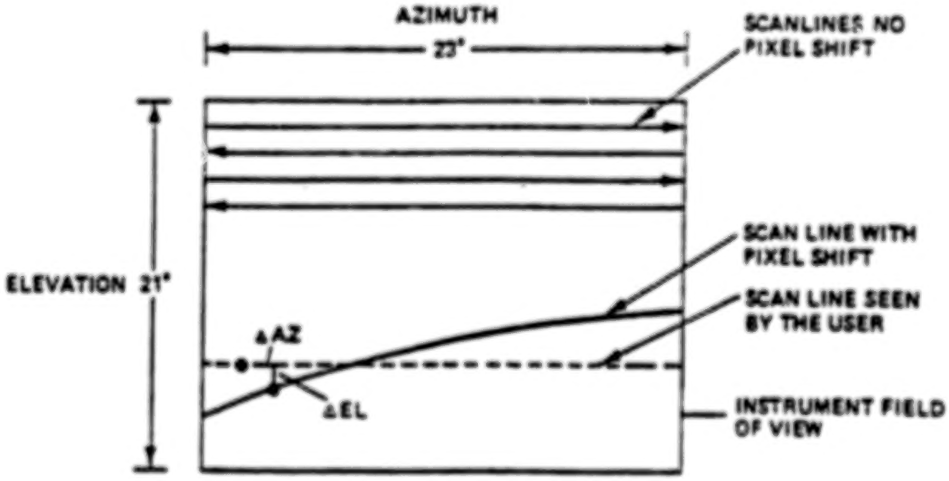

Figure 7. Image Motion Compensation (IMC) System

Orbital drift is caused mainly by the geopotential field (zonal and tesseral harmonic terms), solar and lunar gravity, and solar radiation pressure. The orbital effects on the image are a shift in azimuth due to the east-west drift of the spacecraft from its nominal station and a shift in elevation due to the nonzero inclination of the orbit. Attitude drift effects are caused primarily by solar radiation torques. Attitude effects on the image are on elevation shift due to roll drift, an azimuth shift due to pitch drift, and a combination of azimuth and elevation shifts due to yaw drift and instrument misalignments.

Navigation operation responsibilities for IMC include generating the IMC coefficients and monitoring their uplink, quality assuring the IMC coefficients, and troubleshooting IMC anomalies. Residuals of computed IMC coefficients against the orbit and attitude solutions are monitored. Large residuals are investigated, and corrective action is taken before the coefficients are uplinked and made operational. IMC quality checking is also performed using the OATS. IMC data are received and checked for consistency with the IMC model.

2.4 DATA MONITORING

Data are monitored regularly to check INR accuracy requirements, stationkeeping requirements, and the health and safety of the spacecraft. Landmark observations are processed, and their residuals are computed based on the predicted orbit and attitude. Abnormally large numbers of landmark residuals above the threshold are investigated, and corrective action is taken. Star observations are also monitored, as discussed in Section 2.2.

3.0 NAVIGATION SUPPORT

Stationkeeping maneuvers are performed to control the inclination (north-south stationkeeping maneuvers) and subsatellite longitude (east-west stationkeeping and station change maneuvers). Maneuvers at the end of mission life are also performed to dispose of the spacecraft. Attitude reorientation is a continuous process controlled by the onboard attitude and orbit control system. Navigation support for this is provided through housekeeping operations.

3.1 NORTH-SOUTH STATIONKEEPING

The average inclination drift at geosynchronous altitude is approximately 0.86 degree per year. This requires north-south stationkeeping maneuvers approximately every 2.8 months to maintain a 0.1-degree inclination. Maneuver dates are predicted by periodically generating a spacecraft ephemeris in the OATS based on the current OATS orbit solution. Approximately 1 week before the projected maneuver date, the OATS is used to determine the thruster firings required to move the spacecraft orbit to its target. The target orbit is the orbit having an inclination at the opposite end of the inclination constraint box. This is achieved by a "node flip"; that is, the roll thrusters, pointing southward, are fired at the descending node such that it becomes the ascending node. Approximately 2 hours before the start of the maneuver, the DIRA is turned on and calibrated. This is discussed further in Section 3.3. Postmaneuver attitude instabilities can last for as much as 6 hours, causing a serious impact on normal imaging operations. Following each maneuver, thruster firing data and propellant system temperature and pressure data are collected. These data are used for calibrating the thrusters and managing propellant use.

3.2 EAST-WEST STATIONKEEPING

East-west stationkeeping maneuvers are performed to maintain or change the subsatellite longitude. Nominal stations for the operational GOES satellites are 75 degrees west longitude (GOES-East) and 135 degrees west longitude (GOES-West). Stored satellites will be positioned with regard to their intended use and the health status of the operational satellites. The direction and rate of drift of the subsatellite longitude depends on its position relative to a stable longitude node of 105.5 degrees west. For the operational spacecraft stations, east-west stationkeeping maneuvers occur approximately every 2.5 months. Station change maneuvers occur as required. Their frequency depends on the desired use for the spacecraft or on the health and safety of the spacecraft.

East-west stationkeeping maneuver dates are predicted by periodically generating a spacecraft ephemeris in the OATS based on the current OATS orbit solution. Maneuvers take place on or before the date on which the east-west stationkeeping constraint is violated. Maneuvers are planned such that the thruster firings provide an impulse to the spacecraft so that its east-west drift keeps it within its station longitude limits for the longest period of time. Similarly, station change maneuvers are planned such that the thruster firings provide an impulse to the spacecraft so that its east-west drift brings it to its desired station in a given period of time. Postmaneuver attitude instabilities can last for as much as 6 hours, causing a serious impact on normal imaging operations. Maneuver monitoring occurs in the same manner as for north-south maneuvers. Thruster data are collected after each east-west maneuver so that thruster calibration and propellant management can be performed.

3.3 DIRA CALIBRATION

Approximately 2 hours before the start of a maneuver, the DIRA is turned on so that roll, pitch, and yaw DIRA angle data can be collected by the OATS for DIRA calibration. Roll and yaw data are used to determine an average drift rate in those directions, pitch data, which include the orbital drift rate that maintains spacecraft Earth pointing, are also used to determine an average drift rate. These drift rates are used to calibrate the DIRA. DIRA angle data may be monitored during the process for unexpected attitude drift.

3.4 PLUME IMPINGEMENT

Before the start of a north-south stationkeeping maneuver, the solar array is placed in a park position to minimize roll thruster plume impingement. However, solar array heating still occurs. Consequently, there is a constraint limiting roll thruster continuous firing to 5 minutes, followed by a 5-minute cooling interval before the next firing. This constraint has a significant effect on the duration of north-south stationkeeping maneuvers; for example, a 0.4-degree inclination would require a 15-minute maneuver of which 10 minutes is actual burn time. Plume impingement and heating effects can be minimized by performing north-south stationkeeping maneuvers at optimum times around solstices.

3.5 CONTINGENCIES

Several contingencies are available to handle abnormal events that may occur during a stationkeeping maneuver. A standby communications link is ready in the event that communications are lost just before the start of a maneuver. If communications are lost during a maneuver, that maneuver is terminated. The effect of the completed part of the maneuver is determined, and the remainder is rescheduled and replanned if necessary.

If abnormal attitude changes occur during a stationkeeping event, there is the possibility of regaining attitude control by entering either Sun or Earth reacquisition mode in the AOCS.

4.0 HOUSEKEEPING SUPPORT

Housekeeping operations are part of the activities supported by the OATS. Housekeeping includes attitude control through unloading of angular momentum from the momentum wheels, trim tab positioning, and DIRA calibration. Housekeeping operations occur daily and are scheduled so as not to interfere with the imaging process.

4.1 ATTITUDE CONTROL

Nominal attitude control for GOES-Next will be performed by the two pitch momentum wheels (Figure 8). Both wheels operate to maintain Earth pointing throughout the orbit. Pitch is controlled by a speed modulation of both wheels. Roll and yaw are controlled by roll-yaw quarter-orbit coupling. Roll errors cause a differential modulation of wheel speed producing a yaw momentum increment. Attitude errors created during stationkeeping maneuvers are controlled by unloading roll and yaw momentum with thruster firings.

4.2 TRIM TAB POSITIONING

The trim tab is used to compensate the solar array for the solar radiation pressure torque. The trim tab angle can be stepped daily. The OATS determines the angle at which the trim tab is to be set based on the solar torque. The OATS also generates the commands for setting the trim tab angle.

4.3 DIRA CALIBRATION

The DIRA is composed of three mutually perpendicular rate integrating gyros. They are oriented along the roll, pitch, and yaw axes and are used to measure attitude changes in those directions.

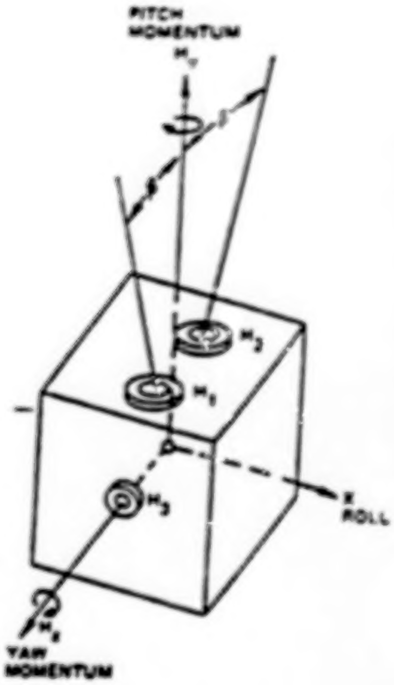

Figure 8. Momentum/Reaction Wheel Configuration

Following turn-on and warmup of the DIRA, the OATS collects at least 30 minutes of roll, pitch, and yaw DIRA angle data. The pitch data are corrected for the orbital rate. Each set of data are then curve-fit to produce an average drift rate in each direction. The OATs prepares commands for these drift rates to be uplinked to the spacecraft. Once they are uplinked, the DIRA is reset to initiate their use.

5.0 SUMMARY

The GOES-Next series of spacecraft will present a more demanding requirement on operations than the current GOES satellites. The new system of INR using image motion compensation for better imaging calls for daily generation of IMC coefficients based on orbital and attitude motions of the spacecraft and instrument thermal distortions. Three-axis attitude stabilization requires daily housekeeping activities that are not performed on the current dual-spin spacecraft. Potential impacts on normal imaging operations, such as those that will occur during stationkeeping maneuvers, also pose an operational problem. Consequently, NOAA is currently preparing for daily operations of these spacecraft. As part of this preparation, they are developing methods of reducing the impacts to imaging. An early mission evaluation period is also planned to evaluate spacecraft performance. Once this evaluation is complete, the GOES-Next system should provide improved and accurate weather forecasts into the next century.

ACKNOWLEDGMENTS

The authors wish to thank K. Kelly (NOAA), M. Suranno (NOAA), R. Johnson (Computer Sciences Corporation), and J. Dunham (Computer Sciences Corporation) for their thoughtful comments during preparation of this paper. They are also grateful to R. Pendley (Computer Sciences Corporation) and to the Technical Publications Department for their assistance in producing this paper.

BIBLIOGRAPHY

Ford Aerospace and Communications Corporation/Western Development Laboratories Division, WDL-TR1093, GOES IJK/LM Image Navigation and Registration, DRL 300-06, Volume 1 - Non-Proprietary Information, January 15, 1987

--, WDL-TP4077, GOES I/J/K Best and Final Offer, Volume II, Part 1 - Technical Approach (Book 1), April 1985 (Proprietary)

Ford Aerospace and Communications Corporation, GOES-PCC-TM-0789 Revision B, North-South, East-West, Stationkeeping Time Lines, R. Ripley, August 17, 1987

--, GOES-PCC-TM-1648, Mathematical Foundation of the Orbit and Attitude Determination Program, K. M. Ong, October 7, 1987

N89-15961

CORRELATIONS BETWEEN SOLAR ACTIVITY AND OPERATIONALLY DETERMINED SATELLITE DRAG VARIATION PARAMETERS*

E. A. Smith, Computer Sciences Corporation (CSC)

ABSTRACT

Operational orbit determination of the Earth Radiation Budget Satellite (ERBS) and the Solar Maximum Mission (SMM) spacecraft using the Goddard Trajectory Determination System (GTDS) in the Flight Dynamics Facility (FDF) of the Goddard Space Flight Center (GSFC) has yielded an orbit solution data base of 3 years for ERBS and 8 years for SMM. One of the parameters in each data base is the drag variation parameter used in the GTDS atmospheric drag model; this parameter is solved for routinely to accommodate the different atmospheric densities as they are encountered solution to solution. These two data bases of the drag variation parameter solutions are analyzed to evaluate correlations in the variations of the parameter with changes in the 10.7-centimeter wavelength solar flux, F10.7, and the geomagnetic index.

The data for SMM span a wider range of solar flux values and show a stronger correlation. The data for ERBS, which is at a higher altitude and inclination than SMM, show a significant degree of scatter. For both satellites, the data indicate that changes in the drag variation parameter are more strongly correlated with the F10.7 solar flux than with the geomagnetic index. Correlations with the geomagnetic index are apparent only for severe geomagnetic storm conditions.

Results from this analysis enhance the understanding of the drag model and the accommodation of atmospheric density variations in operational orbit determination support. The resulting improvements in operations support procedures will be important for continued maintenance of the quality and accuracy of orbit solutions and propagations during periods of high solar flux. The results of this analysis for SMM have contributed directly to analysis currently being performed to predict the SMM reentry date.

---

*This work was supported by the National Aeronautics and Space Administration (NASA)/Goddard Space Flight Center (GSFC), Greenbelt, Maryland, under Contract NAS 5-31500.

1. INTRODUCTION

Operational orbit determination at the Goddard Space Flight Center (GSFC) Flight Dynamics Facility (FDF) using the Goddard Trajectory Determination System (GTDS) has yielded a data base of orbit solutions for the Earth Radiation Budget Satellite (ERBS) that exceeds 3 years in length. Similarly, the data base of orbit solutions for the Solar Maximum Mission (SMM) spacecraft currently approaches 8 years in length. These solutions consist of six-parameter orbital state vectors, which represent the position and velocity vectors at the solution epoch, and an atmospheric drag force scaling parameter, ρ_1, called the drag variation parameter. This parameter is solved for routinely to accommodate differences between modeled and actual drag effects from solution to solution. The combined data bases of ρ_1 solutions are analyzed in this paper to evaluate correlations in the variations of ρ_1 with changes in the 10.7-centimeter wavelength solar flux (F10.7) and the geomagnetic index, A_p.

The degree of correlation of ρ_1 with the solar flux values is evaluated in this paper to demonstrate the degree to which ρ_1 actually accommodates changes in the atmospheric density relative to other phenomena, such as the geopotential model and tracking errors. Atmospheric density models correlate the atmospheric density with the F10.7 solar flux and the geomagnetic activity. The 10.7-centimeter (2800-megahertz) solar radio flux is reported from Ottawa, Canada, and is measured in units of 10^{-22} watts per meter^2 per hertz. The geomagnetic index, A_p, is a measure of the amplitude of magnetic field disturbances based on a planetary average.

The F10.7 solar flux and A_p values reported over the period covered by this analysis were obtained from Solar-Geophysical Data Prompt Reports, published by the National Oceanic and Atmospheric Administration (NOAA) on a monthly basis. The values were entered into a master data base available for use for any spacecraft. The solar flux is characterized by smooth variations with a periodicity corresponding to the 27-day solar rotation.

The geomagnetic index is characterized by short intense bursts at random intervals, with the bursts sometimes being correlated with the solar rotation period.

The GTDS atmospheric drag force modeling, which includes the Harris-Priester atmospheric density model, is discussed in Section 2. Section 3 describes the orbit determination support procedures followed in the GSFC FDF for the ERBS and SMM spacecraft. The data analyses for ERBS and SMM are presented Sections 4 and 5, respectively. Section 6 gives the summary and conclusions for this study.

2. THE GTDS ATMOSPHERIC DRAG MODEL

In GTDS, the atmospheric drag force, $\vec{F}_D$, acting on a spacecraft is modeled by the following equation:

$$\vec{F}_D = -\frac{1}{2} \rho \vec{V}_r |\vec{V}_r| C_D A (1 + \rho_1) \qquad (1)$$

where ρ = atmospheric density

$\vec{V}_r$ = velocity of the spacecraft with respect to the atmosphere

C_D = spacecraft drag coefficient

A = spacecraft reference cross-sectional area

ρ_1 = drag variation parameter, which is a scale factor error coefficient on the $C_D\rho$ product

The density, ρ, is obtained in GTDS using the Harris-Priester atmospheric density model (References 2 through 4) in the form of 10 density profile tables (Tables HP1 through HP10) corresponding to 10 discrete values of the F10.7 solar flux. These tables provide minimum and maximum values of the atmospheric density at discrete altitude points. The Harris-Priester model averages the semiannual and seasonal-latitudinal variations, but it does not attempt to account for the extreme ultraviolet 27-day effect or for variations in the geomagnetic index, A_p.

The GTDS atmospheric drag model also includes a diurnal bulge, which is a region of increased atmospheric density on the sunlit hemisphere of the Earth. The density variation due to the diurnal bulge is modeled as proportional to $\cos^2(\alpha/2)$, where α is the angle between the spacecraft position vector and the apex of the diurnal bulge. The average density is the arithmetic average of the maximum value, which occurs at the apex of the diurnal bulge, and the minimum value, which occurs at the nadir of the diurnal bulge.

The profiles of the atmospheric densities for a range of altitudes relevant to the SMM mission are illustrated in Figure 1. Table 1 gives the Harris-Priester table numbers, the corresponding F10.7 solar flux values, and the range of solar flux values for which each table is used operationally.

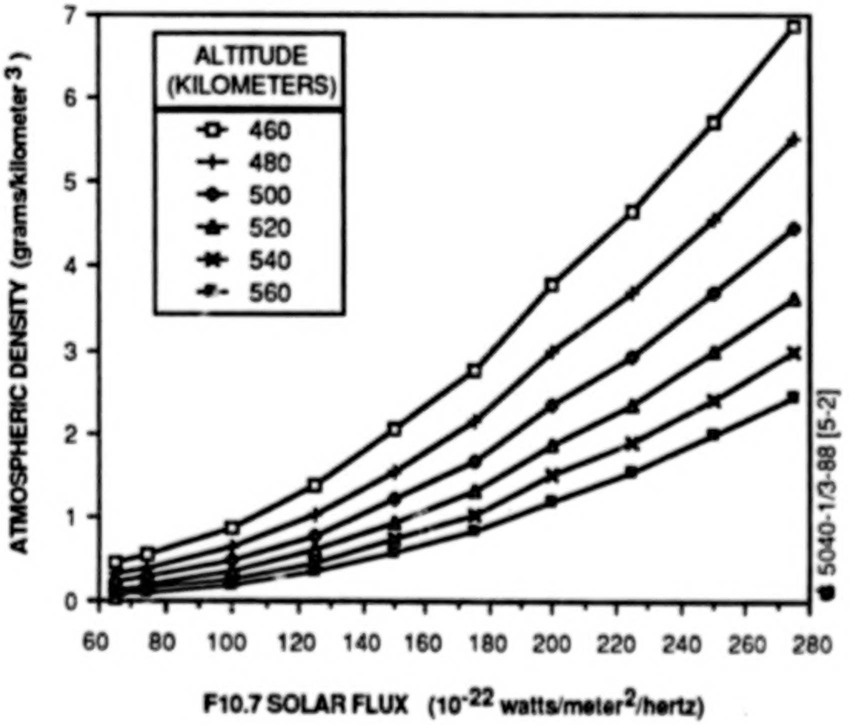

Figure 1. Harris-Priester Standard Atmospheric Densities as a Function of the F10.7 Solar Flux for Altitudes Relevant to SMM

Table 1. GTDS Harris-Priester Atmospheric Density Tables

HARRIS-PRIESTER (HP) TABLE NO.	F10.7 SOLAR FLUX VALUE (10^{-22} watts/meter^2/hertz)	F10.7 SOLAR FLUX VALUE RANGE FOR HP TABLE OPERATIONAL USE (10^{-22} watts/meter^2/hertz)
HP1	65	NOT USED
HP2	75	LESS THAN 88
HP3	100	88 - 112
HP4	125	113 - 137
HP5	150	138 - 162
HP6	175	163 - 187
HP7	200	188 - 212
HP8	225	213 - 237
HP9	250	238 - 262
HP10	275	263 - 287

5040-2/3-88 [5-2]

In the GTDS drag model, the drag variation parameter, ρ_1, is solved for in the differential correction process to accommodate drag variations relative to the nominal values provided by the Harris-Priester table and the spacecraft drag coefficient and to account for drag-like effects from other unmodeled perturbations. If drag is an important perturbing force on a spacecraft, it is necessary to solve for ρ_1, since the density tables corresponding to 10 discrete values of the solar flux cannot properly represent the density and resulting drag force for a continuum of solar flux values. The drag variation parameter, ρ_1, can therefore be utilized as a parameter for interpolating between the Harris-Priester tables to determine densities corresponding to intermediate values of the F10.7 solar flux.

For an F10.7 solar flux value less than 88, Harris-Priester Table HP2 (see Table 1 above), which is based on an F10.7 solar flux value of 75, is used operationally . For an F10.7 solar flux value between 88 and 112, Table HP3, based on an F10.7 solar flux value of 100, is used. Similarly, for higher values of the solar flux, the closest standard table is used, as indicated in the last column of Table 1. Table HP1 is not used operationally.

3. ORBIT DETERMINATION SUPPORT PROCEDURES FOR ERBS AND SMM

Operational orbit support for ERBS consists of two orbit solutions per week, on Tuesday and Friday. The orbit solution on Tuesday uses a tracking data arc of 5 days and 10 hours, ending on Tuesday at 10 hours UTC. The Friday orbit solution uses a tracking data arc of 4 days and 10 hours, ending on Friday at 10 hours UTC. The geopotential model used is the Goddard Earth Model-9 (GEM-9), truncated to order and degree 8. The drag variation parameter, ρ_1, is solved for in each orbit solution, and the value obtained is used in the generation of two ephemerides: a 21-day ephemeris produced on each solution date and a 47-day ephemeris produced each Tuesday. In addition to these predicted ephemerides, a 1-week merged definitive ephemeris is prepared each week for delivery to the ERBS experimenters at NASA's Langley Research Center (LaRC).

Operational orbit support for SMM consists of an orbit solution every other day. These orbit solutions use a tracking data arc of 2 days and 10 hours. The geopotential model used is the GEM-9, truncated to order and degree 16, although over the history of SMM mission support values higher and lower than 16 have been used. The ρ_1 parameter is solved for in each solution, and the value obtained is used in the generation of a 12-day ephemeris on each solution date and a 37-day ephemeris once a week. In addition, each 58-hour definitive ephemeris is delivered to the SMM experimenters.

To quality assure the solutions for each spacecraft, ephemeris comparison runs are made, using the GTDS Ephemeris Comparison (COMPARE) Program, on consecutive orbit solutions over the respective overlap intervals. The maximum position difference from this comparison is a measure of the consistency of the orbit solutions. A second quality check is made by comparing the current orbit solution with an ephemeris propagated from the solution before last.

4. ERBS DATA ANALYSIS

The ERBS orbit has maintained a nearly constant semimajor axis of 6981 kilometers (corresponding to an altitude of 603 kilometers) since the start of the mission in October 1984. During this period, the solar flux has been near the minimum of its 11-year cycle, and relatively low drag forces have been present. Although no significant orbital decay has occurred, the drag force is still considered to be an important perturbation, and ρ_1 is solved for in the orbit solution. For spacecraft at higher altitudes (i.e., Landsat-4 and Landsat-5 at 700 kilometers and Nimbus-7 at 950 kilometers), the drag force becomes less significant and solving for ρ_1 leads to nonphysical values.

The F10.7 solar flux and geomagnetic index values for the epoch dates of the ERBS orbit solutions are presented in Figure 2 for the period from October 1984 to October 1987. The corresponding ρ_1 values from the operational orbit solutions are shown in Figure 3. Since more than one Harris-Priester table was used during this time period, the solved-for ρ_1 data have been normalized to reflect the solved-for atmospheric density adjustment relative to Table HP2 (F10.7 solar flux value = 75) for an altitude of 600 kilometers.

To verify the normalization procedure, GTDS runs were made to determine the ρ_1 differences that correspond to the difference between Tables HP3 and HP2. Using Table HP3 and a ρ_1 value of -0.47 gave a zero along-track error at the end of the 1-day propagation when compared with an ephemeris using Table HP2 and a ρ_1 value of 0.00. Similarly, using Table HP2 and a ρ_1 value of +0.89 gave a zero along-track error after 1 day when compared with an ephemeris using Table HP3 and a ρ_1 value of 0.00. These values are

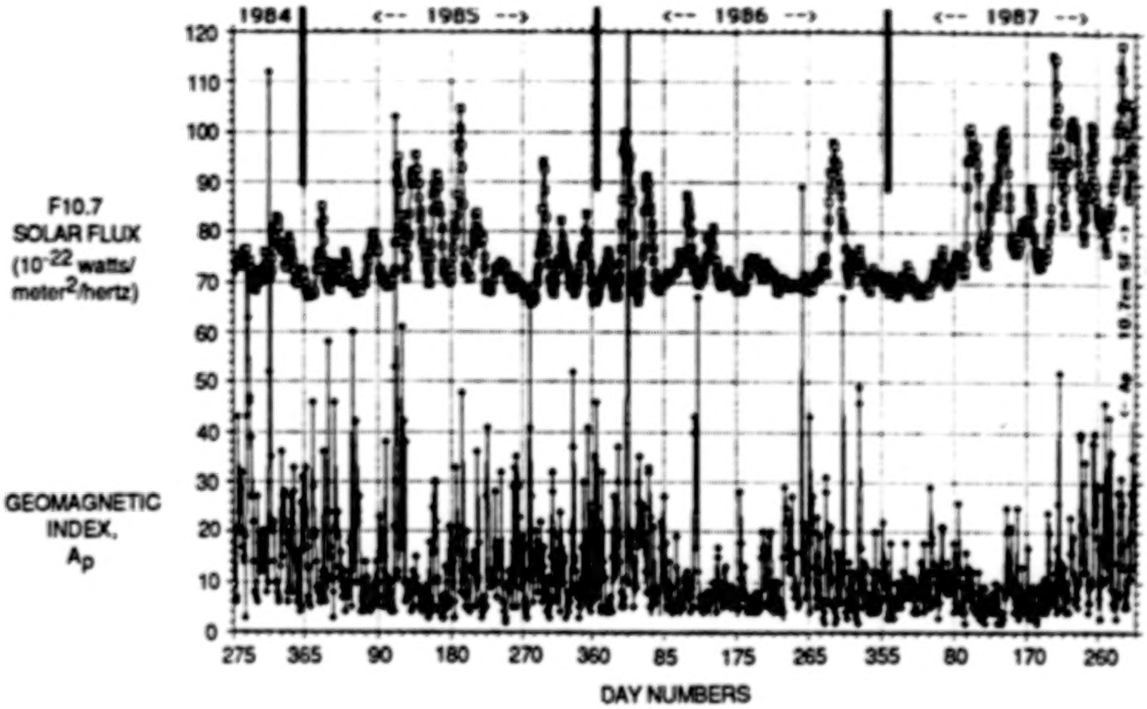

Figure 2. F10.7 Solar Flux and Geomagnetic Index Values for ERGS Orbit Solution Epoch Dates

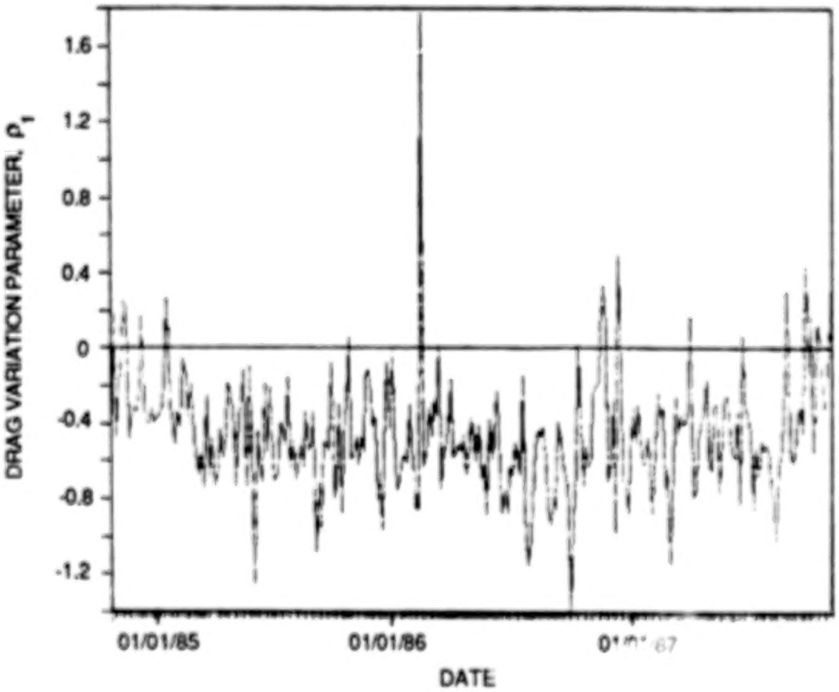

Figure 3. Drag Variation Parameter Valu. From ERBS Operational Orbit Solutions

ORIGINAL PAGE IS
OF POOR QUALITY

consistent with those determined by taking the ratio of the average densities for an altitude of 600 kilometers from Tables HP2 and HP3.

Most of the operational ρ_1 data were associated with Table HP2; the operational data associated with Table HP3 were converted to the equivalent for Table HP2 by the normalization procedure, which is described in Appendix A. Only the HP2 and HP3 tables were used for the ERBS study, since no F10.7 solar flux values above 112 were encountered during the 3 years covered by the ERBS data.

The normalized ρ_1 values from the ERBS orbit solutions are plotted versus the F10.7 solar flux in Figure 4 and versus the geomagnetic index in Figure 5. No clear correlation can be seen from these plots. The correlation coefficients, R, are the following: $R_{F10.7} = 0.182$ and $R_{Ap} = 0.459$. The data are characterized by a large amount of noise that obscures any evident trend. Possible reasons for the observed noise are the following:

1. Errors in the solved-for ρ_1 due to the length of the tracking data arc

2. Errors in the F10.7 solar flux and geomagnetic index values used

3. Modeling errors with drag-like effects

To investigate the errors in ρ_1 due to the tracking arc length, the ρ_1 data were segmented into values from 4-day arcs and values from 5-day arcs. No significant difference was observed between the two samples. Specifically, the average value of ρ_1 for the 4-day arcs was -0.4691, while for the 5-day arcs, the average value of ρ_1 was -0.4613. Errors in the F10.7 solar flux or geomagnetic index values arise because the values used were the values on the solution epoch date and not on an average value over the tracking data arc. To evaluate these errors, the arithmetic mean of the F10.7 solar flux and geomagnetic index values over the tracking data

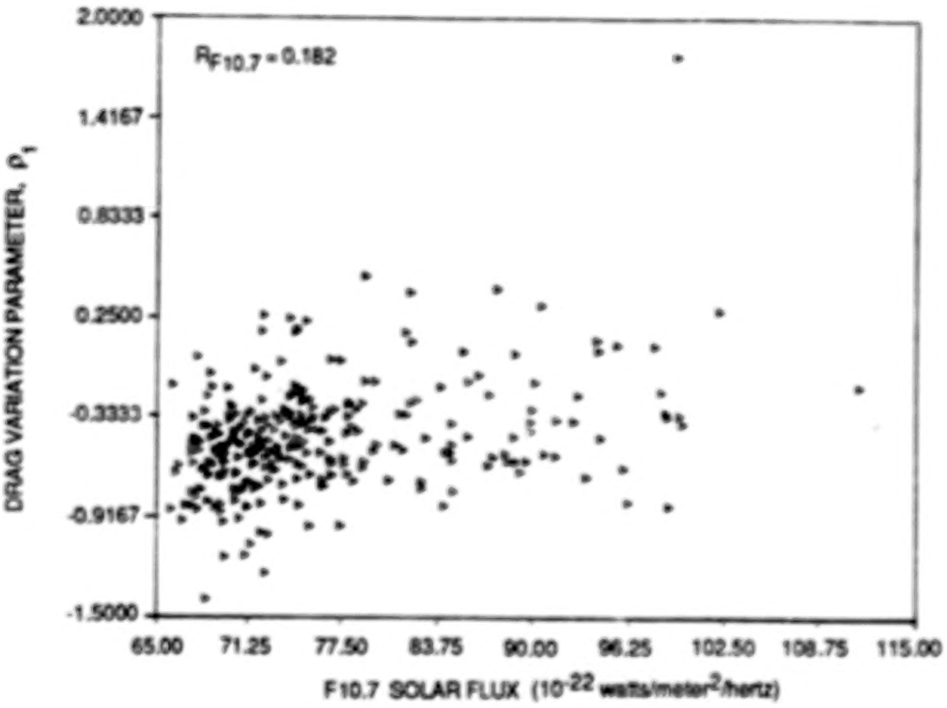

Figure 4. Normalized ERBS Drag Variation Parameter Values as a Function of the F10.7 Solar Flux From October 1984 to October 1987

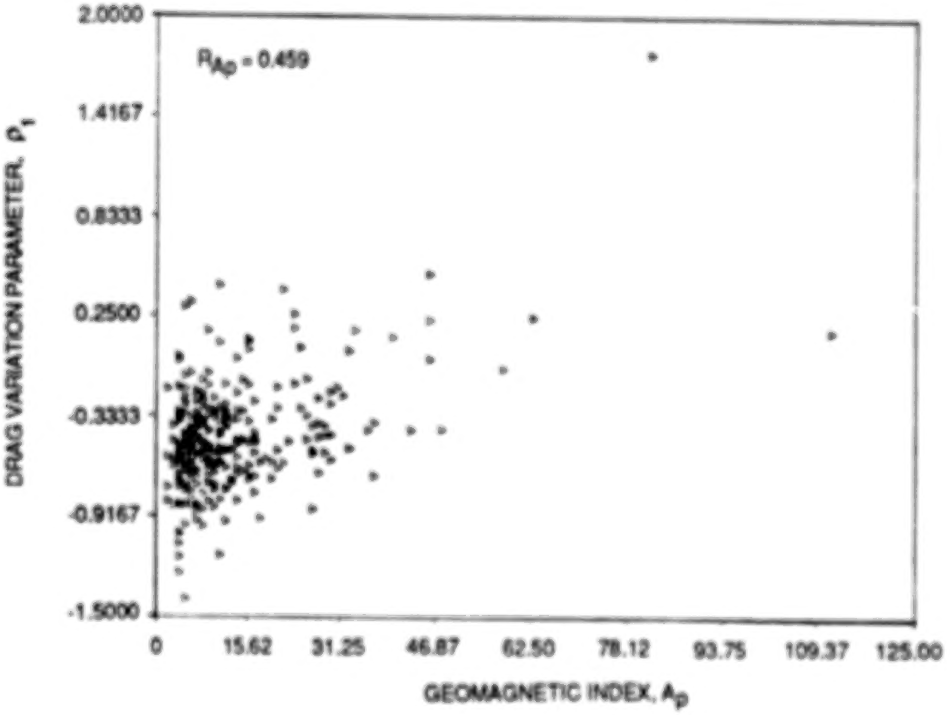

Figure 5. Normalized ERBS Drag Variation Parameter Values as a Function of the Geomagnetic Index From October 1984 to October 1987

arc were used rather than the values on the epoch date; only a slight reduction in the noise resulted. The F10.7 correlation coefficient, $R_{F10.7}$, increased slightly, from 0.182 to 0.235, when the arithemetic mean values were used. Likewise, the A_p correlation coefficient, R_{Ap}, increased from 0.459 to 0.559. It was therefore concluded that the noise appears to reflect modeling errors intrinsic to other factors in the propagation model and input data.

5. SMM DATA ANALYSES

The SMM orbit analysis is described in Section 5.1. Section 5.2 presents a description of a method to improve the drag model by adjusting the SMM drag coefficient. Section 5.3 discusses ephemeris propagation and reentry predictions for SMM.

5.1 SMM ORBIT ANALYSIS

SMM was launched on February 14, 1980, and by October 1987 the drag force had caused the semimajor axis to decay from 6952 kilometers (574 kilometers altitude) to 6865 kilometers (487 kilometers altitude). SMM orbit solutions from launch through the end of October 1987 have been used to study the effects of solar flux variations on the atmospheric density as estimated by the GTDS solved-for ρ_1 values. For each orbit solution, the following are tabulated: (1) the observed values of the F10.7 solar flux and the geomagnetic index, (2) the Harris-Priester table used in the orbit solution, and (3) the solved-for value of ρ_1.

For consistency, all ρ_1 values were normalized to reflect the empirical atmospheric densities, as was done for the ERBS data. Because the SMM altitude was rapidly decaying during the period several years ago when the solar flux was high, the conversion algorithm constants varied with the spacecraft altitude and, therefore, with the mission year. For specific mission years, density table values corresponding to the spacecraft altitudes given below were used:

Mission Year	Spacecraft Altitude (kilometers)
1980	560
1981	540
1982	520
1983	500
1984	500
1985	480
1986	480
1987	480

Figure 1 shows the F10.7 solar flux as a function of the atmospheric density for each of these altitudes. The details of the conversion algorithm for SMM are given in Appendix B.

The empirical atmospheric densities for SMM are shown in Figure 6 as a function of the observed F10.7 solar flux on the epoch date. As expected, a clear correlation between the solar flux and the atmospheric density is evident in this figure ($R_{F10.7} = 0.863$). The densities plotted as a function of the geomagnetic index, A_p, in Figure 7 show a weak correlation ($R_{Ap} = 0.247$).

5.2 ADJUSTING THE SMM DRAG COEFFICIENT TO CALIBRATE THE DENSITY MODELING

A clear correlation between the atmospheric density and the observed F10.7 solar flux is demonstrated by the analysis presented in Section 5.1. For values of the F10.7 solar flux that lie between the Harris-Priester tables values, an expected value of ρ_1 can be determined by interpolation. The ρ_1 values obtained from the operational orbit solutions average approximately -0.6, while those obtained by interpolating the Harris-Priester table values to the observed solar flux/average approximately 0.0; therefore,

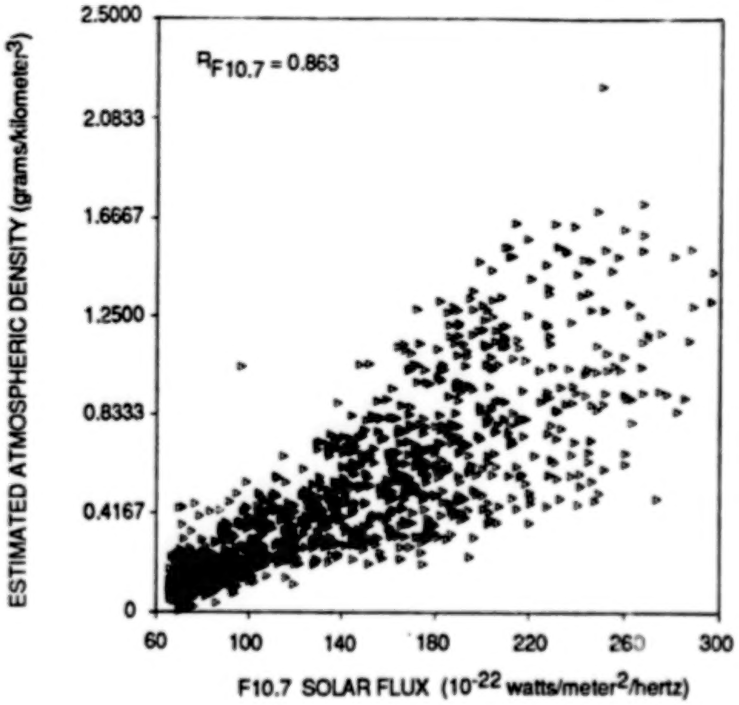

Figure 6. SMM Estimated Atmospheric Density as a Function of the F10.7 Solar Flux From Launch to October 1987

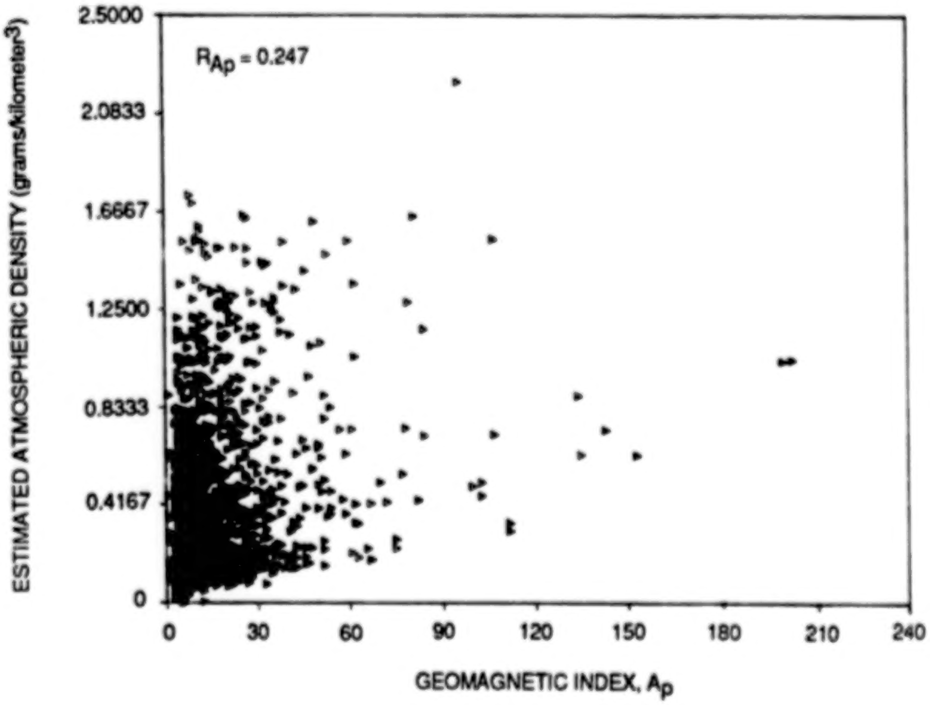

Figure 7. SMM Estimated Atmospheric Density as A Function of the Geomagnetic Index From Launch to October 1987

it is clear that the expected values are significantly different from those actually seen in the SMM orbit solutions. A likely source of this difference is the failure to account for attitude-dependent drag variations.

Since some of the error in the drag model originates from the time-dependence of the spacecraft attitude with respect to the relative velocity vector, the approach taken was to determine a value of the drag coefficient that results in ρ_1 values near those expected from interpolating the Harris-Priester tables to the actual F10.7 solar flux level. This procedure effectively calibrates the drag modeling such that the term $\rho\ (1 + \rho_1)$ provides a direct estimate of the actual atmospheric density.

Drag coefficient normalization was performed using the empirical densities derived from the solved-for ρ_1 values. The drag coefficient value that results in atmospheric density values consistent with the solar flux levels in the range 150 to 200 was found to be 1.38. Further refinement of this result is possible using GTDS propagations and comparisons with past evolution of the SMM orbit during the previous solar maximum.

5.3 EPHEMERIS PROPAGATION AND REENTRY PREDICTIONS FOR SMM

Predictions of the monthly averages of the F10.7 solar flux are available from the Atmospheric Sciences Division, Marshall Space Flight Center (MSFC) (Reference 5). For the months April 1987 through January 1988, the actual observed monthly averages have been calculated and are in good agreement with the predicted averages (see Table 2). For each month in 1988 and 1989, the estimated monthly average F10.7 solar flux has been converted to an expected value of ρ_1 for the appropriate Harris-Priester table, following the procedure described in Appendix B. Using the calibrated value of 1.38 for the drag coefficient, the SMM orbit was propagated using GTDS on a month-by-month basis. For each month, the selected Harris-Priester table and the expected ρ_1 value (see Table 3) were incorporated into the drag model. The resulting ephemeris predicts that the SMM reentry will occur in February 1990.

Table 2. MSFC Predicted F10.7 Solar Flux and the Observed F10.7 Solar Flux From April 1987 Through January 1988

MONTH	F10.7 SOLAR FLUX VALUE (10^{-22} watts/meter^2/hertz)	
	MSFC PREDICTED	OBSERVED
APRIL 1987	80.3	84.9
MAY 1987	82.3	87.8
JUNE 1987	84.5	77.9
JULY 1987	87.2	84.2
AUGUST 1987	90.7	90.0
SEPTEMBER 1987	94.2	86.1
OCTOBER 1987	97.8	98.1
NOVEMBER 1987	103.1	101.1
DECEMBER 1987	109.3	94.9
JANUARY 1988	115.3	108.8

5040-3/3-88 [5-2]

Table 3. MSFC Best-Estimate Monthly Average F10.7 Solar Flux, Selected Harris-Priester Table, and Expected Drag Density Variation Parameter From January 1988 Through February 1990

MONTH	MSFC BEST-ESTIMATE MONTHLY AVERAGE F10.7 SOLAR FLUX (10^{-22} watts/meter^2/hertz)	HARRIS-PRIESTER TABLE NO.	ρ_1
JANUARY 1988	115.3	HP4	-0.1454
FEBRUARY 1988	121.7	HP4	-0.0495
MARCH 1988	128.4	HP4	0.0673
APRIL 1988	133.9	HP4	0.1761
MAY 1988	138.8	HP5	-0.1483
JUNE 1988	143.2	HP5	-0.0900
JULY 1988	148.3	HP5	-0.0225
AUGUST 1988	154.2	HP5	0.0652
SEPTEMBER 1988	160.4	HP5	0.1615
OCTOBER 1988	167.0	HP6	-0.0895
NOVEMBER 1988	172.9	HP6	-0.0235
DECEMBER 1988	178.2	HP6	0.0501
JANUARY 1989	182.7	HP6	0.1152
FEBRUARY 1989	187.9	HP7	-0.1317
MARCH 1989	191.6	HP7	-0.0915
APRIL 1989	194.1	HP7	-0.0642
MAY 1989	198.6	HP7	-0.0152
JUNE 1989	202.4	HP7	0.0215
JULY 1989	205.5	HP7	0.0493
AUGUST 1989	208.6	HP7	0.0771
SEPTEMBER 1989	210.0	HP7	0.0897
OCTOBER 1989	210.2	HP7	0.0915
NOVEMBER 1989	211.4	HP7	0.1022
DECEMBER 1989	212.9	HP8	-0.0886
JANUARY 1990	215.6	HP8	-0.0688
FEBRUARY 1990	218.1	HP8	-0.0505

5040-4/3-88 [5-2]

6. SUMMARY AND CONCLUSIONS

A study based on an operational data base of solved-for drag variation parameter values for 3 years of ERBS orbit solutions and 8 years of SMM orbit solutions has been presented in this paper. After adjustments to these data to account for variations in the associated Harris-Priester table, a clear correlation ($R_{F10.7} = 0.863$) of the estimated atmospheric density with the F10.7 solar flux has been demonstrated for SMM. Thus, the inclusion of the solved-for ρ_1 parameter in the orbital solution for SMM primarily accommodates the effects of drag on the orbit. In doing this, the solved-for ρ_1 acts to interpolate the atmospheric density when the actual F10.7 solar flux values are between the values of the standard Harris-Priester tables; it also accommodates variations in the spacecraft effective drag coefficient resulting from daily science operations.

For ERBS, which is at a higher altitude and with solar activity levels near the solar minimum, no strong correlation was found between the estimated atmospheric density and the F10.7 solar flux or the geomagnetic index. The higher level of noise illustrated by the plots of ρ_1 as a function of the F10.7 solar flux and the geomagnetic index indicate that for this spacecraft the solved-for ρ_1 plays a large role in the accommodation of effects in the orbit propagation model that are not directly associated with atmospheric density and drag. One possible source of these errors is the effects of resonance of the spacecraft orbital period with geopotential harmonic coefficients.

As a part of the SMM study, the drag model was calibrated by adjusting the drag coefficient in such a way that densities estimated using the ρ_1 values from the data base were in good agreement with density values obtained by interpolating the Harris-Priester table values. The results of this analysis have contributed directly to studies currently being performed in the orbit operations area of GSFC's FDF to predict the reentry date of the SMM. Estimates based on the calibrated SMM drag model and on the MSFC predictions of the F10.7 solar flux levels indicate that SMM will reenter the atmosphere in February 1990. As indicated in Table 2, the most recent solar flux observations are lower than the MSFC predictions. If this trend continues, the SMM reentry will occur later than the February prediction.

APPENDIX A. DRAG VARIATION PARAMETER (ρ_1) DATA STANDARDIZATION METHOD FOR ERBS

Assuming that the value of the spacecraft drag coefficient is correct and that there are no other modeling errors affecting the drag calculation, then the drag variation parameter, ρ_1, is a measure of the difference between the actual atmospheric density and the atmospheric density in the model being used. For example, a ρ_1 value of -0.5 means 50 percent less atmospheric density, while a ρ_1 value of +0.5 means 50 percent more atmospheric density, etc.

For the ERBS altitude (600 kilometers), the atmospheric density values for the HP2 and HP3 tables are given in Table 4. The table gives both a minimum and a maximum density.

Table 4. Harris-Priester Atmospheric Densities at an Altitude of 600 Kilometers

HARRIS-PRIESTER TABLE NO.	F10.7 SOLAR FLUX VALUE (10^{-22} watts/meter^2/hertz)	ATMOSPHERIC DENSITY (kilograms/kilometer^3)	
		MINIMUM	MAXIMUM
HP2	75	0.00001109	0.0001137
HP3	100	0.00002088	0.0002146

5040-5/3-88 [5-2]

Dividing the value from Table HP2 by the value from Table HP3 yields 0.53. The result is the same to two significant digits whether the minimum or maximum values are used.

Using the factor 0.53, the GTDS analysis results can be replicated. The atmospheric densities from Table HP2 are 47 percent less than those from Table HP3, so -0.47 is the theoretical ρ_1 value for converting density values from Table HP3 to Table HP2. Similarly, the Table HP3 density values are 1.89 times as large as the Table HP2 values, or 89 percent more dense; thus, +0.89 is the theoretical ρ_1 value for converting density values from Table HP2 to Table HP3.

The transformation equation can then be derived, making use of the fact that the actual atmospheric density is the same regardless of the Harris-Priester table being used. The density, ρ, is given by

$$\rho = (1 + \rho_1)\ \rho_0 \qquad \text{(A-1)}$$

where ρ_0 is the tabulated density in the Harris-Priester table being used. The value from the Harris-Priester table is included as the argument of the variable. Equation (A-1) leads to the following expression:

$$\rho = [1 + \rho_1(2)]\ \rho_0(2) = [1 + \rho_1(3)]\ \rho_0(3) \qquad \text{(A-2)}$$

where the number in parentheses corresponds to the Harris-Priester table being used.

Next, $\rho_1(2)$ can be solved for as

$$\rho_1(2) = \frac{\rho_0(3)}{\rho_0(2)}\ [1 + \rho_1(3)] - 1 \qquad \text{(A-3)}$$

Using the actual density ratio for ERBS yields

$$\rho_1(2) = 1.89\ [1 + \rho_1(3)] - 1 \qquad \text{(A-4)}$$

APPENDIX B. DRAG VARIATION PARAMETER (ρ_1) DATA STANDARDIZATION METHOD FOR SMM

The standardization procedure used for ERBS (Appendix A) was inadequate for standardizing the SMM data for the following reasons:

1. The SMM data require the use of Harris-Priester tables ranging from Table HP2 to HP10. With such a large spread, standardization to a single table would result in a loss of precision.

2. More than one altitude was encountered in the SMM data, and the conversion factor ratios are altitude dependent.

3. At the lower altitudes, different ratios are obtained depending on whether the minimum or maximum tabulated densities are used. This requires the determination of an average density.

The average value for the atmospheric density was determined to be the arithmetic mean of the maximum and minimum densities. This is established by integrating the cosine-squared dependence over a diurnal cycle, as follows:

$$\frac{1}{\pi}\int_0^{\pi} \cos^2\Theta \, d\Theta = \frac{1}{2\pi}\int_0^{\pi} (1 + \cos 2\Theta)\, d\Theta = \frac{1}{2\pi}\left[\Theta + \frac{1}{2}\sin 2\Theta\right]\Bigg|_0^{\pi} = \frac{1}{2} \quad \text{(B-1)}$$

The empirical density is then calculated by taking the average density for the Harris-Priester table being used and multiplying it by the factor $(1 + \rho_1)$.

A further refinement in the analysis is to use the average densities to calculate expected ρ_1 values for values of the F10.7 solar flux between the table values. The average densities and interpolating values of ρ_1 are given in Table 5. The ρ_1 (UP) column gives the value of ρ_1 that accounts for a step up to the next highest Harris-Priester table. It is determined by

$$\frac{\rho(HP+1)}{\rho(HP)} - 1$$

The ρ_1 (DOWN) column contains the value of ρ_1 that accounts for a step down to the next lowest Harris-Priester table. It is determined by

$$\frac{\rho(HP-1)}{\rho(HP)} - 1$$

To determine a value of ρ_1 given a value of the F10.7 solar flux, the difference between the given F10.7 solar flux value and the standard value for the table (ΔF10.7) is divided by 25 (the spacing between tables) and is then multiplied by the appropriate interpolating value of ρ_1. For example, for the case where the F10.7 solar flux is 115.3 and SMM is at 480 kilometers altitude, the following determination is made:

1. The given F10.7 solar flux value of 115.3 is closest to the solar flux value of 125 for Harris-Priester Table HP4, but is lower than the table value.

2. The expected ρ_1 is then determined as

$$\rho_1 = \frac{125 - 115.3}{25} (-0.3745) = -0.1454 \qquad \text{(B-2)}$$

Table 5. Average Atmospheric Densities and Drag Variation Parameter Values to be Used for Interpolation

ALTITUDE (kilometers)	HARRIS-PRIESTER TABLE NO.	F10.7 SOLAR FLUX VALUE (10^{-22} watts/ meter^2/hertz)	AVERAGE ATMOSPHERIC DENSITY (grams/kilometer ^{3})	INTERPOLATING VALUES OF P_1	
				P_1 (DOWN)	P_1 (DOWN)
560	HP2	75	0.1112	-0.2054	0.8210
	HP3	100	0.2025	-0.4509	0.7353
	HP4	125	0.3514	-0.4237	0.6417
	HP5	150	0.5769	-0.3909	0.4287
	HP6	175	0.8242	-0.3000	0.4596
	HP7	200	1.203	-0.3149	0.2793
	HP8	225	1.539	-0.2183	0.2833
	HP9	250	1.975	-0.2208	0.2415
	HP10	275	2.452	-0.1945	0.1945
540	HP2	75	0.1501	-0.2001	0.7855
	HP3	100	0.2680	-0.4399	0.7015
	HP4	125	0.4560	-0.4123	0.6132
	HP5	150	0.7356	-0.3801	0.4111
	HP6	175	1.038	-0.2913	0.4422
	HP7	200	1.497	-0.3066	0.2685
	HP8	225	1.899	-0.2117	0.2728
	HP9	250	2.417	-0.2143	0.2333
	HP10	275	2.981	-0.1892	0.1892
520	HP2	75	0.2042	-0.1983	0.7473
	HP3	100	0.3568	-0.4277	0.6676
	HP4	125	0.5950	-0.4003	0.5857
	HP5	150	0.9435	-0.3694	0.3916
	HP6	175	1.313	-0.2814	0.4265
	HP7	200	1.873	-0.2990	0.2568
	HP8	225	2.354	-0.2043	0.2630
	HP9	250	2.973	-0.2082	0.2254
	HP10	275	3.643	-0.1839	0.1839
500	HP2	75	0.2798	-0.1873	0.7091
	HP3	100	0.4782	-0.4149	0.6338
	HP4	125	0.7813	-0.3879	0.5577
	HP5	150	1.217	-0.3580	0.3739
	HP6	175	1.672	-0.2721	0.4085
	HP7	200	2.355	-0.2900	0.2467
	HP8	225	2.935	-0.1979	0.2524
	HP9	250	3.677	-0.2015	0.2170
	HP10	275	4.475	-0.1783	0.1783
480	HP2	75	0.3863	-0.1802	0.6710
	HP3	100	0.6455	-0.4015	0.5988
	HP4	125	1.0320	-0.3745	0.4952
	HP5	150	1.543	-0.3312	0.3882
	HP6	175	2.142	-0.2796	0.3917
	HP7	200	2.981	-0.2814	0.2352
	HP8	225	3.682	-0.1904	0.2423
	HP9	250	4.574	-0.1950	0.2081
	HP10	275	5.526	-0.1723	0.1723

5040 6/3-88 [5-2]

REFERENCES

1. Goddard Space Flight Center, X-582-76-77, Mathematical Theory of the Goddard Trajectory Determination System, A. J. Fuchs, C. E. Velez, and J. O. Cappellari, Jr. (editors), April 1976

2. Harris, I. and W. Priester, "Time Dependent Structure of the Upper Atmosphere," Journal of Atmospheric Sciences, Vol. 19, No. 4, July 1952

3. Goddard Space Flight Center, NASA-TN-D-144, Theoretical Models for the Solar Cycle Variation of the Upper Atmosphere, I. Harris and W. Priester, August 1962

4. Harris, I. and W. Priester, "Atmospheric Structure and Its Variations in the Region From 120 to 80 KM," COSPAR International Reference Atmosphere (CIRA) 1965, Space Research IV. Amsterdam, Holland: North Holland Publishing Company, 1965

5. Marshall Space Flight Center, Memorandum EL01 (184-87), Solar Activity Inputs for Upper Atmospheric Models Used in Programs to Estimate Spacecraft Orbital Lifetime, G. D. Hopson, October 14, 1987

N89-15962

EVALUATION OF ADVANCED GEOPOTENTIAL MODELS FOR OPERATIONAL ORBIT DETERMINATION*

M. S. Radomski, B. E. Davis, and M. V. Samii
Computer Sciences Corporation (CSC)

C. J. Engel and C. E. Doll
Goddard Space Flight Center (GSFC)

ABSTRACT

To meet future orbit determination accuracy requirements for different National Aeronautics and Space Administration (NASA) projects, analyses are performed using Tracking and Data Relay Satellite System (TDRSS) tracking measurements and orbit determination improvements in areas such as the modeling of the Earth's gravitational field. Current operational requirements are satisfied using the Goddard Earth Model-9 (GEM-9) geopotential model with the harmonic expansion truncated at order and degree 21 (21-by-21). This study evaluates the performance of 36-by-36 geopotential models, such as the GEM-10B and Preliminary Goddard Solution-3117 (PGS-3117) models.

The Earth Radiation Budget Satellite (ERBS) and Landsat-5 are the spacecraft considered in this study. Series of orbit determination solutions are generated for 34-hour arcs with 10-hour overlaps using the batch weighted-least-squares method. Orbit determination consistency is evaluated by comparing ephemerides during the 10-hour overlap periods. The sensitivity of the solutions to variations in the tracking data distribution is also considered. The principal source of tracking data is TDRSS, but Ground Spaceflight Tracking and Data Network (GSTDN) data are also considered.

The orbit consistencies are improved, relative to GEM-9 (21-by-21) results, by an average of 7 meters out of 34 meters for ERBS and 7 meters out of 56 meters for Landsat-5. The detailed results and conclusions of the comparative evaluation of the effects of geopotential models on the accuracy of orbit determination results are presented.

---

*This work was supported by the National Aeronautics and Space Administation (NASA)/Goddard Space Flight Center (GSFC), Greenbelt, Maryland, Contract NAS 5-31500.

1. INTRODUCTION

The Tracking and Data Relay Satellite System (TDRSS) has been providing routine operational tracking support to TDRSS user satellites with a single relay spacecraft, Tracking and Data Relay Satellite-East (TDRS-E), for approximately 4 years. The completed TDRSS will comprise two operational relay satellites and one in-orbit spare. The operational satellites will be located at 41 degrees west longitude and 171 degrees west longitude and will communicate with the White Sands Ground Terminal (WSGT) at White Sands, New Mexico. Selected TDRSS users receive some tracking support from the Ground Spaceflight Tracking and Data Network (GSTDN). While GSTDN provides approximately 15-percent visibility coverage, TDRSS can provide 85-percent to 100-percent visibility coverage.

The Bilateration Ranging Transponder System (BRTS) is used to provide tracking measurements for the relay spacecraft. BRTS is a system of four ground-based unmanned facilities that contain transponders similar to those flown on user spacecraft. The positions of the BRTS transponders are known so that ranging information can be used to determine the orbits of the TDRSs. The BRTS facilities are located at WSGT; Ascension Island; American Samoa; and Alice Springs, Australia. TDRS-E and TDRS-Spare (TDRS-S) will be supported by the BRTS transponders at WSGT and Ascension Island, while TDRS-West (TDRS-W) will be supported by the BRTS transponders at Alice Springs, American Samoa, and WSGT.

While orbit determination requirements for currently operational spacecraft missions are satisfied by the orbit determination methods currently in place, meeting the more stringent definitive and predictive accuracy requirements for future missions requires an ongoing effort to improve orbit determination methods in such areas as force modeling, geophysical modeling, observation modeling, observation correction, estimation methods, orbit propagation, and numerical methods. The gravitational forces of the nonspherical Earth are the largest forces perturbing the orbits of low Earth-orbiting spacecraft. Continued improvement in the modeling of the gravitational geopotential is crucial to future improvements in orbit determination accuracy. This paper reports on evaluations of the effectiveness of certain improved geopotential models when applied to orbit determination in an operational environment.

The geopotential models used are supplied by the Geodynamics Branch at the Goddard Space Flight Center (GSFC). The Goddard Earth Model-9 (GEM-9) (Reference 1) is a pre-Laser Dynamics Satellite (LAGEOS) model determined solely from observations of orbiting spacecraft and containing harmonic expansion terms up to the 30th degree and order. The geopotential model used at GSFC's Flight Dynamics Facility (FDF) for routine operational orbit determination of low Earth-orbiting spacecraft is the truncation of GEM-9 at 21st order and degree, referred to as GEM-9 (21 x 21). For TDRS orbit determination, the GEM-9 (8 x 8) model is used, since the higher-degree terms have been found to have a negligible effect for geosynchronous orbits. The GEM-10B model (Reference 2) is a 36-by-36 model based on spacecraft observations and surface gravimetry. The GEM-L2A model is a modification of the GEM-L2 model (Reference 3), a 30-by-30 "satellite only" model which, because of its extensive use of data from the LAGEOS spacecraft, is considered to be very accurate at long wavelengths. The GEM-L2A (8 x 8) model has been used for some of the TDRS-E orbit solutions in the studies reported in this paper. The Preliminary Goddard Solution-3117 (PGS-3117) model is a preliminary version of the model that has been published as GEM-T1 (Reference 4). GEM-T1 is a 36-by-36 "satellite only" model developed in support of the upcoming Topography Experiment (TOPEX) mission.

Section 2 of this paper describes the orbit determination methods utilized and the methods of evaluating geopotentials using orbit determination results. Section 3 discusses the results of the orbit determination studies, and Section 4 presents the conclusions.

2. METHODS OF ORBIT DETERMINATION AND GEOPOTENTIAL MODEL EVALUATION

The methods of orbit determination and geopotential model evaluation used in this study are described in Sections 2.1 and 2.2, respectively.

2.1 ORBIT DETERMINATION METHODOLOGY

The orbit determination methods used in this study are basically those used for operational orbit determination at GSFC. The batch weighted-least-squares algorithm implemented in the Goddard Trajectory Determination System (GTDS) (Reference 5) solves for the set of orbital elements and other parameters that minimizes the difference between observed and calculated values of selected tracking data over a solution arc. Estimated parameters include the spacecraft state at epoch and, optionally, one or more free parameters of the force model and/or the observation model. In GTDS, several different force models, as well as a selection of orbit propagators, numerical integrators, observation correction models, and dynamic observation editing options are available. The general options used for the studies described in this paper are summarized in Table 1.

The first step in orbit determination with GTDS is use of the Differential Correction (DC) Program to find the solution parameters at a designated epoch that best fit the tracking measurements using the batch weighted-least-squares method. The Ephemeris Generation (EPHEM) Program regenerates the ephemerides from the epoch solution. In this study, analysis is performed only with definitive ephemerides that are generated over the tracking data span.

To evaluate the orbit determination consistency achievable with a particular choice of options, a series of seven or eight daily 34-hour solutions is performed with 10-hour overlaps between successive arcs. The Ephemeris Comparison (COMPARE) Program is used to determine the maximum position differences between the definitive ephemerides for successive solutions in the 10-hour overlap time period. These six or seven overlap comparisons are a measure of the orbit determination consistency.

Table 1. Parameters and Options for User and Relay Spacecraft Orbit Determination

PARAMETER OR OPTION	VALUE OF PARAMETER OR OPTION CHOSEN	
	USER	TDRS
INTEGRATION TYPE	FIXED-STEP COWELL	FIXED-STEP COWELL
COORDINATE SYSTEM OF INTEGRATION	MEAN OF 1950.0	MEAN OF 1950.0
INTEGRATION STEP SIZE (SECONDS)	60.0	600.0
GEOPOTENTIAL MODELS	GEM-9 (21 x 21) GEM-10B (36 x 36) PGS-3117 (36 x 36)	GEM-9 (8 x 8) GEM-L2A (8 x 8)
ATMOSPHERIC DENSITY MODEL	HARRIS-PRIESTER (F = 75)	N/A
SOLAR AND LUNAR EPHEMERIDES	DE-118[a]	DE-118[a]
SOLAR REFLECTIVITY COEFFICIENT (C_R)	1.2	ESTIMATED
COEFFICIENT OF DRAG (C_D)	2.2	N/A
ESTIMATED PARAMETERS	STATE, DRAG SCALING PARAMETER (ρ_1)	STATE, SOLAR REFLECTIVITY COEFFICIENT (C_R)
DIFFERENTIAL CORRECTION (DC) CONVERGENCE PARAMETER	0.005	0.005
DC EDITING	3σ	3σ
IONOSPHERIC REFRACTION CORRECTION	YES (BENT MODEL)	YES (BENT MODEL)
TROPOSPHERIC REFRACTION CORRECTION	YES	YES
ANTENNA MOUNT CORRECTION	NO	NO
TRACKING DATA	TDRSS OR TDRSS + GSTDN	BRTS

[a] DE-118 INDICATES JET PROPULSION LABORATORY (JPL) DEVELOPMENT EPHEMERIS 118.

5038-17/3-88 [5-2]

When more than one set of orbit determination options is under study, the entire series is repeated with each of the different sets of options. In addition, the COMPARE Program may be used to obtain the maximum position difference between corresponding ephemerides from different series. These parallel comparisons measure the total effect of the difference between two sets of options on the trajectories determined in two series of solutions.

The detailed results presented in this paper are from studies in which TDRS orbits, predetermined using only BRTS data, were input and remained fixed during the user spacecraft solution process. An alternative mode of orbit determination would solve for both user and relay spacecraft variables simultaneously, allowing the TDRSS tracking observations of the user to directly influence both orbits. While the latter mode offers certain operational benefits when only a single user spacecraft is under study, in the current operational environment, more accurate TDRS orbits are obtained in isolation from the greater uncertainties of the orbit determination of low Earth-orbiting users. Some of the geopotential modeling studies reported in this paper have been repeated in the simultaneous orbit determination mode, with results that are essentially the same as far as geopotential model evaluation is concerned (References 6 and 7).

2.2 GEOPOTENTIAL MODEL EVALUATION METHODOLOGY

The gravitational field of the nonspherical Earth is modeled in GTDS using the standard expansion in spherical harmonic functions (Reference 5), truncated at a fixed maximum degree and order. Different geopotential models correspond to different values of the harmonic expansion coefficients. The standard operational version of GTDS is only capable of including 21 degrees and orders. A special version of GTDS, called GATFITR, which can utilize up to 36 degrees and orders, was used for this study. GATFITR enables the use of the GEM-10B, PGS-3117, and GEM-T1 gravitational models.

With the TDRS orbit predetermined, it is possible to use a different geopotential model for user orbit determination. This is also possible with GATFITR in the simultaneous orbit determination mode. User orbit determination studies of the 36-by-36 models were sometimes repeated with two versions of the pregenerated TDRS-E orbits; one set of TDRS-E orbits was generated with GEM-9 (8 x 8) and another was generated with GEM-L2A (8 x 8). It was found that the geopotential used for TDRS orbit determination did not significantly affect the evaluation of the user geopotential. All studies in which GEM-9 (21 x 21) was employed for the user spacecraft used TDRS-E orbits corresponding to GEM-9 (8 x 8).

For some of the time periods studied, orbit determination was performed using only TDRSS tracking data, while for other time periods both TDRSS and GSTDN data were used. The former case is characteristic of operational orbit determination in the near future, while the latter is characteristic of the present.

For one of the Earth Radiation Budget Satellite (ERBS) evaluation periods, high TDRSS tracking coverage permitted good quality orbit determination with subsets of the available data. In this case, the series of solutions was repeated with two different tracking data distribution subsets in addition to the full data complement. Parallel consistency of solutions generated for corresponding arcs for the different data distributions was evaluated. High consistency of this type, as well as overlap consistency, is desirable for an effective geopotential model for operational orbit determination. For a given arc, the better the overall modeling, the less the solution should depend on the particular data used for orbit determination.

As a general rule, weighted root-mean-square (RMS) residuals and similar measures of goodness of fit are of limited utility in analytical comparisons of orbit determination solution results, because the dynamic residual editing process eliminates the most discrepant data from the statistics. Considerations of such measures in References 6, 7, and 8 support the conclusions presented in this paper but are not discussed here.

3. RESULTS AND DISCUSSION

The spacecraft arcs studied in this analysis are described in Section 3.1. The results of the Landsat-5 study are presented in Section 3.2, and the results of the ERBS studies with full data and with data distribution subsets are given in Sections 3.3 and 3.4, respectively.

3.1 SPACECRAFT ARCS STUDIED

The TDRSS user spacecraft chosen for this study were ERBS and Landsat-5. Their orbital characteristics and those of the TDRS-E are shown in Table 2.

Three intervals of approximately 1-week duration were selected for study. Table 3 defines these time periods and describes that two-way tracking data used for orbit determination in each period. Landsat-5 was studied in only

Table 2. Characteristics of TDRS-E and the TDRSS User Spacecraft

SPACECRAFT	SEMIMAJOR AXIS (kilometers)	ECCENTRICITY	INCLINATION (degrees)	PERIGEE HEIGHT (kilometers)
ERBS	6981	0.000275	57.00	598
LANDSAT-5	7078	0.000105	97.98	687
TDRS-E	42,166	0.000222	0.98	35,779

5038-18/3-88 [5-2]

Table 3. Tracking Data Periods, Pass Frequency, and Data Acceptance Statistics

SPACECRAFT	TIMESPAN (GMT)	AVERAGE NUMBER OF PASSES PER DAY		AVERAGE NUMBER OF ACCEPTED OBSERVATIONS PER 34-HOUR ARC			
				TDRSS		GSTDN	
		TDRSS	GSTDN	RANGE	DOPPLER	RANGE	DOPPLER
LANDSAT-5	16 JUNE 1986 AT 0^h TO 23 JUNE 1986 AT 10^h	6.2	1.6	455	461	78	131
ERBS	12 AUGUST 1985 AT 0^h TO 19 AUGUST 1985 AT 10^h	6.9	2.2	1046	1073	67	76
ERBS	16 JUNE 1986 AT 0^h TO 23 JUNE 1986 AT 10^h	6.3	2.2	909	906	82	100
ERBS	11 JANUARY 1987 AT 0^h TO 19 JANUARY 1987 AT 10^h	7.5	–	1203	1164	–	–

5038-19/3-88 [5-2]

one of these intervals, and ERBS was studied in all three. The pass counts given in Table 3 include every pass that was not completely flagged as invalid at the tracking station. The observation counts include only the measurements surviving the differential correction (DC) dynamic residual editing in the baseline DCs using GEM-9 (21 x 21) for the user spacecraft. The studies are referred to by the acronyms LAND86, ERBS85, ERBS86, and ERBS87, in the order given in Table 3.

3.2 LANDSAT-5 RESULTS

Three series of orbit determinations were performed in the LAND86 study. The geopotential models applied to the user spacecraft were the GEM-9 (21 x 21) and GEM-10B (36 x 36) models. Solutions for the latter model were obtained using TDRS-E orbits pregenerated with the GEM-9 (8 x 8) model and also with the GEM-L2A (8 x 8) model. Figure 1 gives a plot of the overlap

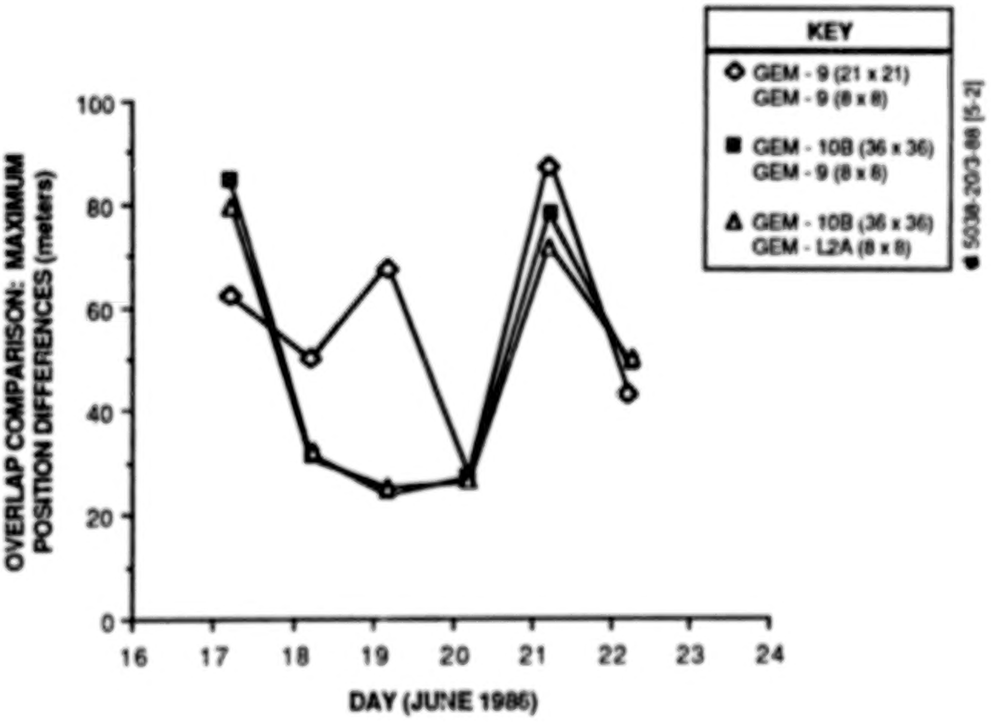

Figure 1. Maximum Overlap Comparisons for Landsat-5

comparisons as a function of the day in which the 10-hour overlap period occurs. Table 4 lists the respective means and standard deviations of these collections of six comparisons for all series. For LAND86, the improvement in the mean overlap comparison from using the GEM-10B geopotential model for Landsat-5 orbit determination is 7.2 ± 9.5 meters (mean and standard deviation in the mean of the differences between corresponding overlap comparisons). The differences between the user results obtained with the two different relay geopotential models are not significant.

Table 4. Statistical Summary of Overlap Comparisons for Series Using All Available Data

STUDY NAME	GEOPOTENTIAL MODELS		MAXIMUM OVERLAP COMPARISONS		
	USER	RELAY	NUMBER OF COMPARISONS	MEAN (METERS)	STANDARD DEVIATION (METERS)
LAND86	GEM-9 (21 x 21)	GEM-9 (8 x 8)	6	56.35	19.29
	GEM-10B (36 x 36)	GEM-9 (8 x 8)	6	49.17	24.17
	GEM-10B (36 x 36)	GEM-L2A (8 x 8)	6	47.51	22.08
ERBS85	GEM-9 (21 x 21)	GEM-9 (8 x 8)	6	21.24	10.30
	GEM-10B (36 x 36)	GEM-9 (8 x 8)	6	26.60	10.67
	GEM-10B (36 x 36)	GEM-L2A (8 x 8)	6	27.00	11.67
ERBS86	GEM-9 (21 x 21)	GEM-9 (8 x 8)	6	33.33	12.75
	GEM-10B (36 x 36)	GEM-9 (8 x 8)	6	24.20	11.62
	GEM-10B (36 x 36)	GEM-L2A (8 x 8)	6	23.79	12.06
ERBS87	GEM-9 (21 x 21)	GEM-9 (8 x 8)	6	47.82	6.13
	GEM-10B (36 x 36)	GEM-L2A (8 x 8)	6	29.34	10.62
	PGS-3117 (36 x 36)	GEM-L2A (8 x 8)	6	25.20	8.26
	PGS-3117 (36 x 36)	GEM-9 (8 x 8)	6	24.62	8.57
	GEM-9 (21 x 21)	GEM-9 (8 x 8)	7	46.77	6.23
	PGS-3117 (36 x 36)	GEM-9 (8 x 8)	7	22.64	8.72

5038-21/3-88 [5-2]

3.3 ERBS RESULTS WITH FULL DATA

For the ERBS85 and ERBS86 studies, the combinations of user and relay geopotential models for which series of solutions were obtained were the same as in the LAND86 study. The overlap comparisons from these series are plotted in Figure 2. The summary statistics of the overlap comparisons from each of these series are given in Table 4. The average improvements in overlap comparisons from using the GEM-10B (36 x 36) model instead of the GEM-9 (21 x 21) model are 9.1 ± 9.1 meters for ERBS86 and -5.4 ± 7.7 meters for ERBS85.

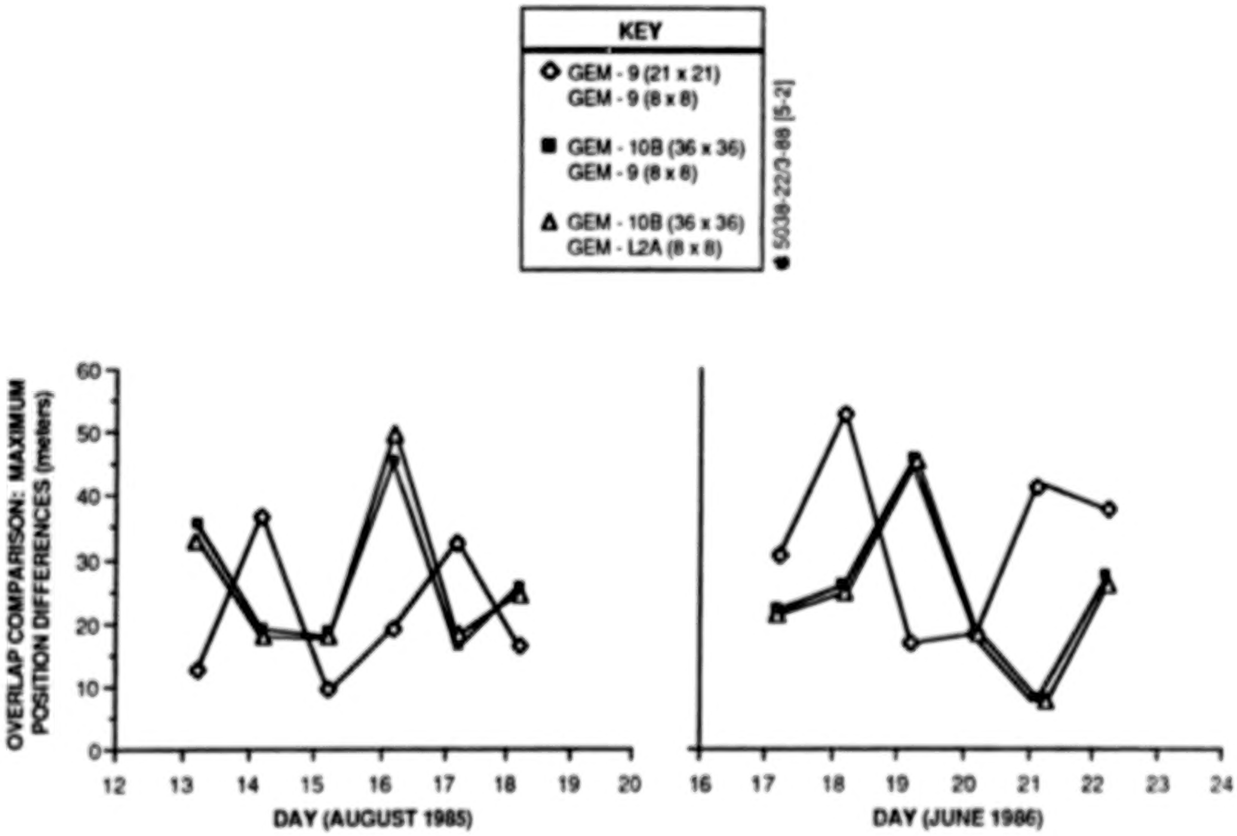

Figure 2. Maximum Overlap Comparisons for ERBS: ERBS85 and ERBS86 Studies

The combinations of user and relay geopotential models for which the ERBS87 orbit determination series were performed were given in Table 4 along with the overlap comparison summary statistics for the first 7 days of each series and for the full 8 days where applicable. Only the GEM-9 (21 x 21) and the PGS-3117 (36 x 36) user series that employ the GEM-9 (8 x 8) TDRS-E orbits were carried out for 8 days.

Figure 3 shows a plot of the overlap comparisons for these series. The differences between overlap comparisons obtained with different TDRS-E geopotential models is again insignificant. The average gain in consistency

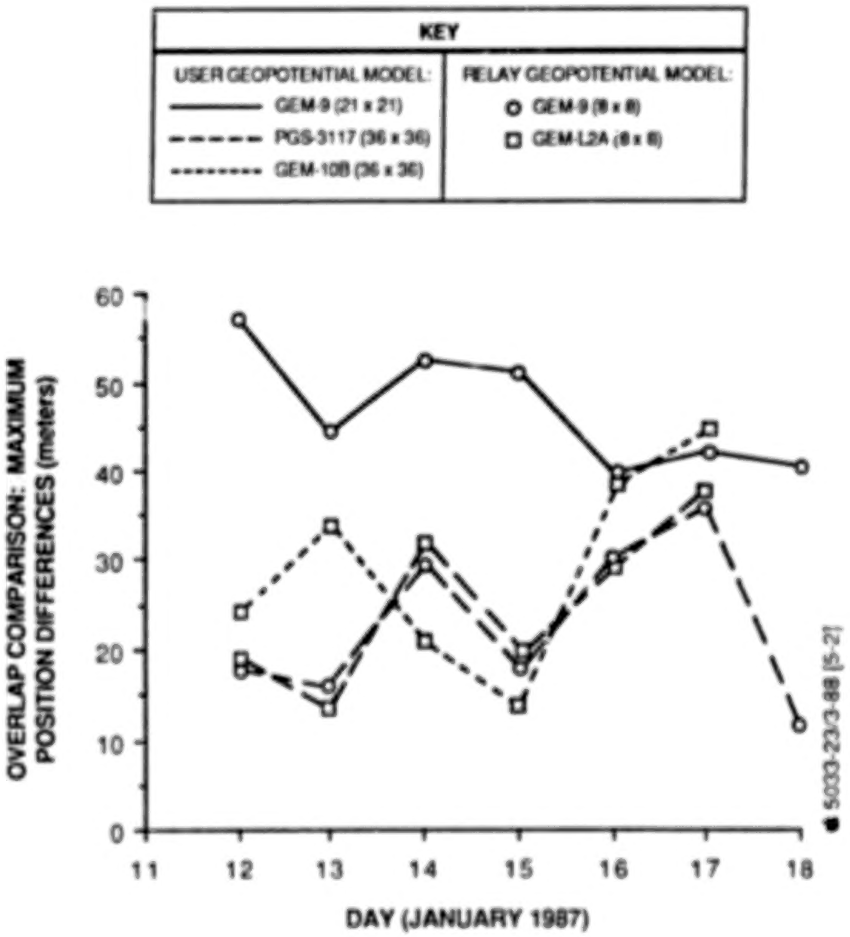

Figure 3. Maximum Overlap Comparisons for ERBS87

relative to GEM-9 (21 x 21) is 18.5 ± 7.1 meters for GEM-10B (36 x 36) and 22.6 ± 5.4 meters for PGS-3117 (36 x 36) [both calculated using six overlaps and the GEM-L2A (8 x 8) model for the TDRS-E orbits].

The improvements in consistency obtained from using the larger potential models in the ERBS87 study is more pronounced than in the other studies. The difference, if it is fair to compare results from different years, comes from degraded consistency of the GEM-9 (21 x 21) orbits (47.8 meters average) relative to the ERBS85 and ERBS86 studies (27.3 meters average), rather than from improved consistency of the orbits obtained with the 36-by-36 models. The degradation is rather consistent throughout the ERBS87 week, which suggests that it is not a random variation. A likely explanation is that the exclusion of GSTDN data in the ERBS87 solutions degrades the consistency of GEM-9 (21 x 21) orbit solutions more than it does the consistency of the PGS-3117 (36 x 36) and GEM-10B (36 x 36) solutions.

3.4 ERBS RESULTS WITH DATA DISTRIBUTION SUBSETS

The GEM-9 (21 x 21) and PGS-3117 (36 x 36) studies of ERBS87 were repeated with two other data distributions consisting of subsets of the available two-way TDRSS tracking data. For these additional studies, the TDRS-E orbits were estimated with the GEM-9 (8 x 8) model. The full data distribution, called dd1, is described in Table 3. Data distribution dd2, nominally a four-pass-per-day tracking schedule, was obtained by deleting approximately every other whole pass. Data distribution dd3 was obtained by shortening every individual tracking pass in dd1 to exactly 5 minutes of valid data (from an average of 20 minutes). The dd2 data distribution consisted of 3.7 passes per day, and the DC editing accepted an average of 57[illegible] range and 539 Doppler observations per 34-hour arc. The dd3 data distribution consisted of 7.5 passes per day, and the DC editing accepted an average of 314 range and 315 Doppler observations per 34-hour arc.

The overlap comparisons resulting from the six series using each of three data distributions with each of two geopotential models are plotted in Figure 4 and statistically summarized in Table 5. As expected from the previously described ERBS87 results, the consistency obtained with the PGS-3117 (36 x 36) model is better for all these data distributions than that obtained with the GEM-9 (21 x 21) model. Furthermore, consistency is more seriously degraded by restricting the tracking data coverage with GEM-9 (21 x 21) than with PGS-3117 (36 x 36).

Thirty-four-hour definitive parallel comparisons were performed between the ephemerides for corresponding arcs with different data distributions. Such comparisons quantify the sensitivity of orbit determination results to data selection variation. Both the dd2 and dd3 data distributions were compared with the dd1 distribution. The maximum position differences from these parallel comparisons are plotted in Figure 5 and are statistically summarized in Table 6. On 4 of the 8 days, orbits determined with the GEM-9 (21 x 21) model are markedly more sensitive to the difference between dd1 and dd2 data selections than those determined with the PGS-3117 (36 x 36) model. The results for data distribution dd3 do not strongly differentiate between the two geopotential models used.

4. CONCLUSIONS

The 36-by-36 Goddard geopotential models produced generally better orbit determination consistency for the user spacecraft than did the GEM-9 (21 x 21) model in three out of four studies. For the GEM-10B (36 x 36) model, the average gain in consistency for 18 ERBS overlap comparisons in three studies was 7.4 ± 5.0 meters, resulting in an average consistency of 26.7 meters. The average gain in consistency for the one Landsat-5 study was 7.2 ± 9.5 meters, resulting in an average consistency of 49.2 meters. The PGS-3117 (36 x 36) model, in the one ERBS study in which it was used, improved the consistency by an average of 22.6 ± 5.4 meters, to the 26-meter

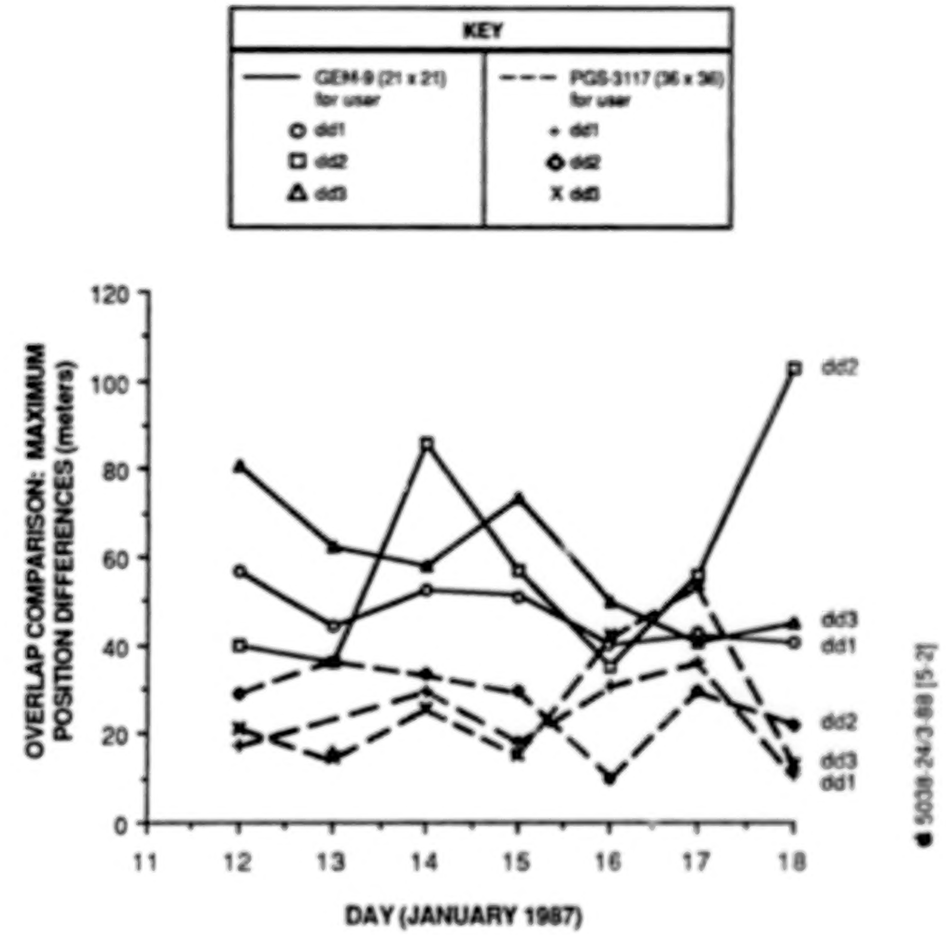

Figure 4. Maximum Overlap Comparisons for ERBS87 With Variable Data Distributions

Table 5. Summary Statistics for ERBS87 Overlap Comparisons With Variable Data Distributions

GEOPOTENTIAL MODEL	DATA DISTRIBUTION	OVERLAP COMPARISON: MAXIMUM POSITION DIFFERENCE (meters)			
		MEAN	STANDARD DEVIATION	MAXIMUM	MINIMUM
GEM-9 (21 x 21)	dd1	46.77	6.23	56.90	39.78
GEM-9 (21 x 21)	dd2	58.76	24.24	102.68	34.75
GEM-9 (21 x 21)	dd3	58.29	13.77	80.68	40.11
PGS-3117 (36 x 36)	dd1	22.64	8.72	36.20	10.77
PGS-3117 (36 x 36)	dd2	26.94	8.11	35.89	9.82
PGS-3117 (36 x 36)	dd3	26.42	14.41	53.55	13.05

5038-25/3-88 [5-2]

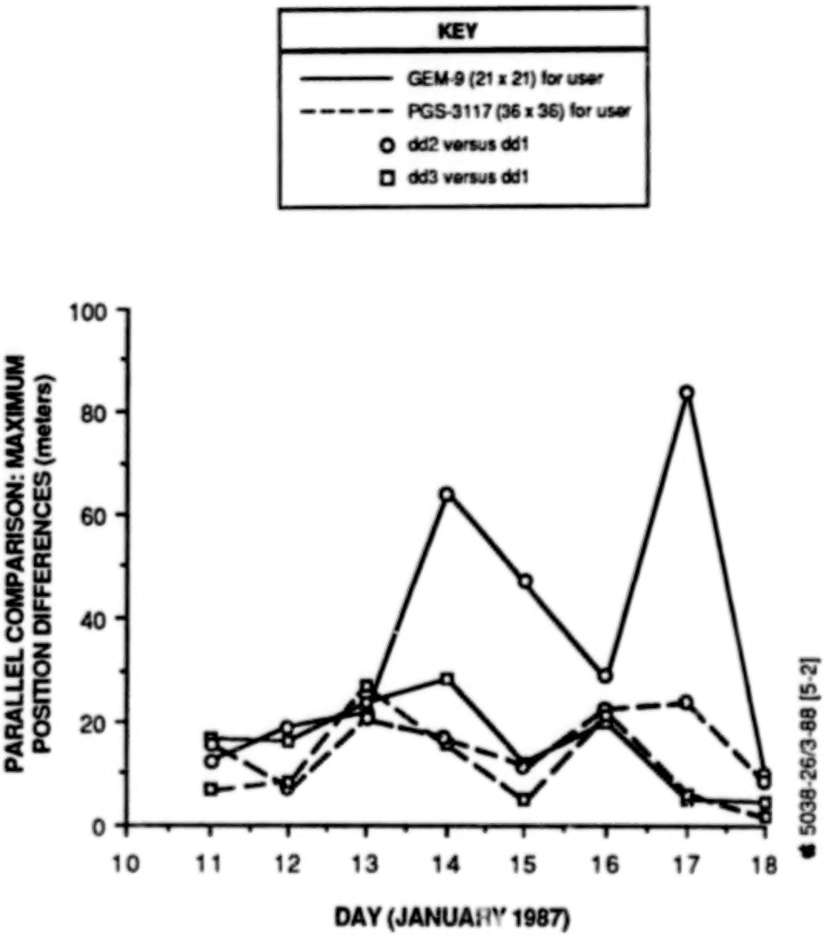

Figure 5. Parallel Comparisons Between ERBS87 Solutions With Different Data Distributions

Table 6. Summary Statistics for Parallel Comparisons Between ERBS87 Solutions With Different Data Distributions

GEOPOTENTIAL MODEL	DATA DISTRIBUTIONS COMPARED	PARALLEL COMPARISON: MAXIMUM POSITION DIFFERENCE (meters)			
		MEAN	STANDARD DEVIATION	MAXIMUM	MINIMUM
GEM-9 (21 x 21)	dd1 VERSUS dd2	35.88	25.06	84.11	9.78
GEM-9 (21 x 21)	dd1 VERSUS dd3	15.84	7.83	28.34	4.81
PGS-3117 (36 x 36)	dd1 VERSUS dd2	15.95	6.02	23.96	7.45
PGS-3117 (36 x 36)	dd1 VERSUS dd3	11.53	8.35	27.06	1.87

5038-27/3-88 [5-2]

level, performing slightly better than the GEM-10B (36 x 36) model (by 4.1 ± 4.5 meters in the average overlap comparison). There is, however, no clear indication of superiority of either of the 36-by-36 models studied over the other.

The overall average improvement in overlap comparison consistency, which is 7.4 ± 4.3 meters, can be considered significant. The ERBS87 study is the only one of the four in which the decrease in overlap comparisons, from GEM-9 (21 x 21) results to GEM-10B (36 x 36) or PGS-3117 (36 x 36) results, is consistent across the period of study. The results of the ERBS87 study alone demonstrate that, if it is required to achieve and maintain orbit determination consistency better than 40 meters, GEM-9 (21 x 21) must be improved upon and that GEM-10B (36 x 36) and/or PGS-3117 (36 x 36) can support such requirements.

The superiority of the 36-by-36 gravity models becomes more evident as the data complement becomes more restricted. The experiments with data distribution show that the overall consistency obtained with the PGS-3117 (36 x 36) model degrades less rapidly with tracking coverage than does that obtained with the GEM-9 (21 x 21) model. Furthermore, it is a reasonable conjecture that the decrease in consistency of GEM-9 (21 x 21) solutions in the ERBS87 study relative to the ERBS85 and ERBS86 studies, which leaves the other gravity models clearly superior, is due to the exclusion of GSTDN data.

Varying the tracking coverage appears to be an effective means of evaluating gravity models for operational orbit determination. The superiority of the PGS-3117 (36 x 36) model over the GEM-9 (21 x 21) model, shown in the overlap comparisons in the ERBS87 study (with full data), is strongly confirmed by the superior consistency that was observed with respect to deletion of tracking passes. This technique may also prove useful for comparative evaluation of other variations in orbit determination techniques.

REFERENCES

1. Goddard Space Flight Center, X-921-77-246, Gravity Model Improvement Using GEOS-3, F. J. Lerch, S. M. Klosko, R. E. Laubscher, and C. A. Wagner, 1977

2. Lerch, F. J., B. H. Putney, C. A. Wagner, and S. M. Klosko, "Goddard Earth Models for Oceanographic Applications (GEM 10B and 10C)," Marine Geodesy, Vol.5, No.2, pp. 145-187, 1981

3. Lerch, F. J., S. M. Klosko, and G. B. Patel, "Gravity Model Developmen From Lageos," Geophysical Research Letters, Vol. 9, No. 11, pp. 1263-1266, 1982

4. National Aeronautics and Space Administration, Technical Memorandum 4019, An Improved Model of the Earth's Gravitational Field: GEM-T1, J. G. March et al., July 1987

5. Goddard Space Flight Center, X-582-76-77, Mathematical Theory of the Goddard Trajectory Determination System, A. J. Fuchs, C. E. Velez, and J. O. Cappellari, Jr. (editors), April 1976

6. Computer Sciences Corporation, CSC/TM-86/6723, Analysis of Operational Orbit Determination Techniques, M. Radomski and B. Davis, December 1986

7. Computer Sciences Corporation, CSC/TM-87/6710, Analysis Report 87001, Operational Orbit Techniques Compendium of Analysis Reports: Dual Geopotential Model for Relay and Target Spacecraft in the Goddard Trajectory Determination System (GTDS) Environment, B. Davis and M. Radomski, June 1987

8. Computer Sciences Corporation, CSC/TM-87/6710, Analysis Report 87003, Operational Orbit Techniques Compendium of Analysis Reports: Effects of Simultaneous Variation of Tracking Schedules and Geopotential Models on TDRSS User Orbit Determination, B. Davis and M. Radomski, October 1987

NASA
National Aeronautics and Space Administration

Report Documentation Page

1. Report No. NASA CP-3011

2. Government Accession No.

3. Recipient's Catalog No.

4. Title and Subtitle
Flight Mechanics/Estimation Theory Symposium - 1988

5. Report Date SEPTEMBER 1988

6. Performing Organization Code

7. Author(s)
Thomas Stengle (Editor)

8. Performing Organization Report No. 88B0224

9. Performing Organization Name and Address
Flight Dynamics Division
Goddard Space Flight Center
Greenbelt, Maryland 20771

10. Work Unit No.

11. Contract or Grant No.

12. Sponsoring Agency Name and Address
National Aeronautics and Space Administration
Washington, D.C. 20546-0001

13. Type of Report and Period Covered Conference Publication

14. Sponsoring Agency Code

15. Supplementary Notes

16. Abstract

This conference publication includes 28 papers and abstracts presented at the Flight Mechanics/Estimation Theory Symposium on May 10-11, 1988. Sponsored by the Flight Dynamics Division of Goddard Space Flight Center, this symposium features technical papers on a wide range of issue related to orbit-attitude prediction, determination and control; attitude sensor calibration; attitude determination error analysis; attitude dynamics; and orbit decay and maneuver strategy. Government, industry, and the academic community participated in the preparation and presentation of these papers.

17. Key Words (Suggested by Author(s))
Flight Mechanics, Spacecraft Dynamics, Estimation Theory, Orbit Determination, Attitude Determination, Mission Analysis

18. Distribution Statement
Unclassified-Unlimited

Subject Category 13

19. Security Classif. (of this report) Unclassified

20. Security Classif. (of this page) Unclassified

21. No. of pages 620

22. Price A99

NASA FORM 1626 OCT 86

NASA-Langley, 1988

END

DATE

FILMED

APR 12 1989